FINAL TECHNICAL REPORT FOR

OFFICE OF NAVAL RESEARCH

O.N.R. YOUNG INVESTIGATOR PROGRAM

GRANT NO. N00014-96-1-0691

Development of Testing Methodologies for Nonlinear Solid State Actuation Materials

and incorporated project

Performance Models for Underwater Transducers Incorporating Nonlinear Active Materials

Grant Period: May 1, 1996 to Sept. 30, 2001

PRINCIPAL INVESTIGATOR

Dr. Nesbitt W. Hagood, IV
nwh@ContinuumPhotonics.com
(978) 670-4910

Department of Aeronautics and Astronautics
Massachusetts Institute of Technology
Cambridge, MA 02139

DISTRIBUTION STATEMENT A
Approved for Public Release
Distribution Unlimited

BEST AVAILABLE COPY
20030805 088

"Development of Testing Methodologies for Nonlinear Solid State Actuation Materials"
and
"Performance Models for Underwater Transducers Incorporating Nonlinear Active Materials"

Abstract

A derivation is presented and demonstrated for finding actuation efficiency and work output for electromechanically fully coupled, non-linear systems working against generalized quasi-static loads. A component testing facility with programmable impedance and closed-loop capability was designed, built, and operated to measure work output and actuation efficiency of a discrete actuator working against both linear and non-linear loads. The complete design of the testing facility is presented with an overview of the rationale behind its design decisions. Increases in the mechanical work output of the actuator were found to be possible by using non-linear loads instead of linear loads. Theory and formulation are presented, suitable for modeling and performance analysis of actuator and sensor devices composed of deformable, electromechanically coupled, highly insulating materials with non-linear response functions. The testing facility was renovated and used for feed-forward open-loop test methodology utilizing a Force-Voltage model developed from Ritz Formulation. Linear tests correlated well with theoretical prediction. Results show actuation efficiency of a non-linear system is about 200% that of a linear system, and its work output is about 245% that of the linear system. Research is recommended on behavior and performance of active materials and actuation efficiency of piezoelectrically-driven systems under dynamic loads.

A Collection of 3 ResearchTheses
Supervised by Dr. Nesbitt W. Hagood, IV
O.N.R. Young Investigator Program
Grant No. N00014-96-1-0691

"Actuation Efficiency and Work Flow in Piezoelectrically Driven Linear and Non-linear Systems", by Yong Shi,132 p., June 2001.

"Analysis of Nonlinear Electroelastic Continua with Electric Conduction", by John E. Harper, 137 p., June 1999.

"Study of Work Flow in Piezoelectrically Driven Linear and Non-linear Systems," by Malinda K. Lutz, 160 p., June 1999.

BEST AVAILABLE COPY

Actuation Efficiency and Work Flow in piezoelectrically Driven Linear and Non-linear Systems

by

Yong Shi

B. Eng., National University of Defense Technology, P. R. China (1985)

Submitted to the Department of Aeronautics and Astronautics
in partial fulfillment of the requirements for the degree of

Master of Science

at the

MASSACHUSETTS INSTITUTE OF TECHNOLOGY

June 2001

© Massachusetts Institute of Technology 2001. All rights reserved.

The author hereby grants to MASSACHUSETTS INSTITUTE OF TECHNOLOGY
permission to reproduce and
to distribute copies of this thesis document in whole or in part.

Signature of Author .....
Department of Aeronautics and Astronautics
2 May 2001

Certified by .....
Nesbitt W. Hagood, IV
Associate Professor, Thesis Supervisor
Thesis Supervisor

Accepted by .....
Wallace E. Vander Velde
Professor of Aeronautics and Astronautics
Chair, Committee on Graduate Students

MASSACHUSETTS INSTITUTE OF TECHNOLOGY
SEP 11 2001
LIBRARIES

AERO

BEST AVAILABLE COPY

Actuation Efficiency and Work Flow in piezoelectrically Driven Linear and Non-linear Systems

by

Yong Shi

Submitted to the Department of Aeronautics and Astronautics
on 2 Feb. 2001, in partial fulfillment of the
requirements for the degree of
Master of Science

Abstract

It is generally believed that the maximum actuation efficiency of piezoelectrically driven systems is a quarter of the material coupling coefficient squared. This maximum value is reached when the stiffness ratio of structure and piezo stack equals to one. However, previous study indicts that load coupling has significant influence on the work flow and actuation efficiency in the systems. Theoretical coupled analysis of such systems has shown that the actuation efficiency is the highest at the stiffness ratio larger than one and this maximum value is much higher than that predicted by the uncoupled analysis when coupling coefficient is relatively high. Moreover, for non-linear systems, the actuation efficiency can be twice as high as that of linear systems. The objectives of this research is to verify the theoretical coupled analysis experimentally and explore the possibility for the mechanical work to be done into the environment. To do this, a testing facility has been designed and built with programmable impedances and closed loop test capability. However, the feedback control method is not fast enough in determining the voltage for the driving stack which has limited the test frequency. Meanwhile, the original mechanical design can not guarantee the accurate measurement of mechanical work. Renovation on the existing tester has been made and feed forward open loop test methodology has been used utilizing a Force-Voltage model developed from Ritz Formulation. Linear test results correlate very well with the theoretical prediction. Two non-linear functions have been chosen for non-linear tests. The results have shown that the actuation efficiency of non-linear systems is much higher than that of linear systems. The actuation efficiency of system simulated by non-linear function 1 is about 200% that of linear systems and the work output of this system is about 254% that of the linear systems. These test results exactly proved out the theoretical prediction of non-linear loading systems. The capability of modeling and testing of non-conservative thermodynamic cycles have also been demonstrated which make it possible to take advantage of the mechanical work out of the systems.

Thesis Supervisor: Nesbitt W. Hagood, IV
Title: Associate Professor, Thesis Supervisor

Acknowledgements

It is with heartfelt gratitude that I dedicate this thesis to all those who have played a role in the successful completion of my research. I would like to thank Ching-Yu Lin, David Roberson, Mauro Atlalla, Chris Dunn, Viresh Wickramasinghe, Timothy Glenn as well as all my lab-mates and roommates who are always ready to help me in every expect from the tester design, test setup, data acquisition and handling, signal analysis and the using of different equipment or instrument and software in the lab, just to mention a few. Their sincere helps make my research a lot easier and my working at AMSL a wonderful memory.

I am also very grateful to my Chinese friends here and I would also like to thank my family–my parents, my wife, my brother and sisters. I am very grateful to my parents who love me and worry about me all the time. My special thanks go to my wife Zhihong. It is her love which actually makes all this becoming true. I still remember all the sufferings in the past two years, the pain from legs and the pain from research. She is always standing by my side taking care of me and encouraging me. There is no word which could express my love and thanks to her. I would also like to dedicate this thesis to my son-Caleb who will come to this word very soon.

Funding for this research was provided by the Office of Naval Research (ONR) Young Investigator's Program. under contract N00014-1-0691, and monitored by Wallace Smith.

Nomenclature

α	Stiffness ratio, load stiffness divided by material stiffnes
A	Cross-sectional area of the material
A_{p1}	Cross-sectional area of the piezoelectric material, or the sample stack
A_{p2}	Cross-sectional area of the driving stack
A_s	Cross-sectional area of the structure
C_{p1}^S	Capacitance of the system under constant strain
c_{33}^E	Young's modulus of the active material in the "three-three" direction under constant electric field
c_0	Linear part of the Young's modulus of non-linear loads
c_s	Young's modulus of the structure
c_x	Non-linear part of the Young's modulus of non-linear loads
δ	Variation operator
d	Derivative operator
D_3	Electric displacement in the active material in the "three" direction
d_{33}	Electromechanical coupling term of the active material in the "three-three" direction
ε_0	Dielectric constant of free space
ε_{33}^S	Dielectric constant of the active material in the "three-three" direction under constant strain
ε_{33}^T	Dielectric constant of the active material in the "three-three" direction under constant stress

E_3	Electric field in the active material in the "three" direction
e_t	Electromechanical coupling of active materials
e_{33}	Electromechanical coupling of active materials in the "three-three" direction
f_1	Generalized force vector of the active material of the sample stack
f_2	Generalized force vector of the driving stack
F_{bl}	Blocked the force of the active material
F_{linear}	Blocked the force of the active material
F_{linear}	Linear Load
$F_{non-linear1}$	Non-linear load 1
$F_{non-linear2}$	Non-linear load 2
f_s	Generalized force vector of the structure
K_{p1}^E	Stiffness of the active material under constant electric field
k_s	Stiffness of the structure
k_{33}	Material coupling coefficient of the active material
l	Length of material or structure
l_{p1}	Length of active material
l_s	Length of structure
η	Actuation efficiency of systems
$\eta_{\max}$	Maximum actuation efficiency of systems
N	Number of layers in piezoelectric stack
θ_1	Electromechanical coupling of the active material
θ_2	Electromechanical coupling of the driving stack
Q_1	Charge vector of the active material
Q_2	Charge vector of the driving stack
S_3	Strain in "three" direction of the active material
s_{33}^E	Elastic constant of the active material in the "three-three" direction under constant electric field

s_{33}^D	Elastic constant of the active material in the "three-three" direction at open circuit
T_3	Elastic constant of the active material in the "three-three" direction at open circuit
t_l	Thickness of the stack layers
V_0	Initial voltage to the sample stack
V_1	Voltage applied to the active material or the sample stack during testing
V_2	Voltage applied to the driving stack
V_f	Final voltage to the sample stack
$V_{\max}$	Maximum voltage applied during tests
V_{p1}	Volume of the active material or the sample stack
W_E	Electric Work
W_M	Mechanical work
W_{in}	Work into the system
W_{out}	Work out of the system
x_0	Initial displacement
x	Displacement of the system
x_1	Displacement of the active materials
x_2	Displacement of the driving stack
x_{free} or x_f	Free displacement of the system
Ψ_E	Electric mode shape
Ψ_M	Mechanical mode shape

Contents

1 Introduction **16**

1.1 Motivation 16

1.2 Objective 17

1.3 Previous Work 17

1.3.1 Material Coupling Coefficient. 17

1.3.2 Berlincount's Work 18

1.3.3 Lesieutre and Davis' Work 18

1.3.4 Spangler and Hall's Work 19

1.3.5 Giurgiutiu's Work 20

1.3.6 C. L. Davis' Work 21

1.3.7 M. Mitrovic's Work 21

1.3.8 Lutz and Hagood's Work 22

1.4 Approach 23

1.5 Organization of the Document 24

2 Analysis of the Work Flow and Actuation Efficiency of Electromechanically Coupled Systems **26**

2.1 Definition of Work Terms 27

2.1.1 Mechanical Work 28

2.1.2 Electrical Work 28

2.1.3 Actuation Efficiency 28

2.2 Linear and Non-linear Systems 29

2.3 General Analysis 30
2.3.1 Linear Constitutive Equations 31
2.3.2 Governing Equations for the coupled systems 31
2.3.3 Compatibility and Equilibrium 32
2.3.4 Electrical Work 32
2.3.5 Mechanical Work 33
2.3.6 Actuation Efficiency 33
2.4 One Dimensional Linear Systems 34
2.4.1 Expressions for Linear Systems 34
2.4.2 Constitutive Equations 34
2.4.3 Finding the Constants in Work Expressions 35
2.4.4 Simplified Expressions for Electrical and Mechanical Work 36
2.4.5 Actuation Efficiency 37
2.4.6 Discussion on Actuation Efficiency 37
2.5 One dimensional Non-linear Systems 38
2.5.1 General Analysis 38
2.5.2 Mechanical and electrical Work in terms of Displacement 39
2.5.3 Simplified Expressions for Mechanical and Electrical Work 40
2.5.4 Actuation Efficiency 41
2.6 Comparison of Linear and Non-linear Systems 41
2.7 Summary 43

3 Renovation on the Existing Component Testing Facility 44
3.1 The existing Component Tester 44
3.1.1 Design Requirements 44
3.1.2 Main Features of the Component Tester 45
3.2 Previous Test Results 46
3.2.1 Material Properties Measurement 46
3.2.2 Linear Test Results 47
3.2.3 Nonlinear Test Results 49
3.3 Analysis of the Problems 49

3.3.1 Electrical Work Measurement 50
3.3.2 Mechanical Work Measurement 51
3.4 Re-design of the Load Transfer Device 56
3.4.1 Initial design 56
3.4.2 Vibration Measurement and Improvement on the Design 56
3.5 Validation of the New Design 60
3.5.1 Stiffness Measurement 60
3.5.2 Capacitance Measurement 65
3.6 Summary 66

4 One Dimensional Linear and Non-linear Tests 68
4.1 FeedBack Test Approach 68
4.2 FeedForward Test Approach 71
4.3 Material Properties of Test sample 71
4.3.1 Test Sample Physical Parameters 71
4.3.2 Stiffness and Elastic Constants 73
4.3.3 Capacitance and Dielectric Constant 73
4.3.4 Electromechanical Coupling Term 78
4.3.5 Material Coupling Coefficient 79
4.3.6 Material Properties Summary 79
4.4 Actuating Voltage for Test Sample 80
4.4.1 Linear and non-linear Functions 80
4.4.2 Actuating Voltage for Sumitomo Stack 81
4.5 Voltage-Force Model 83
4.5.1 Model Development 84
4.5.2 Experimental Determination of model coefficients 86
4.6 Theoretical Predictions for systems driven by Sumitomo Stack 86
4.7 Linear Tests 88
4.8 Non-linear Tests 91
4.8.1 Non-linear system 1 96
4.8.2 Non-linear system 2 101

4.9 Comparison and Discussion 106
4.10 Summary 107

5 Non-Conservative Systems **108**
5.1 Net Work in Conservative Systems 108
5.2 Non-Conservative System and Its Efficiency 108
5.2.1 Non-Conservative Cycles 108
5.2.2 Efficiency 110
5.3 Experimental Demonstration 110
5.3.1 Simulation Methods 110
5.3.2 Test Results 110
5.4 Summary 115

6 Conclusions and Recommendations for Future Work **117**
6.1 Conclusions on the Linear and the Non-linear Tests 117
6.2 Conclusions on Non-Conservative Systems 118
6.3 Recommendation for Future Work 119

A Component Testing Facility Drawings **123**

List of Figures

2-1 Piezoelectrically Driven One Dimensional Model 27

2-2 Material and Structure Loading Line for the Linear Systems 29

2-3 Comparison of Linear and Non-linear Functions 30

2-4 Comparison of Actuation Efficiency of Linear Systems with Different k_{33} 38

2-5 Max. Actuation Efficiency vs. k_{33} for 1D Linear Systems 39

2-6 Comparison of Electrical and Mechanical Work for 1D Systems 42

2-7 Comparison of Actuation Efficiency for 1D systems 42

3-1 The Original Component Testing Facility 45

3-2 Determination of k_{33} for Sumitomo Stack 47

3-3 Mechanical Work vs. Stiffness Ratio α for Linear Systems 48

3-4 Electrical Work vs. Stiffness Ratio α for Linear Systems 48

3-5 Actuation Efficiency vs. Stiffness Ratio α for Linear Systems 49

3-6 Comparison of Actuation Efficiency for Linear and Non-linear Systems 50

3-7 Time Trace of from Previous Test 51

3-8 Stiffness of PETI-1 vs. Applied Preload 53

3-9 The Original Alignment Mechanism 53

3-10 Stiffness of the Alignment Mechanism vs.Preload 54

3-11 The Original Cage System for Load Transfer and Protection 55

3-12 New Design of the Load Transfer System 57

3-13 Transfer Function of the Transverse Velocity of Test Sample to the Input to Drive 57

3-14 Transverse Vibraton of Test Sample at Time 1 58

3-15 Transverse Vibration at Time 2 58

3-16 Transverse Vibration at Time 3 59
3-17 Transverse Vibration at Time 4 59
3-18 Transverse Vibration at Time 5 59
3-19 Transverse Vibration at Time 6 59
3-20 Improvement on the New Design by Providing Springs for Preload 60
3-21 New Design of the Load Transfer Systems1 61
3-22 New Design of the Load Transfer System 2 61
3-23 Overall View of the New Tester 62
3-24 Force Calibration for the New Design 63
3-25 Comparison of Displacement measured by Two MTI Probes 64
3-26 Comparison of Displacement Measured by MTI Probes and Strain Gages 64
3-27 Stiffness Measured from MTI probes and Strain Gages 65
3-28 Capacitance Measurement for Standard Capacitor 66

4-1 Time Trace for Linear Test at 0.05 Hz, Assumed Stiffness 3000 lbs/in 69
4-2 Time Trace for Linear Test at 1 Hz, Assumed Stiffness 3000 lbs/in 70
4-3 Time Trace for Linear Test at 10 Hz, Assumed stiffness 3000 lbs/in 70
4-4 Feedforward open loop test approach 72
4-5 Time Trace of Displacement and Force for Stack Stiffness Measurement 75
4-6 Force vs. Displacement for Stack Stiffness Measurement 75
4-7 Time Trace of Current and Voltage for Capacitance Measurement 76
4-8 Charge vs. Volatge for Capacitance Measurement 77
4-9 Time Trace of Displacement and Voltage for Stack d_{33} Measurement 78
4-10 Displacement vs. Voltage for Stack d_{33} Measurement 79
4-11 Linear and Non-linear Functions in terms of Displacement of the Actuator 81
4-12 Voltage vs. Displacement from Coupled Analysis 83
4-13 Three Component System for Voltage-Force Model 84
4-14 Force vs. Voltage V1 for Voltage-Force Model 87
4-15 Force vs. Voltage V1 and V2 for Voltage-Force Model 87
4-16 Prediction of Mechanical Work for Systems Driven by Sumitomom Satck 88
4-17 Prediction of Electrical Work for Systems Driven by Sumitomo Satck 89

4-18 Prediction of Actuation Efficiency for Systems Driven by Sumitomo Satck 89
4-19 Typical Displacement Measurement for Linear Tests 91
4-20 Typical Force Measurement for Linear Tests 92
4-21 Typical Current and Voltage Measurement for Linear Tests 92
4-22 The Resentative Cycle for Computing Work Terms 93
4-23 Typical Effective Stiffness Determined from Actaul Data 93
4-24 Typical Mechanical Work from Theory and Experiment for Linear Test 94
4-25 Typical Electrical Work from Theory and Experiment for Linear Tests 94
4-26 Actuation Efficiency as a Function of Stiffness Rato Ks/K_{33}^{E} for Linear Tests . . 95
4-27 Predicted Displacement and Force for Non-linear Test 1 96
4-28 Predicted Voltage to the Driving Stack for Non-linear Test 1 97
4-29 Measured Displacement of Sample for Non-linear System 1 97
4-30 Measured Force in the System for Non-linear System 1 98
4-31 Measured Volatge and Current for Non-linear Test 1 98
4-32 Representative Cycle for Work terms for Non-linear 1 99
4-33 Simulated Force vs. Displacement for Non-linear1 99
4-34 Mechanical Work out Comparison for Non-linear System 1 100
4-35 Electrical Work in Comparison for Non-linear System 1 100
4-36 Predicted Force and Displacement for Non-linear 2 101
4-37 Computed Voltage to Driving Stack for Non-liner 2 102
4-38 Measured Displacement of Sample for Non-linear System 2 102
4-39 Measured Force in the system for Non-linear System 2 103
4-40 Measured Current and Voltage for Non-linear System 2 103
4-41 Representative Cycle for determining Work Terms for non-linear 2 104
4-42 Simulated Force vs. Displacement for Non-linear System 2 104
4-43 Mechanical Work out Comparison for Non-linear system 2 105
4-44 Electrical Work in Comparison for Non-linear system 2 105
4-45 Comparison of Mechanical Work for Linear and Non-linear Systems 106
4-46 Comparison of Electrical Work for Linear and Non-linear Systems 107

5-1 Comparison of non-linear function 1 with a Non-conservative Cycle 109

5-2 Different Non-Conservative Thermodynamic Cycles 109
5-3 Voltage to the Sample and Driving Stacks 111
5-4 Displacement Measurement for a Non-Conservative Cycle 111
5-5 Force Measurement for a Non-Conservative Cycle 112
5-6 Current and Voltage Measurement for a Non-Conservative Cycle 112
5-7 Representative Cycle for Determining Work and Efficiency 113
5-8 Comparison of the Non-Conservative Cycle 1 and the Actually Simulated Cycle 113
5-9 Net Mechanical Work Done by a Non-Conservative Cycle 114
5-10 Net Electrical Work into a Non-Conservative Cycle 114
5-11 Mechanical work and electric work vs. Sstress on the sample stack 115
5-12 Efficiency of non-conservative cycles vs. stress on the sample stack 116

A-1 Assembly Drawing of the Renovated Component Tester 124
A-2 Adaptor 2 Drawing 125
A-3 Adaptor 6 Drawing 126
A-4 Adaptor 7 Drawing 127
A-5 Adaptor 9 Drawing 128
A-6 Linear Bearing Mounting Plate Drwaing 129
A-7 Adaptor 3 Drawing 130
A-8 Adaptor 4 Drawing 131
A-9 Adaptor 5 Drawing 132

List of Tables

3.1 Driving Stack Parameters 46

3.2 Sumitomo Stack Parameters 47

3.3 Al Bar Stiffness Measurement 52

4.1 Sumitomo Stack Physical Parameters 72

4.2 Sumitomo Measured Stiffness at open Circuit, ... 74

4.3 Sumitomo Stack Measured Compliance st Open Circuit 74

4.4 Sumitomo Stack Measured Stiffness at Short Circuit 74

4.5 Sumitomo Stack Measured Compliance at Short Ciucuit 74

4.6 Measured Capacitance and Dielectric Constant for Sumitomo Stack 77

4.7 The Measured Material Properties for Sumitomo Stack 80

4.8 Comparison of Actuation Efficiency for Linear and Non-linear Systems 106

Chapter 1

Introduction

1.1 Motivation

Recently piezoelectric actuators have been extensively used for different applications, such as, precise positioning[Karl, 2000] and [Roberts, 1999], vibration suppression[Hagood, 1991] and [Binghamand, 1999], and ultrasonic motors [Bar-Cohen, 1999] and [Frank, 1999, spie]. Moreover, their special characteristics have also made them popular in micro-systems as well as in optical device applications [Varadan, 2000, spie]. However, to use these actuators efficiently, it is necessary to evaluate and understand the material response, energy flow and actuation efficiency in the system at working conditions.

Piezoelectric materials have been initially developed for sensors applications initially which focus on low power properties. For example, the linear material model is valid for low electric field. These properties are not appropriate for the applications of actuators which are used at high frequency, high electric field, and high mechanical loads. Furthermore, standard assumptions about the efficiency of piezoelectrically driven systems neglect the electromechanical coupling in the system. These pending problems also necessitate the study of work flow and actuation efficiency in such systems.

1.2 Objective

The objective of this research is to closely examine the work input, work output and actuation efficiency in a fully coupled system. Different expressions such as material coupling coefficient, device coupling coefficient, and efficiency of coupling elements have been used traditionally to describe the systems. Actuation efficiency, which is a thermodynamic efficiency expression defined by the ratio of mechanical work out and electrical work in, may best describe coupled systems.

Previous theoretical analysis [Malindal, 1999] has shown that the actuation efficiency of one dimensional linear systems reaches the highest when the stiffness ratio of the structure and the active material is larger than one. This peak value of actuation efficiency is much higher than the prediction of the coupling element efficiency of Hall [Hall, 1996]when the coupling coefficient is relatively high. However, for active materials working against non-linear loads, it is possible to significantly increase the actuation efficiency in the systems. So another objective of this research is to validate the theoretical derivation and verify the analysis results experimentally, then to explore the possibility for the mechanical work out of the system to be done to the environment.

1.3 Previous Work

1.3.1 Material Coupling Coefficient.

Much work has been done in the area of material characterization of actuators and the efficiency analysis of the systems. However, people tend to use different expressions to describe and compare the efficiency of systems according to their specific application and interests. Material coupling coefficient has long been regarded as a measure of the capability of active materials transduce mechanical work to electrical work and vice versa. Material coupling coefficient k_{33} is defined as [IEEE,1978]

$$k_{33}^2 = \frac{W_{out}}{W_{in}} = \frac{d_{33}^2}{s_{33}^E \varepsilon_{33}^T} \tag{1.1}$$

However, material coupling coefficient only describes the interaction of the mechanical and electrical states in the active materials itself. The conditions under which the material cou-

pling coefficient is derived are idealized work conditions. The interaction or coupling between the active materials and the structures, which are driven by the interrelation of force and displacement as well as that of charge and voltage, have all been neglected. Materials coupling coefficient itself is not an accurate measure of actuation efficiency of systems.

1.3.2 Berlincount's Work

Berlincourt [Berlincount, 1971] found out that boundary conditions, times and orders at which mechanical load and electrical load were applied could also change the efficiency of the systems. He defined an effective coupling factor after he studied the differences in efficiency of a few different cycles. By using these different loading cycles, he changed the amount of energy extracted from the systems. For example, he claimed that one of the loading cycles increased the effective coupling factor of PZT-4 to 0.81 while the material coupling coefficient of this material is only 0.70. He also showed the influence of boundary conditions on efficiency. The effective coupling factor of a thin disk with clamped edges was increased to 0.68 compared to the material coupling coefficient of 0.50. He then examined the efficiency of the systems under ideal linear or non-linear loads assuming one-time energy conversion, which was associated with polarization or depolarization of active materials. The mechanical work of the systems using such non-linear loads doubled that using linear loads. However, the effective coupling factor Berlincourt defined still focused on the information obtained from the material coupling coefficient, and it did not include the information of the structures that the active materials worked against. The study of the one-time conversion process considered the dependence on the structures which the active materials worked against, but the complete depolarization of the active materials assumed made it difficult to apply this theory to real cyclic operation.

1.3.3 Lesieutre and Davis' Work

Lesieutre and Davis [Lesieutre, 1997]defined a device coupling coefficient when they studied the changes of material coupling coefficient of a bender device, which composed of two piezoelectric wafers bonded to a substrate with a destabilizing preload on both ends. They still used the same work cycle as used by the material coupling coefficient. By means of simplifying the Rayleigh-Ritz formulation presented by Hagood, Chung and Von Flotow[Hagood, 1990], they

destabilized the matrix relation to describe the system. Then, they assumed the proper mechanical and electrical mode shapes and found out the corresponding stiffness, capacitance and electromechanical coupling of the bender without preload. They also discussed the influence of the axial preload on the stiffness of the bender. Finally, they defined the apparent actuation efficiency and proper actuation efficiency. The apparent actuation efficiency did not include the work done by preload, while the proper actuation efficiency included it. They claimed that the work by preload could not be considered a steady-state source of energy in the system, so the proper actuation efficiency expression was correct. Although the device coupling coefficient still looked at the energy conversion of the active materials, it included the effect of the external load. It described the actuation efficiency of a special coupled systems with distributed elements and could hardly be applied to general cases.

1.3.4 Spangler and Hall's Work

When studying the discrete actuation systems for helicopter rotor control, Spangler and Hall and later Hall and Prechtl [Hall, 1996] defined an impedance matched efficiency expression. This expression came from the mathematical study of the linear material load line and linear structure load line on a stress-strain diagram. The intersection of the two lines was the stress-strain state for a specific load or electric field condition. The area under the material load line represented the maximum energy for mechanical work in the active materials, while the area under the structure load line represented the total strain energy in the structure. They found out that at most one quarter of the actuation stain energy could be usefully applied to actuating a control surface.

$$\eta_{\max} = \frac{W_{M\,\max}}{W_{Esystem}} = \frac{1}{4}\frac{W_{Msystem}}{W_{Esystem}} = \frac{1}{4}k_{33}^2 \tag{1.2}$$

This mathematical optimum occurred at the impedance matched conditions when the stiffness ratio of the structure and the actuator is one. This impedance matched efficiency served well in their research, however, they did not take into account the effect of the load, which the systems worked against, had on the Electrical work into the systems. Therefore, this efficiency expression is still not a true thermodynamic actuation efficiency for the systems studied.

1.3.5 Giurgiutiu's Work

Giurgiutiu et al [Giurgiutiu, 1997] studied this effect in 1994. They assumed active materials such as piezo actuators behaved like electrical capacitors. Under non-load conditions, the electrical work stored was

$$E^*_{elec} = \frac{1}{2}CV^2 \tag{1.3}$$

This is actually the W_{in} in 1.1. However, when external load was applied onto the active materials, the electrical energy stored inside changed. Giurgiutiu et al modulated their capacitances under external load by the stiffness ration of structures and the active materials. They found the resulting electrical work to be

$$E_{elec} = (1 - k^2\frac{r}{1+r}) * (\frac{1}{2}CV^2) = (1 - k^2\frac{r}{1+r})E^*_{elec} \tag{1.4}$$

Where r is the stiffness ratio of structures and active materials. In 1997, Giurgiutiu et al tried to find the actuation efficiency of a system where a PZT actuator operating against a mechanical load under static and dynamic conditions. For the static case, they found the mechanical work out to be

$$E_{out} = \frac{r}{(1+r)^2}E^*_{mech} \tag{1.5}$$

Where E^*_{mech} is actually the ideal work out resulting from electromechanical conversion, i.e. the W_{out} in 1.1. They also found mathematically that E_{out} had a maximum value at $r = 1$.

$$E_{out-\max} = \frac{1}{4}E^*_{mech} \tag{1.6}$$

When finding the actuation efficiency of the systems, instead of using the ratio of 1.5 to 1.4, they used the ratio of 1.6 to 1.4 which resulted in

$$\eta = \frac{1}{4}\frac{k^2}{1 - k^2\frac{r}{r+1}} \tag{1.7}$$

Where k^2 is actually $k^2_{33} = \frac{W_{out}}{W_{in}}$ in 1.1. This expression actually has an implied condition which is $r = 1$, so it is not the correct expression. However, they seemed to have used the correct expression to find the maximum value for the actuation efficiency of the system. Actually this

has been verified mathematically. Giurgiutiu et al also extended their work to dynamic analysis for a similar case, but they did not experimentally verify their analytical results for both static and dynamic cases.

1.3.6 C. L. Davis' Work

Davis et al [Davis, 1999] used a different approach than that used by Giurgiutiu to estimate the actuation efficiency of structurally integrated active materials. They converted the one dimensional linear constitutive equation of piezo element into a set of two equations in the frequency domain. Then, they found the complex electrical power consumed by the piezo element and the mechanical power delivered to the mechanical load. They defined their actuation efficiency of the system as the ratio of this mechanical energy to this electrical energy. Their expression was in the frequency domain expressed as

$$\eta = k^2 \frac{\alpha}{(1+\alpha) * [1 + (1-k^2) * \alpha]} \tag{1.8}$$

Where α here is the ratio of the mechanical load impedance to the effective mechanical impedance of the piezo element. In a static one-dimensional case, α is actually r as defined in 1.4, and k is actually k_{33} as in 1.1. After a simple algebraic operation, we can rewrite equation 1.8 as:

$$\eta = \frac{\frac{\alpha}{(1+\alpha)^2} k^2}{1 - k^2 \frac{\alpha}{1+\alpha}} \tag{1.9}$$

Actuation efficiency expressed by Equation 1.9 is exactly the same as the expression of Giurgiutiu if we use the ratio of 1.5 to 1.4 in their study. Davis et al also extended their work into dynamic analysis, however, like Giurgiutiu et al, they did not experimentally verify their work either.

1.3.7 M. Mitrovic's Work

M. Mitrovic et al [Mitrovic, 1999] conducted a series of experiments to understand the behavior of piezoelectric materials under electrical, mechanical, and combined electromechanical loading conditions. They evaluated parameters such as strain output, permittivity, mechanical stiffness, energy density and material coupling coefficient as a function of mechanical preload and

electrical field applied. Unlike the work discussed above, their work was mainly experimental. They tested five different commercially available piezoelectric stack actuators and found the stiffness dependence on preload and applied electrical field. They also found out that piezoelectric coefficients and the energy density delivered by the actuator initially increased when mechanical preload was applied, however, higher preload had the adverse effect on the stacks' response. The tests were conducted on a 22 kip Instron 8516 servo-hydraulic test frame. The mechanical loading frequency was from 0.1 Hz to 40 Hz, while the electrical load frequency was only 0.1 Hz and 1 Hz. Although they tried to determine the optimum conditions under which the piezo actuators could be operated and did found some interesting results in mechanical power delivered from the actuators and electrical power delivered to the actuators, they did not discuss the actuation efficiency of the systems as a whole. In addition, they did not theoretically analyze the systems and did not make any prediction as explanations for the test results.

1.3.8 Lutz and Hagood's Work

Lutz and Hagood [Malinda, 1999] studied the actuation efficiency and work flow both analytically and experimentally. They were also able to extend their work for the systems where piezo actuators working against not only linear loads but also non-linear loads. They used a different approach than those used by Giurgiutiu or Davis and studied this problem almost at the same time. The method they utilized was the Rayleigh-Ritz formulation presented by Hagood, Chung and Von Flotow[Hagood, 1990], simplified for quasi-static analysis. They found out that load coupling had significant influence on the work flow and actuation efficiency of the systems. For linear loading systems, their analysis has shown that the actuation efficiency is the highest when the stiffness ratio is larger than one. This maximum value is much higher than that predicted by the uncoupled analysis when the material coupling coefficient is relatively high, while for non-linear loading systems, actuation efficiency can be twice as high as that of the linear systems. The analytical results for linear systems actually agree very well with those found by Giurgiutiu [Giurgiutiu, 1997] and Davis [Davis, 1999]. The equation for linear systems in [Malinda, 1999] has typos. To verify the analytical results, a testing facility was designed and built to measure the actual work input, work output, and actuation efficiency of a discrete actuator working against both linear and non-linear loads. The testing facility was

designed for load application with programmable impedances and closed loop testing capability at frequency up to 1 kHz compared to the maximum testing frequency of 40 Hz for an Instron testing machine. However, due to some mechanical and control problems, it was difficult to measure mechanical and electrical work accurately. Not much valid experimental data was obtained, and further exploration was needed.

1.4 Approach

The work discussed in this thesis is a follow-up of Malinda and Hagood's work. For the purpose of mathematically verifying the theories derived by them and also for the completeness of this document, the expressions for work input, work output and actuation efficiency will be derived again using the Rayleigh-Ritz formulation presented by Hagood, Chung and Von Flotow [Hagood, 1990] at the beginning, and will be compared to those derived previously. General expressions will be derived first in terms of the actuating voltage of the piezo actuators and then applied to the chosen linear and non-linear cases. Due to the difficulty in finding the close form solution for the displacement of the actuators in terms of the applied voltage to them, expressions for the work and actuation efficiency in terms of displacement of the piezo actuators will also be derived. The results predicted by the theoretical analysis for linear and non-linear systems will be compared and contrasted.

Then, experimental data from previous work will be studied and summarized, so as to find out the remaining problems. Methods used to determine the material properties such as stiffness, capacitance, electromechanical and coupling terms as well as the methods for measuring mechanical work and electrical work will all be examined. Proper renovation and validation on the existing test facility will be made to guarantee accurate measurements. For the linear and non-linear actuation tests, the feed back control methodology will also be checked, and improvements will be made accordingly.

For the convenience of comparing with the test results obtained before, the same Sumitomo stack actuator, as used by Lutz, will still be used as the test sample. The experimental data from linear and non-linear tests will be compared with the theoretical prediction, and an expansion of this work to non-conservative systems will be discussed.

1.5 Organization of the Document

This document is organized in the same way as the problem is approached.

Chapter 2 presents the theoretical derivation of the mechanical work, electrical work, and actuation efficiency for linear and non-linear systems. It begins by defining work terms and actuation efficiency as well as the constitutive relation for piezo active materials, followed by the mathematical derivation using the Rayleigh-Ritz formulation mention above. Then it shows the application of the general expressions to both linear and non-linear cases in terms of either voltage to the active material or the displacement of it during the actuation tests. The analytical results for linear and non-linear systems are compared and discussed at the end.

Chapter 3 presents the redesign of the important mechanical part of the tester and the validation of the test methods. It summarizes the previous test results and some insights on the remaining problems first followed by discussing the test results from the laser vibrometer, which reveals the serious bending effect of the sample during tests. After that, possible improvements based on the tests and previous analysis has are discussed, and the new design of the load transfer device is exhibited too. Finally, it shows the validation test results made on the new test facility. These tests include calibration of force, displacement, stiffness, and capacitance measurement which guarantee the correct measurement of mechanical and electrical work.

Chapter 4 presents the test results and their correlation with theoretical prediction. It begins by discussing the problem of the former feed back control test methodology and presents the proposed feed forward method. Then, it displays the derived Voltage-Force model using the Rayleigh-Ritz formulation for the simulated actuator-structure-actuator system. Afterwards, linear test results are presented first and compared with the theoretical prediction and the data found in the literature. For the non-linear tests, the two non-linear functions chosen are analyzed and the driving voltage for the sample is determined, then the determination of voltage for the driving stack is shown using the established Voltage-Force model. The non-linear test results are compared with the theoretical prediction and linear test results.

Chapter 5 discusses the possibility for mechanical work to be done on the environment. The linear and non-linear tests discussed above are all for conservative systems. This chapter shows that the net work in these systems is zero. To take advantage of the mechanical work from the actuator, proper thermodynamic cycle should be chosen so that the net work in the system is

not zero. Possible thermodynamic cycles used in other applications is presented as a reference. The out of phase actuation of the driving stack and the sample stack at the same frequency is demonstrated to be such a thermodynamic cycle. The experimental results are also compared with the analytical results at the end.

Chapter 6 concludes the document and the research. It highlights the important test and analytical results in the research and their correlation with each other. The possibility for the mechanical work to be done on the environment is also emphasized. Then recommendations for future work in this area are presented, and recommendation are made to extand the application of piezo actuators and take further advantage of them.

Chapter 2

Analysis of the Work Flow and Actuation Efficiency of Electromechanically Coupled Systems

The system analyzed and the method used in this research are essentially the same as those used by Malinda and Hagood. The purpose to include this part of work is for the completeness of this document and a verification of the previous work. In addition, Malinda just found a close form solution for linear systems in terms of the applied voltage to the active materials, while for non-linear systems she had to rely on numerical results for work input and output. This is not convenient because the independent variable in her expression is voltage to the sample stack, however, there is no close form expression for the displacement of the active materials in terms of the applied voltage for non-linear cases, which can be seen from the compatibility equation derived later. To derive a close form expression, we should choose displacement of the active materials as the independent variable.

The system studied is a generalized system comprised of an electromechanically coupled core with a generalized energy input, working against a generalized load which has some defined linear or non-linear relation. The coupled core could be a variety of systems such

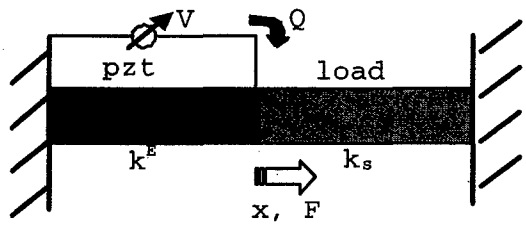

Figure 2-1: Piezoelectrically Driven One Dimensional Model

as a discrete actuator and the magnification mechanism, a mechanically coupled system or a hydraulic actuation system. The input into the system could be any generalized work pair like charge and voltage or current and voltage. The output of the system could be another work pair like displacement and force or strain and stress.

The generalized expression will be derived first, then applied to linear or non-linear cases for discrete piezo actuator systems. In order to compare and discuss different systems, it is necessary to define work input, work output and actuation efficiency in the beginning.

2.1 Definition of Work Terms

The system which will be studied has been shown in Figure 2-1. Work input is defined as the electrical work, while work output is defined as the mechanical work. The actuation efficiency is then a true thermodynamical efficiency defined as the ratio of mechanical work to electrical work. Each of the work terms is defined below.

2.1.1 Mechanical Work

The mechanical work of a system is described as the integral of force times the derivative of displacement:

$$W_M = \int_{x_0}^{x_f} F dx \tag{2.1}$$

Or it can be defined in terms of stress and strain as:

$$W_M = \int_{Vol} \int_{s} T ds \cdot dVol \tag{2.2}$$

2.1.2 Electrical Work

Electrical work of a system is defined in the same way as mechanical work is defined. It is the integral of voltage times the derivative of charge:

$$W_E = \int_{Q_0}^{Q_f} V dQ \tag{2.3}$$

Or it can be defined in terms of electrical field and electrical displacement as

$$W_E = \int_{Vol} \int_{D} E dD \cdot dVol \tag{2.4}$$

2.1.3 Actuation Efficiency

As being discussed in the previous chapter, the material coupling coefficient is not a good measure to describe the efficiency of a device or a system, while actuation efficiency is a viable metric. It is defined as the work out of the system divided by the work into the system when working over a typical operation cycle. As mentioned before, work input is defined as the electrical work, while work out is defined as the mechanical work. Therefore, actuation efficiency is expressed as

$$\eta = \frac{W_{out}}{W_{in}} = \frac{W_M}{W_E} \tag{2.5}$$

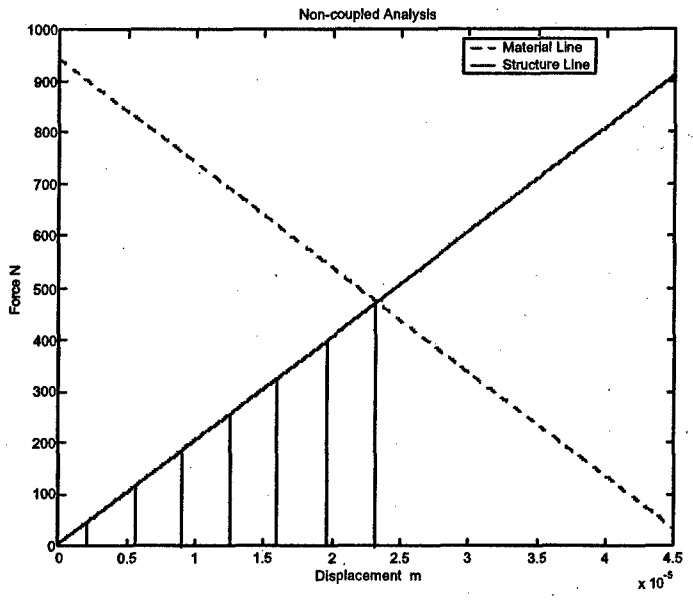

Figure 2-2: Material and Structure Loading Line for the Linear Systems

2.2 Linear and Non-linear Systems

The motivation for looking into non-linear systems comes from the diagram showing the intersection of a material load line and a structure load line on a force-displacement diagram, shown in figure 2-2.

The area under the structure load line from the origin to the intersection is the actual mechanical work of the system. The area under the material load line is the total amount of energy available to do mechanical work. So if a structure load line, such as a curve, can encompass more area under the material load line before it intersect with the structure load line, it is possible that more mechanical work can be done on the structure. Thus, the actuation efficiency of the system will be increased. Such curves do exist and we can call them non-linear loading functions, while the corresponding systems called non-linear systems. Two sample non-linear loading functions are shown in Fig. 2-3. They are essentially the same functions defined by Malinda for the purpose of comparison and discussion.

Linear loading function:

$$\frac{F_{linear}}{F_{bl}} = \frac{x}{x_{free}} \tag{2.6}$$

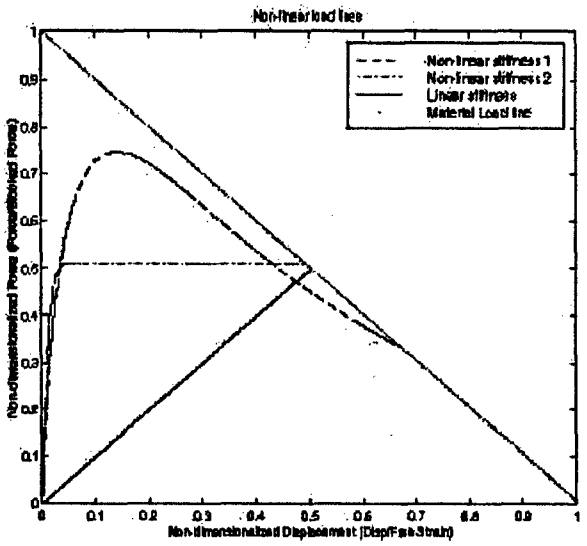

Figure 2-3: Comparison of Linear and Non-linear Functions

Non-linear loading function 1:

$$\frac{F_{non-linear1}}{F_{bl}} = \frac{x}{x_{free}} \left(41 \exp^{-5.45\left(\frac{x}{x_{free}}\right)^{\frac{1}{2}}} \right) \tag{2.7}$$

Non-linear loading function 2:

$$\frac{F_{non-linear2}}{F_{bl}} = \frac{1}{2} \left(\tanh \left(66 \frac{x}{x_{free}} \right) \right) \tag{2.8}$$

2.3 General Analysis

The object we are going to study here is a piezo actuator. The linear constitutive equations of the piezoelectric are presented first, then the general actuator and sensor equations derived by Hagood et al [Hagood, 1990] are introduced. The work terms are derived using the actuator and sensor equations and then applied to one dimensional linear and non-linear cases.

2.3.1 Linear Constitutive Equations

For small stresses and electric fields, piezoelectric materials follow a linear set of governing equations which describe the electrical and mechanical interaction of the materials. The equation can be expressed as

$$\begin{Bmatrix} S \\ D \end{Bmatrix} = \begin{bmatrix} s^D & d_t \\ d & \varepsilon^T \end{bmatrix} \begin{Bmatrix} T \\ E \end{Bmatrix} \tag{2.9}$$

These equations have four system states: T, the stress in six directions; E, the electric field in three directions; S, the strain in six directions; D, the electric displacement in three directions. The materials constitutive relation is a nine by nine matrix. This matrix can be reduced using either plain stress, plain strain assumptions, or by assuming one dimensional relations. Most of the work in this document will be using one dimensional relations, which is a two by two matrix.

2.3.2 Governing Equations for the coupled systems

The governing equations for the piezo active materials are the simplified actuator equation and sensor equation for quasi-static cases, which can be expressed as [Hagood, 1990]

$$\begin{bmatrix} K_{p1}^E & -\theta_1 \\ \theta_1 & C_{p1}^S \end{bmatrix} \begin{Bmatrix} x_1 \\ V_1 \end{Bmatrix} = \begin{Bmatrix} f_1 \\ Q_1 \end{Bmatrix} \tag{2.10}$$

Where K_{p1}^E is the stiffness matrix for the active materials; θ_1 is the electromechanical coupling terms; C_{p1}^S is the capacitance of the active materials under constant strain and x_1, V_1, f_1 and Q_1 are the displacement, voltage, force and charge vector respectively. Dynamic terms are neglected since the tests were done quasistatically.

For the non-piezoelectric structure, force-displacement relation can be written as:

$$f_s = k_s x_s \tag{2.11}$$

Where k_s is the stiffness of the structure and can be either linear or non-linear with respect to x_s, the displacement of the structure.

2.3.3 Compatibility and Equilibrium

The states of the structure and active material are related by compatibility and equilibrium requirements.

Force equilibrium:

$$f_1 = f_s \tag{2.12}$$

Compatibility:

$$x_1 = -x_s = x \tag{2.13}$$

From equation 2.10 we have

$$K_{p1}^E x_1 - \theta_1 V_1 = f_1 \tag{2.14}$$

Substitute equation 2.12 and equation 4.21, we have

$$x = \frac{\theta_1 V_1}{k_s + K_{p1}^E} \tag{2.15}$$

This is an implicit relationship between V_1 and x. which is automatically satisfied during the test. Therefore, this equation can be used to determine displacement of the active material when a voltage is applied or for an expected displacement, the required voltage can be determined by solving this equation iteratively.

2.3.4 Electrical Work

Electrical work is defined in equation 2.3.

From equation 2.10:

$$Q_1 = \theta_1^T x + C_{p1}^S V_1 \tag{2.16}$$

Substitute equation 2.15 into 4.18, we have

$$Q_1 = \theta_1^T \frac{\theta_1 V_1}{k_s + K_{p1}^E} + C_{p1}^S V_1 = \left(\frac{\theta_1^T \theta_1}{k_s + K_{p1}^E} + C_{p1}^S \right) V_1 \tag{2.17}$$

Then the variation of Q_1 in terms of V_1 can be expressed as

$$\delta Q_1 = \left[\frac{\theta_1^T \theta_1}{k_s + K_{p1}^E} + C_{p1}^S - \frac{\theta_1^T \theta_1 V_1}{(k_s + K_{p1}^E)^2} \frac{dk_s}{dx} \frac{dx}{dV_1} \right] \delta V_1 \tag{2.18}$$

Substitute equation 2.18 into equation 2.3, we have the electrical work expressed as

$$W_E = \int_{V_0}^{V_f} \left[\frac{\theta_1^T \theta_1 V_1}{k_s + K_{p1}^E} + C_{p1}^S V_1 - \frac{\theta_1^T \theta_1 V_1^2}{(k_s + K_{p1}^E)^2} \frac{dk_s}{dx} \frac{dx}{dV_1} \right] \delta V_1 \tag{2.19}$$

2.3.5 Mechanical Work

Mechanical work is defined in equation 2.1, where

$$F = k_s x \tag{2.20}$$

Finding the variation of x using equation 2.15, we have

$$\delta x = \left[\frac{\theta_1}{k_s + K_{p1}^E} - \frac{\theta_1 V_1}{(k_s + K_{p1}^E)^2} \frac{dk_s}{dx} \frac{dx}{dV_1} \right] \delta V_1 \tag{2.21}$$

Substitute equation 2.20 and equation 2.21 into 2.1, we will have the mechanical work expressed as

$$W_M = \int_{V_0}^{V_f} \frac{k_s \theta_1^T \theta_1 V_1}{(k_s + K_{p1}^E)^2} \left[1 - \frac{V_1}{k_s + K_{p1}^E} \frac{dk_s}{dx} \frac{dx}{dV_1} \right] \delta V_1 \tag{2.22}$$

2.3.6 Actuation Efficiency

The actuation efficiency of the system is defined in equation 2.5, which is simply the ratio of equation 2.22 to equation 2.19.

2.4 One Dimensional Linear Systems

2.4.1 Expressions for Linear Systems

The systems discussed here has been shown in Fig. 2-1. For linear systems,

$$\frac{dk_s}{dx} = 0 \tag{2.23}$$

And assume $V_0 = 0$ and $V_f = V_1$, equation 2.19 and equation 2.22 can be simplified and expressed as

$$W_E = \frac{1}{2}V_1^2\left(\frac{\theta_1^T\theta_1}{k_s + K_{p1}^E} + C_{p1}^S\right) \tag{2.24}$$

$$W_M = \frac{1}{2}V_1^2\frac{k_s\theta_1^T\theta_1}{(k_s + C_{p1}^S)^2} \tag{2.25}$$

2.4.2 Constitutive Equations

The central axis of the actuator and structure is regarded as the 3-direction of the systems. Linear material relations is used and constitutive equations 2.9 is simplified for one dimensional cases. The one dimensional constitutive equations in 3-direction can be written as

$$\begin{Bmatrix} S_3 \\ D_3 \end{Bmatrix} = \begin{bmatrix} s_{33}^E & d_{33} \\ d_{33} & \epsilon_{33}^T \end{bmatrix} \begin{Bmatrix} T_3 \\ E_3 \end{Bmatrix} \tag{2.26}$$

This equation can be rewritten to have strain as the free variable, then

$$\begin{Bmatrix} T_3 \\ D_3 \end{Bmatrix} = \begin{bmatrix} c_{33}^E & -e_{33} \\ e_{33} & \epsilon_{33}^S \end{bmatrix} \begin{Bmatrix} S_3 \\ E_3 \end{Bmatrix} \tag{2.27}$$

From equation 2.26 and equation 2.27 we can find the following relations

$$c_{33}^E = \frac{1}{s_{33}^E} \tag{2.28}$$

$$e_{33} = d_{33}c_{33}^E \tag{2.29}$$

$$\varepsilon_{33}^{S} = \varepsilon_{33}^{T} - d_{33}^{2} c_{33}^{E} \tag{2.30}$$

2.4.3 Finding the Constants in Work Expressions

To find the constants in the work expressions, i.e. equation 2.24 and equation 2.25, The Ritz method is used. Electrical and mechanical mode shapes , which satisfy the prescribed voltage boundary conditions and the geometric boundary conditions of this specific problem respectively are assumed as

$$\Psi_E = \frac{x}{l_{p1}} \tag{2.31}$$

$$\Psi_M = \frac{x}{l_{p1}} \tag{2.32}$$

The assumed mode shapes can be used to find C_{p1}^{S}, K_{p1}^{E} and θ_1 using the equation developed by Hagood et al [Hagood, 1990]

$$\begin{aligned} K_{p1}^{E} &= \int_{V_{p1}} N_x^T c^E N_x dV_{p1} \\ &= \int_{V_{p1}} \frac{1}{l_{p1}} c_{33}^{E} \frac{1}{l_{p1}} dV_{p1} \\ &= \frac{c_{33}^{E} A_{p1}}{l_{p1}} \end{aligned} \tag{2.33}$$

$$\begin{aligned} \theta_1 &= \int_{V_{p1}} N_x^T e_t N_v dV_{p1} \\ &= \int_{V_{p1}} \frac{1}{l_{p1}} e_{33} \frac{1}{l_{p1}} dV_{p1} \\ &= \frac{e_{33} A_{p1}}{l_{p1}} \end{aligned} \tag{2.34}$$

$$\begin{aligned} C_{p1}^{S} &= \int_{V_{p1}} N_v^T \varepsilon^S N_v dV_{p1} \\ &= \int_{V_{p1}} \frac{1}{l_{p1}} \varepsilon_{33}^{S} \frac{1}{l_{p1}} dV_{p1} \\ &= \frac{\varepsilon_{33}^{S} A_{p1}}{l_{p1}} \end{aligned} \tag{2.35}$$

For a one dimensional linear structure, we have

$$k_s = \frac{A_s}{l_s} c_s \tag{2.36}$$

2.4.4 Simplified Expressions for Electrical and Mechanical Work

Assume that the structure and the piezoelectric have the same effective length and the same cross sectional area, then we have

$$A_s = A_{p1} = A \tag{2.37}$$

$$l_s = l_{p1} = l \tag{2.38}$$

Substitute equation 2.33, 2.34, 2.35, 2.36, 2.37 and 2.38 into equation 2.24 and 2.25, we will be able to find the simplified expressions for mechanical work , electric work and actuation efficiency.

Mechanical Work

$$W_M = \frac{1}{2}\frac{A}{l} V_1^2 \frac{c_s e_{33}^2}{(c_{33}^E + c_s)^2} \tag{2.39}$$

Electrical Work

$$W_E = \frac{1}{2}\frac{A}{l} V_1^2 \left(\varepsilon_{33}^S + \frac{e_{33}^2}{c_{33}^E + c_s} \right) \tag{2.40}$$

We can further simplify these two equations by taking advantage of the material coupling coefficient expressed as

$$k_{33}^2 = \frac{d_{33}^2}{s_{33}^E \varepsilon_{33}^T} \tag{2.41}$$

And the relation expressed in equations 2.28, 2.29 and 2.30. Then the mechanical work and electrical work will be

Mechanical Work

$$W_M = \frac{1}{2}\frac{A}{l} V_1^2 \varepsilon_{33}^T k_{33}^2 \frac{\alpha}{(1+\alpha)^2} \tag{2.42}$$

Electrical Work

$$W_E = \frac{1}{2}\frac{A}{l}V_1^2\varepsilon_{33}^T\left(1 - \frac{\alpha}{1+\alpha}k_{33}^2\right) \tag{2.43}$$

Where

$$\alpha = \frac{c_s}{c_{33}^E} = \frac{k_s}{k_{p1}^E} \tag{2.44}$$

2.4.5 Actuation Efficiency

Actuation efficiency of the one dimensional linear system can be determined by equation 2.42 and 2.43, which is

$$\eta = \frac{W_{out}}{W_{in}} = \frac{k_{33}^2\frac{\alpha}{(1+\alpha)^2}}{1 - \frac{\alpha}{1+\alpha}k_{33}^2} \tag{2.45}$$

This expression is exactly the same as which derived by Giurgiutiu [Giurgiutiu, 1997] and Davis [Davis, 1999] respectively, but we use a different approach here.

It can be shown mathematically that equation 2.45 has a peak at

$$\alpha = \frac{1}{\sqrt{1-k_{33}^2}} \tag{2.46}$$

And the maximum value is

$$\eta_{\max} = \frac{k_{33}^2}{\left(1+\sqrt{1-k_{33}^2}\right)^2} \tag{2.47}$$

2.4.6 Discussion on Actuation Efficiency

To better understand the expression we have derived here, actuation efficiency is plotted in Fig. 2-4 with the impedance matched system efficiency by Hall and Prechtl, equation 1.2, for comparison.

This figure shows that when material coupling coefficient is small, the actuation efficiency correlates the impedance matched systems efficiency. However, when material coupling coefficient is significantly large, there is a big difference between the two due to higher electromechanical coupling. In addition, the peak value of the actuation efficiency occurs at a stiffness ratio larger than one, while the impedance matched system efficiency always occurs at the impedance matched condition.

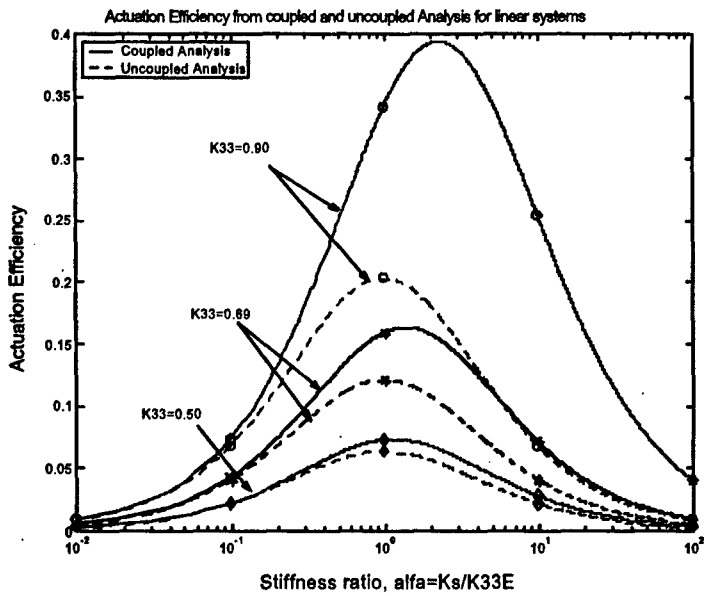

Figure 2-4: Comparison of Actuation Efficiency of Linear Systems with Different k_{33}

The relations of peak actuation efficiency and the corresponding stiffness ratio with the material coupling coefficient is illustrated in Fig.2-5.

2.5 One dimensional Non-linear Systems

2.5.1 General Analysis

In genaral, we can not find a close form solution for mechanical work and electrical work in terms of V_1, the applied voltage to test sample. For the convenience of analysis, we can use equation 2.20 and equation 2.36 to rewrite the non-linear functions, equation 2.7 and 2.8, in the following form:

$$f_s = k_s x = \frac{c_0 c_x A_s}{l_s} x \tag{2.48}$$

Where c_0 is a constant independent of x, and c_x is the non-linear part of the stiffness.

For nonlinear function 1:

$$c_x = 41 \exp^{-5.45\left(\frac{x}{x_{free}}\right)^{\frac{1}{2}}} \tag{2.49}$$

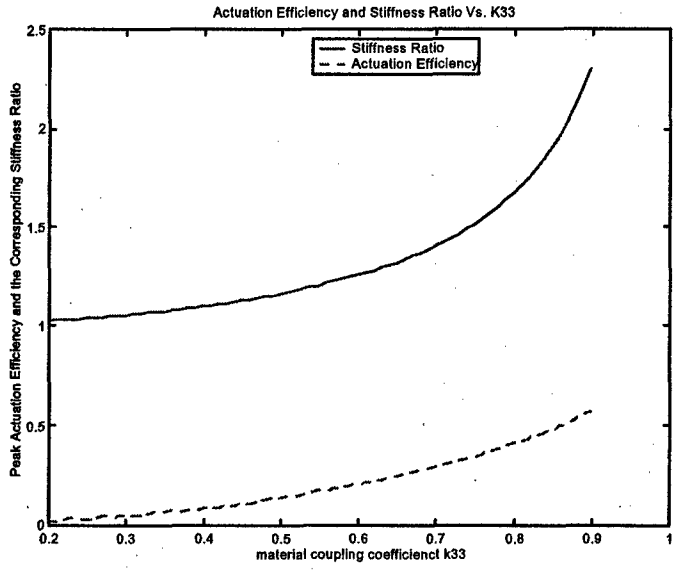

Figure 2-5: Max. Actuation Efficiency vs. k_{33} for 1D Linear Systems

For non-linear function 2:

$$c_x = \frac{1}{2x}\left(\tanh\left(66\frac{x}{x_{free}}\right)\right) \tag{2.50}$$

If we substitute equation 2.49, into equation 2.15, for example, we will have

$$x = \frac{\theta_1 V_1}{\frac{c_0 A_s}{l_s} 41 \exp^{-5.45\left(\frac{x}{x_{free}}\right)^{\frac{1}{2}}} + K_{p1}^E} \tag{2.51}$$

It is obvious that there is no close form solution for x in terms of V_1. Therefore, we can not find close form solutions for mechanical work and electrical work for such non-linear systems by simply substituting equation 2.51 in to equation 2.19 and equation 2.22. To find a close form solution, we need to express mechanical and electrical work in terms of the displacement of the active materials.

2.5.2 Mechanical and electrical Work in terms of Displacement

Electrical and mechanical work is still the same as defined in equation 2.3 and equation 2.1.

Mechanical work

$$W_M = \int_{x_0}^{x_f} k_s x dx \tag{2.52}$$

Electrical work

$$W_E = \int_{Q_0}^{Q_f} V_1 dQ_1 \tag{2.53}$$

From equation 2.15, we have

$$V_1 = \frac{k_s + K_{p1}^E}{\theta_1} x \tag{2.54}$$

Substitute equation 2.54 into 4.18, we have

$$Q_1 = \theta_1^T x + C_{p1}^S \frac{k_s + K_{p1}^E}{\theta_1} x \tag{2.55}$$

Then the variation of Q_1 in terms of x can be expressed as

$$dQ_1 = \left[\theta_1^T + \frac{C_{p1}^S}{\theta_1} \left(k_s + K_{p1}^E\right) + \frac{C_{p1}^S}{\theta_1} \frac{dk_s}{dx} x \right] dx \tag{2.56}$$

Substitute equation 2.54 and equation 2.56 into equation 2.53, we have

$$W_E = \int_{x_0}^{x_f} \frac{k_s + K_{p1}^E}{\theta_1} x \cdot \left[\theta_1^T + \frac{C_{p1}^S}{\theta_1} \left(k_s + K_{p1}^E\right) + \frac{C_{p1}^S}{\theta_1} \frac{dk_s}{dx} x \right] dx \tag{2.57}$$

2.5.3 Simplified Expressions for Mechanical and Electrical Work

As we have done for linear systems, we also need to assume mode shapes for the non-linear systems so as to find the material constants in equation 2.52 and equation 2.57. Here we assume the same electrical and mechanical mode shapes as in linear analysis. Therefore, we can simply substitute equation 2.33, 2.34, 2.35, 2.37, 2.38, and $k_s = \frac{c_0 c_x A_s}{l_s}$ from 2.48 into equation 2.52 and 2.57, and obtain

Mechanical work

$$W_M = \frac{c_{33}^E A}{l} \alpha \int_{x_0}^{x_f} c_x x dx \tag{2.58}$$

Electrical work

$$W_E = \frac{c_{33}^E A}{l}\int_{x_0}^{x_f}(1+\alpha c_x)\,x dx + \frac{(c_{33}^E)^2 A}{l}\frac{\varepsilon_{33}^S}{e_{33}^2}\int_{x_0}^{x_f}(1+\alpha c_x)^2\,x dx + \tag{2.59}$$

$$+\frac{c_0 c_{33}^E A}{l}\frac{\varepsilon_{33}^S}{e_{33}^2}\int_{x_0}^{x_f}(1+\alpha c_x)\,x^2\frac{dc_x}{dx}dx \tag{2.60}$$

Again we can further simplify the expression by utilizing equation 2.41, 2.28, 2.29 and 2.30. Then, the final expression for electrical work can be written as

$$W_E = \frac{c_{33}^E A}{l}\int_{x_0}^{x_f}(1+\alpha c_x)\,x dx + \frac{c_{33}^E A}{l}\left(\frac{1}{k_{33}^2}-1\right)\int_{x_0}^{x_f}(1+\alpha c_x)^2\,x dx + \tag{2.61}$$

$$+\frac{c_{33}^E A}{l}\alpha\left(\frac{1}{k_{33}^2}-1\right)\int_{x_0}^{x_f}(1+\alpha c_x)\,x^2\frac{dc_x}{dx}dx \tag{2.62}$$

Where

$$\alpha = \frac{c_0}{c_{33}^E} \tag{2.63}$$

Now if we substitute equation 2.49 or equation 2.50 into 2.58 and 2.61 respectively, we can obtain the close form solutions for mechanical work and electrical work for these two cases. However, the solutions are very long and it is much easier to evaluate the integrals numerically. Even though, it is still more convenient to use equation 2.58 and equation 2.61 rather than use 2.22 and 2.19.

2.5.4 Actuation Efficiency

Similarly, the actuation efficiency of one dimensional non-linear systems can be found by dividing equation 2.58 with equation 2.61.

2.6 Comparison of Linear and Non-linear Systems

Assume the stiffness of both the active materials are one and the material coupling coefficient is 0.75. Mechanical work, electrical work and actuation efficiency of both the linear and non-linear systems has been shown in Fig. 2-6 and Fig. 2-7.

It is obvious that the work output and actuation efficiency of the non-linear systems is much higher than that of the linear system. For non-linear system 1, the actuation efficiency is almost

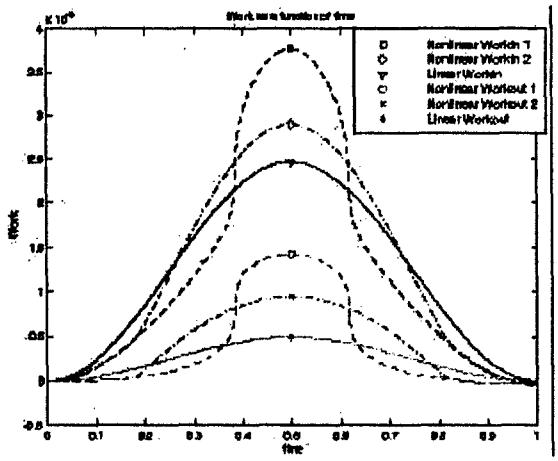

Figure 2-6: Comparison of Electrical and Mechanical Work for 1D Systems

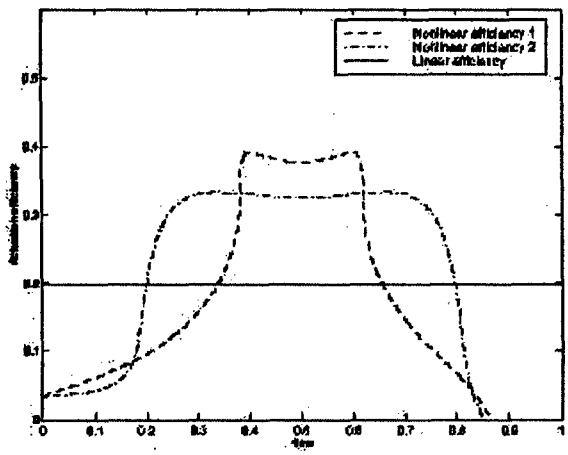

Figure 2-7: Comparison of Actuation Efficiency for 1D systems

doubled, while the work output is almost tripled.

2.7 Summary

Equations for the electric work, mechanical work and actuation efficiency for both the one dimensional linear and non-linear systems have been derived.

For linear systems, the analysis has shown that when material coupling coefficient is small, the actuation efficiency correlates the impedance matched systems efficiency. However, when material coupling coefficient is significantly large, there is a big difference between the two due to higher electromechanical coupling. In addition, the peak value of the actuation efficiency occurs when the stiffness ratio is larger than one, while the maximum impedance matched system efficiency always occurs at the impedance matched condition. The maximum actuation efficiency of the linear systems can be increased significantly when the material coupling coefficient of the active materials become large. For a given active materials whose material coupling coefficient is a constant, the stiffness of the structure should be carefully chosen to maximize the actuation efficiency of the system.

It has also been shown theoretically that the work output and actuation efficiency of the non-linear systems is much higher than that of the linear system. For non-linear system 1, the actuation efficiency is almost doubled, while the work output is almost tripled

Chapter 3

Renovation on the Existing Component Testing Facility

A component test facility has already been designed and built previously by Lutz [Malinda1, 1999] in order to verify the theoretical derivation of the mechanical, electrical work and actuation efficiency for both linear and non-linear systems. The picture in Fig. 3-1 shows the compressive component testing machine. However, due to some mechanical problems, force and displacement or the mechanical work from the active materials can not be measured accurately which necessitates a renovation on the tester. For a basis of discussion, the existing component tester is briefly introduced and the remaining problems are discussed, then the new design is presented and validated.

3.1 The existing Component Tester

3.1.1 Design Requirements

The main design requirements for this tester include:

- providing uniaxial testing with load application up to 8900 N and programmable impedances with a force resolution of 100 mN;
- To provide closed-loop testing capabilities at frequencies up to 1 KHz

BEST AVAILABLE COPY

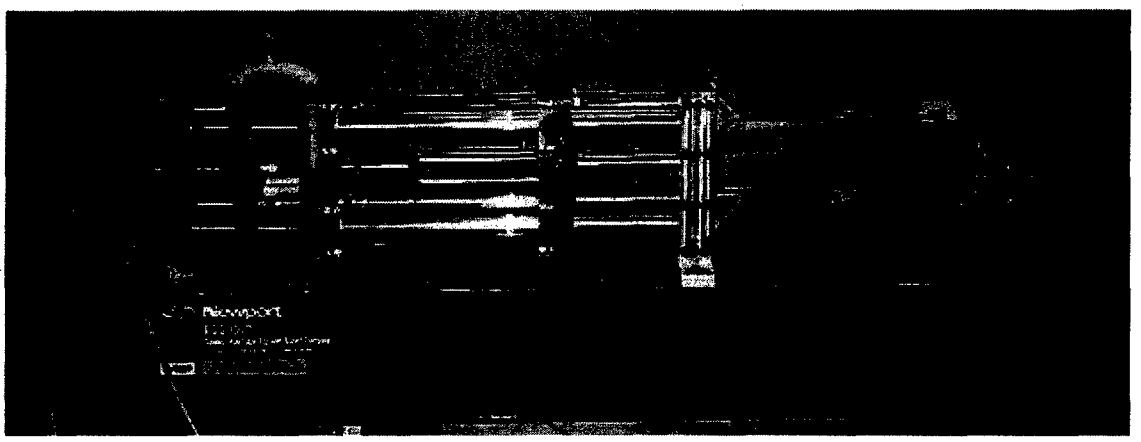

Figure 3-1: The Original Component Testing Facility

- To provide a testing facility that accommodates samples 0-120 mm long
- To provide the capability to perform 'free strain' and 'blocked force' tests
- To compensate for non-parallelism in the sample faces
- The ability to test most kinds of piezoelectric, electrostrictive, magnetostrictive and shape memory materials

3.1.2 Main Features of the Component Tester

The component tester actually built satisfies some of these requirements, such as loading capability and frequency range. The mechanical part consists of a large scale linear positioning system, which can provide preload to the sample, and two sets of driving piezo stacks, which can be chosen according to the applications. An alignment mechanism has been designed to compensate for the bending effect during the test. All the tests are controlled through the National Instrument/Labview data acquisition system. The feedback control of the systems mentioned above have also been implemented in Labview.

Specifications for some of the key components are listed below for reference:

- Preload: Flexline linear positioner, up to 20 kN.

- Optical displacement sensors: MTI 2000, range 0.127-0.510 mm, resolution 25 m, frequency up to 20 kHz.
- Entran load cell: 13.35 KN, resolution 4.5 N, frequency up to 700 Hz
- Kistler load cell: 22.250 KN, resolution 4.5 N, frequency up to 3000Hz
- Trek amplifier: Model 609 D-6, output voltage range 0 to ±4 KV, DC or peak AC; output current range 0 to 20 mA, DC or peak AC; voltage monitor ratio 1V/1000 V, accuracy 0.1% of full scale; current monitor ratio 1V/2 mA, accuracy 0.5% of full scale.
- Amplifier for Driving Stack: +800 V, -800 V or ±400 V.; 1 A per channel, 1.5 A peak.
- Driving stacks: Data shown in Table 3.1 below.

	Small Stacks	Large Stacks
Max. Displacement (no load)	78.74 m	182.88 m
Stiffness	105.64×10^6 N/m	45.20×10^6 N/m
Capacitance	1.28 F	3.00 F
Diameter	30.86 mm	30.86 mm
Overall Length	97.28 mm	184.15 mm

Table 3.1: Driving Stack Parameters

3.2 Previous Test Results

3.2.1 Material Properties Measurement

Material properties of piezo stacks such as open circuit stiffness, short circuit stiffness, dielectric constant and electromechanical coupling terms are required in the theoretical prediction of the mechanical and electrical work and actuation efficiency. The correct measurement of these properties is also a good validation of the methods used for the measurement of basic parameters including displacement, force, current and voltage. These basic parameters are the key parameters for acquiring mechanical and electrical work experimentally.

The test sample chosen is Sumitomo stack MLA-20B. The tested properties measured by Lutz [Malinda1,1999], are listed in Table 3.2 below.

	Units	Ave. Value	Max. Value	Max.Value
Elastic constant	10^{-12} m^2/N	31.3	34.5	27.5
Dielectric Constant	$\varepsilon_{33}^T/\varepsilon_0$	4015	4818	3215
Electromechanical coupling	10^{-12} m/V	785	824	746

Table 3.2: Sumitomo Stack Parameters

Method of Obtaining Value			**Coupling Coefficient k_{33}^2**	**Data Label**
Bulk Material			**0.72**	**-**
Measured Stack Resonance			**0.44**	**-**
max s_{33}^E	**max ε_{33}^T**	**max d_{33}**	**0.675**	**Theory 1**
min s_{33}^E	**min ε_{33}^T**	**min d_{33}**	**0.843**	**Theory 2**
mean s_{33}^E	**mean ε_{33}^T**	**mean d_{33}**	**0.745**	**Theory 3**
max s_{33}^E	**max ε_{33}^T**	**min d_{33}**	**0.611**	**Theory 4**
min s_{33}^E	**min ε_{33}^T**	**max d_{33}**	**0.932**	**Theory 5**

Figure 3-2: Determination of k_{33} for Sumitomo Stack

From table 3.2, we can see that the material properties actually could not be measure accurately. For this reason, the material coupling coefficient could not be determined accurately either. Different combination of the data listed in Table 3.2 had to be used to find a better estimation of the material coupling coefficient, which is shown in following Fig. 3-2 [Malinda1, 1999].

The k_{33} estimated in this table varies from 0.44 to 0.932 which has a difference of more than 100%. It is obvious that the mechanical work and electrical work can not be predicted accurately.

3.2.2 Linear Test Results

The mechanical work, electrical work and actuation efficiency of the linear tests is shown in Fig. 3-3, Fig. 3-4 and Fig. 3-5 respectively [Malinda1,1999]. Theory 1 to Theory 5 represents the five theoretical predictions using the five different estimated k_{33}^2.

Figure 3-3: Mechanical Work vs. Stiffness Ratio α for Linear Systems

Figure 3-4: Electrical Work vs. Stiffness Ratio α for Linear Systems

BEST AVAILABLE COPY

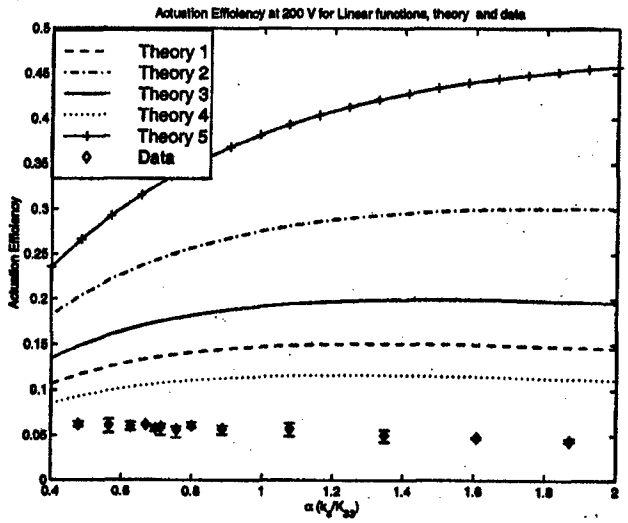

Figure 3-5: Actuation Efficiency vs. Stiffness Ratio α for Linear Systems

3.2.3 Nonlinear Test Results

No much data was obtained for non-linear tests [Malinda1,1999]. The actuation efficiency comparison for linear and non-linear systems is shown in Fig. 3-6.

Form the figures shown above, it is obvious that the experimental data do not match the theoretical prediction.

3.3 Analysis of the Problems

The accurate measurement of electrical and mechanical work is the basis for the comparison of theoretical prediction and experimental data. From previous discussion we know that the theoretical prediction could not be made accurately because of the bad material property data. This actually implies that the mechanical work and electrical work could not be measured accurately either since the basic parameters required are the same, such as current, voltage, displacement and force.

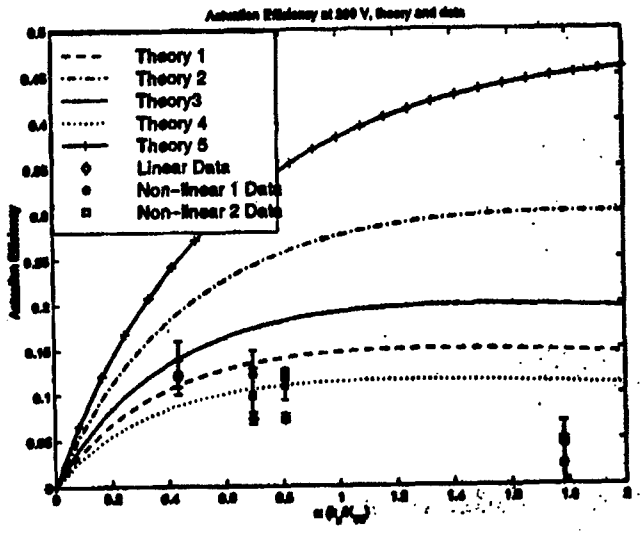

Figure 3-6: Comparison of Actuation Efficiency for Linear and Non-linear Systems

3.3.1 Electrical Work Measurement

The time trace of a representative test is shown in Fig. 3-7. It is obvious that the data is unaccessible, which could be one of the reasons for the mismatch of electrical work from prediction and experiment.

Form this figure, we can also find that the length of the test is 20 seconds, using half a sine wave. The driving frequency of the test is then 1/40 Hz, i.e. 0.025 Hz. The applied voltage to the sample is 200 V, which can also be seen from the figure. The nominal capacitance of the Sumitomo stack MLA-20B is 800 nF at free condition. From these data we can estimate the magnitude of the current in the systems which is:

$$\begin{aligned} I &= 2\ fVF \qquad (3.1) \\ &= 2 \times 3.14 \times 0.025 \times 200 \times 800 \times 10^{-9} \\ &= 0.025 \text{ mA} \end{aligned}$$

The current magnitude computed is so small that it is far below the lowest value of an accurate measurement for the current monitor of the Trek amplifier, which is about $0.5\% \times 20 =$

BEST AVAILABLE COPY

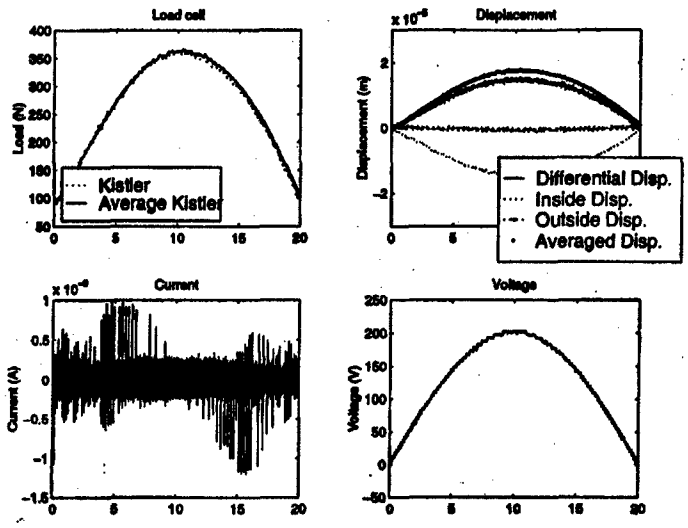

Figure 3-7: Time Trace of from Previous Test

0.1 mA. This value can be found from the specification of the Trek amplifier listed before. The current measurement problem could be solved by simply increasing the test frequency so that the current magnitude is high enough for the current monitor. However, the driving frequency is actually limited by the capability of the control system of the tester. An improvement in the control method should be made to guarantee an better current measurement. This will be demonstrated later in this chapter. The voltage measurement should have no problem and this will be demonstrated later too.

3.3.2 Mechanical Work Measurement

The mechanical work measurement seemed to be a very difficult problem. To get an idea of the displacement and force measurement accuracy, stiffness of an Aluminum bar was measured first.

Aluminum Bar Stiffness Measurement

The Al bar measured has a length of 0.0832 m, diameter of ϕ 0.008 m and the theoretical stiffness of it is 4.229×10^7 N/m. The Aluminum bar was placed on the different locations

	Test 1		Test 2		Test 3	
	Align.	No Align.	Align	No Align.	Align	No. Align.
Kis.10^7 N/m	2.3001	2.3110	3.2283	4.5397	2.0136	3.7400
Ent. 10^7 N/m	1.9266	1.9350	2.9663	4.0373	1.6331	2.600

Table 3.3: Al Bar Stiffness Measurement

on the sample plate of the tester. The test were done under two conditions: testing with the alignment mechanism or without the alignment mechanism. When tested with the alignment mechanism, the stiffness of the Al bar should be

$$K = \frac{1}{\frac{1}{K_{measu.}} - \frac{1}{K_{align.}}} \tag{3.2}$$

The displacement of the Al bar was measured by the MTI Fotonic sensors, and force was measured by both Entran and Kistler load cells. The results are listed in Table 3.3.

It was obvious that the stiffness measured did not match the theoretical value when tested without the alignment mechanism. The alignment mechanism was designed to remove the bending effect during tests, however, the data measured with the alignment mechanism was questionable also. In addition to the Aluminum bar stiffness measurement, several plastic bars were measured and the data was also unaccessible, which has been shown in Fig. 3-8.

This necessitated the accurate stiffness measurement of the alignment mechanism.

Alignment Mechanism Stiffness Measurement

The alignment mechanism is shown Fig. 3-9. It consists of two circular plates connected by a thin bar which is designed to compensate for the un-parallelism of both the test sample and the champing plates.

The stiffness of the alignment mechanism measured was unexpected which showed a stiffness change with respect to the preload applied on it. Fig. 3-10 shows the results.

Cage Assembly

Besides the problem of the alignment mechanism, the cage assembly caused some problems also. The cage assembly was designed and built for two purposes mainly. First the cage provides the capability of transferring load from the driving stacks to the test sample, and the convenience

BEST AVAILABLE COPY

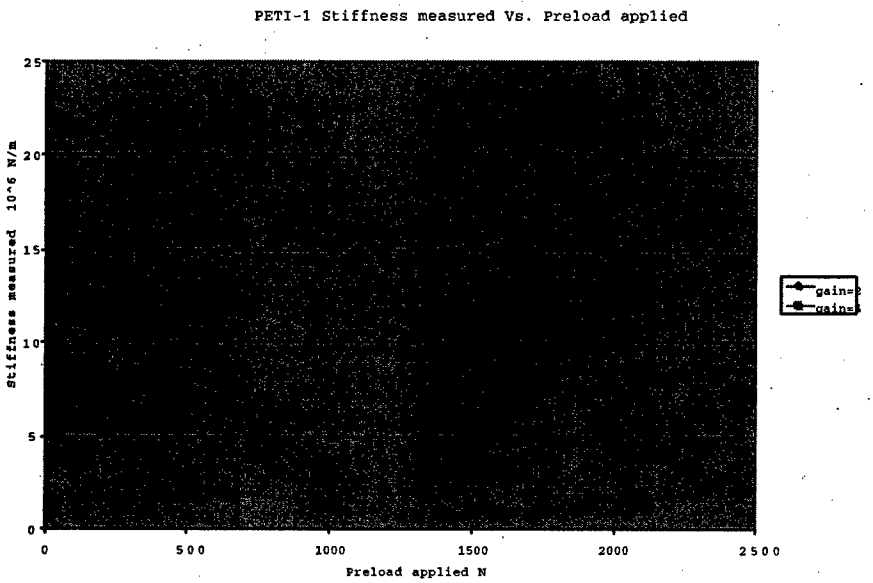

Figure 3-8: Stiffness of PETI-1 vs. Applied Preload

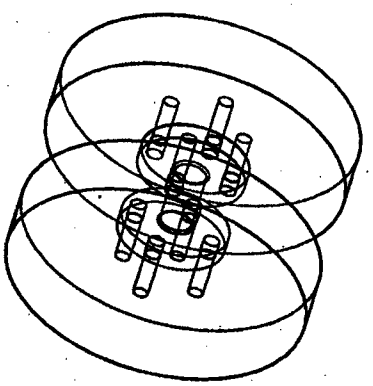

Figure 3-9: The Original Alignment Mechanism

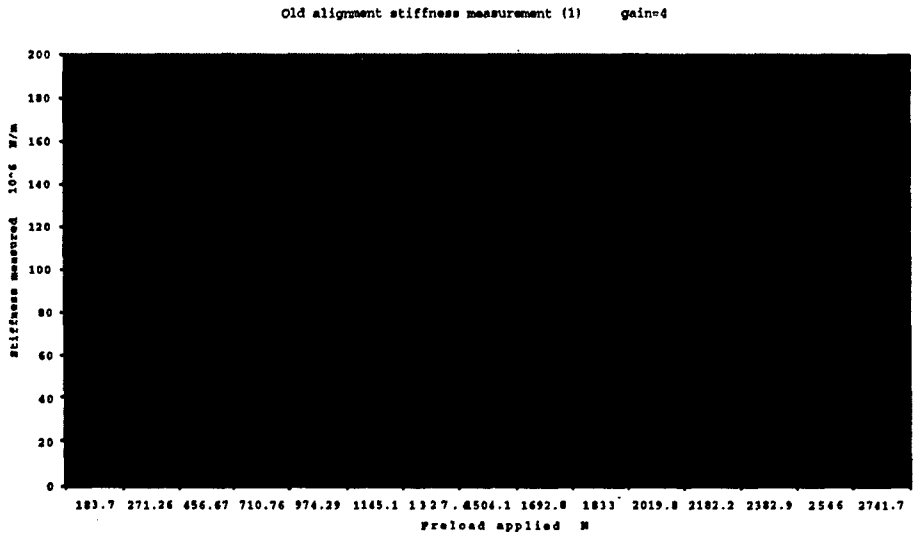

Figure 3-10: Stiffness of the Alignment Mechanism vs.Preload

for the displacement measurement of the sample. The load was transferred through two thin flextures. Second, the cage provides the protection of the loading and testing systems in case of serious misalignment. This was done by reinforcing the loading and testing systems through this cage mounted on the four rods. A picture of the cage assembly is shown in Fig. 3-11.

It was found, however, the stiffness of the flextures, and the friction between the rods and the bushing of the cage was too high. In addition, test sample was placed on one side of the cage and the load cells for force measurement were all placed on the other side of the cage. This made it very hard to determine the accurate displacement of the sample and the actual load on it.

Other Considerations

In addition to the problems discussed above, the MTI probes caused some problems also. MTI probes were used to measure the displacement of the test sample when it was actuated. However, it was difficult to get repeatable displacement measurements for the same test at the beginning. This turned out to be caused by problems in calibrating the MTI probes, such as finding the peak value. The MTI probes has to be calibrated very carefully.

BEST AVAILABLE COPY

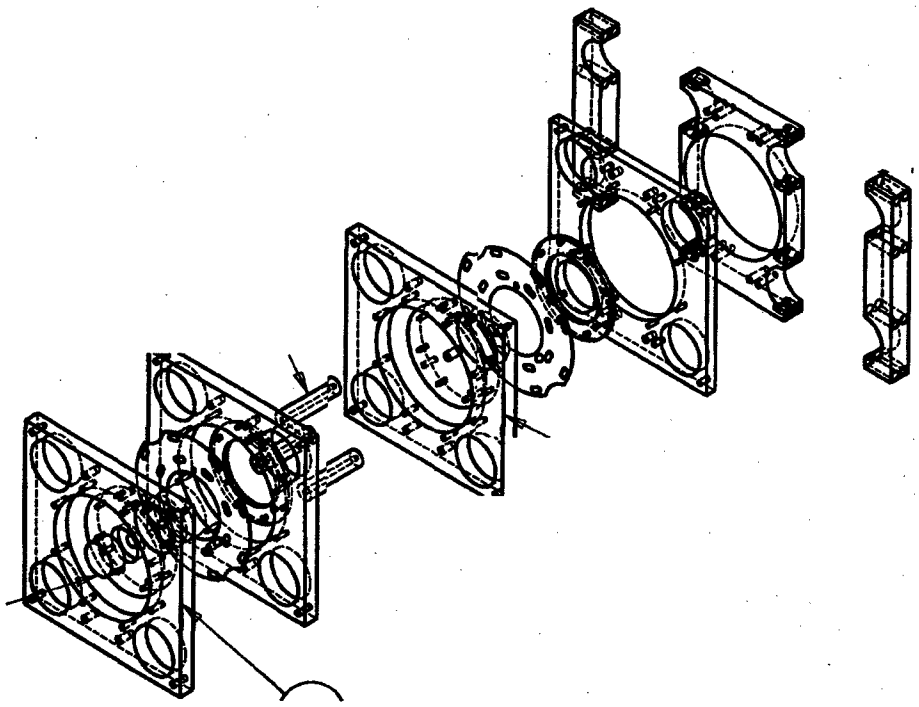

Figure 3-11: The Original Cage System for Load Transfer and Protection

Another remaining problem is the different force measurement from Entan and Kistler load cell as shown in Table 3-3. The measurement from Kistler is very reliable which will be demonstrated later in this chapter. The difference is caused by Entran load cell which is a strain gauge type load cell which needed to be calibrated every time before it is used.

From the discussion above, we can see that the alignment and the load transferring device of the component tester should be improved or replaced. Some modification on the existing cage could not guarantee the improvement of performance, therefore, a new design was made and built to replace the cage assembly.

3.4 Re-design of the Load Transfer Device

3.4.1 Initial design

The objectives of this design was to replace the cage assembly and the alignment mechanism for accurate force and displacement measurements and safe tests. As a result, the alignment mechanism was replaced by the spherical joint connection between different mechanical parts, and the cage assembly was replaced by a linear bearing system. For a protection of the loading system, the bearing system was mounted on a plate which again was mounted on the four rods. A schematic view of this design is shown is Fig. 3-12.

From the figure we can see that the Kistler load cells (load cell1) is on the sample side and Entran load cell (load cell 2) is on the other side of the linear bearing. The connection between different parts are all spherical joints. In addition, the configuration of the loading systems can be changed freely according to request because we have designed and built different connectors.

3.4.2 Vibration Measurement and Improvement on the Design

To validate this new tester configuration, Polytec CLV 100 Laser Vibrometer was used to monitor the transverse vibration of the tester during test. The transverse vibration of different parts of the tester were monitored one by one. The information obtained from the test sample itself seemed to be more important. The transfer function of the test sample, a steel tube with the similar stiffness as the piezo stack, is shown in Fig. 3-13.

From the transfer function we can see the peak at about 400 Hz as well as other peaks.

BEST AVAILABLE COPY

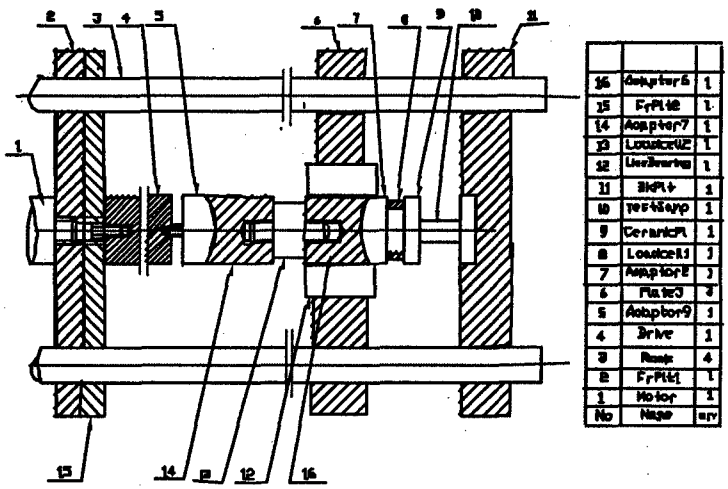

Figure 3-12: New Design of the Load Transfer System

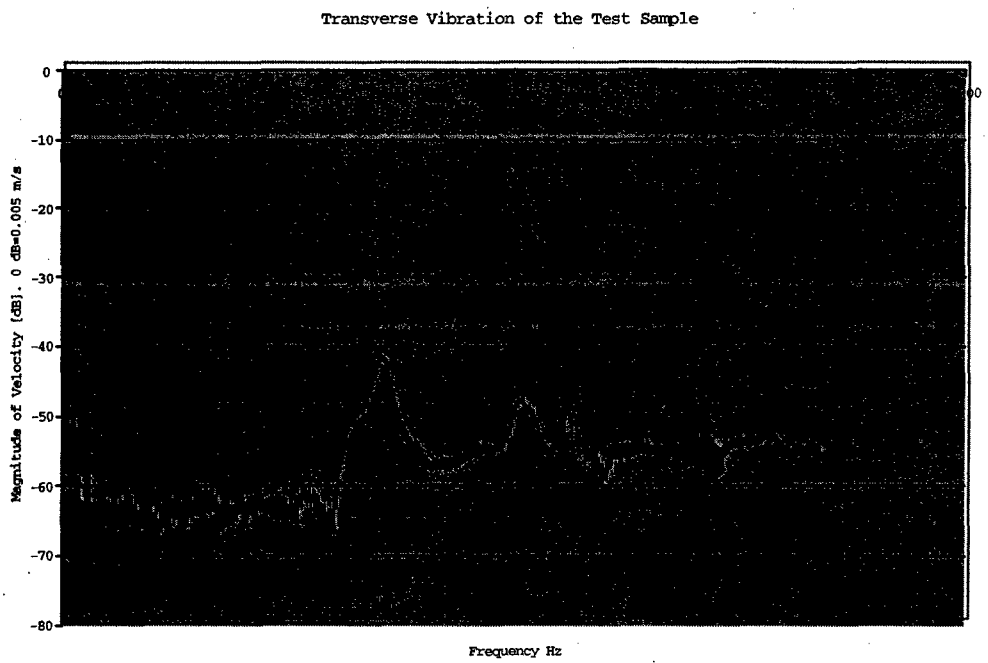

Figure 3-13: Transfer Function of the Transverse Velocity of Test Sample to the Input to Drive

Figure 3-14: Transverse Vibraton of Test Sample at Time 1

Figure 3-15: Transverse Vibration at Time 2

Pictures shown in Fig. 3-14 to 3-19 provides information in detail about the transverse vibration of the test sample at this frequency.

Fig. 3-14 shows the picture for the transverse vibration at the peak frequency for a start moment. The transverse vibration is more obvious when check the pictures in a timely order.

From this series of pictures, we could find that the left side of the sample had bad contact with the clamping plate of the tester. The lower left part of the sample vibrated much more severely than that of the upper left part. This means that the misalignment of the sample with the tester was larger than what the spherical joints could compensate for. For this reason, three springs were mounted between the joint and the plate, where the linear bearing was mounted, as shown in Fig. 3-20. The springs could provide enough preload to the sample so that the position of the sample could be adjusted carefully before the driving system pressed on it.

Pictures of the new design are shown in Fig. 3-21 and Fig. 3-22. The improvement seemed

BEST AVAILABLE COPY

Figure 3-16: Transverse Vibration at Time 3

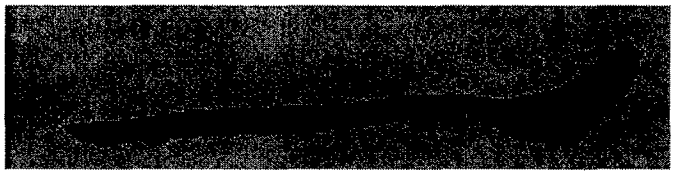

Figure 3-17: Transverse Vibration at Time 4

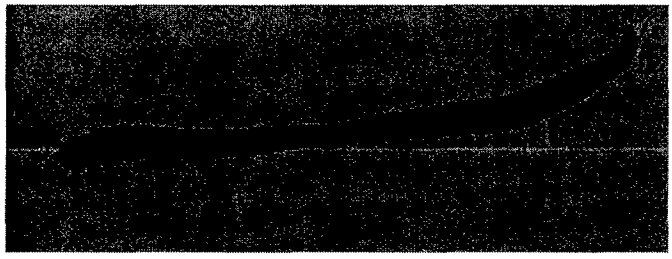

Figure 3-18: Transverse Vibration at Time 5

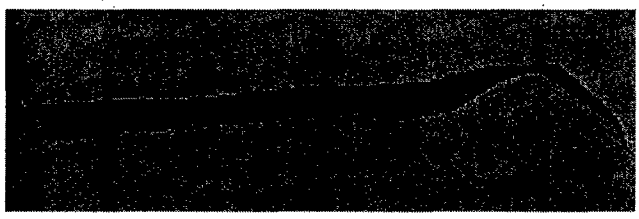

Figure 3-19: Transverse Vibration at Time 6

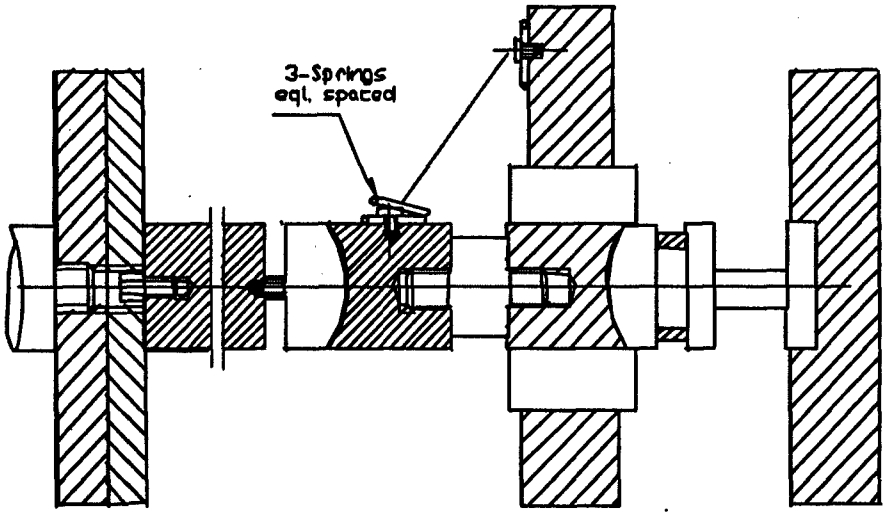

Figure 3-20: Improvement on the New Design by Providing Springs for Preload

very effective because the transverse vibration was suppressed.

3.5 Validation of the New Design

The validation tests were conducted to verify the correct measurement of displacement, force voltage and current or charge. The current and voltage validation is done by capacitance measurement of standard capacitor, and the force and displacement validation was done by stiffness measurement.

3.5.1 Stiffness Measurement

To measure the stiffness of sample correctly, the load cells, which measure force, and the Fotonic sensors, which measure displacement were calibrated first.

Load Cell Calibration

The load cells, Kistler 9212 and Entran miniature, were compared with the standard load cell of the Instron testing machine, Kistler 9300. The results showed a very good match while the calibration of the kistler load cell was adjusted to be 100 N/V and that of the Entran load

BEST AVAILABLE COPY

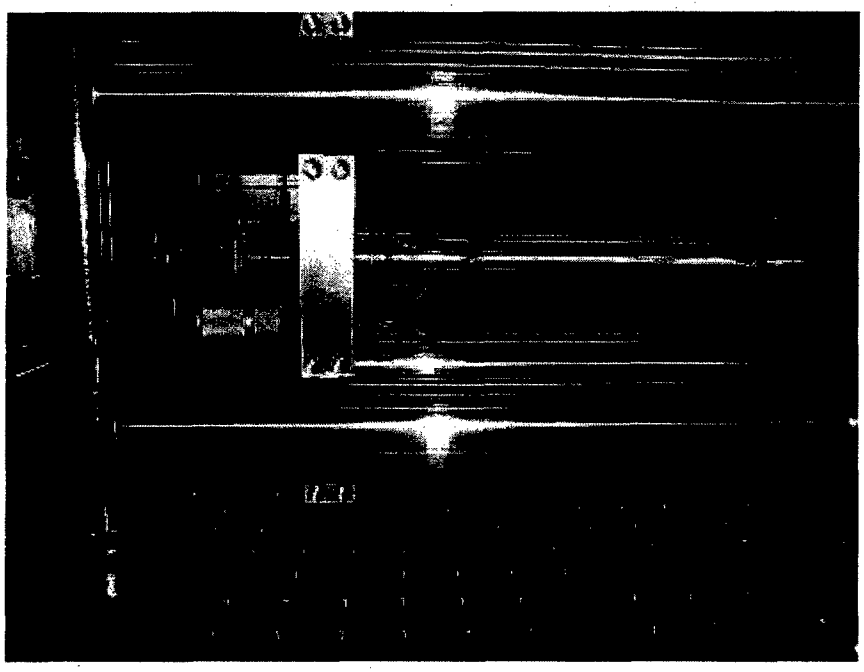

Figure 3-21: New Design of the Load Transfer Systems1

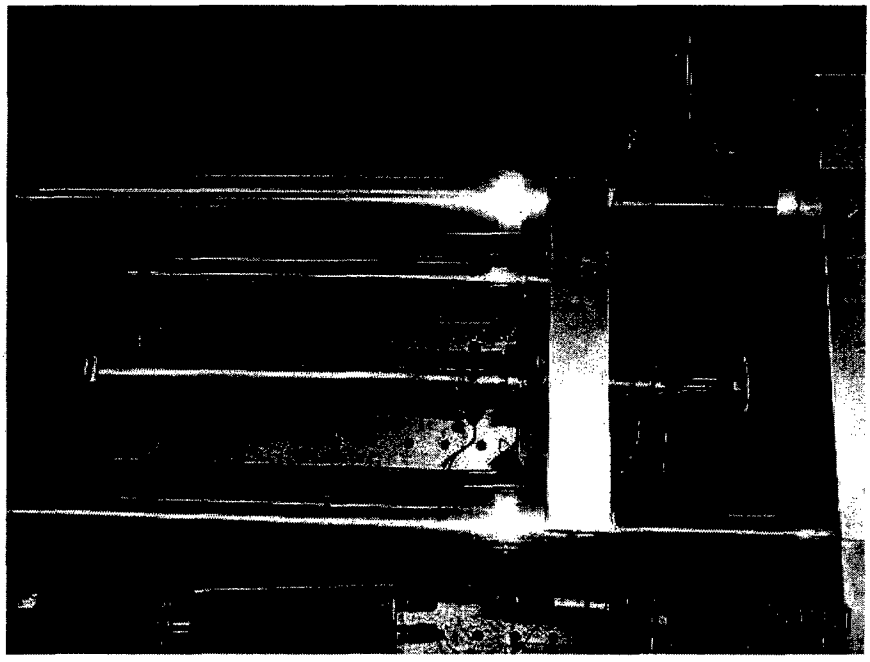

Figure 3-22: New Design of the Load Transfer System 2

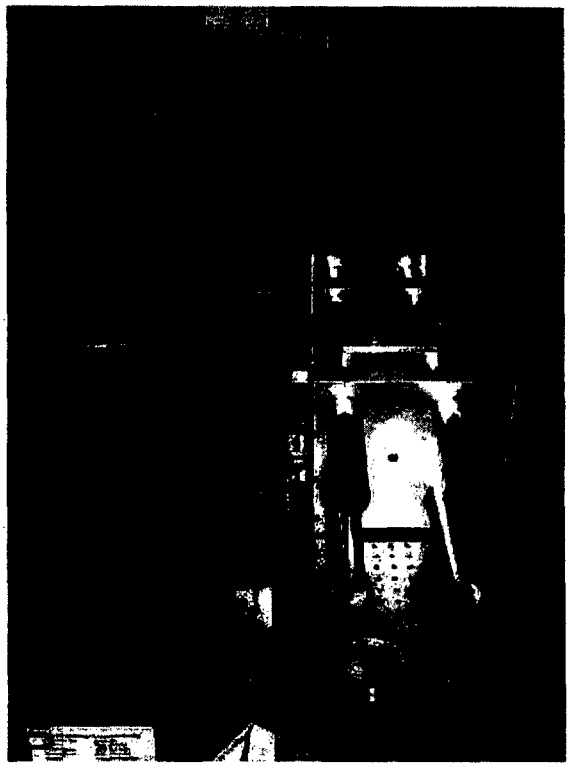

Figure 3-23: Overall View of the New Tester

BEST AVAILABLE COPY

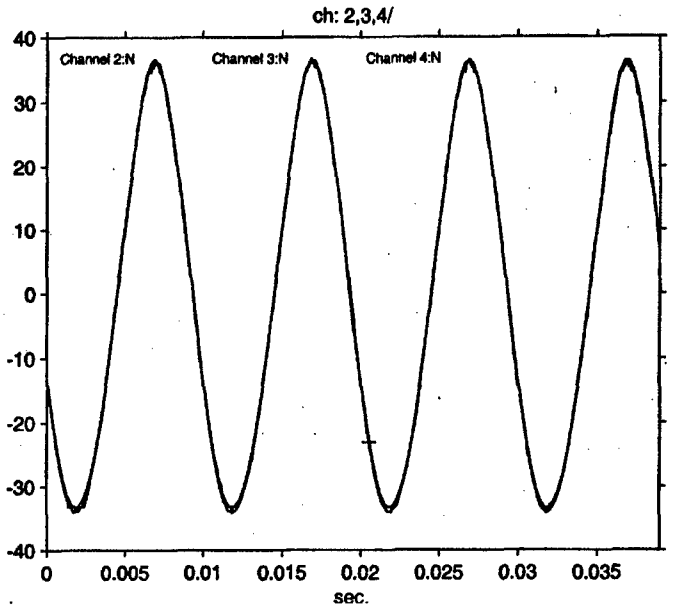

Figure 3-24: Force Calibration for the New Design

cell was 1570 N/V. The comparison is shown in Fig. 3-24. In this figure, channel 2,3 and 4 represents Kistler 9300, Kistler 9212 and Entran miniature respectively.

Fotonic Sensor Calibration

The displacement of the two Fotonic sensors, also called MTI probes, were compared with each other first. Then the displacement of a sample measured by the two Fotonic sensors (differential displacement) and strain gauges was compared. The results were comparable as seen in Fig. 3-25 and Fig. 3-26.

Stiffness Measurement

The sample used for the stiffness test was a steel tube: ϕ12.65 mm $\times$ 0.15 mm $\times$ 101.55 mm. Three equally spaced strain gages were bonded on the outer surface of the sample. The measured stiffness by the strain gages and the Fotonic sensors was compared in Fig. 3-27. The Kistler load cell was used to measure force.

The stiffness measured by strain gages and Fotonic sensors are very close as can be seen

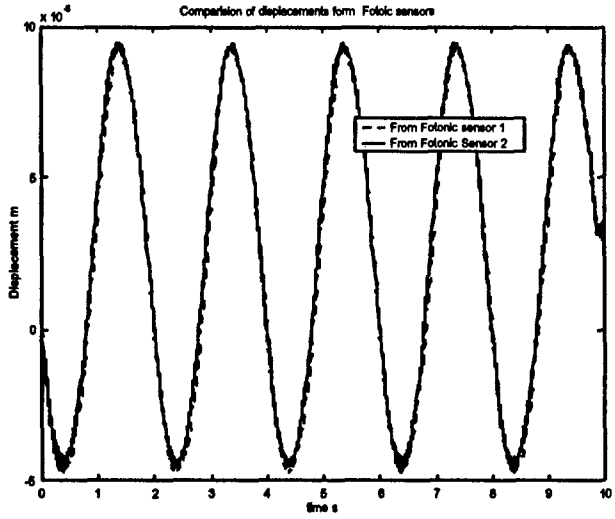

Figure 3-25: Comparison of Displacement measured by Two MTI Probes

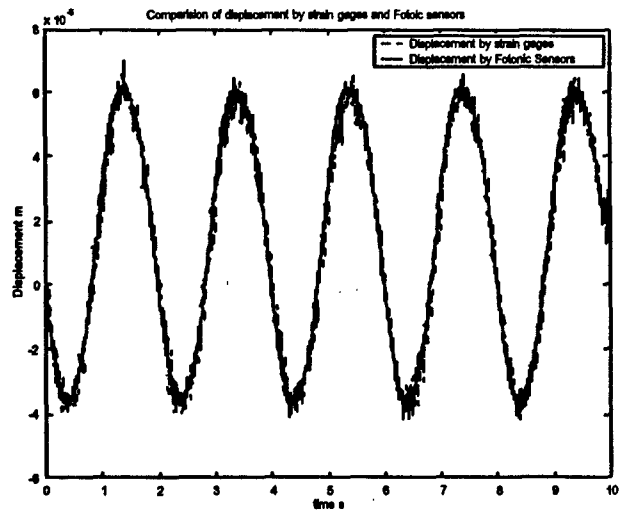

Figure 3-26: Comparison of Displacement Measured by MTI Probes and Strain Gages

BEST AVAILABLE COPY

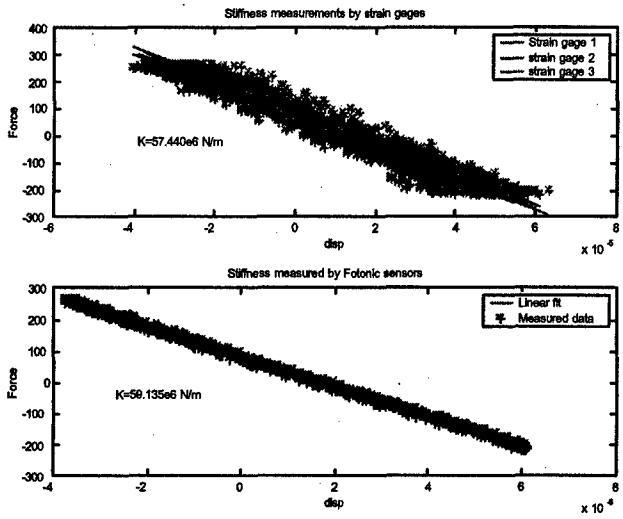

Figure 3-27: Stiffness Measured from MTI probes and Strain Gages

from the figure: 57.440×10^6 N/m and 59.135×10^6 N/m respectively.

3.5.2 Capacitance Measurement

The capacitor used for this test was a standard capacitor with a nominal capacitance of 800 nF, which was close to the capacitance of the Sumitomo piezo stack. The capacitance was determined by

$$Q = CV \tag{3.3}$$

Where Q was determined by integrating current monitored by the Trek amplifier over time, and V directly came from the voltage monitor of the Trek amplifier. A set of representative curves have been shown in Fig. 3-28.

As can be seen from the figure, the measured capacitance 791.39 nF has very good correlation with the nominal value 800 nF (1% error). The test was conducted at a frequency of 10 Hz. At this frequency and an applied voltage of 225 V, it is possible to compute the magnitude of

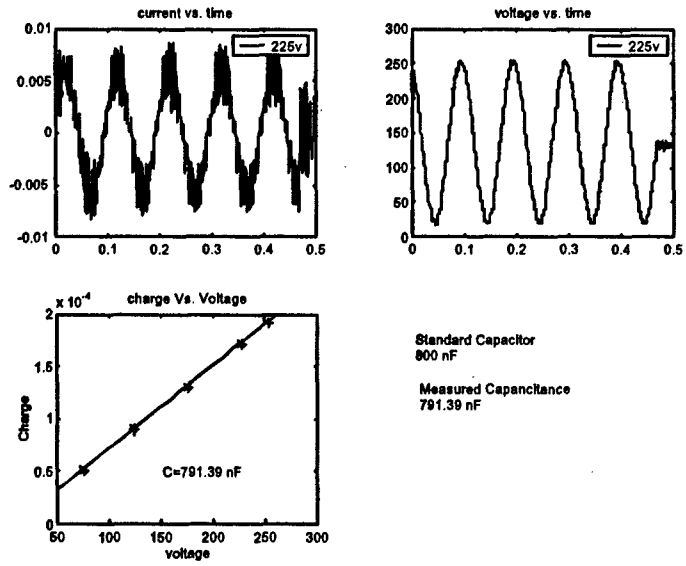

Figure 3-28: Capacitance Measurement for Standard Capacitor

the current in the circuit using equation 3.1 as following:

$$
\begin{aligned}
I &= 2\ fVF \\
&= 2 \times 3.14 \times 10 \times 225 \times 800 \times 10^{-9} \\
&= 11.30 \text{ mA}
\end{aligned}
$$

This magnitude of current is well within the range of an accurate measurement as can be seen from the figure. This proved out our suggestion made early about increasing the test frequency for linear and non-linear tests.

3.6 Summary

The renovation and validation of the component tester has been presented. The status of the existing component tester and the test results from it have been discussed. Both the electrical work and mechanical work could not be measured accurately in those tests. The poor electrical work measurement is caused by the low test frequency. The current magnitude computed for a typical linear test done before is about 0.025 mA, which is far below the

lowest value of an accurate measurement. The current monitor of the Trek amplifier is capable of measuring a current as low as about 0.1 mA. The current measurement problem has been solved by increasing the test frequency so that the current magnitude is high enough for accurate measurements. This has been demonstrated by a capacitance test. When the test frequency is raised to 10 Hz for a standard capacitor with a similar capacitance as the sample stack, the computed magnitude of current is 11.30 mA, and the current signal is very clean. Capacitance measurement of a standard capacitor (800 nF) has been used as a validation of the voltage and current measurement method. The actual measured capacitance of this capacitor is 791.39 nF.

The poor mechanical work measured is caused by the load transfer systems, and the misalignment during the tests. The cage assembly has been replaced by a linear bearing system, while the alignment mechanism has been replaced by spherical joint connectors. A laser vibrometer has been used to monitor the transverse vibration due to misalignment. An adjustment mechanism has been applied for fine adjustment of the position of the sample stack. Stiffness measurement of a steel tube has been chosen as the validation method for the force and displacement measurement. Displacement has been measured using both the MTI probes and 3 strain gages on the tube, while the force is measured by the Kistler load cell. The stiffness of which measured by the strain gages and MTI probes are very close which are 57.440×10^6 N/m, and 59.135×10^6 N/m respectively.

As a conclusion, the renovation of the component tester is validated, and the measurement methods for displacement, force, current and voltage are reliable.

Chapter 4

One Dimensional Linear and Non-linear Tests

In order to verify the theoretical prediction made in chapter 2, linear and non-linear tests were to be conducted. In this chapter, the linear and non-linear test approach and test results will be presented. The original feedback approach which was used by Lutz [Malindal, 1999] will be examined and the problems of this approach will be discussed, then a new test approach proposed. The linear and non-linear test results will be compared and contrasted at the end of this chapter.

4.1 FeedBack Test Approach

A feedback closed loop control method was originally chosen for the linear and non-linear tests. The idea was to provide the capability of testing a sample against a programmable impedance, either linear or non-linear. The input to this control loop is the displacement and force information from the Fotonic sensors and the load cells. The output from this control loop is the voltage level to supply to the driving stacks. For an assumed structure stiffness or impedance, the voltage level to the driving stacks is determined first by detecting what the desired change of force in the system is, then finding the corresponding change in electrical field to satisfy this requirement. This is analogous to finding a root of an equation using iteration method.

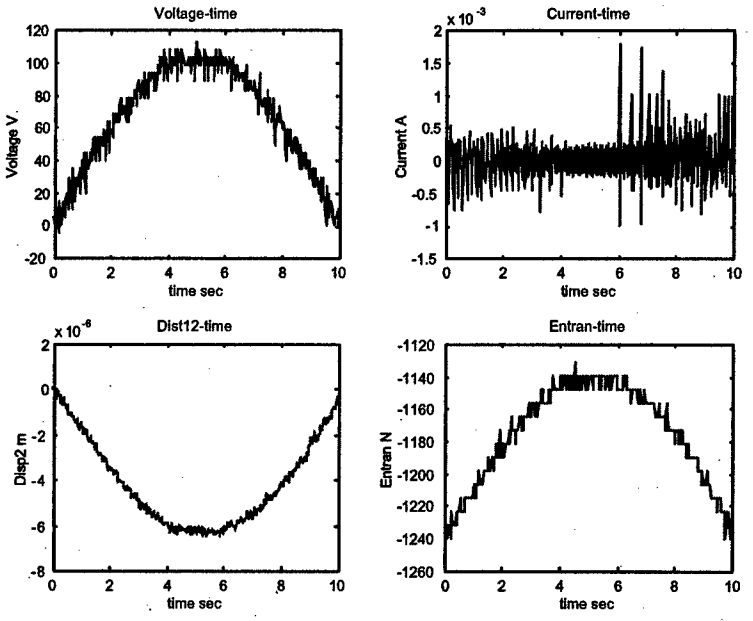

Figure 4-1: Time Trace for Linear Test at 0.05 Hz, Assumed Stiffness 3000 lbs/in

To do the linear and non-linear tests planned successfully, it is important to determine whether to use feedback close loop control or other methods. From the discussion in the last chapter, it has been demonstrated that increasing the test frequency could solve the problem of a noisy current signal. To verify this assumption for linear or non-linear tests, some tests have been done on the component tester before it was renovated. The renovation on the tester was mainly for improving force and displacement measurement. Renovation did not influence the current and voltage measurement at all since these two parameters were obtained from the current and voltage monitors of the Trek amplifier. Therefore, the linear tests should still be valid for checking current and voltage measurement. Some of the test results have been shown in the following figures. The test frequency has been increased form 0.05 Hz to 10 Hz.

The input signal for these tests was half a sine wave. From Fig.4-1, Fig4-2 and Fig.4-3 we can see that at 0.05 Hz and 1 Hz the current signal is noisy as predicted, however, the system becomes unsteady at 10 Hz, thereby making the situation worse.

A MATLAB simulation of the process for the feedback controller to determine the voltage level for the driving stacks according to the applied voltage to the sample stack has been

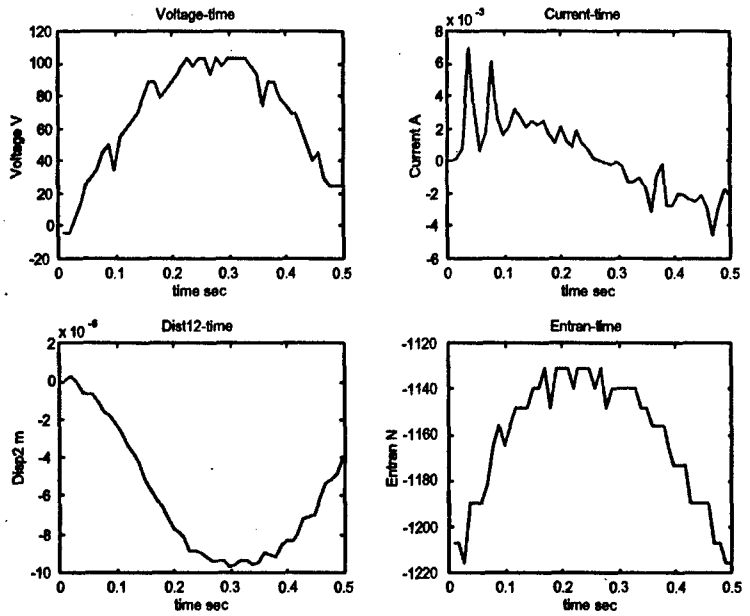

Figure 4-2: Time Trace for Linear Test at 1 Hz, Assumed Stiffness 3000 lbs/in

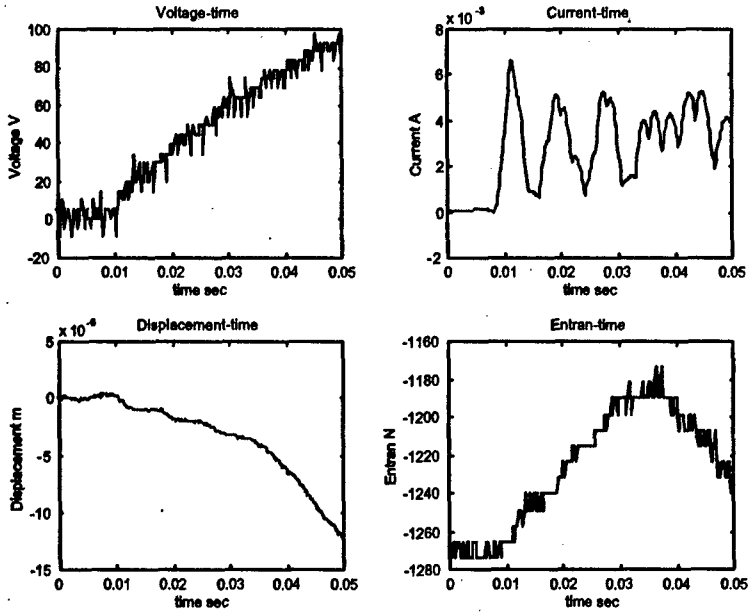

Figure 4-3: Time Trace for Linear Test at 10 Hz, Assumed stiffness 3000 lbs/in

conducted. A given sine wave was applied to the sample stack for an assumed structure stiffness. The input sine wave signal (one cycle) was represented by 2000 points for accuracy. The objective was to find the sine wave signal to the driving stacks represented by another set of 2000 corresponding points using iteration method. The simulation has shown that the computer requires about 25 minutes to find the 2000 corresponding voltage value. If reducing the points to 100, it still need about 150 seconds. However, to drive the test at 10 Hz, for example, requires the computer to find the 100 points or 2000 points within 0.1 seconds. This is a probable cause for why the system goes unsteady when testing at 10 Hz. A different method should be considered for successful linear and non-linear tests.

4.2 FeedForward Test Approach

From the discussion of the last section, it is unlikely to determine the drive voltage for the driving stacks using feed back controller. A possible solution is to solve for the driving voltage in advance, which leads to the feed forward open loop control method. The principle of this method has been shown by the block diagram in Fig. 4-4.

From Fig.4-4, it was seen that a Voltage-Force model is required to compute the voltage to the driving stacks. The material properties of the test sample Sumitomo stack are also needed. The non-linear functions shown in this figure could also be linear functions. An easier way to perform the linear tests will be shown later in this chapter.

4.3 Material Properties of Test sample

The material properties of the test sample Sumitomo stack is required not only in theoretical prediction, but also in defining the linear and non-linear functions, determining the voltage-displacement relation and establishing the Voltage-Force model. The methods used to measure the material properties in this section are those methods validated in Chapter 3.

4.3.1 Test Sample Physical Parameters

The test sample chosen is the Sumitomo stack MLA-20B for comparison with the data obtained by Malinda. The physical parameters are shown in Table 4.1

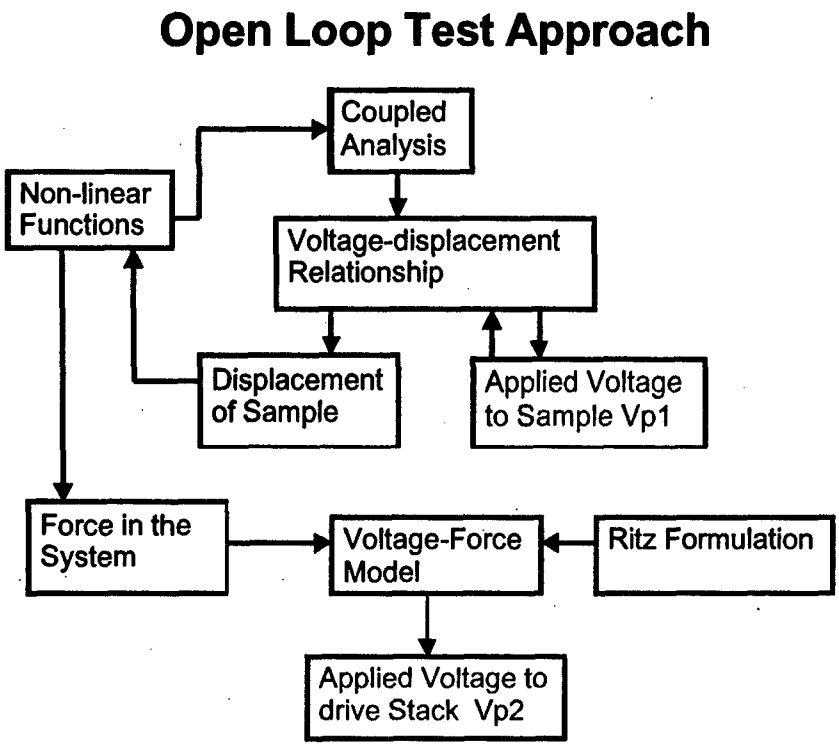

Figure 4-4: Feedforward open loop test approach

Total Length mm	41
Active Length mm	37
Section Area mm^2	23.4
Layer Thickness mm	0.18
Number of Layers	200
Max. Applied Voltage V	250

Table 4.1: Sumitomo Stack Physical Parameters

4.3.2 Stiffness and Elastic Constants

The stack stiffness test were performed on the component tester. The sample was placed on the clamping plate, then pressed and held by the three springs. The position of the stack was carefully adjusted to make sure it had a good contact with the clamping plates. After that, a preload was applied to the stack gradually while the Entran load cell was used to monitor the increase of the preload. The preload was maintained to be around 150 N and this preload was used for all of the tests including both the linear and nonlinear tests for the Sumitomo stack. It was found that preload had some influence on the test results and it was necessary to minimize it.

The tests were done through the actuation of one long stack in the loading systems. This configuration was kept through out all the tests including linear and non-linear tests. The driving signal to the driving stack was a sine wave with a frequency of 10 Hz and voltage level of 160 V, 200 V or 240 V. The Sumitomo stack was tested at both open circuit and short circuit conditions. k^D and k^E were found through the ratio of force to displacement measured, while s_{33}^D and s_{33}^E were found from the following equations:

$$s_{33}^D = \frac{A}{k^D l} \tag{4.1}$$

and

$$s_{33}^E = \frac{A}{k^E l} \tag{4.2}$$

The measured value for $k_{p1}^D 10^6$ N/m have been shown in Table 4.2, where Test 1, 2 , 3 indict that the driving voltage of the driving stack is 160 V, 200V and 240 V respectively, and it was the same in the tables for S_{33}^D, K^E and S_{33}^E. Measured Value for S_{33}^D 10^{-12} m^2/N, k_{p1}^E 10^{-12} N/m and S_{33}^E 10^{-12} m^2/N has been listed in Table 4.3, Table 4.4 and Table 4.5 respectively.

Typical time trace and force-displacement relation curves are shown in Fig.4-5 and Fig. 4-6.

4.3.3 Capacitance and Dielectric Constant

The capacitance of the Sumitomo stack was measured in the same way as the standard capacitor was measured in Chapter 3. Here the Sumitomo stack was placed on a support to restrain it

	k_{p1}^{D} 10^6 N/m							
Test1	39.983	39.996	40.024	40.039	40.051	39.974	40.086	39.865
Test2	41.107	40.988	41.049	41.058	41.077	41.094	41.015	41.125
Test3	41.749	41.635	41.654	41.708	41.712	41.727	41.747	41.763
Average	40.924							

Table 4.2: Sumitomo Measured Stiffness at open Circuit,

	S_{33}^{D} 10^{-12} m^2/N							
Test1	15.865	15.835	15.812	15.801	15.795	15.791	15.821	15.777
Test2	15.385	15.430	15.407	15.403	15.396	15.390	15.378	15.420
Test3	15.148	15.190	15.183	15.163	15.162	15.157	15.149	15,143
Average	15.458							

Table 4.3: Sumitomo Stack Measured Compliance st Open Circuit

	k_{p1}^{E} 10^{-12} N/m							
Test1	20.872	20.904	20.914	20.930	20.949	20.955	20.935	20.972
Test2	20.865	20.885	20.899	20.913	20.931	20.932	20.950	20.953
Test3	20.884	20.932	20.970	20.968	21.007	21.027	21.037	21.052
Average	20.943							

Table 4.4: Sumitomo Stack Measured Stiffness at Short Circuit

	S_{33}^{E} 10^{-12} m^2/N							
Test1	30.301	30.255	30.239	30.216	30.188	30.180	30.210	30.155
Test2	30.311	30.282	30.261	30.242	30.216	30.214	30.188	30.183
Test3	30.282	30.214	30.158	30.162	30.106	30.078	30.063	30.041
Average	30.198							

Table 4.5: Sumitomo Stack Measured Compliance at Short Ciucuit

BEST AVAILABLE COPY

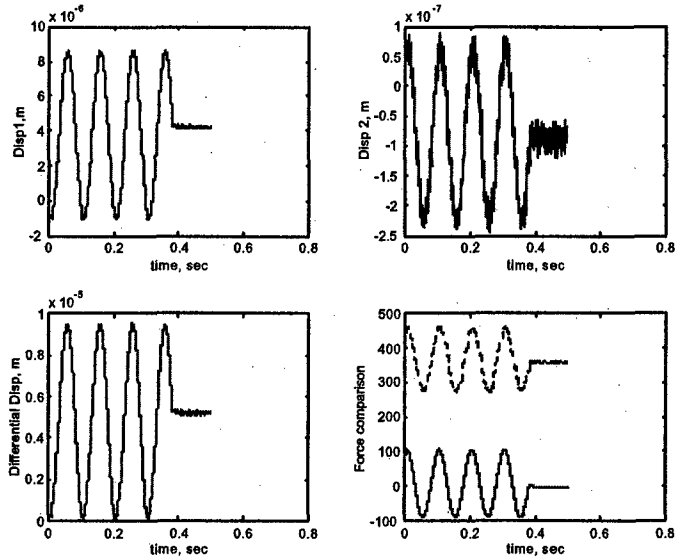

Figure 4-5: Time Trace of Displacement and Force for Stack Stiffness Measurement

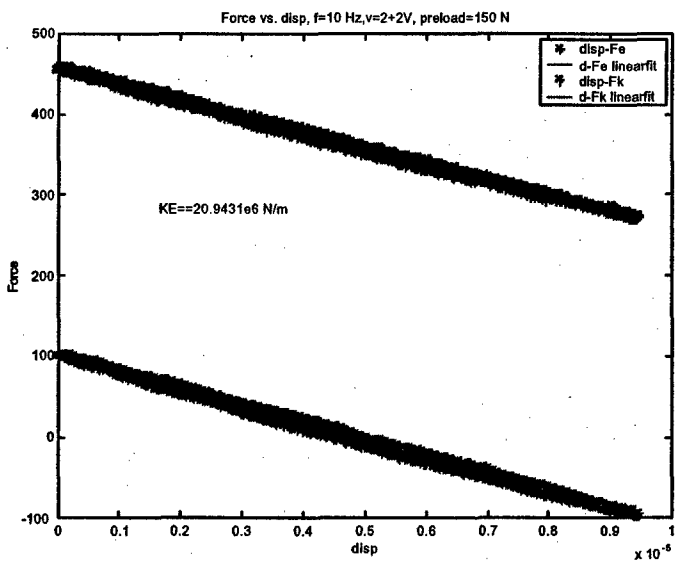

Figure 4-6: Force vs. Displacement for Stack Stiffness Measurement

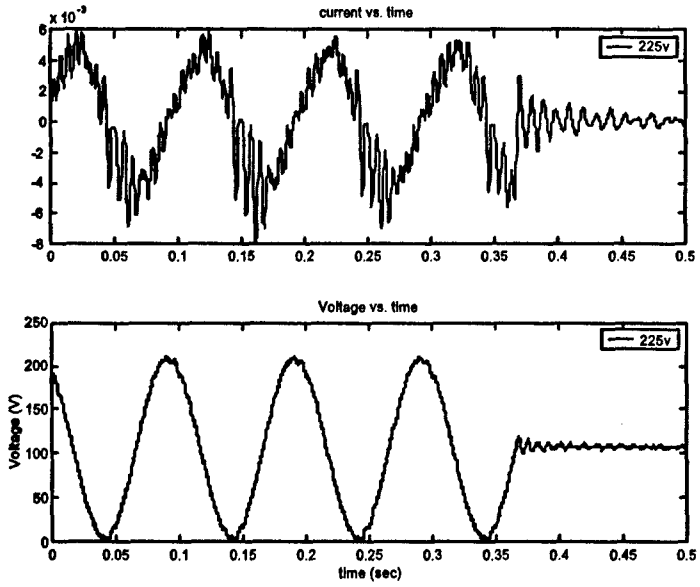

Figure 4-7: Time Trace of Current and Voltage for Capacitance Measurement

at either ends, while different levels of voltage were applied to it, while the current signal going to the stack was measured. The current measured was integrated over time to find the charge value which was then used to find capacitance as described by 3.3. The driving frequency was 10 Hz and the signal used as input to the Trek amplifier was

$$V_{appl} = \frac{1}{2}V_{\max}\sin(20\ \ t) + \frac{1}{2}V_{\max} \tag{4.3}$$

Where $V_{\max}$ ranges from 25 V to 225 V.

The dielectric constant under constant stress can be found from the measured capacitance for the stack. The equation used to determine ε_{33}^{T} is

$$\varepsilon_{33}^{T} = \frac{C^{T}t_{l}}{AN} \tag{4.4}$$

The measured capacitance and dielectric constant have been shown in Table 4.6. and the typical representative time trace curve and voltage-charge relation is shown in Fig. 4-7 and 4-8.

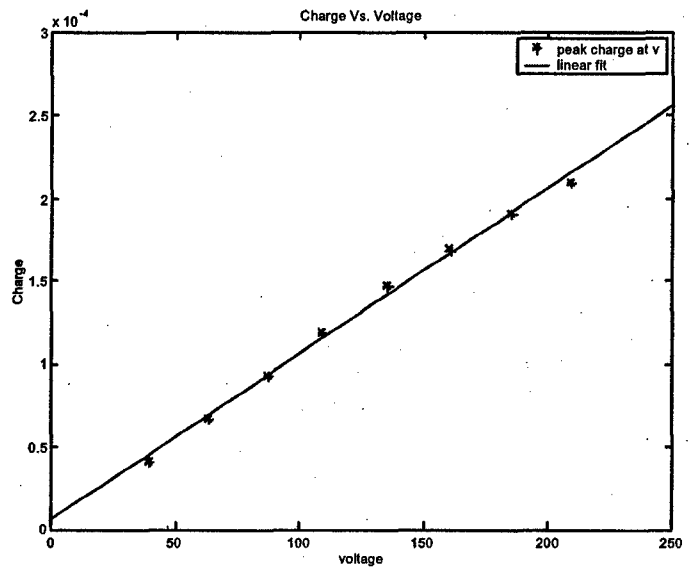

Figure 4-8: Charge vs. Volatge for Capacitance Measurement

C nF	1004.0	1008.0	999.79	999.37	1022.7	1013.8	1001.2
C Ave.	1006.98 nF						
ε_{33}^{T}	38730 F/m						
$\varepsilon_{33}^{T}/\varepsilon_0$	4376.3						

Table 4.6: Measured Capacitance and Dielectric Constant for Sumitomo Stack

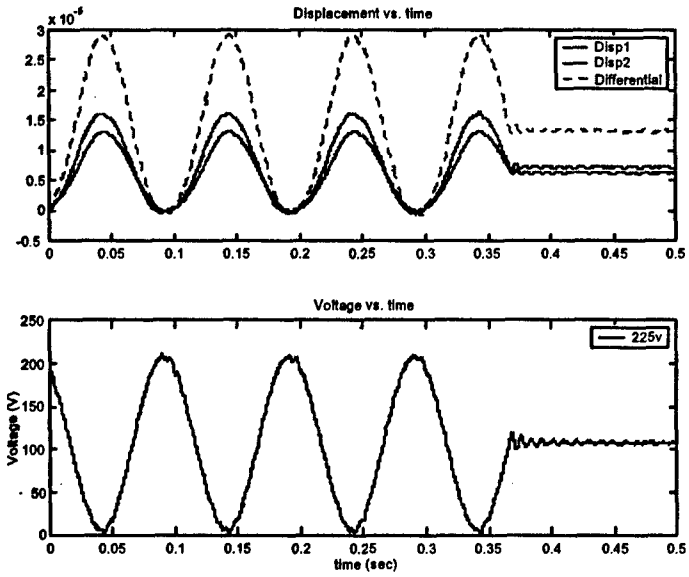

Figure 4-9: Time Trace of Displacement and Voltage for Stack d_{33} Measurement

4.3.4 Electromechanical Coupling Term

The test for measuring the electromechanical coupling term was similar to the capacitance measurement test. The driving frequency used was 10 Hz and the applied voltage to the driving stack was the same as shown in 4.3. Current and voltage was monitored in the same manner. The difference between the two tests was that the actuator was placed on the support and held in a horizontal position, while two Fotonic sensors were used to measure the displacement of the Sumitomo stack during actuation. The electromechanical coupling term was found using the following equation.

$$d_{33} = \frac{(\frac{x}{V})t_l}{l} \tag{4.5}$$

The measured electromechanical coupling term was shown in Table 4.7. and the typical representative time trace curve and voltage-displacement relation is shown in Fig. 4-9 and 4-10.

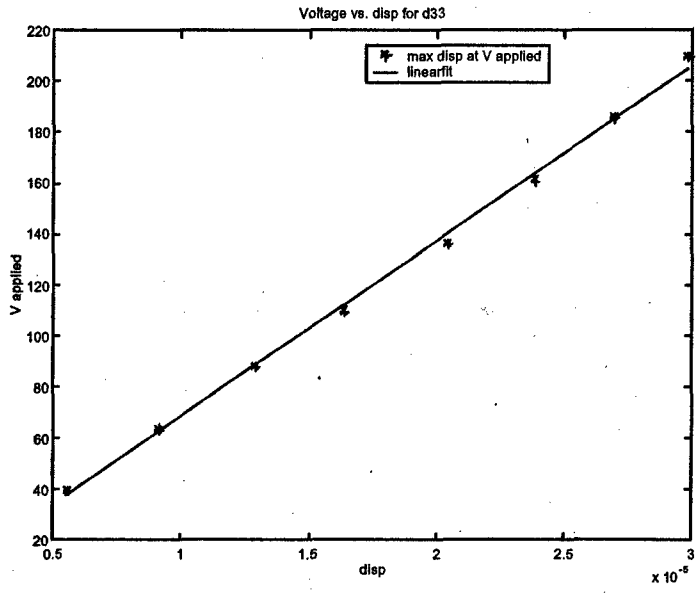

Figure 4-10: Displacement vs. Voltage for Stack d_{33} Measurement

4.3.5 Material Coupling Coefficient

The material coupling coefficient can be determined based on the material properties which have be measured using equation 1.1. The computed the material coupling coefficient k_{33} for Sumitomo stack was 0.6928.

4.3.6 Material Properties Summary

The measured material properties are summarized in Table 4.7. The accuracy of the measured material properties of the Sumitomo stack can be examined through the equation which related s^D and s^E:

$$s^D = s^E - d_t(\varepsilon)^{-1}d \tag{4.6}$$

For one dimensional systems, equation 4.6 can be simplified as

$$s_{33}^D = s_{33}^E - d_{33}(\varepsilon_{33}^T)^{-1}d_{33} \tag{4.7}$$

	Specification	Measured Value
Stiffness k^E 10^6 N/m		20.934
Stiffness k^D 10^6 N/m		40.924
Elastic Constant s_{33}^E 10^{-12} m^2/N		30.198
Elastic Constant s_{33}^D 10^{-12} m^2/N		15.458
Capacitance nF	800±20%	1006.98
Dielectric Constant $\varepsilon_{33}^T/\varepsilon_0$	3570	4376.3
Electromechanical Coupling d_{33} 10^{-12} m/V	778	728.987
Material Coupling Coefficient k_{33}		0.6928

Table 4.7: The Measured Material Properties for Sumitomo Stack

Substitute the material properties listed in Table 4.7, we can find S_{33}^D:

$$\begin{aligned} s_{33}^D &= 30.198 \times 10^{-12} - \frac{(728.987 \times 10^{-12})^2}{4376.3 \times 8.85 \times 10^{-12}} \\ &= 16.477 \times 10^{-12} \end{aligned}$$

There is only a 6% error between the computed s_{33}^D and the measured s_{33}^D in the table.

4.4 Actuating Voltage for Test Sample

4.4.1 Linear and non-linear Functions

With the material properties of the Sumitomo stack measured, it is possible to rewrite equations 2.6, 2.7 and 2.8 for the convenience of analysis. The three loading functions can be written in the form of equation 2.48:

$$f_{lin} = \alpha k_{p1}^E x \tag{4.8}$$

$$f_{non1} = \alpha k_{p1}^E \cdot 41x \cdot \exp\left(-5.45\left(\frac{x}{x_{free}}\right)^{0.5}\right) \tag{4.9}$$

$$f_{non2} = \alpha k_{p1}^E \cdot 0.5x_{free} \tanh\left(66\frac{x}{x_{free}}\right) \tag{4.10}$$

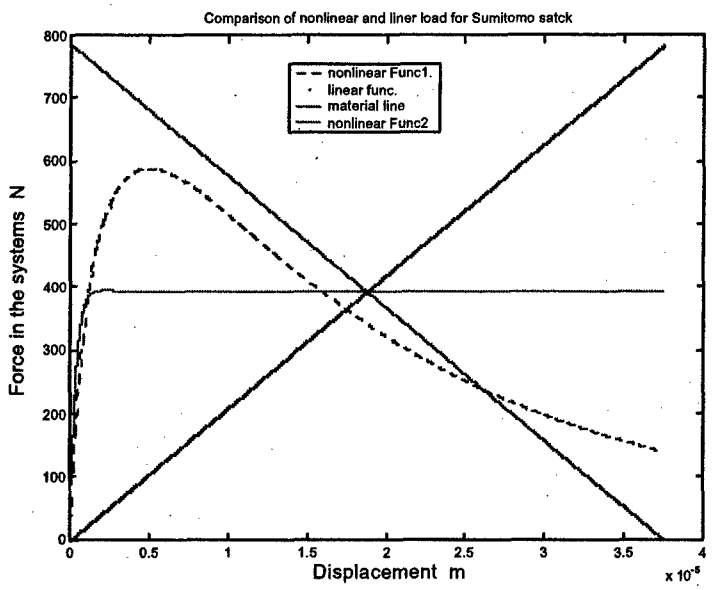

Figure 4-11: Linear and Non-linear Functions in terms of Displacement of the Actuator

And the material load line can be written as:

$$f_{material} = k_{p1}^{E} x_{free} - \alpha k_{p1}^{E} x \tag{4.11}$$

Where α is the stiffness ratio,which is the same as in equation 2.44 and 2.63. x_{free} is the maximum free displacement of the Sumitomo Stack, which can be expressed as

$$x_{free} = V_{\max} d_{33} \frac{l}{t_t} \tag{4.12}$$

The new linear and non-linear loading functions in terms of displacement have been shown in Fig. 4-11.

4.4.2 Actuating Voltage for Sumitomo Stack

The actuating voltage is not an important parameter for linear tests as long as the voltage is high enough for accurate current measurement. However, from the Fig. 4-11, we can see that the initial stiffness of the non-linear functions shown is very high. In order to allow the Sumitomo

stack to do more work under non-linear conditions than it could under linear conditions, the actuator should overcome this initial stiffness, and approach the maximum displacement or the displacement at balanced conditions, which are at the intersections of the material line and linear or non-linear loading lines. From the coupled analysis, however, we have found that the maximum displacement the actuator could approach is determined by the actuating voltage of the actuator.

To determine the actuating voltage for the test sample actuator, voltage-displacement relation from the coupled analysis as expressed by equation 2.15 was to be written in a convenient form. k_s for the linear and non-linear functions can be found by dividing the right hand side of equation 4.8, 4.9 and 4.10. Substitute these stiffness terms and the coefficients terms in K_{p1}^E and θ_1 expressed by equation 2.33 and 2.34, the new expression of the voltage-displacement relation for the linear and non-linear cases becomes:

Linear function:

$$V = \frac{1+\alpha}{d_{33}l} t_l \tag{4.13}$$

Non-linear 1:

$$V = \frac{1 + 41\alpha \exp\left(-5.45\left(\frac{x}{x_{free}}\right)^{0.5}\right)}{d_{33}l} x t_l \tag{4.14}$$

Non-linear 2:

$$V = \frac{x + \frac{1}{2}\alpha x_{free} \tanh\left(66\frac{x}{x_{free}}\right)}{d_{33}l} t_l \tag{4.15}$$

For $\alpha = 1$, the voltage-displacement relations for different loading functions are shown in Fig. 4-12.

A close check of the voltage-displacement curve of non-linear function 1 has shown that the voltage should be higher than 235 V for the actuator to overcome the initial stiffness and generate large enough displacement. A higher voltage, however, is too close to the maximum allowed voltage of the actuator and could destroy the actuator. For non-linear function 2 this voltage can go lower, while for linear functions, it could go even lower. However, for the purpose of comparison of the linear and non-linear systems, we should drive the actuator at the same magnitude of voltage. 235 V has been chosen as the magnitude of test sample actuating voltage for all of the actuation tests in this research. As discussed in the stack material properties

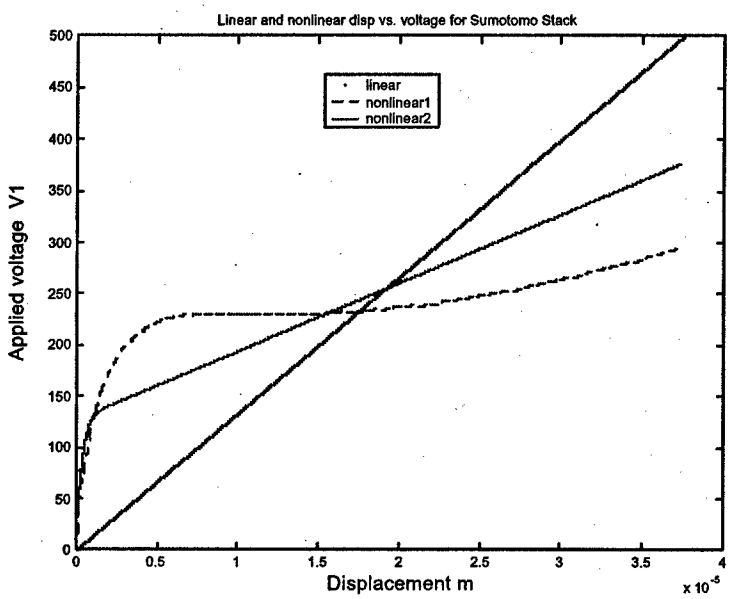

Figure 4-12: Voltage vs. Displacement from Coupled Analysis

measurement, an offset voltage was applied to the actuator to prevent the driving voltage from being negative, which may depolarize the sample. The applied voltage to the test sample, the Sumitomo stack, has been determined as

$$V_1 = 235\left(\frac{1}{2}\sin\left(20\ \ t + \frac{3}{2}\ \right) + \frac{1}{2}\right) \tag{4.16}$$

4.5 Voltage-Force Model

From the feed forward approach diagram shown in Fig. 4-4, it is obvious that an accurate Voltage-Force Model is critical in determining the driving voltage for driving stacks from the required force in the system. The model has been developed in the same way as that of the coupled analysis was develpoed in chapter 2. However, here there are three components instead of two: the test sample piezo stack, the structure (connectors and load cells), and the driving piezo stacks. The system is shown as in Fig. 4-13.

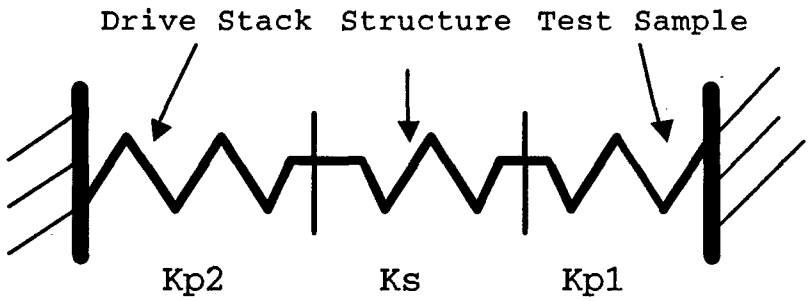

Figure 4-13: Three Component System for Voltage-Force Model

4.5.1 Model Development

The method used for the model development is the same as that used for the coupled analysis derived in Chapter 2. The governing equations for the piezo active materials are the simplified actuator equation and sensor equation for quasi-static cases as in Chapter 2.

For the sample stack, the equations are exactly the same as equation 2.10. For the convenience of discussion, they are listed here again:

$$\begin{bmatrix} K_{p1}^{E} & -\theta_1 \\ \theta_1 & C_{p1}^{S} \end{bmatrix} \begin{Bmatrix} x_1 \\ V_1 \end{Bmatrix} = \begin{Bmatrix} f_1 \\ Q_1 \end{Bmatrix} \tag{4.17}$$

For the driving stack, they can be expressed as

$$\begin{bmatrix} K_{p2}^{E} & -\theta_2 \\ \theta_2 & C_{p2}^{S} \end{bmatrix} \begin{Bmatrix} x_2 \\ V_2 \end{Bmatrix} = \begin{Bmatrix} f_2 \\ Q_2 \end{Bmatrix} \tag{4.18}$$

For the structure, it can be expressed as

$$k_s x_s = f_s \tag{4.19}$$

The force balance equation in the system is given by:

$$f_1 = f_2 = f_s \tag{4.20a}$$

The compatibility equation is given by:

$$x_1 = -\left(x_2 + x_s\right) \tag{4.21}$$

From equation 4.17, 4.18, 4.19, 4.20a and 4.21, we can find out that

$$f = \frac{\frac{\theta_1 V1}{K_{p1}^E} + \frac{\theta_2 V2}{K_{p2}^E}}{\frac{1}{K_{p1}^E} + \frac{1}{K_{p2}^E} + \frac{1}{K_s}} \tag{4.22}$$

Assuming the same mechanical and electrical mode shapes as described by equation 2.31 and 2.32, we can find the coefficients in equation 4.22 using the same equations as shown in 2.33 and 2.34. Then the force model can be written as

$$f = \frac{d_{33p1} V1 + d_{33p2} V_2}{\frac{1}{K_{p1}^E} + \frac{1}{K_{p2}^E} + \frac{1}{K_s}} \tag{4.23}$$

Where $d_{33p1} = d_{33}\frac{l}{t_i}$ is the effective electromechanical coupling terms for the Sumitomo stack and d_{33p2} is that of the driving stack. From this equation we can see that if all the stiffness terms and the d_{33p2} are determined, we can find the driving voltage V_2 according to the sample voltage V_1 and the force in the system f. However, there are two problems which make it difficult to for us predict the driving voltage accurately using equation 4.23. First, this model is developed based on a simplified three component systems, assuming the system is clamped at both ends. Actually this is not true and there will be some displacement at both ends. An accurate model should include a few more springs in series or in parallel. Second, the three unknown coefficients in equation 4.23 should be measured accurately. Even if this has been done, the developed model still needs to be verified experimentally. For these considerations, we will determine the model in the form of this equation directly from experiments. This has been proven to be a very effective way.

4.5.2 Experimental Determination of model coefficients

The Voltage-Force expressed in equation 4.23 can be written as

$$f = aV_1 + bV_2 \tag{4.24}$$

where a and b are undetermined.

The two coefficients were determined in two steps. First, the test sample was actuated, while the driving stack was at constant electrical field, i.e. $V_2 = 0$. The magnitude of the applied voltage to the test sample varied from a small voltage to its maximum, while the force in the system was recorded. The coefficient a was found from the linear fit of the peak V_1 vs. peak f relation. Second, both the sample stack and the driving stack were actuated to find coefficient b using the determined a. Since it was determined that the magnitude of test sample actuating voltage would be 235 V for all tests, the voltage expressed by equation 4.16 has been applied to test sample. The voltage applied to the driving stack is in the same form as expressed by equation 4.16, while the magnitude of the voltage varied from the lowest to the highest. The phase and frequency of the applied voltage to sample stack and driving stack were all the same. The frequency was 10 Hz with a phase difference of zero.

The experimental voltage-force relations are shown in Fig. 4-14 and Fig. 4-15. The experimental determined Voltage-Force Model can be expressed as

$$f = 2.1394V_1 + 1.3859V_2 \tag{4.25}$$

4.6 Theoretical Predictions for systems driven by Sumitomo Stack

With the material properties measured, actuating voltage and frequency chosen and the Voltage-Force Model determined, it is possible toperform the linear and non-linear tests. The theoretical prediction of the electrical and mechanical work and actuation efficiency of the systems driven by the Sumitomo stack can provide some information for comparison. The linear and non-linear functions used are the same as those expressed in equation 4.8, 4.9 and 4.10. The driving

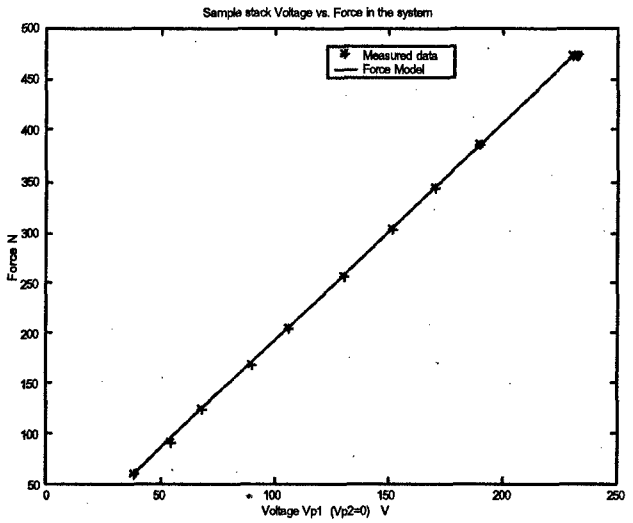

Figure 4-14: Force vs. Voltage V1 for Voltage-Force Model

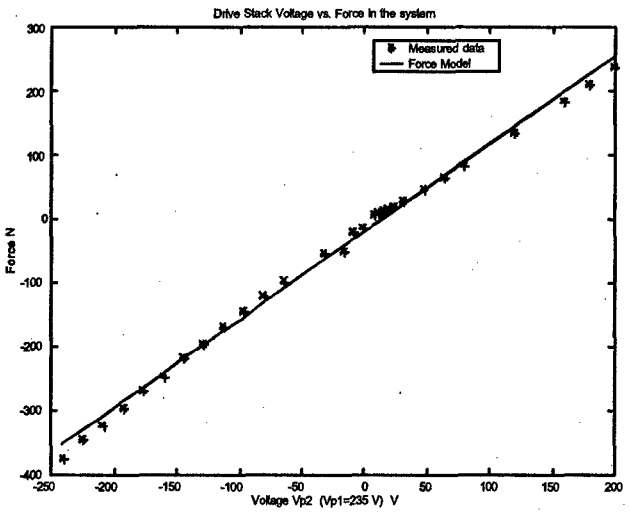

Figure 4-15: Force vs. Voltage V1 and V2 for Voltage-Force Model

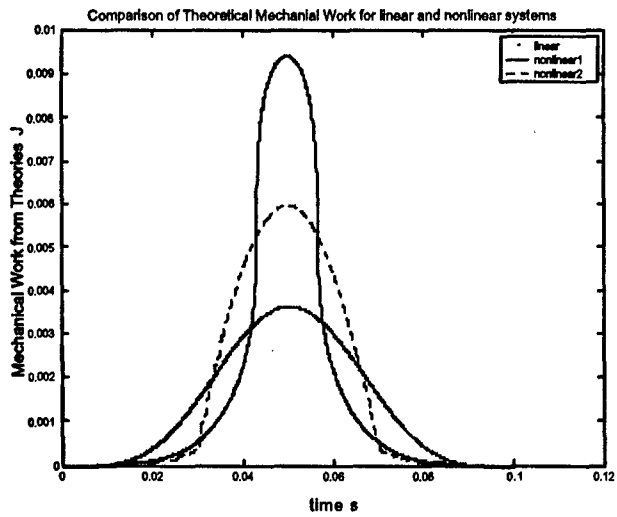

Figure 4-16: Prediction of Mechanical Work for Systems Driven by Sumitomom Satck

frequency for both the sample stack and the driving stack was 10 Hz and the actuating voltage of the sample stack was the same as expressed in equation 4.16. The stiffness ratio α is assumed to be 1. The results have been shown in Fig. 4-16, Fig. 4-17 and Fig. 4-18.

From these figures, we can obtain the similar information as was done in chapter 2. However, the system discussed here is real and the material properties used are measured. The mechanical work out of non-linear system1 is about 254% that of linear system, while the actuation efficiency of non-linear 1 is about 200% that of linear systems.

4.7 Linear Tests

As mentioned early, the linear tests have been done in a relatively easier way than the non-linear tests. Voltage was applied to both the sample stack, the Sumitomo stack, and the driving stack. The phase and the frequency of the applied voltage for the two stacks was all the same. The frequency chosen was 10 Hz and the phase difference was zero. The applied voltage to the sample stack was expressed by equation 4.16, while the voltage to the driving stack was either increased from zero to a higher magnitude gradually, simulating a higher structure stiffness or decreased from zero to a lower magnitude gradually, simulating a lower structure

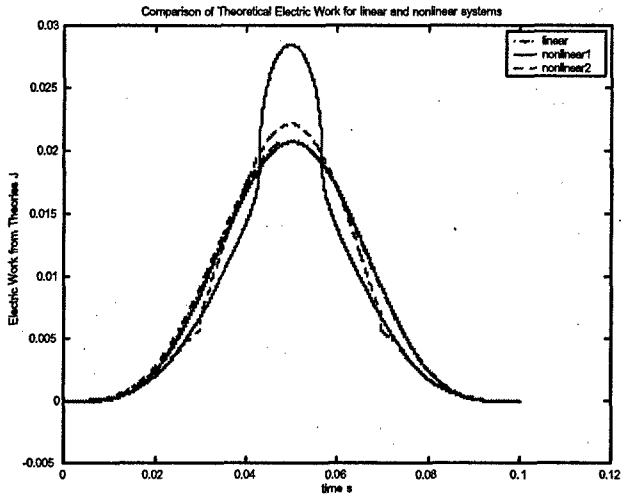

Figure 4-17: Prediction of Electrical Work for Systems Driven by Sumitomo Satck

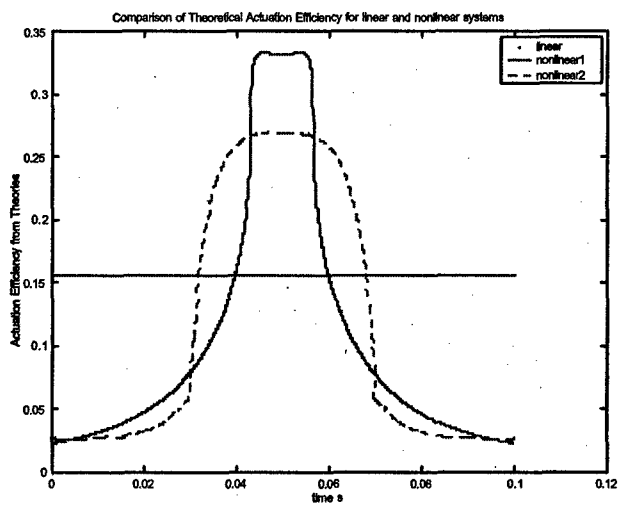

Figure 4-18: Prediction of Actuation Efficiency for Systems Driven by Sumitomo Satck

stiffness. During the voltage increasing or decreasing process, the displacement of the sample stack and the force in the systems was monitored carefully to prevent the sample stack from being over compressed by the driving stack or the sample stack dropping off. Effective stiffness of the structure was determined from the measured displacement and force data because the displacement of the structure was assumed to be the negative of that of the sample stack as expressed the compatibility equation 4.21.

The current and voltage in the circuit was obtained from the current and voltage monitor of the Trek amplifier, while the displacement and force data were taken from the Fotonic sensors, Kistler and Entran load cells.

The test results have been shown in the following figures. Fig. 4-19, Fig. 4-21 and Fig. 4-20 shows the measurement of the basic parameters. Fig. 4-22 shows the representative cycle for determining the effective stiffness, mechanical work, electrical work and actuation efficiency. These results have been shown in Fig. 4-23, 4-25, 4-24 and 4-26 where the experimental data were compared with the theoretical predications. The actuation efficiency was shown as a function of the stiffness ratio α.

The experimental mechanical and electrical work have been obtained from the following equations

$$W_M = \int_{x_0}^{x_f} F dx \tag{4.26}$$

$$W_E = \int_{t_0}^{t_f} VI dt \tag{4.27}$$

The experimental actuation efficiency was obtained from the ratio of the peak mechanical work to that of the electrical work.

The theoretical prediction for the mechanical work and electrical work was obtained from the following equations:

$$W_M = \frac{1}{2} N^2 \frac{A}{l} V_1^2 \varepsilon_{33}^T k_{33}^2 \frac{\alpha}{(1+\alpha)^2} \tag{4.28}$$

$$W_E = \frac{1}{2} N^2 \frac{A}{l} V_1^2 \varepsilon_{33}^T \left(1 - \frac{\alpha}{1+\alpha} k_{33}^2\right) \tag{4.29}$$

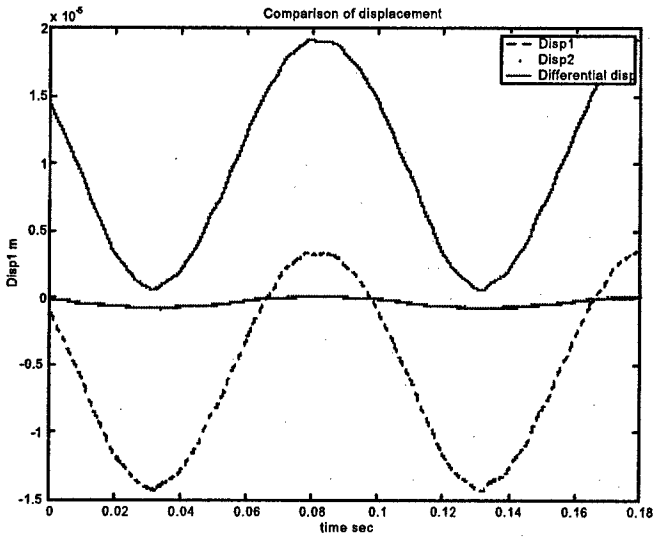

Figure 4-19: Typical Displacement Measurement for Linear Tests

And the actuation efficiency was from the ratio of the two equations as expressed by equation 2.45.

From these figures, we can see that the experimental data of the mechanical work, electrical work and actuation efficiency correlate with the theoretical prediction very well.

4.8 Non-linear Tests

The test approach of non-linear tests was exactly as shown in Fig. 4-4. Voltage with the same frequency and the same phase were applied to both the sample stack and the driving stack. However, unlike in linear tests, the applied voltage to the driving stack was determined according to the Voltage-Force Model, while force was determined from the chosen non-linear loading functions and voltage applied to the sample stack was the same as expressed by equation 4.16. The frequency chosen was still 10 Hz and the phase difference of the two applied voltage was zero. The current and voltage in the circuit was obtained from the current and voltage monitor of the Trek amplifier, while the displacement and force data was taken from the Fotonic sensors and Kistler and Entran load cells.

The experimental mechanical and electrical work has been obtained using equation 4.26 and

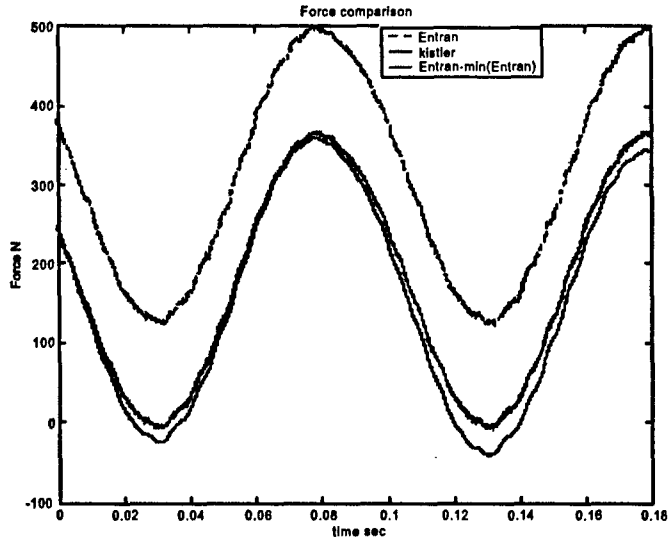

Figure 4-20: Typical Force Measurement for Linear Tests

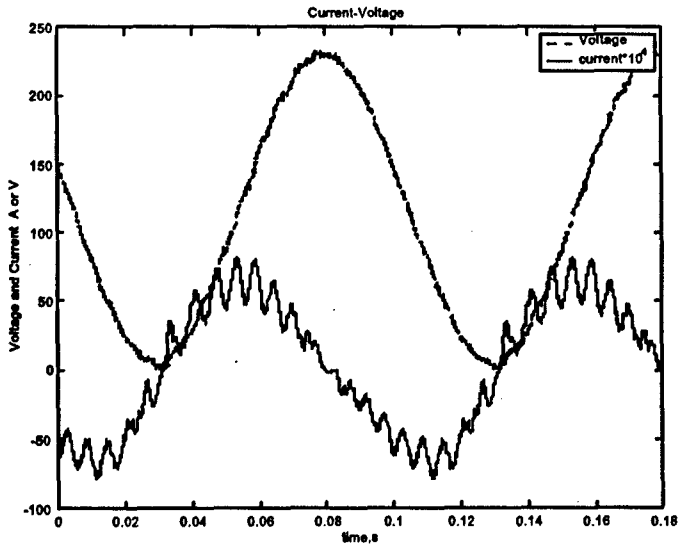

Figure 4-21: Typical Current and Voltage Measurement for Linear Tests

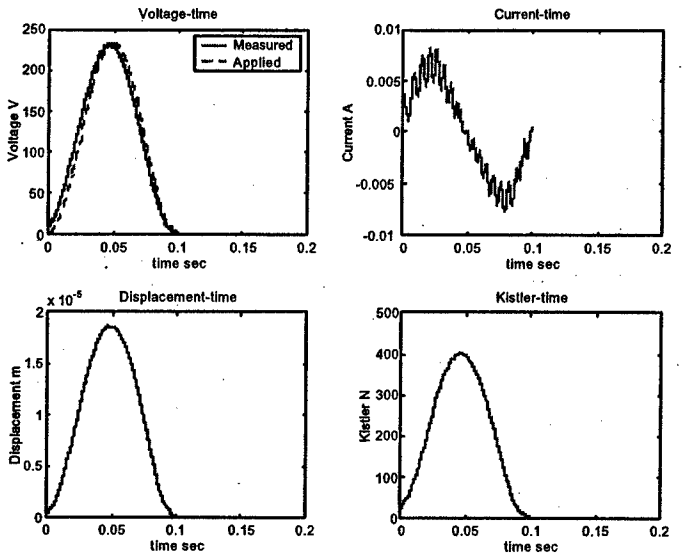

Figure 4-22: The Resentative Cycle for Computing Work Terms

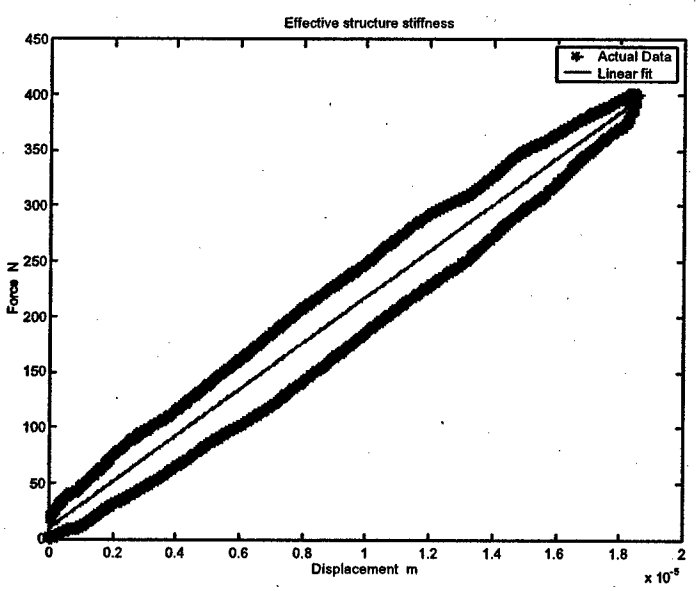

Figure 4-23: Typical Effective Stiffness Determined from Actaul Data

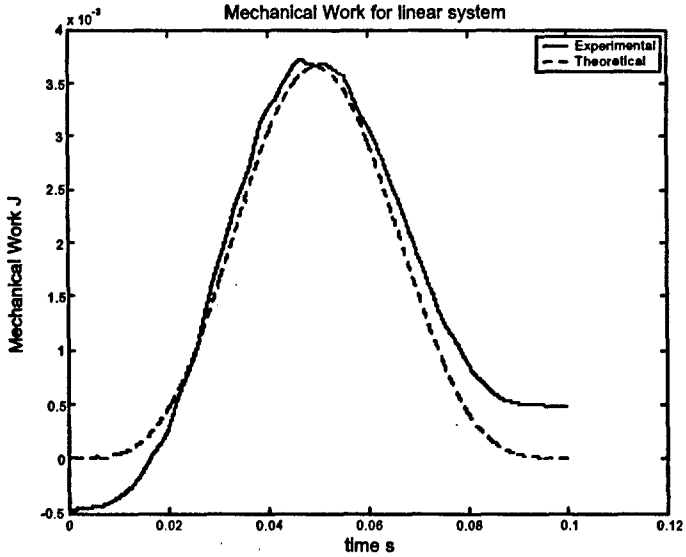

Figure 4-24: Typical Mechanical Work from Theory and Experiment for Linear Test

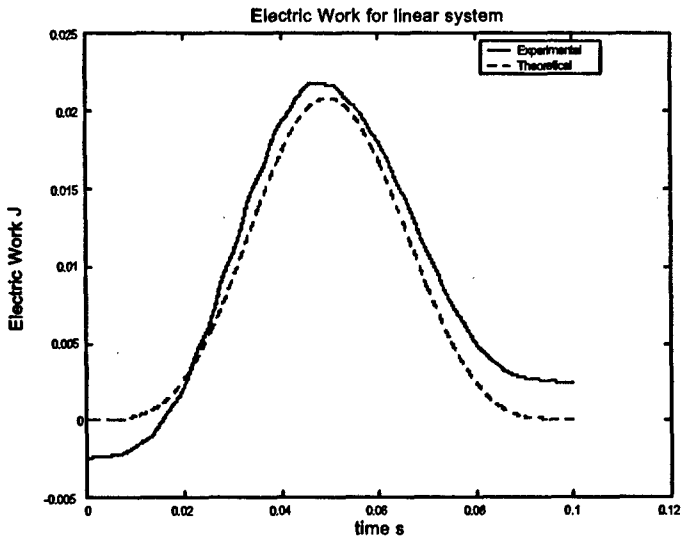

Figure 4-25: Typical Electrical Work from Theory and Experiment for Linear Tests

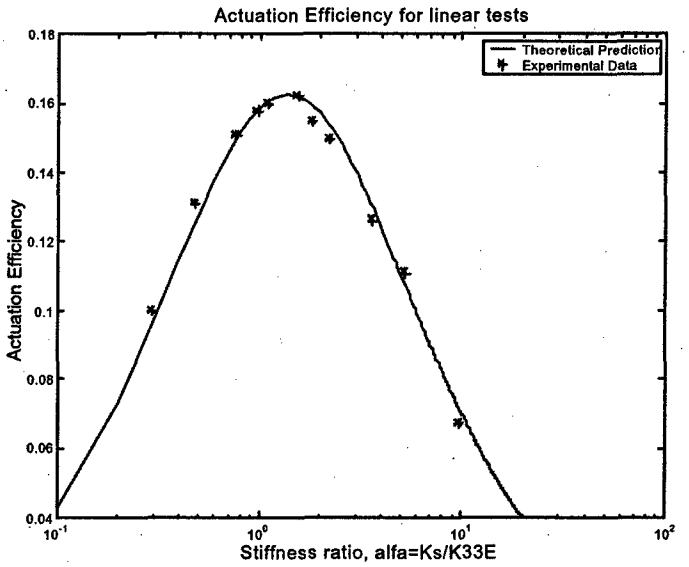

Figure 4-26: Actuation Efficiency as a Function of Stiffness Rato Ks/K_{33}^{E} for Linear Tests

equation 4.27. Similarly the actuation efficiency was determined by the ratio of peak mechanical work to peak electrical work.

The theoretical mechanical work and electrical work has been determined by the following equations which is the same as expressed in Chapter 2 and are listed here for convenience. α was chosen to be 0.96 for safety consideration.

$$W_M = \frac{c_{33}^E A}{l} \alpha \int_{x_0}^{x_f} c_x x dx \tag{4.30}$$

$$W_E = \frac{c_{33}^E A}{l} \int_{x_0}^{x_f} (1 + \alpha c_x) x dx + \frac{c_{33}^E A}{l} \left(\frac{1}{k_{33}^2} - 1 \right) \int_{x_0}^{x_f} (1 + \alpha c_x)^2 x dx + \tag{4.31}$$

$$+ \frac{c_{33}^E A}{l} \alpha \left(\frac{1}{k_{33}^2} - 1 \right) \int_{x_0}^{x_f} (1 + \alpha c_x) x^2 \frac{dc_x}{dx} dx \tag{4.32}$$

The actuation efficiency was determined by the ratio of equation 4.30 and equation 4.31. For non-linear system 1 and 2, the non-linear part of the stiffness is expressed by equation 2.49 and equation 2.50 respectively.

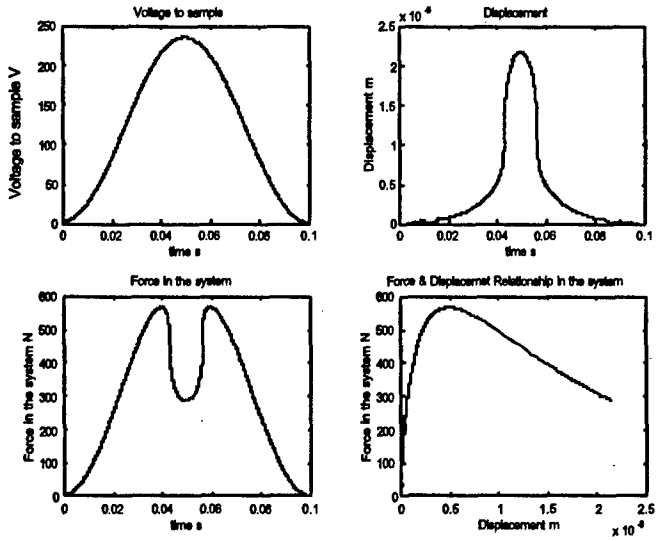

Figure 4-27: Predicted Displacement and Force for Non-linear Test 1

4.8.1 Non-linear system 1

Determination of Voltage to Drive Stack

As mentioned above, voltage to the driving stack was determined from the Voltage-Force model. The theoretically predicted displacement of the sample stack and the force in the system as well as the driving voltage to driving stack have been shown in Fig. 4-27 and 4-28.

Test Results

Test results have been shown in the following figures. Fig. 4-29, Fig. 4-30 and Fig. 4-31 show the measurement of basic parameters. Fig. 4-32 shows the representative cycle which was used to determine the experimental mechanical and electrical work and the actually simulated force-displacement relationship. Fig. 4-33, Fig. 4-34 and Fig. 4-35 shows the simulated force-displacement relationship, the mechanical work out and the electrical work in.

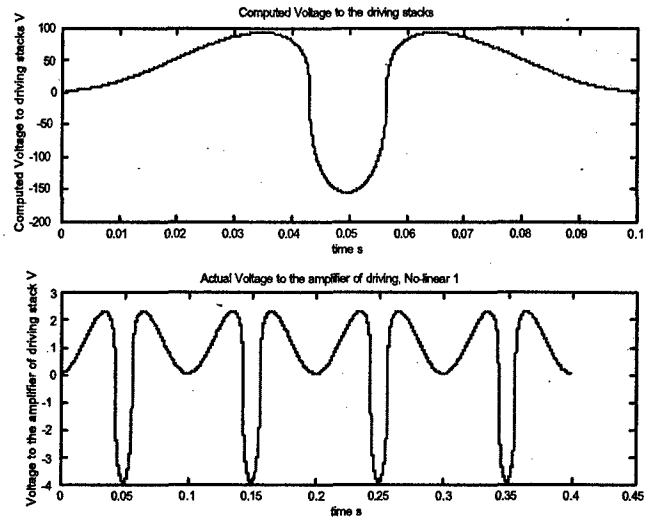

Figure 4-28: Predicted Voltage to the Driving Stack for Non-linear Test 1

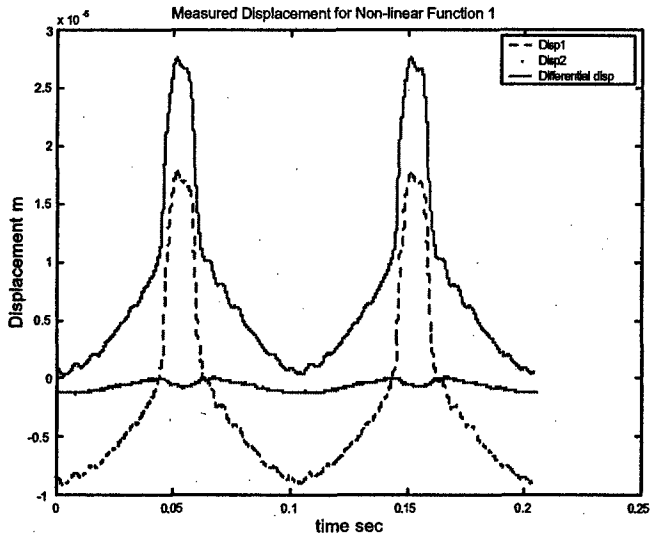

Figure 4-29: Measured Displacement of Sample for Non-linear System 1

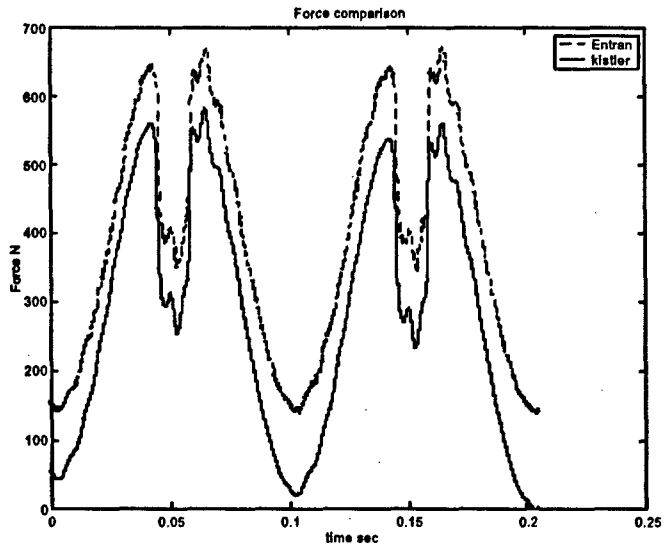

Figure 4-30: Measured Force in the System for Non-linear System 1

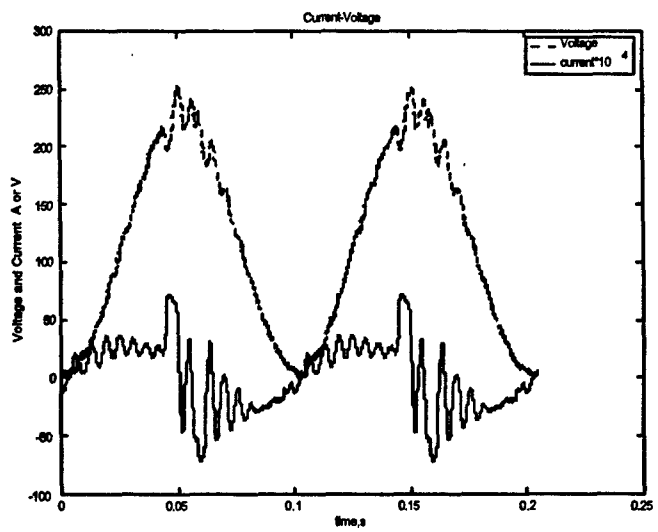

Figure 4-31: Measured Volatge and Current for Non-linear Test 1

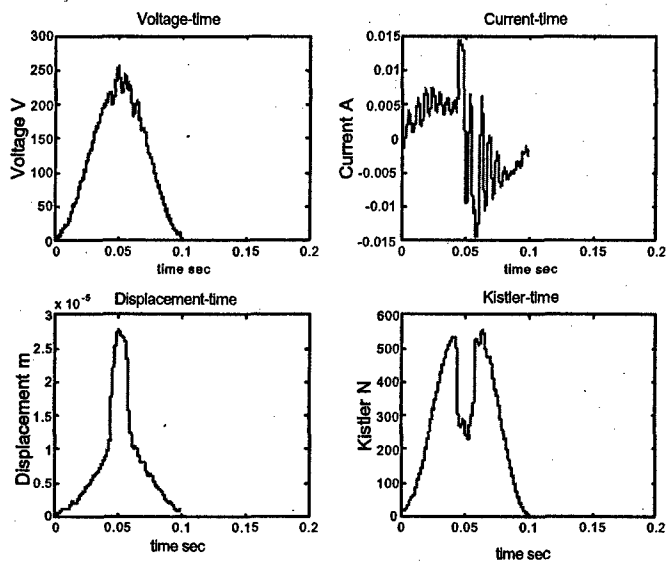

Figure 4-32: Representative Cycle for Work terms for Non-linear 1

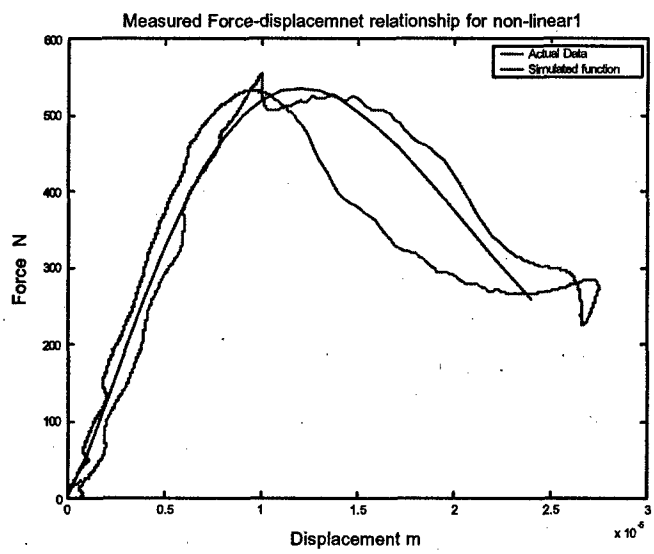

Figure 4-33: Simulated Force vs. Displacement for Non-linear1

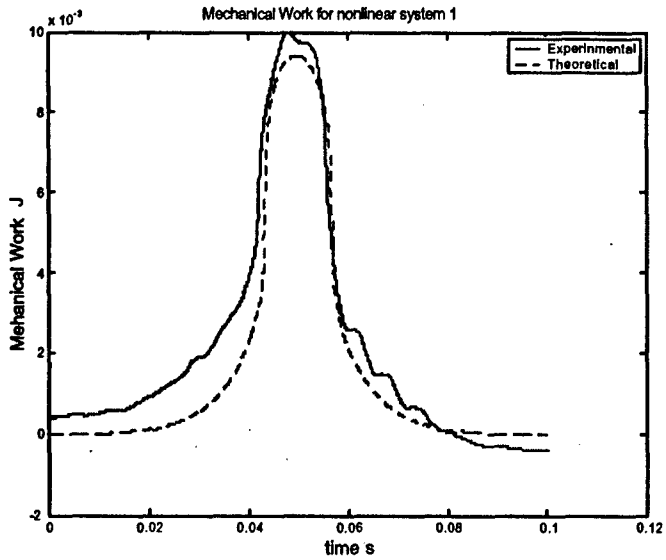

Figure 4-34: Mechanical Work out Comparison for Non-linear System 1

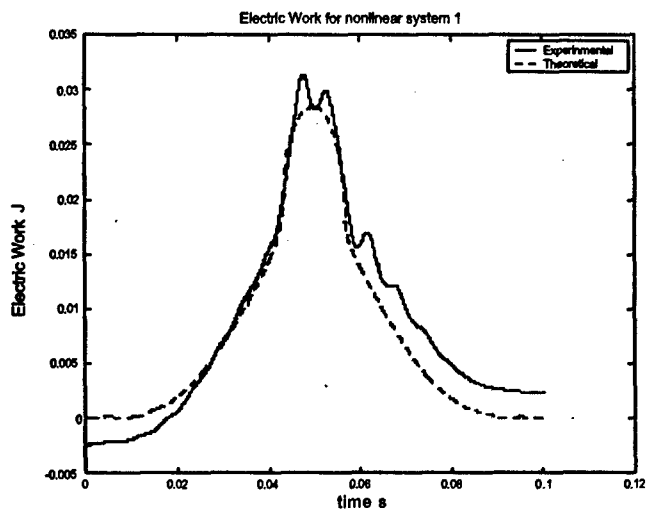

Figure 4-35: Electrical Work in Comparison for Non-linear System 1

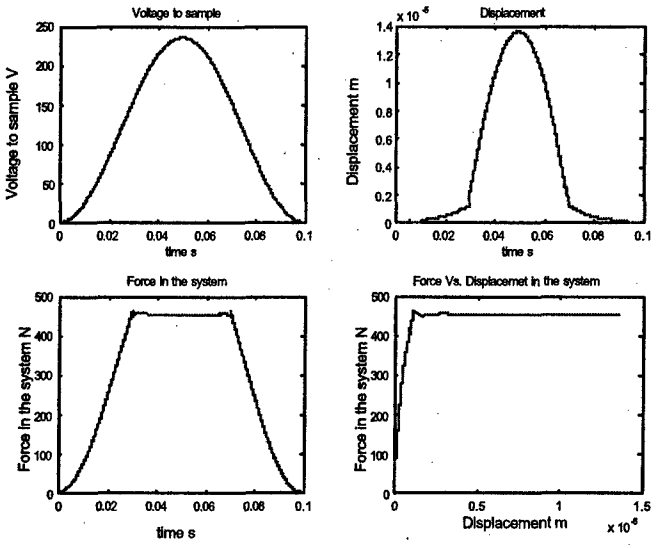

Figure 4-36: Predicted Force and Displacement for Non-linear 2

4.8.2 Non-linear system 2

Determination of Voltage to Drive Stack

Similar to non-linear systems 1, voltage to the driving stack for non-linear system 2 was also determined from the Voltage-Force model. The theoretically predicted displacement of the sample stack, the force in the system, as well as the driving voltage to driving stack, have been shown in Fig. 4-36 and 4-37.

Test Results

Test results have been shown in the following figures. Fig. 4-38, Fig. 4-39 and Fig. 4-40 shows the measurement of the basic parameters. Fig. 4-41 shows the representative cycle which was used to determine the experimental mechanical and electrical work and the simulated force-displacement relationship. Fig. 4-42, Fig. 4-43 and Fig. 4-44 shows the simulated force-displacement relationship, the mechanical work out and electrical work in.

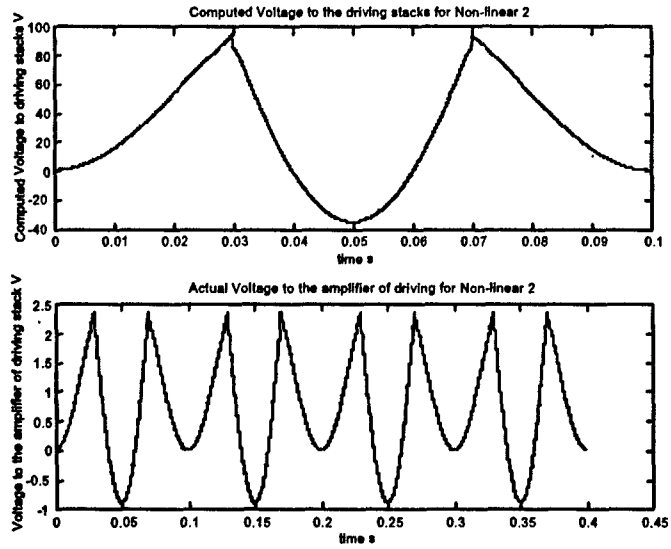

Figure 4-37: Computed Voltage to Driving Stack for Non-liner 2

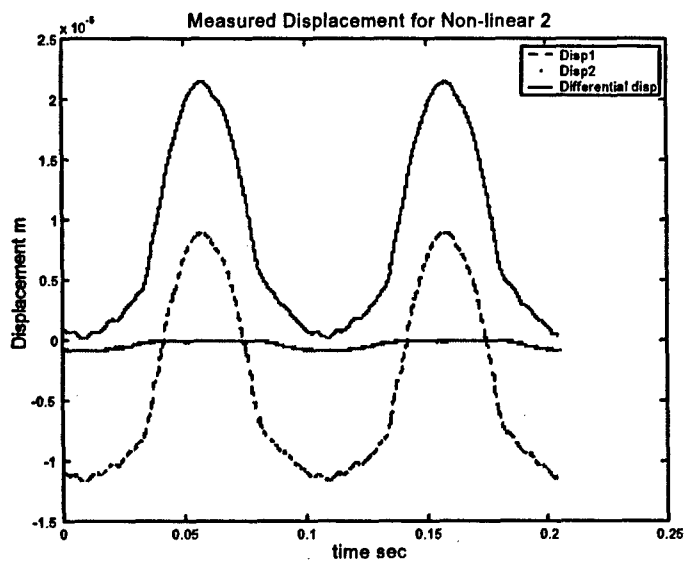

Figure 4-38: Measured Displacement of Sample for Non-linear System 2

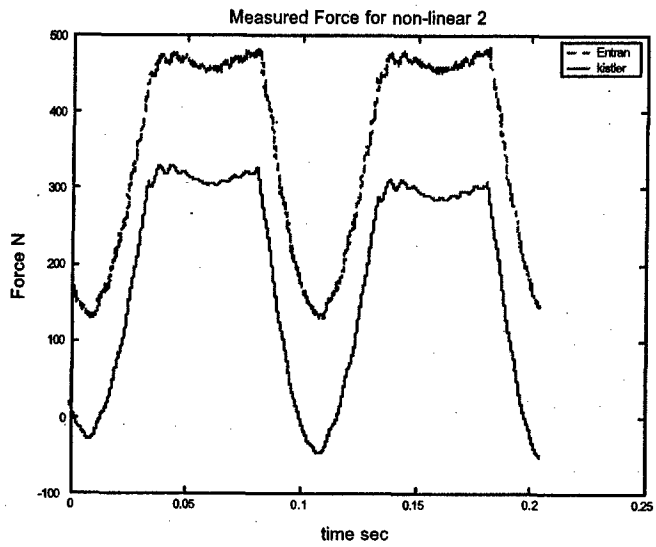

Figure 4-39: Measured Force in the system for Non-linear System 2

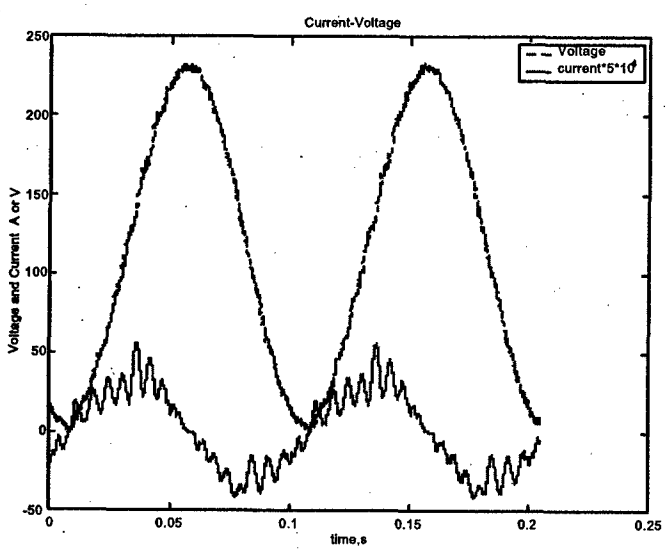

Figure 4-40: Measured Current and Voltage for Non-linear System 2

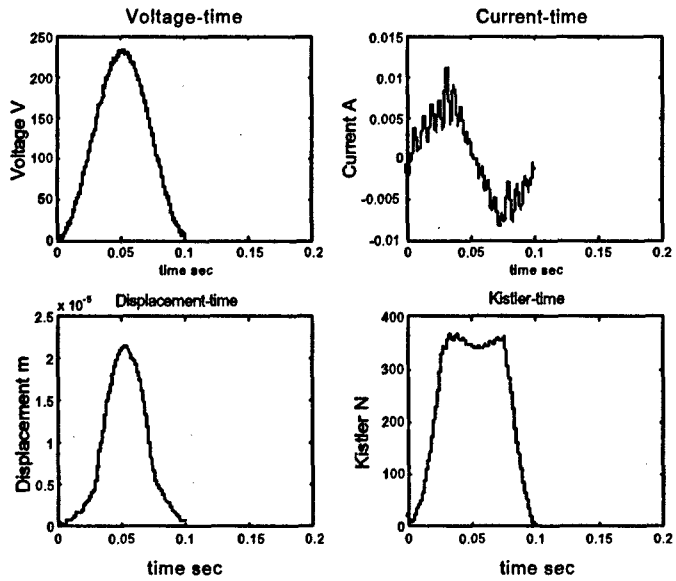

Figure 4-41: Representative Cycle for determining Work Terms for non-linear 2

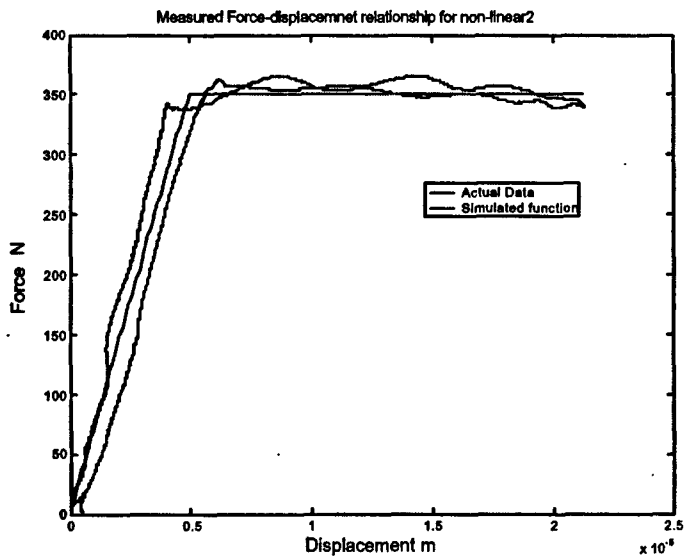

Figure 4-42: Simulated Force vs. Displacement for Non-linear System 2

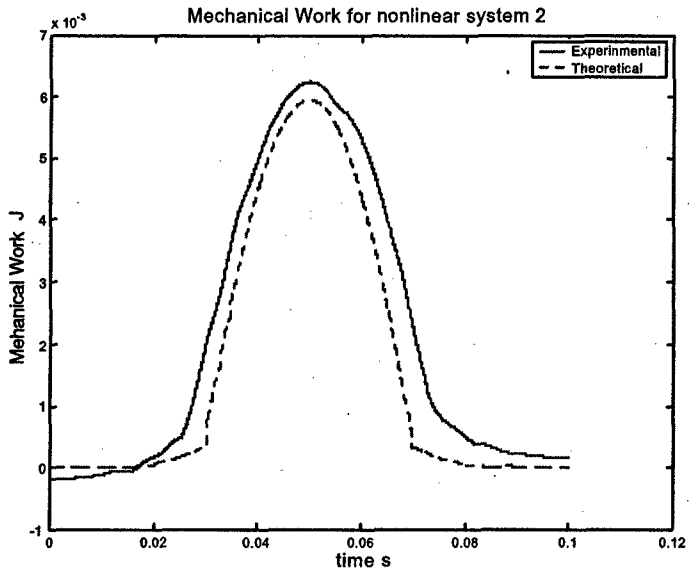

Figure 4-43: Mechanical Work out Comparison for Non-linear system 2

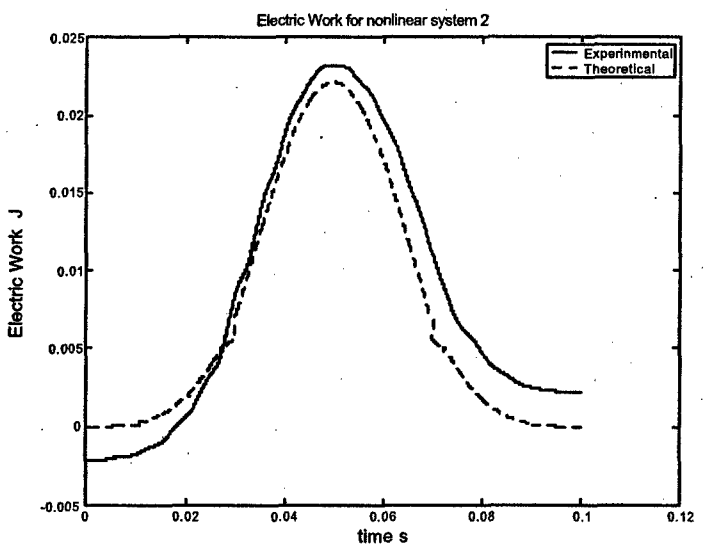

Figure 4-44: Electrical Work in Comparison for Non-linear system 2

	Linear System	Non-linear System 1	Non-linear System 2
Predicted	0.1578	0.3321	0.2693
Measured	0.1496	0.3181	0.2596

Table 4.8: Comparison of Actuation Efficiency for Linear and Non-linear Systems

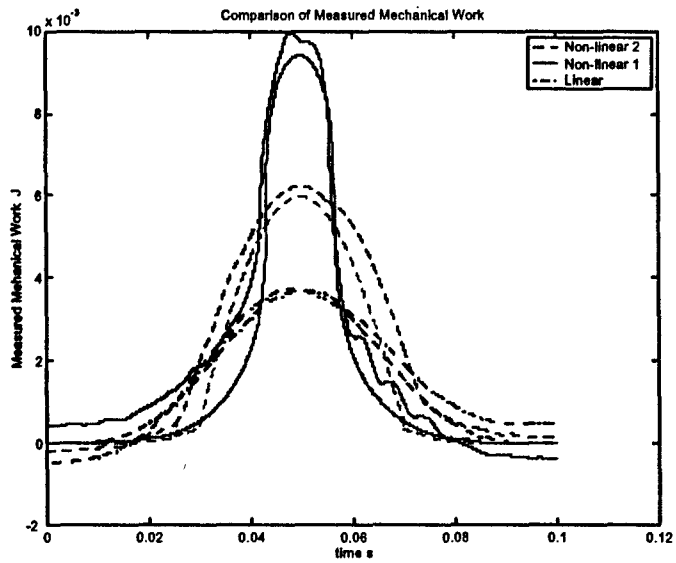

Figure 4-45: Comparison of Mechanical Work for Linear and Non-linear Systems

4.9 Comparison and Discussion

The experimental and theoretical mechanical work and electrical work for both linear and non-linear systems has been compared in Fig. 4-45 and Fig. 4-46. The actuation efficiency of the linear and non-linear systems was listed in Table 4.8. The stiffness ratio α is 0.96.

From the table we can see that actuation efficiency of the non-linear systems is about 200% that of the linear systems. From the figures of mechanical work of the linear and nonlinear systems, we can see that the mechanical work out of the non-linear system is about 250% that of the linear systems. The theoretical predictions correlate with experimental results very well. This has verified theoretical prediction made in Chapter 2.

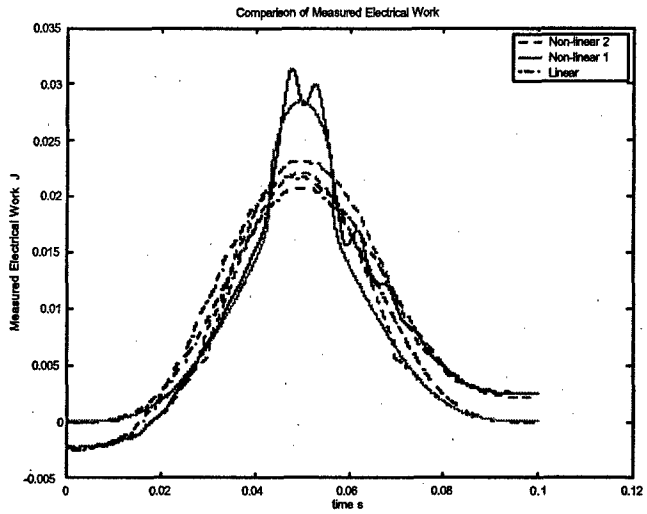

Figure 4-46: Comparison of Electrical Work for Linear and Non-linear Systems

4.10 Summary

All the linear and non-linear test results and their correlation with theoretical prediction have been discussed. The feedback control methodology used previously and have been replaced by a feedforward approach. The Voltage-Force model needed for the simulated actuator-structure-actuator system has been derived using the Rayleigh-Ritz formulation, and the related coefficient in its expression have been determined by experiment. The magnitude of the voltage to the sample stack is 235 V for all the linear and the non-linear tests, while the frequency of all the test is 10 Hz. For the linear systems, the test results have shown that the actuation efficiency is the highest when the stiffness ratio is larger than one, and this maximum value is much higher than that of the uncoupled analysis. For non-linear systems, the actuation efficiency of systems simulated by non-linear function 1 is about 200% that of the linear systems, while the work output of this system is about 250% that of the linear systems. The test results have exactly proved out the theoretical predictions.

Chapter 5

Non-Conservative Systems

5.1 Net Work in Conservative Systems

Up to now, all the systems discussed are conservative systems. The net electrical work input to the systems and the net mechanical work out of the systems is all zero. This can be seen from Fig. 4-45 and Fig. 4-46. To do actual work on the environment, we need to choose non-conservative thermodynamic cycles.

5.2 Non-Conservative System and Its Efficiency

5.2.1 Non-Conservative Cycles

Highly non-linear functions can be used as thermodynamic cycles to do work on the environment. Such a cycle could be a circle or an elliptical circle or any other functions. The comparison of such a thermodynamic cycle with the non-linear function 1 analyzed in the previous chapters has been shown in. Fig. 5-1. A few more different such cycles have been shown in Fig. 5-2.

The general equation of the non-conservative cycles shown in 5-2 can be expressed as

$$\begin{aligned} x &= d_1 \cos(\theta) + d_2 \sin(\theta) + d_{0x} \\ f &= d_3 \cos(\theta) + d_4 \sin(\theta) + d_{0f} \end{aligned} \tag{5.1}$$

Where $\theta = 0$ - 2 is an independent variable. $d_1, d_2, d_3, d_4, d_{0x}$ and d_{0f} are all constants.

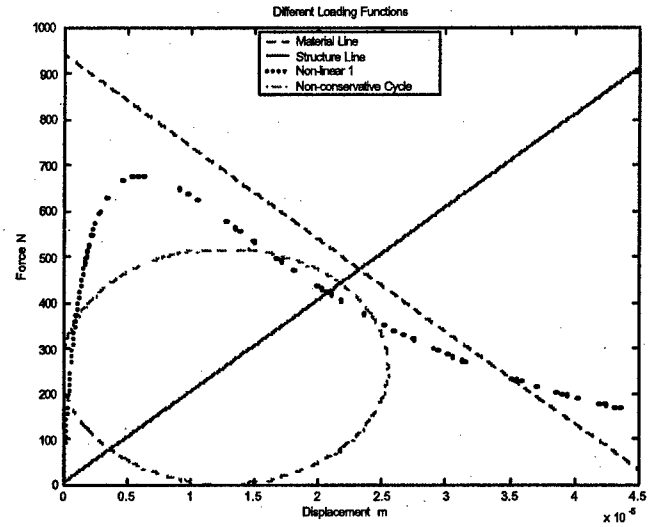

Figure 5-1: Comparison of non-linear function 1 with a Non-conservative Cycle

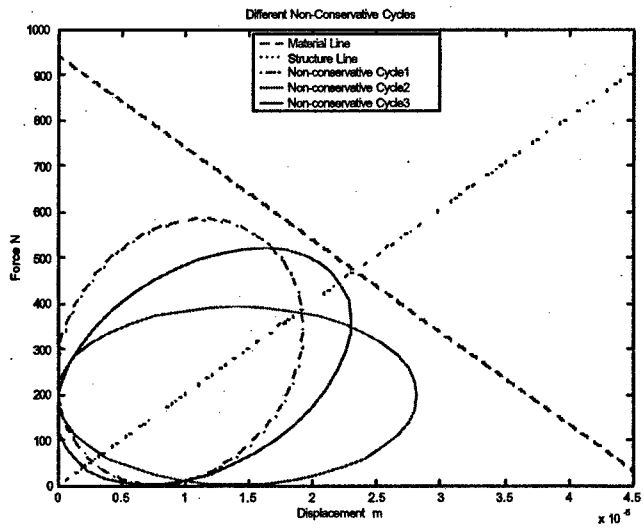

Figure 5-2: Different Non-Conservative Thermodynamic Cycles

5.2.2 Efficiency

For these non-conservative systems, The net work into the systems and net work out of the systems is not zero. The efficiency of the cycles can be defined as the ratio of net mechanical work out to net electrical work in expressed as

$$\eta = \frac{Net_Wm_out}{Net_We_in} \tag{5.2}$$

Where Net_Wm_out is net the mechanical work done on the environment, and Net_We_in is the net electrical work into the systems.

5.3 Experimental Demonstration

5.3.1 Simulation Methods

The non-conservative cycles shown in Fig. 5-2 can be simulated by driving the sample stack and the driving stack simultaneously, and maintaining a constant phase difference between the voltage to the sample and the voltage to the driving stack. For the purpose of demonstration, non-conservative cycle 1 shown in Fig. 5-2 has been chosen as an example. The test frequency and the driving voltage to the sample stack is the same as in the linear and the non-linear tests in Chapter 4. The driving voltage to the driving stack has been increased gradually to find out its influence on mechanical and electrical work as well as efficiency of the cycles simulated. The phase shift of the voltage to the driving stack is /2.

Fig. 5-3 has shown the voltage to the sample and the driving stack for such an example.

5.3.2 Test Results

The test results have been shown in the following figures. Fig. 5-4, Fig. 5-5 and Fig. 5-6 show the measurement of basic parameters such as displacement, force, current and voltage. Fig. 5-7 shows the representative cycle which has be used to determine the experimental mechanical and electrical work and the simulated force-displacement relationship. Fig. 5-8, Fig. 5-10 and Fig. 5-9 show the simulated force-displacement relationship, the net mechanical work out and net electrical work in. for this cycle.

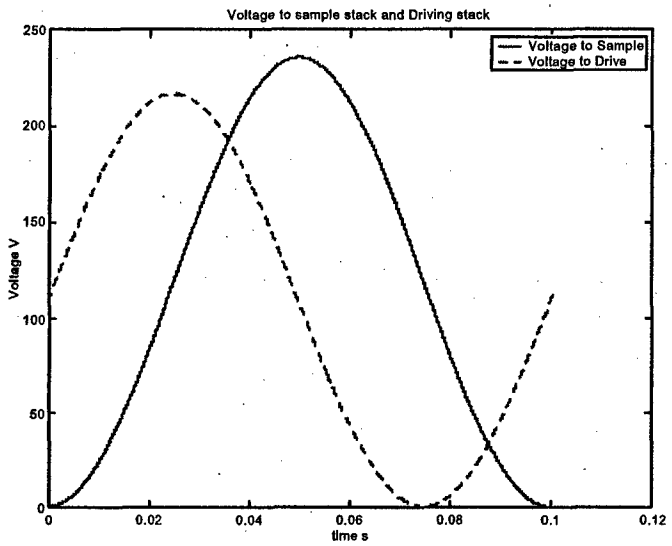

Figure 5-3: Voltage to the Sample and Driving Stacks

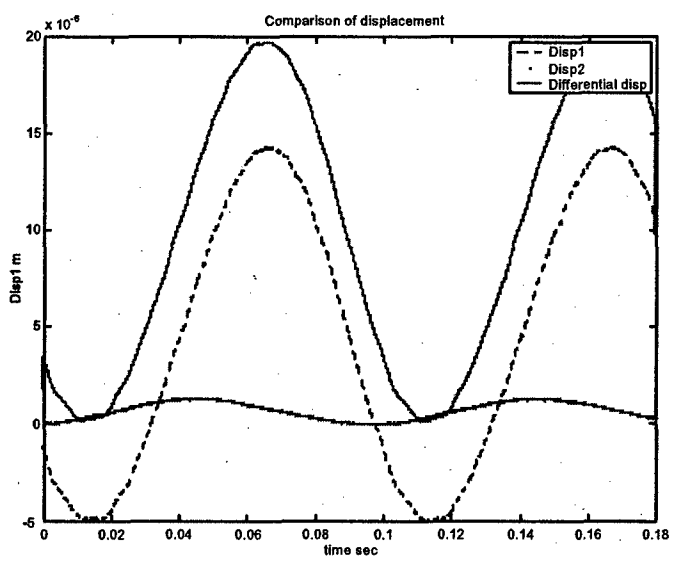

Figure 5-4: Displacement Measurement for a Non-Conservative Cycle

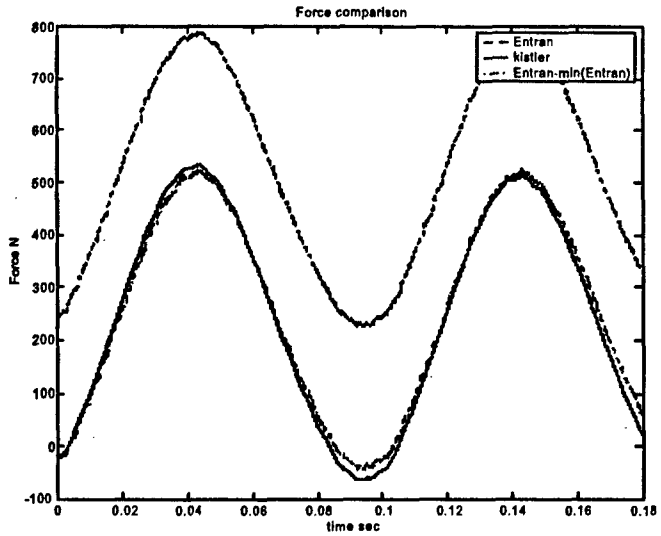

Figure 5-5: Force Measurement for a Non-Conservative Cycle

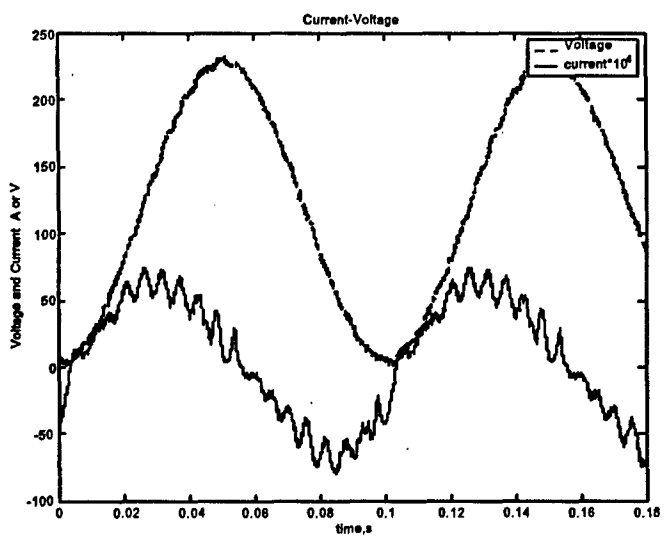

Figure 5-6: Current and Voltage Measurement for a Non-Conservative Cycle

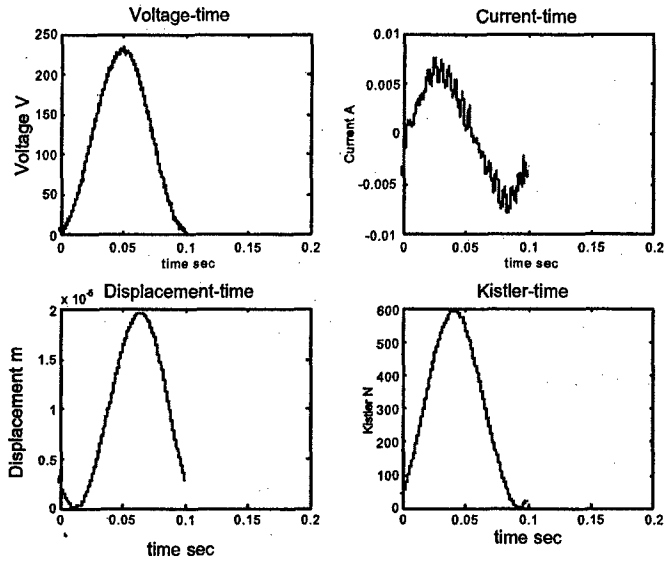

Figure 5-7: Representative Cycle for Determining Work and Efficiency

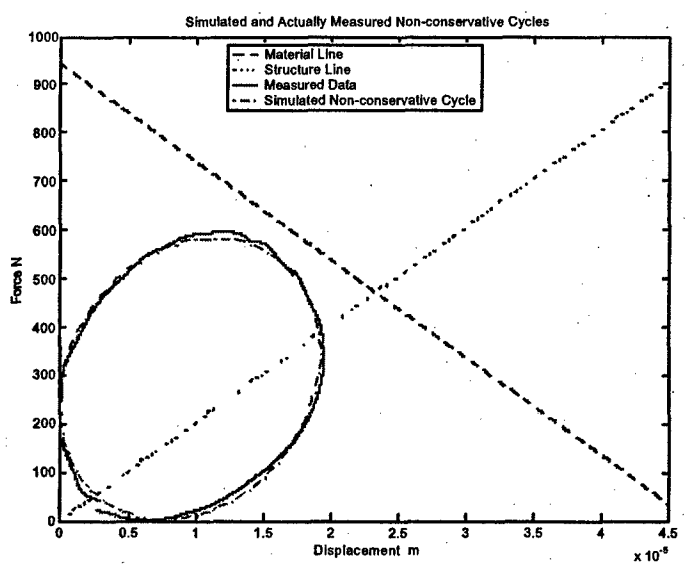

Figure 5-8: Comparison of the Non-Conservative Cycle 1 and the Actually Simulated Cycle

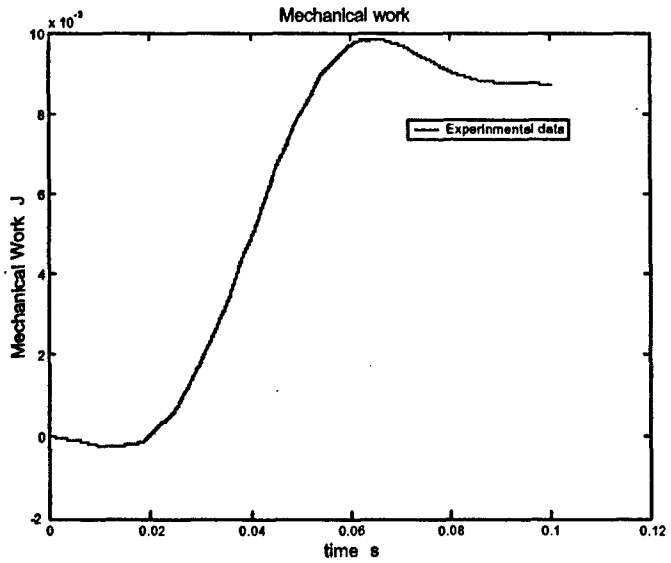

Figure 5-9: Net Mechanical Work Done by a Non-Conservative Cycle

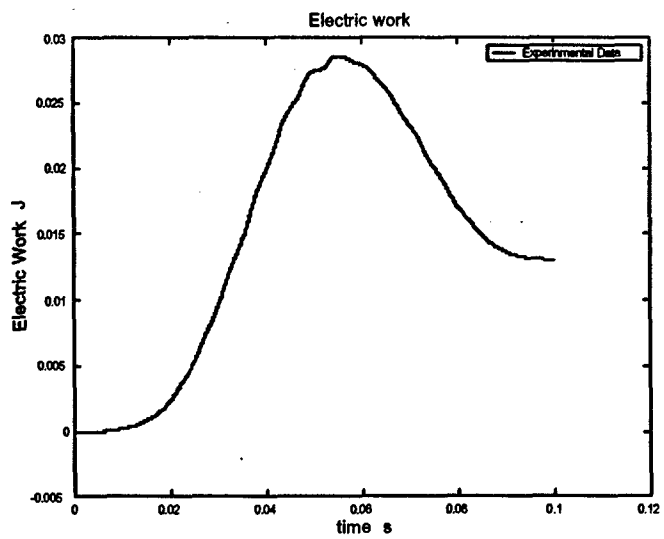

Figure 5-10: Net Electrical Work into a Non-Conservative Cycle

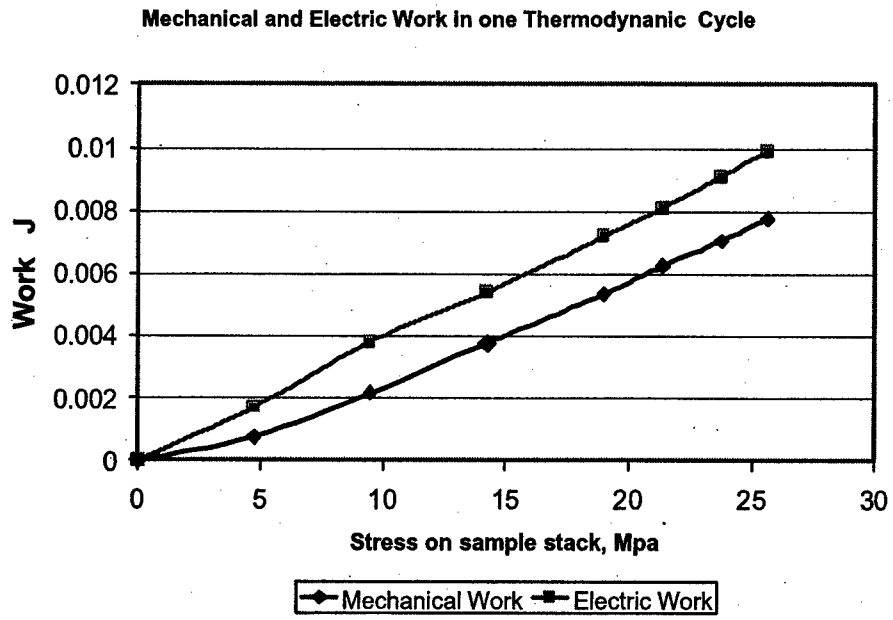

Figure 5-11: Mechanical work and electric work vs. Sstress on the sample stack

The influence of driving voltage to the driving stack on the mechanical work, electrical work and efficiency of the cycles have been shown in Fig. 5-12 and 5-11.

5.4 Summary

It has been shown that for the thermodynamic cycles chosen here the net work out of the systems is not zero. The non-conservative cycle 1 has been successfully simulated by driving the test sample and the driving stack simultaneously but maintaining a phase shift between the two driving voltages. The efficiency of the cycles increases with the increasing of the magnitude of voltage to the driving stack.

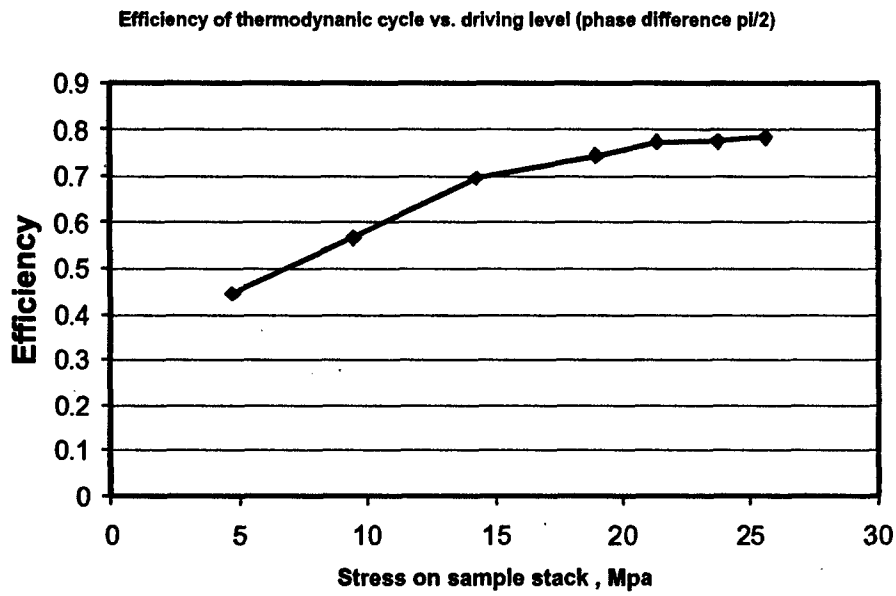

Figure 5-12: Efficiency of non-conservative cycles vs. stress on the sample stack

Chapter 6

Conclusions and Recommendations for Future Work

6.1 Conclusions on the Linear and the Non-linear Tests

The work presented has demonstrated that actuation efficiency viable metric coupled systems. Different expressions such as material coupling coefficient, device coupling coefficient and actuation efficiency, which have been used to describe and evaluate the energy flow and efficiency of coupled systems, have been compared and contrasted. It has been found that load coupling effects the performance for both linear and non-linear systems. The true thermodynamic actuation efficiency expressed as the ratio of work output to work input of a system can incorporate the coupling effects better than material coupling coefficient. Thus, actuation efficiency is more efficient and more accurate in evaluating the performance and behavior of a system.

Through the coupled analysis and tests of piezoelectrically driven systems, the performance of linear systems have been better understood. For a linear system in which a piezoelectrically active material working against a linear load, it is believed traditionally that the maximum efficiency of systems is a quarter of the material coupling coefficient squared. This maximum is reached when the stiffness ratio of structure and piezo active material equals one. However, the coupled analysis and tests in this research have shown that actuation efficiency is the highest when the stiffness ratio is larger than one, and this maximum value is much higher than that of the uncoupled analysis, although the efficiency of the uncoupled analysis does increase when

material coupling coefficient increases. These results agree very well with those found from the literature, and have been verified by the linear tests in this research. The test results correlate with theoretical prediction very well.

For a non-linear system in which a piezoelectrically active material working against a non-linear load, the coupled analysis has found out that it is possible to significantly increase the work output and actuation efficiency of the system. Two non-linear functions have been chosen for the demonstration. The test results have shown that the actuation efficiency of non-linear systems is much higher than that of linear systems. The actuation efficiency of systems simulated by non-linear function 1 is about 200% of that of the linear systems, while the work output of this system is about 254% of that of the linear systems. This has also been verified by tests.

The renovation of the component tester has proven to be a success. The previous tester was designed and built with programmable impedance and closed loop test capability. However, the feed back control method is not fast enough in determining the voltage for the driving stack which has limited the test frequency. Meanwhile, the original mechanical design can not guarantee the accurate measurement of mechanical work. Therefore, renovation of this tester is essential in experimental verification of the linear and non-linear theoretical predictions. The load transfer system of the tester has been redesigned and feedforward open loop test methodology has used instead of the feedback control. All the linear and non-linear tests have been conducted on the renovated test facility, and the theoretical predictions about the linear and non-linear systems have been experimentally verified.

6.2 Conclusions on Non-Conservative Systems

All the linear and non-linear tests done are for conservative systems. The net work on the environment has been shown to be zero. To do work into environment, non-conservative cycles have been chosen. Such cycles could be a circle or an elliptical circle. The efficiency of such a thermodynamic cycle can be defined as the ratio of net mechanical work out to the net electrical work in.

The net work out of the systems for non-conservative cycle 1 has been demonstrated to be

non-zero. The systems have been simulated by driving the test sample and the driving stack simultaneously but maintaining a phase shift between the two driving voltages. The efficiency of the cycles increases with the increasing of the magnitude of voltage to the driving stack.

6.3 Recommendation for Future Work

This research has shown that the actuation efficiency of the non-linear systems is almost twice as high as that of the linear systems, and for the non-conservative systems, work can be done on the environment. This will highly reduce the complexity of the actuation systems for some applications such as a pump. However, the non-linear loading device and non-conservative cycle device must be designed and built first. A method of achieving such a non-linear system is to configure two springs into a triangle and looking at the behavior of the springs as they are loaded through the central platform they are connected, as explained in [Malinda1, 1999].

The analysis and tests presented here are all in quasi-static region. However, in some cases such the helicopter rotor blade and airplane wing applications, active materials undergo dynamic load. The behavior and performance of active materials and the actuation efficiency of the piezoelectrically driven systems under dynamic loads should be explored also.

Bibliography

[Bar-Cohen, 1999] Y. Bar-Cohen, X. Bao, et. al., "Rotary ultrasonic motors actuated by travelling flexural wave", *Proceedings of SPIE, Smart Structures and Materials 1999, Vol. 3668,* pp. 698-704, 1-4 March 1999, New Port Beach, California.

[Binghamand, 1999] B. S. Bingham, N. W. Hagood, M. J. Atalla, "Performance comparison of feedback and feedforward structural-acoustic control techniques", *Proceedings of SPIE, Smart Structures and Materials 1999, Vol. 3668,* pp. 698-704, 1-4 March 1999, New Port Beach, California.

[Berlincount, 1971] D. Berlincount, "Piezoelectric crystals and ceramics," *Ultrasonic Transducer Materials,* O. E. Mattiat, ed., Plenum Press, New York, 1971.

[Davis, 1999] C. L. Davis, F. T. Calkins te. al. " Predicting actuation efficiency of structurally integrated active materials" *Proceedings of SPIE, Smart Structures and Materials 1999, Vol. 3674,* pp. 476-486.

[Frank, 1999] J. E. Frank, G. H. Koopmann, et. al. "Design and performance of a high-force piezoelectric inchworm model," *Proceedings of SPIE, Smart Structures and Materials 1999, Vol. 3668,* pp. 717-723, 1-4 March 1999, New Port Beach, California.

[Giurgiutiu, 1997] "Power and energy characteristics of solid-state induced-strain actuators for static and dynamic applications," *Journal of Intelligent Material Systems and Structures,* Vol. 8, September 1997.

[Hagood, 1990] N. Hagood, W. Chung, and A. von Flowtow, " Modeling of piezoelectric actuator dynamics for active structural control," *Journal of Intelligent Material Systems and Structures* 1[3], pp. 327-354, 1990.

[Hagood, 1991] N. W. Hagood, A. V. Flotow, "Damping of structural vibrations with piezoelectric materials and passive electrical networks" *Journal of Sound and Vibration,* 146(2), pp243-268, 1991.

[Hall, 1996] S. R. Hall, E. Prechtl, "Development of a piezoelectric servoflap for helicopter rotor control, " *Smart Materials and Structures,* Vol. 5, pp. 26-34, 1996.

[IEEE,1978] *IEEE Standard on Piezoelectricity,* IEEE, inc., 1978.

[Karl, 2000] K. Spanner, "Breakthrough in piezo actuator application," *Proceedings of the 7th International Conference on New Actuators,* B.2.0, 19-21 June 2000, Bremen, Germany.

[Lesieutre, 1997] G. Lesieutre, C. Davis, " Can a coupling coefficient of a piezoelectric device be higher than those of its active material ?," *Journal of Intelligent Material Systems and Structures* 8[10], p. 859, 1997.

[Malindal, 1999] M. K. Lutz, "Study of work flow in piezoelectrically driven linear and non-linear systems," *Master Thesis,* Department of Aeronautics and Astronautics, Massachusetts Institute of Technology, 1999.

[Malinda, 1999] M. K. Lutz, N. W. Hagood, "Actuation efficiency in piezoelectrically driven linear and non-linear systems", *Proceedings of SPIE, Smart Structures and Materials 1999, Vol. 3668,* pp. 780-796, 1-4 March 1999, New Port Beach, California.

[Mitrovic, 1999] M. Mitrovic, G. P. Carman, et. al. "Electromechanical characterization of piezoelectric stack actuators," *Proceedings of SPIE, Smart Structures and Materials 1999, Vol. 3668,* pp. 586-601, 1-4 March 1999, New Port Beach, California.

[Roberts, 1999] D. Roberts, "Development of a linear piezoelectric motor based upon the inchworm model," *Proceedings of SPIE, Smart Structures and Materials 1999, Vol. 3668,* pp. 705-716, 1-4 March 1999, New Port Beach, California.

[Varadan, 2000] V. K. Varadan, V. V. Varadan, " Microsensors, microelectromechanical systems (MEMS), and electronics for smart structures and systems," *Smart Materials and Structures,* Vol. 9, pp. 953-972.,2000.

Appendix A

Component Testing Facility Drawings

The following pages contain the complete set of the mechanical drawings for the renovation of the Component Testing Facility. The materials used and the tolerances of each part have been specified on each of the drawings.

BEST AVAILABLE COPY

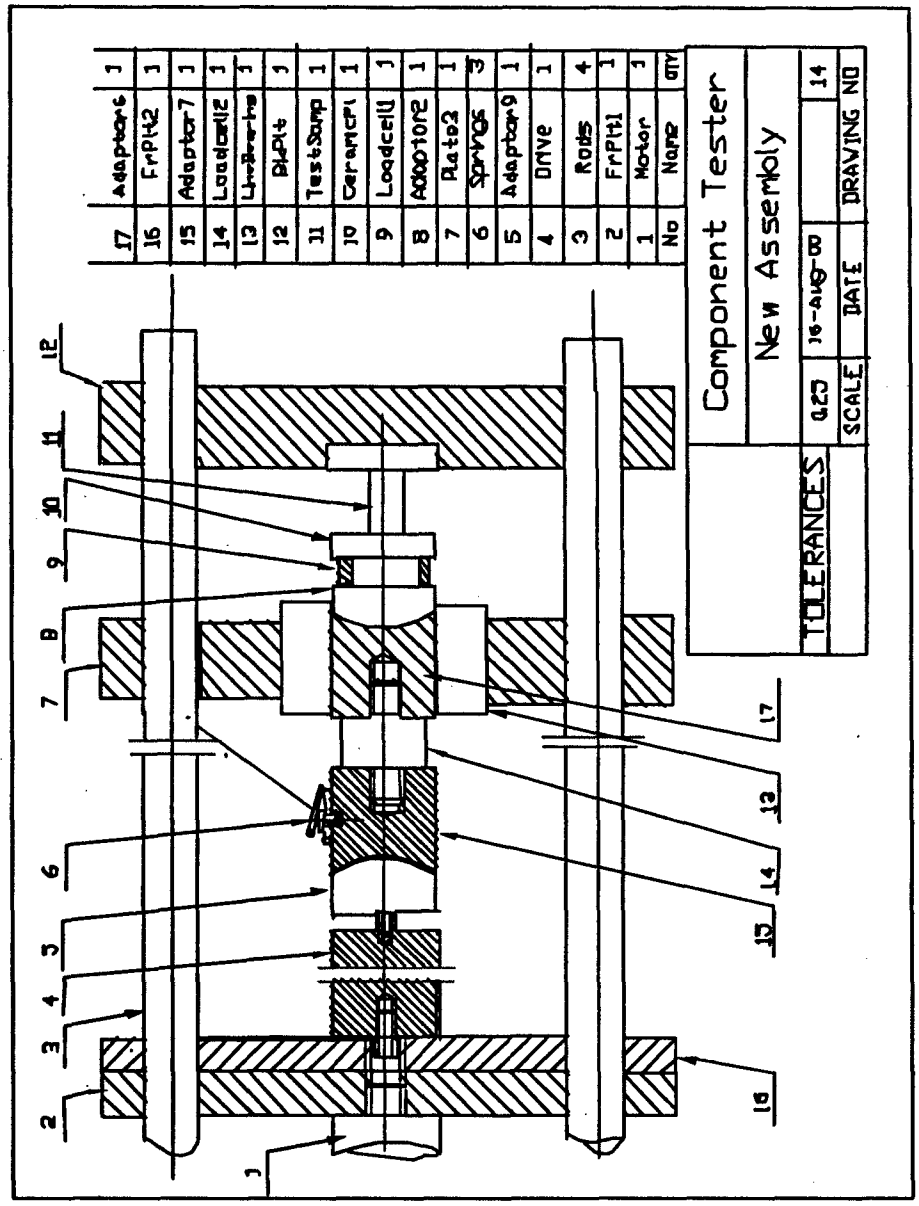

Figure A-1: Assembly Drawing of the Renovated Component Tester

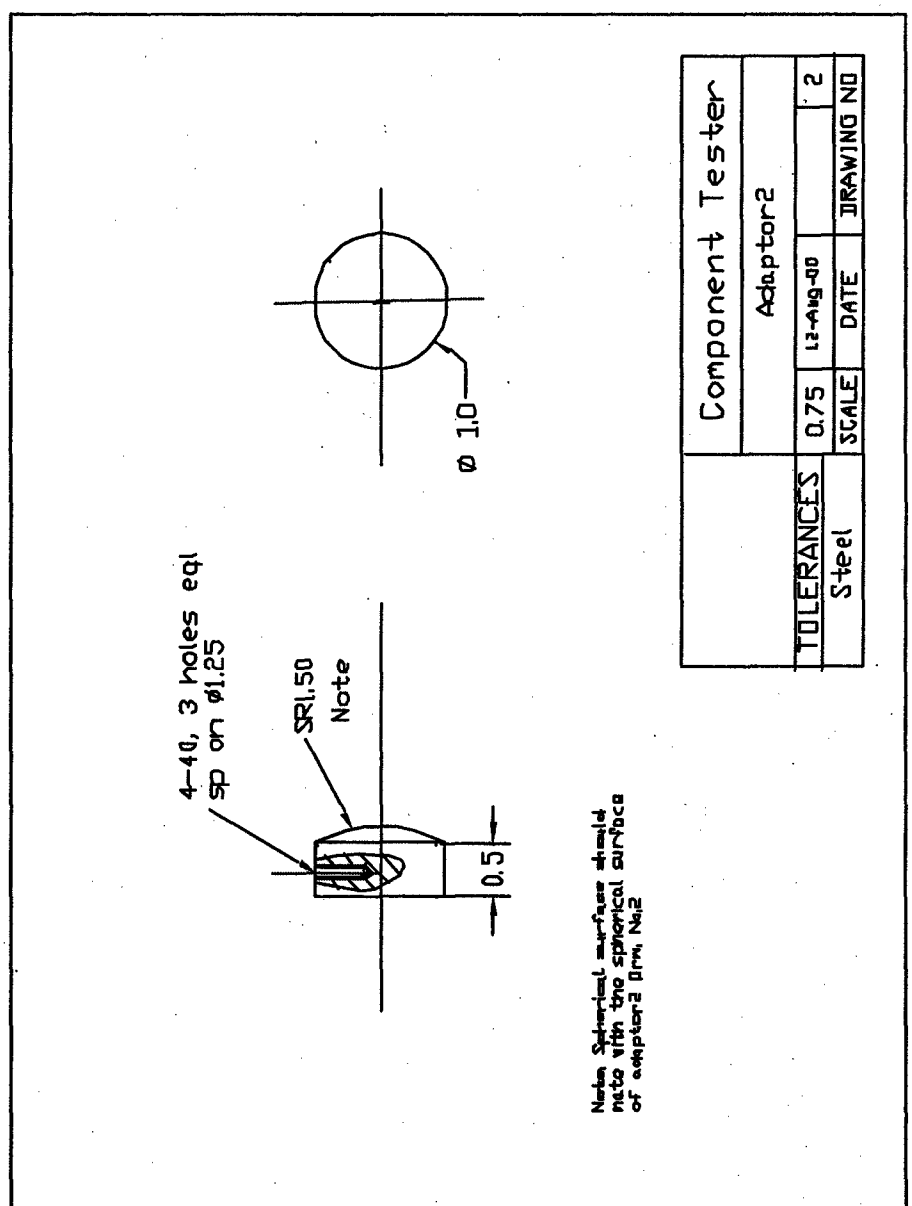

Figure A-2: Adaptor 2 Drawing

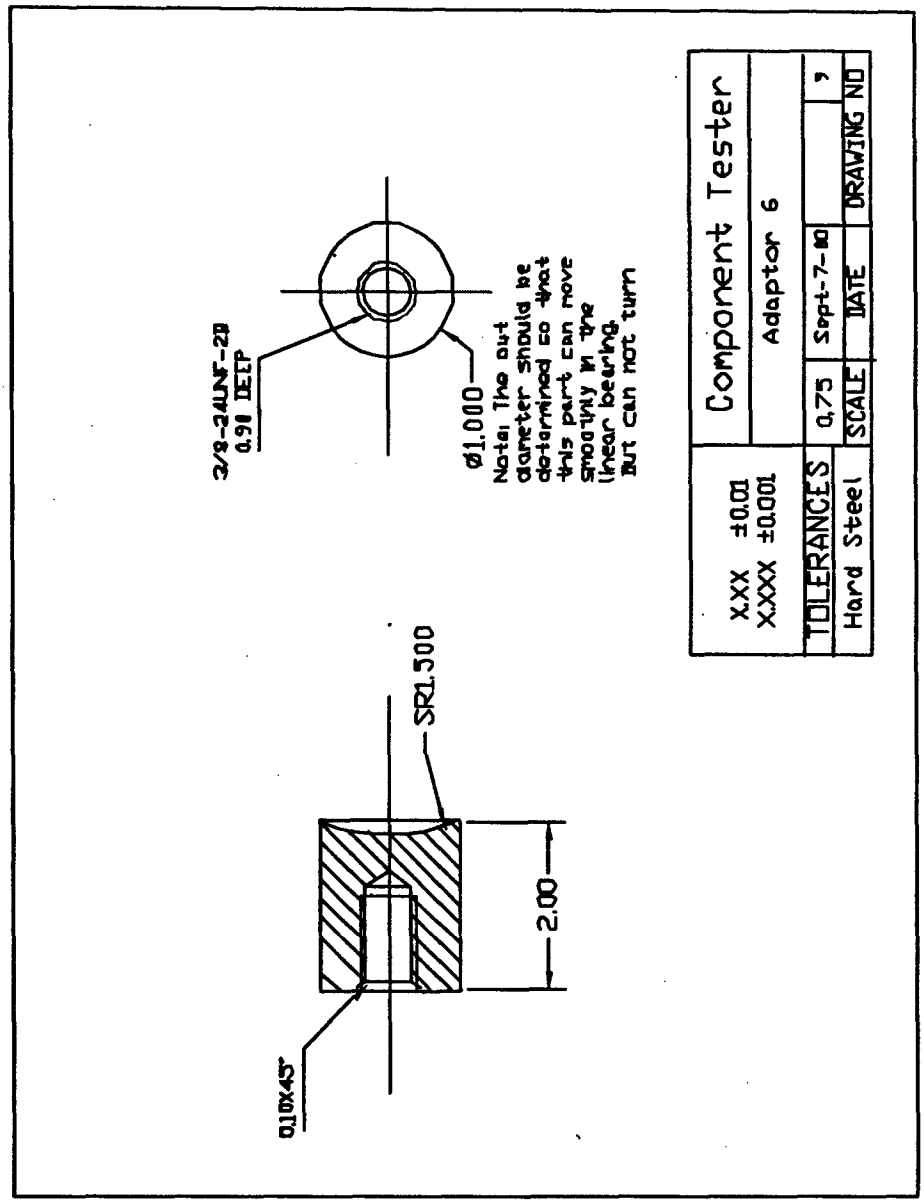

Figure A-3: Adaptor 6 Drawing

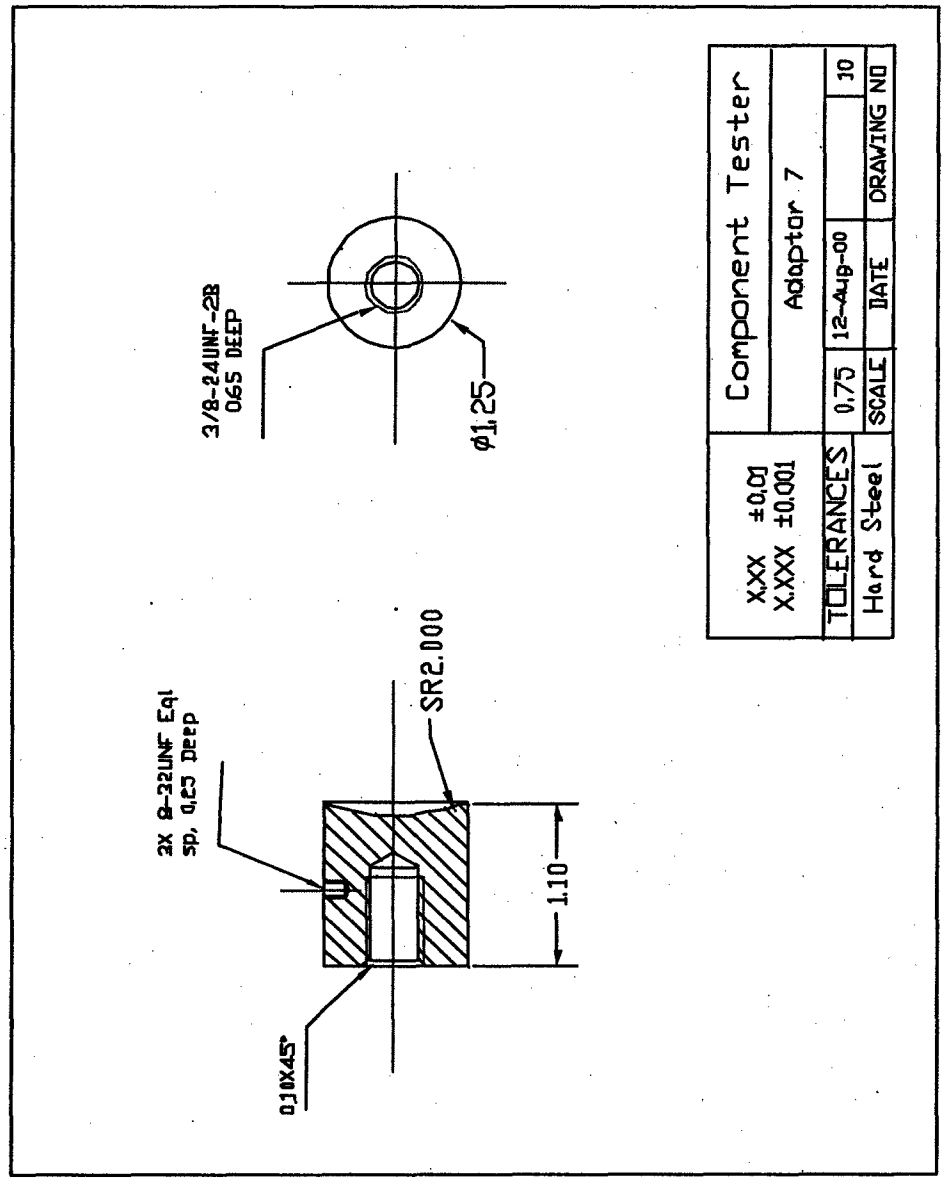

Figure A-4: Adaptor 7 Drawing

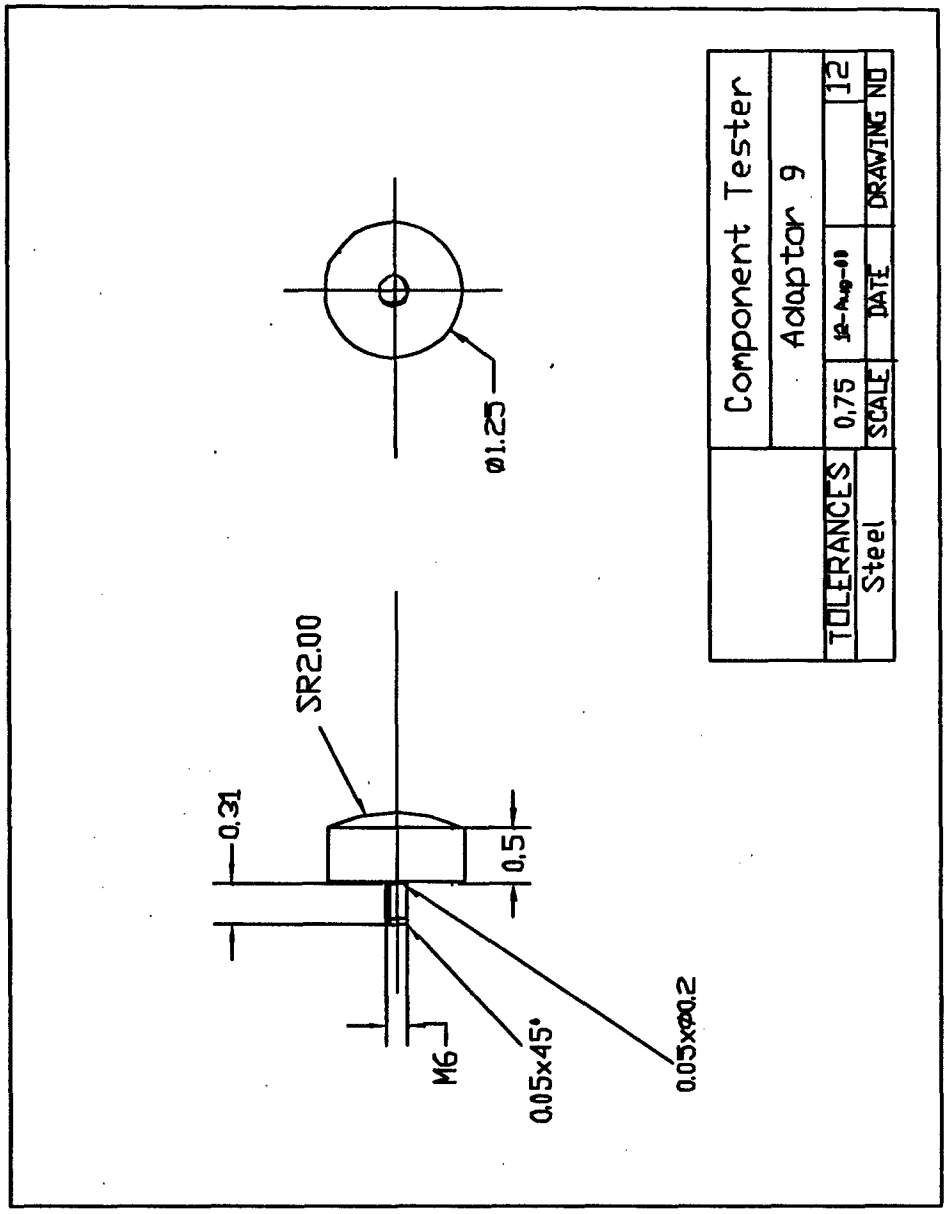

Figure A-5: Adaptor 9 Drawing

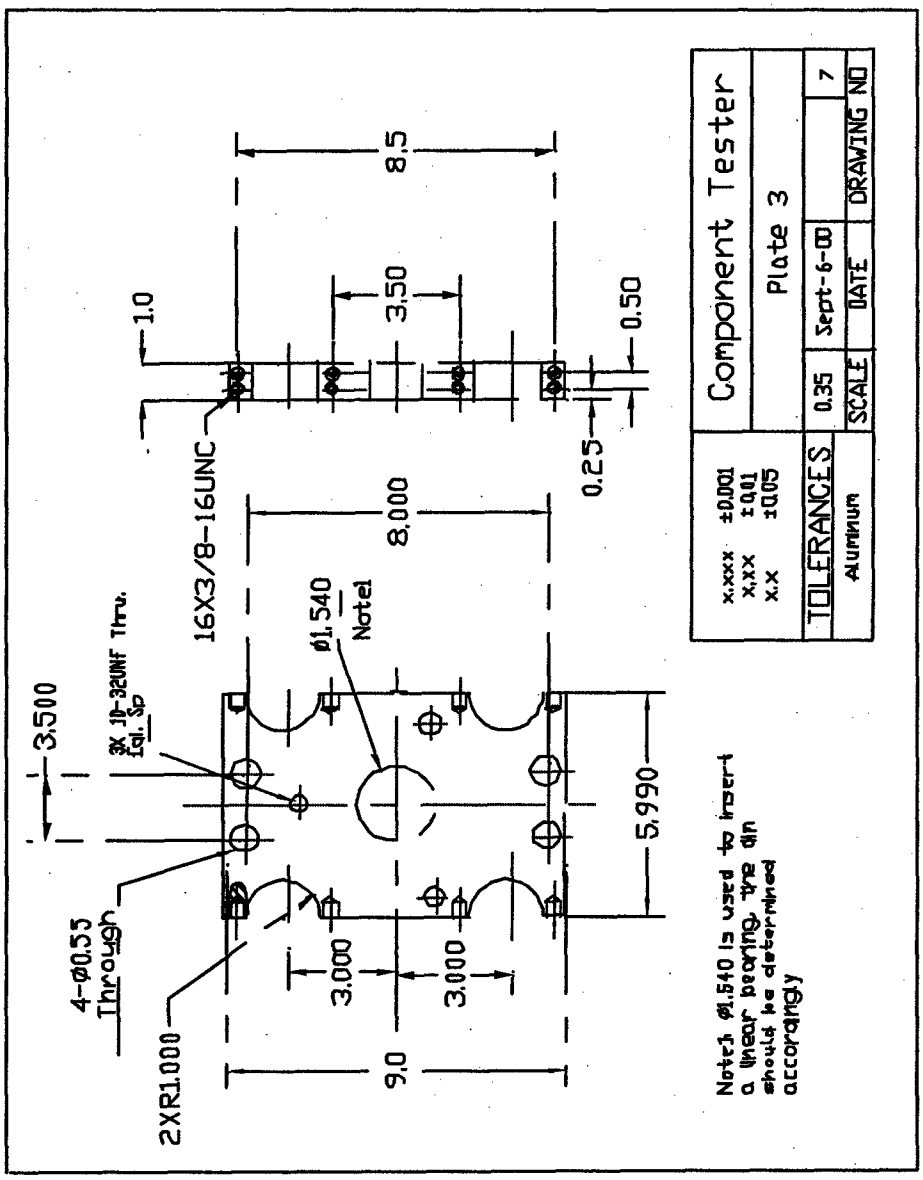

Figure A-6: Linear Bearing Mounting Plate Drwaing

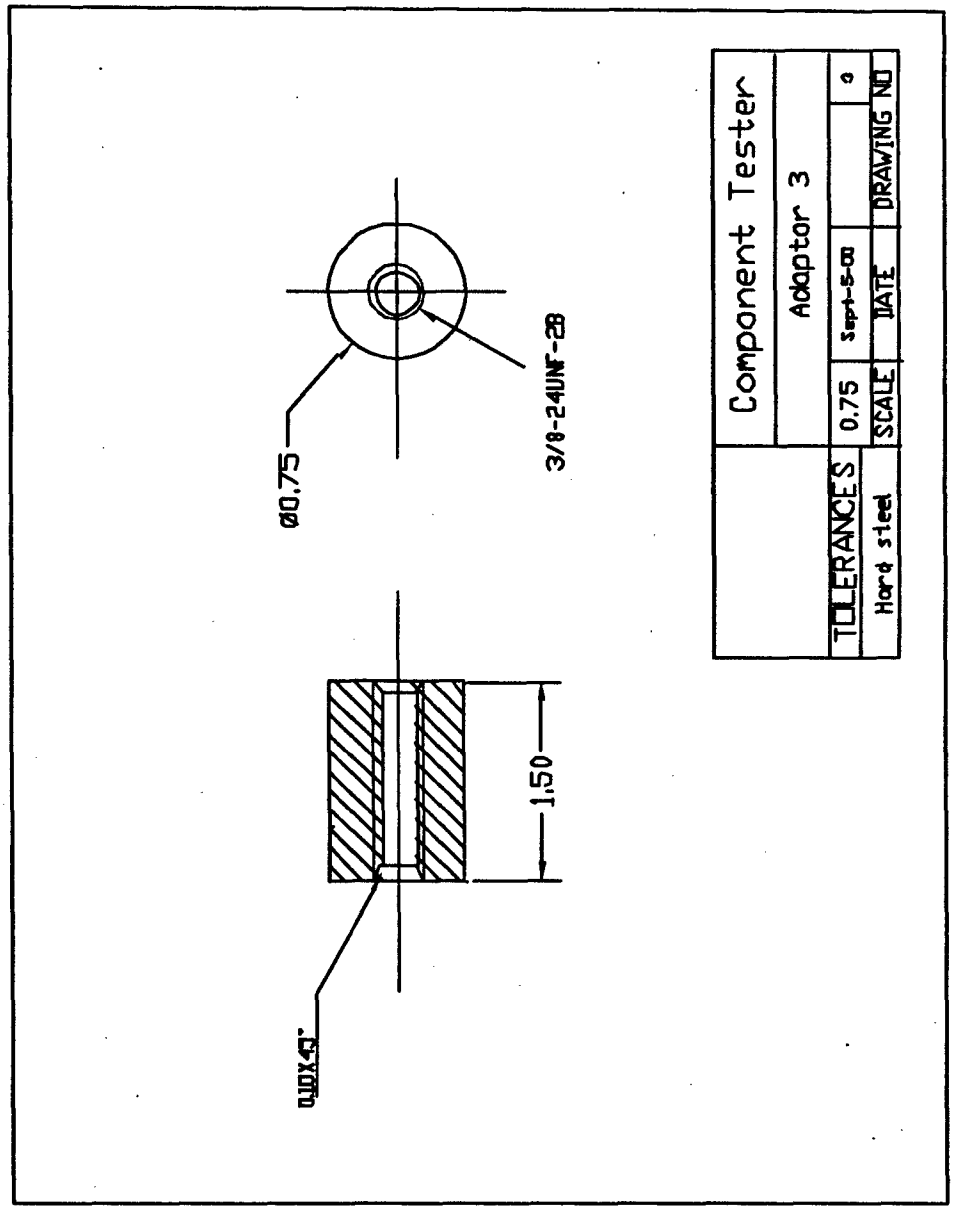

Figure A-7: Adaptor 3 Drawing

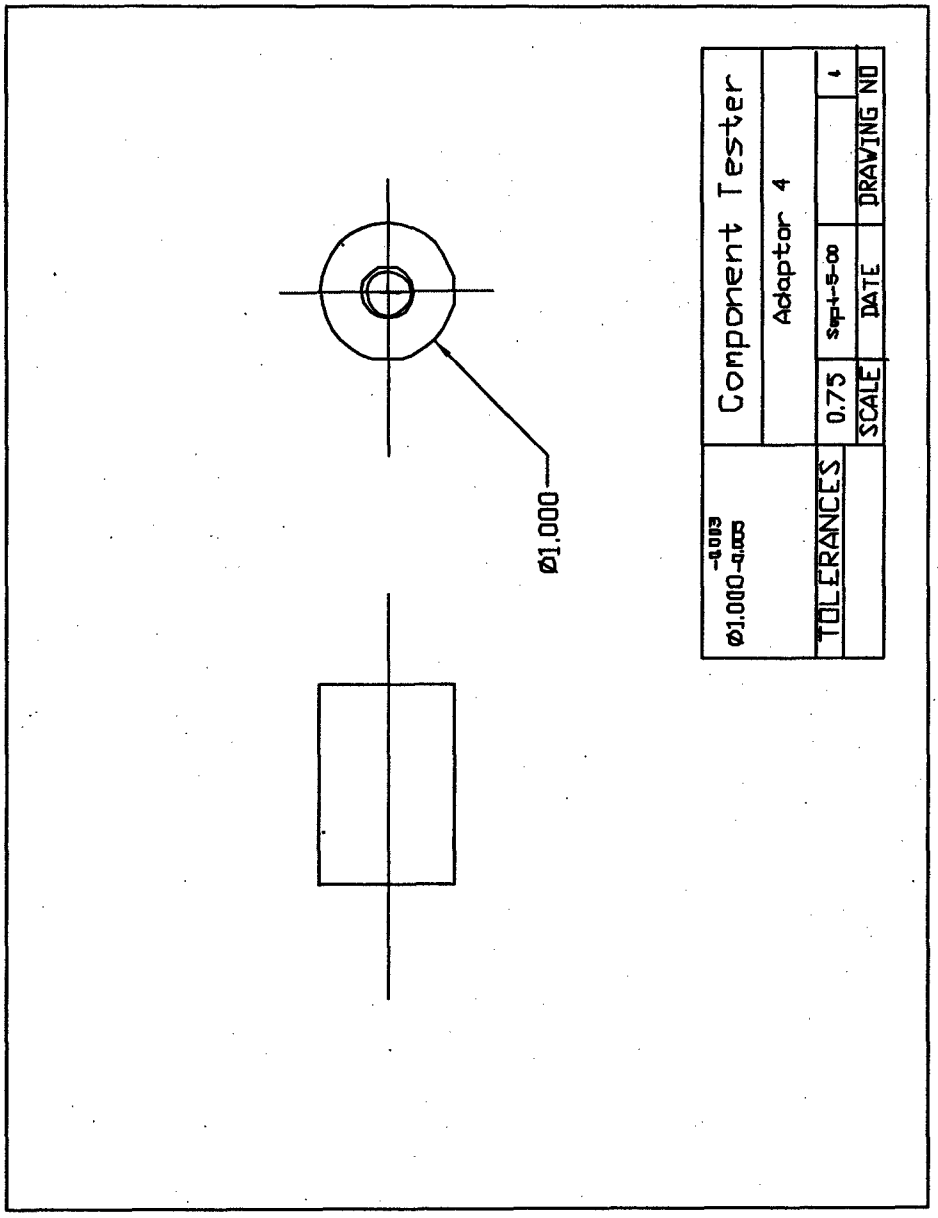

Figure A-8: Adaptor 4 Drawing

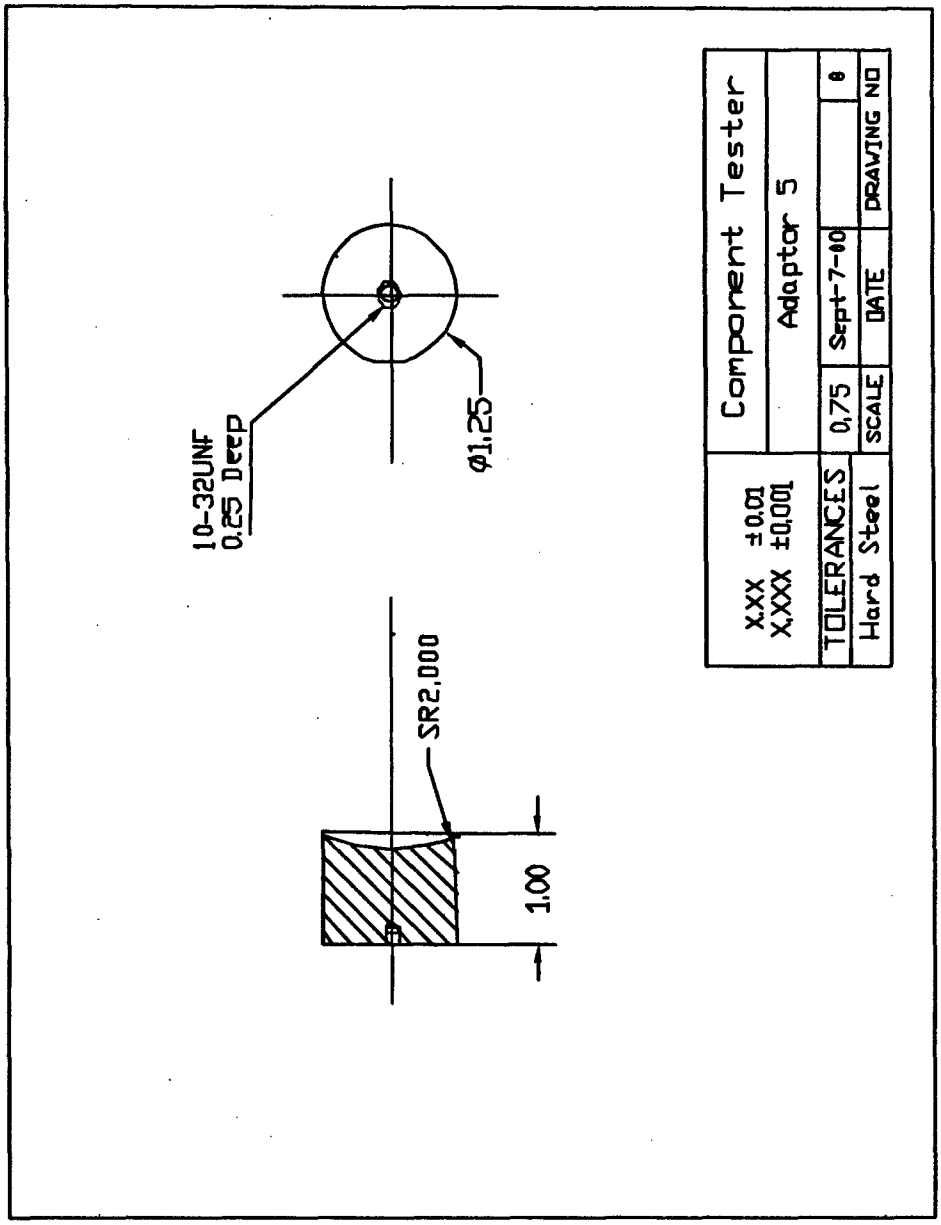

Figure A-9: Adaptor 5 Drawing

Analysis of Nonlinear Electroelastic Continua with Electric Conduction

by

John E. Harper

B.S. Aeronautical Engineering (1995)
Rensselaer Polytechnic Institute

Submitted to the Department of Aeronautics and Astronautics
in partial fulfillment of the requirements for the degree of

Master of Science in Aeronautics and Astronautics

at the

MASSACHUSETTS INSTITUTE OF TECHNOLOGY

June 1999

© Massachusetts Institute of Technology 1999. All rights reserved.

Author .....
Department of Aeronautics and Astronautics
May 21, 1999

Certified by .....
Nesbitt W. Hagood IV
Associate Professor
Thesis Supervisor

Accepted by .....
Jaime Peraire
Chairman, Department Graduate Committee

MASSACHUSETTS INSTITUTE OF TECHNOLOGY
JUL 15 1999
LIBRARIES

Aero

Analysis of Nonlinear Electroelastic Continua with Electric Conduction

by
John E. Harper

Submitted to the Department of Aeronautics and Astronautics
on May 21, 1999, in partial fulfillment of the
requirements for the degree of
Master of Science in Aeronautics and Astronautics

Abstract

This thesis presents the nonlinear theory for large deformation electroelastic continua with electric conduction. This theory is suitable for modeling actuator and sensor devices composed of deformable, electromechanically coupled, highly insulating materials. Consistency is proven between the large deformation theory and the classical Poynting vector based piezoelectric small deformation theory, extended for electric conduction. A result is that electric body forces, realized mathematically as electric surface tractions, are retained in the small deformation approximation. A finite element formulation is presented suitable for performance analysis of deformable electromechanical actuator and sensor devices composed of highly insulating materials with nonlinear response functions, under the small deformation approximation. Results demonstrate the significant cumulative effects of a weak electric current flow for electric voltage DC offset loading of a highly electrically insulating composite device.

Thesis Supervisor: Nesbitt W. Hagood IV
Title: Associate Professor

Acknowledgments

This work was supported under sponsorship by ONR Grant N00014-96-1-0691 with Dr. Wallace Smith serving as technical monitor, and under ARO Grant DAAH04-95-1-0104 with Dr. Gary Anderson serving as technical monitor.

Contents

1 Introduction **13**

1.1 Motivation 13
1.2 Objective 13
1.3 Background 14
1.4 Thesis Contributions 16
1.5 Thesis Outline 16

2 Large Deformation Electroelastic Equations **19**

2.1 Introduction 19
2.2 Bodies, Deformations, and Motions 19
2.3 Observer Transformations 21
2.4 Fields, Deformations, and Integral Theorems 22
2.5 Fundamental Axioms of Electromagnetics and Thermomechanics . . . 30
2.6 Maxwell's Equations 32
2.7 EQS Maxwell Equations 34
2.8 Conservation of Mass 36
2.9 Balance of Momentum 37
2.10 Balance of Moment of Momentum 39
2.11 Electromagnetic Power 41
2.12 Conservation of Energy: Electroelastic Continua 42
2.13 Entropy Inequality 47
2.14 Surfaces of Discontinuity 47
2.15 Jump Conditions 50
2.16 Objective Fields and Reference Configurations 52
2.17 Axioms of Constitutive Theory 54
2.18 Constitutive Function Restrictions 55
2.19 Constitutive Equations: Spatial Fields 58
2.20 Material Fields 60
2.21 Equations in Material Fields 62
2.22 Surfaces of Discontinuity: Material Fields 68
2.23 Jump Conditions: Material Fields 69
2.24 Constitutive Equations in Material Fields 71
2.25 Equation Summary: Spatial Fields 75
2.26 Equation Summary: Material Fields 76

3 Small Deformation Approximations **79**
3.1 Introduction 79
3.2 Large Deformation Equations: Material Fields 79
3.3 Small Deformation Equations: Material Fields 80

4 Finite Element Formulations **85**
4.1 Introduction 85
4.2 Electroelastic SDA Equations 85
4.3 Weak Forms of Equations 87
4.4 Solution Technique 89
4.4.1 Choice of Independent Variables 91
4.5 Finite Element Formulation 92
4.5.1 Mixed Weak Form 92
4.5.2 Mixed Weak Form Rewritten 92
4.5.3 Test Functions Defined 93
4.5.4 Introducing Test Functions 93
4.5.5 Shape Functions Defined 93
4.5.6 Introducing Constitutive and Shape Functions 94
4.5.7 Jacobian Matrices 94
4.5.8 Define Loading Interpolation Functions 95
4.5.9 Residual Vectors 95

5 Results **97**
5.1 Introduction 97
5.2 Charge Relaxation and Time Scales 97
5.3 Example: Active Fiber Composite 101
5.3.1 Material Model: Polarizable Piezoelectric 101
5.3.2 Analysis Results 106

6 Conclusions **113**

A Integral Theorems **115**

B Finite Element Formulations **117**
B.1 Weak Forms: No Electric Conduction 117
B.2 Finite Element Formulation I 119
B.2.1 Weak Form 119
B.2.2 Weak Form Rewritten 119
B.2.3 Test Functions Defined 119
B.2.4 Shape Functions Defined 120
B.2.5 Introducing Test Functions 120
B.2.6 Newton's Method at Time t 120
B.2.7 Introducing Constitutive and Shape Function 121
B.2.8 Jacobian Matrices 121
B.2.9 Define Loading Interpolation Functions 122

B.2.10 Residual Vectors 122
B.3 Finite Element Formulation II 123
B.3.1 Mixed Weak Form 123
B.3.2 Mixed Weak Form Rewritten 123
B.3.3 Test Functions Defined 123
B.3.4 Shape Functions Defined 124
B.3.5 Introducing Test Functions 124
B.3.6 Introducing Constitutive and Shape Functions 124
B.3.7 Jacobian Matrices 125
B.3.8 Define Loading Interpolation Functions 126
B.3.9 Residual Vectors 126

C Electric Conduction Measurements **127**

D Epoxy Material Model **129**

E Classical Small Deformation Derivation **131**
E.1 Introduction 131
E.1.1 Conservation of energy 131

List of Figures

2-1 Motion χ_t from $\mathcal{B}_o$ to $\mathcal{B}_t$. 20
2-2 Surface of discontinuity for generalized Gauss' theorem. 48
2-3 Line of discontinuity for generalized Stokes' theorem. 50

5-1 Two layer body geometry: Example 5.2.3. 98
5-2 Active fiber composite: finite element mesh. 107
5-3 Active fiber composite dimensions, in $[m] * 10^{-6}$. 107
5-4 Voltage response through thickness. 108
5-5 Axial end face displacement. 109
5-6 Transverse centerline displacements. 109
5-7 Average axial and transverse strains. 110
5-8 Fiber centerline strains. 110
5-9 Fiber centerline electric field response. 111
5-10 Fiber centerline stress response. 111

C-1 Electric conduction measurement circuit. 127

List of Tables

5.1 Charge relaxation time constants. 101

Chapter 1

Introduction

1.1 Motivation

Engineering analysis techniques are used in design and development of actuator and sensor devices to predict the performance of a candidate design. Accurate device analysis allows the engineer to optimize a design for a given performance objective and constraints. Alternately, inaccurate device analysis could lead to poor designs and device failure.

This thesis considers analysis of highly electrically insulating deformable bodies subject to electrical and mechanical loading. The response of such highly insulating devices can be influenced or dominated by the cumulative effects of a very weak electric current flow. Much of the engineering analysis literature is concerned with perfect electrically insulating deformable bodies. The perfect insulator approximation is only accurate provided the time scales of loading are sufficiently fast to prevent the cumulative effects of a weak electric current flow. Device designs based on perfect insulator analyses are likely to fail when subjected to sufficiently slow time scale loadings.

1.2 Objective

This thesis will report on the mathematical abstraction of deformable electromechanical actuator and sensor devices composed of highly electrically insulating materials. A first objective is to present a clear exposition with detailed proofs of the nonlinear large deformation theory of electroelastic continua with electric conduction. A second objective is to investigate the consistency between this general electroelastic continua theory and the classical small deformation piezoelectric theory based on Poynting vector interpretations, extended for electric conduction. A third objective is to develop an engineering analysis tool for deformable electromechanical actuator and sensor devices composed of highly insulating materials with nonlinear response functions (e.g., repolarizable piezoelectric ceramic material), suitable for arbitrary device geometry and loading conditions.

1.3 Background

An excellent monograph on the analysis of electroelastic perfect electrically insulating bodies subject to the assumption of small deformations is TIERSTEN's [29] *Linear Piezoelectric Plate Vibrations.* TIERSTEN presents the balance of energy equation for the classical small deformation theory based on the notion of Poynting's vector as the electric energy flux vector across a surface. The result is a local form of the energy expression containing the scalar product of electric field vector with the time derivative of electric displacement vector. The theory presented in TIERSTEN's monograph can be extended to include the effects of weak electric current density by retaining the electric current density term in Poynting's vector and appending to the system of equations the entropy inequality axiom. As noted by TIERSTEN, the effects of large deformation and electric body forces have been ignored. A natural question to ask is how accurate is this small deformation theory compared to the general large deformation theory, and what are the effects of the ignored electric body forces? This question can be answered by studying the large deformation theory of electroelastic continua and the consequences of introducing a small deformation approximation.

A large deformation theory of electroelastic continua, independent of Poynting vector interpretations, has been developed. See DIXON & ERINGEN [9], MAUGIN & ERINGEN [17] , ERINGEN & MAUGIN [11] for derivations based on a space (volume) averaging procedure, and TIERSTEN [30], TIERSTEN & TSAI [35], and DE LORENZI & TIERSTEN [8] for derivations based on a well defined model of interpenetrating continua. A necessary prerequisite would be a study of large deformation continuum mechanics theory, see ERINGEN [10], OGDEN [21], and GURTIN [15]. We remark that these two derivations result in equivalent theories, and it is worthwhile to study both approaches. An excellent monograph summarizing this large deformation electromagnetic theory is ERINGEN & MAUGIN's [11] *Electrodynamics of Continua I* which contains as a special case the electroelastic theory with electric conduction that we are interested in.

Solutions of the large deformation equations can be difficult to obtain, and therefore introduction of a small deformation approximation is frequently carried out in the literature. Examples of small deformation analyses, usually superposed on a large deformation, have been presented, for example, by TIERSTEN [31, 33, 32, 34], BAUMHAUER & TIERSTEN [3], TIERSTEN & TSAI [35], DE LORENZI & TIERSTEN [8], and also MAUGIN, ET AL [19], ERINGEN & MAUGIN [11], ERINGEN [12], MAUGIN & POUGET [18], ANI & MAUGIN [1].

In all of the above works, the starting point of the analyses are the large deformation electroelastic equations. Reduction to the small deformation equations make explicit exactly what terms are being neglected. Clearly it is desirable to begin an analysis from such a framework. A natural question to ask is, are the equations used in the classical small deformation theory, based on Poynting vector interpretations, consistent with the large deformation theory? The primary equation of concern is the balance of energy expression. Indeed, THURSTON [26] has asked this consistency question regarding the perfectly insulating electromagnetic continua theory. He introduces a total energy function as the sum of an internal energy function and a free

space energy term, then transforms the energy equation in terms of the total energy function to material fields. THURSTON demonstrates that introducing a so-called thermostatic approximation, that ignores certain velocity and magnetization terms, will result in an energy expression that simplifies under the small deformation approximation to the classical energy expression derived using Poynting's vector. Use of the thermostatic approximation is not very satisfactory of a reconciliation between the two theories, and suggests the classical small deformation piezoelectric theory is not consistent with the general electroelastic theory.

THURSTON's result, however, is very interesting. Indeed, the unsatisfactory thermostatic approximation is not needed if the energy equation[1] is restricted from electromagnetic continua to electroelastic continua. Although THURSTON does not emphasize this, the transformed energy expression for electroelastic continua will be exactly consistent, under the small deformation approximation, with the classical energy expression based on Poynting's vector.

MCCARTHY & TIERSTEN [20], working with large deformation semiconducting electroelastic continua, present a transformation for the balance of energy in terms of material fields. The derived balance of energy expression[2], under the small deformation approximation and simplified to electric conduction, will be exactly consistent with the classical form of the energy expression relying on Poynting's vector when extended to include electric conduction.

An approach using THURSTON's transformed energy expression for perfectly insulating continua and MCCARTHY & TIERSTEN's transformed energy expression for semiconducting continua can be used to prove consistency between the large deformation electroelastic continua with electric conduction and the classical small deformation piezoelectric theory relying on Poynting's vector interpretation, extended for electric conduction. Such a study is certainly worthwhile, as it exposes the assumptions and approximations inherent in the classical small deformation theory, including the role of electric body forces.

TIERSTEN's monograph *Linear Piezoelectric Plate Vibrations* is concerned with the analysis of highly electrically insulating piezoelectric bodies in vibration, and therefore does not consider the effects of electric conduction. In fact, highly insulating materials are almost always assumed to be perfectly insulating. It is important to recall that all highly insulating materials, classified in the engineering literature as electrical insulators, will support non-zero electric conduction currents, usually referred to as leakage currents in elementary physics texts [39, 38, 16]. Under sufficiently fast dynamic loading of a highly insulating body, the cumulative effects of weak electric conduction currents are typically negligible, and the perfect insulator approximation may very well be an excellent one.

On the other hand, if the loading time scales are such that very weak electric currents have a cumulative effect, then an analysis based on the perfect insulator approximation could be very inaccurate. Consider the example of a highly insulating piezoelectric device under a sufficiently high frequency sinusoidal electrical loading.

[1]See eq. 13.48 on p.162 of [26]

[2]See eq. 3.16 on p.35 of [20]

In this case, the pefect insulator approximation may be an excellent one. However, consider the same device under identical high frequency electrical loading, but with an additional electric voltage DC offset. After a sufficiently long period of time the cumulative effects of the weak electric current flow will dominate the voltage offset response. This is an example of a typical loading condition on highly insulating devices when electric conduction will in general be signifcant.

1.4 Thesis Contributions

This thesis is based on the recognition that highly electrically insulating actuator and sensor devices under general electrical and mechanical loading must be analysed in the framework of electroelastic continua with electric conduction. This thesis presents a detailed account of the nonlinear theory for large deformation highly insulating electroelastic continua with electric conduction, and proves the consistency between this theory and the classical small deformation piezoelectric theory based on Poynting vector interpretations, extended for electric conduction. The essential step is proving the equivalence of the balance of energy equations in the two theories. A consequence is that electric body forces, recognized mathematically as electric surface tractions, are naturally retained in the small deformation approximation. Finally, this thesis presents a finite element formulation suitable for performance analysis of deformable electromechanical actuator and sensor devices composed of highly insulating materials with nonlinear response functions (e.g., repolarizable piezoelectric ceramic material) and arbitrary device geometries, under the small deformation approximation.

1.5 Thesis Outline

Our presentation is in the framework of continuum physics. We introduce the notion of a body as a collection of points. Deformation is a mapping of the body from some reference configuration to a new deformed configuration. The notion of change of observer and change of reference configuration is introduced. These will be needed for deducing restrictions on the constitutive functions, as required by our constitutive theory axioms. Mathematical results essential to the development are presented. Fundamental axioms of the continuum physics theory are presented in terms of spatial fields. Differential equations are derived from the integral form statements. Jump conditions are derived from integral form statements extended to include surfaces of discontinuity. Constitutive equations are derived in terms of an internal energy function and a total energy function. We introduce the notion of material fields, and systematically derive equivalent material field representations of the global and local equations. Constitutive equations are derived from the material fields, which automatically satisfy the material objectivity axiom. Jump conditions in material fields are derived from integral form statements extended to surfaces of discontininuity. These are needed to piece together solutions across material discontinuities, and specialize to boundary conditions on the bounding surface of a body. The small

deformation approximation is introduced to simplify the governing equations. A weak form of the resulting small deformation equations is presented as a starting point for our finite element formulation. Solution techniques for the finite element equations are presented, with results from analysis of a piezoelectric fiber embedded in an epoxy matrix under an electric voltage DC offset loading, using a nonlinear material model for repolarization.

Chapter 2

Large Deformation Electroelastic Equations

2.1 Introduction

This chapter presents essential theorems and proofs in the nonlinear large deformation theory of electroelastic continua with electric conduction. The differential equations and jump conditions needed for device analysis are summarized in chapter 3 for convenience.

2.2 Bodies, Deformations, and Motions

[1] Bodies have the property that they occupy regions of three dimensional Euclidean point space $\mathcal{E}$. An arbitrary point x in $\mathcal{E}$ is associated with a position vector $\boldsymbol{x}$ in three dimensional Euclidean vector space $\mathbf{E}$, relative to an arbitrarily choosen origin point $o \in \mathcal{E}$. For fixed o, x and $\boldsymbol{x}$ have a unique correspondence, and we can identify the point x with the vector $\boldsymbol{x}$. When o is fixed in $\mathcal{E}$, we use $\boldsymbol{x}$ to denote both a point in $\mathcal{E}$ and its corresponding position vector in $\mathbf{E}$.

We define a body $\mathcal{B}$ as a regular region[1] in $\mathcal{E}$. In general, $\mathcal{B}$ will occupy different regions of $\mathcal{E}$ at different times[2] $t \in \mathbf{R}$. For convenience we choose one such region $\mathcal{B}_o$ as the reference configuration of $\mathcal{B}$. Points in the body can be identified with their positions in $\mathcal{B}_o$. We call points $\boldsymbol{X} \in \mathcal{B}_o$ material points. A deformation $\hat{\chi}$ carries the body from its reference configuration $\mathcal{B}_o$ to a deformed configuration $\mathcal{B}_d$ and carries each material point $\boldsymbol{X}$ to a point $\boldsymbol{x}$,

$$\hat{\chi} : \mathcal{B}_o \to \mathcal{E},$$
$$\hat{\chi} : \boldsymbol{X} \mapsto \boldsymbol{x},$$

[1]This section is based on OGDEN [21, pp. 77-83]

[1]A closed region is the closure of a connected, open set in $\mathcal{E}$. A regular region is a closed region with piecewise smooth boundary.

[2]The set of real numbers is denoted by $\mathbf{R}$.

where we write,

$$\mathcal{B}_d = \hat{\chi}(\mathcal{B}_o).$$

The motion χ_t of $\mathcal{B}$ is a smooth one-parameter family of deformations parameterized

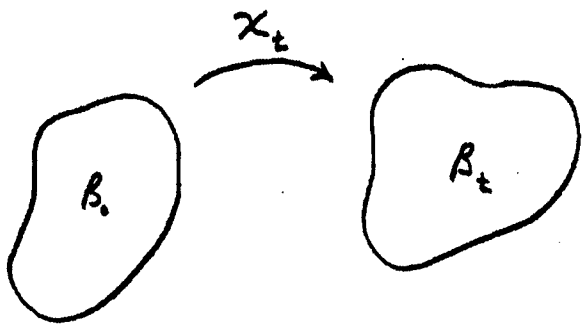

Figure 2-1: Motion χ_t from $\mathcal{B}_o$ to $\mathcal{B}_t$.

by time t. The region $\mathcal{B}_t$ is called the current configuration of $\mathcal{B}$, and the point $\boldsymbol{x}$ is called the spatial point occupied by the material point $\boldsymbol{X}$ at time t,

$$\begin{aligned} \chi_t &: \mathcal{B}_o \to \mathcal{E}, \\ \chi_t &: \boldsymbol{X} \mapsto \boldsymbol{x}. \end{aligned}$$

We write

$$\begin{aligned} \mathcal{B}_t &= \chi(\mathcal{B}_o, t), \\ \boldsymbol{x} &= \chi(\boldsymbol{X}, t). \end{aligned}$$

Axiom 2.2.1 (Axiom of Continuity) [2] *Throughout the body $\mathcal{B}$ the motion χ_t and its inverse are single-valued and as many times continuously differentiable as required.*

The inverse mapping χ_t^{-1} takes the deformed body $\mathcal{B}_t$ back to its reference configuration $\mathcal{B}_o$. We write

$$\begin{aligned} \mathcal{B}_o &= \chi^{-1}(\mathcal{B}_t, t), \\ \boldsymbol{X} &= \chi^{-1}(\boldsymbol{x}, t). \end{aligned}$$

If we choose our reference time corresponding to $\mathcal{B}_o$, at $t = 0$, then the reference configuration $\mathcal{B}_o$ necessarily satisfies

$$\begin{aligned} \mathcal{B}_o &= \chi(\mathcal{B}_o, 0), \\ \mathcal{B}_o &= \chi^{-1}(\mathcal{B}_o, 0). \end{aligned}$$

[2] TRUESDELL & TOUPIN [37, p. 243]

2.3 Observer Transformations

[3] Suppose an event in the physical world manifests itself at a point of Euclidean point space $\mathcal{E}$ and at a time in $\mathbb{R}$. This event will be recorded by an observer O as occuring at $(\boldsymbol{x}, t)$. If $\boldsymbol{x}$ and $\boldsymbol{x}_o$ are distinct points of $\mathcal{E}$ and t and t_o are distinct times in $\mathbb{R}$, then two events observed by O at $(\boldsymbol{x}_o, t_o)$ and $(\boldsymbol{x}, t)$ are seperated by a distance $\|\boldsymbol{x} - \boldsymbol{x}_o\|$ in $\mathcal{E}$ and a time interval $t - t_o$ in $\mathbb{R}$. The definition of an observer transformation is based on the notion that different observers must agree about distance and time intervals between events.

Definition 2.3.1 (Change of Observer) *An observer transformation or change of observer is defined as any transformation that takes $(\boldsymbol{x}_o, t_o)$ and $(\boldsymbol{x}, t)$ to $(\boldsymbol{x}_o^*, t_o^*)$ and $(\boldsymbol{x}^*, t^*)$, such that distances and time intervals are preserved,* [4]

$$\begin{aligned} \|\boldsymbol{x} - \boldsymbol{x}_o\| &= \|\boldsymbol{x}^* - \boldsymbol{x}_o^*\| \,, \\ t - t_o &= t^* - t_o^* \,. \end{aligned}$$

The general form of such a transformation is,

$$\begin{aligned} \boldsymbol{x}^* &= \boldsymbol{Q}(t)\,\boldsymbol{x} + \boldsymbol{b}(t) \,, \qquad t^* = t - a \\ \boldsymbol{Q}'\boldsymbol{Q} &= \boldsymbol{Q}\boldsymbol{Q}' = \boldsymbol{I} \\ \det(\boldsymbol{Q}) &= \pm 1, \end{aligned}$$

where a is an arbitrary scalar, $\boldsymbol{b}(t)$ is an arbitrary vector, and $\boldsymbol{Q}(t)$ is an arbitrary orthogonal tensor. It is convenient to restrict $\boldsymbol{Q}(t)$ to arbitrary proper orthogonal tensors, such that $\det(\boldsymbol{Q}) = 1$.

Remark 2.3.2 (Observer Transformation) *For the motion χ_t of a body $\mathcal{B}$, an observer transformation or change in observer χ_t^* is,*

$$\begin{aligned} \chi^*(\boldsymbol{X}, t^*) &= \boldsymbol{Q}(t)\,\chi(\boldsymbol{X}, t) + \boldsymbol{b}(t) \qquad t^* = t - a. \\ \boldsymbol{Q}'\boldsymbol{Q} &= \boldsymbol{Q}\boldsymbol{Q}' = \boldsymbol{I} \\ \det(\boldsymbol{Q}) &= 1 \,. \end{aligned} \tag{2.1}$$

A transformation (2.1) that takes $(\boldsymbol{x}, t)$ to $(\boldsymbol{x}^*, t^*)$ is interpreted as a change of observer from O to O^*, such that the event recorded by O at $(\boldsymbol{x}, t)$ is the same event as that recorded by O^* at $(\boldsymbol{x}^*, t^*)$. In general, the description of a physical quantity associated with the motion χ_t of a body $\mathcal{B}$ depends on the choice of observer. Such a distinction will be important for deducing restrictions on constitutive equations for material response.

[3] This section is based on OGDEN [21, pp. 73-77] and GURTIN [15, pp. 139-145]

[4] *The 2-norm is defined by,* $\|x_i\| = \left(\sum_{i=1}^{3} x_i^2\right)^{1/2}$

2.4 Fields, Deformations, and Integral Theorems

[5] To introduce definitions of material and spatial fields, we define the reference set $\mathcal{T}_o$ and the trajectory set $\mathcal{T}$ as

$$\begin{aligned} \mathcal{T}_o &= \{(\boldsymbol{X}, t) \,|\, \boldsymbol{X} \in \mathcal{B}_o,\, t \in \mathbf{R}\}, \\ \mathcal{T} &= \{(\boldsymbol{x}, t) \,|\, \boldsymbol{x} \in \mathcal{B}_t,\, t \in \mathbf{R}\}. \end{aligned}$$

Definition 2.4.1 (Material and Spatial Fields) *A material field is a function with domain $\mathcal{T}_o$. A spatial field is a function with domain $\mathcal{T}$.*

Remark 2.4.2 (Fields) *All fields defined over $\mathcal{T}$ are assumed to be as many times continuously differentiable as required. Surfaces and lines of discontinuity will be addressed in section 2.14.*

Much of the theory presented involves integrals over volumes, surfaces, and lines contained in either $\mathcal{B}_o$ or $\mathcal{B}_t$. Here we introduce notation to distinguish between sets of points in the two configurations.

Definition 2.4.3 (Volumes, Surfaces, and Lines in $\mathcal{B}_o$ and $\mathcal{B}$)

- *A material volume V_o is a volume in $\mathcal{B}_o$. The material volume V is the volume in $\mathcal{B}_t$ occupied by the material points $\boldsymbol{X} \in V_o$ at time t,*

$$V = \chi(V_o, t).$$

- *A material surface S_o is a surface in $\mathcal{B}_o$. The material surface S is the surface in $\mathcal{B}_t$ occupied by the material points $\boldsymbol{X} \in S_o$ at time t,*

$$S = \chi(S_o, t).$$

- *A material line C_o is a line in $\mathcal{B}_o$. The material line C is the line in $\mathcal{B}_t$ occupied by the material points $\boldsymbol{X} \in C_o$ at time t,*

$$C = \chi(C_o, t).$$

Many of the proofs will be made more transparent by introducing a Cartesian coordinate system and manipulating vectors and tensors in their component form.

Definition 2.4.4 (Cartesian Coordinate System) *Material and spatial fields will be referred to a single Cartesian coordinate system fixed in $\mathcal{E}$. The set of basis vectors for this system will be denoted by either $\boldsymbol{i}_k$ or $\boldsymbol{i}_K$, with indices $k, K = 1, 2, 3$.*

[5] This section is based on ERINGEN [10, pp. 5-92] and GURTIN [15, pp. 41-85]

Definition 2.4.5 (Summation Convention) *Summation over once repeated indices is understood.*

For example,

$$X_M \boldsymbol{i}_M = X_1 \boldsymbol{i}_1 + X_2 \boldsymbol{i}_2 + X_3 \boldsymbol{i}_3.$$

A material point located in the reference configuration $\mathcal{B}_o$ by $\boldsymbol{P}$ and in the current configuration $\mathcal{B}_t$ by $\boldsymbol{p}$ are represented in the Cartesian coordinate system by

$$\begin{aligned} \boldsymbol{P} &= X_M \boldsymbol{i}_M, \\ \boldsymbol{p} &= x_k \boldsymbol{i}_k. \end{aligned}$$

Definition 2.4.6 (Component Notation Convention) *Components associated with the reference configuration $\mathcal{B}_o$ will consistently have capital indices. Components associated with the current configuration $\mathcal{B}_t$ will consistently have lower case indices.*

Frequently both spatial and material fields will be presented and manipulated in their component form. For example, a spatial vector field $\boldsymbol{A}$, a material tensor field $\boldsymbol{B}$, and a two-point tensor field $\boldsymbol{F}$ are referred to the Cartesian coordinate system by[1]

$$\begin{aligned} \boldsymbol{A} &= A_k \, \boldsymbol{i}_k, \\ \boldsymbol{B} &= B_{RS} \, \boldsymbol{i}_R \otimes \boldsymbol{i}_S, \\ \boldsymbol{F} &= F_{kR} \, \boldsymbol{i}_k \otimes \boldsymbol{i}_R. \end{aligned} \tag{2.2}$$

Consistent with our convention, the fields $\boldsymbol{A}$, $\boldsymbol{B}$, and $\boldsymbol{F}$ can be written in component form as A_k, B_{RS}, and F_{kR} respectively. Similarly, the motion $\boldsymbol{\chi}_t$ of a body may be written in component form as

$$x_k = \chi_k \left(X_M, t \right), \tag{2.3}$$

$$X_M = \chi_M^{-1} \left(x_k, t \right). \tag{2.4}$$

We will occasionally abuse notation by not distinguishing between the function and its value in (2.3) and (2.4). For example,

$$\begin{aligned} \frac{\partial x_k}{\partial X_M} &\equiv \frac{\partial \chi_k \left(X_J, t \right)}{\partial X_M}, \\ \frac{\partial X_M}{\partial x_k} &\equiv \frac{\partial \chi_M^{-1} \left(x_j, t \right)}{\partial x_k}. \end{aligned}$$

Integral transformations will be needed to rewrite conservation laws originally defined over $\mathcal{B}_t$, in terms of fields over $\mathcal{B}_o$. For example, if boundary conditions are only known in terms of the reference configuration $\mathcal{B}_o$, then it can be useful to rewrite the governing equations in terms of fields over $\mathcal{B}_o$.

[1]The tensor product (or dyadic product) of two vectors $\boldsymbol{a}$ and $\boldsymbol{b}$ is denoted $\boldsymbol{a} \otimes \boldsymbol{b}$ and has Cartesian components $(\boldsymbol{a} \otimes \boldsymbol{b})_{ij} = a_i b_j$

Definition 2.4.7 (Jacobian Determinant) *The Jacobian determinant J is assumed to be strictly positive for all time t,*

$$J = \det\left(\frac{\partial x_k}{\partial X_M}\right) > 0.$$

Theorem 2.4.8 (Transformations of Arc, Area, and Volume) *A material element of arc dx_i in the current configuration $\mathcal{B}_t$ is related to its element of arc dX_J in the reference configuration $\mathcal{B}_o$ by*

$$dx_i = \frac{\partial x_i}{\partial X_J}\, dX_J. \tag{2.5}$$

A material element of area $n_i\, dS$ in $\mathcal{B}_t$ is related to its element of area $N_J\, dS_o$ in $\mathcal{B}_o$ by

$$n_i\, dS = J\frac{\partial X_J}{\partial x_i} N_J\, dS_o. \tag{2.6}$$

A material element of volume dV in $\mathcal{B}_t$ is related to its element of volume dV_o in $\mathcal{B}_o$ by

$$dV = J\, dV_o. \tag{2.7}$$

Proof. See ERINGEN [10, pp. 45-48] or OGDEN [21, pp. 83-89] for a proof. ■

Definition 2.4.9 (Kronecker Delta) *The Kronecker delta symbol, δ_{ij}, is defined by*

$$\delta_{ij} = \begin{cases} 1 & i = j \\ 0 & i \neq j \end{cases}$$

Consider a material vector field A_K and a spatial tensor field B_{ij}. It can be verified directly from definition 2.4.9 that the Kronecker delta symbol has the property of changing indices,

$$\begin{aligned} A_K\, \delta_{KM} &= A_M, \\ B_{ij}\, \delta_{jk} &= B_{ik}. \end{aligned}$$

Definition 2.4.10 (Alternating Symbol) *The alternating symbol, ε_{ijk}, is defined by*

$$\varepsilon_{ijk} = \begin{cases} 1 & \textit{if } (ijk) \textit{ is a cyclic permutation of } (123) \\ -1 & \textit{if } (ijk) \textit{ is an anti-cyclic permutation of } (123) \\ 0 & \textit{otherwise} \end{cases}$$

Consider two spatial vector fields $\boldsymbol{a}$ and $\boldsymbol{b}$. It can be verified directly from definition 2.4.10 that the vector cross product of two vectors and the alternating symbol are

related by,

$$(\boldsymbol{a} \times \boldsymbol{b})_i = \varepsilon_{ijk} a_j b_k. \tag{2.8}$$

A direct consequence of (2.8) is an expression for the curl of a vector field in terms of the alternating symbol,

$$(\boldsymbol{\nabla} \times \boldsymbol{b})_i = \varepsilon_{ijk} b_{k,j}.$$

Useful expressions for the determinant and cofactor of a 3×3 matrix A_{ij} in terms of the alternating symbol are[6]

$$\begin{aligned} \det(A_{ij}) &= \frac{1}{6}\varepsilon_{ijk}\varepsilon_{pqr}A_{ip}A_{jq}A_{kr}, \\ \text{cofactor}(A_{ip}) &= \frac{1}{2}\varepsilon_{ijk}\varepsilon_{pqr}A_{jq}A_{kr}. \end{aligned} \tag{2.9}$$

Recall, the cofactor matrix and determinant satisfy[7]

$$\det(A_{ij})(A_{ij})^{-1} = \text{cofactor}(A_{ji}). \tag{2.10}$$

Consider a material tensor field T_{JK}. It can be verified directly from definition 2.4.10 that the equation

$$\varepsilon_{IJK} T_{JK} = 0$$

implies that the anti-symmetric components of T_{JK} are identically zero,

$$T_{[JK]} = 0.$$

Using (2.3) and (2.4) for fixed time t we obtain

$$dx_k = \frac{\partial x_k}{\partial X_M} dX_M, \tag{2.11}$$

$$dX_M = \frac{\partial X_M}{\partial x_k} dx_k. \tag{2.12}$$

From the chain-rule of differention, we obtain the useful relations

$$\begin{aligned} \frac{\partial x_k}{\partial X_M}\frac{\partial X_M}{\partial x_l} &= \delta_{kl}, \\ \frac{\partial X_M}{\partial x_k}\frac{\partial x_k}{\partial X_N} &= \delta_{MN}. \end{aligned}$$

[6]See SEGEL [23, pp. 14-23] for discussion on the alternating symbol and determinants
[7]See STRANG [24, pp. 211-227]

We will frequently introduce a symmetric/anti-symmetric decomposition in our proofs and statements. To simplify our presentation we introduce the following notation.

Definition 2.4.11 (S/A Decomposition) *The symmetric/anti-symmetric (S/A) decomposition of a tensor A_{ij} is defined as*

$$\begin{aligned} A_{(ij)} &= \frac{1}{2}(A_{ij} + A_{ji}) \\ A_{[ij]} &= \frac{1}{2}(A_{ij} - A_{ji}) \\ A_{ij} &= A_{(ij)} + A_{[ij]}. \end{aligned}$$

The deformation and strain tensors introduced next will appear when transforming our equations from spatial to material fields. They also appear when material response functions depending on the displacement gradient are required to be invariant under observer transformations.

Definition 2.4.12 (Deformation and Strain Tensors) *The deformation tensor C_{MN} and the strain tensor E_{MN} are defined as*

$$\begin{aligned} C_{MN}(X_L, t) &= \frac{\partial x_k}{\partial X_M}\frac{\partial x_k}{\partial X_N}, \\ E_{MN}(X_L, t) &= \frac{1}{2}\left(\frac{\partial x_k}{\partial X_M}\frac{\partial x_k}{\partial X_N} - \delta_{MN}\right). \end{aligned}$$

The significance of these tensors is illustrated below. Consider elements $d\boldsymbol{P}$ in $\mathcal{B}_o$ and $d\boldsymbol{p}$ in $\mathcal{B}_t$,

$$\begin{aligned} d\boldsymbol{P} &= dX_M \boldsymbol{i}_M, \\ d\boldsymbol{p} &= dx_k \boldsymbol{i}_k. \end{aligned}$$

The square of these elements are

$$\begin{aligned} dS^2 &= dX_M\, dX_M, \\ ds^2 &= dx_k\, dx_k \\ &= \frac{\partial x_k}{\partial X_M}\frac{\partial x_k}{\partial X_N} dX_M\, dX_N, \\ &= C_{MN}\, dX_M\, dX_N. \end{aligned}$$

The measure of change of length for the same material points in $\mathcal{B}_o$ and $\mathcal{B}_t$ is

$$\begin{aligned} ds^2 - dS^2 &= \left(\frac{\partial x_k}{\partial X_M}\frac{\partial x_k}{\partial X_N} - \delta_{MN}\right) dX_M\, dX_N, \\ &= 2E_{MN}\, dX_M\, dX_N. \end{aligned}$$

Definition 2.4.13 (Comma Notation) *A comma followed by an index denotes*

partial differentiation with respect to a coordinate. For example,

$$\begin{aligned} x_{k,M} &= \frac{\partial x_k}{\partial X_M}, \\ X_{M,k} &= \frac{\partial X_M}{\partial x_k}. \end{aligned}$$

In continuum physics theory, the time rate of change following a material point X_k is frequently encountered. We therefore introduce the following notation.

Definition 2.4.14 (Material Time Derivative) *The material time derivative operator is defined as the time rate of change following a material particle X_M,*

$$\frac{d}{dt}(\,) = \dot{(\,)} = \frac{\partial}{\partial t}(\,)\bigg|_{X_M}.$$

Definition 2.4.15 (Material Velocity) *The material velocity field v_k is defined as*

$$v_k = \frac{\partial \chi_k(X_J, t)}{\partial t}\bigg|_{X_M}.$$

Proposition 2.4.16 (Material Time Derivative: Spatial Fields) *The material time derivative of any spatial field $\phi(x_k, t)$ is*

$$\frac{d\phi}{dt} = \frac{\partial \phi}{\partial t} + v_k\,\phi_{,k}. \tag{2.13}$$

Proof. Introducing $x_k = \chi_k(X_K, t)$ and using the chain rule

$$\begin{aligned} \frac{d\phi}{dt} = \dot{\phi} &= \frac{\partial \phi}{\partial t} + \frac{\partial \phi}{\partial x_k}\frac{\partial x_k}{\partial t}\bigg|_{X_M}, \\ &= \frac{\partial \phi}{\partial t} + v_k\,\phi_{,k}. \end{aligned}$$

■

In continuum mechanics it is natural to express balance laws in terms of integrals over material lines, material surfaces, and material volumes in $\mathcal{B}_t$. Below we state some results that will be useful in working with such integrals.

Lemma 2.4.17 *The material time derivative of the Jacobian determinant J is*

$$\dot{J} = J v_{k,k} \tag{2.14}$$

Proof. From (2.9) we write

$$J = \frac{1}{6}\varepsilon_{ijk}\varepsilon_{IJK}x_{i,I}x_{j,J}x_{k,K}.$$

Differentiating J with respect to $x_{r,R}$ and using (2.9) and (2.10),

$$\begin{aligned}\frac{\partial J}{\partial x_{r,R}} &= \frac{1}{2}\varepsilon_{rjk}\varepsilon_{RJK}x_{j,J}x_{k,K}. \\ &= \text{cofactor}\,(x_{r,R}) \\ &= JX_{R,r}.\end{aligned}$$

Taking the material time derivative of J

$$\dot{J} = \frac{\partial J}{\partial x_{r,R}}\frac{d}{dt}(x_{r,R}) = JX_{R,r}v_{r,R}$$

proves (2.14). ■

Lemma 2.4.18 *The material time derivative of the deformation gradient $X_{J,k}$ is*

$$\frac{d}{dt}(X_{J,i}) = -X_{J,k}\,v_{k,i} \tag{2.15}$$

Proof. Take the material time derivative of

$$X_{J,k}\,x_{k,K} = \delta_{JK},$$

and multiply the result by $X_{K,i}$ to obtain

$$\begin{aligned}\frac{d}{dt}(X_{J,i}) &= -X_{J,k}\,v_{k,n}\,x_{n,K}\,X_{K,i} \\ &= -X_{J,k}\,v_{k,n}\,\delta_{ni}. \end{aligned}\tag{2.16}$$

Equation (2.16) proves (2.15). ■

Below we derive three useful theorems for material time derivatives of integrals over material lines, material surfaces, and material volumes in $\mathcal{B}_t$.

Remark 2.4.19 (Integrals over Elements of $\mathcal{B}_o$) *According to definition 2.4.14, the material time derivative operates holding material points $\boldsymbol{X} \in \mathcal{B}_o$ constant, therefore, the material time derivative operator commutes with integrals defined over elements in $\mathcal{B}_o$.*

Theorem 2.4.20 (Material Time Derivative: Line Integral) *The material time derivative of a line integral of any spatial field ϕ over a material line C in $\mathcal{B}_t$ is*

$$\frac{d}{dt}\int_C \phi\,dx_i = \int_C \left(\dot{\phi}\,dx_i + \phi v_{i,j}\,dx_j\right). \tag{2.17}$$

Proof. Transform the integral over elements in $\mathcal{B}_t$ to an integral over elements in $\mathcal{B}_o$ using (2.5), commute the material time derivative operator with the integral over

C_o, and transform the integral back into an integral over elements in $\mathcal{B}_t$,

$$\begin{aligned}
\frac{d}{dt}\int_C \phi\, dx_i &= \frac{d}{dt}\int_{C_o} \phi x_{i,J}\, dX_J \\
&= \int_{C_o} \left(\dot{\phi} x_{i,J} + \phi v_{i,J}\right) dX_J \\
&= \int_C \left(\dot{\phi} x_{i,J} + \phi v_{i,J}\right) X_{J,j}\, dx_j \\
&= \int_C \left(\dot{\phi}\, \delta_{ij} + \phi v_{i,j}\right) dx_j. \qquad (2.18)
\end{aligned}$$

Equation (2.18) proves (2.17). ■

Theorem 2.4.21 (Material Time Derivative: Surface Integral) *The material time derivative of a surface integral of any spatial field ϕ over a material surface S in $\mathcal{B}_t$ is*

$$\frac{d}{dt}\int_S \phi n_i\, dS = \int_S \left[\left(\dot{\phi} + \phi v_{k,k}\right) n_i - \phi v_{k,i} n_k\right] dS\,. \qquad (2.19)$$

Proof. Transform the integral over elements in $\mathcal{B}_t$ to an integral over elements in $\mathcal{B}_o$ using (2.6), commute the material time derivative operator with the integral over S_o, use the relations (2.14) and (2.15), and transform the integral back into an integral over elements in $\mathcal{B}_t$,

$$\begin{aligned}
\frac{d}{dt}\int_S \phi n_i\, dS &= \frac{d}{dt}\int_{S_o} \phi J X_{J,i} N_J\, dS_o \\
&= \int_{S_o} \left[\dot{\phi} J X_{J,i} + \phi \dot{J} X_{J,i} + \phi J \frac{d}{dt}\left(X_{J,i}\right)\right] N_J\, dS_o \\
&= \int_{S_o} \left[\dot{\phi} J X_{J,i} + \phi J v_{k,k} X_{J,i} - \phi J X_{J,k} v_{k,i}\right] N_J\, dS_o \\
&= \int_S J\left[\left(\dot{\phi} + \phi v_{k,k}\right) X_{J,i} - \phi v_{k,i} X_{J,k}\right] J^{-1} x_{r,J}\, n_r\, dS \\
&= \int_S \left[\left(\dot{\phi} + \phi v_{k,k}\right) \delta_{ir} - \phi v_{k,i}\, \delta_{kr}\right] n_r\, dS\,. \qquad (2.20)
\end{aligned}$$

Equation (2.20) proves (2.19). ■

Theorem 2.4.22 (Material Time Derivative: Volume Integral) *The material time derivative of a volume integral of any spatial field ϕ over a material volume V in $\mathcal{B}_t$ is*

$$\frac{d}{dt}\int_V \phi\, dV = \int_V \left(\dot{\phi} + \phi v_{k,k}\right) dV\,. \qquad (2.21)$$

$$\frac{d}{dt}\int_V \phi\, dV = \int_V \left[\frac{\partial \phi}{\partial t} + \left(\phi v_k\right)_{,k}\right] dV \qquad (2.22)$$

Proof. Transform the integral over elements in $\mathcal{B}_t$ to an integral over elements in $\mathcal{B}_o$ using (2.7), commute the material time derivative operator with the integral over V_o,

use the relation (2.14), and transform the integral back into an integral over elements in $\mathcal{B}_t$,

$$\begin{aligned}
\frac{d}{dt}\int_V \phi\, dV &= \frac{d}{dt}\int_{V_o} \phi J\, dV_o \\
&= \int_{V_o} \left(\dot{\phi} J + \phi \dot{J}\right) dV_o \\
&= \int_{V_o} \left(\dot{\phi} + \phi v_{k,k}\right) J\, dV_o \\
&= \int_V \left(\dot{\phi} + \phi v_{k,k}\right) dV\,. \qquad (2.23)
\end{aligned}$$

Equation (2.23) proves (2.21). Using (2.13) in (2.21) proves (2.22). ■

2.5 Fundamental Axioms of Electromagnetics and Thermomechanics

[8] This section presents the fundamental axioms of electromagnetics and thermomechanics for deformable continua, including both fluids and solids. The electromagnetic equations are presented in terms of rationalized MKS units[9]. The axioms of electromagnetism are defined over spatially fixed line, surface, and volume integrals. In our presentation below, we take these integrals to coincide at time t with the deformed body $\mathcal{B}_t$.

Definition 2.5.1 (Fields)

$$\begin{aligned}
\epsilon_o &= \textit{permittivity of free space} \\
\mu_o &= \textit{permeability of free space} \\
\boldsymbol{E} &= \textit{electric field vector in } \mathcal{B}_t \\
\boldsymbol{H} &= \textit{magnetic field vector in } \mathcal{B}_t \\
\boldsymbol{P} &= \textit{polarization vector in } \mathcal{B}_t \\
\boldsymbol{D} &= \textit{electric displacement vector in } \mathcal{B}_t \\
\boldsymbol{D} &= \epsilon_o \boldsymbol{E} + \boldsymbol{P}, \\
\boldsymbol{M} &= \textit{magnetization vector in } \mathcal{B}_t \\
\boldsymbol{B} &= \textit{magnetic induction vector in } \mathcal{B}_t \\
\boldsymbol{H} &= \frac{1}{\mu_o}\boldsymbol{B} - \boldsymbol{M}, \\
q^F &= \textit{free charge per unit volume in } \mathcal{B}_t \\
\boldsymbol{J}' &= \textit{electric conduction current in } \mathcal{B}_t \textit{ (with respect to fixed frame)} \\
\boldsymbol{J} &= \textit{total electric current in } \mathcal{B}_t \textit{ (with respect to fixed frame)}
\end{aligned}$$

[8] This section is based on ERINGEN & MAUGIN [11, pp. 72-81]
[9] See ERINGEN & MAUGIN [11, p. 406]

$$
\begin{aligned}
\boldsymbol{J} &= \boldsymbol{J}' + q^F \boldsymbol{v} \\
\rho &= \textit{mass per unit volume in } \mathcal{B}_t, \\
\rho_o &= \textit{mass per unit volume in } \mathcal{B}_o, \\
f_i^E &= \textit{electromagnetic or electric force per unit volume in } \mathcal{B}_t, \\
f_i &= \textit{non-electromagnetic force per unit mass}, \\
t_i &= \textit{force per unit area in } \mathcal{B}_t, \\
t_i &= \tau_{ji} n_j, \\
\tau_{ji} &= \textit{Cauchy stress tensor}, \\
C_k^E &= \textit{electromagnetic or electric body couple per unit volume in } \mathcal{B}_t, \\
\epsilon &= \textit{internal energy per unit mass}, \\
\Sigma &= \textit{electromagnetic or electric power per unit volume in } \mathcal{B}_t, \\
h &= \textit{heat power per unit mass}, \\
q &= \textit{heat flux per unit area in } \mathcal{B}_t, \\
\eta &= \textit{entropy per unit mass}, \\
\Theta &= \textit{absolute temperature.}
\end{aligned}
$$

Axiom 2.5.2 (Gauss' Law)

$$\oint_S \boldsymbol{D} \cdot \boldsymbol{n}\, dS = \int_V q^F\, dV. \tag{2.24}$$

Axiom 2.5.3 (Conservation of Magnetic Flux)

$$\oint_S \boldsymbol{B} \cdot \boldsymbol{n}\, dS = 0. \tag{2.25}$$

Axiom 2.5.4 (Faraday's Law)

$$\oint_C \boldsymbol{E} \cdot d\boldsymbol{x} = -\frac{\partial}{\partial t} \int_S \boldsymbol{B} \cdot \boldsymbol{n}\, dS. \tag{2.26}$$

Axiom 2.5.5 (Ampere's Law)

$$\oint_C \boldsymbol{H} \cdot d\boldsymbol{x} = \int_S \boldsymbol{J} \cdot \boldsymbol{n}\, dS + \frac{\partial}{\partial t} \int_S \boldsymbol{D} \cdot \boldsymbol{n}\, dS. \tag{2.27}$$

Axiom 2.5.6 (Conservation of Mass) *The total mass of a material body $\mathcal{B}$ is unchanged during the motion χ_t of the body.*

$$\int_V \rho\, dV = \int_{V_o} \rho_o\, dV_o \tag{2.28}$$

Axiom 2.5.7 (Balance of Momentum) *The time rate of change of momentum of the material body is equal to the resultant force acting upon the body.*

$$\frac{d}{dt} \int_V \rho v_i\, dV = \int_V \left(\rho f_i + f_i^E\right) dV + \oint_S t_i\, dS. \tag{2.29}$$

Axiom 2.5.8 (Balance of Moment of Momentum) *The time rate of moment of momentum of the material body is equal to the resultant moment of all forces and the resultant of all couples acting on the body.*

$$\frac{d}{dt}\int_V \boldsymbol{x}\times\rho\boldsymbol{v}\,dV = \int_V \left[\boldsymbol{x}\times\left(\rho\boldsymbol{f}+\boldsymbol{f}^E\right)+\boldsymbol{C}^E\right]dV + \oint_S \boldsymbol{x}\times\boldsymbol{t}\,dS\,. \tag{2.30}$$

or in component form,

$$\frac{d}{dt}\int_V \varepsilon_{knj}x_n\rho v_j\,dV = \int_V \left[\varepsilon_{knj}x_n\left(\rho f_j+f_j^E\right)+C_k^E\right]dV + \oint_S \varepsilon_{knj}x_n t_j\,dS\,. \tag{2.31}$$

Axiom 2.5.9 (Conservation of Energy) *The time rate of change of the sum of the internal and kinetic energies of a material body, considered as a closed system, is equal to the sum of the rate of work of all forces and couples and the energies that enter or leave the body per unit time.*

$$\begin{aligned}\frac{d}{dt}\int_V\left(\frac{1}{2}\rho v_i v_i+\rho\epsilon\right)dV &= \int_V\left(\Sigma+\rho h+\rho f_i v_i\right)dV\\ &+ \oint_S\left(t_i v_i - q_i n_i\right)dS\,.\end{aligned} \tag{2.32}$$

Axiom 2.5.10 (Law of Entropy) *The time rate of the total entropy is never less than the sum of the entropy supply due to body sources and the entropy influx through the surface of the body.*

$$\frac{d}{dt}\int_V \rho\eta\,dV \geq \int_V \rho\frac{h}{\Theta}\,dV - \oint_S \frac{q_i}{\Theta}n_i\,dS\,. \tag{2.33}$$

Axiom 2.5.11 (Postulate of Localization) *The axioms hold true for any volume element in V, any surface element in S, and any line element in C.*

2.6 Maxwell's Equations

This section deduces the local balance laws from the global axioms.

Theorem 2.6.1 (Maxwell's Equations) *The local equations (2.34)-(2.37) are equivalent to (2.24)-(2.27),*

$$\nabla\cdot\boldsymbol{D} = q^F, \tag{2.34}$$

$$\nabla\cdot\boldsymbol{B} = 0, \tag{2.35}$$

$$\nabla\times\boldsymbol{E} = -\frac{\partial\boldsymbol{B}}{\partial t}, \tag{2.36}$$

$$\nabla\times\boldsymbol{H} = \boldsymbol{J}+\frac{\partial\boldsymbol{D}}{\partial t}. \tag{2.37}$$

Proof. Commute the partial time derivative with the spatially fixed integrals (coinciding at time t with $\mathcal{B}_t$). Applying (A.1), (A.2) to (2.24)-(2.27), and invoking the postulate of localization proves (2.34)-(2.37). ∎

Proposition 2.6.2 (Conservation of Charge) *The conservation of charge equation,*

$$\nabla \cdot \boldsymbol{J} + \frac{\partial q^F}{\partial t} = 0, \tag{2.38}$$

is a consequence of Maxwell's equations (2.34) and (2.37).

Proof. Take the partial time derivative of (2.34) and the divergence of (2.37),

$$\frac{\partial}{\partial t}(\nabla \cdot \boldsymbol{D}) = \frac{\partial q^F}{\partial t} \quad \rightarrow \quad \nabla \cdot \frac{\partial \boldsymbol{D}}{\partial t} = \frac{\partial q^F}{\partial t}, \tag{2.39}$$

$$\nabla \cdot \left(\boldsymbol{J} + \frac{\partial \boldsymbol{D}}{\partial t}\right) = \nabla \cdot (\nabla \times \boldsymbol{H}) \quad \rightarrow \quad \nabla \cdot \left(\boldsymbol{J} + \frac{\partial \boldsymbol{D}}{\partial t}\right) = 0. \tag{2.40}$$

Equation (2.38) follows from (2.39) and (2.40). ■

Definition 2.6.3 (Electromagnetic Energy of Free Space) *The electromagnetic energy of free space U^F is defined as*

$$U^F = \frac{1}{2}\left(\epsilon_o \boldsymbol{E} \cdot \boldsymbol{E} + \frac{1}{\mu_o}\boldsymbol{B} \cdot \boldsymbol{B}\right). \tag{2.41}$$

Theorem 2.6.4 (Poynting's Theorem) *All fields satisfying Maxwell's equations (2.34)-(2.37) satisfy the identities*

$$\boldsymbol{E} \cdot \boldsymbol{J} + \boldsymbol{E} \cdot \frac{\partial \boldsymbol{D}}{\partial t} + \boldsymbol{H} \cdot \frac{\partial \boldsymbol{B}}{\partial t} = -\nabla \cdot (\boldsymbol{E} \times \boldsymbol{H}), \tag{2.42}$$

$$\boldsymbol{E} \cdot \boldsymbol{J} + \boldsymbol{E} \cdot \frac{\partial \boldsymbol{P}}{\partial t} - \boldsymbol{M} \cdot \frac{\partial \boldsymbol{B}}{\partial t} + \frac{\partial U^F}{\partial t} = -\nabla \cdot (\boldsymbol{E} \times \boldsymbol{H}). \tag{2.43}$$

Proof. Take scalar product of (2.37) with $\boldsymbol{E}$, and using the vector identity

$$\nabla \cdot (\boldsymbol{E} \times \boldsymbol{H}) = \boldsymbol{H} \cdot (\nabla \times \boldsymbol{E}) - \boldsymbol{E} \cdot (\nabla \times \boldsymbol{H}),$$

obtain

$$\boldsymbol{E} \cdot \boldsymbol{J} = \boldsymbol{H} \cdot (\nabla \times \boldsymbol{E}) - \nabla \cdot (\boldsymbol{E} \times \boldsymbol{H}) - \boldsymbol{E} \cdot \frac{\partial \boldsymbol{D}}{\partial t}. \tag{2.44}$$

Using (2.36) in (2.44) proves (2.42). Using (2.41) in (2.42) proves (2.43). ■

Remark 2.6.5 (Poynting's Vector) *The vector $(\boldsymbol{E} \times \boldsymbol{H})$ in (2.42) and (2.43) is called Poynting's vector and its surface integral is interpreted as the surface flux of electromagnetic energy. In integral form, Poynting's theorem appears mathematically as a conservation statement, with Poynting's vector as a surface flux term,*

$$\int_V \left(\boldsymbol{E} \cdot \boldsymbol{J} + \boldsymbol{E} \cdot \frac{\partial \boldsymbol{D}}{\partial t} + \boldsymbol{H} \cdot \frac{\partial \boldsymbol{B}}{\partial t}\right) dV = -\oint_S (\boldsymbol{E} \times \boldsymbol{H}) \cdot \boldsymbol{n}\, dS.$$

Physical arguments in support of the Poynting vector interpretation can be found in STRATTON [25].

2.7 EQS Maxwell Equations

In this section the electroquasistatic (EQS) Maxwell equations are defined. These equations are Maxwell's equations (2.34)-(2.37) with the magnetic induction term assumed negligible, see HAUS & MELCHER [16], and TIERSTEN [27]. The EQS equations are a good approximation for materials with small electric current flow, where magnetic fields are presumed negligible.

Definition 2.7.1 (EQS Field) *The EQS electric displacement $\boldsymbol{D}$ is defined as*

$$\boldsymbol{D} = \epsilon_o \boldsymbol{E} + \boldsymbol{P}. \tag{2.45}$$

Definition 2.7.2 (Negligible Magnetic Induction) *The magnetic induction and its partial time derivative are assumed negligibly small,*

$$\frac{\partial \boldsymbol{B}}{\partial t} \approx 0, \tag{2.46}$$

$$\boldsymbol{B} \approx 0. \tag{2.47}$$

Remark 2.7.3 (Approximations) *Equation (2.46) is the usual EQS approximation, permitting a non-zero static magnetic induction field. Equation (2.47) is an additional approximation used to eliminate magnetic terms from the electromagnetic body force and body couple equations (2.73) and (2.80).*

The EQS Maxwell equations are,

$$\nabla \cdot \boldsymbol{D} = q^F, \tag{2.48}$$

$$\nabla \cdot \boldsymbol{B} = 0, \tag{2.49}$$

$$\nabla \times \boldsymbol{E} \approx 0, \tag{2.50}$$

$$\nabla \times \boldsymbol{H} = \boldsymbol{J} + \frac{\partial \boldsymbol{D}}{\partial t}. \tag{2.51}$$

The magnetic field term $\boldsymbol{H}$ can be eliminated by taking the divergence of (2.51) and the partial time derivative of (2.48) to form the conservation of charge statement (2.38). If $\boldsymbol{H}$ is desired it can always be determined from (2.51) once $\boldsymbol{D}$ and $\boldsymbol{E}$ are known. From this point on the EQS Maxwell equations will be defined by:

Definition 2.7.4 (EQS Maxwell Equations)

$$\nabla \cdot \boldsymbol{D} = q^F, \tag{2.52}$$

$$\nabla \times \boldsymbol{E} = 0 \quad \rightarrow \quad \boldsymbol{E} = -\nabla \phi, \tag{2.53}$$

$$\nabla \cdot \boldsymbol{J} + \frac{\partial q^F}{\partial t} = 0. \tag{2.54}$$

Definition 2.7.5 (EQS Poynting Vector) *The EQS Poynting vector* $(\boldsymbol{E} \times \boldsymbol{H})^{EQS}$ *is understood as notation for a vector and is defined by*

$$(\boldsymbol{E} \times \boldsymbol{H})^{EQS} = \phi \left(\boldsymbol{J} + \frac{\partial \boldsymbol{D}}{\partial t} \right). \tag{2.55}$$

Definition 2.7.6 (Electric Energy of Free Space) *The electric energy of free space* U^F *is defined*

$$U^F = \frac{1}{2} \epsilon_o \boldsymbol{E} \cdot \boldsymbol{E}. \tag{2.56}$$

under the EQS approximation.

Theorem 2.7.7 (EQS Poynting's Theorem) *All fields satisfying the EQS Maxwell equations (2.52)-(2.54) satisfy the identities*

$$\boldsymbol{E} \cdot \boldsymbol{J} + \boldsymbol{E} \cdot \frac{\partial \boldsymbol{D}}{\partial t} = -\boldsymbol{\nabla} \cdot (\boldsymbol{E} \times \boldsymbol{H})^{EQS}, \tag{2.57}$$

$$\boldsymbol{E} \cdot \boldsymbol{J} + \boldsymbol{E} \cdot \frac{\partial \boldsymbol{P}}{\partial t} + \frac{\partial U^F}{\partial t} = -\boldsymbol{\nabla} \cdot (\boldsymbol{E} \times \boldsymbol{H})^{EQS}. \tag{2.58}$$

Proof. Using (2.53) and the vector identity

$$\boldsymbol{\nabla} \times (\phi \boldsymbol{H}) = \boldsymbol{\nabla} \phi \times \boldsymbol{H} + \phi \boldsymbol{\nabla} \times \boldsymbol{H},$$

gives

$$\begin{aligned} -\boldsymbol{\nabla} \cdot (\boldsymbol{E} \times \boldsymbol{H}) &= \boldsymbol{\nabla} \cdot [\boldsymbol{\nabla} \times (\phi \boldsymbol{H})] - \boldsymbol{\nabla} \cdot (\phi \boldsymbol{\nabla} \times \boldsymbol{H}), \\ &= -\boldsymbol{\nabla} \cdot (\phi \boldsymbol{\nabla} \times \boldsymbol{H}). \end{aligned} \tag{2.59}$$

Using (2.37), (2.59), (2.55), and (2.46) in (2.42) proves (2.57). Using (2.45) and (2.56) in (2.57) proves (2.58). ■

We will find it convenient to work with a reduced form of the EQS Maxwell equations that do not contain free charge q^F explicitly. First we note the integral form of the EQS equations.

Proposition 2.7.8 (EQS Maxwell: Integral Form) *The integral form of the EQS Maxwell equations (2.52)-(2.54) are*

$$\oint_S D_i n_i \, dS = \int_V q^F \, dV \tag{2.60}$$

$$\oint_C E_i \, dx_i = 0 \tag{2.61}$$

$$\frac{d}{dt} \int_V q^F \, dV + \oint_S J_i' n_i \, dS = 0 \,, \qquad J_i' = J_i - q^F v_i \tag{2.62}$$

Proof. Integrating (2.52) over a material volume V in spatial coordinates and using (A.1) proves (2.60). Integrating (2.53) over an open material surface S in spatial

coordinates and using (A.2) proves (2.61). Integrate (2.54) over a material volume V in spatial coordinates and use (A.1) to obtain

$$\oint_S J_i n_i \, dS + \int_V \frac{\partial q^F}{\partial t} \, dV = 0. \tag{2.63}$$

Using (2.22) and (A.1) in (2.63) proves (2.62). ■

Proposition 2.7.9 (Reduced EQS Maxwell: Integral Form) *The EQS Maxwell equations (2.60)-(2.62) are equivalent to*

$$\frac{d}{dt} \oint_S D_i n_i \, dS + \oint_S J_i' n_i \, dS = 0 \tag{2.64}$$

$$\oint_C E_i \, dx_i = 0 \tag{2.65}$$

Proof. Taking the material time derivative of (2.60) and using in (2.62) proves (2.64). ■

It will be useful to define the following convective time derivative.

Definition 2.7.10 (Convective Time Derivative) *The convective time derivative of a spatial vector field D_i is defined as*

$$D_i^* = \dot{D}_i + D_i v_{k,k} - D_k v_{i,k} \tag{2.66}$$

This definition is motivated by (2.19) and satisfies

$$\frac{d}{dt} \oint_S D_i n_i \, dS = \oint_S D_i^* n_i \, dS \, . \tag{2.67}$$

Proposition 2.7.11 (Reduced EQS Maxwell: Local Form) *The local form of the reduced EQS Maxwell equations (2.64) and (2.65) are*

$$(D_i^* + J_i')_{,i} = 0 \tag{2.68}$$

$$(\nabla \times \boldsymbol{E})_i = 0 \quad \longrightarrow \quad E_i = -\phi_{,i} \tag{2.69}$$

Proof. Equation (2.67) in (2.64) and postulate of localization proves (2.68). Equation (A.2) in (2.65) and postulate of localization proves (2.69). ■

2.8 Conservation of Mass

This section derives the local form of conservation of mass, and also presents a useful material derivative relation.

Theorem 2.8.1 (Local Conservation of Mass) *Local conservation of mass equivalent to (2.28) is*

$$\dot{\rho} + \rho v_{k,k} = 0. \tag{2.70}$$

Proof. Taking the material time derivative of (2.28), using (2.22)

$$\int_V (\dot{\rho} + \rho v_{k,k})\, dV \;=\; 0, \tag{2.71}$$

and taking (2.71) for arbitrary volumes V (postulate of localization) proves (2.70). ■

Proposition 2.8.2 (Material Derivative Relation) *Any spatial field ϕ satisfies the following identity for integrals over a material volume V*

$$\frac{d}{dt}\int_V \rho\phi\, dV = \int_V \rho\dot{\phi}\, dV\,. \tag{2.72}$$

Proof. Consider an aribtrary function ϕ. Using (2.21) and conservation of mass (2.70) we obtain the useful relation

$$\begin{aligned}
\frac{d}{dt}\int_V \rho\phi\, dV &= \int_V \frac{d}{dt}(\rho\phi) + (\rho\phi)v_{k,k}\, dV\,,\\
&= \int_V \rho\dot{\phi} + \phi\,(\dot{\rho} + \rho v_{k,k})\, dV\,,\\
&= \int_V \rho\dot{\phi}\, dV\,.
\end{aligned}$$

■

2.9 Balance of Momentum

Expressions for electromagnetic body force density f_i^E acting on deformable continua have been derived in DIXON & ERINGEN [9], MAUGIN & ERINGEN [17], ERINGEN & MAUGIN [11] based on volume (space) averaging techniques, and in DE LORENZI & TIERSTEN [8] based on a well-defined interpenetrating continua model. The DE LORENZI & TIERSTEN paper is a generalization of earlier works by TIERSTEN [30] and TIERSTEN & TSAI [35].

Definition 2.9.1 (Electromagnetic Body Force) *A polarizable, magnetizable, and electrically conducting deformable media will experience an electromagnetic body force per unit volume in $\mathcal{B}_t$ (to a first approximation) of the form*[10]

$$f_i^E = q^F E_i + P_j E_{i,j} + \varepsilon_{ijk} v_j P_n B_{k,n} + \rho\varepsilon_{ijk}\dot{\Pi}_j B_k + M'_n B_{n,i} + \varepsilon_{ijk} J_j B_k. \tag{2.73}$$
$$\Pi_i = \frac{P_i}{\rho}, \qquad M'_i = M_i + (\boldsymbol{v}\times\boldsymbol{P})_i\,.$$

Introducing approximation (2.47) eliminates magnetic force density terms from (2.73) resulting in the electric body force density definition.

[10]See DE LORENZI & TIERSTEN [8, eq. 3.44, p. 944]. Equation (2.73) is equivalent to ERINGEN & MAUGIN [11, eq. 3.5.26, p. 59]

Definition 2.9.2 (Electrical Body Force) *A polarizable and electrically conducting deformable media will experience an electric body force per unit volume in $\mathcal{B}_t$ (to a first approximation) of the form*

$$f_i^E = q^F E_i + P_j E_{i,j}. \tag{2.74}$$

Proposition 2.9.3 (Electrical Stress Tensor) *The electrical body force density f_i^E defined by (2.74) can be written as the divergence of a second order tensor τ_{ji}^E*

$$\begin{aligned} f_i^E &= \tau_{ji,j}^E, && (2.75)\\ \tau_{ji}^E &= P_j E_i + \epsilon_o E_j E_i - \frac{1}{2}\epsilon_o E_k E_k \delta_{ji}, \\ &= D_j E_i - U^F \delta_{ji}. && (2.76) \end{aligned}$$

Proof. Taking divergence of (2.76) and using (2.52), (2.45), and (2.56)

$$\begin{aligned} \tau_{ji,j}^E &= (D_j E_i)_{,j} - \frac{1}{2}\epsilon_o (E_k E_k \delta_{ji})_{,j}, \\ &= D_{j,j} E_i + D_j E_{i,j} - \epsilon_o E_j E_{j,i}, \\ &= q^F E_i + P_j E_{i,j}. \end{aligned}$$

■

Theorem 2.9.4 (Local Balance of Momentum) *Local balance of momentum statements equivalent to (2.29) are*

$$\left(\tau_{ji} + \tau_{ji}^E\right)_{,j} + \rho\left(f_i - \dot{v}_i\right) = 0, \tag{2.77}$$

$$\tau_{ji,j} + f_i^E + \rho\left(f_i - \dot{v}_i\right) = 0. \tag{2.78}$$

Proof. From (2.72)

$$\frac{d}{dt}\int_V \rho v_i \, dV = \int_V \rho \dot{v}_i \, dV.$$

and noting

$$\begin{aligned} \oint_S \left[t_i(n_j) + t_i^E(n_j)\right] dS &= \oint_S \left(\tau_{ji} + \tau_{ji}^E\right) n_j \, dS, \\ &= \int_V \left(\tau_{ji} + \tau_{ji}^E\right)_{,j} dV. \end{aligned}$$

our balance of momentum statement becomes

$$\int_V \left[\left(\tau_{ji} + \tau_{ji}^E\right)_{,j} + f_i - \rho \dot{v}_i\right] dV. \tag{2.79}$$

Taking (2.79) for arbitrary volumes V (postulate of localization) proves (2.77). Using equation (2.74) in (2.77) proves (2.78). ■

2.10 Balance of Moment of Momentum

An expression for the electromagnetic body couple density C_i^E in deformable continua is derived in ERINGEN & MAUGIN [11] based on a volume (space) averaging techniques.

Definition 2.10.1 (Electromagnetic Body Couple) *A polarizable, magnetizable, and electrically conducting deformable media will experience an electrical body couple per unit volume in $\mathcal{B}_t$ (to a first approximation) of the form*[11]

$$\boldsymbol{C}^E = \boldsymbol{P} \times \boldsymbol{E} + \boldsymbol{M} \times \boldsymbol{B} + \boldsymbol{v} \times (\boldsymbol{P} \times \boldsymbol{B}). \tag{2.80}$$

Introducing approximation (2.47) eliminates magnetic couple terms from (2.80) resulting in the electrical body couple definition:

Definition 2.10.2 (Electrical Body Couple) *A polarizable and electrically conducting deformable media will experience an electrical body couple per unit volume in $\mathcal{B}_t$ (to a first approximation) of the form*

$$\begin{aligned} C_i^E &= e_{ijk} P_j E_k, \\ \boldsymbol{C}^E &= \boldsymbol{P} \times \boldsymbol{E}. \end{aligned} \tag{2.81}$$

Theorem 2.10.3 (Local Balance of Moment of Momemtum) *Local balance of moment of momentum equivalent to (2.31) is*

$$\tau_{[nj]} = E_{[n} P_{j]}. \tag{2.82}$$

Proof. Noting

$$\begin{aligned} \oint_S \varepsilon_{knj} x_n \tau_{ij} n_i \, dS &= \int_V \left(\varepsilon_{knj} x_n \tau_{ji}\right)_{,i} dV \\ &= \int_V \varepsilon_{knj} \left(x_{n,i} \tau_{ij} + x_n \tau_{ij,i}\right) dV, \\ &= \int_V \varepsilon_{knj} \left(\delta_{ni} \tau_{ij} + x_n \tau_{ij,i}\right) dV, \\ &= \int_V \varepsilon_{knj} \left(\tau_{nj} + x_n \tau_{ij,i}\right) dV. \end{aligned} \tag{2.83}$$

Using (2.21)

$$\begin{aligned} \frac{d}{dt} \int_V \varepsilon_{knj} x_n \rho v_j \, dV &= \int_V \left[\frac{d}{dt}\left(\varepsilon_{knj} x_n \rho v_j\right) + \varepsilon_{knj} x_n \rho v_j v_{k,k}\right] dV, \\ &= \int_V \varepsilon_{knj} \left(v_n \rho v_j + x_n \dot{\rho} v_j + x_n \rho \dot{v}_j + x_n \rho v_j v_{k,k}\right) dV. \end{aligned} \tag{2.84}$$

[11] See ERINGEN & MAUGIN [11, eq. 3.5.32, p. 60]

Using (2.83) and (2.84), (2.31) becomes

$$\int_V \varepsilon_{knj}\left[x_n v_j\left(\dot{\rho}+\rho v_{k,k}\right)-x_n\left(-\rho\dot{v}_j+\rho f_j+f_j^E+\tau_{ij,i}\right)-\tau_{nj}\right]dV$$
$$=\int_V C_k^E\,dV\,. \tag{2.85}$$

Using (2.70) and (2.78), (2.85) becomes

$$\int_V\left(\varepsilon_{knj}\tau_{nj}+C_k^E\right)dV=0 \quad\rightarrow\quad \varepsilon_{knj}\tau_{nj}+C_k^E=0. \tag{2.86}$$

Recalling (2.81), (2.86) becomes

$$\begin{aligned}\varepsilon_{knj}\left(\tau_{nj}+P_nE_j\right) &= 0 \quad\rightarrow\quad \tau_{[nj]}+P_{[n}E_{j]}=0,\\ \tau_{[nj]} &= -P_{[n}E_{j]}.\end{aligned} \tag{2.87}$$

Using the anti-symmetric relationship

$$-P_{[n}E_{j]}=E_{[n}P_{j]}.$$

in (2.87) proves (2.82). ■

Definition 2.10.4 (Partial and Total Stress Tensors) *The partial and total stress tensors τ_{ji}^P and τ_{ji}^T are defined as*

$$\tau_{ji}^P = \tau_{ji}+P_jE_i, \tag{2.88}$$
$$\tau_{ji}^T = \tau_{ji}+\tau_{ji}^E, \tag{2.89}$$
$$= \tau_{ji}+D_jE_i-U^F\delta_{ij}. \tag{2.90}$$

The stress tensors τ_{ji}^P and τ_{ji}^T defined above appear in our presentation of the constitutive equations.

Proposition 2.10.5 (Symmetry of Partial and Total Tensors) *Tensors τ_{ji}^P and τ_{ji}^T are symmetric*

$$\tau_{[ji]}^P=0 \tag{2.91}$$
$$\tau_{[ji]}^T=0 \tag{2.92}$$

Proof. Recalling the fact

$$E_{[j}P_{i]}=-P_{[j}E_{i]}$$

and using (2.82) we obtain the anti-symmetric part of τ_{ji} as

$$\tau_{[ji]}=-P_{[j}E_{i]}. \tag{2.93}$$

Introducing the S/A decomposition of τ^P_{ji} and using (2.93)

$$\begin{aligned}\tau^P_{ji} &= \tau^P_{(ji)} + \tau^P_{[ji]} \\ &= \tau_{(ji)} + \tau_{[ji]} + P_{(j}E_{i)} + P_{[j}E_{i]} \\ &= \tau_{(ji)} + P_{(j}E_{i)} \end{aligned} \tag{2.94}$$

Equation (2.94) proves (2.91). Similarly decomposing τ^T_{ji} and using (2.93)

$$\begin{aligned}\tau^T_{ji} &= \tau^T_{(ji)} + \tau^T_{[ji]} \\ &= \tau_{(ji)} + \tau_{[ji]} + P_{(j}E_{i)} + P_{[j}E_{i]} + \epsilon_o E_j E_i - U^F \delta_{ij} \\ &= \tau_{(ji)} + P_{(j}E_{i)} + \epsilon_o E_j E_i - U^F \delta_{ij} \end{aligned} \tag{2.95}$$

Equation (2.95) proves (2.92). ■

2.11 Electromagnetic Power

[12] Expressions for the electromagnetic power density Σ for deformable continua have been derived in DIXON & ERINGEN [9], MAUGIN & ERINGEN [17], ERINGEN & MAUGIN [11] based on volume (space) averaging technqiues, and in DE LORENZI & TIERSTEN [8] based on a well-defined interpenetrating continua model. The DE LORENZI & TIERSTEN paper is a generalization of earlier works by TIERSTEN [30] and TIERSTEN & TSAI [35].

Definition 2.11.1 (Electromagnetic Power Density) *A polarizable, magnetizable, and electrically conducting deformable media has electromagnetic power per unit volume in $\mathcal{B}_t$ (to a first approximation) of the form*[13].

$$\Sigma = \left(P_i E_{j,i} + q^F E_j\right) v_j + E_i \rho \dot{\Pi}_i + J'_i E_i - M'_i \frac{\partial B_i}{\partial t}, \tag{2.96}$$

$$\begin{aligned}\Pi_i &= \frac{P_i}{\rho}, \\ J'_i &= J_i - q^F v_i, \\ M'_i &= M_i + (\boldsymbol{v} \times \boldsymbol{P})_i .\end{aligned} \tag{2.97}$$

Proposition 2.11.2 (Equivalent Electromagnetic Power) *Electromagnetic power density Σ is equivalent to*

$$\Sigma = E_i \frac{\partial P_i}{\partial t} - M_i \frac{\partial B_i}{\partial t} + J_i E_i + (E_i P_i v_j)_{,j}. \tag{2.98}$$

[12] This section is based on THURSTON [26, pp. 157-163]

[13] See DE LORENZI & TIERSTEN [8, eq. 4.4, p.944]. Equation 2.96 is equivalent to ERINGEN & MAUGIN [11, eq. 3.5.41, p. 61]

Proof.

$$\dot{\Pi}_i = \frac{d}{dt}\left(\frac{P_i}{\rho}\right) = \rho^{-1}\dot{P}_i - \rho^{-2}P_i\dot{\rho}.$$

Using (2.70)

$$\begin{aligned}
\dot{\Pi}_i &= \rho^{-1}\dot{P}_i + \rho^{-2}P_i\rho v_{j,j}, \\
\rho\dot{\Pi}_i &= \dot{P}_i + P_i v_{k,k}, && (2.99) \\
&= \frac{\partial P_i}{\partial t} + v_k P_{i,k} + P_i v_{k,k}. && (2.100)
\end{aligned}$$

Recalling the Maxwell equation (2.36),

$$-M_i'\frac{\partial B_i}{\partial t} = -M_i\frac{\partial B_i}{\partial t} + (\boldsymbol{v}\times\boldsymbol{P})_i(\boldsymbol{\nabla}\times\boldsymbol{E})_i.$$

Noting the vector identity,

$$(\boldsymbol{v}\times\boldsymbol{P})_i(\boldsymbol{\nabla}\times\boldsymbol{E})_i = v_k E_{i,k}P_i - P_k E_{i,k}v_i,$$

we obtain

$$\begin{aligned}
-M_i'\frac{\partial B_i}{\partial t} &= -M_i\frac{\partial B_i}{\partial t} + v_k E_{i,k}P_i - P_k E_{i,k}v_i, \\
\Sigma &= E_i\frac{\partial P_i}{\partial t} + E_i P_i v_{j,j} + J_i E_i - M_i\frac{\partial B_i}{\partial t} \\
&+ v_j E_{i,j}P_i + E_i v_j P_{i,j}. && (2.101)
\end{aligned}$$

Grouping terms to obtain $(E_iP_iv_j)_{,j}$ in (2.101) proves (2.98). ∎

2.12 Conservation of Energy: Electroelastic Continua

In this section we establish a series of equivalent statements for conservation of energy.

Theorem 2.12.1 (Conservation of Energy I) *Conservation of energy for electroelastic continua is*

$$\begin{aligned}
\frac{d}{dt}\int_V\left(\frac{1}{2}\rho v_i v_i + \rho\epsilon\right)dV &= \int_V(\Sigma + \rho h + \rho f_i v_i)\,dV \\
&+ \oint_S(t_j v_j - q_i n_i)\,dS\,, && (2.102) \\
\Sigma &= \rho E_i\dot{\Pi}_i + \left(P_i E_{j,i} + q^F E_j\right)v_j + J_i' E_i, && (2.103) \\
\Pi_i &= \frac{P_i}{\rho}, && (2.104) \\
J_i' &= J_i - q^F v_i, && (2.105)
\end{aligned}$$

$$t_j = \tau_{ij} n_i. \tag{2.106}$$

Proof. Theorem 2.12.1 follows immediately from axiom 2.5.9 and definition 2.96 by introducing the EQS approximation (2.46). ■

Proposition 2.12.2 (Equivalent Electric Power Densities) *Electric power density Σ is equivalent to*

$$\Sigma = \rho E_i \dot{\Pi}_i + P_i E_{j,i} v_j + J_i E_i, \tag{2.107}$$

$$\Sigma = E_i \dot{P}_i + E_i P_i v_{j,j} + P_i E_{j,i} v_j + J_i E_i, \tag{2.108}$$

$$\Sigma = E_i \frac{\partial P_i}{\partial t} + (P_i E_i v_j)_{,j} + J_i E_i, \tag{2.109}$$

$$\Sigma = -\frac{\partial U^F}{\partial t} - (\boldsymbol{E} \times \boldsymbol{H})^{EQS}_{i,i} + (P_i E_i v_j)_{,j}. \tag{2.110}$$

Proof. Equation (2.107) follows immediately from (2.103) by using (2.105) and canceling $q^F v_i$ terms. From (2.99)

$$\rho E_i \dot{\Pi}_i = E_i \dot{P}_i + E_i P_i v_{j,j}.$$

Using this in (2.107) proves (2.108). Using (2.46) in (2.98) proves (2.109). ■

Remark 2.12.3 *We can verify that (2.109) is equivalent to (2.108) in the electroelastic approximation by noting $E_i = -\phi_{,i}$ implies*

$$E_{i,j} = -\phi_{,ij} = -\phi_{,ji} = E_{j,i}.$$

Proposition 2.12.4 (Conservation of Energy II) *Conservation of energy statement equivalent to (2.102) is*

$$\frac{d}{dt}\int_V \left(\frac{1}{2}\rho v_i v_i + \rho\epsilon + U^F\right) dV = \int_V \rho\left(h + f_i v_i\right) dV$$
$$+ \oint_S \left[U^F v_i - (\boldsymbol{E} \times \boldsymbol{H})^{EQS}_i + P_j E_j v_i\right] n_i \, dS$$
$$+ \oint_S \left(t_j v_j - q_i n_i\right) dS. \tag{2.111}$$

$$t_j = \tau_{ij} n_i. \tag{2.112}$$

Proof. Adding the term

$$\frac{d}{dt}\int_V U^F \, dV$$

to both sides of (2.102) with (2.110), use (2.19) to obtain

$$\frac{d}{dt}\int_V U^F \, dV = \int_V \left[\frac{\partial U^F}{\partial t} + (U^F v_i)_{,i}\right] dV.$$

Canceling like terms and using the divergence theorem (A.1) proves (2.111). ■

Definition 2.12.5 (Total Energy) *The total energy density U is defined*

$$U = \epsilon + \rho^{-1} U^F \quad \rightarrow \quad \rho U = \rho\epsilon + U^F. \tag{2.113}$$

Theorem 2.12.6 (Conservation of Energy III) *Conservation of energy statement equivalent to (2.102) is* [14]

$$\begin{aligned}\frac{d}{dt}\int_V \left(\frac{1}{2}\rho v_i v_i + \rho U\right) dV &= \int_V \left[E_i \dot{D}_i + \left(U^F + E_i P_i\right) v_{j,j} + P_i E_{j,i} v_j\right] dV \\ &+ \int_V \left(J_i E_i + \rho h + \rho f_i v_i\right) dV \\ &+ \oint_S \left(t_i v_i - q_i n_i\right) dS. \end{aligned} \tag{2.114}$$

Proof. Using (2.17) and (2.102) with (2.108) we can write

$$\begin{aligned}&\frac{d}{dt}\int_V \left(\frac{1}{2}\rho v_i v_i + \rho U\right) dV = \int_V \left(\dot{U}^F + U^F v_{i,i}\right) dV + \frac{d}{dt}\int_V \left(\frac{1}{2}\rho v_i v_i + \rho\epsilon\right) dV, \\ &= \int_V \left(\dot{U}^F + U^F v_{i,i} + E_i \dot{P}_i + E_i P_i v_{j,j} + P_i E_{j,i} v_j\right) dV \\ &+ \int_V \left(J_i E_i + \rho h + \rho f_i v_i\right) dV + \oint_S \left(t_i v_i - q_i n_i\right) dS. \end{aligned} \tag{2.115}$$

Using (2.45) and (2.56) in (2.115) proves (2.114). ■

Next we are interested in simplifying these integral expression and arriving at local forms of energy balance.

Theorem 2.12.7 (Local Conservation of Energy Statements) *Local conservation of energy statements equivalent to (2.102) with (2.108) and to (2.114) are*

$$\rho\dot{\epsilon} = E_i \dot{P}_i + \left[\tau_{ji} + E_k P_k \delta_{ij}\right] v_{i,j} + J_i' E_i + \rho h - q_{i,i}, \tag{2.116}$$

$$\rho\dot{U} = E_i \dot{D}_i + \left[\tau_{ji} + (U^F + E_k P_k)\delta_{ij}\right] v_{i,j} + J_i' E_i + \rho h - q_{i,i}. \tag{2.117}$$

Proof. Using equation (2.72)

$$\frac{d}{dt}\int_V \left(\frac{1}{2}\rho v_i v_i + \rho U\right) dV = \int_V \left(\rho v_i \dot{v}_i + \rho\dot{U}\right) dV. \tag{2.118}$$

From divergence theorem

$$\begin{aligned}\oint_S \left(t_i v_i - q_i n_i\right) dS &= \oint_S \left(\tau_{ji} n_j v_i - q_i n_i\right) dS, \\ &= \int_V \left[\left(\tau_{ji} v_i\right)_{,j} - q_{i,i}\right] dV. \end{aligned} \tag{2.119}$$

Using (2.118), (2.119), and balance of momentum

$$\tau_{ji,j} + q^F E_i + P_j E_{i,j} + \rho\left(f_i - \dot{v}_i\right) = 0.$$

[14] This form of the energy expression is motivated by THURSTON [26, eq. 13.47, p. 162]

in (2.102) with (2.108) and (2.114) we obtain

$$\int_V \rho\dot{\epsilon}\, dV = \int_V \left[E_i\dot{P}_i + E_kP_kv_{i,i} + \tau_{ji}v_{i,j} + J_i'E_i + \rho h - q_{i,i}\right] dV\,, \quad (2.120)$$

$$\int_V \rho\dot{U}\, dV = \int_V \left[E_i\dot{D}_i + (U^F + E_iP_i)v_{j,j} + \tau_{ji}v_{i,j} + J_i'E_i + \rho h - q_{i,i}\right] dV\,. \quad (2.121)$$

respectively. Requiring (2.120) and (2.121) to hold for arbitrary volumes V (postulate of localization) proves (2.116) and (2.117). ■

The next integral form of the energy statement will be particularly useful when deriving jump conditions of the energy across a moving surface of discontinuity.

Theorem 2.12.8 (Conservation of Energy IV: Global Form) *Conservation of energy statement equivalent to (2.102) is* [15]

$$\begin{aligned}\frac{d}{dt}\int_V \left(\frac{1}{2}\rho v_iv_i + \rho\epsilon + U^F\right) dV &= \int_V \rho\left(h + f_iv_i\right) dV \\ &+ \oint_S \left[\left(\tau_{ij} + \tau_{ij}^E\right)v_j - \phi\left(J_i' + D_i^*\right) - q_i\right] dS \end{aligned} \quad (2.122)$$

where the convective derivative D^* is defined in (2.66).

Proof. From (2.111), (2.56), and (2.55),

$$\begin{aligned}\frac{d}{dt}\int_V \left(\frac{1}{2}\rho v_iv_i + \rho\epsilon + U^F\right) dV &= \int_V \rho\left(h + f_iv_i\right) dV \\ + \oint_S \left[\frac{1}{2}\epsilon_oE_kE_kv_i - \phi\left(J_i + \frac{\partial D_i}{\partial t}\right) + P_jE_jv_i\right] n_i\, dS \\ &+ \oint_S \left(t_{ij}v_j - q_i\right) n_i\, dS\,. \end{aligned} \quad (2.123)$$

Noting $\tau_{ij}^E = D_iE_j - \left(\frac{1}{2}\right)\epsilon_oE_kE_k\delta_{ij}$,

$$\begin{aligned}\frac{1}{2}\epsilon_oE_kE_kv_i + P_kE_kv_i &= \left(\frac{1}{2}\epsilon_oE_k + P_k + \frac{1}{2}\epsilon_oE_k\right)E_kv_i - \frac{1}{2}\epsilon_oE_kE_kv_i \\ &= D_kE_kv_i - \frac{1}{2}\epsilon_oE_kE_kv_i \\ &= \tau_{ij}^Ev_j + D_kE_kv_i - D_iE_jv_j. \end{aligned} \quad (2.124)$$

Next consider the term we temporarily define as t,

$$\begin{aligned} t &= \oint_S \left(D_kE_kv_i - D_iE_jv_j\right) n_i\, dS \\ &= \int_V \left(D_kE_kv_i - D_iE_jv_j\right)_{,i}\, dV\,. \end{aligned}$$

[15] This conservation of energy equation was derived by McCarthy & Tiersten [20, eq. 3.13, p. 35], in the context of semiconducting continua.

Introducing $E_k = -\phi_{,k}$,

$$E_{k,j} = -\phi_{,jk} = -\phi_{,kj} = E_{j,k}.$$

then,

$$\begin{aligned} t &= \int_V (D_k v_i)_{,i} E_k + D_i v_j E_{i,j} - E_j (D_i v_j)_{,i} - D_i v_j E_{j,i} \, dV \\ &= \int_V (D_k v_i)_{,i} E_k - E_k (D_i v_k)_{,i} \, dV \\ &= \int_V \phi_{,k} (D_i v_k - D_k v_i)_{,i} \, dV \\ &= \int_V \left[\phi (D_i v_k - D_k v_i)_{,i}\right]_{,k} - \phi (D_i v_k - D_k v_i)_{,ik} \, dV \end{aligned}$$

Noting that $(D_i v_k - D_k v_i)_{,ik} = 0$ and using (2.52),

$$\begin{aligned} t &= \int_V \left[\phi (D_i v_k - D_k v_i)_{,i}\right]_{,k} dV \\ &= \oint_S \phi (D_i v_k - D_k v_i)_{,i} n_k \, dS \\ &= \oint_S \phi \left(q^F v_k + D_i v_{k,i} - D_{k,i} v_i - D_k v_{i,i}\right) n_k \, dS . \end{aligned} \tag{2.125}$$

Using (2.124) and (2.125) in (2.123) gives

$$\begin{aligned} \frac{d}{dt} \int_V \left(\frac{1}{2}\rho v_i v_i + \rho\epsilon + U^F\right) dV &= \int_V \rho (h + f_i v_i) \, dV + \oint_S \left[\left(\tau_{ij} + \tau_{ij}^E\right) v_j\right] n_i \, dS \\ + \oint_S \left[\phi \left(q^F v_i - J_i - \frac{\partial D_i}{\partial t} - D_{i,k} v_k + D_k v_{i,k} - D_i v_{k,k}\right) - q_i\right] n_i \, dS . \end{aligned} \tag{2.126}$$

Using $J_i' = J_i - q^F v_i$ and (2.13) in (2.126) gives,

$$\begin{aligned} \frac{d}{dt} \int_V \left(\frac{1}{2}\rho v_i v_i + \rho\epsilon + U^F\right) dV &= \int_V \rho (h + f_i v_i) \, dV \\ + \oint_S \left[\left(\tau_{ij} + \tau_{ij}^E\right) v_j + \phi \left(-J_i' - \dot{D}_i + D_k v_{i,k} - D_i v_{k,k}\right) - q_i\right] n_i \, dS . \end{aligned} \tag{2.127}$$

Finally using (2.66) in (2.127) proves (2.122). ■

Theorem 2.12.9 (Conservation of Energy IV: Local Form) *The local form of conservation of energy statement for (2.122), in terms of the function $U = \epsilon + \rho^{-1} U^F$, is*

$$\rho \dot{U} = \rho h + \left(\tau_{ij} + \tau_{ij}^E\right) v_{j,i} + E_i \left(J_i' + D_i^*\right) - q_{i,i} \tag{2.128}$$

Proof. Using (A.1), (2.72) and the postulate of localization with (2.122) gives,

$$\rho \dot{v}_i v_i + \rho \dot{U} = \rho h + \rho f_i v_i + \left(\tau_{ij} + \tau_{ij}^E\right)_{,i} v_j + \left(\tau_{ij} + \tau_{ij}^E\right) v_{j,i}$$

$$- \quad \phi_{,i}\left(J_i' + D_i^*\right) - \phi\left(J_i' + D_i^*\right)_{,i} - q_{i,i}. \tag{2.129}$$

Using (2.77) and (2.64) in (2.129) proves (2.128). ■

2.13 Entropy Inequality

Theorem 2.13.1 (Local Entropy Inequality) *Local entropy inequality statement equivalent to (2.33) is*

$$\rho\dot{\eta} + \left(\frac{q_i}{\Theta}\right)_{,i} - \rho\frac{h}{\Theta} \geq 0, \tag{2.130}$$

$$\rho\Theta\dot{\eta} + q_{i,i} - q_i\Theta^{-1}\Theta_{,i} - \rho h \geq 0. \tag{2.131}$$

Proof. Using (2.72)

$$\frac{d}{dt}\int_V \rho\eta\, dV = \int_V \rho\dot{\eta}\, dV\,.$$

and noting

$$\oint_S \frac{q_i}{\Theta} n_i\, dS = \int_V \left(\frac{q_i}{\Theta}\right)_{,i} dV\,.$$

we obtain

$$\int_V \left[\rho\dot{\eta} + \left(\frac{q_i}{\Theta}\right)_{,i} - \rho\frac{h}{\Theta}\right] dV \geq 0. \tag{2.132}$$

Taking (2.132) for arbitrary volumes V (postulate of localization) proves (2.130). Expanding divergence term in (2.130) and multiplying by Θ proves (2.131). ■

2.14 Surfaces of Discontinuity

[16] In this section we generalize our global balance laws to include moving surfaces of discontinuity.

Definition 2.14.1 (Discontinuity Surfaces and Lines) *A surface (line) on which a material or spatial field is not continuous, is called a surface (line) of discontinuity.*

Discontinuity surfaces such as shock waves in nonlinear wave propagation problems frequently arise in applications. In this section we derive generalized expressions for Gauss, Stokes, and material time derivative theorems. These will allow us to extend our global balance laws to include surfaces and lines of discontinuity. Application of the postulate of localization will result in jump conditions that fields must satisfy across such surfaces and lines.

[16] This section is based on ERINGEN [10, pp. 427-429]

Recall the Gauss theorem for a spatial vector field A_k,

$$\int_V A_{k,k}\, dV = \oint_S A_k n_k\, dS$$

where S is the material surface enclosing the material volume V in spatial coordinates. We extend this theorem to regions containing a discontinuity surface with the following theorem.

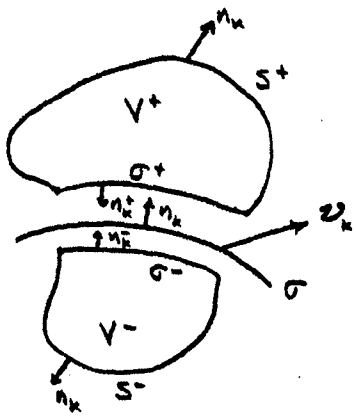

Figure 2-2: Surface of discontinuity for generalized Gauss' theorem.

Theorem 2.14.2 (Generalized Gauss) *A spatial field A_k defined over a material volume V in $\mathcal{B}_t$, bounded by surface S, and containing a surface of discontinuity σ satisfies the integral statement,*

$$\begin{aligned} \oint_{S-\sigma} A_k n_k\, dS &= \int_{V-\sigma} A_{k,k}\, dV + \int_\sigma [\![A_k]\!] n_k\, dS \qquad (2.133) \\ [\![A_k]\!] &= A_k^+ - A_k^- \\ V-\sigma &= V^+ + V^- \\ S-\sigma &= S^+ + S^- \end{aligned}$$

where A_k^+ and A_k^- are the limiting values of A_k as the discontinuity surface σ is approached from the positive n_k side and negative n_k side, respectively.

Proof. From the Gauss theorem,

$$\begin{aligned} \int_{V^+} A_{k,k}\, dV &= \int_{S^+} A_k n_k\, dS + \int_{\sigma^+} A_k n_k^+\, dS \\ \int_{V^-} A_{k,k}\, dV &= \int_{S^-} A_k n_k\, dS + \int_{\sigma^-} A_k n_k^-\, dS \end{aligned}$$

In the limit as $\sigma^+ \to \sigma$, $n_k^+ \to -n_k$. In the limit as $\sigma^- \to \sigma$, $n_k^- \to n_k$. Then taking the limit as σ^+ and σ^- approach the discontinuity surface σ,

$$\int_{V^+ + V^-} A_{k,k}\, dV = \int_{S^+ + S^-} A_k n_k\, dS - \int_\sigma [\![A_k]\!] n_k\, dS\,. \qquad (2.134)$$

Equation (2.134) proves (2.133). ■

We use this generalized Gauss theorem to obtain the following useful generalized integral theorem.

Theorem 2.14.3 (Generalized Material Derivative Statement) *A spatial field ϕ defined over a material volume V in $\mathcal{B}_t$ and containing a surface of discontinuity σ moving with absolute velocity ν_k satisfies the integral statement,*

$$\begin{aligned} \frac{d}{dt}\int_{V-\sigma} \phi\, dV &= \int_{V-\sigma} \dot{\phi} + \phi v_{k,k}\, dV + \int_{\sigma} [\![\, \phi\,(v_k - \nu_k)\,]\!]\, n_k\, dS \\ [\![\, A_k \,]\!] &= A_k^+ - A_k^- \\ V - \sigma &= V^+ + V^- \\ S - \sigma &= S^+ + S^-. \end{aligned} \tag{2.135}$$

Proof.

$$\begin{aligned} \frac{d}{dt}\int_{V^+} \phi\, dV &= \int_{V^+} \frac{\partial \phi}{\partial t}\, dV + \int_{S^+} \phi v_k n_k\, dS + \int_{\sigma^+} \phi \nu_k n_k^+\, dS \\ \frac{d}{dt}\int_{V^-} \phi\, dV &= \int_{V^-} \frac{\partial \phi}{\partial t}\, dV + \int_{S^-} \phi v_k n_k\, dS + \int_{\sigma^-} \phi \nu_k n_k^-\, dS\,. \end{aligned}$$

In the limit as $\sigma^+ \to \sigma$, $n_k^+ \to -n_k$. In the limit as $\sigma^- \to \sigma$, $n_k^- \to n_k$. Then taking the limit as σ^+ and σ^- approach the discontinuity surface σ,

$$\begin{aligned} \frac{d}{dt}\int_{V^+ + V^-} \phi\, dV &= \int_{V^+ + V^-} \frac{\partial \phi}{\partial t}\, dV + \int_{S^+ + S^-} \phi v_k n_k\, dS \\ &- \int_{\sigma} [\![\, \phi \,]\!]\, \nu_k n_k\, dS\,. \end{aligned}$$

From the generalized Gauss theorem,

$$\int_{S-\sigma} \phi v_k n_k\, dS = \int_{V-\sigma} (\phi v_k)_{,k}\, dV + \int_{\sigma} [\![\, \phi v_k \,]\!]\, n_k\, dS\,.$$

Then noting that ν_k commutes with $[\![\,\cdot\,]\!]$ operator,

$$\frac{d}{dt}\int_{V-\sigma} \phi\, dV = \int_{V-\sigma} \left(\frac{\partial \phi}{\partial t} + \phi_{,k} v_k + \phi v_{k,k} \right) dV + \int_{\sigma} [\![\, \phi\,(v_k - \nu_k)\,]\!]\, n_k\, dS\,. \tag{2.136}$$

Using (2.13) in (2.136) proves (2.135). ■

We will require a generalized version of Stokes's theorem to account for a line of discontinuity in a surface S.

Theorem 2.14.4 (Generalized Stokes') *A spatial field A_k defined over an open material surface S in $\mathcal{B}_t$, bounded by the line C, and containing a line of discontinuity γ satisfies the integral statement,*

$$\oint_{C-\gamma} A_i\, dx_i = \int_{S-\gamma} (\boldsymbol{\nabla} \times \boldsymbol{A})_i\, n_i\, dS + \int_{\gamma} [\![\, A_i \,]\!]\, dx_i \tag{2.137}$$

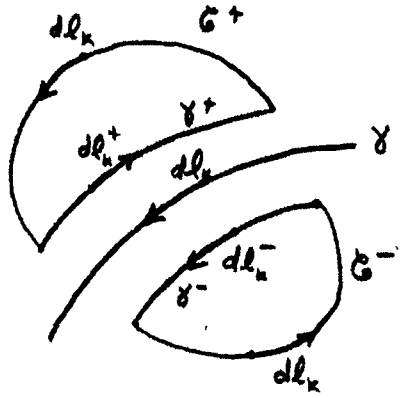

Figure 2-3: Line of discontinuity for generalized Stokes' theorem.

$$
\begin{aligned}
[A_i] &= A_i^+ - A_i^- \\
S - \gamma &= S^+ + S^- \\
C - \gamma &= C^+ + C^- .
\end{aligned}
$$

Proof. From Stokes' theorem,

$$
\begin{aligned}
\int_{S+} (\nabla \times \boldsymbol{A})_i \, n_i \, dS &= \int_{C^+} A_i \, dx_i + \int_{\gamma^+} A_i \, dx_i^+ \\
\int_{S-} (\nabla \times \boldsymbol{A})_i \, n_i \, dS &= \int_{C^-} A_i \, dx_i + \int_{\gamma^-} A_i \, dx_i^-
\end{aligned}
$$

In the limit as $\gamma^+ \to \gamma$, $dx_k^+ \to -dx_k$. In the limit as $\gamma^- \to \gamma$, $dx_k^- \to dx_k$. Then taking the limit as γ^+ and γ^- approach the discontinuity line γ,

$$
\int_{S^+ + S^-} (\nabla \times \boldsymbol{A})_i \, n_i \, dS = \int_{C^+ + C^-} A_i \, dx_i - \int_{\gamma} [A_i] \, dx_i
$$

proves (2.137). ■

2.15 Jump Conditions

In this section we use the generalized theorems derived earlier to obtain jump conditions across surfaces of discontinuity. First we summarize in convenient integral form the electroelastic EQS equations.

Proposition 2.15.1 (Integral EQS Electroelastic Equations: Spatial Form)

$$
\begin{aligned}
\oint_{S-\sigma} (D_i^* + J_i') \, n_i \, dS &= 0 \\
\oint_{C-\gamma} E_i \, dx_i &= 0
\end{aligned}
$$

$$
\begin{aligned}
\frac{d}{dt}\int_{V-\sigma}\rho\,dV &= 0 \\
\frac{d}{dt}\int_{V-\sigma}\rho v_i\,dV &= \oint_{S-\sigma}\left(\tau_{ji}+\tau_{ji}^{E}\right)dS+\int_{V-\sigma}\rho f_i\,dV \qquad (2.138)\\
\frac{d}{dt}\int_{V-\sigma}\left(\frac{1}{2}\rho v_i v_i+\rho\epsilon+U^F\right)dV &= \int_{V-\sigma}\rho\left(h+f_i v_i\right)dV \\
&\quad+\oint_{S-\sigma}\left[\left(\tau_{ij}+\tau_{ij}^{E}\right)v_j-\phi\left(J_i'+D_i^*\right)-q_i\right]dS \\
\frac{d}{dt}\int_{V-\sigma}\rho\eta\,dV &\geq \int_{V-\sigma}\rho\frac{h}{\Theta}\,dV-\oint_{S-\sigma}\frac{q_i}{\Theta}n_i\,dS
\end{aligned}
$$

Jump conditions are obtained by applying the three generalized integral theorems derived earlier and valid for volumes containing a surface discontinuity moving at velocity ν_k. Applying the postulate of localization then results in differential equations derived earlier and new jump conditions across the discontinuity surface and discontinuity line.

The above procedure is straight forward and will be illustrated for the balance of momentum equation.

Example 2.15.2 (Jump Condition Calculations) Applying (2.133) and (2.135) gives

$$
\begin{aligned}
\frac{d}{dt}\int_{V-\sigma}(\rho v_i)\,dV &= \int_{V-\sigma}\left[\frac{d}{dt}(\rho v_i)+(\rho v_i)\,v_{k,k}\right]dV \\
&\quad+\int_{\sigma}[\![\,\rho v_i\left(v_k-\nu_k\right)]\!]\,n_k\,dS \qquad (2.139)\\
\oint_{S-\sigma}\left(\tau_{ji}+\tau_{ji}^{E}\right)n_j\,dS &= \int_{V-\sigma}\left(\tau_{ji}+\tau_{ji}^{E}\right)dV+\int_{\sigma}[\![\,\tau_{ji}+\tau_{ji}^{E}\,]\!]\,n_j\,dS \qquad (2.140)
\end{aligned}
$$

Using (2.139) and (2.140) in (2.138), the global momentum balance laws for a volume containing a discontinuity surface moving with absolute velocity ν_k, becomes

$$
\begin{aligned}
\int_{V-\sigma}\left[\frac{d}{dt}(\rho v_i)+(\rho v_i)\,v_{k,k}\right]dV &+ \int_{\sigma}[\![\,\rho v_i\left(v_j-\nu_j\right)-\left(\tau_{ji}+\tau_{ji}^{E}\right)]\!]\,n_j\,dS \\
&= \int_{V-\sigma}\left(\tau_{ji}+\tau_{ji}^{E}\right)_{,j}+\rho f_i\,dV
\end{aligned}
$$

From the postulate of localization we obtain

$$
\begin{aligned}
\frac{d}{dt}(\rho v_i)+(\rho v_i)\,v_{k,k} &= \left(\tau_{ji}+\tau_{ji}^{E}\right)_{,j}+\rho f_i && \text{in } V-\sigma \\
[\![\,\rho v_i\left(v_j-\nu_j\right)]\!]\,n_j &= [\![\,\tau_{ji}+\tau_{ji}^{E}\,]\!]\,n_j && \text{across } \sigma.
\end{aligned}
$$

The differential equation is equivalent to local form for balance of momentum we derived earlier. The jump condition across the moving discontinuity surface σ is new.

Here we summarize the corresponding jump conditions for the EQS electroelastic equations in spatial fields.

Proposition 2.15.3 (Jump Conditions: Moving Surface of Discontinuity)

$$
\begin{aligned}
[\![D_i^* + J_i']\!] n_i &= 0 && \textit{across } \sigma \\
[\![\phi]\!] &= 0 && \textit{across } \gamma \\
[\![x_k]\!] &= 0 && \textit{across } \sigma \\
[\![\rho (v_k - \nu_k)]\!] n_k &= 0 && \textit{across } \sigma \\
[\![\rho v_i (v_k - \nu_k)]\!] n_j &= [\![\tau_{ji} + \tau_{ji}^E]\!] n_j && \textit{across } \sigma \\
[\![\left(\frac{1}{2}\rho v_j v_j + \rho\epsilon + U^F\right) (v_i - \nu_i)]\!] n_i &= \\
[\![\left(\tau_{ij} + \tau_{ij}^E\right) v_j - \phi (J_i' + D_i^*) - q_i]\!] n_i && \textit{across } \sigma \\
[\![\rho\eta (v_j - \nu_j)]\!] n_j &\geq -[\![\frac{q_j}{\Theta}]\!] n_j && \textit{across } \sigma
\end{aligned}
$$

Proposition 2.15.4 (Jump Conditions: Material Surface of Discontinuity)

$$
\begin{aligned}
[\![D_i^* + J_i']\!] n_i &= 0 && \textit{across } \sigma \\
[\![\phi]\!] &= 0 && \textit{across } \gamma \\
[\![x_k]\!] &= 0 && \textit{across } \sigma \\
[\![\tau_{ji} + \tau_{ji}^E]\!] n_j &= 0 && \textit{across } \sigma \\
[\![\left(\tau_{ij} + \tau_{ij}^E\right) v_j - \phi (J_i' + D_i^*) - q_i]\!] n_i &= 0 && \textit{across } \sigma \\
[\![\frac{q_j}{\Theta}]\!] n_j &\geq 0 && \textit{across } \sigma
\end{aligned}
$$

2.16 Objective Fields and Reference Configurations

[17] In this section we define the notion of an objective field. Objective fields are quantities that are independent of observer or form invariant under observer transformations. In the following section we introduce three axioms of constitutive theory. One of these requires that material response functions be independent of observer, that is, objective. This notion is then used to deduce restrictions on the allowable class of material response functions. For example, material objectivity restricts a scalar function depending on the deformation gradient $x_{i,K}$, which is not an objective function, to a scalar function depending on the strain tensor E_{JK}, which is an objective function. In this manner, the strain tensor arises naturally in the mathematical description of material response. Next we introduce change of reference configuration. Material symmetries can be characterized by a required invariance under a class of reference configuration transformations.

Prior to stating our definition of objective fields, we define arbitrary line elements $d\boldsymbol{x}_1, d\boldsymbol{x}_2$ in $\mathcal{B}_t$ and line elements $d\boldsymbol{X}_1, d\boldsymbol{X}_2$ in $\mathcal{B}_o$. Under an observer transformation

[17] This section is based on OGDEN [21, pp. 133-137] and GURTIN [15, pp. 165-175]

(2.1) the material line elements remain unchanged and spatial line elements transform as,

$$d\boldsymbol{x}_k^* = \boldsymbol{Q}(t)\, d\boldsymbol{x}_k \quad \text{for} \quad k = 1, 2.$$

Definition 2.16.1 (Objective Fields) *Objective scalar, vector, tensor, and two-point tensor fields with domains both in $\mathcal{T}$ and $\mathcal{T}_o$ are defined according to transformations under a change in observer. Consider the following fields,*

- *A spatial scalar field ϕ*
- *A material scalar field Φ*
- *A spatial vector field $\boldsymbol{A} = A_j \boldsymbol{i}_j$*
- *A material vector field $\boldsymbol{H} = H_K \boldsymbol{i}_K$*
- *A spatial tensor field $\boldsymbol{B} = B_{ij} \boldsymbol{i}_i \otimes \boldsymbol{i}_j$*
- *A material tensor field $\boldsymbol{M} = M_{RS} \boldsymbol{i}_R \otimes \boldsymbol{i}_S$*
- *A spatial two-point tensor field $\boldsymbol{G} = G_{Ki} \boldsymbol{i}_K \otimes \boldsymbol{i}_i$*
- *A material two-point tensor field $\boldsymbol{F} = F_{iK} \boldsymbol{i}_i \otimes \boldsymbol{i}_K$*

These fields are said to be objective if,

$$\begin{aligned}
\phi^*(\boldsymbol{x}^*, t^*) &= \phi(\boldsymbol{x}, t), \\
\Phi^*(\boldsymbol{X}, t^*) &= \Phi(\boldsymbol{X}, t) \\
d\boldsymbol{x}_1^{*\prime} \boldsymbol{A}^*(\boldsymbol{x}^*, t^*) &= d\boldsymbol{x}_1{}' \boldsymbol{A}(\boldsymbol{x}, t), \\
d\boldsymbol{X}_1{}' \boldsymbol{H}^*(\boldsymbol{X}, t^*) &= d\boldsymbol{X}_1{}' \boldsymbol{H}(\boldsymbol{X}, t), \\
d\boldsymbol{x}_1^{*\prime} \boldsymbol{B}^*(\boldsymbol{x}^*, t^*)\, d\boldsymbol{x}_2^* &= d\boldsymbol{x}_1{}' \boldsymbol{B}(\boldsymbol{x}, t)\, d\boldsymbol{x}_2, \\
d\boldsymbol{X}_1{}' \boldsymbol{M}^*(\boldsymbol{X}^*, t^*)\, d\boldsymbol{X}_2 &= d\boldsymbol{X}_1{}' \boldsymbol{M}(\boldsymbol{X}, t)\, d\boldsymbol{X}_2, \\
d\boldsymbol{X}_1{}' \boldsymbol{G}^*(\boldsymbol{x}^*, t^*)\, d\boldsymbol{x}_1^* &= d\boldsymbol{X}_1{}' \boldsymbol{G}(\boldsymbol{x}, t)\, d\boldsymbol{x}_1, \\
d\boldsymbol{x}_1^{*\prime} \boldsymbol{F}^*(\boldsymbol{X}, t^*)\, d\boldsymbol{X}_1 &= d\boldsymbol{x}_1{}' \boldsymbol{F}(\boldsymbol{X}, t)\, d\boldsymbol{X}_1.
\end{aligned}$$

Recall, for example, that $\phi^*(\boldsymbol{x}^*, t^*)$ and $\phi(\boldsymbol{x}, t)$ are quantities associated with the same event as recorded by two different observers, O^* and O respectively.

Remark 2.16.2 (Objective Fields) *Definition 2.16.1 implies the following transformation requirements for objective fields under a change in observer (2.1):*

$$\phi^*(\boldsymbol{x}^*, t^*) = \phi(\boldsymbol{x}, t). \tag{2.141}$$

$$\Phi^*(\boldsymbol{X}, t^*) = \Phi(\boldsymbol{X}, t). \tag{2.142}$$

$$\boldsymbol{A}^*(\boldsymbol{x}^*, t^*) = \boldsymbol{Q}(t) \boldsymbol{A}(\boldsymbol{x}, t). \tag{2.143}$$

$$\boldsymbol{H}^*(\boldsymbol{X}, t^*) = \boldsymbol{H}(\boldsymbol{X}, t). \tag{2.144}$$

$$\boldsymbol{B}^*(\boldsymbol{x}^*, t^*) = \boldsymbol{Q}(t) \boldsymbol{B}(\boldsymbol{x}, t) \boldsymbol{Q}(t)'. \tag{2.145}$$

$$
\begin{aligned}
\boldsymbol{M}^*(\boldsymbol{X}^*, t^*) &= \boldsymbol{M}(\boldsymbol{X}, t). && (2.146)\\
\boldsymbol{G}^*(\boldsymbol{x}^*, t^*) &= \boldsymbol{G}(\boldsymbol{x}, t)\boldsymbol{Q}(t)'. && (2.147)\\
\boldsymbol{F}^*(\boldsymbol{X}, t^*) &= \boldsymbol{Q}(t)\boldsymbol{F}(\boldsymbol{X}, t). && (2.148)
\end{aligned}
$$

Definition 2.16.3 (Change of Reference Configuration) *A change of reference configuration is a deformation $\boldsymbol{\kappa}_o$ that takes $\mathcal{B}_o$ to a new reference configuration $\overline{\mathcal{B}}_o$ and takes material points $\boldsymbol{X}$ to new material points $\overline{\boldsymbol{X}}$,*

$$
\begin{aligned}
\boldsymbol{\kappa}_o : \mathcal{B}_o &\rightarrow \mathcal{E},\\
\boldsymbol{\kappa}_o : \boldsymbol{X} &\mapsto \overline{\boldsymbol{X}}.
\end{aligned}
$$

We write

$$
\begin{aligned}
\overline{\mathcal{B}}_o &= \boldsymbol{\kappa}_o(\mathcal{B}_o)\\
\overline{\boldsymbol{X}} &= \boldsymbol{\kappa}_o(\boldsymbol{X})
\end{aligned}
$$

2.17 Axioms of Constitutive Theory

[18] We introduce three axioms of constitutive theory that must be satisfied by any material response or constitutive equations. These axioms will be used to restrict the class of equations that may describe material response.

Axiom 2.17.1 (Admissibility) *The constitutive equations must be consistent with the fundamental axioms of electromagnetics and thermomechanics.*

Axiom 2.17.2 (Material Objectivity) *The constitutive response functions must be independent of observer.*

Axiom 2.17.3 (Material Symmetry) *The constitutive response functions must be scalar invariant with respect to a group of transformations of the reference configuration representing the material symmetry conditions.*

Recall, an observer transformation (2.1) that takes $(\boldsymbol{x}, t)$ to $(\boldsymbol{x}^*, t^*)$ is interpreted as a change in observer from O to O^*, such that the event recorded by O at $(\boldsymbol{x}, t)$ is the same event as that recorded by O^* at $(\boldsymbol{x}^*, t^*)$. Consider a scalar ϵ, vector $\boldsymbol{f}$, and tensor $\boldsymbol{A}$ defined over $\mathcal{B}_t$ corresponding to a particular event at $(\boldsymbol{x}, t)$ as recorded by O. If O^* observes this same event, measured at $(\boldsymbol{x}^*, t^*)$ according to O^*, then O^* must necessarily measure the scalar as $\epsilon^* = \epsilon$, the vector as $\boldsymbol{f}^* = \boldsymbol{Q}(t)\boldsymbol{f}$, and the tensor as $A^* = \boldsymbol{Q}(t)A\boldsymbol{Q}(t)'$. In other words, the observers O and O^* measure the same event. An event is necessarily independent of observer, and therefore the scalar, vector, and tensor quantities corresponding to the event are objective fields, and transform according to remark 2.16.2 under an observer transformation. Consider an event, with corresponding fields $\epsilon, \Theta, \boldsymbol{E}, \boldsymbol{D}, \boldsymbol{J}', \boldsymbol{\tau}^T$ measured by O at $(\boldsymbol{x}, t)$. These

[18] The axioms are based on ERINGEN & MAUGIN [11, pp. 133-144]

fields are necessarily objective fields, and transform according to remark 2.16.2 under a change of observer.

The axiom of material objectivity requires that material response *functions* are independent of observer. Here it is important to distinguish between the material response function, and its value. Material objectivity is a powerful axiom that imposes restrictions on the set of admissible material response functions. The next section clarifies this discussion with some examples.

2.18 Constitutive Function Restrictions

[19] Suppose we deduce or assume the following constitutive equations relative to the reference configuration $\mathcal{B}_o$,

$$\begin{aligned} \epsilon(\boldsymbol{x},t) &= \hat{\epsilon}(\chi(\boldsymbol{X},t)), \\ \boldsymbol{E}(\boldsymbol{x},t) &= \hat{\boldsymbol{E}}(\chi(\boldsymbol{X},t)), \\ \boldsymbol{\tau}(\boldsymbol{x},t) &= \hat{\boldsymbol{\tau}}(\chi(\boldsymbol{X},t)). \end{aligned}$$

As remarked in the previous section, the fields ϵ, $\boldsymbol{E}$, and $\boldsymbol{\tau}$ transform objectively under a change in observer,

$$\begin{aligned} \epsilon^*(\boldsymbol{x}^*,t^*) &= \epsilon(\boldsymbol{x},t), \\ \boldsymbol{E}^*(\boldsymbol{x}^*,t^*) &= \boldsymbol{Q}(t)\boldsymbol{E}(\boldsymbol{x},t), \\ \boldsymbol{\tau}^*(\boldsymbol{x}^*,t^*) &= \boldsymbol{Q}(t)\boldsymbol{\tau}(\boldsymbol{x},t)\boldsymbol{Q}'(t). \end{aligned}$$

Using the constitutive equations we obtain,

$$\begin{aligned} \epsilon^*(\boldsymbol{x}^*,t^*) &= \hat{\epsilon}(\chi(\boldsymbol{X},t)), \\ \boldsymbol{E}^*(\boldsymbol{x}^*,t^*) &= \boldsymbol{Q}(t)\hat{\boldsymbol{E}}(\chi(\boldsymbol{X},t)), \\ \boldsymbol{\tau}^*(\boldsymbol{x}^*,t^*) &= \boldsymbol{Q}(t)\hat{\boldsymbol{\tau}}(\chi(\boldsymbol{X},t))\boldsymbol{Q}'(t). \end{aligned}$$

The axiom of material objectivity requires the material response functions $\hat{\epsilon}$, $\hat{\boldsymbol{E}}$, and $\hat{\boldsymbol{\tau}}$ to be the independent of observer. This implies

$$\begin{aligned} \epsilon^*(\boldsymbol{x}^*,t^*) &= \hat{\epsilon}(\chi^*(\boldsymbol{X},t^*)), \\ \boldsymbol{E}^*(\boldsymbol{x}^*,t^*) &= \hat{\boldsymbol{E}}(\chi^*(\boldsymbol{X},t^*)), \\ \boldsymbol{\tau}^*(\boldsymbol{x}^*,t^*) &= \hat{\boldsymbol{\tau}}(\chi^*(\boldsymbol{X},t^*)). \end{aligned}$$

and therefore,

$$\begin{aligned} \hat{\epsilon}(\chi(\boldsymbol{X},t)) &= \hat{\epsilon}(\chi^*(\boldsymbol{X},t^*)), \\ \boldsymbol{Q}(t)\hat{\boldsymbol{E}}(\chi(\boldsymbol{X},t)) &= \hat{\boldsymbol{E}}(\chi^*(\boldsymbol{X},t^*)), \end{aligned}$$

[19] See COLEMAN & NOLL [7, pp. 170-173], TRUESDELL & NOLL [36, pp. 41-47], and GURTIN [15, pp. 143-145] for a discussion of constitutive function restrictions and the principle of objectivity

$$Q(t)\hat{\tau}(\chi(X,t))\,Q'(t) = \hat{\tau}(\chi^*(X,t^*)).$$

These equations are the mathematical statement of material objectivity, and must be satisfied by $\hat{\epsilon}$, $\hat{E}$, and $\hat{\tau}$ for all possible proper orthogonal $Q(t)$.

Next, we write the deformation gradient in direct notation as

$$F = \frac{\partial \chi(X,t)}{\partial X}.$$

To make the restrictions more explicit, suppose we deduce or assume the constitutive equations are

$$\begin{aligned} \epsilon(x,t) &= \hat{\epsilon}(F), \\ E(x,t) &= \hat{E}(F), \\ \tau(x,t) &= \hat{\tau}(F). \end{aligned}$$

Under a change of observer, F transforms as

$$\begin{aligned} F^* &= \frac{\partial \chi^*(X,t)}{\partial X} \\ &= Q(t)F. \end{aligned}$$

From our previous result, the axiom of objectivity imposes the following restrictions on the material response functions,

$$\begin{aligned} \hat{\epsilon}(F) &= \hat{\epsilon}(Q(t)F), \\ Q(t)\hat{E}(F) &= \hat{E}(Q(t)F), \\ Q(t)\hat{\tau}(F)\,Q'(t) &= \hat{\tau}(Q(t)F). \end{aligned}$$

Next we consider the restrictions imposed by the axiom of material symmetry on the constitutive functions. Consider the change in reference configuration from $\mathcal{B}_o$ and $\overline{\mathcal{B}}_o$,

$$\begin{aligned} \kappa_o(X) &= S'X \\ S'S &= SS' = I \\ \det(S) &= 1. \end{aligned}$$

The motion with respect to the new reference configuration is

$$\begin{aligned} \overline{\chi}_t : \overline{\mathcal{B}}_o &\to \mathcal{B}_t \\ \overline{\chi}_t : \overline{X} &\mapsto x \end{aligned}$$

We write

$$\mathcal{B}_t = \overline{\chi}\left(\overline{\mathcal{B}}_o, t\right)$$

$$\boldsymbol{x} = \overline{\chi}\left(\overline{\boldsymbol{X}}, t\right)$$

The deformation gradient with respect to the new reference configuration is

$$\begin{aligned}\overline{\boldsymbol{F}} &= \frac{\partial \overline{\chi}\left(\overline{\boldsymbol{X}}, t\right)}{\partial \overline{\boldsymbol{X}}} \\ &= \boldsymbol{F}\boldsymbol{S}\end{aligned}$$

With respect to the two reference configurations $\mathcal{B}_o$ and $\overline{\mathcal{B}}_o$, the constitutive equations are

$$\begin{aligned}\epsilon(\boldsymbol{x}, t) &= \hat{\epsilon}(\boldsymbol{F}), \\ \boldsymbol{E}(\boldsymbol{x}, t) &= \hat{\boldsymbol{E}}(\boldsymbol{F}), \\ \boldsymbol{\tau}(\boldsymbol{x}, t) &= \hat{\boldsymbol{\tau}}(\boldsymbol{F})\end{aligned}$$

$$\begin{aligned}\epsilon(\boldsymbol{x}, t) &= \overline{\epsilon}\left(\overline{\boldsymbol{F}}\right), \\ \boldsymbol{E}(\boldsymbol{x}, t) &= \overline{\boldsymbol{E}}\left(\overline{\boldsymbol{F}}\right), \\ \boldsymbol{\tau}(\boldsymbol{x}, t) &= \overline{\boldsymbol{\tau}}\left(\overline{\boldsymbol{F}}\right).\end{aligned}$$

Suppose that the response of the material relative to $\mathcal{B}_o$ is always indistinguishable from that relative to $\overline{\mathcal{B}}_o$ for all proper orthogonal tensors $\boldsymbol{S}$ in the set of transformations $\mathcal{S}$, such that

$$\begin{aligned}\hat{\epsilon} \equiv \overline{\epsilon} &\rightarrow \hat{\epsilon}(\boldsymbol{F}) = \hat{\epsilon}(\boldsymbol{F}\boldsymbol{S}), \\ \hat{\boldsymbol{E}} \equiv \overline{\boldsymbol{E}} &\rightarrow \hat{\boldsymbol{E}}(\boldsymbol{F}) = \hat{\boldsymbol{E}}(\boldsymbol{F}\boldsymbol{S}), \\ \hat{\boldsymbol{\tau}} \equiv \overline{\boldsymbol{\tau}} &\rightarrow \hat{\boldsymbol{\tau}}(\boldsymbol{F}) = \hat{\boldsymbol{\tau}}(\boldsymbol{F}\boldsymbol{S}).\end{aligned}$$

The set $\mathcal{S}$ is said to characterize the symmetry of the material relative to the reference configuration $\mathcal{B}_o$. If we replace $\boldsymbol{F}$ with $\boldsymbol{F}\boldsymbol{S}'$ we obtain

$$\begin{aligned}\hat{\epsilon}(\boldsymbol{F}\boldsymbol{S}') &= \hat{\epsilon}(\boldsymbol{F}), \\ \hat{\boldsymbol{E}}(\boldsymbol{F}\boldsymbol{S}') &= \hat{\boldsymbol{E}}(\boldsymbol{F}), \\ \hat{\boldsymbol{\tau}}(\boldsymbol{F}\boldsymbol{S}') &= \hat{\boldsymbol{\tau}}(\boldsymbol{F}).\end{aligned}$$

This shows that if $\boldsymbol{S} \in \mathcal{S}$ then $\boldsymbol{S}' \in \mathcal{S}$. Combining the imposed restriction from material symmetry with the imposed restriction from material objectivity and choosing $\boldsymbol{Q} = \boldsymbol{S}$, implies the restriction that the response functions are invariant under $\mathcal{S}$,

$$\begin{aligned}\hat{\epsilon}(\boldsymbol{F}) &= \hat{\epsilon}(\boldsymbol{S}\boldsymbol{F}\boldsymbol{S}'), \\ \boldsymbol{S}\hat{\boldsymbol{E}}(\boldsymbol{F}) &= \hat{\boldsymbol{E}}(\boldsymbol{S}\boldsymbol{F}\boldsymbol{S}'), \\ \boldsymbol{S}\hat{\boldsymbol{\tau}}\boldsymbol{S}'(\boldsymbol{F}) &= \hat{\boldsymbol{\tau}}(\boldsymbol{S}\boldsymbol{F}\boldsymbol{S}').\end{aligned}$$

2.19 Constitutive Equations: Spatial Fields

This section uses the conservation of energy and entropy inequality equations, under the axiom of admissibility, to derive restrictions on material response functions. The result is a set of relations between material response functions and partial derivatives of a scalar energy response function.

The axiom of admissibility requires material response functions to be consistent with the fundamental axioms of electromagnetics and thermomechanics, in particular the conservation of energy and entropy inequality equations. It is useful to form the so-called Clausius-Duhem (C-D) inequality by eliminating the heat flux and heat source terms from the entropy inequality (2.131) and conservation of energy equation, either (2.116) or (2.117). The resulting inequality is required to be satisfied for all independent processes. The resulting necessary and sufficient conditions yield general constitutive equations that govern material response. These constitutive equations are in terms of first derivatives of energy functions, $\hat{\epsilon}$ or $\hat{U}$. The axioms of material objectivity and material symmetry can then be applied to deduce further restrictions on these equations.

Proposition 2.19.1 (Local C-D Inequality Statements: Spatial Fields) *The local form of the C-D inequality statements are*

$$\rho\Theta\dot{\eta} - \rho\dot{\epsilon} + E_i\dot{P}_i + (\tau_{ji} + E_kP_k\delta_{ij})\, v_{i,j} + J_i'E_i - q_i\Theta^{-1}\Theta_{,i} \geq 0 \quad (2.149)$$

$$\rho\Theta\dot{\eta} - \rho\dot{U} + E_i\dot{D}_i + \left[\tau_{ji} + (U^F + E_kP_k)\delta_{ij}\right] v_{i,j} + J_i'E_i - q_i\Theta^{-1}\Theta_{,i} \geq 0 \quad (2.150)$$

Proof. The C-D inequalities are obtained by eliminating $(q_{i,i} - \rho h)$ from the entropy inequality (2.131) using conservation of energy statements. Reodering (2.116) and (2.117)

$$\begin{aligned} q_{i,i} - \rho h &= -\rho\dot{\epsilon} + E_i\dot{P}_i + (\tau_{ji} + E_kP_k\delta_{ij})\, v_{i,j} + J_i'E_i \\ q_{i,i} - \rho h &= -\rho\dot{U} + E_i\dot{D}_i + \left[\tau_{ji} + (U^F + E_kP_k)\delta_{ij}\right] v_{i,j} + J_i'E_i \end{aligned}$$

and using in (2.131) proves (2.149) and (2.150). ■

Consider the following,

$$v_{i,j} = X_{K,j}v_{i,K} = X_{K,j}\frac{d}{dt}(x_{i,K}). \quad (2.151)$$

Then equations (2.149) and (2.150) together with (2.151) motivate the assumption that

$$\epsilon = \hat{\epsilon}(\eta, P_i, x_{i,K}) \quad (2.152)$$

$$U = \hat{U}(\eta, D_i, x_{i,K}) \quad (2.153)$$

Taking the material time derivatives of (2.152) and (2.153),

$$\dot{\epsilon} = \frac{\partial \hat{\epsilon}}{\partial \eta}\dot{\eta} + \frac{\partial \hat{\epsilon}}{\partial P_i}\dot{P}_i + \frac{\partial \hat{\epsilon}}{\partial (x_{i,K})}\frac{d}{dt}(x_{i,K}) \tag{2.154}$$

$$\dot{U} = \frac{\partial \hat{U}}{\partial \eta}\dot{\eta} + \frac{\partial \hat{U}}{\partial D_i}\dot{D}_i + \frac{\partial \hat{U}}{\partial (x_{i,K})}\frac{d}{dt}(x_{i,K}). \tag{2.155}$$

Using (2.154) and (2.155) in equations (2.149) and (2.150) respectively we obtain

$$\begin{aligned}&\rho\left(\Theta - \frac{\partial \hat{\epsilon}}{\partial \eta}\right)\dot{\eta} + \left(E_i - \rho\frac{\partial \hat{\epsilon}}{\partial P_i}\right)\dot{P}_i + J_i' E_i - q_i \Theta^{-1}\Theta_{,i} \\ &+ \left[\left(\tau_{ji} + E_n P_n \delta_{ij}\right) X_{K,j} - \rho\frac{\partial \hat{\epsilon}}{\partial (x_{i,K})}\right]\frac{d}{dt}(x_{i,K}) \geq 0\end{aligned} \tag{2.156}$$

$$\begin{aligned}&\rho\left(\Theta - \frac{\partial \hat{U}}{\partial \eta}\right)\dot{\eta} + \left(E_i - \rho\frac{\partial \hat{U}}{\partial D_i}\right)\dot{D}_i + J_i' E_i - q_i \Theta^{-1}\Theta_{,i} \\ &+ \left(\left[\tau_{ji} + \left(U^F + E_n P_n\right)\delta_{ij}\right] X_{K,j} - \rho\frac{\partial \hat{U}}{\partial (x_{i,K})}\right)\frac{d}{dt}(x_{i,K}) \geq 0.\end{aligned} \tag{2.157}$$

Inequalities (2.156) and (2.157) are linear in $\dot{\eta}, \dot{P}_i, \dot{\overline{x_{i,J}}}$, and $\dot{\eta}, \dot{D}_i, \dot{\overline{x_{i,J}}}$ respectively, and must be satisfied for all independent variations of these quantities. Necessary and sufficient conditions are

$$J_i' E_i - q_i \Theta^{-1}\Theta_{,i} \geq 0$$

$$\Theta = \frac{\partial \hat{\epsilon}}{\partial \eta} \tag{2.158}$$

$$E_i = \rho\frac{\partial \hat{\epsilon}}{\partial P_i} \tag{2.159}$$

$$\left(\tau_{ji} + E_n P_n \delta_{ij}\right) X_{K,j} = \rho\frac{\partial \hat{\epsilon}}{\partial (x_{i,K})} \tag{2.160}$$

and

$$J_i' E_i - q_i \Theta^{-1}\Theta_{,i} \geq 0$$

$$\Theta = \frac{\partial \hat{U}}{\partial \eta} \tag{2.161}$$

$$E_i = \rho\frac{\partial \hat{U}}{\partial D_i} \tag{2.162}$$

$$\left[\tau_{ji} + \left(U^F + E_n P_n\right)\delta_{ij}\right] X_{K,j} = \rho\frac{\partial \hat{U}}{\partial (x_{i,K})} \tag{2.163}$$

Equations (2.158) - (2.160) and (2.161) - (2.163) are restrictions imposed by combined

statements of balance of energy and entropy inequality, as required by the axiom of admissibility. The energy functions $\hat{\epsilon}$ and $\hat{U}$ can not be arbitrary functions of their arguments, they must satisfy the axiom of material objectivity and material symmetry. Instead of deriving these conditions here, it turns out the material objectivity will be satisfied if the constitutive equations are derived from the C-D inequality written in terms of material fields, as introduced in the next section. See TIERSTEN [28, pp. 1309-1310] for an example of material objectivity calculations.

Next we derive the heat conduction equation by simplifying the conservation of energy equation with the constitutive equations. Substitute (2.158)-(2.160), (2.154) and (2.161)-(2.163), (2.155) into the energy equations (2.156) and (2.157), respectively. Both result in a heat conduction equation,

$$\rho\Theta\dot{\eta} + q_{i,i} = \rho h + J_i' E_i.$$

2.20 Material Fields

In this section we introduce material fields. In typical continuum mechanics problems, the material points x_k in the deformed body $\mathcal{B}_t$ are part of the solution, and therefore unknown a priori. Loading and boundary conditions are usually known at material points X_M on the undeformed body $\mathcal{B}_o$. The fundamental axioms and resulting differential equations and jump conditions are stated in terms of spatial fields defined over the deformed and a priori unknown body B_t. It can be convenient, in particular for approximate theories, to rewrite the equations in terms of fields defined over the known reference configuration $\mathcal{B}_o$. Transformations of arc, area, and volume (2.5)-(2.7) relating elements in $\mathcal{B}_t$ to elements in $\mathcal{B}_o$ can be used to introduce relevant fields defined over $\mathcal{B}_o$. These fields are called material fields and are introduced below.

Consider a spatial scalar field q^F. A corresponding material field $\mathcal{Q}^F$ can be defined such that the volume integral of $\mathcal{Q}^F$ over a material volume V_o in $\mathcal{B}_o$ is equal to the volume integral of q^F over the corresponding material volume V in $\mathcal{B}_t$,

$$\int_{V_o} \mathcal{Q}^F \, dV_o = \int_V q^F \, dV \,. \tag{2.164}$$

The required relationship between $\mathcal{Q}^F$ and q^F can be derived using (2.7),

$$\begin{aligned} \int_{V_o} \mathcal{Q}^F \, dV_o &= \int_V q^F \, dV \\ &= \int_{V_o} q^F J \, dV_o \,. \end{aligned}$$

The material field $\mathcal{Q}^F$ required to satisfy (2.164) is then,

$$\mathcal{Q}^F = J q^F.$$

Consider a spatial vector field D_i. A corresponding material field $\mathcal{D}_J$ can be defined such that the surface integral of $\mathcal{D}_J$ over a material surface S_o in $\mathcal{B}_o$ is equal to the

surface integral of D_i over the corresponding material surface S in $\mathcal{B}_t$,

$$\int_{S_o} \mathcal{D}_J N_J \, dS_o = \int_S D_i n_i \, dS \,. \tag{2.165}$$

The required relationship between $\mathcal{D}_J$ and D_i can be derived using (2.6),

$$\begin{aligned} \int_{S_o} \mathcal{D}_J N_J \, dS_o &= \int_S D_i n_i \, dS \\ &= \int_{S_o} D_i J X_{J,i} N_J \, dS_o \,. \end{aligned}$$

The material field $\mathcal{D}_J$ required to satisfy (2.165) is then,

$$\mathcal{D}_J = J X_{J,i} D_i.$$

Consider another spatial vector field E_i. A corresponding material field $\mathcal{E}_J$ can be defined such that the line integral of $\mathcal{E}_J$ over a material line C_o in $\mathcal{B}_o$ is equal to the line integral of E_i over the corresponding material line C in $\mathcal{B}_t$,

$$\int_{C_o} \mathcal{E}_J \, dX_J = \int_C E_i \, dx_i. \tag{2.166}$$

The required relationship between $\mathcal{E}_J$ and E_i can be derived using (2.5),

$$\begin{aligned} \int_{C_o} \mathcal{E}_J \, dX_J &= \int_C E_i \, dx_i \\ &= \int_{C_o} E_i x_{i,J} \, dX_J. \end{aligned}$$

The material field $\mathcal{E}_J$ required to satisfy (2.166) is then,

$$\mathcal{E}_J = x_{i,J} E_i.$$

We note, the same defintion for $\mathcal{E}_J$ would have been obtained if it were defined in terms of $\mathcal{D}_K$, E_i, and D_j by,

$$\int_{V_o} \mathcal{E}_J \mathcal{D}_J \, dV_o = \int_V E_i D_i \, dV \,,$$

Definition 2.20.1 (Material Fields) *For convenience we define all material fields below. Their definitions will be motivated in the proofs that follow.*

$$\begin{aligned} \mathcal{Q}^F = J q^F \quad &\rightarrow \quad q^F = J^{-1} \mathcal{Q}^F && (2.167) \\ \mathcal{P}_J = J X_{J,i} P_i \quad &\rightarrow \quad P_i = J^{-1} x_{i,J} \mathcal{P}_J && (2.168) \\ \mathcal{D}_J = J X_{J,i} D_i \quad &\rightarrow \quad D_i = J^{-1} x_{i,J} \mathcal{D}_J && (2.169) \\ \mathcal{E}_J = x_{i,J} E_i \quad &\rightarrow \quad E_i = X_{J,i} \mathcal{E}_J && (2.170) \\ \mathcal{J}'_J = J X_{J,i} J'_i \quad &\rightarrow \quad J'_i = J^{-1} x_{i,J} \mathcal{J}'_J && (2.171) \end{aligned}$$

$$\mathcal{Q}_J = JX_{J,i}q_i \quad \rightarrow \quad q_i = J^{-1}x_{i,J}\mathcal{Q}_J \tag{2.172}$$
$$T^P_{Si} = JX_{S,j}\tau^P_{ji} \quad \rightarrow \quad \tau^P_{ji} = J^{-1}T^P_{Si}x_{j,S} \tag{2.173}$$
$$T^E_{Si} = JX_{S,j}\tau^E_{ji} \quad \rightarrow \quad \tau^E_{ji} = J^{-1}x_{j,S}T^E_{Si} \tag{2.174}$$
$$\mathcal{T}^P_{SR} = JX_{S,j}X_{R,i}\tau^P_{ji} \quad \rightarrow \quad \tau^P_{ji} = J^{-1}x_{j,S}x_{i,R}\mathcal{T}^P_{SR} \tag{2.175}$$
$$\mathcal{T}^T_{SR} = JX_{S,j}X_{R,i}\tau^T_{ji} \quad \rightarrow \quad \tau^T_{ji} = J^{-1}x_{j,S}x_{i,R}\mathcal{T}^T_{SR} \tag{2.176}$$

2.21 Equations in Material Fields

[20] The material form of the thermomechanical and EQS Maxwell equations will be systematically derived by integrating the local equations over a material surface or volume in $\mathcal{B}_t$ and introducing the appropriate transformations of elements of arc, area, or volume in $\mathcal{B}_o$. The resulting expressions are the global material forms of the original local spatial equations.

Theorem 2.21.1 (Global EQS Maxwell Equations: Material Fields) *The global form of the EQS Maxwell equations is,*

$$\oint_{S_o} \mathcal{D}_J N_J \, dS_o = \int_{V_o} \mathcal{Q}^F \, dV_o, \tag{2.177}$$
$$\int_{C_o} \mathcal{E}_J \, dX_J = 0, \tag{2.178}$$
$$\frac{d}{dt}\int_{V_o} \mathcal{Q}^F \, dV_o + \oint_{S_o} \mathcal{J}'_J N_J \, dS_o = 0. \tag{2.179}$$

Proof. Integrate (2.52) and (2.54) over a material volume V in spatial coordinates and integrate (2.53) over a material surface S in spatial coordinates, and using (2.22), (A.1), and (A.2),

$$\oint_S D_i n_i \, dS = \int_V q^F \, dV, \tag{2.180}$$
$$\int_C E_i \, dx_i = 0, \tag{2.181}$$
$$\oint_S J_i n_i \, dS + \frac{d}{dt}\int_V q^F \, dV - \oint_S q^F v_i n_i \, dS = 0. \tag{2.182}$$

Using (2.97) and introducing transformations (2.5)-(2.7) in (2.180)-(2.182) gives

$$\oint_{S_o} D_i J X_{J,i} N_J \, dS_o = \int_{V_o} q^F J \, dV_o, \tag{2.183}$$
$$\int_{C_o} E_i \frac{\partial x_i}{\partial X_J} \, dX_J = 0, \tag{2.184}$$
$$\frac{d}{dt}\int_{V_o} q^F J \, dV_o + \oint_{S_o} J'_i X_{J,i} N_J \, dS_o = 0. \tag{2.185}$$

[20] Conservation of energy equations in material fields are based on THURSTON [26, pp. 157-165]

Using (2.167), (2.169), (2.170), and (2.171) in (2.183) - (2.185) proves (2.177) - (2.179). ■

Theorem 2.21.2 (Local EQS Maxwell Equations: Material Fields)

$$\begin{aligned} \mathcal{D}_{J,J} &= \mathcal{Q}^F, && (2.186)\\ \epsilon_{IJK}\mathcal{E}_{K,J} &= 0 \quad \longrightarrow \quad \mathcal{E}_J = -\phi_{,J}, && (2.187)\\ \dot{\mathcal{Q}}^F + \mathcal{J}'_{J,J} &= 0. && (2.188) \end{aligned}$$

Proof. Noting the material time derivative commutes with the volume integral over a material volume and using (A.1) and (A.2) in (2.177)-(2.179) and requiring the integrals hold for arbitrary volumes V_o and surfaces S_o in the appropriate relations (postulate of localization) proves (2.186)-(2.188). ■

It will be convenient to work with a reduced form of the EQS equations.

Theorem 2.21.3 (Reduced EQS Maxwell: Integral Form and Material Fields)

$$\begin{aligned} \oint_{S_o} \left(\dot{\mathcal{D}}_J + \mathcal{J}'_J\right) N_J \, dS_o &= 0\\ \int_{C_o} \mathcal{E}_J \, dX_J &= 0 \end{aligned}$$

Proof. Immediate consequence of (2.180)-(2.182). ■

Theorem 2.21.4 (Reduced EQS Maxwell: Local Form and Material Fields)

$$\begin{aligned} \left(\dot{\mathcal{D}}_J + \mathcal{J}'_J\right)_{,J} &= 0\\ \epsilon_{IJK}\mathcal{E}_{K,J} &= 0 \quad \longrightarrow \quad \mathcal{E}_J = -\phi_{,J}. \end{aligned}$$

Theorem 2.21.5 (Conservation of Mass: Material Fields) *Global and local conservation of mass in material form is equivalent to (2.28) is*

$$\begin{aligned} \int_V \rho \, dV &= \int_{V_o} \rho_o \, dV_o, && (2.189)\\ J\rho &= \rho_o. && (2.190) \end{aligned}$$

Proof. Equation (2.189) is a restatement of axiom 2.5.6. Using (2.7), (2.189) becomes

$$\int_{V_o} (J\rho - \rho_o) \, dV_o = 0.$$

Using postulate of localization proves (2.190). ■

Theorem 2.21.6 (Balance of Momentum: Material Fields) *Global and local balance of momentum in material form is*

$$\oint_{S_o} \left(T_{Ji} + T^E_{Ji}\right) N_J \, dS_o + \int_{V_o} \rho_o \left(f_i - \dot{v}_i\right) dV_o = 0, \tag{2.191}$$

$$\left(T_{Ji} + T^E_{Ji}\right)_{,J} + \rho_o \left(f_i - \dot{v}_i\right) = 0. \tag{2.192}$$

Proof. Integrate (2.77) over a material volume V in spatial (deformed) coordinates and use the divergence theorem (A.1),

$$\oint_S \left(\tau_{ji} + \tau^E_{ji}\right) n_i \, dS + \int_V \rho \left(f_i - \dot{v}_i\right) dV = 0. \tag{2.193}$$

Using the transformations (2.6) and (2.7) in (2.193),

$$\oint_{S_o} \left(\tau_{ji} + \tau^E_{ji}\right) J X_{J,i} N_J \, dS_o + \int_{V_o} \rho \left(f_i - \dot{v}_i\right) J \, dV_o = 0. \tag{2.194}$$

Using (2.173) and (2.174) in (2.194) proves (2.191). Using divergence theorem (A.1) in (2.191) and requiring to hold for arbitrary volumes V_o (postulate of localization) proves (2.192). ■

Theorem 2.21.7 (Symmetry of Partial and Total Tensors: Material Fields) *The material stress tensors $\mathcal{T}^T_{SR}$ and $\mathcal{T}^P_{SR}$ are symmetric,*

$$\mathcal{T}^T_{[SR]} = 0, \tag{2.195}$$

$$\mathcal{T}^P_{[SR]} = 0 \tag{2.196}$$

Proof. From (2.91),

$$\tau^T_{ji} = \tau^T_{ij}. \tag{2.197}$$

Introducing (2.176) into (2.197),

$$\mathcal{T}^T_{SR} x_{j,S} x_{i,R} J^{-1} = \mathcal{T}^T_{MN} x_{i,M} x_{j,N} J^{-1} \tag{2.198}$$

Multiplying (2.198) by $J X_{S,j} X_{R,i}$ gives,

$$\begin{aligned} \mathcal{T}^T_{SR} &= X_{S,j} X_{R,i} x_{i,M} x_{j,N} \mathcal{T}^T_{MN}, \\ &= \delta_{SN} \delta_{RM} \mathcal{T}^T_{MN}, \\ &= \mathcal{T}^T_{RS}. \end{aligned} \tag{2.199}$$

Equation (2.199) proves (2.195). Repeating the calculations using (2.91) and (2.175) proves (2.196). ■

Prior to establishing the material forms of local conservation of energy expressions, we must derive total derivative expressions.

Proposition 2.21.8 (Material Derivative: Spatial and Material Field) *Defining $\mathcal{A}_J = JX_{J,i}A_i$, the material derivative of A_i is*

$$\dot{A}_i = \dot{\mathcal{A}}_J x_{i,J} J^{-1} + A_k v_{i,k} - A_i v_{k,k}. \tag{2.200}$$

Proof. Taking the material derivative of A_i

$$\dot{A}_i = \dot{\mathcal{A}}_J x_{i,J} J^{-1} + \mathcal{A}_J \frac{d}{dt}(x_{i,J}) J^{-1} - \mathcal{A}_J x_{i,J} J^{-2} \dot{J}$$

Using (2.14) and (2.201),

$$\frac{d}{dt}(x_{i,J}) = v_{i,J} = v_{i,k} x_{k,J}, \tag{2.201}$$

proves (2.200). ■

Lemma 2.21.9 (Local Conservation of Energy) *Local conservation of energy equations equivalent to (2.116) and (2.117) are*

$$\rho\dot{\epsilon} = \mathcal{E}_J \dot{\mathcal{P}}_J J^{-1} + \tau^P_{ji} v_{i,j} + J'_i E_i + \rho h - q_{i,i} \tag{2.202}$$

$$\rho\dot{U} = \mathcal{E}_J \dot{\mathcal{D}}_J J^{-1} + \tau^T_{ji} v_{i,j} + J'_i E_i + \rho h - q_{i,i} \tag{2.203}$$

Proof. Using theorem 2.21.8, $\dot{P}_i$ and $\dot{D}_i$ are,

$$\dot{P}_i = \dot{\mathcal{P}}_J x_{i,J} J^{-1} + P_k v_{i,k} - P_i v_{k,k}, \tag{2.204}$$

$$\dot{D}_i = \dot{\mathcal{D}}_J x_{i,J} J^{-1} + D_k v_{i,k} - D_i v_{k,k}. \tag{2.205}$$

Using (2.170),(2.190),(2.204), and (2.205) in (2.116) and (2.117) obtain

$$\rho\dot{\epsilon} = \mathcal{E}_J \dot{\mathcal{P}}_J J^{-1} + [\tau_{ji} + P_j E_i] v_{i,j} + J'_i E_i + \rho h - q_{i,i} \tag{2.206}$$

$$\rho\dot{U} = \mathcal{E}_J \dot{\mathcal{D}}_J J^{-1} + \left[\tau_{ji} + D_j E_i - U^F \delta_{ij}\right] v_{i,j} + J'_i E_i + \rho h - q_{i,i} \tag{2.207}$$

Rewriting (2.206) and (2.207) using (2.88) and (2.90) proves (2.206) and (2.207) ■

Definition 2.21.10 (Strain Rate Decomposition) *The S/A decomposition of $v_{i,j}$ is defined as*

$$d_{ij} = v_{(i,j)}, \qquad w_{ij} = v_{[i,j]}$$

$$v_{i,j} = d_{ij} + w_{ij} \tag{2.208}$$

Proposition 2.21.11 (Partial and Total Stress Power Densities) *Stress power densities $\tau^P_{ji} v_{i,j}$ and $\tau^T_{ji} v_{i,j}$ simplify to*

$$\tau^P_{ji} v_{i,j} = \tau^P_{ji} d_{ij} \tag{2.209}$$

$$\tau^T_{ji} v_{i,j} = \tau^T_{ji} d_{ij} \tag{2.210}$$

Proof. Using (2.91) in the form $\tau^P_{ji} = \tau^P_{(ji)}$

$$\begin{aligned}\tau^P_{ji} v_{i,j} &= \tau^P_{(ji)} v_{i,j} \\ &= \tau^P_{(ij)} (d_{ij} + w_{ij}) \\ &= \tau^P_{ji} d_{ij}\end{aligned}$$

Equation (2.210) is similarly proved using (2.92) in the form $\tau^T_{ji} = \tau^T_{(ji)}$. ■

Proposition 2.21.12 (Symmetric Strain Rate: Material Fields)

$$d_{pq} = X_{R,p} X_{S,q} \dot{E}_{RS}$$

Proof.

$$\begin{aligned}C_{RS} &= x_{k,R} x_{k,S} = \delta_{RS} + 2E_{RS} \\ \dot{C}_{RS} &= v_{k,R} x_{k,S} + x_{k,R} v_{k,S} = 2\dot{E}_{RS}\end{aligned}$$

Multiplying through by $X_{R,p} X_{S,q}$

$$X_{R,p} X_{S,q} \dot{C}_{RS} = v_{k,p} \delta_{kq} + \delta_{kp} v_{k,q} = 2X_{R,p} X_{S,q} \dot{E}_{RS}$$

or

$$v_{q,p} + v_{p,q} = X_{R,p} X_{S,q} \dot{C}_{RS} = 2X_{R,p} X_{S,q} \dot{E}_{RS}$$

From (2.208)

$$\begin{aligned}d_{qp} &= \frac{1}{2}(v_{q,p} + v_{p,q}) \\ &= \frac{1}{2} X_{R,p} X_{S,q} \dot{C}_{RS} && (2.211) \\ &= X_{R,p} X_{S,q} \dot{E}_{RS} && (2.212)\end{aligned}$$

■

Proposition 2.21.13 (Partial and Total Stress Power Densities: Material Fields) *Stress power densities $\tau^P_{ji} v_{i,j}$ and $\tau^T_{ji} v_{i,j}$ are identically*

$$\begin{aligned}\tau^P_{ji} v_{i,j} &= \tau^P_{ji} X_{R,i} X_{S,j} \dot{E}_{RS} && (2.213) \\ \tau^T_{ji} v_{i,j} &= \tau^T_{ji} X_{R,i} X_{S,j} \dot{E}_{RS} && (2.214)\end{aligned}$$

Proof. Equation (2.209) with (2.212) proves (2.213). Similarly, (2.210) with (2.212) proves (2.214). ■

Theorem 2.21.14 (Local Conservation of Energy: Material Fields) *Global and local onservation of energy statements equivalent to (2.116) and (2.117) in material*

fields are

$$\rho_o\dot{\epsilon} = \mathcal{E}_J\dot{\mathcal{P}}_J + \mathcal{T}^P_{SR}\dot{E}_{RS} + \mathcal{J}'_J\mathcal{E}_J + \rho_o h - \mathcal{Q}_{J,J} \tag{2.215}$$

$$\rho_o\dot{U} = \mathcal{E}_J\dot{\mathcal{D}}_J + \mathcal{T}^T_{SR}\dot{E}_{RS} + \mathcal{J}'_J\mathcal{E}_J + \rho_o h - \mathcal{Q}_{J,J} \tag{2.216}$$

Proof. Integrate (2.202) and (2.203) over a material domain V in spatial coordinates and use the divergence theorem (A.1),

$$\int_V \rho\dot{\epsilon}\, dV = \int_V \left(\mathcal{E}_J\dot{\mathcal{P}}_J J^{-1} + \tau^P_{ji}v_{i,j} + J'_iE_i + \rho h\right) dV - \oint_S q_i n_i\, dS\,, \tag{2.217}$$

$$\int_V \rho\dot{U}\, dV = \int_V \left(\mathcal{E}_J\dot{\mathcal{D}}_J J^{-1} + \tau^T_{ji}v_{i,j} + J'_iE_i + \rho h\right) dV - \oint_S q_i n_i\, dS\,. \tag{2.218}$$

Introducing transformations (2.6) and (2.7) gives,

$$\begin{aligned}\int_{V_o} \rho\dot{\epsilon} J\, dV_o &= \int_{V_o} \left(\mathcal{E}_J\dot{\mathcal{P}}_J J^{-1} + \tau^P_{ji}v_{i,j} + J'_iE_i + \rho h\right) J\, dV_o \\ &- \oint_{S_o} q_i J X_{J,i} N_J\, dS_o \end{aligned} \tag{2.219}$$

$$\begin{aligned}\int_{V_o} \rho\dot{U} J\, dV_o &= \int_{V_o} \left(\mathcal{E}_J\dot{\mathcal{D}}_J J^{-1} + \tau^T_{ji}v_{i,j} + J'_iE_i + \rho h\right) J\, dV_o \\ &- \oint_{S_o} q_i J X_{J,i} N_J\, dS_o\,. \end{aligned} \tag{2.220}$$

Using (2.190), (2.170), (2.171), (2.172), (2.175), (2.176), (2.213), and (2.214) in (2.219) and (2.220) gives,

$$\begin{aligned}\int_{V_o} \rho_o\dot{\epsilon}\, dV_o &= \int_{V_o} \left(\mathcal{E}_J\dot{\mathcal{P}}_J + \mathcal{T}^P_{SR}\dot{E}_{RS} + \mathcal{J}'_J\mathcal{E}_J + \rho_o h\right) dV_o \\ &- \oint_{S_o} \mathcal{Q}_J N_J\, dS_o \end{aligned} \tag{2.221}$$

$$\begin{aligned}\int_{V_o} \rho_o\dot{U}\, dV_o &= \int_{V_o} \left(\mathcal{E}_J\dot{\mathcal{D}}_J + \mathcal{T}^T_{SR}\dot{E}_{RS} + \mathcal{J}'_J\mathcal{E}_J + \rho_o h\right) dV_o \\ &- \oint_{S_o} \mathcal{Q}_J N_J\, dS_o\,. \end{aligned} \tag{2.222}$$

Using the divergence theorem (A.1) in (2.221) and (2.222) and requiring the result to hold for arbitrary V_o proves (2.215) and (2.216). ■

Theorem 2.21.15 (Global Conservation of Energy: Material Fields)

$$\begin{aligned}\frac{d}{dt}\int_V \left(\frac{1}{2}\rho_o v_i v_i + \rho_o U\right) dV &= \int_V \rho_o\left(h + f_i v_i\right) dV + \\ \oint_{S_o} &\left[\left(T_{Jj} + T^E_{Jj}\right) v_j - \phi\left(\mathcal{J}'_J + \dot{\mathcal{D}}_J\right) - \mathcal{Q}_J\right] N_J\, dS_o \end{aligned} \tag{2.223}$$

Proof. Using (2.200) and (2.66),

$$\begin{aligned} D^*_i &= \dot{D}_i + D_i v_{k,k} - D_k v_{i,k} \\ \dot{\mathcal{D}}_J &= D^*_i J X_{J,i}. \end{aligned} \tag{2.224}$$

Using (2.224), and appropriate entries from definition 2.20.1 in (2.122) proves (2.223). ■

Theorem 2.21.16 (Entropy Inequality: Material Fields) *Global and local entropy inequality statements equivalent to (2.130) in material fields are*

$$\int_{V_o} \rho_o \dot{\eta}\, dV_o + \oint_{S_o} \frac{\mathcal{Q}_J}{\Theta} N_J\, dS_o - \int_{V_o} \rho_o \frac{h}{\Theta}\, dV_o \geq 0, \tag{2.225}$$

$$\rho_o \Theta \dot{\eta} + \mathcal{Q}_{J,J} - \mathcal{Q}_J \Theta^{-1} \Theta_{,J} - \rho_o h \geq 0. \tag{2.226}$$

Proof. Integrate the product of Θ with (2.131) over a material volume V in spatial coordinates and using the divergence theorem (A.1) obtain

$$\int_V \rho \dot{\eta}\, dV + \oint_S \frac{q_i}{\Theta} n_i\, dS - \int_V \rho \frac{h}{\Theta}\, dV \geq 0. \tag{2.227}$$

Using transformations (2.6) and (2.7) in (2.227),

$$\int_{V_o} \rho \dot{\eta} J\, dV_o + \oint_{S_o} \frac{q_i}{\Theta} J X_{J,i} N_J\, dS_o - \int_{V_o} \rho \frac{h}{\Theta} J\, dV_o \geq 0. \tag{2.228}$$

Using (2.190) and (2.172) in (2.228) proves (2.225). Using the divergence theorem (A.1) in (2.225) and requiring the statement to hold for arbitrary volumes V_o, and multiplying the result by Θ proves (2.226). ■

2.22 Surfaces of Discontinuity: Material Fields

In this section we generalize our global balance statements in material fields to include surfaces of discontinuity moving with absolute velocity ν_k. We note that Gauss and Stokes' theorems remain unchanged for material coordinates. Therefore the derivations for generalized integral theorems are valid.

Theorem 2.22.1 (Generalized Gauss: Material Fields) *A material field A_M defined over a material volume V_o in $\mathcal{B}_o$, bounded by surface S_o, and containing a surface of discontinuity σ_o satisfies the integral statement,*

$$\begin{aligned} \oint_{S_o - \sigma_o} A_M N_M\, dS_o &= \int_{V_o - \sigma_o} A_{M,M}\, dV_o + \int_{\sigma_o} [\![A_M]\!] N_M\, dS_o \\ [\![A_K]\!] &= A_K^+ + A_K^- \\ V_o - \sigma_o &= V_o^+ + V_o^- \\ S_o - \sigma_o &= S_o^+ + S_o^- \end{aligned} \tag{2.229}$$

Proof. Equation (2.229) is a restatement in material coordinates of (2.133). ■

Theorem 2.22.2 (Generalized Stokes: Material Fields) *A material field A_M defined over an open material surface S_o in $\mathcal{B}_o$, bounded by the line C_o, and con-*

taining a line of discontinuity γ_o satisfies the integral statement,

$$\begin{aligned}
\oint_{C_o-\gamma_o} A_K\, dX_K &= \int_{S_o-\gamma_o} \epsilon_{IJK} A_{K,J} N_I\, dS_o + \int_{\gamma_o} [\![A_K]\!]\, dX_K \qquad (2.230)\\
[\![A_K]\!] &= A_K^+ + A_K^-\\
S_o - \gamma_o &= S_o^+ + S_o^-\\
C_o - \gamma_o &= C_o^+ + C_o^-
\end{aligned}$$

Proof. Equation (2.230) is a restatement in material coordinates of (2.137). ■

Theorem 2.22.3 (Generalized Total Derivative: Material Fields) *A material field ϕJ defined over a material volume V_o in $\mathcal{B}_o$ and containing a surface of discontinuity σ_o moving with absolute velocity ν_k satisfies the integral statement,*

$$\begin{aligned}
\frac{d}{dt}\int_{V_o-\sigma_o} \phi J\, dV_o &= \int_{V_o-\sigma_o} \left(\dot{\phi} + \phi v_{k,k}\right) J\, dV_o\\
&+ \int_{\sigma_o} [\![\phi\left(v_k - \nu_k\right) J X_{J,k}]\!]\, N_J\, dS_o \qquad (2.231)\\
[\![A_K]\!] &= A_K^+ + A_K^-\\
V_o - \sigma_o &= V_o^+ + V_o^-\\
S_o - \sigma_o &= S_o^+ + S_o^-
\end{aligned}$$

Proof. Using theorem 2.4.8 in (2.135) and noting that normals n_k and N_J commute with the jump operator $[\![\cdot]\!]$ proves (2.231). ■

2.23 Jump Conditions: Material Fields

In this section we generalize global balance statements to include surfaces of discontinuity moving with velocity ν_k.

Proposition 2.23.1 (Integral EQS Electroelastic Equations: Material Form)

$$\begin{aligned}
\oint_{S_o-\sigma_o} \left(\dot{\mathcal{D}}_J + \mathcal{J}'_J\right) N_J\, dS_o &= 0\\
\int_{C_o-\gamma_o} \mathcal{E}_J\, dX_J &= 0\\
\frac{d}{dt}\int_{V_o-\sigma_o} \rho J\, dV_o &= 0\\
\frac{d}{dt}\int_{V_o-\sigma_o} \rho v_i J\, dV_o = \int_{V_o-\sigma_o} \rho_o f_i\, dV_o &+ \oint_{S_o-\sigma_o} \left(T_{Ji} + T^E_{Ji}\right) N_J\, dS_o\\
\frac{d}{dt}\int_{V_o-\sigma_o} \left(\frac{1}{2}\rho v_i v_i + \rho U\right) J\, dV_o &= \int_{V_o-\sigma_o} \rho_o\left(h + f_i v_i\right) dV_o\\
&+ \oint_{S_o-\sigma_o} \left[\left(T_{Jj} + T^E_{Jj}\right) v_j - \phi\left(\mathcal{J}'_J + \dot{\mathcal{D}}_J\right) - \mathcal{Q}_J\right] N_J\, dS_o\\
\frac{d}{dt}\int_{V_o-\sigma_o} \rho\eta J\, dV_o &\geq \int_{V_o-\sigma_o} \rho_o h\, dV_o - \oint_{S_o-\sigma_o} \frac{\mathcal{Q}_J}{\Theta} N_J\, dS_o\,.
\end{aligned}$$

We obtain local differential equations and jump conditions by applying the generalized integral theorems followed by the postulate of localization to the global balance laws. The resulting local equations will be identical to those derived earlier, however the jump conditions across the moving surface of discontinuity will be new. We present an example considering the balance of momentum equation.

Example 2.23.2 (Jump Condition Calculation: Material Fields) Consider the integral balance of momentum equations and apply the general integral theorems (2.231) and (2.229),

$$\begin{aligned}
\frac{d}{dt}\int_{V_o-\sigma_o}(\rho v_i)\,J\,dV_o &= \int_{V_o-\sigma_o}\left[\frac{d}{dt}(\rho v_i)+(\rho v_i)\,v_{k,k}\right]J\,dV_o \\
&+ \int_{\sigma_o}\left[\rho v_i\,(v_k-\nu_k)\,JX_{J,k}\right]N_J\,dS_o \\
\oint_{S_o-\sigma_o}\left(T_{Ji}+T^E_{Ji}\right)N_J\,dS_o &= \int_{V_o-\sigma_o}\left(T_{Ji}+T^E_{Ji}\right)_{,J}dV_o \\
&+ \int_{\sigma_o}\left[T_{Ji}+T^E_{Ji}\right]N_J\,dS_o\,.
\end{aligned}$$

Substituting these in integral balance law we obtain,

$$\begin{aligned}
&\int_{V_o-\sigma_o}\left[\frac{d}{dt}(\rho v_i)+(\rho v_i)\,v_{k,k}\right]J\,dV_o+\int_{\sigma_o}\left[\rho_o v_i\,(v_k-\nu_k)\,X_{J,k}\right]N_J\,dS_o \\
&\quad=\int_{V_o-\sigma_o}\left[\rho_o h+\left(T_{Ji}+T^E_{Ji}\right)_{,J}\right]dV_o+\int_{\sigma_o}\left[T_{Ji}+T^E_{Ji}\right]N_J\,dS_o\,.
\end{aligned}$$

applying the postulate of localization we obtain

$$\begin{aligned}
J\frac{d}{dt}(\rho v_i)+J\,(\rho v_i)\,v_{k,k} &= \rho_o h+\left(T_{Ji}+T^E_{Ji}\right)_{,J} && \text{in } V_o-\sigma_o \\
\left[\rho_o v_i\,(v_k-\nu_k)\,X_{J,k}\right]N_J &= \left[T_{Ji}+T^E_{Ji}\right]N_J && \text{across } \sigma_o
\end{aligned}$$

The local equations are equivalent to those derived before, however the jump conditions that must be satisfied across a moving surface of discontinuity are new.

Proposition 2.23.3 (Jump Conditions: Moving Surface of Discontinuity)

$$\begin{aligned}
\left[\dot{\mathcal{D}}_J+\mathcal{J}'_J\right]N_J &= 0 && \textit{across } \sigma_o \\
\left[\phi\right] &= 0 && \textit{across } \gamma_o \\
\left[x_k\right] &= 0 && \textit{across } \sigma_o \\
\left[\rho_o\,(v_k-\nu_k)\,X_{J,k}\right]N_J &= 0 && \textit{across } \sigma_o \\
\left[\rho_o v_i\,(v_k-\nu_k)\,X_{J,k}\right]N_J &= \left[T_{Ji}+T^E_{Ji}\right]N_J && \textit{across } \sigma_o \\
\left[\left(\frac{1}{2}\rho_o v_i v_i+\rho_o U\right)(v_k-\nu_k)\,X_{J,k}\right]N_J &= && \\
\left[\left(T_{Jj}+T^E_{Jj}\right)v_j-\phi\left(\mathcal{J}'_J+\dot{\mathcal{D}}_J\right)-\mathcal{Q}_J\right]N_J && && \textit{across } \sigma_o
\end{aligned}$$

$$[\![\rho_o \eta (v_k - \nu_k) X_{J,k}]\!] N_J \geq -[\![\frac{\mathcal{Q}_J}{\Theta}]\!] N_J \qquad \textit{across } \sigma_o$$

Proposition 2.23.4 (Jump Conditions: Material Surface of Discontinuity)

$$\begin{aligned}
[\![\dot{\mathcal{D}}_J + \mathcal{J}'_J]\!] N_J &= 0 && \textit{across } \sigma_o \\
[\![\phi]\!] &= 0 && \textit{across } \gamma_o \\
[\![x_k]\!] &= 0 && \textit{across } \sigma_o \\
[\![T_{Ji} + T^E_{Ji}]\!] N_J &= 0 && \textit{across } \sigma_o \\
[\![\left(T_{Jj} + T^E_{Jj}\right) v_j - \phi\left(\mathcal{J}'_J + \dot{\mathcal{D}}_J\right) - \mathcal{Q}_J]\!] N_J &= 0 && \textit{across } \sigma_o \\
[\![\frac{\mathcal{Q}_J}{\Theta}]\!] N_J &\geq 0 && \textit{across } \sigma_o
\end{aligned}$$

2.24 Constitutive Equations in Material Fields

In this section we derive restrictions on material response functions imposed by the conservation of energy and entropy inequality equations, in terms of material fields. The resulting material response functions satisfy the axiom of material objectivity without further restriction. Additional restrictions will be imposed by the axiom of material symmetry.

Theorem 2.24.1 (Local C-D Inequality Statements in Material Fields) *The Clausius-Duhem inequalities in material fields are*

$$\rho_o \Theta \dot{\eta} - \rho_o \dot{\epsilon} + \mathcal{E}_J \dot{\mathcal{P}}_J + \mathcal{T}^P_{SR} \dot{E}_{RS} + \mathcal{J}'_J \mathcal{E}_J - \mathcal{Q}_J \Theta^{-1} \Theta_{,J} \geq 0 \tag{2.232}$$

$$\rho_o \Theta \dot{\eta} - \rho_o \dot{U} + \mathcal{E}_J \dot{\mathcal{D}}_J + \mathcal{T}^T_{SR} \dot{E}_{RS} + \mathcal{J}'_J \mathcal{E}_J - \mathcal{Q}_J \Theta^{-1} \Theta_{,J} \geq 0 \tag{2.233}$$

Proof. Using (2.215) and (2.216) in (2.226) proves (2.232) and (2.233). ∎

Equations (2.232) and (2.233) motivate the assumed functional forms

$$\epsilon = \hat{\epsilon}\left(\eta, \mathcal{P}_J, E_{RS}\right) \tag{2.234}$$

$$U = \hat{U}\left(\eta, \mathcal{D}_J, E_{RS}\right) \tag{2.235}$$

for ϵ and U. We note that $\hat{\epsilon}$ and $\hat{U}$ in this assumed form satisfy the axiom of material objectivity, they are objective functions. Procedures identical to section 2.19 can be used to obtain constitutive equations in terms of derivatives on the potential functions. The result is a material characterization based on either $\hat{\epsilon}$ or $\hat{U}$, described as functions of $(\eta, \mathcal{P}_J, E_{RS})$ or $(\eta, \mathcal{D}_J, E_{RS})$. Characterizing a material in terms of these fields may be inconvenient. Legendre transformations can be used to change independent variables in the material response functions.

We introduce the following Legendre transformation to switch independent variables from η to the absolute temperature Θ. Inspection of (2.232) and (2.233) motivates

$$\epsilon \;=\; \Psi_1 + \Theta\eta \quad \rightarrow \quad \dot{\epsilon} = \dot{\Psi}_1 + \dot{\Theta}\eta + \Theta\dot{\eta} \tag{2.236}$$

$$U = \Psi_2 + \Theta\eta \quad \rightarrow \quad \dot{U} = \dot{\Psi}_2 + \dot{\Theta}\eta + \Theta\dot{\eta}. \tag{2.237}$$

Based on this inspection we define the following Legendre transformations.

Definition 2.24.2 (Legendre Transforms I) *Legendre transformations Ψ_1 and Ψ_2 are defined as*

$$\begin{aligned} \Psi_1 &= \epsilon - \Theta\eta \\ \Psi_2 &= U - \Theta\eta \end{aligned}$$

Theorem 2.24.3 (Legendre Transformed C-D Inequality Statements) *Local Clausius-Duhem inequalities equivalent to (2.232) and (2.233) are*

$$-\rho_o\left(\dot{\Psi}_1 + \dot{\Theta}\eta\right) + \mathcal{E}_J\dot{\mathcal{P}}_J + \mathcal{T}^P_{SR}\dot{E}_{RS} + \mathcal{J}'_J\mathcal{E}_J - \mathcal{Q}_J\Theta^{-1}\Theta_{,J} \geq 0 \tag{2.238}$$

$$-\rho_o\left(\dot{\Psi}_2 + \dot{\Theta}\eta\right) + \mathcal{E}_J\dot{\mathcal{D}}_J + \mathcal{T}^T_{SR}\dot{E}_{RS} + \mathcal{J}'_J\mathcal{E}_J - \mathcal{Q}_J\Theta^{-1}\Theta_{,J} \geq 0 \tag{2.239}$$

Proof. Using (2.236) and (2.237) in (2.232) and (2.233) proves (2.238) and (2.239). ■

Equations (2.238) and (2.239) motivate the objective functional forms

$$\begin{aligned} \rho_o\Psi_1 &= \overline{\Psi}_1\left(\Theta, \mathcal{P}_J, E_{RS}\right) \\ \rho_o\Psi_2 &= \overline{\Psi}_2\left(\Theta, \mathcal{D}_J, E_{RS}\right) \end{aligned}$$

Assuming these true

$$\rho_o\dot{\Psi}_1 = \frac{\partial\overline{\Psi}_1}{\partial\Theta}\dot{\Theta} + \frac{\partial\overline{\Psi}_1}{\partial\mathcal{P}_J}\dot{\mathcal{P}}_J + \frac{\partial\overline{\Psi}_1}{\partial E_{RS}}\dot{E}_{RS} \tag{2.240}$$

$$\rho_o\dot{\Psi}_2 = \frac{\partial\overline{\Psi}_2}{\partial\Theta}\dot{\Theta} + \frac{\partial\overline{\Psi}_2}{\partial\mathcal{D}_J}\dot{\mathcal{D}}_J + \frac{\partial\overline{\Psi}_2}{\partial E_{RS}}\dot{E}_{RS} \tag{2.241}$$

Using (2.240) and (2.241) in (2.238) and (2.239)

$$\begin{aligned} -\left(\rho_o\eta + \frac{\partial\overline{\Psi}_1}{\partial\Theta}\right)\dot{\Theta} + \left(\mathcal{E}_J - \frac{\partial\overline{\Psi}_1}{\partial\mathcal{P}_J}\right)\dot{\mathcal{P}}_J &+ \left(\mathcal{T}^P_{SR} - \frac{\partial\overline{\Psi}_1}{\partial E_{RS}}\right)\dot{E}_{RS} \\ &+ \mathcal{J}'_J\mathcal{E}_J - \mathcal{Q}_J\Theta^{-1}\Theta_{,J} \geq 0 \end{aligned} \tag{2.242}$$

$$\begin{aligned} -\left(\rho_o\eta + \frac{\partial\overline{\Psi}_2}{\partial\Theta}\right)\dot{\Theta} + \left(\mathcal{E}_J - \frac{\partial\overline{\Psi}_2}{\partial\mathcal{D}_J}\right)\dot{\mathcal{D}}_J &+ \left(\mathcal{T}^T_{SR} - \frac{\partial\overline{\Psi}_2}{\partial E_{RS}}\right)\dot{E}_{RS} \\ &+ \mathcal{J}'_J\mathcal{E}_J - \mathcal{Q}_J\Theta^{-1}\Theta_{,J} \geq 0 \end{aligned} \tag{2.243}$$

Necessary and sufficient conditions are

$$\begin{aligned} \rho_o\eta &= -\frac{\partial\overline{\Psi}_1}{\partial\Theta}, \quad \mathcal{E}_J = \frac{\partial\overline{\Psi}_1}{\partial\mathcal{P}_J}, \quad \mathcal{T}^P_{SR} = \frac{\partial\overline{\Psi}_1}{\partial E_{RS}} \\ \mathcal{J}'_J\mathcal{E}_J &- \mathcal{Q}_J\Theta^{-1}\Theta_{,J} \geq 0 \end{aligned} \tag{2.244}$$

and

$$\begin{aligned} \rho_o\eta &= -\frac{\partial\overline{\Psi}_2}{\partial\Theta}, \qquad \mathcal{E}_J = \frac{\partial\overline{\Psi}_2}{\partial\mathcal{D}_J}, \qquad \mathcal{T}^T_{SR} = \frac{\partial\overline{\Psi}_2}{\partial E_{RS}} \\ \mathcal{J}'_J\mathcal{E}_J &- \mathcal{Q}_J\Theta^{-1}\Theta_{,J} \geq 0 \end{aligned} \tag{2.245}$$

Theorem 2.24.4 (Legendre Transformed Conservation of Energy Statements) *Local conservation of energy statements equivalent to (2.215) and (2.216) are*

$$\rho_o\left(\dot{\Psi}_1 + \dot{\Theta}\eta + \Theta\dot{\eta}\right) = \mathcal{E}_J\dot{\mathcal{P}}_J + \mathcal{T}^P_{SR}\dot{E}_{RS} + \mathcal{J}'_J\mathcal{E}_J + \rho_o h - \mathcal{Q}_{J,J} \tag{2.246}$$

$$\rho_o\left(\dot{\Psi}_2 + \dot{\Theta}\eta + \Theta\dot{\eta}\right) = \mathcal{E}_J\dot{\mathcal{D}}_J + \mathcal{T}^T_{SR}\dot{E}_{RS} + \mathcal{J}'_J\mathcal{E}_J + \rho_o h - \mathcal{Q}_{J,J} \tag{2.247}$$

Proof. Using (2.236) and (2.237) in (2.215) and (2.216) proves (2.246) and (2.247). ■

We obtain our equations of heat conduction by simplifying the conservation of energy equations (2.246) and (2.247).

Theorem 2.24.5 (Local Heat Conduction in Material Fields) *The local heat conduction equation in material fields is*

$$\rho_o\Theta\dot{\eta} = \mathcal{J}'_J\mathcal{E}_J + \rho_o h - \mathcal{Q}_{J,J} \tag{2.248}$$

Proof. Using (2.244) and (2.245) in (2.246) and (2.247) proves (2.248). ■

Another useful Legendre transformation changes the independent variables from $(\eta, \mathcal{P}_J, E_{RS})$ or $(\eta, \mathcal{D}_J, E_{RS})$ to $(\Theta, \mathcal{E}_J, E_{RS})$. Inspection of (2.232) and (2.233) motivates

$$\epsilon = \Psi_3 + \Theta\eta + \mathcal{E}_J\mathcal{P}_J\rho_o^{-1} \tag{2.249}$$

$$U = \Psi_4 + \Theta\eta + \mathcal{E}_J\mathcal{D}_J\rho_o^{-1} \tag{2.250}$$

which gives

$$\begin{aligned} \dot{\epsilon} &= \dot{\Psi}_3 + \dot{\Theta}\eta + \Theta\dot{\eta} + \dot{\mathcal{E}}_J\mathcal{P}_J\rho_o^{-1} + \mathcal{E}_J\dot{\mathcal{P}}_J\rho_o^{-1} \\ \dot{U} &= \dot{\Psi}_4 + \dot{\Theta}\eta + \Theta\dot{\eta} + \dot{\mathcal{E}}_J\mathcal{D}_J\rho_o^{-1} + \mathcal{E}_J\dot{\mathcal{D}}_J\rho_o^{-1}. \end{aligned}$$

Based on this inspection we define the Legendre transformations

Definition 2.24.6 (Legendre Transforms II) *Legendre transformations Ψ_1 and Ψ_2 are defined as*

$$\begin{aligned} \Psi_3 &= \epsilon - \Theta\eta - \mathcal{E}_J\mathcal{P}_J\rho_o^{-1} \\ \Psi_4 &= U - \Theta\eta - \mathcal{E}_J\mathcal{D}_J\rho_o^{-1} \end{aligned}$$

Theorem 2.24.7 (Legendre Transformed Local C-D Inequality Statements II) *Local Clausius-Duhem inequalities equivalent to (2.232) and (2.233) are*

$$-\rho_o\left(\dot{\Psi}_3 + \dot{\Theta}\eta\right) - \mathcal{P}_J\dot{\mathcal{E}}_J + \mathcal{T}^P_{SR}\dot{E}_{RS} + \mathcal{J}'_J\mathcal{E}_J - \mathcal{Q}_J\Theta^{-1}\Theta_{,J} \geq 0 \tag{2.251}$$

$$-\rho_o\left(\dot{\Psi}_4+\dot{\Theta}\eta\right)-\mathcal{D}_J\dot{\mathcal{E}}_J+\mathcal{T}^T_{SR}\dot{E}_{RS}+\mathcal{J}'_J\mathcal{E}_J-\mathcal{Q}_J\Theta^{-1}\Theta_{,J}\ \geq\ 0 \qquad (2.252)$$

Proof. Using (2.249) and (2.250) in (2.232) and (2.233) proves (2.251) and (2.252). ■

Equations (2.251) and (2.252) motivate the objective functional forms

$$\begin{aligned}\rho_o\Psi_3 &= \overline{\Psi}_3\left(\Theta,\mathcal{E}_J,E_{RS}\right)\\ \rho_o\Psi_4 &= \overline{\Psi}_4\left(\Theta,\mathcal{E}_J,E_{RS}\right)\end{aligned}$$

Assuming these true

$$\rho_o\dot{\Psi}_3 = \frac{\partial\overline{\Psi}_3}{\partial\Theta}\dot{\Theta}+\frac{\partial\overline{\Psi}_3}{\partial\mathcal{E}_J}\dot{\mathcal{E}}_J+\frac{\partial\overline{\Psi}_3}{\partial E_{RS}}\dot{E}_{RS} \qquad (2.253)$$

$$\rho_o\dot{\Psi}_4 = \frac{\partial\overline{\Psi}_4}{\partial\Theta}\dot{\Theta}+\frac{\partial\overline{\Psi}_4}{\partial\mathcal{E}_J}\dot{\mathcal{E}}_J+\frac{\partial\overline{\Psi}_4}{\partial E_{RS}}\dot{E}_{RS} \qquad (2.254)$$

Using (2.253) and (2.254) in (2.251) and (2.252)

$$\begin{aligned}-\left(\rho_o\eta+\frac{\partial\overline{\Psi}_3}{\partial\Theta}\right)\dot{\Theta}+\left(\mathcal{P}_J+\frac{\partial\overline{\Psi}_3}{\partial\mathcal{E}_J}\right)\dot{\mathcal{E}}_J &+ \left(\mathcal{T}^P_{SR}-\frac{\partial\overline{\Psi}_3}{\partial E_{RS}}\right)\dot{E}_{RS}\\ &+ \mathcal{J}'_J\mathcal{E}_J-\mathcal{Q}_J\Theta^{-1}\Theta_{,J}\geq 0 \qquad (2.255)\end{aligned}$$

$$\begin{aligned}-\left(\rho_o\eta+\frac{\partial\overline{\Psi}_4}{\partial\Theta}\right)\dot{\Theta}+\left(\mathcal{D}_J+\frac{\partial\overline{\Psi}_4}{\partial\mathcal{E}_J}\right)\dot{\mathcal{E}}_J &+ \left(\mathcal{T}^T_{SR}-\frac{\partial\overline{\Psi}_4}{\partial E_{RS}}\right)\dot{E}_{RS}\\ &+ \mathcal{J}'_J\mathcal{E}_J-\mathcal{Q}_J\Theta^{-1}\Theta_{,J}\geq 0 \qquad (2.256)\end{aligned}$$

Necessary and sufficient conditions are

$$\begin{aligned}\rho_o\eta &= -\frac{\partial\overline{\Psi}_3}{\partial\Theta}, \quad \mathcal{P}_J=-\frac{\partial\overline{\Psi}_3}{\partial\mathcal{E}_J}, \quad \mathcal{T}^P_{SR}=\frac{\partial\overline{\Psi}_3}{\partial E_{RS}} \qquad (2.257)\\ \mathcal{J}'_J\mathcal{E}_J &- \mathcal{Q}_J\Theta^{-1}\Theta_{,J}\geq 0\end{aligned}$$

and

$$\begin{aligned}\rho_o\eta &= -\frac{\partial\overline{\Psi}_4}{\partial\Theta}, \quad \mathcal{D}_J=-\frac{\partial\overline{\Psi}_4}{\partial\mathcal{E}_J}, \quad \mathcal{T}^T_{SR}=\frac{\partial\overline{\Psi}_4}{\partial E_{RS}} \qquad (2.258)\\ \mathcal{J}'_J\mathcal{E}_J &- \mathcal{Q}_J\Theta^{-1}\Theta_{,J}\geq 0\end{aligned}$$

Theorem 2.24.8 (Legendre Transformed Local Conservation of Energy II) *Local conservation of energy statements equivalent to (2.215) and (2.216) are*

$$\rho_o\left(\dot{\Psi}_1+\dot{\Theta}\eta+\Theta\dot{\eta}\right) = -\mathcal{P}_J\dot{\mathcal{E}}_J+\mathcal{T}^P_{SR}\dot{E}_{RS}+\mathcal{J}'_J\mathcal{E}_J+\rho_o h-\mathcal{Q}_{J,J} \qquad (2.259)$$

$$\rho_o\left(\dot{\Psi}_2+\dot{\Theta}\eta+\Theta\dot{\eta}\right) = -\mathcal{D}_J\dot{\mathcal{E}}_J+\mathcal{T}^T_{SR}\dot{E}_{RS}+\mathcal{J}'_J\mathcal{E}_J+\rho_o h-\mathcal{Q}_{J,J} \qquad (2.260)$$

Proof. Using (2.249) and (2.250) in (2.215) and (2.216) proves (2.259) and (2.260). ■

We obtain our equations of heat conduction by simplifying the conservation of energy equations (2.259) and (2.260).

Theorem 2.24.9 (Local Heat Conduction in Material Fields) *The local heat conduction equation in material fields is*

$$\rho_o \Theta \dot{\eta} = \mathcal{J}_J' \mathcal{E}_J + \rho_o h - \mathcal{Q}_{J,J} \tag{2.261}$$

Proof. Using (2.257) and (2.258) in (2.259) and (2.260) proves (2.261). ■

2.25 Equation Summary: Spatial Fields

Here we summarize the local equations and jump conditions for deformable electroelastic continua with electric conduction, in terms of spatial fields [21].

$$\begin{aligned}
(D_i^* + J_i')_{,i} &= 0 \\
E_i + \phi_{,i} &= 0 \\
\dot{\rho} + \rho v_{k,k} &= 0 \\
\left(\tau_{ji} + \tau_{ji}^E\right)_{,j} + \rho\left(f_i - \dot{v}_i\right) &= 0 \\
\tau_{[ji]}^T = 0 \qquad \text{where } \tau_{ji}^T &= \tau_{ji} + \tau_{ji}^E \\
\rho \dot{U} = \left(\tau_{ij} + \tau_{ij}^E\right) v_{j,i} + E_i\left(J_i' + D_i^*\right) + \rho h - q_{i,i} \\
\rho \dot{\eta} \geq \rho \frac{h}{\Theta} - \left(\frac{q_i}{\Theta}\right)_{,i} \\
\rho \Theta \dot{\eta} = E_i J_i' + \rho h - q_{i,i}
\end{aligned}$$

Jump conditions across a material surface of discontinuity, such as the bounding surface of a material body are,

$$\begin{aligned}
[\![D_i^* + J_i']\!] n_i &= 0 && \text{across } \sigma \\
[\![\phi]\!] &= 0 && \text{across } \gamma \\
[\![x_k]\!] &= 0 && \text{across } \sigma \\
[\![\tau_{ji} + \tau_{ji}^E]\!] n_j &= 0 && \text{across } \sigma \\
[\![\left(\tau_{ij} + \tau_{ij}^E\right) v_j - \phi\left(J_i' + D_i^*\right) - q_i]\!] n_i &= 0 && \text{across } \sigma \\
[\![\frac{q_j}{\Theta}]\!] n_j &\geq 0 && \text{across } \sigma
\end{aligned}$$

[21] The convective time derivative D_i^* is defined in (2.66)

The system of equations is not closed without constitutive equations describing the material response.

$$\begin{aligned} \Psi_2 &= U - \Theta\eta \\ \rho_o\Psi_2 &= \overline{\Psi}_2(\Theta, \mathcal{D}_J, E_{RS}) \end{aligned}$$

Then from our results obtained earlier,

$$\eta = \frac{1}{\rho_o}\frac{\partial\overline{\Psi}_2}{\partial\Theta}, \qquad E_i = X_{J,i}\frac{\partial\overline{\Psi}_2}{\partial\mathcal{D}_J}, \qquad \tau^T_{ji} = J^{-1}x_{j,S}x_{i,R}\frac{\partial\overline{\Psi}_2}{\partial E_{RS}}$$

Additionally we have,

$$\begin{aligned} J'_i &= J^{-1}x_{i,J}\overline{\mathcal{J}'_J}(\mathcal{D}_J, E_{RS}, \Theta, \Theta_{,K}) \\ q_i &= J^{-1}x_{i,J}\overline{\mathcal{Q}_J}(\mathcal{D}_J, E_{RS}, \Theta, \Theta_{,K}) \end{aligned}$$

subject to the restriction

$$J'_iE_i - q_i\Theta^{-1}\Theta_{,i} \geq 0.$$

Remark 2.25.1 (Perfect Electrically Insulating Bodies) *The above system of equations specializes to perfectly insulating bodies by constraining conduction current density $J'_i = 0$ inside the body. The bounding surface of the body may have a non-zero prescribed current density. We can append this modified system of equations with the original EQS Maxwell equations if we introduce a surface charge density w^F on the discontinuity surface σ,*

$$\begin{aligned} \oint_S D_in_i\,dS &= \int_V q^F\,dV \\ D_{i,i} &= q^F \\ [D_i]\,n_i &= w^F \qquad \textit{across } \sigma. \end{aligned}$$

2.26 Equation Summary: Material Fields

Here we summarize the local equations and jump conditions for deformable electroelastic continua with electric conduction, in terms of material fields.

$$\begin{aligned} \left(\dot{\mathcal{D}}_J + \mathcal{J}'_J\right)_{,J} &= 0 \\ \mathcal{E}_J + \phi_{,J} &= 0 \\ J\rho &= \rho_o \\ \left(\mathcal{T}_{JK}x_{i,K} + \mathcal{T}^E_{JK}x_{i,K}\right)_{,J} + \rho_o(f_i - \dot{v}_i) &= 0 \\ \mathcal{T}^T_{[JK]} = 0\,, \qquad \mathcal{T}^T_{JK} &= \mathcal{T}_{JK} + \mathcal{T}^E_{JK} \\ \rho_o\dot{U} = \left(\mathcal{T}_{SR} + \mathcal{T}^E_{SR}\right)\dot{E}_{RS} + \mathcal{E}_J\left(\mathcal{J}'_J + \dot{\mathcal{D}}_J\right) &+ \rho_oh - \mathcal{Q}_{J,J} \end{aligned}$$

$$\rho\dot{\eta} \geq \rho_o \frac{h}{\Theta} - \left(\frac{\mathcal{Q}_J}{\Theta}\right)_{,J}$$
$$\rho\Theta\dot{\eta} = \mathcal{E}_J \mathcal{J}'_J + \rho_o h - \mathcal{Q}_{J,J}$$

Jump conditions across a material surface of discontinuity, such as the bounding surface of a material body are,

$$\begin{aligned}
[\![\dot{\mathcal{D}}_J + \mathcal{J}'_J]\!]\, N_J &= 0 && \text{across } \sigma_o \\
[\![\phi]\!] &= 0 && \text{across } \gamma_o \\
[\![x_k]\!] &= 0 && \text{across } \sigma_o \\
[\![\mathcal{T}_{JK} x_{i,K} + \mathcal{T}^E_{JK} x_{i,K}]\!]\, N_J &= 0 && \text{across } \sigma_o \\
[\![\left(\mathcal{T}_{JK} x_{j,K} + \mathcal{T}^E_{JK} x_{j,K}\right) v_j - \phi\left(\mathcal{J}'_J + \dot{\mathcal{D}}_J\right) - \mathcal{Q}_J]\!]\, N_J &= 0 && \text{across } \sigma_o \\
[\![\frac{\mathcal{Q}_J}{\Theta}]\!]\, N_J &\geq 0 && \text{across } \sigma_o
\end{aligned}$$

The system of equations is not closed without constitutive equations describing the material response.

$$\Psi_2 = U - \Theta\eta\,, \qquad \rho_o \Psi_2 = \overline{\Psi}_2\left(\Theta, \mathcal{D}_J, E_{RS}\right)$$
$$\eta = \frac{1}{\rho_o}\frac{\partial \overline{\Psi}_2}{\partial \Theta}\,, \qquad \mathcal{E}_J = \frac{\partial \overline{\Psi}_2}{\partial \mathcal{D}_J}\,, \qquad \mathcal{T}^T_{SR} = \frac{\partial \overline{\Psi}_2}{\partial E_{RS}}.$$

Additionally, subject to the inequality constraint,

$$\begin{aligned}
\mathcal{J}'_J &= \overline{\mathcal{J}'_J}\left(\mathcal{D}_J, E_{RS}, \Theta, \Theta_{,K}\right) \\
\mathcal{Q}_J &= \overline{\mathcal{Q}_J}\left(\mathcal{D}_J, E_{RS}, \Theta, \Theta_{,K}\right) \\
\mathcal{J}'_J \mathcal{E}_J - \mathcal{Q}_J \Theta^{-1} \Theta_{,J} &\geq 0.
\end{aligned}$$

Remark 2.26.1 (Perfect Electrically Insulating Bodies) *The general system of equations specializes to perfectly insulating bodies by constraining conduction current density $\mathcal{J}'_J = 0$ inside the body. The bounding surface of the body may have a non-zero prescribed current density. We can append this modified system of equations with the original EQS Maxwell equations if we introduce a surface charge density $\mathcal{W}^F$ on the discontinuity surface σ_o,*

$$\begin{aligned}
\oint_{S_o} \mathcal{D}_J N_J \, dS_o &= \int_{V_o} \mathcal{Q}^F \, dV_o \\
\mathcal{D}_{J,J} &= \mathcal{Q}^F \\
[\![\mathcal{D}_J]\!]\, N_J &= \mathcal{W}^F \qquad \textit{across } \sigma_o.
\end{aligned}$$

Remark 2.26.2 (Rigid and Static Bodies) *The general system of equations specializes to rigid and static bodies by constraining the strain tensor $E_{RS} = 0$ and the velocity vector $v_i = 0$. We can append this modified system of equations with the original EQS Maxwell equations if we introduce a surface charge density $\mathcal{W}^F$ on the*

discontinuity surface σ_o.

$$\oint_{S_o} \mathcal{D}_J N_J \, dS_o = \int_{V_o} \mathcal{Q}^F \, dV_o$$

$$\oint_{S_o} \mathcal{J}'_J N_J \, dS_o = -\frac{d}{dt} \int_{V_o} \mathcal{Q}^F \, dV_o$$

$$\mathcal{D}_{J,J} = \mathcal{Q}^F$$

$$\mathcal{J}'_{J,J} = -\dot{\mathcal{Q}}^F$$

$$[\![\mathcal{D}_J]\!] N_J = \mathcal{W}^F \qquad \textit{across } \sigma_o.$$

$$[\![\mathcal{J}'_J]\!] N_J = -\dot{\mathcal{W}}^F \qquad \textit{across } \sigma_o.$$

Chapter 3

Small Deformation Approximations

3.1 Introduction

The purpose of this chapter is to introduce the small deformation approximation (SDA) into the general EQS electroelastic equations summarized below. The resulting SDA equations are greatly simplified and specialize to the classical linear piezoelectric equations, extended to include electrical conduction. A result is that electric body forces, realized mathematically as electric surface tractions, are retained in the small deformation approximation.

3.2 Large Deformation Equations: Material Fields

Below we present a summary of the general EQS electroelastic equations with electric conduction in material fields.

$$
\begin{aligned}
\left(\dot{\mathcal{D}}_J + \mathcal{J}'_J\right)_{,J} &= 0 \\
\mathcal{E}_J + \phi_{,J} &= 0 \\
J\rho &= \rho_o \\
\left(\mathcal{T}_{JK} x_{i,K} + \mathcal{T}^E_{JK} x_{i,K}\right)_{,J} + \rho_o \left(f_i - \dot{v}_i\right) &= 0 \\
\mathcal{T}^T_{[JK]} = 0\,, \qquad \mathcal{T}^T_{JK} &= \mathcal{T}_{JK} + \mathcal{T}^E_{JK} \\
\rho_o \dot{U} = \left(\mathcal{T}_{SR} + \mathcal{T}^E_{SR}\right) \dot{E}_{RS} + \mathcal{E}_J \left(\mathcal{J}'_J + \dot{\mathcal{D}}_J\right) &+ \rho_o h - \mathcal{Q}_{J,J} \\
\rho_o \dot{\eta} \geq \rho_o \frac{h}{\Theta} &- \left(\frac{\mathcal{Q}_J}{\Theta}\right)_{,J} \\
\rho_o \Theta \dot{\eta} = \mathcal{E}_J \mathcal{J}'_J &+ \rho_o h - \mathcal{Q}_{J,J}
\end{aligned}
$$

Jump conditions across material surfaces of discontinuity, such as the bounding surface of a material body are,

$$
\begin{aligned}
[\![\dot{\mathcal{D}}_J + \mathcal{J}'_J]\!]\, N_J &= 0 \qquad \text{across } \sigma_o \\
[\![\phi]\!] &= 0 \qquad \text{across } \gamma_o
\end{aligned}
$$

$$
\begin{aligned}
[\,\mathcal{T}_{JK}x_{i,K} + \mathcal{T}^E_{JK}x_{i,K}\,]\,N_J &= 0 \qquad \text{across } \sigma_o \\
[\,\left(\mathcal{T}_{JK}x_{j,K} + \mathcal{T}^E_{JK}x_{j,K}\right)v_j - \phi\left(\mathcal{J}'_J + \dot{\mathcal{D}}_J\right) - \mathcal{Q}_J\,]\,N_J &= 0 \qquad \text{across } \sigma_o \\
[\,\frac{\mathcal{Q}_J}{\Theta}\,]\,N_J &\geq 0 \qquad \text{across } \sigma_o
\end{aligned}
$$

The system of equations is not closed without constitutive equations describing the material response.

$$
\begin{aligned}
\Psi_2 = U - \Theta\eta\,, \qquad \rho_o\Psi_2 &= \overline{\Psi}_2\left(\Theta, \mathcal{D}_J, E_{RS}\right) \\
\eta = \frac{1}{\rho_o}\frac{\partial\overline{\Psi}_2}{\partial\Theta}\,, \qquad \mathcal{E}_J = \frac{\partial\overline{\Psi}_2}{\partial\mathcal{D}_J}\,, \qquad \mathcal{T}^T_{SR} &= \frac{\partial\overline{\Psi}_2}{\partial E_{RS}}.
\end{aligned}
$$

Additionally, subject to the inequality constraint,

$$
\begin{aligned}
\mathcal{J}'_J &= \overline{\mathcal{J}'_J}\left(\mathcal{D}_J, E_{RS}, \Theta, \Theta_{,K}\right) \\
\mathcal{Q}_J &= \overline{\mathcal{Q}_J}\left(\mathcal{D}_J, E_{RS}, \Theta, \Theta_{,K}\right) \\
\mathcal{J}'_J\mathcal{E}_J - \mathcal{Q}_J\Theta^{-1}\Theta_{,J} &\geq 0.
\end{aligned}
$$

Remark 3.2.1 (Material Time Derivative: Material Fields) *Material fields such as $\mathcal{D}_J$ are defined over material points X_j in $\mathcal{B}_o$. The material time derivative of a material field is simply a partial derivative with respect to time,*[1]

$$
\begin{aligned}
\dot{\mathcal{D}}_J &= \frac{\partial\mathcal{D}_J\left(X_J, t\right)}{\partial t} \\
v_i &= \frac{\partial\chi_i\left(X_J, t\right)}{\partial t}.
\end{aligned}
$$

3.3 Small Deformation Equations: Material Fields

The material form of the large deformation equations summarized above are particularly useful for deriving approximate theories. The difficulty with the above expression is that $x_{j,K}$ is part of the solution, and unknown a priori. We can greatly simplify the above equations by introducing the small deformation approximation. First we define the mechanical displacement vector.

Definition 3.3.1 (Mechanical Displacement) *A mechanical displacement vector u_M is defined as*

$$
x_k = \left(X_M + u_M\right)\delta_{Mk}, \tag{3.1}
$$

Introducing u_M into $x_{j,K}$, E_{MN}, and v_k gives

$$
x_{j,K} = \delta_{jK} + \frac{\partial u_M}{\partial X_K}\delta_{Mj}
$$

[1] *Compare to the spatial field description where a nonlinear convective term that arises*

$$
\begin{aligned}
E_{MN} &= \frac{1}{2}\left(\frac{\partial u_M}{\partial X_N} + \frac{\partial u_N}{\partial X_M} + \frac{\partial u_K}{\partial X_M}\frac{\partial u_K}{\partial X_N}\right) \\
v_k &= \dot{u}_M \delta_{Mk}.
\end{aligned}
$$

Definition 3.3.2 (Small Deformation Approximation (SDA)) *The displacement gradient and its material derivative are assumed small,*

$$
\left|\frac{\partial u_K}{\partial X_J}\right| \ll 1 \quad \textit{for each } K, J = 1..3, \tag{3.2}
$$

$$
\left|\frac{\partial \dot{u}_K}{\partial X_J}\right| \ll 1 \quad \textit{for each } K, J = 1..3. \tag{3.3}
$$

Remark 3.3.3 (Simplifications Under SDA) *The SDA implies the following approximations,*

$$
\begin{aligned}
x_{j,K} &= \delta_{jK} + \frac{\partial u_M}{\partial X_K}\delta_{Mj} \approx \delta_{jK} \\
J &= \det\left(\frac{\partial x_i}{\partial X_J}\right) \approx 1. \\
E_{MN} &= \frac{1}{2}\left(\frac{\partial u_M}{\partial X_N} + \frac{\partial u_N}{\partial X_M} + \frac{\partial u_K}{\partial X_M}\frac{\partial u_K}{\partial X_N}\right) \\
&\approx \frac{1}{2}\left(\frac{\partial u_M}{\partial X_N} + \frac{\partial u_N}{\partial X_M}\right)
\end{aligned} \tag{3.4}
$$

It is interesting to note that $x_{i,K} \approx \delta_{iK}$ and $J \approx 1$ imply that all spatial and material fields in definition 2.20.1 are indistinguishable in the SDA approximation. This suggests the extreme nature of the simplification.

Theorem 3.3.4 (EQS Electroelastic SDA Equations) *The EQS electroelastic equations under the SDA approximation simplify to the following:*

$$
\begin{aligned}
\left(\dot{\mathcal{D}}_J + \mathcal{J}'_J\right)_{,J} &= 0 \\
\mathcal{E}_J + \phi_{,J} &= 0 \\
\left(\mathcal{T}_{JK}\delta_{iK} + \mathcal{T}^E_{JK}\delta_{iK}\right)_{,J} + \rho_o\left(f_i - \dot{v}_i\right) &= 0 \\
\mathcal{T}^T_{[JK]} = 0\,, \qquad \mathcal{T}^T_{JK} &= \mathcal{T}_{JK} + \mathcal{T}^E_{JK} \\
\rho_o\dot{U} = \left(\mathcal{T}_{SR} + \mathcal{T}^E_{SR}\right)\dot{\overline{E}}_{RS} + \mathcal{E}_J\left(\mathcal{J}'_J + \dot{\mathcal{D}}_J\right) &+ \rho_o h - \mathcal{Q}_{J,J} \\
\rho_o\dot{\eta} &\geq \rho_o\frac{h}{\Theta} - \left(\frac{\mathcal{Q}_J}{\Theta}\right)_{,J} \\
\rho_o\Theta\dot{\eta} &= \mathcal{E}_J\mathcal{J}'_J + \rho_o h - \mathcal{Q}_{J,J} \\
\dot{\overline{E}}_{MN} &= \frac{1}{2}\left(\frac{\partial u_M}{\partial X_N} + \frac{\partial u_N}{\partial X_M}\right)
\end{aligned}
$$

The corresponding jump conditions across material surfaces of discontinuity, such as the bounding surface of a material body, are

$$
\begin{aligned}
[\dot{\mathcal{D}}_J + \mathcal{J}'_J]\, N_J &= 0 && \text{across } \sigma_o \\
[\phi] &= 0 && \text{across } \gamma_o \\
[u_M] &= 0 && \text{across } \sigma_o \\
[\mathcal{T}_{JK}\delta_{iK} + \mathcal{T}^E_{JK}\delta_{iK}]\, N_J &= 0 && \text{across } \sigma_o \\
[\left(\mathcal{T}_{JK}\delta_{jK} + \mathcal{T}^E_{JK}\delta_{jK}\right) v_j - \phi\left(\mathcal{J}'_J + \dot{\mathcal{D}}_J\right) - \mathcal{Q}_J]\, N_J &= 0 && \text{across } \sigma_o \\
[\frac{\mathcal{Q}_J}{\Theta}]\, N_J &\geq 0 && \text{across } \sigma_o
\end{aligned}
$$

The system of equations is not closed without constitutive equations describing the material response.

$$
\Psi_2 = U - \Theta\eta\,, \qquad \rho_o\Psi_2 = \overline{\Psi}_2\left(\Theta, \mathcal{D}_J, \overline{E}_{RS}\right)
$$

$$
\eta = \frac{1}{\rho_o}\frac{\partial\overline{\Psi}_2}{\partial\Theta}\,, \qquad \mathcal{E}_J = \frac{\partial\overline{\Psi}_2}{\partial\mathcal{D}_J}\,, \qquad \mathcal{T}^T_{SR} = \frac{\partial\overline{\Psi}_2}{\partial\overline{E}_{RS}}.
$$

Additionally, subject to the inequality constraint,

$$
\begin{aligned}
\mathcal{J}'_J &= \overline{\mathcal{J}'_J}\left(\mathcal{D}_J, \overline{E}_{RS}, \Theta, \Theta_{,K}\right) \\
\mathcal{Q}_J &= \overline{\mathcal{Q}_J}\left(\mathcal{D}_J, \overline{E}_{RS}, \Theta, \Theta_{,K}\right) \\
\mathcal{J}'_J\mathcal{E}_J &- \mathcal{Q}_J\Theta^{-1}\Theta_{,J} \geq 0.
\end{aligned}
$$

Remark 3.3.5 (Perfect Electrically Insulating Bodies) *The general system of equations specializes to perfectly insulating bodies by constraining conduction current density $\mathcal{J}'_J = 0$ inside the body. The bounding surface of the body may have a non-zero prescribed current density. We can append this modified system of equations with the original EQS Maxwell equations if we introduce a surface charge density $\mathcal{W}^F$ on the discontinuity surface σ_o,*

$$
\begin{aligned}
\oint_{S_o} \mathcal{D}_J N_J\, dS_o &= \int_{V_o} \mathcal{Q}^F\, dV_o \\
\mathcal{D}_{J,J} &= \mathcal{Q}^F \\
[\mathcal{D}_J]\, N_J &= \mathcal{W}^F \qquad \text{across } \sigma_o.
\end{aligned} \tag{3.5}
$$

Remark 3.3.6 (Rigid and Static Bodies) *The general system of equations specializes to rigid and static bodies by constraining the strain tensor $E_{RS} = 0$ and the velocity vector $v_i = 0$. We can append this modified system of equations with the original EQS Maxwell equations if we introduce a surface charge density $\mathcal{W}^F$ on the discontinuity surface σ_o.*

$$
\oint_{S_o} \mathcal{D}_J N_J\, dS_o = \int_{V_o} \mathcal{Q}^F\, dV_o
$$

$$\oint_{S_o} \mathcal{J}'_J N_J \, dS_o = -\frac{d}{dt} \int_{V_o} \mathcal{Q}^F \, dV_o$$

$$\mathcal{D}_{J,J} = \mathcal{Q}^F$$

$$\mathcal{J}'_{J,J} = -\dot{\mathcal{Q}}^F$$

$$[\![\mathcal{D}_J]\!] N_J = \mathcal{W}^F \qquad \textit{across } \sigma_o.$$

$$[\![\mathcal{J}'_J]\!] N_J = -\dot{\mathcal{W}}^F \qquad \textit{across } \sigma_o.$$

Chapter 4

Finite Element Formulations

4.1 Introduction

The current and following chapters will consider solution of the EQS electroelastic SDA equations presented in theorem 3.3.4. Restricting ourself to the simplified equations, it is convenient to introduce new notation.

4.2 Electroelastic SDA Equations

Definition 4.2.1 (Notation) *The notation in theorem 3.3.4 is changed as follows:*

$$
\begin{aligned}
u_M &\to u_i & \mathcal{D}_J &\to D_i \\
\mathcal{Q}^F &\to q^F & \mathcal{W}^F &\to w^F \\
\mathcal{J}'_J &\to J_i & \mathcal{E}_J &\to E_i \\
\phi &\to \phi & \mathcal{T}_{JK} &\to \tau_{ij} \\
\mathcal{T}^E_{JK} &\to \tau^E_{ij} & \rho_o f_i &\to f_i \\
v_i &\to v_i & \mathcal{T}^T_{JK} &\to \tau^T_{ij} \\
\rho_o U &\to U & \overline{E}_{RS} &\to \epsilon_{ij} \\
h &\to h & \mathcal{Q}_J &\to q_i \\
\eta &\to \eta & \Theta &\to \Theta \\
N_J &\to n_j & V_o &\to V \\
S_o &\to S & C_o &\to C
\end{aligned}
$$

Next we present the SDA equations in the new notation.

Theorem 4.2.2 (EQS Electroelastic SDA Equations)

$$
\begin{aligned}
\left(\dot{D}_i + J_i\right)_{,i} &= 0 \\
E_i + \phi_{,i} &= 0 \\
\left(\tau_{jk} + \tau^E_{jk}\right)_{,j} + f_i - \rho_o \dot{v}_i &= 0
\end{aligned}
$$

$$\tau^T_{[jk]} = 0 \,, \qquad \tau^T_{jk} = \tau_{jk} + \tau^E_{jk}$$
$$\dot{U} = \left(\tau_{ji} + \tau^E_{ji}\right)\dot{\epsilon}_{ij} + E_k\left(J_k + \dot{D}_k\right) + \rho_o h - q_{k,k}$$
$$\rho_o\dot{\eta} \geq \rho_o\frac{h}{\Theta} - \left(\frac{q_j}{\Theta}\right)_{,j}$$
$$\rho_o\Theta\dot{\eta} = E_k J_k + \rho_o h - q_{k,k}$$
$$\epsilon_{ij} = \frac{1}{2}\left(u_{i,j} + u_{j,i}\right)$$

Jump conditions across a material surface of discontinuity, such as the bounding surface of a material body are,

$$\begin{aligned}
[\,\dot{D}_i + J_i\,]\,n_i &= 0 && \textit{across } \sigma_o \\
[\,\phi\,] &= 0 && \textit{across } \gamma_o \\
[\,u_i\,] &= 0 && \textit{across } \sigma_o \\
[\,\tau_{jk} + \tau^E_{jk}\,]\,n_j &= 0 && \textit{across } \sigma_o \\
[\,\left(\tau_{jk} + \tau^E_{jk}\right)v_k - \phi\left(J_j + \dot{D}_j\right) - q_j\,]\,n_j &= 0 && \textit{across } \sigma_o \\
[\,\frac{q_j}{\Theta}\,]\,n_j &\geq 0 && \textit{across } \sigma_o
\end{aligned}$$

The system of equations is not closed without the constitutive equations describing the material response.

$$\Psi_2 = U - \Theta\eta \,, \qquad \rho_o\Psi_2 = \overline{\Psi}_2\left(\Theta, D_j, \epsilon_{ij}\right)$$
$$\eta = \frac{1}{\rho_o}\frac{\partial\overline{\Psi}_2}{\partial\Theta} \,, \qquad E_j = \frac{\partial\overline{\Psi}_2}{\partial D_j} \,, \qquad \tau^T_{ji} = \frac{\partial\overline{\Psi}_2}{\partial\epsilon_{ij}}.$$

Additionally, subject to the inequality constraint,

$$J_j = \overline{J_j}\left(D_j, \epsilon_{ij}, \Theta, \Theta_{,k}\right)$$
$$q_j = \overline{q_j}\left(D_j, \epsilon_{ij}, \Theta, \Theta_{,k}\right)$$
$$J_j E_j - q_j\Theta^{-1}\Theta_{,j} \geq 0.$$

Remark 4.2.3 (Perfect Electrically Insulating Bodies) *The general system of equations specializes to perfectly insulating bodies by constraining conduction current density $J_i = 0$ inside the body. The bounding surface of the body may have a non-zero prescribed current density. We can append this modified system of equations with the original EQS Maxwell equations if we introduce a surface charge density w^F on the discontinuity surface σ_o,*

$$\begin{aligned}
\oint_S D_i n_i \, dS &= \int_V q^F \, dV \\
D_{i,i} &= q^F \\
[\,D_i\,]\,n_i &= w^F \qquad \textit{across } \sigma_o.
\end{aligned} \tag{4.1}$$

Remark 4.2.4 (Rigid and Static Bodies) *The general system of equations spe-*

cializes to rigid and static bodies by constraining the strain tensor $\epsilon_{ij} = 0$ and the velocity vector $v_i = 0$. We can append this modified system of equations with the original EQS Maxwell equations if we introduce a surface charge density w^F on the discontinuity surface σ_o.

$$
\begin{aligned}
\oint_S D_i n_i \, dS &= \int_V q^F \, dV \\
\oint_S J_i n_i \, dS &= -\frac{\partial}{\partial t} \int_V q^F \, dV \\
D_{i,i} &= q^F \\
J_{i,i} &= -\dot{q}^F \\
[\![D_i]\!] \, n_i &= w^F \qquad \textit{across } \sigma_o. \\
[\![J_i]\!] \, n_i &= -\dot{w}^F \qquad \textit{across } \sigma_o.
\end{aligned}
$$

4.3 Weak Forms of Equations

In this section we obtain the weak form of the balance of momentum and Maxwell EQS equations suitable for a finite element analysis.

Theorem 4.3.1 (Balance of Momentum: Weak Form) *A material volume V bounded by surface $S = S_f + S_u$ is subject to mechanical surface tractions $f_i^{S_f}$ on S_f, mechanical displacement constraints $u_i^{S_u}$ on S_u, and body force density f_i^B in V. The electric stress tractions t_i^E outside the material volume V are assumed negligible, consistent with an assumption of zero electric fields E_i outside V. The balance of momentum equations and corresponding jump conditions across S are*

$$
\tau^T_{ji,j} + f_i^B = \rho_o \frac{\partial^2 u_i}{\partial t^2} \qquad \tau^T_{[ji]} = 0
$$

$$
\tau^T_{ji} n_j = f_i^{S_f} \ \textit{on } S_f \qquad u_i = u_i^{S_u} \ \textit{on } S_u.
$$

Consider a weighting function $\overline{u}_i$ and tensor $\overline{\epsilon}_{ij}$, defined over the material volume V, such that

$$
\overline{u}_i = 0 \ \textit{on } S_u \qquad \overline{\epsilon}_{ij} = \frac{1}{2}\left(\overline{u}_{i,j} + \overline{u}_{j,i}\right).
$$

Then the balance of momentum equations and jump conditions have the equivalent weak form,

$$
\begin{aligned}
\int_V \tau^T_{ji} \overline{\epsilon}_{ij} \, dV + \int_V \rho_o \frac{\partial^2 u_i}{\partial t^2} \overline{u}_i \, dV &= \int_V f_i^B \overline{u}_i \, dV + \int_{S_f} f_i^{S_f} \overline{u}_i \, dS_f, \qquad (4.2) \\
u_i &= u_i^{S_u} \ \textit{on } S_u
\end{aligned}
$$

Proof. Multiply the balance of momentum equation through by $\overline{u}_i$ and integrate over V,

$$\int_V \left(\tau^T_{ji,j} + f^B_i\right) \overline{u}_i \, dV = \int_V \rho_o \frac{\partial^2 u_i}{\partial t^2} \overline{u}_i \, dV \, .$$

Use the chain rule to eliminate derivatives from τ^T_{ji},

$$(\tau^T_{ji}\overline{u}_i)_{,j} = \tau^T_{ji,j}\overline{u}_i + \tau^T_{ji}\overline{u}_{i,j}.$$

Use the identity

$$\int_V (\tau^T_{ji}\overline{u}_i)_{,j} \, dV = \oint_S \tau^T_{ji}\overline{u}_i n_j \, dS \, ,$$

and $\tau^T_{[ji]} = 0 \rightarrow \tau^T_{ji} = \tau^T_{ij}$, such that

$$\tau^T_{ji}\overline{u}_{i,j} = \tau^T_{ji}\frac{1}{2}(\overline{u}_{i,j} + \overline{u}_{j,i}) = \tau^T_{ji}\overline{\epsilon}_{ij},$$

to obtain

$$\oint_S \tau^T_{ji}\overline{u}_i n_j \, dS - \int_V \tau^T_{ji}\overline{\epsilon}_{ij} \, dV + \int_V \left(f^B_i - \rho_o \frac{\partial^2 u_i}{\partial t^2}\right) \overline{u}_i \, dV = 0.$$

Use the jump condition and constraint

$$\tau^T_{ji} n_j = f^{S_f}_i \text{ on } S_f \qquad \overline{u}_i = 0 \text{ on } S_u$$

to obtain a weak form of the linear momentum balance

$$\int_V \tau^T_{ji}\overline{\epsilon}_{ij} \, dV + \int_V \rho_o \frac{\partial^2 u_i}{\partial t^2} \overline{u}_i \, dV = \int_V f^B_i \overline{u}_i \, dV + \int_S f^{S_f}_i \overline{u}_i \, dS \, .$$

■

Theorem 4.3.2 (EQS Maxwell: Weak Form) *A material volume V bounded by surface $S = S_q + S_\phi$ is subject to electric current density $\boldsymbol{J}^{\text{ext}} \cdot \boldsymbol{n} = J^{S_q}$ on S_q and electric voltage constraints ϕ^{S_ϕ} on S_ϕ. The electric displacement fields $\boldsymbol{D}$ and their time derivatives are assumed negligible outside the material volume V. The conservation of charge equation and corresponding jump conditions across S are*

$$\boldsymbol{\nabla} \cdot \left(\dot{\boldsymbol{D}} + \boldsymbol{J}\right) = 0 \qquad \left(\dot{\boldsymbol{D}} + \boldsymbol{J}\right) \cdot \boldsymbol{n} = J^{S_q} \text{ on } S_q \qquad \phi = \phi^{S_\phi} \text{ on } S_\phi$$

Consider a weighting function $\overline{\phi}$ and vector $\overline{\boldsymbol{E}}$, defined over the material volume V, such that

$$\overline{\phi} = 0 \text{ on } S_\phi \qquad \overline{\boldsymbol{E}} = -\boldsymbol{\nabla}\phi$$

Then the conservation of charge equation and jump conditions have the equivalent

equivalent weak form,

$$\begin{aligned}\int_V \left(\dot{\boldsymbol{D}} + \boldsymbol{J}\right) \cdot \overline{\boldsymbol{E}}\, dV &= -\int_{S_q} J^{S_q} \overline{\phi}\, dS_q \\ \phi &= \phi^{S_\phi} \text{ on } S_\phi\end{aligned}$$

Proof. Multiply the conservation of charge equation through by $\overline{\phi}$ and integrate over V,

$$\int_V \boldsymbol{\nabla} \cdot \left(\dot{\boldsymbol{D}} + \boldsymbol{J}\right) \overline{\phi}\, dV = 0$$

Use the chain rule to eliminate derivatives from $\left(\dot{\boldsymbol{D}} + \boldsymbol{J}\right)$,

$$\boldsymbol{\nabla} \cdot \left[\left(\dot{\boldsymbol{D}} + \boldsymbol{J}\right) \overline{\phi}\right] = \boldsymbol{\nabla} \cdot \left(\dot{\boldsymbol{D}} + \boldsymbol{J}\right) \overline{\phi} + \left(\dot{\boldsymbol{D}} + \boldsymbol{J}\right) \cdot \boldsymbol{\nabla} \overline{\phi}.$$

Use the identity

$$\int_V \boldsymbol{\nabla} \cdot \left[\left(\dot{\boldsymbol{D}} + \boldsymbol{J}\right) \overline{\phi}\right] dV = \oint_S \left[\left(\dot{\boldsymbol{D}} + \boldsymbol{J}\right) \overline{\phi}\right] \cdot \boldsymbol{n}\, dS,$$

to obtain

$$\oint_S \left(\dot{\boldsymbol{D}} + \boldsymbol{J}\right) \cdot \boldsymbol{n} \overline{\phi}\, dS + \int_V \left(\dot{\boldsymbol{D}} + \boldsymbol{J}\right) \cdot \overline{\boldsymbol{E}}\, dV = 0.$$

Use the jump condition and constraint,

$$\left(\dot{\boldsymbol{D}} + \boldsymbol{J}\right) \cdot \boldsymbol{n} = J^{S_q} \text{ on } S_q \qquad \overline{\phi} = 0 \text{ on } S_\phi$$

to obtain

$$\int_V \left(\dot{\boldsymbol{D}} + \boldsymbol{J}\right) \cdot \overline{\boldsymbol{E}}\, dV = -\oint_{S_q} J^{S_q} \overline{\phi}\, dS_q.$$

■

4.4 Solution Technique

Standard techniques have been developed for the finite element solution of a system of differential equations. These take as a starting point the weak form of the governing equations, see BATHE [2] for finite element procedures in the context of continuum mechanics of solids. Finite element procedures will be used to spatially discretize the weak form equations, and finite difference techniques will be used to discretize the equations over time. The result is a finite degree of freedom system of algebraic equations. In this thesis we are interested in presenting a finite element formulation suitable for nonlinear material response functions. In this case, the resulting system of algebraic equations will also be nonlinear. Below we present our notation for solving the nonlinear system of algebraic equations using Newton's method. We present this

to motivate the form of our finite element formulation in the following sections, which anticipate a Newton method solution.

Our finite element formulations[1] will result in the following system of nonlinear ordinary differential equations

$$Res\left(\boldsymbol{\xi}, \dot{\boldsymbol{\xi}}, \ddot{\boldsymbol{\xi}}\right) = 0,$$

where $\boldsymbol{\xi}$ is our vector of nodal unknowns. Anticipating a finite difference discretization in time, we write the equations at some specified time $t + \Delta t$,

$$\boldsymbol{Res}(\boldsymbol{\xi}_{t+\Delta t}, \dot{\boldsymbol{\xi}}_{t+\Delta t}, \ddot{\boldsymbol{\xi}}_{t+\Delta t}) = 0.$$

This system will be discretized using an implicit finite difference technique,

$$\begin{aligned} \dot{\boldsymbol{\xi}}_{t+\Delta t} &= \dot{\boldsymbol{\xi}}_{t+\Delta t}(\boldsymbol{\xi}_{t+\Delta t}, \boldsymbol{\xi}_t, \dot{\boldsymbol{\xi}}_t, \ddot{\boldsymbol{\xi}}_t), \\ \ddot{\boldsymbol{\xi}}_{t+\Delta t} &= \ddot{\boldsymbol{\xi}}_{t+\Delta t}(\boldsymbol{\xi}_{t+\Delta t}, \boldsymbol{\xi}_t, \dot{\boldsymbol{\xi}}_t, \ddot{\boldsymbol{\xi}}_t). \end{aligned}$$

Dropping the explicit dependence on variables at time t, because they are known at time $t + \Delta t$, we obtain

$$\boldsymbol{Res}(\boldsymbol{\xi}_{t+\Delta t}, \dot{\boldsymbol{\xi}}_{t+\Delta t}(\boldsymbol{\xi}_{t+\Delta t}), \ddot{\boldsymbol{\xi}}_{t+\Delta t}(\boldsymbol{\xi}_{t+\Delta t})) = 0.$$

Redefining such that

$$\boldsymbol{\xi}_{t+\Delta t} \longrightarrow \boldsymbol{\xi}$$

we introduce

$$\begin{aligned} \delta\boldsymbol{\xi} &\triangleq \boldsymbol{\xi}^{\nu+1} - \boldsymbol{\xi}^{\nu}, \\ \boldsymbol{Res}^{\nu} &\triangleq \boldsymbol{Res}(\boldsymbol{\xi}^{\nu}) \end{aligned}$$

where ν is the iteration level for a Newton method solution technique. Consider our equations at iteration level $\nu + 1$ and introduce a first order Taylor series expansion,

$$\begin{aligned} \boldsymbol{Res}^{\nu+1} &\simeq \boldsymbol{Res}^{\nu} + \left.\frac{\partial \boldsymbol{Res}}{\partial \boldsymbol{\xi}}\right|^{\nu} \delta\boldsymbol{\xi} + \left.\frac{\partial \boldsymbol{Res}}{\partial \dot{\boldsymbol{\xi}}}\right|^{\nu} \left.\frac{\partial \dot{\boldsymbol{\xi}}}{\partial \boldsymbol{\xi}}\right|^{\nu} \delta\boldsymbol{\xi} + \left.\frac{\partial \boldsymbol{Res}}{\partial \ddot{\boldsymbol{\xi}}}\right|^{\nu} \left.\frac{\partial \ddot{\boldsymbol{\xi}}}{\partial \boldsymbol{\xi}}\right|^{\nu} \delta\boldsymbol{\xi} + \cdots \\ &= \boldsymbol{Res}^{\nu} + \left[\frac{\partial \boldsymbol{Res}}{\partial \boldsymbol{\xi}} + \frac{\partial \boldsymbol{Res}}{\partial \dot{\boldsymbol{\xi}}}\frac{\partial \dot{\boldsymbol{\xi}}}{\partial \boldsymbol{\xi}} + \frac{\partial \boldsymbol{Res}}{\partial \ddot{\boldsymbol{\xi}}}\frac{\partial \ddot{\boldsymbol{\xi}}}{\partial \boldsymbol{\xi}}\right]^{\nu} \delta\boldsymbol{\xi} + \cdots \end{aligned}$$

or

$$\boldsymbol{Res}^{\nu+1} \simeq \boldsymbol{Res}^{\nu} + J^{\nu}\delta\boldsymbol{\xi}$$

where we have implicitly defined the Jacobian matrix J^{ν}. Newton's method is entirely

[1]See BATHE [2] for details of standard finite element procedures

based on the following two statements

$$\begin{aligned} \boldsymbol{Res}^{\nu+1} &\simeq \boldsymbol{Res}^{\nu} + J^{\nu}\delta\boldsymbol{\xi} \\ \boldsymbol{Res}^{\nu+1} &= 0 \end{aligned}$$

resulting in Newton's method equations that are solved iteratively

$$J^{\nu}\delta\boldsymbol{\xi} = -\boldsymbol{Res}^{\nu}.$$

until components of the residual vector $\boldsymbol{Res}^{\nu}$ are sufficiently small.

4.4.1 Choice of Independent Variables

Boundary conditions and the functional dependence of available constitutive relations are what determines the choice of independent variables in our problem formulation. For convenience we introduce Voight notation to replace the symmetric tensors τ_{ji}^{T} and ϵ_{ij} with $\boldsymbol{T}$ and $\boldsymbol{S}$,

$$\begin{aligned} \boldsymbol{T} &= \begin{bmatrix} \tau_{11}^{T} & \tau_{22}^{T} & \tau_{33}^{T} & \tau_{32}^{T} & \tau_{13}^{T} & \tau_{12}^{T} \end{bmatrix}' \\ \boldsymbol{S} &= \begin{bmatrix} \epsilon_{11} & \epsilon_{22} & \epsilon_{33} & 2\epsilon_{32} & 2\epsilon_{13} & 2\epsilon_{12} \end{bmatrix}' \end{aligned}$$

The jump conditions involve mechanical displacement $\boldsymbol{u}$ and voltage ϕ specification on the corresponding domain boundaries. Therefore, our finite element formulation must have $\boldsymbol{u}$ and ϕ for independent variables. In the conventional formulation we would have available,

$$\boldsymbol{T} = \boldsymbol{T}(\boldsymbol{S}, \boldsymbol{E}) \qquad \boldsymbol{S} = \boldsymbol{S}(\boldsymbol{S}, \boldsymbol{E}).$$

From our definitions of strain and electric field,

$$\boldsymbol{S} = \boldsymbol{S}(\boldsymbol{u}) \qquad \boldsymbol{E} = \boldsymbol{E}(\phi).$$

Therefore our constitutive relations and jump conditions are known in terms of the same independent variables. In this case the weak form of the equations presented earlier are suitable.

It turns out however that constitutive relations may not be avaialable in the above form for a given material. Electroelastic materials with hysteresis may have constitutive relations of the form

$$\boldsymbol{T} = \boldsymbol{T}(\boldsymbol{S}, \boldsymbol{D}) \qquad \boldsymbol{E} = \boldsymbol{E}(\boldsymbol{S}, \boldsymbol{D}),$$

where these nonlinear relations may not be easily inverted. In this case, our boundary conditions require $\boldsymbol{u}, \phi$ as independent variables and our constitutive equations are in terms of $\boldsymbol{S}(\boldsymbol{u}), \boldsymbol{D}$.

Consider the weak formulations presented earlier. Prior to introducing our constitutive relations, the weak forms have $\boldsymbol{T}, \boldsymbol{u}$, and $\boldsymbol{D}$ as independent variables. For

closure of the equations we require constitutive relations, without them our system of equations is underdetermined. We can introduce $\boldsymbol{T} = \boldsymbol{T}(\boldsymbol{S}, \boldsymbol{D})$, but not $\boldsymbol{E} = \boldsymbol{E}(\boldsymbol{S}, \boldsymbol{D})$. To accomodate this second constitutive relation we introduce the electric potential definition

$$\boldsymbol{E} + \nabla\phi = \boldsymbol{0}.$$

This equation can be made suitable for finite element procedures by puting it in a weak form. This is accomplished by multiplying the electric potential equation by $\overline{\boldsymbol{D}}$ and integrating over the volume V[2],

$$\int_V (\boldsymbol{E} + \nabla\phi) \cdot \overline{\boldsymbol{D}}\, dV = 0.$$

4.5 Finite Element Formulation

This section starts from the mixed weak form of the small deformation electroelastic equations with electric conduction. A finite element formulation is presented that anticipates a Newton method solution of the resulting nonlinear discretized equations. The formulation can be implemented using four node, three dimensional, isoparametric finite elements presented in BATHE [2, pp. 375, 979-987] and a backward Euler finite difference (implicit) time integration[3]. Note that similar finite element formulations for perfect electrically insulating materials are presented in appendix B.

4.5.1 Mixed Weak Form

$$\int_V \boldsymbol{T} \cdot \overline{\boldsymbol{S}}\, dV + \int_V \rho_o \frac{\partial^2 \boldsymbol{u}}{\partial t^2} \cdot \overline{\boldsymbol{u}}\, dV - \int_V \boldsymbol{f}^B \cdot \overline{\boldsymbol{u}}\, dV - \int_{S_f} \boldsymbol{f}^{S_f} \cdot \overline{\boldsymbol{u}}^{S_f}\, dS_f = 0$$
$$\int_V (\frac{\partial \boldsymbol{D}}{\partial t} + \boldsymbol{J}) \cdot \overline{\boldsymbol{E}}\, dV + \oint_S J^{S_q} \overline{\phi}^{S_q}\, dS = 0$$
$$\int_V (\boldsymbol{E} + \nabla\phi) \cdot \overline{\boldsymbol{D}}\, dV = 0$$

4.5.2 Mixed Weak Form Rewritten

$$\int_V \overline{\boldsymbol{S}}' \boldsymbol{T}\, dV + \int_V \overline{\boldsymbol{u}}' \rho_o \frac{\partial^2 \boldsymbol{u}}{\partial t^2}\, dV - \int_V \overline{\boldsymbol{u}}' \boldsymbol{f}^B\, dV - \int_{S_f} \overline{\boldsymbol{u}}^{Sf\,\prime} \boldsymbol{f}^{S_f}\, dS_f = (0)$$
$$\int_V \overline{\boldsymbol{E}}' (\frac{\partial \boldsymbol{D}}{\partial t} + \boldsymbol{J})\, dV + \int_{S_q} \overline{\phi}^{S_q\,\prime} J^{S_q}\, dS_q$$
$$\int_V \overline{\boldsymbol{D}}' (\boldsymbol{E} + \nabla\phi)\, dV = 0$$

[2]This procedure is equivalent to a mixed variational equation derived by GHANDI [13]
[3]See BATHE [2, pp. 830-835]

4.5.3 Test Functions Defined

$$
\begin{aligned}
\overline{\boldsymbol{u}}(x_i,t) &= H_u(x_i)\hat{\overline{\boldsymbol{u}}}(t) \\
\overline{\boldsymbol{u}}^{S_f}(x_i,t) &= H_u^{S_f}(x_i)\hat{\overline{\boldsymbol{u}}}(t) \\
\overline{\boldsymbol{S}}(\overline{\boldsymbol{u}}(x_i,t)) &= B_u(x_i)\hat{\overline{\boldsymbol{u}}}(t) \\
\overline{\phi}(x_i,t) &= H_\phi(x_i)\hat{\overline{\phi}}(t) \\
\overline{\phi}^{S_q}(x_i,t) &= H_\phi^{S_q}(x_i)\hat{\overline{\phi}}(t) \\
\overline{\boldsymbol{E}}(\overline{\phi}(x_i,t)) &= -B_\phi(x_i)\hat{\overline{\phi}}(t) \\
\overline{\boldsymbol{D}}(x_i,t) &= H_D(x_i)\hat{\overline{\boldsymbol{D}}}(t)
\end{aligned}
$$

4.5.4 Introducing Test Functions

$$
\begin{aligned}
&\hat{\overline{\boldsymbol{u}}}'\left\{\int_V B_u{}'\boldsymbol{T}\,dV + \int_V H_u{}'\rho_o\frac{\partial^2\boldsymbol{u}}{\partial t^2}\,dV - \int_V H_u{}'\boldsymbol{f}^B\,dV - \int_{S_f} H_u^{S_f}{}'\boldsymbol{f}^{S_f}\,dS_f\right\} = 0 \\
&\hat{\overline{\phi}}'\left\{\int_V -B_\phi{}'(\frac{\partial\boldsymbol{D}}{\partial t} + \boldsymbol{J})\,dV + \int_{S_q} H_\phi^{S_q}{}'J^{S_q}\,dS_q\right\} = 0 \\
&\hat{\overline{\boldsymbol{D}}}'\left\{\int_V H_D{}'(\boldsymbol{E} + \boldsymbol{\nabla}\phi)\,dV\right\} = 0
\end{aligned}
$$

We require the weak form to hold for all $\hat{\overline{\boldsymbol{u}}}(t), \hat{\overline{\phi}}(t), \hat{\overline{\boldsymbol{D}}}(t)$. A necessary condition is that $\{\,\} = 0$,

$$
\begin{bmatrix} \int_V \rho_o H_u{}'\boldsymbol{u}_{,tt}\,dV \\ \boldsymbol{0} \\ \boldsymbol{0} \end{bmatrix} + \begin{bmatrix} \boldsymbol{0} \\ \int_V B_\phi{}'\boldsymbol{D}_{,t}\,dV \\ \boldsymbol{0} \end{bmatrix} + \begin{bmatrix} \int_V B_u{}'\boldsymbol{T}\,dV \\ \int_V B_\phi{}'\boldsymbol{J}\,dV \\ \int_V H_D{}'(\boldsymbol{E} + \boldsymbol{\nabla}\phi)\,dV \end{bmatrix}
- \begin{bmatrix} \int_V H_u{}'\boldsymbol{f}^B\,dV \\ \boldsymbol{0} \\ \boldsymbol{0} \end{bmatrix} - \begin{bmatrix} \int_{S_f} H_u^{S_f}{}'\boldsymbol{f}^{S_f}\,dS_f \\ \boldsymbol{0} \\ \boldsymbol{0} \end{bmatrix} - \begin{bmatrix} \boldsymbol{0} \\ \int_{S_q} H_\phi^{S_q}{}'J^{S_q}\,dS_q \\ \boldsymbol{0} \end{bmatrix} = \boldsymbol{0}
$$

or

$$
\boldsymbol{FI}^m + \boldsymbol{FI}^c + \boldsymbol{FI}^k - \boldsymbol{FE}^b - \boldsymbol{FE}^{S_f} - \boldsymbol{FE}^{S_q} = \boldsymbol{0}
$$

4.5.5 Shape Functions Defined

$$
\begin{aligned}
\boldsymbol{u}(x_i,t) &= H_u(x_i)\hat{\boldsymbol{u}}(t) \\
\boldsymbol{S}(\boldsymbol{u}(x_i,t)) &= B_u(x_i)\hat{\boldsymbol{u}}(t) \\
\phi(x_i,t) &= H_\phi(x_i)\hat{\phi}(t) \\
\boldsymbol{\nabla}\phi(\phi(x_i,t)) &= B_\phi(x_i)\hat{\phi}(t) \\
\boldsymbol{D}(x_i,t) &= H_D(x_i)\hat{\boldsymbol{D}}(t)
\end{aligned}
$$

The shape functions have been chosen identical to the corresponding test functions (Galerkin's method).

4.5.6 Introducing Constitutive and Shape Functions

$$
\begin{aligned}
\boldsymbol{T} &= \boldsymbol{T}(\boldsymbol{S}(\boldsymbol{\xi}), \boldsymbol{D}(\boldsymbol{\xi})) \\
\boldsymbol{E} &= \boldsymbol{E}(\boldsymbol{S}(\boldsymbol{\xi}), \boldsymbol{D}(\boldsymbol{\xi})) \\
\boldsymbol{J} &= \boldsymbol{J}(\boldsymbol{E})
\end{aligned}
$$

and using the chain rule

$$
\begin{aligned}
\frac{\partial \boldsymbol{T}}{\partial \boldsymbol{\xi}} &= \frac{\partial \boldsymbol{T}}{\partial \boldsymbol{S}}\frac{\partial \boldsymbol{S}}{\partial \boldsymbol{\xi}} + \frac{\partial \boldsymbol{T}}{\partial \boldsymbol{D}}\frac{\partial \boldsymbol{D}}{\partial \boldsymbol{\xi}} \\
&= \begin{bmatrix} C_{uu} \end{bmatrix}\begin{bmatrix} B_u & 0 & 0 \end{bmatrix} + \begin{bmatrix} C_{ud} \end{bmatrix}\begin{bmatrix} 0 & 0 & H_d \end{bmatrix} \\
\frac{\partial \boldsymbol{J}}{\partial \boldsymbol{\xi}} &= \frac{\partial \boldsymbol{J}}{\partial \boldsymbol{\nabla}\phi}\frac{\partial \boldsymbol{\nabla}\phi}{\partial \boldsymbol{\xi}} \\
&= \begin{bmatrix} C_{q\phi} \end{bmatrix}\begin{bmatrix} 0 & B_\phi & 0 \end{bmatrix} \\
\frac{\partial(\boldsymbol{E} + \boldsymbol{\nabla}\phi)}{\partial \boldsymbol{\xi}} &= \frac{\partial \boldsymbol{E}}{\partial \boldsymbol{S}}\frac{\partial \boldsymbol{S}}{\partial \boldsymbol{\xi}} + \frac{\partial \boldsymbol{E}}{\partial \boldsymbol{D}}\frac{\partial \boldsymbol{D}}{\partial \boldsymbol{\xi}} + \frac{\partial \boldsymbol{\nabla}\phi}{\partial \boldsymbol{\xi}} \\
&= \begin{bmatrix} C_{du} \end{bmatrix}\begin{bmatrix} B_u & 0 & 0 \end{bmatrix} + \begin{bmatrix} C_{dd} \end{bmatrix}\begin{bmatrix} 0 & 0 & H_d \end{bmatrix} + \begin{bmatrix} 0 & B_\phi & 0 \end{bmatrix}
\end{aligned}
$$

or

$$
\begin{aligned}
\frac{\partial \boldsymbol{T}}{\partial \boldsymbol{\xi}} &= \begin{bmatrix} C_{uu}B_u & 0 & C_{ud}H_d \end{bmatrix} \\
\frac{\partial \boldsymbol{J}}{\partial \boldsymbol{\xi}} &= \begin{bmatrix} 0 & C_{q\phi}B_\phi & 0 \end{bmatrix} \\
\frac{\partial(\boldsymbol{E} + \boldsymbol{\nabla}\phi)}{\partial \boldsymbol{\xi}} &= \begin{bmatrix} C_{du}B_u & B_\phi & C_{dd}H_d \end{bmatrix}
\end{aligned}
$$

4.5.7 Jacobian Matrices

$$
\begin{aligned}
\frac{\partial \boldsymbol{FI}^m}{\partial \ddot{\boldsymbol{\xi}}} &= \int_V \begin{bmatrix} \rho_o H_u{}' H_u & 0 & 0 \\ 0 & 0 & 0 \\ 0 & 0 & 0 \end{bmatrix} dV \\
&= \int_V \rho_o H_m{}' H_m \, dV = J^m \\
\frac{\partial \boldsymbol{FI}^c}{\partial \dot{\boldsymbol{\xi}}} &= \int_V \begin{bmatrix} 0 & 0 & 0 \\ 0 & 0 & B_\phi{}' H_d \\ 0 & 0 & 0 \end{bmatrix} dV
\end{aligned}
$$

$$
\begin{aligned}
&= \int_V H_{c1}{}' H_{c2}\, dV = J^c \\
\frac{\partial \boldsymbol{FI}^k}{\partial \boldsymbol{\xi}} &= \int_V \begin{bmatrix} B_u{}' C_{uu} B_u & 0 & B_u{}' C_{ud} H_d \\ 0 & B_\phi{}' C_{q\phi} B_\phi & 0 \\ H_d{}' C_{du} B_u & H_d{}' B_\phi & H_d{}' C_{dd} H_d \end{bmatrix} dV \\
&= \int_V \begin{bmatrix} B_u & 0 & 0 \\ 0 & B_\phi & 0 \\ 0 & 0 & H_d \end{bmatrix}' \begin{bmatrix} C_{uu} & 0 & C_{ud} \\ 0 & C_{q\phi} & 0 \\ C_{du} & I & C_{dd} \end{bmatrix} \begin{bmatrix} B_u & 0 & 0 \\ 0 & B_\phi & 0 \\ 0 & 0 & H_d \end{bmatrix} dV \\
&= \int_V B' C B\, dV \\
&= J^k
\end{aligned}
$$

4.5.8 Define Loading Interpolation Functions

$$
\begin{aligned}
\boldsymbol{f}^B(x_i, t) &= H_{bf}(x_i) \boldsymbol{B_f}(t) \\
\boldsymbol{f}^{S_f}(x_i, t) &= H_{sf}(x_i) \boldsymbol{S_f}(t) \\
J^{S_q}(x_i, t) &= H_{sq}(x_i) \boldsymbol{S_q}(t)
\end{aligned}
$$

4.5.9 Residual Vectors

$$
\begin{aligned}
\boldsymbol{FI}^m &= \int_V \rho_o H_m{}' H_m\, dV\, \ddot{\boldsymbol{\xi}} = J^m \ddot{\boldsymbol{\xi}} \\
\boldsymbol{FI}^c &= \int_V H_{c1}{}' H_{c2}\, dV\, \dot{\boldsymbol{\xi}} = J^c \dot{\boldsymbol{\xi}} \\
\boldsymbol{FI}^k &= \int_V B' \begin{bmatrix} \boldsymbol{T} \\ \boldsymbol{J} \\ (\boldsymbol{E} + \boldsymbol{\nabla}\phi) \end{bmatrix} dV \\
\boldsymbol{FE}^b &= \int_V \begin{bmatrix} H_u{}' \\ 0 \\ 0 \end{bmatrix} \boldsymbol{f}^B\, dV = \int_V H' \boldsymbol{f}^B\, dV \\
&= \int_V H' H_{bf}\, dV\, \boldsymbol{B_f} = FE_{bf} \boldsymbol{B_f} \\
\boldsymbol{FE}^{S_f} &= \int_{S_f} \begin{bmatrix} H_u^{S_f}{}' \\ 0 \\ 0 \end{bmatrix} \boldsymbol{f}^{S_f}\, dS_f = \int_{S_f} H_{su}{}' \boldsymbol{f}^{S_f}\, dS_f \\
&= \int_{S_f} H_{su}{}' H_{sf}\, dS_f\, \boldsymbol{S_f} = FE_{sf} \boldsymbol{S_f}
\end{aligned}
$$

$$
\begin{aligned}
\boldsymbol{FE}^{S_q} &= \int_{S_q} \begin{bmatrix} 0 \\ H_\phi^{S_q\,\prime} \\ 0 \end{bmatrix} J^{S_q}\, dS_q = \int_{S_q} H_{s\phi}{}' J^{S_q}\, dS_q \\
&= \int_{S_q} H_{s\phi}{}' H_{sq}\, dS_q\, \boldsymbol{S_q} = FE_{sq} \boldsymbol{S_q}
\end{aligned}
$$

Chapter 5

Results

5.1 Introduction

In this chapter we present some classical examples of electric conduction in rigid and static bodies to establish significance of the charge relaxation time constant for linear materials. Analysis results are then presented under a typical loading condition where electric conduction in a highly insulating electromechanical device will eventually dominate the device response. Specifically, we present results for electric voltage DC offset loading of an active fiber composite (AFC) device using a nonlinear material model for repolarizable piezoelectric ceramic. DC offset loading is common in applications to maximize the effective linear range of device operation.

5.2 Charge Relaxation and Time Scales

Example 5.2.1 (Rigid and Static Body) We consider a rigid $\epsilon_{ij} = 0$ and static $v_i = 0$ body. Then the governing equation is

$$\left(\dot{D}_i + J_i\right)_{,i} = 0. \tag{5.1}$$

Assuming a steady state response exists, then at steady state,

$$\frac{d}{dt} = 0 \rightarrow J_{i,i} = 0 \tag{5.2}$$

the response of the body is completely dominated by electrical conduction.

Example 5.2.2 (Rigid and Static Body, Uniform and Linear Material) We consider a rigid $\epsilon_{ij} = 0$ and static $v_i = 0$ body. Then the governing differential equations are

$$D_{i,i} = q^F \qquad J_{i,i} + \frac{\partial q^F}{\partial t} = 0. \tag{5.3}$$

Additionally, consider the body composed of a homogeneous and linear material,

$$\begin{aligned} J_i(x_i,t) &= \sigma E_i(x_i,t) \qquad \sigma \in \mathbf{R}_{>0} \\ D_i(x_i,t) &= \epsilon E_i(x_i,t) \qquad \epsilon \in \mathbf{R}_{>0}. \end{aligned} \tag{5.4}$$

Differentiating these constitutive relations,

$$J_{i,i} = \sigma E_{i,i} \qquad E_{i,i} = \frac{1}{\epsilon} D_{i,i} \qquad \rightarrow J_{i,i} = \frac{\sigma}{\epsilon} D_{i,i} \tag{5.5}$$

Using (5.5) and (5.3) gives a first order differential equation for free charge density $q^F(x_i,t)$

$$\frac{\partial q^F}{\partial t} + \left(\frac{\sigma}{\epsilon}\right) q^F = 0 \qquad q^F(x_i,0) = q_o^F(x_i)$$

This differential equation has solution,

$$q^F(x_i,t) = q_o^F(x_i)\, e^{-t/\tau} \qquad \tau = \frac{\epsilon}{\sigma} \tag{5.6}$$

Therefore charge relaxes exponentially with time constant $\tau = \epsilon/\sigma$.

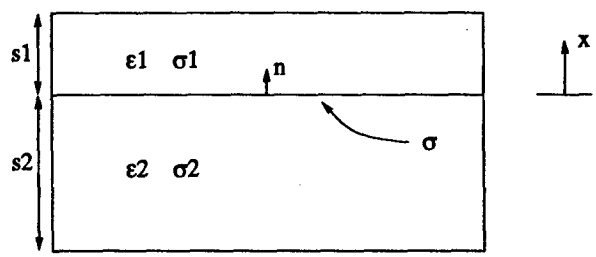

Figure 5-1: Two layer body geometry: Example 5.2.3.

Example 5.2.3 (Rigid and Static Body, Piecewise Uniform and Linear Material) We consider a rigid $\epsilon_{ij} = 0$ and static $v_i = 0$ body. Then the governing differential equations and jump conditions are

$$\begin{aligned} & & D_{i,i} = q^F & \qquad E_i + \phi_{,i} = 0 \\ [D_i]\, n_i = w^F & & [\dot{D}_i + J_i]\, n_i = 0 & \qquad [\phi] = 0. \end{aligned} \tag{5.7}$$

Consider the electric voltage boundary conditions,

$$\phi^1(s_1,t) = 0 \qquad \phi^2(-s_2,t) = V(t). \tag{5.8}$$

The body geometry and loading conditions are consistent with a one dimensional spatial fields approximation,

$$D_i(x_i,t) \rightarrow D(x,t)$$

$$
\begin{aligned}
E_i\left(x_i, t\right) &\rightarrow E\left(x, t\right) \\
\phi\left(x_i, t\right) &\rightarrow \phi\left(x, t\right)
\end{aligned}
\tag{5.9}
$$

The body is composed of two layers of uniform and linear material, distinguished by superscripts,

$$
\begin{aligned}
D^k\left(x, t\right) &= \epsilon^k E^k\left(x, t\right) \qquad & \epsilon^k \in \mathbb{R}_{>0} \\
J^k\left(x, t\right) &= \sigma^k E^k\left(x, t\right) \qquad & \sigma^k \in \mathbb{R}_{>0}
\end{aligned}
\tag{5.10}
$$

Consider the initial condition on free charge density $q^F\left(x, t\right) = 0$. Then, from example 5.2.2 we see that $q^F\left(x, t\right) = 0$ for all time $t \in \mathbb{R}_{>0}$. Then in each uniform region $k \in \{1, 2\}$ we have

$$
\frac{\partial D^k\left(x, t\right)}{\partial x} = 0. \tag{5.11}
$$

Therefore the fields D^k and E^k are spatially uniform

$$
D^k\left(x, t\right) \rightarrow D^k\left(t\right) \qquad E^k\left(x, t\right) \rightarrow E^k\left(t\right) \qquad J^k\left(x, t\right) \rightarrow J^k\left(t\right)
$$

Imposing the boundary conditions

$$
\phi^1\left(s_1, t\right) = 0 \qquad \phi^2\left(-s_2, t\right) = V\left(t\right) \tag{5.12}
$$

and integrating the electric field/potential equation through the thickness

$$
\begin{aligned}
\int_{-s_2}^{0} E^2(t)\, dx + \int_{0}^{s_1} E^1(t)\, dx &= -\int_{-s_2}^{0} \frac{\partial \phi^2(x,t)}{\partial x}\, dx - \int_{0}^{s_1} \frac{\partial \phi^1(x,t)}{\partial x}\, dx \\
&= -\phi^1(s_1, t) + \phi^2(-s_2, t) = V(t)
\end{aligned}
\tag{5.13}
$$

gives

$$
E^1(t)^1 + E^2(t) s_2 = V(t). \tag{5.14}
$$

Using the jump condition across σ_o,

$$
\dot{D}^1 + J^1 = \dot{D}^2 + J^2 \rightarrow \epsilon^1 \dot{E}^1 + \sigma^1 E^1 = \epsilon^2 \dot{E}^2 + \sigma^2 E^2 \tag{5.15}
$$

Using (5.14) in (5.15) yields the following differential equations for E^1 and E^2,

$$
\begin{aligned}
\left(\epsilon^2 s_1 + \epsilon^1 s_2\right) \dot{E}^1(t) + \left(\sigma^2 s_1 + \sigma^1 s_2\right) E^1(t) &= \frac{\epsilon^2}{s_2} \dot{V}(t) + \frac{\sigma^2}{s_2} V(t) \\
\left(\epsilon^2 s_1 + \epsilon^1 s_2\right) \dot{E}^2(t) + \left(\sigma^2 s_1 + \sigma^1 s_2\right) E^2(t) &= \frac{\epsilon^1}{s_1} \dot{V}(t) + \frac{\sigma^1}{s_1} V(t)
\end{aligned}
$$

Defining the following constants,

$$\tau = \frac{\epsilon^2 s_1 + \epsilon^1 s_2}{\sigma^2 s_1 + \sigma^1 s_2} \qquad \alpha^1 = \frac{\epsilon^2}{s_2\left(\epsilon^2 s_1 + \epsilon^1 s_2\right)} \qquad \beta^1 = \frac{\sigma^2}{s_2\left(\epsilon^2 s_1 + \epsilon^1 s_2\right)}$$

$$\alpha^2 = \frac{\epsilon^1}{s_1\left(\epsilon^2 s_1 + \epsilon^1 s_2\right)} \qquad \beta^2 = \frac{\sigma^1}{s_1\left(\epsilon^2 s_1 + \epsilon^1 s_2\right)}$$

we obtain

$$\dot{E}^1(t) + \frac{1}{\tau}E^1(t) = \alpha^1\dot{V}(t) + \beta^1 V(t)$$
$$\dot{E}^2(t) + \frac{1}{\tau}E^2(t) = \alpha^2\dot{V}(t) + \beta^2 V(t).$$

Consider response to a step input $V(t) = \hat{V}$. Then at time $t = 0^+$ we have $w^F = 0$. Using the jump condition across σ_o

$$[\,D_i\,]\,n_i = 0 \rightarrow \epsilon^1 E^1(0^+) = \epsilon^2 E^2(0^+) \tag{5.16}$$

and (5.14) gives initial conditions at $t = 0^+$,

$$E^1(0^+) = \frac{\epsilon^2\hat{V}}{\epsilon^2 s_1 + \epsilon^1 s_2} \qquad E^2(0^+) = \frac{\epsilon^1\hat{V}}{\epsilon^2 s_1 + \epsilon^1 s_2} \tag{5.17}$$

The step response of the two layer body is

$$E^1(t) = \frac{\sigma^2\hat{V}}{\sigma^2 s_1 + \sigma^1 s_2}\left(1 - e^{-t/\tau}\right) + \frac{\epsilon^2\hat{V}}{\epsilon^2 s_1 + \epsilon^1 s_2}e^{-t/\tau}$$
$$E^2(t) = \frac{\sigma^1\hat{V}}{\sigma^2 s_1 + \sigma^1 s_2}\left(1 - e^{-t/\tau}\right) + \frac{\epsilon^1\hat{V}}{\epsilon^2 s_1 + \epsilon^1 s_2}e^{-t/\tau} \tag{5.18}$$

For t/τ small the electrical response is that of a perfectly insulating material. For t/τ large the electrical response is dominated by electrical conduction. Most importantly, the electrical response of the body is not determined by the electrical conductivity alone, but rather the geometry weighted ratio of electrical conductivities to permittivities. It can be shown that the electrical time constant for the system is bounded by the time constants for the individual materials, $\tau^1 \leq \tau \leq \tau^2$ [1].

[1]Form the ratios τ/τ^1 and τ/τ^2

Remark 5.2.4 (Time Constants of Engineering Materials) *The effect of electric conduction on the electrical response for linear materials is determined not by electrical conductivity alone, but the ratio of permittivity to conductivity. It is useful to look at order of magnitude values for some common engineering materials* [2].

Table 5.1: Charge relaxation time constants.

Material	σ [*ohm-m*]$^{-1}$	ϵ/ϵ_o	τ [*sec*]
Copper	$5.7\ 10^{7}$	*1.0*	$1.6\ 10^{-19}$
Seawater	$4.0\ 10^{0}$	*80*	$1.8\ 10^{-10}$
Water	$4.0\ 10^{-6}$	*80*	$1.8\ 10^{-4}$
Epoxy, 23° *C*	$2.6\ 10^{-13}$	*4.4*	*150*
Epoxy, 100° *C*	$2.8\ 10^{-12}$	*4.4*	*14*
PZT-5H, 23° *C*	$3.4\ 10^{-12}$	*3400*	*8850*
PZT-5H, 100° *C*	$8.2\ 10^{-12}$	*3400*	*3670*
Corn oil	$4.0\ 10^{-11}$	*2.7*	*.60*
Glass	$1.0\ 10^{-12}$	*8.9*	*79*
Teflon	$1.0\ 10^{-16}$	*5.0*	$4.4\ 10^{5}$
Quartz	$1.0\ 10^{-17}$	*4.0*	$3.5\ 10^{6}$

5.3 Example: Active Fiber Composite

This section presents an analysis of electric voltage DC offset loading of a highly electrically insulating actuator/sensor device. The device is composed of a piezoelectric ceramic fiber embedded in an epoxy matrix, an active fiber composite or AFC device[3]. The analysis considers a nonlinear material model for repolarizable piezoelectric ceramic due to GHANDI [13] and described in the next section. Results demonstrate significant cumulative effects of weak electric conduction currents.

5.3.1 Material Model: Polarizable Piezoelectric

The section describes a nonlinear material model for polarizable piezoelectric ceramics developed by GHANDI [13]. Our first step is to derive constitutive equations with appropriate independent variables from the energy balance and entropy equations. This is accomplished using the balance of energy and entropy inequality equations to form the Clausius-Duhem (C-D) inequality.

$$\dot{U} = \tau^T_{ji}\dot{\epsilon}_{ij} + E_k\dot{D}_k + E_kJ_k + \rho_o h - q_{k,k}$$

[2]The material parameters are from HAUS & MELCHER [16, p. 222,251]. The values for epoxy and PZT-5H were measured using a bridge circuit, see appendix C

[3]See BENT [4, 5], RODGERS [22], and BENT, RODGERS, & HAGOOD [6]

$$\Theta\rho_o\dot{\eta} + q_{j,j} - \rho_o h - q_j\Theta^{-1}\Theta_{,j} \geq 0. \tag{5.19}$$

We form the C-D inequality by eliminating $q_{j,j} - \rho_o h$,

$$\Theta\rho_o\dot{\eta} - \dot{U} + \tau_{ji}^T\dot{\epsilon}_{ij} + E_k\dot{D}_k + E_kJ_k - q_j\Theta^{-1}\Theta_{,j} \geq 0. \tag{5.20}$$

Introduce the Legendre transform $G = U - \rho_o\Theta\eta - \tau_{ji}^T\epsilon_{ij}$, then

$$-\dot{U} = -\dot{G} - \rho_o\dot{\Theta}\eta - \rho_o\Theta\dot{\eta} - \dot{\tau}_{ji}^T\epsilon_{ij} - \tau_{ji}^T\dot{\epsilon}_{ij}. \tag{5.21}$$

The C-D inequality becomes

$$-\dot{G} - \rho_o\dot{\Theta}\eta - \dot{\tau}_{ji}^T\epsilon_{ij} + E_k\dot{D}_k + E_kJ_k - q_j\Theta^{-1}\Theta_{,j} \geq 0. \tag{5.22}$$

Introducing the isothermal approximation $\Theta(x_j, t) = \text{constant}$,

$$-\dot{G} - \dot{\tau}_{ji}^T\epsilon_{ij} + E_k\dot{D}_k + E_kJ_k \geq 0. \tag{5.23}$$

Next we define G as

$$\begin{aligned} G &= \hat{G}\left(\tau_{ji}^T, D_k\right) \\ -\dot{G} &= -\frac{\partial\hat{G}}{\partial D_k}\dot{D}_k - \frac{\partial\hat{G}}{\partial\tau_{ji}^T}\dot{\tau}_{ji}^T. \end{aligned} \tag{5.24}$$

Introducing into the C-D inequality,

$$\left(E_k - \frac{\partial\hat{G}}{\partial D_k}\right)\dot{D}_k - \left(\frac{\partial\hat{G}}{\partial\tau_{ji}^T}\right)\dot{\tau}_{ji}^T + E_kJ_k \geq 0. \tag{5.25}$$

This expression will hold for all independent processes $D_k(x_j, t)$ and $\tau_{ji}^T(x_k, t)$ if and only if,

$$E_k = \frac{\partial\hat{G}}{\partial D_k} \qquad \epsilon_{ij} = -\frac{\partial\hat{G}}{\partial\tau_{ji}^T} \qquad E_kJ_k \geq 0. \tag{5.26}$$

We write,

$$E_k = \hat{E}_k\left(\tau_{ji}^T, D_k\right) \qquad \epsilon_{ij} = \hat{\epsilon}_{ij}\left(\tau_{ji}^T, D_k\right) \qquad J_k = \sigma E_k \qquad \sigma \in \mathbf{R}_{\geq 0}, \tag{5.27}$$

where we have assumed for simplicity a linear and isotropic electrical conduction law that clearly satisfies the required inequality. The material response functions are then completely determined by the scalar function $G = \hat{G}\left(D_k, \tau_{ji}^T\right)$.

GHANDI introduces a memory vector[4] $D_i^*(D_k)$ that by definition does not evolve thermodynamically, such that $\dot{D}_i^* = 0$. This vector is defined to evolve according to

[4]The vector D_i^* is not to be confused, in this small deformation context, with the convective time derivative

an evolution rule, but thermodynamically $D^*(D_k)$ is a constant. Then G is defined by,

$$G = \hat{G}\left(\tau_{ji}^T, D_k, D_i^*(D_k)\right)\Big|_{D_i^*} \tag{5.28}$$

where it is indicated that thermodynamically, D_i^* is held constant. Then we have,

$$\begin{aligned}
E_k &= \hat{E}_k\left(\tau_{ji}^T, D_k, D_k^*(D_j)\right) = \frac{\partial}{\partial D_k}\left(\hat{G}\Big|_{D_i^*}\right) \\
\epsilon_{ij} &= \hat{\epsilon}_{ij}\left(\tau_{ji}^T, D_k, D_k^*(D_j)\right) = -\frac{\partial}{\partial \tau_{ji}^T}\left(\hat{G}\Big|_{D_i^*}\right) \\
J_k &= \sigma E_k \qquad \sigma \in \mathbb{R}_{\geq 0},
\end{aligned} \tag{5.29}$$

Symmetry of ϵ_{ij} and τ_{ji}^T permit introduction of Voight notation,

$$\begin{array}{ll}
(11) \to 1 & (32) = (23) \to 4 \\
(22) \to 2 & (31) = (13) \to 5 \\
(33) \to 3 & (12) = (21) \to 6 \\
\epsilon_{ij} \to S_k & \tau_{ji}^T \to T_k
\end{array}$$

where $k \in \{1, \cdots, 6\}$. Redefining $\hat{E}_k, \hat{S}_k$ consistent with $\hat{E}_k, \hat{\epsilon}_{ij}$ we finally obtain

$$\begin{aligned}
E_k &= \hat{E}_k\left(T_k, D_k, D_k^*(D_j)\right) \\
S_k &= \hat{S}_k\left(T_k, D_k, D_k^*(D_j)\right).
\end{aligned} \tag{5.30}$$

At this point we will drop the component notation and adopt vector notation. Then,

$$\begin{aligned}
\boldsymbol{E} &= \hat{\boldsymbol{E}}\left(\boldsymbol{T}, \boldsymbol{D}, \boldsymbol{D}^*(\boldsymbol{D})\right) \\
\boldsymbol{S} &= \hat{\boldsymbol{S}}\left(\boldsymbol{T}, \boldsymbol{D}, \boldsymbol{D}^*(\boldsymbol{D})\right) \\
&= \boldsymbol{S}^\alpha\left(\boldsymbol{D}, \boldsymbol{D}^*(\boldsymbol{D})\right) + \boldsymbol{S}^\beta\left(\boldsymbol{T}, \boldsymbol{D}, \boldsymbol{D}^*(\boldsymbol{D})\right) \\
&= \boldsymbol{S}^\alpha\left(\boldsymbol{D}, \boldsymbol{D}^*(\boldsymbol{D})\right) + \frac{\partial \boldsymbol{S}^\beta}{\partial \boldsymbol{T}}\left(\boldsymbol{D}, \boldsymbol{D}^*(\boldsymbol{D})\right)\boldsymbol{T} \\
\boldsymbol{J} &= \sigma \boldsymbol{E} \qquad \sigma \in \mathbb{R}_{\geq 0}
\end{aligned} \tag{5.31}$$

emphasizing the linear dependence of $\boldsymbol{S}^\beta$ on $\boldsymbol{T}$. Solving for $\boldsymbol{T}$,

$$\boldsymbol{T} = \hat{\boldsymbol{T}}\left(\boldsymbol{S}, \boldsymbol{D}, \boldsymbol{D}^*(\boldsymbol{D})\right) = \left[\frac{\partial \boldsymbol{S}^\beta}{\partial \boldsymbol{T}}\left(\boldsymbol{D}, \boldsymbol{D}^*(\boldsymbol{D})\right)\right]^{-1}\left(\boldsymbol{S} - \boldsymbol{S}^\alpha\left(\boldsymbol{D}, \boldsymbol{D}^*(\boldsymbol{D})\right)\right) \tag{5.32}$$

The following matrices will be required in the finite element implementation,

$$C_{uu} = \frac{\partial \boldsymbol{T}}{\partial \boldsymbol{S}}\Big|_{\boldsymbol{D}} \qquad C_{ud} = \frac{\partial \boldsymbol{T}}{\partial \boldsymbol{D}}\Big|_{\boldsymbol{S}} \qquad C_{q\phi} = \frac{\partial \boldsymbol{J}}{\partial \boldsymbol{\nabla}\phi} = -\frac{\partial \boldsymbol{J}}{\partial \boldsymbol{E}}$$

$$C_{du} = \left.\frac{\partial \boldsymbol{E}}{\partial \boldsymbol{S}}\right|_{\boldsymbol{D}} \qquad C_{dd} = \left.\frac{\partial \boldsymbol{E}}{\partial \boldsymbol{D}}\right|_{\boldsymbol{S}} \tag{5.33}$$

Remark 5.3.1 (Material Model: Jacobian Matrices)

$$\begin{aligned}
C_{uu} &= \left[\frac{\partial \boldsymbol{S}^{\beta}}{\partial \boldsymbol{T}}\right]^{-1} \\
C_{ud} &= -C_{uu}\left.\frac{\partial \hat{\boldsymbol{S}}}{\partial \boldsymbol{D}}\right|_{\boldsymbol{T}} \\
C_{du} &= \left.\frac{\partial \hat{\boldsymbol{E}}}{\partial \boldsymbol{T}}\right|_{\boldsymbol{D}} C_{uu} \\
C_{dd} &= \left.\frac{\partial \hat{\boldsymbol{E}}}{\partial \boldsymbol{T}}\right|_{\boldsymbol{D}} C_{ud} + \left.\frac{\partial \hat{\boldsymbol{E}}}{\partial \boldsymbol{D}}\right|_{\boldsymbol{T}} \\
C_{q\phi} &= -\sigma \boldsymbol{I}
\end{aligned} \tag{5.34}$$

where,

$$\begin{aligned}
\left.\frac{\partial \hat{\boldsymbol{S}}}{\partial \boldsymbol{D}}\right|_{\boldsymbol{T}} &= \left.\frac{\partial \hat{\boldsymbol{S}}}{\partial \boldsymbol{D}}\right|_{\boldsymbol{T},\boldsymbol{D}^*} + \left.\frac{\partial \hat{\boldsymbol{S}}}{\partial \boldsymbol{D}^*}\right|_{\boldsymbol{T},\boldsymbol{D}} \frac{\partial \boldsymbol{D}^*}{\partial \boldsymbol{D}} \\
\left.\frac{\partial \hat{\boldsymbol{E}}}{\partial \boldsymbol{D}}\right|_{\boldsymbol{T}} &= \left.\frac{\partial \hat{\boldsymbol{E}}}{\partial \boldsymbol{D}}\right|_{\boldsymbol{T},\boldsymbol{D}^*} + \left.\frac{\partial \hat{\boldsymbol{E}}}{\partial \boldsymbol{D}^*}\right|_{\boldsymbol{T},\boldsymbol{D}} \frac{\partial \boldsymbol{D}^*}{\partial \boldsymbol{D}}
\end{aligned} \tag{5.35}$$

Proof. Calculation of C_{uu}, C_{du}, and $C_{q\phi}$ are immediate. Consider C_{ud},

$$\begin{aligned}
&\frac{\partial}{\partial \boldsymbol{D}}\left[\left(\boldsymbol{S} = \boldsymbol{S}^{\alpha}(\boldsymbol{D},\boldsymbol{D}^*(\boldsymbol{D})) + \frac{\partial \boldsymbol{S}^{\beta}}{\partial \boldsymbol{T}}(\boldsymbol{D},\boldsymbol{D}^*(\boldsymbol{D}))\boldsymbol{T}\right)\right|_{\boldsymbol{S}}\right] \\
\rightarrow\ & 0 = \frac{\partial \boldsymbol{S}^{\alpha}}{\partial \boldsymbol{D}}(\boldsymbol{D},\boldsymbol{D}^*(\boldsymbol{D})) + \frac{\partial}{\partial \boldsymbol{D}}\left(\frac{\partial \boldsymbol{S}^{\beta}}{\partial \boldsymbol{T}}(\boldsymbol{D},\boldsymbol{D}^*(\boldsymbol{D}))\right)\boldsymbol{T} \\
\rightarrow\ & 0 = \left.\frac{\partial \hat{\boldsymbol{S}}}{\partial \boldsymbol{D}}\right|_{\boldsymbol{T}} + \frac{\partial \boldsymbol{S}^{\beta}}{\partial \boldsymbol{T}}\left.\frac{\partial \boldsymbol{T}}{\partial \boldsymbol{D}}\right|_{\boldsymbol{S}} \\
\rightarrow\ & \left.\frac{\partial \boldsymbol{T}}{\partial \boldsymbol{D}}\right|_{\boldsymbol{S}} = -C_{uu}\left.\frac{\partial \hat{\boldsymbol{S}}}{\partial \boldsymbol{D}}\right|_{\boldsymbol{T}},
\end{aligned} \tag{5.36}$$

proves the C_{ud} relation. Next consider C_{dd},

$$\begin{aligned}
\left.\frac{\partial \hat{\boldsymbol{E}}}{\partial \boldsymbol{D}}\right|_{\boldsymbol{S}} &= \left.\frac{\partial \hat{\boldsymbol{E}}}{\partial \boldsymbol{T}}\right|_{\boldsymbol{D}}\left.\frac{\partial \boldsymbol{T}}{\partial \boldsymbol{D}}\right|_{\boldsymbol{S}} + \left.\frac{\partial \hat{\boldsymbol{E}}}{\partial \boldsymbol{D}}\right|_{\boldsymbol{T}} \\
&= \left.\frac{\partial \hat{\boldsymbol{E}}}{\partial \boldsymbol{T}}\right|_{\boldsymbol{D}} C_{ud} + \left.\frac{\partial \hat{\boldsymbol{E}}}{\partial \boldsymbol{D}}\right|_{\boldsymbol{T}},
\end{aligned} \tag{5.37}$$

proves the C_{dd} relation. ■

Definition 5.3.2 (Material Model: Memory Variable Evolution Rule)

$$
\begin{aligned}
\overline{\boldsymbol{\Delta}} &= {}^{t+\Delta t}\boldsymbol{D} - {}^{t}\boldsymbol{D}^{*} \\
\left\|\overline{\boldsymbol{\Delta}}\right\| &= \left(\sum_{k=1}^{3} \overline{\Delta}_k^2\right)^{\frac{1}{2}}
\end{aligned}
$$

if $\left\|\overline{\boldsymbol{\Delta}}\right\| < \Delta_{cr}$ *then*

$$
\begin{aligned}
{}^{t+\Delta t}\boldsymbol{D}^{*} &= {}^{t}\boldsymbol{D}^{*} \\
\frac{\partial({}^{t+\Delta t}D_i^{*})}{\partial D_j} &= 0
\end{aligned}
$$

if $\left\|\overline{\boldsymbol{\Delta}}\right\| \geq \Delta_{cr}$ *then*

$$
\begin{aligned}
{}^{t+\Delta t}\boldsymbol{D}^{*} &= {}^{t}\boldsymbol{D}^{*} + \overline{\boldsymbol{\Delta}}\left(1 - \Delta_{cr}\left\|\overline{\boldsymbol{\Delta}}\right\|^{-1}\right) \\
\frac{\partial({}^{t+\Delta t}D_i^{*})}{\partial D_j} &= \delta_{ij}\left(1 - \Delta_{cr}\left\|\overline{\boldsymbol{\Delta}}\right\|^{-1}\right) + \Delta_{cr}\overline{\Delta}_i\overline{\Delta}_j\left\|\overline{\boldsymbol{\Delta}}\right\|^{-3}
\end{aligned}
$$

Definition 5.3.3 (Material Model: Response Function)

$$
\begin{aligned}
G &= \hat{G}\left(\tau_{ji}^{T}, D_k, D_i^{*}(D_k)\right)\Big|_{D_i^{*}} \\
\hat{G} &= \sum_{k=1}^{27} \alpha_k G_k\left(\boldsymbol{T}, \boldsymbol{D}, \boldsymbol{D}^{*}(\boldsymbol{D})\right) \\
E_k &= \hat{E}_k\left(\tau_{ji}^{T}, D_k, D_k^{*}(D_j)\right) = \frac{\partial}{\partial D_k}\left(\hat{G}\Big|_{D_i^{*}}\right) \\
\epsilon_{ij} &= \hat{\epsilon}_{ij}\left(\tau_{ji}^{T}, D_k, D_k^{*}(D_j)\right) = -\frac{\partial}{\partial \tau_{ji}^{T}}\left(\hat{G}\Big|_{D_i^{*}}\right)
\end{aligned}
\tag{5.38}
$$

The α_k are real constants and the G_k are polynomial functions of the following set of tensor invariants of the set $\{\tau_{ji}^{T}, D_i, D_i^{*}\}$ and for convenience we write $a_i = D_i^{*}$.

$$
\begin{aligned}
I_1 &= a_i a_i \\
I_2 &= a_i D_i \\
I_3 &= D_i D_i \\
J_0 &= \tau_{ii}^{T} \\
J_1 &= \tau_{ij}^{T} a_i a_j \\
J_2 &= \tau_{ij}^{T}\left(a_i D_j + a_j D_i\right) \\
J_3 &= \tau_{ij}^{T} D_i D_j \\
K_0 &= \tau_{ij}^{T}\tau_{ji}^{T} \\
K_1 &= \tau_{ik}^{T}\tau_{kj}^{T} a_i a_j \\
K_2 &= \tau_{ik}^{T}\tau_{kj}^{T}\left(a_i D_j + a_j D_i\right) \\
K_3 &= \tau_{ik}^{T}\tau_{kj}^{T} D_i D_j
\end{aligned}
$$

The following coefficients produce stresses τ_{ji}^{T} in $[Pa] * 10^6$ and electric displacements D_k, D_k^* in $[C/m^2]$.

$$
\begin{aligned}
\overline{\Delta} &= 0.02 \\
G_1 &= I_2 & \alpha_1 &= -2.781 * 10^7 \\
G_2 &= I_3 & \alpha_2 &= 1.410 * 10^7 \\
G_3 &= I_3 I_3 & \alpha_3 &= 4.918 * 10^6 \\
G_4 &= J_0 I_1 & \alpha_4 &= 1.540 * 10^5 \\
G_5 &= J_0 I_2 & \alpha_5 &= -3.220 * 10^5 \\
G_6 &= J_0 I_3 & \alpha_6 &= 1.824 * 10^5 \\
G_7 &= J_0 I_3 I_3 & \alpha_7 &= -3.299 * 10^3 \\
G_8 &= J_1 & \alpha_8 &= -3.048 * 10^5 \\
G_9 &= J_1 I_2 & \alpha_9 &= 7.927 * 10^5 \\
G_{10} &= J_2 & \alpha_{10} &= 3.286 * 10^5 \\
G_{11} &= J_3 & \alpha_{11} &= -3.990 * 10^5 \\
G_{12} &= J_3 I_2 & \alpha_{12} &= -2.221 * 10^6 \\
G_{13} &= J_3 I_3 & \alpha_{13} &= 1.477 * 10^6 \\
G_{14} &= J_0 J_0 & \alpha_{14} &= 9.135 * 10^0 \\
G_{15} &= J_0 J_0 I_1 & \alpha_{15} &= 1.691 * 10^3 \\
G_{16} &= J_0 J_0 I_2 & \alpha_{16} &= -3.088 * 10^3 \\
G_{17} &= J_0 J_0 I_3 & \alpha_{17} &= 1.349 * 10^3 \\
G_{18} &= J_0 J_1 & \alpha_{18} &= -5.336 * 10^3 \\
G_{19} &= J_0 J_2 & \alpha_{19} &= 4.965 * 10^3 \\
G_{20} &= J_0 J_3 & \alpha_{20} &= -4.676 * 10^3 \\
G_{21} &= K_0 & \alpha_{21} &= -3.157 * 10^1 \\
G_{22} &= K_0 I_1 & \alpha_{22} &= 1.235 * 10^3 \\
G_{23} &= K_0 I_2 & \alpha_{23} &= -3.316 * 10^3 \\
G_{24} &= K_0 I_3 & \alpha_{24} &= 2.270 * 10^3 \\
G_{25} &= K_1 & \alpha_{25} &= -5.070 * 10^2 \\
G_{26} &= K_2 & \alpha_{26} &= 1.490 * 10^3 \\
G_{27} &= K_3 & \alpha_{27} &= -2.510 * 10^3
\end{aligned}
\tag{5.39}
$$

5.3.2 Analysis Results

In this section we present analysis results demonstrating the transient response of a highly electrically insulating active fiber composite (AFC) device under an electric voltage DC offset loading. Figures 5-4 - 5-10 demonstrate electrical charging response

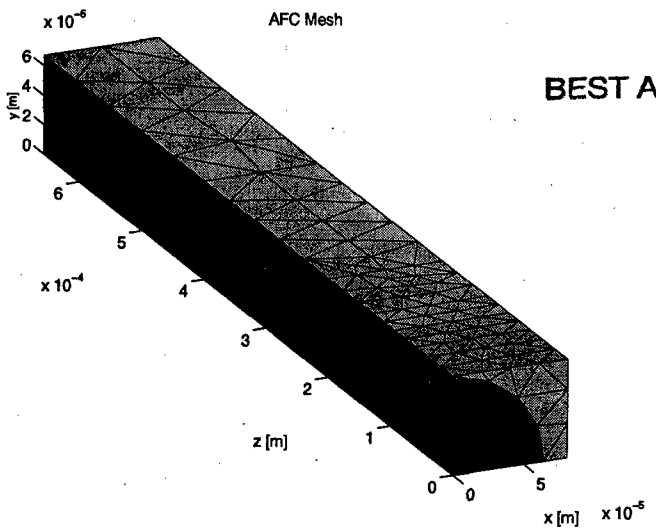

BEST AVAILABLE COPY

Figure 5-2: Active fiber composite: finite element mesh.

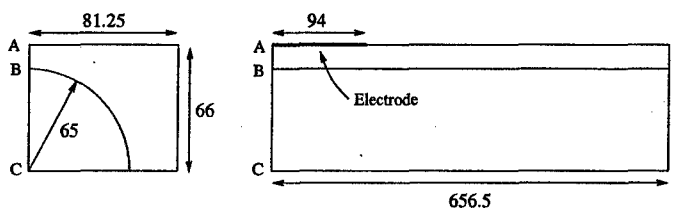

Figure 5-3: Active fiber composite dimensions, in $[m] * 10^{-6}$.

of the AFC device under an electric voltage DC offset loading. This loading condition is used frequently in applications to maximize the linear range of operation. Consider the following loading and boundary conditions.

Definition 5.3.4 (Loading and Boundary Conditions) *The components u_1, u_2, u_3 correspond to mechanical displacement u_i along the coordinate axes x, y, z, respectively. Dimensions for x, y, z are specified in $[m]*10^{-6}$. Boundary conditions imposed are*[5],

$$
\begin{aligned}
x = 0 \;&:\; u_1 = 0 \\
y = 0 \;&:\; u_2 = 0 \\
z = 0 \;&:\; u_3 = 0 \\
z = 656.5 \;&:\; \phi = 0 \\
y = 66,\; 0 \le z \le 94 \;&:\; \phi = \phi^+(t) = \begin{cases} 1050\ [V] & 0^+ \le t \le 1200\ [s] \\ 0\ [V] & 1200 < t \le 1500\ [s] \end{cases}
\end{aligned}
$$

All surfaces not specified have $\left(t_j + t_j^E\right)^+ = 0$ and $\left(\dot{D}_i + J_i\right)^+ = 0$. No mechanical

[5] *These boundary conditions are not symmetry conditions for an AFC device. Symmetry conditions were not enforced due to numerical difficulties.*

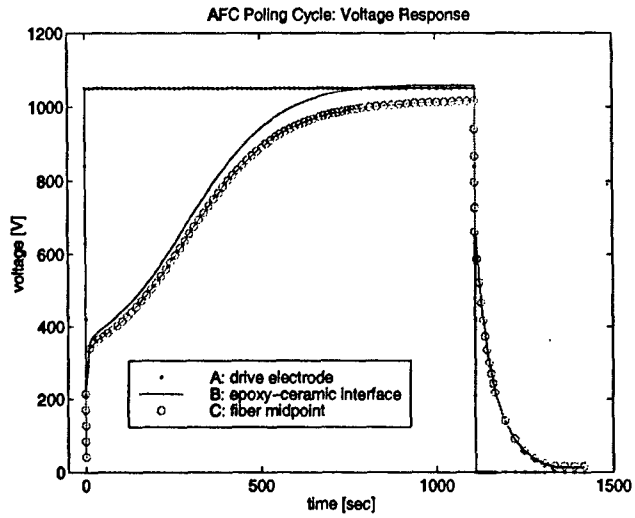

Figure 5-4: Voltage response through thickness.

body forces or inertial terms are included in the analysis. Isothermal conditions are assumed. Electrical conduction values for epoxy and PZT-5H at $100°C$ *from table 5.1 are used. See appendix D for epoxy material model.*

These results demonstrate that electric and stress fields vary considerably over time as a result of weak electric current flow within the material. The results demonstrate a transition between capacitance dominated response during the initial seconds of voltage loading, to an electric conduction dominated response. Over the order of minutes the electric field levels change by a factor of four due to the cumulative effect of weak electric current flow.

The figures demonstrate three interesting points. Weak electric current flow in the highly insulating materials is not negligible, as made clear by the transient response of the device[6]. After the electric field is unloaded to zero, non-zero mechanical displacements, strains, and stresses remain. This is a result of the nonlinear polarization model for the piezoelectric ceramic. Another important feature is the difference in time scales between the initial loading and unloading of electric voltage. Inspection of the figures indicate a charging transient of 1000 seconds for the initial voltage loading. However, the charging transient for voltage unloading is 400 seconds. During the initial voltage loading, the piezoelectric ceramic is repoling, and the effective permittivity is much large than during the voltage unloading. The result of a larger permittivity is a longer effective (linear response) time constant for charge relaxation. This example has demonstrated that a highly electrically insulating body can be dominated by electric conduction under slow time electrical loadings.

[6]A perfectly insulating device would maintain the response at time 0^+ under a constant electric voltage DC offset (not including mechanical inertia effects)

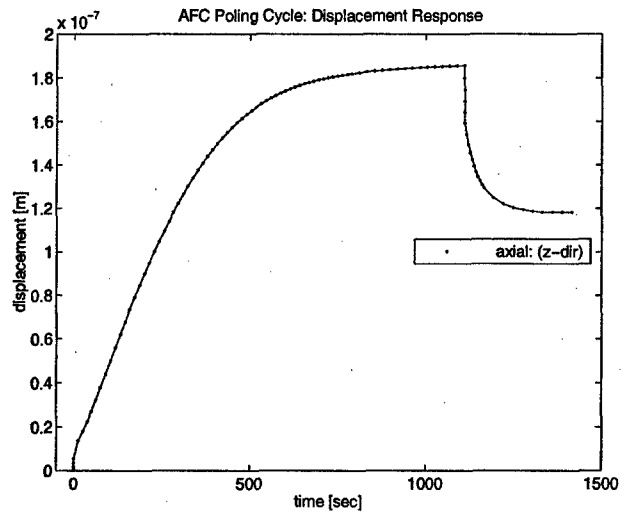

Figure 5-5: Axial end face displacement.

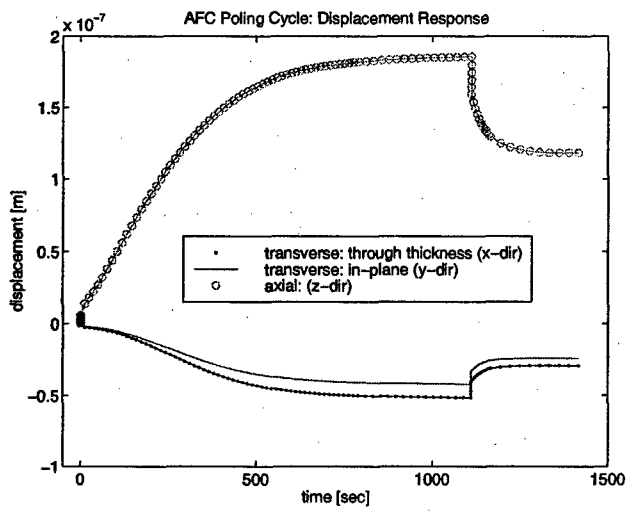

Figure 5-6: Transverse centerline displacements.

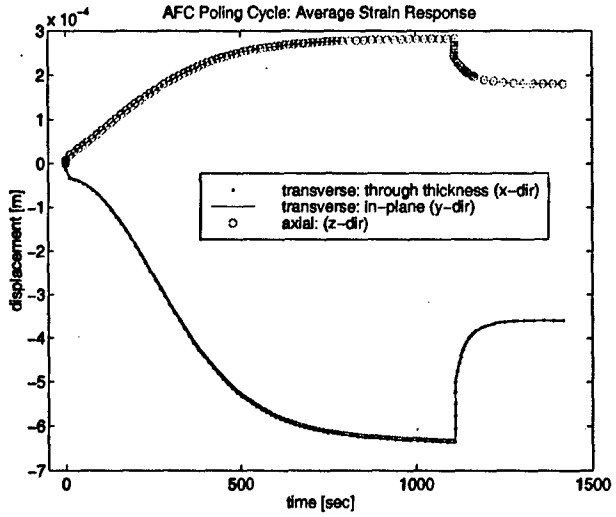

Figure 5-7: Average axial and transverse strains.

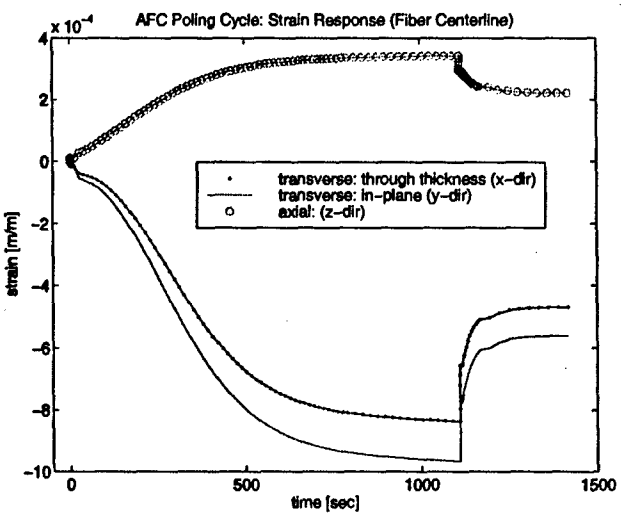

Figure 5-8: Fiber centerline strains.

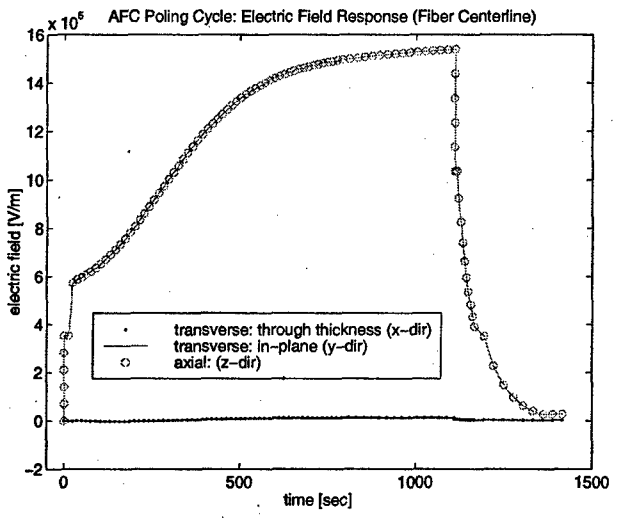

Figure 5-9: Fiber centerline electric field response.

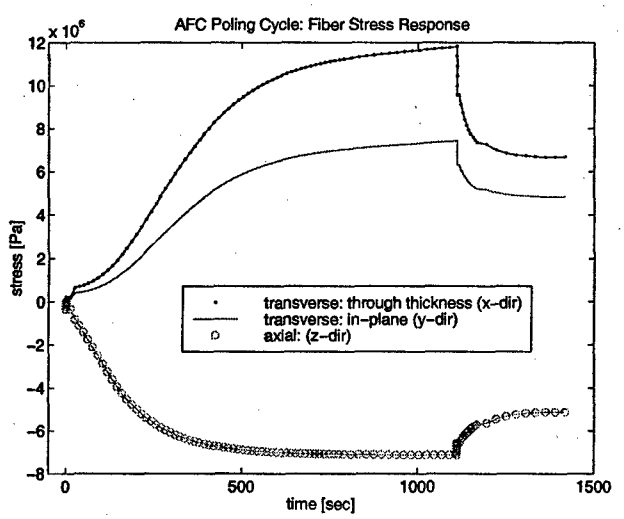

Figure 5-10: Fiber centerline stress response.

Chapter 6

Conclusions

This thesis has reported on the mathematical abstraction of deformable electromechanical actuator and sensor devices composed of highly electrically insulating materials. The presentation included detailed proofs of the nonlinear large deformation theory of electroelastic continua with electric conduction.

Consistency was proven between the large deformation theory and the classical Poynting vector based piezoelectric small deformation theory, extended for electric conduction. A result was that electric body forces, realized mathematically as electric surface tractions, are retained in the small deformation approximation.

A finite element formulation, suitable as an engineering analysis tool, was developed for deformable electromechanical actuator and sensor devices composed of highly insulating materials with nonlinear response functions (e.g., repolarizable piezoelectric ceramic material). The finite element formulation was demonstrated by analyzing the loading response of a highly electrically insulating active fiber composite device. Results demonstrated significant cumulative effects of a weak electric current flow under electric voltage DC offset loading.

Appendix A

Integral Theorems

Theorem A.0.5 (Green-Gauss) *A field $\boldsymbol{A}$ defined over a material volume V in $\mathcal{B}$ and bounded by surface S, satisfies the integral statement,*

$$\int_V \boldsymbol{\nabla} \cdot \boldsymbol{A}\, dV = \oint_S \boldsymbol{A} \cdot \boldsymbol{n}\, dS \tag{A.1}$$

See ERINGEN [10, p. 427].

Theorem A.0.6 (Stokes) *A field $\boldsymbol{A}$ defined over an open material surface S in $\mathcal{B}$ and bounded by the line C, satisfies the integral statement,*

$$\int_S (\boldsymbol{\nabla} \times \boldsymbol{A}) \cdot \boldsymbol{n}\, dS = \oint_l \boldsymbol{A} \cdot d\boldsymbol{l} \tag{A.2}$$

See ERINGEN [10, p. 427].

Appendix B

Finite Element Formulations

B.1 Weak Forms: No Electric Conduction

The equations and finite element formulations presented in this appendix are consistent with notation presented in chapter 4. The equations presented are for small deformation electroelastic continua with no electric conduction.

Theorem B.1.1 (EQS Maxwell w/o Electric Conduction: Weak Form I) *A material volume V bounded by surface $S = S_q + S_\phi$ is subject to surface electric charge density loading q^{S_q} on S_q and electric voltage constraints ϕ^{S_ϕ} on S_ϕ. The electric displacement fields $\boldsymbol{D}$ are assumed negligible outside the material volume V. The EQS Maxwell equation and corresponding jump conditions across S are*

$$\nabla \cdot \boldsymbol{D} = q^F \qquad \boldsymbol{D} \cdot \boldsymbol{n} = -q^{S_q} \text{ on } S_q \qquad \phi = \phi^{S_\phi} \text{ on } S_\phi$$

Consider a weighting function $\overline{\phi}$ and vector $\overline{\boldsymbol{E}}$, defined over the material volume V, such that

$$\overline{\phi} = 0 \text{ on } S_\phi \qquad \overline{\boldsymbol{E}} = -\nabla \phi$$

Then the EQS Maxwell equation and jump conditions have the equivalent weak form,

$$\int_V \boldsymbol{D} \cdot \overline{\boldsymbol{E}}\, dV = \int_V q^F \overline{\phi}\, dV + \int_{S_q} q^{S_q} \overline{\phi}\, dS_q$$

Proof. Multiply the EQS Maxwell equation through by $\overline{\phi}$ and integrate over V,

$$\int_V \nabla \cdot \boldsymbol{D} \overline{\phi}\, dV = \int_V q^F \overline{\phi}\, dV .$$

Use the chain rule to eliminate derivatives from $\nabla \cdot \boldsymbol{D}$,

$$\nabla \cdot \left(\boldsymbol{D}\overline{\phi}\right) = \nabla \cdot \boldsymbol{D}\overline{\phi} + \boldsymbol{D} \cdot \nabla \overline{\phi}$$

Use the identity

$$\int_V \nabla \cdot \left(\boldsymbol{D}\overline{\phi}\right) dV = \oint_S \left(\boldsymbol{D}\overline{\phi}\right) \cdot \boldsymbol{n}\, dS$$

to obtain

$$\oint_S \boldsymbol{D}\overline{\phi} \cdot \boldsymbol{n}\, dS + \int_V \boldsymbol{D} \cdot \overline{\boldsymbol{E}}\, dV = \int_V q^F \overline{\phi}\, dV$$

Use the jump condition and constraint,

$$\boldsymbol{D} \cdot \boldsymbol{n} = -q^{S_q} \text{ on } S_q \qquad \overline{\phi} = 0 \text{ on } S_\phi$$

to obtain

$$\int_V \boldsymbol{D} \cdot \overline{\boldsymbol{E}}\, dV = \int_V q^F \overline{\phi}\, dV + \int_{S_q} q^{S_q} \overline{\phi}\, dS_q$$

■

For convenience we repeat the weak form theorem for balance of momentum from chapter 4.

Theorem B.1.2 (Balance of Momentum: Weak Form) *A material volume V bounded by surface $S = S_f + S_u$ is subject to mechanical surface tractions $f_i^{S_f}$ on S_f, mechanical displacement constraints $u_i^{S_u}$ on S_u, and body force density f_i^B in V. The electric stress tractions t_i^E outside the material volume V are assumed negligible, consistent with an assumption of zero electric fields E_i outside V. The balance of momentum equations and corresponding jump conditions across S are*

$$\tau^T_{ji,j} + f_i^B = \rho_o \frac{\partial^2 u_i}{\partial t^2} \qquad \tau^T_{[ji]} = 0$$
$$\tau^T_{ji} n_j = f_i^{S_f} \text{ on } S_f \qquad u_i = u_i^{S_u} \text{ on } S_u.$$

Consider a weighting function $\overline{u}_i$ and tensor $\overline{\epsilon}_{ij}$, defined over the material volume V, such that

$$\overline{u}_i = 0 \text{ on } S_u \qquad \overline{\epsilon}_{ij} = \frac{1}{2}\left(\overline{u}_{i,j} + \overline{u}_{j,i}\right).$$

Then the balance of momentum equations and jump conditions have the weak form,

$$\begin{aligned} \int_V \tau^T_{ji} \overline{\epsilon}_{ij}\, dV + \int_V \rho_o \frac{\partial^2 u_i}{\partial t^2} \overline{u}_i\, dV &= \int_V f_i^B \overline{u}_i\, dV + \int_{S_f} f_i^{S_f} \overline{u}_i\, dS_f, \\ u_i &= u_i^{S_u} \text{ on } S_u \end{aligned}$$

B.2 Finite Element Formulation I

This section presents a finite element formulation of perfectly electrically insulating electroelastic materials under the small deformation approximation. The formulation is suitable for nonlinear material response functions and anticipates a Newton method solution technique. The formulation is suitable for constitutive equations with strain $\boldsymbol{S}$ and electric field $\boldsymbol{E}$ as independent variables.

B.2.1 Weak Form

$$\int_V \tau_{ji}^T \overline{\epsilon}_{ij}\, dV + \int_V \rho_o \frac{\partial^2 u_i}{\partial t^2} \overline{u}_i\, dV = \int_V f_i^B \overline{u}_i\, dV + \oint_{S_f} f_i^{S_f} \overline{u}_i^{S_f}\, dS_f$$
$$\int_V D_i \overline{E}_i\, dV = \int_V q^B \overline{\phi}\, dV + \int_{S_q} q^{S_q} \overline{\phi}\, dS_q$$

Noting the symmetric of τ_{ji}^T and ϵ_{ij}, we introduce Voight notation

$$\begin{aligned} \boldsymbol{T} &= \begin{bmatrix} \tau_{11}^T & \tau_{22}^T & \tau_{33}^T & \tau_{32}^T & \tau_{13}^T & \tau_{12}^T \end{bmatrix}' \\ \boldsymbol{S} &= \begin{bmatrix} \epsilon_{11} & \epsilon_{22} & \epsilon_{33} & 2\epsilon_{32} & 2\epsilon_{13} & 2\epsilon_{12} \end{bmatrix}' \end{aligned}$$

we obtain

$$\begin{aligned} \int_V \boldsymbol{T} \cdot \overline{\boldsymbol{S}}\, dV + \int_V \rho_o \frac{\partial^2 \boldsymbol{u}}{\partial t^2} \cdot \overline{\boldsymbol{u}}\, dV &= \int_V \boldsymbol{f}^B \cdot \overline{\boldsymbol{u}}\, dV + \int_{S_f} \boldsymbol{f}^{S_f} \cdot \overline{\boldsymbol{u}}^{Sf}\, dS_f \\ \int_V \boldsymbol{D} \cdot \overline{\boldsymbol{E}}\, dV &= \int_V q^B \overline{\phi}\, dV + \int_{S_q} q^{S_q} \overline{\phi}\, dS_q \end{aligned}$$

B.2.2 Weak Form Rewritten

$$\begin{aligned} \int_V \overline{\boldsymbol{S}}' \boldsymbol{T}\, dV + \int_V \overline{\boldsymbol{u}}' \rho_o \frac{\partial^2 \boldsymbol{u}}{\partial t^2}\, dV &= \int_V \overline{\boldsymbol{u}}' \boldsymbol{f}^B\, dV + \int_{S_f} \overline{\boldsymbol{u}}^{Sf\,\prime} \boldsymbol{f}^{S_f}\, dS_f \\ \int_V \overline{\boldsymbol{E}}' \boldsymbol{D}\, dV &= \int_V \overline{\phi}' q^B\, dV + \int_{S_q} \overline{\phi}' q^{S_q}\, dS_q \end{aligned}$$

B.2.3 Test Functions Defined

$$\begin{aligned} \overline{\boldsymbol{u}}(x_i, t) &= H_u(x_i) \hat{\overline{\boldsymbol{u}}}(t) \\ \overline{\boldsymbol{u}}^{S_f}(x_i, t) &= H_u^{S_f}(x_i) \hat{\overline{\boldsymbol{u}}}(t) \\ \overline{\boldsymbol{S}}(\overline{\boldsymbol{u}}(x_i, t)) &= B_u(x_i) \hat{\overline{\boldsymbol{u}}}(t) \\ \overline{\phi}(x_i, t) &= H_\phi(x_i) \hat{\overline{\phi}}(t) \\ \overline{\phi}^{S_q}(x_i, t) &= H_\phi^{S_q}(x_i) \hat{\overline{\phi}}(t) \\ \overline{\boldsymbol{E}}(\overline{\phi}(x_i, t)) &= B_\phi(x_i) \hat{\overline{\phi}}(t) \end{aligned}$$

B.2.4 Shape Functions Defined

$$
\begin{aligned}
\boldsymbol{u}(x_i,t) &= H_u(x_i)\hat{\boldsymbol{u}}(t) \\
\boldsymbol{u}^{S_f}(x_i,t) &= H_u^{S_f}(x_i)\hat{\boldsymbol{u}}(t) \\
\boldsymbol{S}(\overline{\boldsymbol{u}}(x_i,t)) &= B_u(x_i)\hat{\boldsymbol{u}}(t) \\
\phi(x_i,t) &= H_\phi(x_i)\hat{\phi}(t) \\
\phi^{S_q}(x_i,t) &= H_\phi^{S_q}(x_i)\hat{\phi}(t) \\
\boldsymbol{E}(\overline{\phi}(x_i,t)) &= B_\phi(x_i)\hat{\phi}(t)
\end{aligned}
$$

where we have chosen the shape functions identical to corresponding test functions (Galerkin's method).

B.2.5 Introducing Test Functions

$$
\hat{\overline{\boldsymbol{u}}}'\left\{\int_V B_u{}'\boldsymbol{T}\,dV + \int_V H_u{}'\rho_o\frac{\partial^2\boldsymbol{u}}{\partial t^2}\,dV - \int_V H_u{}'\boldsymbol{f}^B\,dV - \int_{S_f} H_u^{S_f}{}'\boldsymbol{f}^{S_f}\,dS_f\right\} = 0
$$

$$
\hat{\overline{\phi}}'\left\{\int_V B_\phi{}'\boldsymbol{D}\,dV - \int_V H_\phi{}'q^B\,dV - \int_{S_q} H_\phi^{S_q}{}'q^{S_q}\,dS_q\right\} = 0
$$

We require the weak form to hold for all $\hat{\boldsymbol{u}}(t), \hat{\phi}(t)$. A necessary condition is $\{\ \} = 0$. We obtain

$$
\begin{bmatrix} \int_V \rho_o H_u{}'\frac{\partial^2\boldsymbol{u}}{\partial t^2}\,dV \\ \boldsymbol{0} \end{bmatrix} + \begin{bmatrix} \int_V B_u{}'\boldsymbol{T}\,dV \\ \int_V B_\phi{}'\boldsymbol{D}\,dV \end{bmatrix} - \begin{bmatrix} \int_V H_u{}'\boldsymbol{f}^B\,dV \\ \int_V H_\phi{}'q^B\,dV \end{bmatrix} +
$$

$$
- \begin{bmatrix} \int_{S_f} H_u^{S_f}{}'\boldsymbol{f}^{S_f}\,dS_f \\ \boldsymbol{0} \end{bmatrix} - \begin{bmatrix} \boldsymbol{0} \\ \int_{S_q} H_\phi^{S_q}{}'q^{S_q}\,dS_q \end{bmatrix} = \boldsymbol{0}
$$

or

$$
\boldsymbol{FI}^m + \boldsymbol{FI}^k - \boldsymbol{FE}^b - \boldsymbol{FE}^{S_f} - \boldsymbol{FE}^{S_q} = \boldsymbol{0}
$$

B.2.6 Newton's Method at Time t

$$
\boldsymbol{\xi} \triangleq \begin{bmatrix} \hat{\boldsymbol{u}} \\ -\hat{\phi} \end{bmatrix}
$$

$$
\boldsymbol{\delta\xi} \triangleq \boldsymbol{\xi}^{\nu+1} - \boldsymbol{\xi}^{\nu}
$$

$$
\boldsymbol{Res}^{\nu} \triangleq \boldsymbol{Res}(\boldsymbol{\xi}^{\nu})
$$

For simplicity we assume $\boldsymbol{f}^B, \boldsymbol{f}^{S_f}, q^B, q^{S_f}$ are independent of $\hat{\boldsymbol{u}}(t), \hat{\phi}(t)$.

$$
\boldsymbol{Res}(\boldsymbol{\xi}, \ddot{\boldsymbol{\xi}}) \triangleq \boldsymbol{FI}^m + \boldsymbol{FI}^k - \boldsymbol{FE}^b - \boldsymbol{FE}^{S_f} - \boldsymbol{FE}^{S_q} \tag{B.1}
$$

$$
\begin{aligned}
\boldsymbol{Res}^{\nu+1} &\simeq \boldsymbol{Res}^{\nu} + \left.\frac{\partial \boldsymbol{Res}}{\partial \boldsymbol{\xi}}\right|_{\nu} \delta\boldsymbol{\xi} + \left.\frac{\partial \boldsymbol{Res}}{\partial \ddot{\boldsymbol{\xi}}}\right|_{\nu} \delta\ddot{\boldsymbol{\xi}} + \cdots \\
\boldsymbol{Res}^{\nu+1} &= \mathbf{0}
\end{aligned}
$$

We obtain the equations for Newton's method

$$
\left.\frac{\partial \boldsymbol{Res}}{\partial \boldsymbol{\xi}}\right|_{\nu} \delta\boldsymbol{\xi} + \left.\frac{\partial \boldsymbol{Res}}{\partial \ddot{\boldsymbol{\xi}}}\right|_{\nu} \delta\ddot{\boldsymbol{\xi}} = -\boldsymbol{Res}^{\nu} \tag{B.2}
$$

where we will introduce a temporal approximation such that

$$
\delta\ddot{\boldsymbol{\xi}} = \boldsymbol{f}(\boldsymbol{\xi}^{\nu}) + F(\boldsymbol{\xi}^{\nu})\delta\boldsymbol{\xi}
$$

This linear system must be solved iteratively, starting from an initial guess, until some norm measure of error is achieved.

B.2.7 Introducing Constitutive and Shape Function

$$
\begin{aligned}
\boldsymbol{T} &= \boldsymbol{T}(\boldsymbol{S}(\boldsymbol{\xi}), \boldsymbol{E}(\boldsymbol{\xi})) \\
\boldsymbol{D} &= \boldsymbol{D}(\boldsymbol{S}(\boldsymbol{\xi}), \boldsymbol{E}(\boldsymbol{\xi}))
\end{aligned}
$$

In anticipation of calculating Jacobian matrices for Newton's method we use the chain rule to define the following matrices.

$$
\begin{aligned}
\frac{\partial \boldsymbol{T}}{\partial \boldsymbol{\xi}} &= \frac{\partial \boldsymbol{T}}{\partial \boldsymbol{S}}\frac{\partial \boldsymbol{S}}{\partial \boldsymbol{\xi}} + \frac{\partial \boldsymbol{T}}{\partial \boldsymbol{E}}\frac{\partial \boldsymbol{E}}{\partial \boldsymbol{\xi}} \\
&= \begin{bmatrix} C_{uu} \end{bmatrix} \begin{bmatrix} B_u & 0 \end{bmatrix} + \begin{bmatrix} C_{u\phi} \end{bmatrix} \begin{bmatrix} 0 & -B_\phi \end{bmatrix}
\end{aligned}
$$

similarly

$$
\begin{aligned}
\frac{\partial \boldsymbol{D}}{\partial \boldsymbol{\xi}} &= \frac{\partial \boldsymbol{D}}{\partial \boldsymbol{S}}\frac{\partial \boldsymbol{S}}{\partial \boldsymbol{\xi}} + \frac{\partial \boldsymbol{D}}{\partial \boldsymbol{E}}\frac{\partial \boldsymbol{E}}{\partial \boldsymbol{\xi}} \\
&= \begin{bmatrix} C_{\phi u} \end{bmatrix} \begin{bmatrix} B_u & 0 \end{bmatrix} + \begin{bmatrix} C_{\phi\phi} \end{bmatrix} \begin{bmatrix} 0 & -B_\phi \end{bmatrix}
\end{aligned}
$$

or

$$
\begin{aligned}
\frac{\partial \boldsymbol{T}}{\partial \boldsymbol{\xi}} &= \begin{bmatrix} C_{uu}B_u & -C_{u\phi}B_\phi \end{bmatrix} \\
\frac{\partial \boldsymbol{D}}{\partial \boldsymbol{\xi}} &= \begin{bmatrix} C_{\phi u}B_u & -C_{\phi\phi}B_\phi \end{bmatrix}
\end{aligned}
$$

B.2.8 Jacobian Matrices

$$
\frac{\partial \boldsymbol{FI}^m}{\partial \ddot{\boldsymbol{\xi}}} = \begin{bmatrix} \int_V \rho_o H_u{}' H_u \, dV & 0 \\ 0 & 0 \end{bmatrix}
$$

$$
\begin{aligned}
&= \int_V \rho_o H_m{}' H_m \, dV \\
&= J^m
\end{aligned}
$$

$$
\begin{aligned}
\frac{\partial \boldsymbol{FI}^k}{\partial \boldsymbol{\xi}} &= \begin{bmatrix} \int_V B_u{}' C_{uu} B_u \, dV & -\int_V B_u{}' C_{u\phi} B_\phi \, dV \\ \int_V B_\phi{}' C_{\phi u} B_u \, dV & -\int_V B_\phi{}' C_{\phi\phi} B_\phi \, dV \end{bmatrix} \\
&= \int_V \begin{bmatrix} B_u & 0 \\ 0 & B_\phi \end{bmatrix}' \begin{bmatrix} C_{uu} & -C_{u\phi} \\ C_{\phi u} & -C_{\phi\phi} \end{bmatrix} \begin{bmatrix} B_u & 0 \\ 0 & B_\phi \end{bmatrix} dV \\
&= \int_V B' C B \, dV \\
&= J^k
\end{aligned}
$$

B.2.9 Define Loading Interpolation Functions

$$
\begin{aligned}
\begin{bmatrix} \boldsymbol{f}^B(x_i, t) \\ q^B(x_i, t) \end{bmatrix} &= H_{bfq}(x_i) \boldsymbol{B_{fq}}(t) \\
\boldsymbol{f}^{S_f}(x_i, t) &= H_{sf}(x_i) \boldsymbol{S_f}(t) \\
q^{S_q} &= H_{sq}(x_i) \boldsymbol{S_q}(t)
\end{aligned}
$$

B.2.10 Residual Vectors

$$
\begin{aligned}
\boldsymbol{FI}^m &= \int_V \rho_o H_m{}' H_m \, dV \, \ddot{\boldsymbol{\xi}} \\
&= J^m \ddot{\boldsymbol{\xi}}
\end{aligned}
$$

$$
\begin{aligned}
\boldsymbol{FI}^k &= \int_V B' \begin{bmatrix} \boldsymbol{T} \\ \boldsymbol{D} \end{bmatrix} dV
\end{aligned}
$$

$$
\begin{aligned}
\boldsymbol{FE}^b &= \int_V \begin{bmatrix} H_u{}' & 0 \\ 0 & H_\phi{}' \end{bmatrix} \begin{bmatrix} \boldsymbol{f}^B \\ q^B \end{bmatrix} dV \\
&= \int_V H' \begin{bmatrix} \boldsymbol{f}^B \\ q^B \end{bmatrix} dV \\
&= \int_V H' H_{bfq} \, dV \, \boldsymbol{B_{fq}} \\
&= FE_{bfq} \boldsymbol{B_{fq}}
\end{aligned}
$$

$$
\begin{aligned}
\boldsymbol{FE}^{S_f} &= \int_{S_f} \begin{bmatrix} H_u^{S_f}{}' \\ 0 \end{bmatrix} \boldsymbol{f}^{S_f} \, dS_f \\
&= \int_{S_f} H_{su}{}' \boldsymbol{f}^{S_f} \, dS_f \\
&= \int_{S_f} H_{su}{}' H_{sf} \, dS_f \, \boldsymbol{S_f}
\end{aligned}
$$

$$
\begin{aligned}
&= FE_{sf}\boldsymbol{S_f} \\
\boldsymbol{FE}^{S_q} &= \int_{S_q} \begin{bmatrix} 0 \\ H_\phi^{S_q\prime} \end{bmatrix} q^{S_q}\, dS_q \\
&= \int_{S_q} H_{s\phi}{}' q^{S_q}\, dS_q \\
&= \int_{S_q} H_{s\phi}{}' H_{sq}\, dS_q\, \boldsymbol{S_q} \\
&= FE_{sq}\boldsymbol{S_q}
\end{aligned}
$$

B.3 Finite Element Formulation II

This section presents a finite element formulation of perfectly electrically insulating electroelastic materials under the small deformation approximation. The formulation is suitable for nonlinear material response functions and anticipates a Newton method solution technique. The formulation is suitable for constitutive equations with strain $\boldsymbol{S}$ and electric displacement $\boldsymbol{D}$ as independent variables.

B.3.1 Mixed Weak Form

$$
\begin{aligned}
\int_V \boldsymbol{T}\cdot\overline{\boldsymbol{S}}\, dV + \int_V \rho_o \frac{\partial^2 \boldsymbol{u}}{\partial t^2}\cdot\overline{\boldsymbol{u}}\, dV - \int_V \boldsymbol{f}^B\overline{\boldsymbol{u}}\, dV - \int_{S_f} \boldsymbol{f}^{S_f}\overline{\boldsymbol{u}}^{S_f}\, dS_f &= 0 \\
\int_V \boldsymbol{D}\cdot\overline{\boldsymbol{E}}\, dV - \int_V q^B\overline{\phi}\, dV - \int_{S_q} q^{S_q}\overline{\phi}\, dS_q &= 0 \\
\int_V (\boldsymbol{E}+\boldsymbol{\nabla}\phi)\cdot\overline{\boldsymbol{D}}\, dV &= 0
\end{aligned}
$$

B.3.2 Mixed Weak Form Rewritten

$$
\begin{aligned}
\int_V \overline{\boldsymbol{S}}'\boldsymbol{T}\, dV + \int_V \overline{\boldsymbol{u}}'\rho_o \frac{\partial^2 \boldsymbol{u}}{\partial t^2}\, dV - \int_V \overline{\boldsymbol{u}}'\boldsymbol{f}^B\, dV - \int_{S_f} \overline{\boldsymbol{u}}^{Sf\prime}\boldsymbol{f}^{S_f}\, dS_f &= (0) \\
\int_V \overline{\boldsymbol{E}}'\boldsymbol{D}\, dV - \int_V \overline{\phi}' q^B\, dV - \int_{S_q} \overline{\phi}' q^{S_q}\, dS_q &= \boldsymbol{0} \\
\int_V \overline{\boldsymbol{D}}'(\boldsymbol{E}+\boldsymbol{\nabla}\phi)\, dV &= 0
\end{aligned}
$$

B.3.3 Test Functions Defined

$$
\begin{aligned}
\overline{\boldsymbol{u}}(x_i,t) &= H_u(x_i)\hat{\overline{\boldsymbol{u}}}(t) \\
\overline{\boldsymbol{u}}^{S_f}(x_i,t) &= H_u^{S_f}(x_i)\hat{\overline{\boldsymbol{u}}}(t) \\
\overline{\boldsymbol{S}}(\overline{\boldsymbol{u}}(x_i,t)) &= B_u(x_i)\hat{\overline{\boldsymbol{u}}}(t) \\
\overline{\phi}(x_i,t) &= H_\phi(x_i)\hat{\overline{\phi}}(t)
\end{aligned}
$$

$$
\begin{aligned}
\overline{\phi}^{S_q}(x_i,t) &= H_\phi^{S_q}(x_i)\hat{\overline{\phi}}(t) \\
\overline{\boldsymbol{E}}(\overline{\phi}(x_i,t)) &= -B_\phi(x_i)\hat{\overline{\phi}}(t) \\
\overline{\boldsymbol{D}}(x_i,t) &= H_D(x_i)\hat{\overline{\boldsymbol{D}}}(t)
\end{aligned}
$$

B.3.4 Shape Functions Defined

$$
\begin{aligned}
\boldsymbol{u}(x_i,t) &= H_u(x_i)\hat{\boldsymbol{u}}(t) \\
\boldsymbol{S}(\boldsymbol{u}(x_i,t)) &= B_u(x_i)\hat{\boldsymbol{u}}(t) \\
\phi(x_i,t) &= H_\phi(x_i)\hat{\phi}(t) \\
\boldsymbol{\nabla}\phi(\phi(x_i,t)) &= B_\phi(x_i)\hat{\phi}(t) \\
\boldsymbol{D}(x_i,t) &= H_D(x_i)\hat{\boldsymbol{D}}(t)
\end{aligned}
$$

where we have chosen the shape functions identical to corresponding test functions (Galerkin's method).

B.3.5 Introducing Test Functions

$$
\begin{aligned}
\hat{\overline{\boldsymbol{u}}}'\left\{\int_V B_u{}'\boldsymbol{T}\,dV + \int_V H_u{}'\rho_o\frac{\partial^2\boldsymbol{u}}{\partial t^2}\,dV - \int_V H_u{}'\boldsymbol{f}^B\,dV - \int_{S_f} H_u^{S_f}{}'\boldsymbol{f}^{S_f}\,dS_f\right\} &= 0 \\
\hat{\overline{\phi}}'\left\{\int_V B_\phi{}'\boldsymbol{D}\,dV - \int_V H_\phi{}'q^B\,dV - \int_{S_q} H_\phi^{S_q}{}'q^{S_q}\,dS_q\right\} &= 0 \\
\hat{\overline{\boldsymbol{D}}}'\left\{\int_V H_D{}'(\boldsymbol{E}+\boldsymbol{\nabla}\phi)\,dV\right\} &= 0
\end{aligned}
$$

We require the weak form to hold for all $\hat{\overline{\boldsymbol{u}}}(t), \hat{\overline{\phi}}(t), \hat{\overline{\boldsymbol{D}}}(t)$. A necessary condition $\longrightarrow \{\} = 0$

$$
\begin{bmatrix} \int_V \rho_o H_u{}'\frac{\partial^2\boldsymbol{u}}{\partial t^2}\,dV \\ \mathbf{0} \\ \mathbf{0} \end{bmatrix} + \begin{bmatrix} \int_V B_u{}'\boldsymbol{T}\,dV \\ \int_V B_\phi{}'\boldsymbol{D}\,dV \\ \int_V H_D{}'(\boldsymbol{E}+\boldsymbol{\nabla}\phi)\,dV \end{bmatrix} - \begin{bmatrix} \int_V H_u{}'\boldsymbol{f}^B\,dV \\ \int_V -H_\phi{}'q^B\,dV \\ \mathbf{0} \end{bmatrix} +
$$

$$
- \begin{bmatrix} \int_{S_f} H_u^{S_f}{}'\boldsymbol{f}^{S_f}\,dS_f \\ \mathbf{0} \\ \mathbf{0} \end{bmatrix} - \begin{bmatrix} \mathbf{0} \\ \int_{S_q} -H_\phi^{S_q}{}'q^{S_q}\,dS_q \\ \mathbf{0} \end{bmatrix} = \mathbf{0}
$$

or

$$
\boldsymbol{FI}^m + \boldsymbol{FI}^k - \boldsymbol{FE}^b - \boldsymbol{FE}^{S_f} - \boldsymbol{FE}^{S_q} = \mathbf{0}
$$

B.3.6 Introducing Constitutive and Shape Functions

$$
\boldsymbol{T} = \boldsymbol{T}(\boldsymbol{S}(\boldsymbol{\xi}), \boldsymbol{D}(\boldsymbol{\xi}))
$$

$$\boldsymbol{E} = \boldsymbol{D}(\boldsymbol{S}(\boldsymbol{\xi}), \boldsymbol{D}(\boldsymbol{\xi}))$$

and using the chain rule

$$\begin{aligned}
\frac{\partial \boldsymbol{T}}{\partial \boldsymbol{\xi}} &= \frac{\partial \boldsymbol{T}}{\partial \boldsymbol{S}}\frac{\partial \boldsymbol{S}}{\partial \boldsymbol{\xi}} + \frac{\partial \boldsymbol{T}}{\partial \boldsymbol{D}}\frac{\partial \boldsymbol{D}}{\partial \boldsymbol{\xi}} \\
&= \begin{bmatrix} C_{uu} \end{bmatrix}\begin{bmatrix} B_u & 0 & 0 \end{bmatrix} + \begin{bmatrix} C_{ud} \end{bmatrix}\begin{bmatrix} 0 & 0 & H_d \end{bmatrix} \\
\frac{\partial \boldsymbol{D}}{\partial \boldsymbol{\xi}} &= \begin{bmatrix} 0 & 0 & H_d \end{bmatrix} \\
\frac{\partial(\boldsymbol{E} + \boldsymbol{\nabla}\phi)}{\partial \boldsymbol{\xi}} &= \frac{\partial \boldsymbol{E}}{\partial \boldsymbol{S}}\frac{\partial \boldsymbol{S}}{\partial \boldsymbol{\xi}} + \frac{\partial \boldsymbol{E}}{\partial \boldsymbol{D}}\frac{\partial \boldsymbol{D}}{\partial \boldsymbol{\xi}} + \frac{\partial \boldsymbol{\nabla}\phi}{\partial \boldsymbol{\xi}} \\
&= \begin{bmatrix} C_{du} \end{bmatrix}\begin{bmatrix} B_u & 0 & 0 \end{bmatrix} + \begin{bmatrix} C_{dd} \end{bmatrix}\begin{bmatrix} 0 & 0 & H_d \end{bmatrix} + \begin{bmatrix} 0 & B_\phi & 0 \end{bmatrix}
\end{aligned}$$

or

$$\begin{aligned}
\frac{\partial \boldsymbol{T}}{\partial \boldsymbol{\xi}} &= \begin{bmatrix} C_{uu}B_u & 0 & C_{ud}H_d \end{bmatrix} \\
\frac{\partial \boldsymbol{D}}{\partial \boldsymbol{\xi}} &= \begin{bmatrix} 0 & 0 & H_d \end{bmatrix} \\
\frac{\partial(\boldsymbol{E} + \boldsymbol{\nabla}\phi)}{\partial \boldsymbol{\xi}} &= \begin{bmatrix} C_{du}B_u & B_\phi & C_{dd}H_d \end{bmatrix}
\end{aligned}$$

B.3.7 Jacobian Matrices

$$\begin{aligned}
\frac{\partial \boldsymbol{FI}^m}{\partial \ddot{\boldsymbol{\xi}}} &= \begin{bmatrix} \int_V \rho_o H_u{}' H_u \, dV & 0 & 0 \\ 0 & 0 & 0 \\ 0 & 0 & 0 \end{bmatrix} \\
&= \int_V \rho_o H_m{}' H_m \, dV = J^m \\
\frac{\partial \boldsymbol{FI}^k}{\partial \boldsymbol{\xi}} &= \begin{bmatrix} \int_V B_u{}' C_{uu} B_u \, dV & 0 & \int_V B_u{}' C_{ud} H_d \, dV \\ 0 & 0 & \int_V B_\phi{}' H_d \, dV \\ \int_V H_d{}' C_{du} B_u \, dV & \int_V H_d{}' B_\phi \, dV & \int_V H_d{}' C_{dd} H_d \, dV \end{bmatrix} \\
&= \int_V \begin{bmatrix} B_u & 0 & 0 \\ 0 & B_\phi & 0 \\ 0 & 0 & H_d \end{bmatrix}' \begin{bmatrix} C_{uu} & 0 & C_{ud} \\ 0 & 0 & I \\ C_{du} & I & C_{dd} \end{bmatrix} \begin{bmatrix} B_u & 0 & 0 \\ 0 & B_\phi & 0 \\ 0 & 0 & H_d \end{bmatrix} dV \\
&= \int_V B' C B \, dV \\
&= J^k
\end{aligned}$$

B.3.8 Define Loading Interpolation Functions

$$\begin{aligned}
\begin{bmatrix} f_i^B(x_i,t) \\ q^B \end{bmatrix} &= H_{bfq}(x_i)\boldsymbol{B_{fq}}(t) \\
\boldsymbol{f}^{S_f}(x_i,t) &= H_{sq}(x_i)\boldsymbol{S_f}(t) \\
q^{S_q}(x_i,t) &= H_{sq}(x_i)\boldsymbol{S_q}(t)
\end{aligned}$$

B.3.9 Residual Vectors

$$\begin{aligned}
\boldsymbol{FI}^m &= \int_V \rho_o H_m{}' H_m \, dV \, \ddot{\boldsymbol{\xi}} = J^m \ddot{\boldsymbol{\xi}} \\
\boldsymbol{FI}^k &= \int_V B' \begin{bmatrix} \boldsymbol{T} \\ \boldsymbol{D} \\ (\boldsymbol{E} + \boldsymbol{\nabla}\phi) \end{bmatrix} dV \\
\boldsymbol{FE}^b &= \int_V \begin{bmatrix} H_u{}' & 0 \\ 0 & -H_\phi{}' \\ 0 & 0 \end{bmatrix} dV = \int_V H' \begin{bmatrix} \boldsymbol{f}^B \\ q^b \end{bmatrix} dV \\
&= \int_V H' H_{bfq} \, dV \, \boldsymbol{B_{fq}} = FE_{bfq} \boldsymbol{B_{fq}} \\
\boldsymbol{FE}^{S_f} &= \int_{S_f} \begin{bmatrix} H_u^{S_f}{}' \\ 0 \\ 0 \end{bmatrix} \boldsymbol{f}^{S_f} \, dS_f = \int_{S_f} H_{su}{}' \boldsymbol{f}^{S_f} \, dS_f \\
&= \int_{S_f} H_{su}{}' H_{sf} \, dS_f \, \boldsymbol{S_f} = FE_{sf} \boldsymbol{S_f} \\
\boldsymbol{FE}^{S_q} &= \int_{S_q} \begin{bmatrix} 0 \\ -H_\phi^{S_q}{}' \\ 0 \end{bmatrix} q^{S_q} \, dS_q = \int_{S_q} H_{s\phi}{}' q^{S_q} \, dS_q \\
&= \int_{S_q} H_{s\phi}{}' H_{sq} \, dS_q \, \boldsymbol{S_q} = FE_{sq} \boldsymbol{S_q}
\end{aligned}$$

Appendix C

Electric Conduction Measurements

Electric conduction values were measured by tuning a potentiometer to zero the voltage V. The measurement is a zero load measurement.

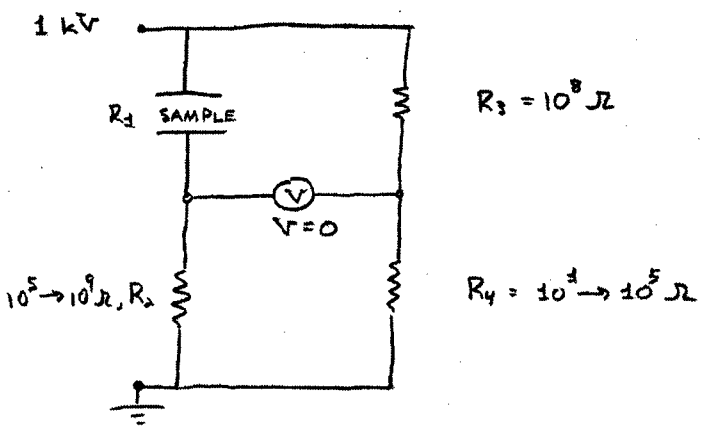

Figure C-1: Electric conduction measurement circuit.

Appendix D

Epoxy Material Model

Here we present a material model for epoxy,

$$\begin{aligned} \tau_{ji}^{T} &= \hat{\tau}_{ji}^{T}\left(\epsilon_{ij}, D_i\right), \\ E_i &= \hat{E}_i\left(\epsilon_{ij}, D_i\right), \\ J_i &= \hat{J}_i\left(\epsilon_{ij}, D_i\right). \end{aligned}$$

Symmetry of ϵ_{ij} and τ_{ji}^{T} permit introduction of Voight notation,

$$\begin{aligned} \boldsymbol{T} &= \left[\begin{array}{cccccc} \tau_{11}^{T} & \tau_{22}^{T} & \tau_{33}^{T} & \tau_{32}^{T} & \tau_{13}^{T} & \tau_{12}^{T} \end{array}\right]' \\ \boldsymbol{S} &= \left[\begin{array}{cccccc} \epsilon_{11} & \epsilon_{22} & \epsilon_{33} & 2\epsilon_{32} & 2\epsilon_{13} & 2\epsilon_{12} \end{array}\right]' \\ \boldsymbol{J} &= \left[\begin{array}{ccc} J_1 & J_2 & J_3 \end{array}\right]' \end{aligned}$$

The linear material model for epoxy in terms of Voight notation is,

$$\begin{aligned} \boldsymbol{T} &= C_{uu}\boldsymbol{S} + C_{ud}\boldsymbol{D}, \\ \boldsymbol{E} &= C_{du}\boldsymbol{S} + C_{dd}\boldsymbol{D}, \\ \boldsymbol{J} &= -C_{q\phi}\boldsymbol{E}. \end{aligned}$$

The following coefficients are for stress $\boldsymbol{T}$ in $[Pa]$, electric field E_i in $[V/m]$, and electric displacement D_i in $[C/m^2]$,

$$\begin{aligned} &C_{uu}(1,1) = C_{uu}(2,2) = C_{uu}(3,3) = 7.708 * 10^{10} \\ &C_{uu}(4,4) = C_{uu}(5,5) = C_{uu}(6,6) = 4.222 * 10^{10} \\ &C_{uu}(1,2) = C_{uu}(1,3) = C_{uu}(2,3) = 2.609 * 10^{10} \\ &C_{uu}(i,j) = C_{uu}(j,i) \\ &C_{uu}(i,j) = 0 \text{ otherwise} \\ \\ &C_{ud}(m,n) = C_{du}(n,m) = 0 \\ &C_{dd}(1,1) = C_{dd}(2,2) = C_{dd}(3,3) = 2.567 * 10^{10} \end{aligned}$$

$$C_{dd}(r,s) = 0 \text{ otherwise}$$

$$C_{q\phi}(1,1) = C_{q\phi}(2,2) = C_{q\phi}(3,3) = -\sigma$$
$$C_{q\phi}(r,s) = 0 \text{ otherwise.}$$

See table 5.1 for values of σ.

Appendix E

Classical Small Deformation Derivation

E.1 Introduction

This appendix presents the classical small deformation piezoelectric equations, extended to include electric conduction and electric body forces. They are based on postulating a conservation of energy statement using Poynting's vector as presented in TIERSTEN [29, pp. 25-39]. We modify the classical equations by including electrical body forces in their surface traction form. This formulation starts from notions of small deformation 'built in'. The main assumption is that Poynting's vector represents the electric energy flux through a surface.

E.1.1 Conservation of energy

After postulating the conservation of energy statement we enforce invariance requirements after GREEN & RIVLIN [14] to obtain linear and angular momentum equations. We could have used momentum and angular momentum equations following TIERSTEN [29] instead of the invariance arguments. The balance of energy equation is postulated in the form[1],

$$\begin{aligned}\frac{\partial}{\partial t}\int_V \left(\frac{1}{2}\rho v_i v_i + U\right) dV &= \int_V f_i v_i \, dV + \oint_S t_i v_i \, dS + \int_V \rho h \, dV - \oint_S q_i n_i \, dS + \\ &\quad \oint_S t_i^E v_i \, dS - \oint_S (\boldsymbol{E} \times \boldsymbol{H})_i \, n_i \, dS \, .\end{aligned}$$

Noting that surface tractions survive a limit process as volume approaches zero and surface remains finite, where a body force like gravity does not, we have exploited this property of electric 'body forces' and written them as electric surface tractions. Note the traction vectors t_i, t_i^E are related to their respective stress tensors by

$$t_i = \tau_{ji} n_j$$

[1]See definition 2.5.1 for field definitions

$$t_i^E = \tau_{ji}^E n_j$$

Also, we utilize the EQS approximation to the Poynting vector

$$(\boldsymbol{E} \times \boldsymbol{H})_i = \phi(J_i + \dot{D}_i)$$

Noting the following

$$\begin{aligned}
\oint_S \tau_{ji} v_i n_j \, dS &= \int_V (\tau_{ji} v_i)_{,j} \, dV \\
\oint_S \tau_{ji}^E v_i n_j \, dS &= \int_V \left(\tau_{ji}^E v_i\right)_{,j} dV \\
\oint_S q_i n_i \, dS &= \int_V q_{i,i} \, dV \\
\oint_S \phi(J_i + \dot{D}_i) n_i \, dS &= \int_V \left[\phi(J_i + \dot{D}_i)\right]_{,i} dV
\end{aligned}$$

we obtain

$$\begin{aligned}
\int_V \left(\rho v_i \dot{v}_i + \dot{U}\right) dV = \int_V f_i v_i \, dV + \int_V (\tau_{ji} v_i)_{,j} \, dV + \int_V \rho h \, dV - \int_V q_{i,i} \, dV \\
+ \int_V \left(\tau_{ji}^E v_i\right)_{,j} dV - \int_V \left[\phi(J_i + \dot{D}_i)\right]_{,i} dV
\end{aligned}$$

Expanding the divergence terms and noting from EQS Maxwell

$$\begin{aligned}
(J_i + \dot{D}_i)_{,i} &= 0 \\
E_i &= -\phi_{,i}
\end{aligned}$$

and by noting this holds for arbitrary volume V we obtain the local for of our energy statement

$$\begin{aligned}
\dot{U} = \left(\tau_{ji,j} + \tau_{ji,j}^E + f_i - \rho \dot{v}_i\right) v_i + \left(\tau_{ji} + \tau_{ji}^E\right) v_{i,j} + \rho h - q_{i,i} \\
+ E_i(J_i + \dot{D}_i)
\end{aligned}$$

We obtain the governing equations of motion by enforcing invariance of our energy expression w.r.t. rigid motion of the body. We first consider a rigid dispacement where b_i is an arbitrary vector

$$v_i \to v_i + b_i$$

We assume during the rigid dispacement that all terms $U, \rho, f_i, \tau_{ji}, \tau_{ji}^E, \rho h, q_i, \phi, J_i, D_i$ remain constant

$$\begin{aligned}
\dot{U} = \left(\tau_{ji,j} + \tau_{ji,j}^E + f_i - \rho \dot{v}_i\right)(v_i + b_i) + \left(\tau_{ji} + \tau_{ji}^E\right) v_{i,j} + \rho h - q_{i,i} \\
+ E_i(J_i + \dot{D}_i)
\end{aligned}$$

Using our energy statement we obtain

$$\left(\tau_{ji,j} + \tau^E_{ji,j} + f_i - \rho\dot{v}_i\right) b_i = 0$$

Requiring this to hold for arbitrary b_i, we obtain our equations of linear momentum

$$(\tau_{ji} + \tau^E_{ji})_{,j} + f_i - \rho\dot{v}_i = 0$$

Using our linear momentum equations in our energy statement it simplifies considerably to

$$\dot{U} = \left(\tau_{ji} + \tau^E_{ji}\right) v_{i,j} + \rho h - q_{i,i} + E_i(J_i + \dot{D}_i)$$

Next we superpose an arbitrary rigid body rotation where Ω_k is arbitrary vector

$$v_i \to v_i + \varepsilon_{ijk} e_j \Omega_k v_{i,j} \to v_{i,j} + \varepsilon_{ijk}\Omega_k$$

we obtain

$$\dot{U} = \left(\tau_{ji} + \tau^E_{ji}\right)(v_{i,j} + \varepsilon_{ijk}\Omega_k)\rho h - q_{i,i} + E_i(J_i + \dot{D}_i)$$

Simplifying using our energy expression

$$(\tau_{ji} + \tau^E_{ji})\varepsilon_{ijk}\Omega_k = 0$$

we require this to hold for arbitrary Ω_k. This requires the anti-symmetric part of $(\tau_{ji} + \tau^E_{ji}) = 0$,or introducing the symmetric and anti-symmetic operators

$$A_{(i,j)} = \frac{1}{2}(A_{ij} + A_{ij})$$
$$A_{[i,j]} = \frac{1}{2}(A_{ij} - A_{ji}),$$

we rewrite this condition as

$$(\tau + \tau^E)_{[j,i]} = 0$$

Rewriting $v_{i,j}$ as the sum of its symmetric and anti-symmetric parts

$$\begin{aligned} v_{i,j} &= \dot{u}_{(i,j)} + \dot{u}_{[i,j]} \\ &= \dot{\epsilon}_{ij} + \dot{\omega}_{ij} \end{aligned}$$

and noting that contraction of a symmetric and anti-symmetric tensor is zero we obtain

$$\begin{aligned} (\tau_{ji} + \tau^E_{ji})v_{i,j} &= (\tau_{ji} + \tau^E_{ji})(\dot{\epsilon}_{ij} + \dot{\omega}_{ij}) \\ &= (\tau_{ji} + \tau^E_{ji})\dot{\epsilon}_{ij} \end{aligned}$$

Finally our energy expression simplifies to

$$\dot{U} = (\tau_{ji} + \tau_{ji}^{E})\dot{\epsilon}_{ij} + \rho h - q_{i,i} + E_i(J_i + \dot{D}_i)$$

Bibliography

[1] W. Ani and G. A. Maugin. Basic equations for shocks in nonlinear electroelastic materials. *J. Acoust. Soc. Am.*, 85(2):599–610, 1989.

[2] K. J. Bathe. *Finite Element Procedures.* Prentice-Hall, 1996.

[3] J. C. Baumhauer and H. F. Tiersten. Nonlinear electroelastic equations for small fields superposed on a bias. *J. Acoust. Soc. Am.*, 54(4):1017–1034, 1973.

[4] A. A. Bent. Piezoelectric fiber composites for structural actuation. Master's thesis, Massachusetts Institute of Technology, 1994.

[5] A. A. Bent. *Active Fiber Composites for Structural Actuation.* PhD thesis, Massachusetts Institute of Technology, 1997.

[6] A. A. Bent, N. W. Hagood, and J. P. Rodgers. Anisotropic actuation with piezoelectric fiber composites. *J. Intell. Mat. Sys. Struct.*, 6(3):338–349, 1995.

[7] B. D. Coleman and W. Noll. The thermodynamics of elastic materials with heat conduction and viscosity. *Arch. Rational Mech. Anal.*, 13:167–178.

[8] H. G. de Lorenzi and H. F. Tiersten. On the interaction of the electromagnetic field with heat conducting deformable semiconductors. *Journal of Mathematical Physics*, 16(4):938–957, 1975.

[9] R. C. Dixon and A. C. Eringen. A dynamical theory of polar elastic dielectrics-i. *Int. J. Engng. Sci.*, 3:359–377, 1965.

[10] A. C. Eringen. *Mechanics of Continua.* John Wiley & Sons, Inc., 1967.

[11] A. C. Eringen and G. A. Maugin. *Electrodynamics of Continua I.* Springer-Verlag, 1990.

[12] C. Eringen. Theory of electromagnetic elastic plates. *Int. J. Engng. Sci.*, 27(4):363–375, 1989.

[13] K. Ghandi. *Nonlinear Modeling and Characterization Techniques for Phase Transitions in Electro-Mechanically Coupled Devices.* PhD thesis, Massachusetts Institute of Technology, 1998.

[14] A. E. Green and R. S. Rivlin. On cauchy's equations of motion. *Z. angew. Math. Phys.*, 15:290–292, 1964.

[15] M. E. Gurtin. *An Introduction to Continuum Mechanics.* Academic Press, 1981.

[16] H. A. Haus and J. R. Melcher. *Electromagnetic Fields and Energy.* Prentice Hall, 1989.

[17] G. A. Maugin and A. C. Eringen. On the equations of the electrodynamics of deformable bodies of finite extent. *Journal de Mecanique*, 16(1):101–147, 1977.

[18] G. A. Maugin and J. Pouget. Electroacoustic equations for one-domain ferroelectric bodies. *J. Acoust. Soc. Am.*, 68(2):575–587, 1980.

[19] G. A. Maugin, J. Pouget, R. Drouot, and B. Collet. *Nonlinear Electromechanical Couplings.* John Wiley & Sons, 1992.

[20] M. F. McCarthy and H. F. Tiersten. On integral forms of the balance laws for deformable semiconductors. *Arch. Rational Mech. Anal.*, 68:27–36, 1978.

[21] R. W. Ogden. *Non-Linear Elastic Deformations.* Dover Publications, Inc., 1997.

[22] J. P. Rodgers. Modeling and manufacturing of adaptive plates incorporating piezoelectric fiber composite plies. Master's thesis, Massachusetts Institute of Technology, 1995.

[23] L. Segel. *Mathematics Applied to Continuum Mechanics.* Dover Publications, Inc., 1987.

[24] G. Strang. *Introduction to Linear Algebra.* Wellesley-Cambridge Press, 1993.

[25] J. A. Stratton. *Electromagnetic Theory.* McGraw-Hill Book Company, Inc., 1941.

[26] R. N. Thurston. Waves in solids. In C. Truesdell, editor, *Encyclopedia of Physics*, volume VIa/4, pages 109–174, 1974.

[27] H. F. Tiersten. The radiation and confinement of electromagnetic energy accompanying the oscillation of piezoelectric crystal plates. In *Recent Advances in Engineering Science*, pages 63–90.

[28] H. F. Tiersten. Coupled magnetomechanical equations for magnetically saturated insulators. *Journal of Mathematical Physics*, 5(9):1298–1318, 1964.

[29] H. F. Tiersten. *Linear Piezoelectric Plate Vibrations.* Plenum Press, 1969.

[30] H. F. Tiersten. On the nonlinear equations of thermo-electroelasticity. *Int. J. Engng. Sci.*, 9:587–604, 1971.

[31] H. F. Tiersten. Nonlinear electroelastic equations cubic in the small field variables. *J. Acoust. Soc. Am.*, 57(3):660–666, 1975.

[32] H. F. Tiersten. Perturbation theory for linear electroelastic equations for small fields superposed on a bias. *J. Acoust. Soc. Am.*, 64(3):832–837, 1978.

[33] H. F. Tiersten. Electroelastic interactions and the piezoelectric equations. *J. Acoust. Soc. Am.*, 70(6):1567–1576, 1981.

[34] H. F. Tiersten. Electroelastic equations for electroded thin plates subject to large driving voltages. *J. Appl. Phys.*, 74(5):3389–3393, 1993.

[35] H. F. Tiersten and C. F. Tsai. On the interaction of the electromagnetic field with heat conducting deformable insulators. *J. Math. Phys.*, 13(3):361–378, 1972.

[36] C. Truesdell and W. Noll. The non-linear field theories of mechanics. In S. Flugge, editor, *Handbuch der Physik*, volume III/3. Springer-Verlag, 1965.

[37] C. Truesdell and R. Toupin. The classical field theories. In S. Flugge, editor, *Encyclopedia of Physics*, volume III/1. Springer-Verlag, 1960.

[38] H. H. Woodson and J. R. Melcher. *Electromechanical Dynamics, Part II: Fields, Forces, and Motion.* Robert E. Krieger Publishing Company, 1968.

[39] M. Zahn. *Electromagnetic Field Theory.* Krieger, 1979.

Study of Work Flow in Piezoelectrically Driven Linear and Non-linear Systems

by

Malinda Kay Lutz

S.B., Aeronautics and Astronautics (1996)
Massachusetts Institute of Technology

Submitted to the Department of Aeronautics and Astronautics
in partial fulfillment of the requirements for the degree of

Master of Science in Aeronautics and Astronautics

at the

MASSACHUSETTS INSTITUTE OF TECHNOLOGY

June 1999

© Massachusetts Institute of Technology 1999. All rights reserved.

Author ..... Malinda K Lutz .....
Department of Aeronautics and Astronautics
May 21, 1999

Certified by ..... Nesbitt W. Hagood, IV .....
Nesbitt W. Hagood, IV
Associate Professor
Thesis Supervisor

Accepted by .....
Jaime Peraire
Chairman, Department Committee on Graduate Students

Aero

MASSACHUSETTS INSTITUTE OF TECHNOLOGY
JUL 15 1999
LIBRARIES

Study of Work Flow in Piezoelectrically Driven Linear and Non-linear Systems

by

Malinda Kay Lutz

Submitted to the Department of Aeronautics and Astronautics
on May 21, 1999, in partial fulfillment of the
requirements for the degree of
Master of Science in Aeronautics and Astronautics

Abstract

Standard assumptions about the efficiency of active systems working against a load neglect the load coupling inherent in these systems. This thesis contains a derivation for finding the actuation efficiency and work output in electro-mechanically coupled systems working against a load. This general derivation is for fully coupled, non-linear systems working against a generalized load. Three example cases are then shown to demonstrate several key aspects of the general derivation. The first example case is a one-dimensional, linear discrete actuator working against a one-dimensional, linear spring load. This example shows the effects of electro-mechanical coupling on the actuation efficiency. The second example case is of a piezoelectric bender first presented by Lesieutre and Davis[1] in their derivation of the device coupling coefficient. The bender example demonstrates the differences between the device coupling coefficient and actuation efficiency as well as the use of the generalized derivation in mechanically complex problems. The final example presented is a one-dimensional, linear discrete actuator working against a one-dimensional, non-linear load in order to demonstrate the possibility of increasing the work output of a system through the use of non-linear loading functions.

To test the theoretical derivation presented, a custom built testing facility was designed and built to measure the work output and actuation efficiency of a discrete actuator working against both linear and non-linear loads. The testing facility was designed for load application with programmable impedances and closed loop testing at frequencies up to 1 kHz. The complete design of the testing facility is presented with an overview of the rationale behind the design decisions made.

Finally, tests were performed on a discrete actuator working against linear and non-linear loading functions. The tests performed on a discrete actuator working against a linear load match the expected work output predicted by the theory. Tests performed on a discrete actuator working against a non-linear load validate that increases in the mechanical work out of the actuator are possible by using non-linear loads instead of linear loads. To illustrate that this is a practical result, the design of a loading device that loads a material non-linearly while loading a spring linearly is presented with its theoretical performance. Recommendations on ways to improve the model, testing methodology, and testing machine concludes the document.

Thesis Supervisor: Nesbitt W. Hagood, IV
Title: Associate Professor

Acknowledgments

Funding for this project was provided through the Office of Naval Research Young Investigator's Program, from Grant No. N00014-96-1-0691 with Dr. Wallace Smith serving as technical monitor. Prof Hagood has also been a remarkable source of ideas and solutions, generally when I needed them most.

Contents

1 Introduction **19**
1.1 Motivation . . . 19
1.2 Objective . . . 20
1.3 Background and Previous Work . . . 20
1.3.1 Material Coupling Coefficient . . . 21
1.3.2 Effective Coupling Factor . . . 26
1.3.3 Device Coupling Coefficient . . . 29
1.3.4 Impedance Matched System Efficiency . . . 30
1.4 Approach . . . 31
1.5 Organization of the Document . . . 32

2 Analysis of the Actuation Efficiency of Electro-mechanically Coupled Systems **35**
2.1 Definition and Metrics . . . 36
2.1.1 Piezoelectric Material Relations . . . 36
2.1.2 Mechanical Work . . . 37
2.1.3 Electrical Work . . . 38
2.1.4 Actuation Efficiency . . . 39
2.2 Uncoupled analysis . . . 40
2.3 General Derivation of the Work Output and Actuation Efficiency . . . 42
2.3.1 General Derivation Framework . . . 43
2.3.2 Work Expressions . . . 44
2.4 Example of a One-dimensional Linear System . . . 46
2.4.1 Material Relations. . . . 46
2.4.2 Electrical and Mechanical Work. . . . 48
2.4.3 Actuation Efficiency. . . . 50
2.4.4 Results of the One-dimensional Simplification . . . 50
2.5 Example of a Bender Device . . . 52
2.5.1 Lesieutre and Davis' results . . . 52
2.5.2 Work output approach . . . 54
2.5.3 Remarks on the Bender Device Example . . . 55
2.6 Coupled Actuation Efficiency of Non-linear Systems . . . 58
2.6.1 Work derivation . . . 58
2.6.2 Remarks on the Non-linear System Derivation . . . 59
2.7 Conclusions . . . 62

3 Design and Validation of the Component Testing Facility **63**
3.1 Motivation for the Component Tester . . . 63

3.2 Component Tester Design Requirements 63
3.3 Review of Commercially Available and Published Designs 64
3.4 Component Testing Facility Design 66
3.4.1 Mechanical Components 67
3.4.2 Electronic Components 68
3.4.3 Support Hardware 70
3.4.4 Thermal Testing Facility Design 70
3.5 Design Issues 71
3.5.1 Compliance Budget 71
3.5.2 Design for High Frequency First Mode 73
3.5.3 Rod and Plate Material Selection 76
3.5.4 Driving Piezostack Selection 77
3.5.5 Amplifier Selection 80
3.5.6 LabVIEW Control Loop 80
3.5.7 Sample Alignment Mechanism 82
3.6 Design Validation 85

4 Validation of Theoretical Results 91
4.1 Testing Methodology 91
4.2 Measurement of Mechanical and Electrical Work 91
4.3 Testing Plan 92
4.4 Test Specimen Selection and Information 92
4.4.1 Sample Selection 92
4.4.2 Sample Information and Characterization 93
4.4.3 Selection of Material Values and Coupling Coefficient 100
4.5 Validation of Linear Loading of Piezoelectric Materials 103
4.6 Validation of Non-linear Loading of Piezoelectric Materials 108
4.7 Non-linear Loading Device 112

5 Conclusions and Recommendations for Future Work 117
5.1 Conclusions of the Derivation of Actuation Efficiency and Work Output in Coupled Systems 117
5.2 Recommendations for Future Work on the Analysis of Coupled Systems 118
5.3 Conclusions of the Design of the Component Testing Facility 119
5.4 Recommendations for Future Work of the Component Testing Facility 119

A Component Testing Facility Drawings 121

List of Figures

1-1 Schematic of general system representation. The electro-mechanical coupling block can be a variety of distributed and discrete systems with linear and non-linear relations. The load element is a generalized work pair with either a linear or non-linear relations. 21

1-2 The loading cycle for the derivation of the material coupling coefficient. This cycle is for the case with Electrical work in and Mechanical work out 23

1-3 The loading cycle for the derivation of the material coupling coefficient. This cycle is for the case with Mechanical work in and Electrical work out 24

1-4 Cycles used by Berlincourt for comparison to the cycle used to derive the material coupling coefficient. 27

1-5 Operational schematic used by Berlincourt to illustrate the use of linear and non-linear dissipative loads. 29

2-1 Schematic of general system representation. The electro-mechanical coupling block can be a variety of distributed and discrete systems with linear and non-linear relations. The load element is a generalized work pair with either a linear or non-linear relations. 36

2-2 Model of a one-dimensional spring/active material system. 40

2-3 Intersection of material and linear structure load lines on a stress-strain diagram. . . 42

2-4 Actuation efficiency variation with structural stiffness for a one-dimensional system of an active material working against a linear load. The actuation efficiency is plotted for varying values of k, the coupling coefficient, and α, the stiffness ratio. 51

2-5 Model of bender structure being analyzed. 52

2-6 Actuation efficiency and device coupling coefficient against the mechanical preload of the system, plotted for $\frac{k_s}{K} = 0.7$. 57

2-7 Work in and work out expressions plotted for varying values of system preload. Values plotted are the maximum work values assuming a 100 V peak input voltage. . 57

2-8 Actuation efficiency and device coupling coefficient against ratio of spring stiffness of the system, plotted for $\frac{P}{P_{cr}} = 0.75$. 57

2-9 Work in and work out expressions plotted for varying values of stiffness ratio. Values plotted are the maximum work values over a cycle with 100 V maximum input voltage. 57

2-10 Linear and non-linear loading functions with the material load line at maximum applied voltage. The area under the curves represent the amount of output work is possible by each. 60

2-11 Instantaneous Work of non-linear loading functions. The first non-linear loading function can increase the work out of the system, compared to the linear load, by a factor of 3. 61

2-12 Actuation efficiency of non-linear loading functions. First non-linear loading function increases the efficiency of the system by a factor of 2. 61

3-1 Schematic of the Compressive Testing Machine including the Electronic Operation of the System. 66
3-2 Compressive Testing Machine 67
3-3 Sketch of Initial Design of a Temperature Testing Facility for use with the Component Testing Facility. 71
3-4 Flow Chart of the Process used in determining the final design decisions of the Compressive Testing Facility. 72
3-5 Sample compliance budget 74
3-6 The four mass dynamic model of the system. 75
3-7 Natural Frequency Comparison for different rod materials and system configurations versus system cost. Rod materials plotted are Steel and Alumina. 77
3-8 Free Deflection comparison of piezoelectric stacks to known samples to be tested. . . 78
3-9 Blocked Force comparison of piezoelectric stacks to samples to be tested. 78
3-10 Natural Frequency comparison of piezoelectric stacks and samples tested. 79
3-11 Transfer function of the compensated and uncompensated control loop for control of the testing machine. 82
3-12 Representative time traces of a sample in the testing machine with the controller driving constant force tests in the presence of sample disturbance. 83
3-13 Mismatch in tested stiffness with theoretical stiffness for an aluminum bar with spherical endcaps under small preload values. 83
3-14 Mismatch in tested stiffness with theoretical stiffness for a steel bar with spherical endcaps under small preload values. 84
3-15 Alignment mechanism designed to compensate for the non-parallelism of sample faces. 84
3-16 Stiffness information for a steel bar tested in the testing machine. The stiffness of the system is shown as seen by the strain gages, the displacement sensors and the expected measurement by the strain gages and displacement sensors. 86
3-17 Stiffness information for an aluminum bar tested in the testing machine. The stiffness of the system is shown as seen by the displacement sensors, the theoretical stiffness, and expected displacement sensor readings. 86
3-18 Variation of the stiffness of an aluminum rod based on position in the testing machine. 87
3-19 Variation of the stiffness of a steel rod based on position in the testing machine. . . 87
3-20 Transfer function from the optical displacement sensors to the input to the stack in the system configuration of the large stack and steel rods. 88
3-21 Transfer function from the Entran load cell to the input to the stack in both system configurations. 89
3-22 Transfer function from the Kistler load cell to the input to the stack in both system configurations. 89
3-23 Transfer functions of the four system configurations as predicted by the four node model. Transfer functions were taken from a force input at mass two to a position measurement at mass three. 90

4-1 Time traces of the force and displacement measurements taken when finding the stiffness of the Sumitomo actuator. 95
4-2 Data taken to find the stiffness of the Sumitomo stack. 95

4-3 Representative time traces of Current and Voltage values measured while finding the capacitance of the Sumitomo actuator. 98
4-4 Test used to find the dielectric constant of the material at varying values of electric field. 98
4-5 Representative time history of voltage and displacement measured when finding the electro-mechanical coupling in the Sumitomo actuator. 99
4-6 Test used to find the electro-mechanical coupling term of the Sumitomo stack at varying values of applied voltage. 100
4-7 Representative time traces of the force, displacement, voltage and current data measured during testing a piezoelectric actuator working against a linear load. 104
4-8 Electrical and Mechanical work of an active material working against a uniaxial load of the same stiffness, time traces. 105
4-9 Maximum work output variation with stiffness ratio for an active material working against a linear load. 106
4-10 Maximum input work variation with stiffness ratio for an active material working against a linear load. 107
4-11 Maximum actuation efficiency variation with stiffness ratio for an active material working against a linear load. 107
4-12 Non-linear and linear loads tested with a 200V stack input voltage, shown with the material load line on a force-displacement graph. 109
4-13 Non-linear and linear loads tested with a 150V stack input voltage, shown with the material load line on a force-displacement graph. 109
4-14 Work output values of the active material when working against linear and non-linear loading functions with an input value of 150 V verses the stiffness ratio of the linear load. Values are compared to the expected work output based on work against a linear function for multiple values of the material constants. 111
4-15 Work output values of the active material when working against linear and non-linear loading functions with an input value of 200 V verses the stiffness ratio of the linear load. Values are compared to the expected work output based on work against a linear function for multiple values of the material constants. 111
4-16 Work input values of the active material when working against linear and non-linear loading functions with an input value of 150 V verses the stiffness ratio of the linear load. Values are compared to the expected work input based on work against a linear function for multiple values of material constants. 111
4-17 Work input values of the active material when working against linear and non-linear loading functions with an input value of 200 V verses the stiffness ratio of the linear load. Values are compared to the expected work input based on work against a linear function for multiple values of material constants. 111
4-18 Actuation efficiency values of the active material when working against linear and non-linear loading functions with an input value of 150 V verses the stiffness ratio of the linear load. Values are compared to the expected work output based on work against a linear function for varying values of coupling coefficient. 112
4-19 Actuation efficiency values of the active material when working against linear and non-linear loading functions with an input value of 200 V verses the stiffness ratio of the linear load. Values are compared to the expected work output based on work against a linear function for varying values of coupling coefficient. 112

4-20 Non-linear loading device. Presented in cross-section. Dimensions labeled are the critical dimensions in the design. 113
4-21 Load lines used in the analysis of the non-linear loading device. 114
4-22 Work in and work out plotted for the non-linear loading device. Looks at the unmodified linear system and the work into and out of the active material and the work into the structure by using the non-linear loading device. 115
4-23 Work efficiency of the system using the proposed design of the non-linear loading device. 115

A-1 Shaded parametric view of the model of the testing facility. 121
A-2 Top Level Assembly Drawing. 122
A-3 Cage Assembly Drawing. 123
A-4 Back Piece of Cage, Assembly Drawing. 124
A-5 Front Piece of Cage, Assembly Drawing. 125
A-6 End Piece Assembly Drawing. 126
A-7 Clamping Plate Clamp Part Drawing. 127
A-8 Clamping Plate 2 Part Drawing. 128
A-9 Flexure Part Drawing. 129
A-10 Half Plate 1 Part Drawing. 130
A-11 Half Plate 3 Part Drawing. 131
A-12 Inside Clamp Part Drawing. 132
A-13 Inside 2 Part Drawing. 133
A-14 Half Plate 2 Part Drawing. 134
A-15 Inside 1 Part Drawing. 135
A-16 Back Plate Part Drawing. 136
A-17 Clamping Plate 1 Part Drawing. 137
A-18 End Block 1 Part Drawing. 138
A-19 End Block 2 Part Drawing. 139
A-20 End Clamp 1 Part Drawing. 140
A-21 End Clamp 2 Part Drawing. 141
A-22 Stack Alignment Mechanism 1 Part Drawing. 142
A-23 Stack Alignment Mechanism 2 Part Drawing. 143
A-24 Alumina Brace Part Drawing. 144
A-25 Steel Braces Part Drawing. 145
A-26 Load Cell Adapter Part Drawing. 146
A-27 Alumina Rod Assembly Drawing. 147
A-28 Alumina Rod Part 1 Drawing. 148
A-29 Alumina Rod Part 2 Drawing. 149
A-30 Alumina Rod Part 3 Drawing. 150
A-31 Sample Alignment Assembly Drawing. 151
A-32 Alignment Flexure Part Drawing. 152
A-33 Sample Alignment Base Part Drawing. 153
A-34 Bottom Shear Panel Part Drawing. 154
A-35 Left Shear Panel Part Drawing. 155
A-36 Right Shear Panel Part Drawing. 156
A-37 Top Shear Panel Part Drawing. 157

List of Tables

2.1 Definition of variables and sample numerical values for bender device problem as used by Lesieutre and Davis. 56

4.1 Physical Characteristics of the Sumitomo Corporation Stack MLA-20B. 93
4.2 Measured and Published material values for Sumitomo MLA-20B Actuator. 94
4.3 Ranges of the Sumitomo material properties used in the theoretical comparison to the data. 101
4.4 Comparison of different possible material coupling coefficient values for the Sumitomo actuator. 102
4.5 Values used in the analysis of the performance possible using the proposed design of the non-linear loading device. 114

Nomenclature

α	Stiffness ratio, load stiffness divided by material stiffness
A/A_{cr}	Cross-sectional area of the material
A_p	Cross-sectional area of piezoelectric material
A_s	Cross-sectional area of structure
β	Angle of the springs
β_i	Initial angle of the springs
b	Base length
$\mathbf{C}^S$	Capacitance of the system under constant strain
C^T	Capacitance of material under constant stress
c_{33}^E	Young's modulus of the active material in the "three-three" direction under constant Electric field
c_{axial}	Axial compliance of plates and rods
c_b^E	Young's Modulus of the base material at constant Electric Field
c_{bend}	Bending compliance of plates
c_p^E	Young's Modulus of the piezoelectric material at constant Electric Field
c_s	Young's modulus of the spring
δ	Variation of the parameter
∂	Partial derivative of the parameter
D_3	Electric Displacement in the active material in the "three" direction
d	Separation distance of pivots
d_{33}	Electro-mechanical coupling term of the active material in the "three-three" direction
ε_0	Dielectric constant of free space
ε_{33}^S	Dielectric constant of the active material in the "three-three" direction under constant strain
ε_{33}^T	Dielectric constant of the active material in the "three-three" direction under constant stress
E	Young's modulus of the material
E_3	Electric Field in the active material in the "three" direction
Ef	Actuation Efficiency
Ef_a	Apparent actuation efficiency
Ef_p	Proper actuation efficiency
e_{13}	Electro-mechanical coupling of the active material in the "one-three" direction
e_{33}	Electro-mechanical coupling of the active material in the "three-three" direction
$\mathbf{F}$	Generalized force vector of the active material
F_{bl}	Blocked force of the actuator
$\mathbf{F_l}$	Generalized Force vector of the load
F_{linear}	Linear force relation

F_{n1}	Force relation of non-linear 1 function
F_{n2}	Force relation of non-linear 2 function
$F_{non-linear1}$	Force relation of non-linear 1 function
$F_{non-linear2}$	Force relation of non-linear 2 function
F_s	Force in the spring
f_a	Anti-resonant frequency of the stack
f_r	Resonant frequency of the stack
$G(s)$	Transfer function of controller
h	Height of the plate
h_b	Height of the base material
h_p	Height of the piezoelectric material
I	Current in system
$\mathbf{K}$	Stiffness matrix of the system
K	Stiffness of the beam in bending
K_{33}	Stiffness of piezoelectric material
K_G	Stiffness reduction of the beam due to axial preload
K_t	Total stiffness of the beam
k_1	Stiffness of side springs
k_2	Stiffness of load spring
k_{33}	Material coupling coefficient in the extensional mode
k_a	Apparent device coupling coefficient
k_{align}	Stiffness of the alignment mechanism
k_{axial}	Axial stiffness of rods
k^E	Stiffness of the piezoelectric material under constant Electric field
$\mathbf{k}_l$	Generalized load stiffness
k_m	Matrix coupling term in beam analysis
k_{meas}	Stiffness measured during testing
k_p	Proper device coupling coefficient
k_s	Stiffness of load or load spring
$k_s(x)$	Stiffness of non-linear load or load spring
L	Length of the beam
l	Length of a rod-shaped material
l_p	Length of piezoelectric material
l_s	Length of structure or spring
$\mathbf{M}$	Mass matrix of the system
η_{mech}	Stiffness ratio relation describing the work output of a system working against a load
N	Number of layers in piezoelectric stack
P	Axial load applied to the beam
$\mathbf{p}$	Electro-mechanical coupling of the system
$\mathbf{Q}$	Charge vector
$q(t)$	Height of the center of the beam as a function of time
S_3	Strain in the active material"three" direction
s	Laplace variable
s_{33}^E	Elastic constant of the active material in the "three-three" direction under constant Electric Field
T_3	Stress in the active material"three" direction

t	Time
t_l	Thickness of the stack layers
t_p	Thickness of the plate
$u(k)$	Control output at update k
$\mathbf{V}$	Vector of applied electric potentials
V_{appl}	Voltage applied to stack during testing
V_i	Initial system voltage
V_f	Final system voltage
V_{max}	Maximum voltage applied during test
Vol	Volume of the piezoelectric material
ω	Frequency of pole or zero
W_E	Electrical Work
W_{in}	Work into the system
W_{ideal_in}	Work into an ideal capacitor
W_{in_E}	Electrical work into the system
W_{in_M}	Mechanical work into the system
W_M	Mechanical Work
W_{out}	Work out of the system
w	Width of the plate
$\mathbf{x}$	Generalized displacement vector
$\mathbf{x_l}$	Generalized load displacement
x	Displacement of system
x_{free}	Free displacement of the actuator
x_i	Initial displacement of the system
x_s	Displacement of spring
x_t	Final displacement of the system
ψ_E	Electrical mode shape
ψ_M	Mechanical mode shape
y	Dimension perpendicular to the beam
$y(k)$	Measurement at time k
ζ	Damping ratio

Chapter 1

Introduction

1.1 Motivation

The properties that active materials exhibit were discovered in the 1950's and linear models of the material behavior were proposed and validated. However, because of technological limitations, these models were defining the stable low power regions of the material. As power generation capabilities have advanced allowing active materials to be used with higher input voltages and currents, the applications for active materials have been expanded and the demands on the materials increased. In recent years, new applications of active materials have demanded that the maximum possible performance is achieved.

To increase the performance of active materials, several avenues have traditionally been explored. Generally advances have been in three classes; either perfecting the modeling of all kinds of active materials in order to accurately predict their performance, especially at the limits; to experiment with different compositions of active materials to maximize the desired characteristics for a certain application; or to use basic active materials in different configurations, for example composites or as single crystals, in order to reduce performance losses found in traditional ceramic wafers. Although these traditional methods of increasing performance focus on the material itself, it is reasonable to assume that another method of increasing performance is to focus on modifying what the active material is being asked to do.

1.2 Objective

The purpose of this thesis is to closely examine the work output and actuation efficiency in the framework of a fully non-linear coupled system. The efficiency expression will be compared to the traditional system comparison methods of the material coupling coefficient[2], device coupling coefficient[1], and impedance matched system efficiency[3, 4]. It is hoped that by examining the work throughput of coupled systems, a better understanding of the effect of coupling terms on an actuation system is achieved.

An additional objective of this project is to explore if the performance metrics of an active material system can be increased by modifying the load that the active material is working against from a linear to a non-linear function. The performance metrics under consideration are the work output and actuation efficiency of the system. The work output is the amount of work going out of the system and into a load at any given time. The actuation efficiency is the work output, typically mechanical work, compared to the work input, typically electrical work.

1.3 Background and Previous Work

Active materials are materials that can predictably deform when an external field is applied, generally a magnetic, electric or thermal field. Special kinds of active materials also have the converse property that they can produce fields when externally deformed. The common classifications of active materials are piezoelectric materials, electrostrictor materials, magnetostrictor materials, and shape memory materials. Each kind of active material has its own unique composition and behavior. This work will be working with piezoelectric materials which have a known mechanical and electrical interaction for their low-power, linear region of behavior. The higher power region becomes non-linear in nature, but this region will not be explicitly considered.

In this thesis, the general system being examined is a base system with coupled mechanical and electrical properties, an electrical work source as input and a mechanical work sink as the output of the system. This general system, shown in fig. 1-1, describes how active materials work in standard operation. The electrical work source is a generalized work source with a generalized charge input and generalized voltage output. The mechanical work sink is a generalized work sink with a generalized displacement output and generalized force input. As is described in Chapter 2, the derivation performed is for a very general system with no constraints on the linearity of the

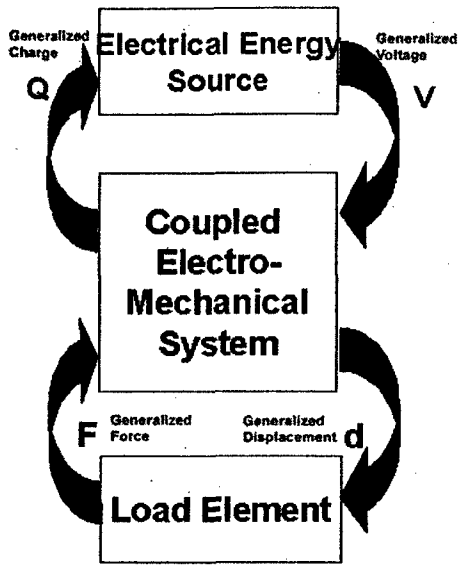

Figure 1-1: Schematic of general system representation. The electro-mechanical coupling block can be a variety of distributed and discrete systems with linear and non-linear relations. The load element is a generalized work pair with either a linear or non-linear relations.

coupling terms of the core system or the interaction of the external work pairs.

When discussing the performance of active materials and active material systems, traditionally just the coupling within the electro-mechanical system has been discussed. These discussions have ranged from the standard material coupling coefficient, an effective coupling factor found when changing the cycle used to find the coupling coefficient, a device coupling coefficient, and an energy transfer metric defined when looking at discrete systems. These metrics will be fully described in the following paragraphs to provide a basis for comparison of the actuation efficiency derived later in the thesis.

1.3.1 Material Coupling Coefficient

One fundamental property of piezoelectric materials is the material coupling coefficient. The IEEE standard on piezoelectricity defines the coupling coefficient as "...non-dimensional coefficients which are useful for the description of a particular piezoelectric material under a particular stress and electric field configuration for conversion of stored energy to mechanical or electrical work"[5]. The coupling coefficient has long been looked on as a measure of the efficiency that a material converts mechanical energy to electrical energy and vice versa. This view has also extended itself to materials

working in a device where the square of the material coupling coefficient represents a value that can be scaled by the load that the material is working against to find the actuation efficiency of the system when working against a load.

The material coupling coefficient for different modes of operation is a standard measure of the worth of a piezoelectric material. The coupling coefficient derivation for piezoelectric materials is presented in the IEEE Standard on Piezoelectricity and is a well known and well documented derivation. However, the derivation is presented here for a background to talk about the other performance metrics.

Derivation of the Material Coupling Coefficient

The coupling coefficient is a unit-less quantity that is defined as the square root of the amount of work produced by an active material divided by the amount of work supplied to the active material under specified loading conditions. In the following paragraphs the derivation method of the material coupling coefficient will be illustrated.

The material coupling coefficient is found by specifying a standardized loading cycle and keeping track of the work put into the system and the work harvested from the system. The coupling coefficient then becomes a measure of how effectively a material can convert energy between its mechanical and electrical states. The coupling coefficient is found by specifying a cycle with either electrical work-in and mechanical work-out, or the reverse cycle of mechanical work-in and electrical work-out. Regardless of the version of the cycle used, for a given directional mode of operation the coupling coefficient is the same. For example, the coupling coefficient in the "one-one" mode is the same regardless of whether mechanical energy was applied or electrical energy was applied, but it is not the same as the coupling coefficient in the "one-three" mode of operation.

To understand where the value of the coupling coefficient comes from, it is necessary to derive the coupling coefficient from the governing equation of the material. The standard work cycle is applied and the equations that express each condition derived. The work cycle is applied with both the mechanical work-in cycle and the electrical work-in cycle so that it is shown that they are the same. The operational mode of the coupling coefficient derived is the "three-three" mode, where the electric field is applied in the three direction and the strain of the system is measured in the three direction. The method of derivation of the coupling coefficient stays the same regardless of the direction applied.

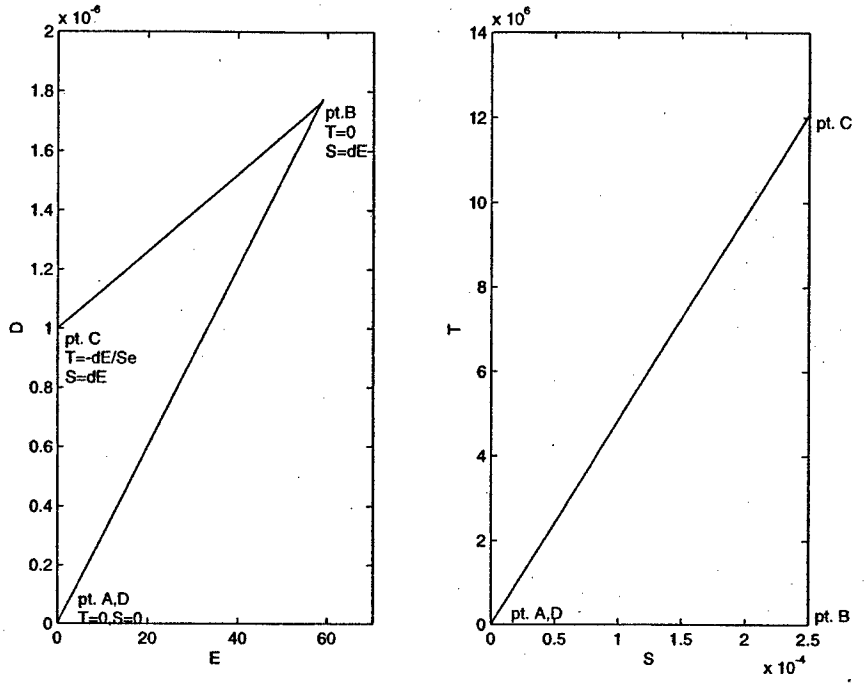

Figure 1-2: The loading cycle for the derivation of the material coupling coefficient. This cycle is for the case with Electrical work in and Mechanical work out

To begin the derivation, it is first necessary to state the governing equation in a one-dimensional form. Since stress, T, and electric field, E, are the desired free variables, the governing equation is shown below.

$$\begin{Bmatrix} S_3 \\ D_3 \end{Bmatrix} = \begin{bmatrix} s_{33}^E & d_{33} \\ d_{33} & \varepsilon_{33}^T \end{bmatrix} \begin{Bmatrix} T_3 \\ E_3 \end{Bmatrix} \tag{1.1}$$

The loading cycles used in the coupling coefficient derivation are found in figures 1-2 and 1-3. The cycle in figure 1-2 is a representation of the coupling coefficient cycle with electrical work-in and mechanical work-out. One graph is how the figure appears from a electrical point of view, the other is how it appears from a mechanical point of view. The cycle begins at point A where all states of the system are zero, the initial condition. Then an electric field is applied across the material under free-stress conditions until point B. From point B to C, the material is clamped so the displacement stays the same as the electric field is removed. Then the material is mechanically unloaded until the material returns to its initial state at point D.

Mathematically, the cycle can be expressed in terms of the governing equation, eqn. (1.1). From

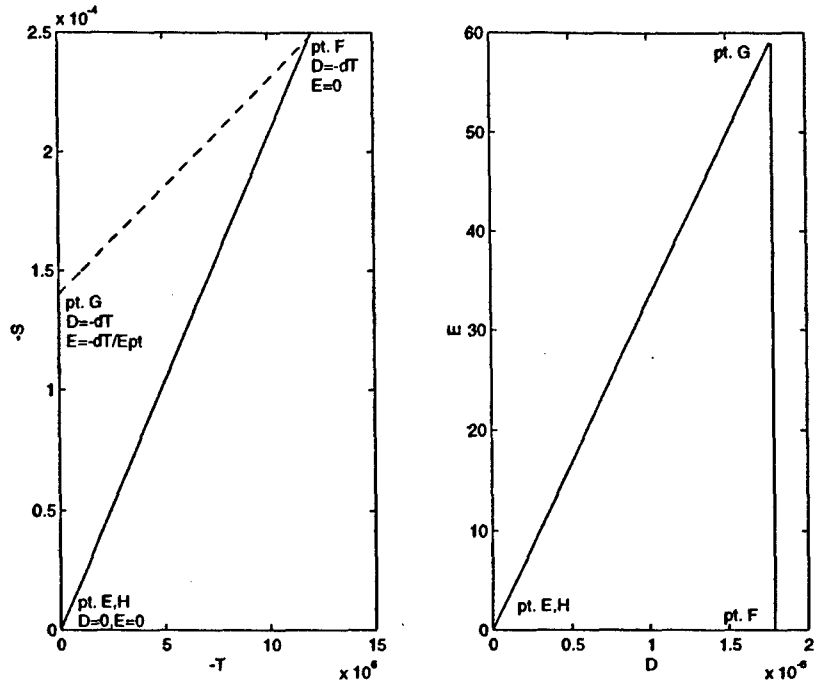

Figure 1-3: The loading cycle for the derivation of the material coupling coefficient. This cycle is for the case with Mechanical work in and Electrical work out

point A to B, the material is loaded in "free-stress" conditions and the work in is electrical work expressed as

$$W_{in} = \int_{\text{Vol}} \int_{D_{3_{min}}}^{D_{3_{max}}} E_3 \delta D_3 \cdot d\text{Vol} \tag{1.2}$$

Since the variation of T is zero, the variation of D becomes

$$\delta D_3 = \varepsilon_{33}^T \delta E_3 \tag{1.3}$$

and then the work in becomes

$$W_{in} = \frac{1}{2} \varepsilon_{33}^T E_{3_{max}}^2 \times \text{Vol} \tag{1.4}$$

From point B to C, the material is clamped and then electrically unloaded. Clamping the structure makes the change in S equal to zero. Therefore

$$0 = d_{33} E_3 + s_{33}^E T_3 \tag{1.5}$$

Rearranging this for an expression for T in terms of E

$$T_3 = -\frac{d_{33}}{s_{33}^E} E_3 \tag{1.6}$$

Then the mechanical work comes from mechanically unloading the system from point C to D while the electric field stays constant.

$$W_{out} = \int_{Vol} \int_{T_{3_{initial}}}^{T_{3_{final}}} T_3 \delta S_3 \cdot d\text{Vol} \tag{1.7}$$

Since the variation in electric field is zero, the variation of strain becomes

$$\delta S_3 = s_{33}^E \delta T_3 \tag{1.8}$$

Substituting equation 1.8 into equation 1.7 and integrating with respect to T results in

$$W_{out} = \frac{1}{2} s_{33}^E T_{3_{initial}}^2 \times \text{Vol} \tag{1.9}$$

However, from equation 1.6 we know that the initial stress for this part of the cycle is based on the maximum stress seen from the maximum electric field. Therefore the substitution of electric field for stress can be used, resulting in

$$W_{out} = \frac{1}{2} \frac{d_{33}^2}{s_{33}^E} E_{3_{max}}^2 \times \text{Vol} \tag{1.10}$$

To find the coupling coefficient, the work out of the system is divided by the work into the system. Therefore, dividing equation 1.10 by equation 1.4, results in

$$k_{33}^2 = \frac{W_{out}}{W_{in}} = \frac{\frac{1}{2} \varepsilon_{33}^T E_{3_{max}}^2 \times \text{Vol}}{\frac{1}{2} \frac{d_{33}^2}{s_{33}^E} E_{3_{max}}^2 \times \text{Vol}} \tag{1.11}$$

Simplifying this expression by cancelling all like terms from the top and bottom

$$k_{33}^2 = \frac{d_{33}^2}{s_{33}^E \varepsilon_{33}^T} \tag{1.12}$$

Equation 1.12 is the square of the material coupling coefficient for the "three-three" or longitudinal direction.

This same expression can also be derived by following the loading cycle shown in figure 1-3. The loading cycle in the figure is the cycle for mechanical work in and electrical work out. Again, half of the figure describes the electrical states of the system while the other half describes the mechanical states of the system. The cycle begins at point E with zero as the initial conditions. Between points E and F, the system is mechanically loaded in an open circuit configuration. Then the material is closed circuited and mechanically unloaded to point G. From points G to H the material is electrically unloaded back to the initial state of the system. Using this loading cycle, it is possible to follow the same mathematical steps as the earlier derivation to find that equation 1.12 also describes the coupling coefficient for this loading cycle.

Discussion of Material Coupling Coefficient

From the derivation, it is obvious that the external mechanical and electrical work is applied on demand and removed when it is no longer desired. In terms of the general system diagram presented in fig. 1-1, the material coupling coefficient only describes the interaction of the mechanical and electrical states in the core system of a single active material, while "disconnecting" the electrical and mechanical work sources when they are no longer desired. Additionally, when the work sources are "connected", they are idealized work sources that have no restrictions on the interaction of their work pairs, the interrelation of force and displacement or charge and voltage. While this idealization makes it difficult to apply the material coupling coefficient directly to systems in which the active material is working, it is a reasonable method of determining the relative worth of different compositions of piezoelectric materials.

1.3.2 Effective Coupling Factor

Berlincourt expanded the idea of the material coupling coefficient by looking at the efficiency of different cycles with both linear and non-linear loads applied[6]. He believed that applying the mechanical and electrical work sources in different orders and at different times might change the efficiency value of the system; therefore, he defined an effective coupling factor based on the different cycles in which the efficiency was found. The effective coupling factor was still dependent on the different boundary conditions of the problem and the different directional characteristics of the electrical and mechanical values. He generally looked at the differences inherent in four different cycles, as shown in fig. 1-4.

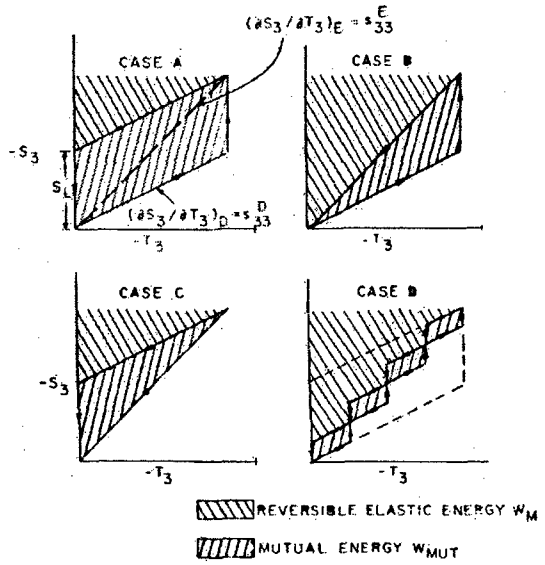

Figure 1-4: Cycles used by Berlincourt for comparison to the cycle used to derive the material coupling coefficient.

The first cycle applies a mechanical load in an open circuit configuration to a certain design stress. At the design stress, the electrical load is attached to the material while keeping the same stress level, adding a change in the strain of the system. Then the electric load is disconnected and the the material mechanically unloaded to zero stress. The electrical load is then reconnected until the strain of the system is again zero. It is assumed that the energy inside the work cycle box is the "mutual energy", the energy available to the electrical load. The energy outside the box is the reversible elastic energy of the system. Therefore, the coupling coefficient was defined as

$$k^2 = \frac{W_{mut}}{W_{mut} + W_M} \tag{1.13}$$

The second and third cycles are the cycles applied if only one of the electrode pairs is available to do work, and both are similar to the cycle applied for the material coupling coefficient. The second cycle is the same beginning as the first cycle, but the electrical load is not disconnected after its initial connection, instead the mechanical load is released with the electrical load connected. The third cycle is the same cycle as is used in the derivation of the material coupling coefficient. The definitions of the effective coupling factor are the same as the definition in the first case, but with the appropriate reversible mechanical energy and mutual energy values used.

The fourth case examined looks at what happens if the built up electrical energy from loading the material open circuited is dissipated at multiple intermediate steps instead of all at once as is done in the first case. Then the mutual energy becomes only the energy enclosed in the small rhombohedrals instead of the amount of energy enclosed in the larger rhombohedral. Additionally, this concept can be expanded to include dissipating energy in the methods used in either the second or third cases. However, the equation that describes this state is the same as the equation that has described the other three states.

Using these different loading cycles does change the amount of energy that can be extracted from the system. For example, Berlincourt claims that the first loading cycle increases the effective coupling factor of PZT-4 to 0.81 compared to the material coupling coefficient of PZT-4 of 0.70. He also considers the case of a thin disk with the edges clamped, quoting that the change in the coupling factor using the first loading case is 0.68 compared to the material coupling coefficient cycle value of 0.50.

Berlincourt then continues by examining the problem of using ideal linear and non-linear loads in a one-time energy conversion of a system rather than a short circuit condition. The one-time energy conversion is associated with the polarization or depolarization of a material. His ideal non-linear load is a load where the entire value of polarization or depolarizing strain is delivered at a single value of electric field or mechanical stress. Using this kind of behavior doubles the work available over using a linear load. Figure 1-5 shows how he uses the linear and non-linear loads in the depolarization cycle.

The first cycle shows the energy dissipated and the reversible energy if the material is depolarized while short circuited. The third cycle shows the amount of mutual energy available if the material is loaded using a linear electrical load, and the second cycle shows the energy available if the ideal non-linear electrical load is used for energy dissipation during depolarization. Since the non-linearities of the material are being considered, the equation to find the effective non-linear coupling factor becomes

$$k_{nf}^2 = \frac{W_{Mut}}{W_{Mut} + W_M + W_{MD}} \tag{1.14}$$

Using the non-linear loading results in a coupling factor of 0.71, which is higher than the linear coupling factor of 0.58. However, these coupling factors are for the complete depoling of the material, and are therefore not sustainable cycle factors, but rather one-time energy extractions.

Throughout the beginning part of this work, Berlincourt was looking at the same type of

BEST AVAILABLE COPY

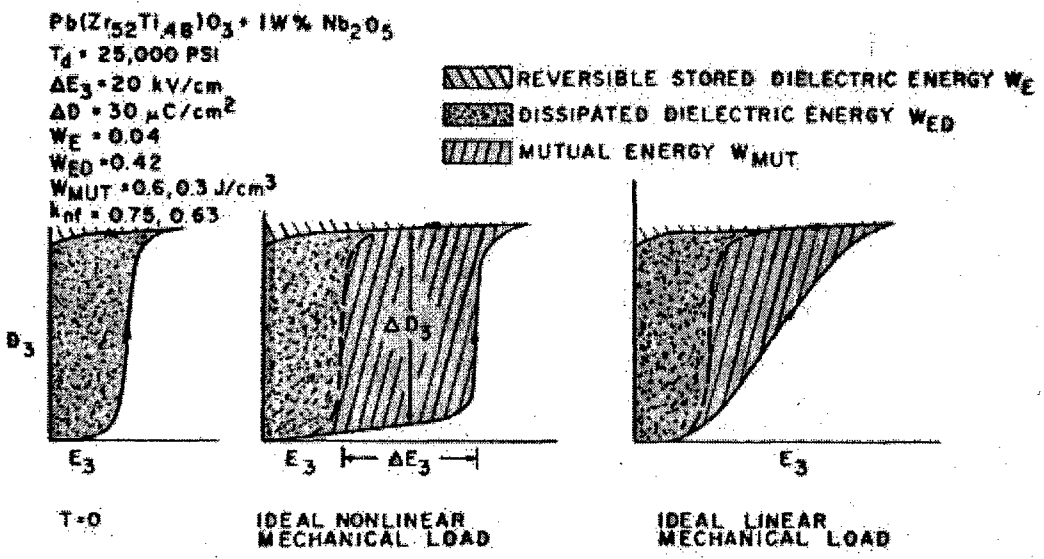

Figure 1-5: Operational schematic used by Berlincourt to illustrate the use of linear and non-linear dissipative loads.

information gathered by the material coupling coefficient; namely, the internal energy conversion of a system with the mechanical and electrical energy sources connected and disconnected at will. Although this work does find ways of using the electrical and mechanical energy sources differently to increase the energy conversion, it still does not allow for the system to change based upon what it is working against. It is still only looking at the energy conversion of a single material in the central core of the general system description with the external electrical and mechanical loads applied at will.

The second part of the work looks at the energy conversion in a one-time process. Although the formulation only allows for a one-time process, the basic formulation does consider the interdependence of the material states on what it is working against. Unfortunately, the reliance of the formulation on the complete depolarization of the material makes it difficult to expand the work done to repetitive cycling done in standard material operation.

1.3.3 Device Coupling Coefficient

In an effort to explain how the coupling coefficient of a material changes when the material is incorporated into a continuous device, Lesieutre and Davis derived a device coupling coefficient. This device coupling coefficient uses the same work cycle that is used by the material coupling

coefficient, but expands the work terms to include the effects of the passive material that the piezoelectric material is incorporated into. Their objective was to determine if this device coupling coefficient could be used to find a device who's energy conversion was higher than the energy conversion of the material it was made from. However, the derivation does provide a framework for the discussion of actuation efficiency.

The derivation of the device coupling coefficient puts the governing equation of the device in a two-by-two block form with charge and displacement as the free variables. The governing equation incorporates both the passive and active components of the device in order to fully describe the inter-workings of the system. Using this governing equation, the device undergoes the same loading cycle as is used in the derivation of the material coupling coefficient to determine an expression for the energy conversion of the composite device. The results of this derivation for an actual device are given in Chapter 2.

In terms of the framework that we are defining as the general operation of a piezoelectric material system, the device coupling coefficient still only looks at the energy conversion of the central core with the external electrical and mechanical load applied at will. However, unlike the material and effective coupling coefficients, the device coupling coefficient does allow for a central core that is more than just a single, active material. By looking at the effects of the passive material on the authority of the active material, a significant step towards looking at the effect of an external load was made.

1.3.4 Impedance Matched System Efficiency

Spangler and Hall and later Hall and Prechtl came close to looking at the effect of the external loading terms on an active material when defining their impedance matched efficiency expression[3, 4]. The work they were doing was focused on discrete actuation systems for helicopter rotor control. Their objective was to find the most efficient method of transferring the motion of the active material, in their case a bender device, to an amplification device to provide the control surface of the the rotor blade. In the course of their investigation, Spangler and Hall discovered that "at most, one-quarter of the actuation strain energy can be usefully applied to actuating a control surface" using linear relations for the transfer mechanism to the control surface[3]. The optimum occurred at the impedance matched condition, where the effective stiffness of the material matched the effective stiffness of the control surface. The equation derived to determine the effect

of different stiffnesses on the transfer efficiency is

$$\eta_{im} = \frac{\frac{k_\delta}{k_B}}{\left(1 + \frac{k_\delta}{k_B}\right)^2} \tag{1.15}$$

where k_δ is the stiffness of the control surface and k_B is the stiffness of the bender device.

This work fits into the general active material system framework presented in fig. 1-1 in a unique way. Instead of the core coupled system that most of the previous work has looked at, the impedance matched system efficiency is looking at a discrete actuator coupled to a transfer mechanism. The single electro-mechanically coupled system box has been replaced by two boxes, one of the active material system and the other of the transfer mechanism. Therefore, there are a set of work pair arrows, force and displacement, between the two boxes within the coupled system box. These secondary arrows encompass the relationship that has been defined by Spangler and Hall. The efficiency derived looks at the efficiency of the strain energy between these two systems. But, the same efficiency can be used to define the efficiency between the electro-mechanically coupled system and the external work sink, the work done on the environment, for linear loads. However, the work by Spangler and Hall still does not address the effect that the load the system is working against has on the work into the system. Therefore, it is not a true thermodynamic system efficiency, but rather a transfer efficiency. The derivation of the transfer efficiency will be shown in Chapter 2 in the uncoupled system analysis.

1.4 Approach

This paper derives a general expression for the work output and actuation efficiency of a system, including external load effects, when working in a typical operational cycle. The expression is derived through the use of a general two-block representation of a coupled system without constraining the coefficients to be linear. The general derivation assumes that the system is working against a generalized load that can be represented by a generalized force, generalized displacement and linear or non-linear load relationships. Through the use of this generalized system framework, expressions for work output and actuation efficiency can be derived.

Three example problems are presented to illustrate the use of the general expressions for real actuation problems. The first example presented is that of a one-dimensional, linear piezoelectric material working against a one-dimensional, linear load. The actuation efficiency expression

for the one-dimensional linear system is compared to the material coupling coefficient and a non-dimensional work output expression to understand the effects of material coupling terms. The second system examined is a piezoelectric bender system; two piezoelectric wafers bonded to a substrate with an applied end-load, first examined by Lesieutre and Davis[1] to explore the concept of a device coupling coefficient. This example fully demonstrates the benefits of using the generalized coupled analysis and provides a comparison of the actuator efficiency to the device coupling coefficient. The third example is of a one-dimensional, linear material working against a one-dimensional, non-linear load. The non-linear loading functions are used to demonstrate how their use can increase the work output and actuation efficiency of active materials.

To validate the theoretical results presented, initial test data was taken for a one-dimensional, linear material working against a linear and non-linear load. The tests were taken using a newly designed testing machine to allow loading of the material through the programmable impedance functionality of the testing machine. This functionality allowed for testing linear and non-linear functions easily sized for the sample tested. Through these tests, comparisons of the resulting work output and actuation efficiency to the expected theoretical results are possible. The tests show that the use of non-linear loading functions can increase the work output and actuation efficiency of a one-dimensional system.

1.5 Organization of the Document

The document is organized in the same way the problem is approached. Chapter 2, **Analysis of the Actuation Efficiency of Electro-mechanically Coupled Systems**, begins by defining the terms and metrics used throughout the derivation. An uncoupled analysis of active material systems is performed to illustrate the error in neglecting the coupling effects of active material systems. Then an accurate method of finding the work throughput of load coupled systems is derived for a general system starting from the integral expressions for work. The results of this derivation are presented and simplified to illustrate the work output and actuation efficiency in three examples.

Chapter 3, **Design and Validation of Component Testing Facility**, presents the design of a general purpose testing facility for uniaxial compressive tests. It was decided that a new testing facility needed to be built to enable testing of materials working against programmable impedances, therefore the design and validation of the testing facility is presented. Since the facility was designed

as a broad-use facility, emphasis is placed on the requirements for the design, the design limitations, and the final performance of the design.

Chapter 4, **Validation of Theoretical Results**, presents the testing methodology used to validate the theory presented in chapter 2. The chapter begins with a general overview of what needed to be tested and how this was to be achieved. Sample selection and material property validation is presented next. The overview is followed by an explanation of the different measurements that were taken for both the linear and non-linear tests by using a stack as the active material tested in the component testing machine with a specified impedance. The results of the linear and non-linear tests are presented. The test results are compared to the theoretical results expected from the derivation. After a comparison has been made, the results are discussed and possible implications presented. The chapter concludes with the design and theoretical performance of a device that could be used to load an active material non-linearly to increase its performance during operation.

Chapter 5, **Conclusions and Recommendations for Future Work**, concludes the document. This chapter presents the overall implications of the work presented in the document and highlights the important points of the research. Then, recommendations for additional work in this area are presented. Conclusions and recommendations are made for expanding the derivation of the use of non-linear loading functions, for increasing the performance of an active material, and for possible improvements and additional features of the Component Testing Device.

Chapter 2

Analysis of the Actuation Efficiency of Electro-mechanically Coupled Systems

In order to discuss and compare the different performance metrics of an actuator system, the system and metrics must be explicitly defined and stated. The system examined is a generalized system comprised of a linear or non-linear electro-mechanically coupled core with a generalized energy source input, working against a generalized load that has some defined linear or non-linear relation. A schematic of the system is shown in fig. 2-1. The coupled electro-mechanical core could be a variety of systems, including a discrete actuator and magnification mechanism, a mechanically coupled system like a bender, or hydraulic actuation system. The input into this system is any generalized scalar work pair, here represented by charge and voltage. The output of the system is another generalized work pair, here represented by force and displacement. The generalized work output could also be represented by a moment-rotation pair, a pressure-volume pair, or any other scalar work product. Because of the general method used in the derivation, the resulting expressions can be used for the analysis of any coupled system.

Work output and actuation efficiency expressions are derived for a generalized system with non-linear material and structural relations that can be expressed in a two-by-two block form. The coupled system is working against a load while externally undisturbed. Three example systems are presented using simplifications of the general expressions. These systems are two one-dimensional spring/actuator systems with a linear and non-linear spring constant, and a preloaded bender

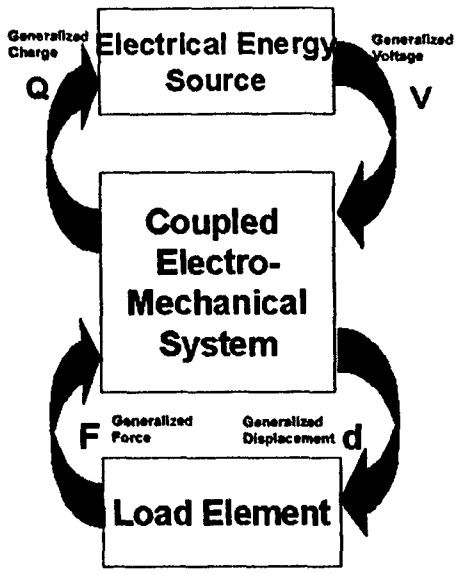

Figure 2-1: Schematic of general system representation. The electro-mechanical coupling block can be a variety of distributed and discrete systems with linear and non-linear relations. The load element is a generalized work pair with either a linear or non-linear relations.

device. For the derivation, a general two block representation of the piezoelectric coupled system is used.

2.1 Definition and Metrics

The metrics that will be compared are the work output of the system and the actuation efficiency. The work output is defined as mechanical work. The actuation efficiency is a true thermodynamic efficiency and is defined as the ratio of the work output to work input. The mathematical definitions for each of these terms are given in the following section, as well as the definitions for other useful terms.

2.1.1 Piezoelectric Material Relations

For the low-power region, piezoelectric materials follow a determined linear set of governing equations that describe the electrical and mechanical interaction of the material. These equations have four system states: **T**, the stress in the system in six directions; **S**, the strain in the system in six directions; **E**, the electric field in the system in three directions; and **D**, the electric displacement in

the system in three directions. These system states combine into two governing equations, making two dependent variables and two independent variables. The dependent variables combine with material constants to give equations for the independent variables. Typically this combination of variables is expressed in matrix form as

$$\begin{Bmatrix} \mathbf{S} \\ \mathbf{D} \end{Bmatrix} = \begin{bmatrix} \mathbf{s^E} & \mathbf{d}^t \\ \mathbf{d} & \varepsilon^{\mathbf{T}} \end{bmatrix} \begin{Bmatrix} \mathbf{T} \\ \mathbf{E} \end{Bmatrix} \tag{2.1}$$

where $\mathbf{s^E}$ is the mechanical stiffness at constant electric field, $\mathbf{d}$ is the electro-mechanical coupling, and $\varepsilon^{\mathbf{T}}$ is the dielectric constant at constant stress. This nine by nine matrix is typically reduced using either plain strain assumptions, plain stress assumptions, or by looking at one-dimensional relations only. Most of the work in this document will be based on a one-dimensional representation of the active material, thereby using only a two by two representation of the entire matrix.

2.1.2 Mechanical Work

The mechanical work of a system is typically described as the integral of force times the derivative of displacement, or mathematically

$$W_M = \int_{x_{initial}}^{x_{final}} F dx \tag{2.2}$$

When assuming a linear force relationship, for example a spring system with $F = kx$, this relationship becomes

$$W_M = \frac{1}{2} k x^2 \tag{2.3}$$

which is the familiar expression for the work done by a spring. In this derivation we will typically be looking at the active material in terms of the force and displacement relations, however the work can also be expressed more generally in terms of the stress and strain state of the system. Therefore, the work expression in equation 2.2 can be transformed into a relationship with stress and strain. The expression that relates force to stress is

$$F = TA \tag{2.4}$$

where A is the cross-sectional area of the material. The expression that relates strain to displacement is

$$S = \frac{x}{l} \tag{2.5}$$

where l is the length of the material.

Substituting the expressions in equations 2.4 and 2.5 into equation 2.2 results in the following expression for mechanical work in terms of stress and strain

$$W_M = \int_{S_{initial}}^{S_{final}} TAldS \tag{2.6}$$

Generalizing this expression to allow for non-constant material properties over a volume is facilitated by combining the area and length terms in equation 2.6 into a volume integral as follows

$$W_M = \int_{\mathrm{Vol}} \int_{S_{initial}}^{S_{final}} TdS \cdot d\mathrm{Vol} \tag{2.7}$$

Either equation 2.2 or equation 2.7 will be used to find the mechanical work of the system. In most actuator systems the mechanical work is the output work of the system. Therefore, the generalized force/displacement product is considered positive when work is being done on the load.

2.1.3 Electrical Work

The electrical work of a system is found in much the same way the mechanical work is found by taking the integral of the voltage times the differential charge. The typical electric work expression is

$$W_E = \int_{Q_{initial}}^{Q_{final}} VdQ \tag{2.8}$$

When using this expression to find the work of a linear system, such as a capacitor with a charge relation of $Q = CV$, this relation becomes

$$W_E = \int_{V_{initial}}^{V_{final}} VCdV \tag{2.9}$$

$$W_E = \frac{1}{2}CV^2 \tag{2.10}$$

which is the typical definition of the work, or energy, in a capacitor. In the derivation we are typically going to look at the system using charge and voltage expression for work, however the work expression can be stated more generally using the electric field and electric displacement of the system. Therefore, equation 2.8 can be transformed into an expression that uses electric field and electric displacement. To do this, expressions relating the electric field and electric displacement

to charge and voltage need to be used. The electric field and voltage relation is

$$E = \frac{V}{t} \tag{2.11}$$

where t is the thickness of the material between the electrodes. The relation of charge to electric displacement is

$$Q = DA \tag{2.12}$$

where A is the area of the electrodes which is typically the cross-sectional area of the material.

Using equations 2.11 and 2.12 in equation 2.8 to find an expression for work that uses electric field and electric displacement results in

$$W_E = \int_{D_{initial}}^{D_{final}} EtAdD \tag{2.13}$$

To find a more general expression that allows for the variation of the material parameters over the volume, it is possible to combine the thickness and area terms into a volume integral over the material as follows

$$W_E = \int_{\mathrm{Vol}} \int_{D_{initial}}^{D_{final}} EdD \cdot d\mathrm{Vol} \tag{2.14}$$

Either equation 2.8 or equation 2.14 will be used to find the electrical work in the system. Again, for most actuator systems the electrical work is the input work to the system. Therefore, the generalized charge/voltage product is positive when work is being done on the coupled system.

2.1.4 Actuation Efficiency

Although the material coupling coefficient describes the efficiency with which a material can convert energy between mechanical and electrical work, the coupling coefficient does not always give a good indication of how a material will work in a real loading cycle. The cycle that the material coupling coefficient is derived for is the cycle that maximizes the work conversion of a system, which is appropriate when determining the best compositions for a given material. However, when working in a device, the material coupling coefficient gives an inflated view of how the material will work when perfect loading conditions do not exist. The loading cycle of a typical device applies and extracts work simultaneously. Because of this, there are load coupling effects that can change the efficiency of a working device. Therefore, a better measure of the efficiency of a device might be a

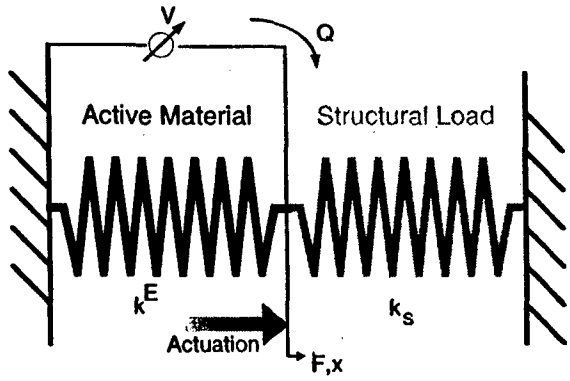

Figure 2-2: Model of a one-dimensional spring/active material system.

ratio of the work out over the work in of a typical loading cycle.

The actuation efficiency of a system is defined as the work out divided by the work in when working over a typical operational cycle of an actuator. In this cycle, the work in is defined as electrical work and the work done on the system is defined as mechanical work. Therefore, the actuation efficiency of a system will be defined mathematically as

$$Ef = \frac{W_{out}}{W_{in}} = \frac{W_M}{W_E} \tag{2.15}$$

2.2 Uncoupled analysis

A general use of an actuator is as a device that is working against a load in only one dimension. Therefore, figure 2-2 shows a typical application of an active material. The figure shows an active material, depicted as a spring with a certain stiffness, working against another spring of a different stiffness that represents a structural load with an associated stiffness. The active material has an applied electric field. The displacement of the attachment point of the two springs is monitored as well as the force in the system. The active material is working one-dimensionally against the load.

By looking at a diagram of the stress-strain relationship of the system in figure 2-2, the current method of finding the actuation efficiency of a system can be explained. A sample figure is shown in figure 2-3. This figure shows the stress-strain relationship of the representative structure, the solid line, and the stress-strain relationship of an active material at a given electrical field, represented by the dashed line. The intersection of these two lines is the stress-strain state of the system at a specific loading, or at a specific electric field. The area under the dashed line representing the

active material is the amount of energy in the active material available for mechanical work at the given electric field as shown in the coupling coefficient derivation, or

$$A_{dashed} = W_{M_{system}} \tag{2.16}$$

The area under the solid line representing the structure is the energy in the structure for any given stress-strain state. The area under the structure line from the intersection of the active material line, represented in the picture by the shaded triangle, represents the amount of work that can be put into the structure, or conversely taken out of the active material. The amount of work represented by this area is referred to as the mechanical work out of the system while working against a load, or

$$A_{shaded} = \int_{x_i}^{x_f} F dx = W_{M_{load}} \tag{2.17}$$

When looking for the actuation efficiency done by the system, it seems reasonable to simply take the amount of work that could be done and compare it to the amount of work actually done on the system since the material coupling coefficient describes the efficiency of the system when the total possible work is done. The ratio of the relative amount of work done can be expressed as a function of the stiffnesses of the load and piezoelectric material as

$$\frac{W_{M_{load}}}{W_{M_{system}}} = \frac{\alpha}{(\alpha+1)^2} \quad \text{where } \alpha = \frac{k_s}{k^E} \tag{2.18}$$

It should be noted that this is the same relationship derived by Spangler and Hall[3]. Mathematically, the maximum area that the shaded triangle can be for linear loads and linear active material relations is a quarter of the area under the material load line which is reached only when the slope of the two lines are equal and opposite, or

$$W_{M_{load_{max}}} = \tfrac{1}{4} W_{M_{system}} \quad \text{when } k^E = -k_s \tag{2.19}$$

The square of the coupling coefficient is the maximum amount of work out divided by the maximum amount of work into the active material, or

$$k^2 = \frac{W_{M_{system}}}{W_{E_{system}}} \tag{2.20}$$

Being able to only get a quarter of the maximum amount of work out of the material translates

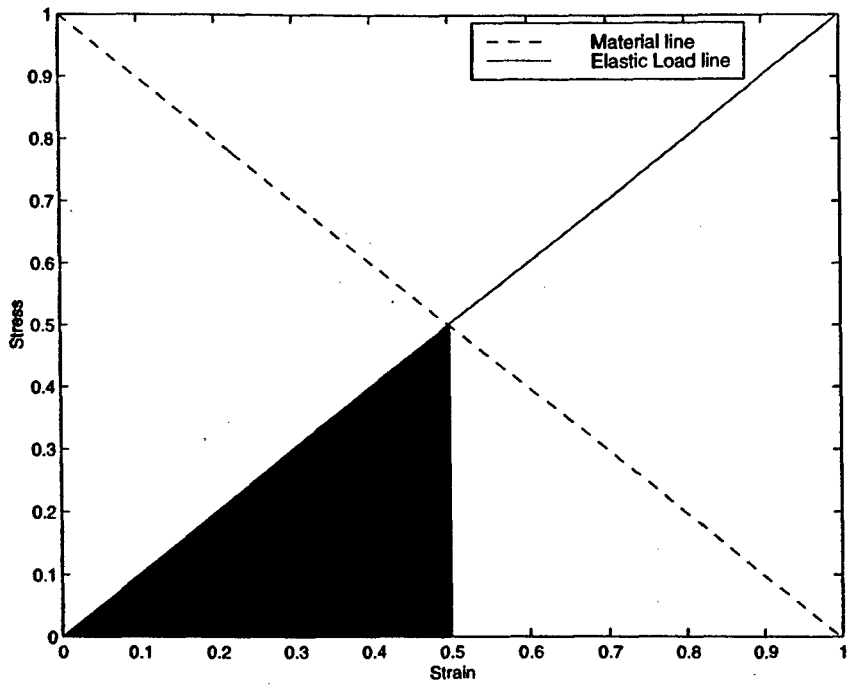

Figure 2-3: Intersection of material and linear structure load lines on a stress-strain diagram.

into being able to get a maximum actuation efficiency of the system of a quarter of the maximum theoretical actuation efficiency, or a quarter of the material coupling coefficient squared. This is shown by

$$\frac{W_{M_{load_{max}}}}{W_{E_{system}}} = \frac{1}{4}\frac{W_{M_{system}}}{W_{E_{system}}} = \frac{1}{4}k^2 \tag{2.21}$$

Although the derivation presented above appears to have no flaws, it doesn't take into consideration the effect that working against a load has on the electrical work into the system. This oversight is remedied in the following section.

2.3 General Derivation of the Work Output and Actuation Efficiency

The derivation of work output and actuation efficiency is initially done for the general case of a coupled system. The derivation is then simplified to look at different example cases. The efficiency is derived for a cycle that a material would see in operation with the active material-structure system externally undisturbed throughout the cycle.

2.3.1 General Derivation Framework

The governing equation for a quasi-static piezoelectric material of general configuration is presented in a general, discrete form. This form can be derived using a variety of methods including Rayleigh-Ritz formulations[7], FEM models, and others; and simplified through the use of static condensation methods.

$$\begin{bmatrix} \mathbf{K}(\mathbf{x},\mathbf{V}) & -\mathbf{p}(\mathbf{x},\mathbf{V})^T \\ \mathbf{p}(\mathbf{x},\mathbf{V}) & \mathbf{C}^S(\mathbf{x},\mathbf{V}) \end{bmatrix} \begin{Bmatrix} \mathbf{x} \\ \mathbf{V} \end{Bmatrix} = \begin{Bmatrix} \mathbf{F} \\ \mathbf{Q} \end{Bmatrix} \tag{2.22}$$

In this equation $\mathbf{x}$ is the displacement vector, $\mathbf{V}$ is the vector of applied electric potentials, $\mathbf{K}$ is the stiffness matrix of the system, $\mathbf{p}$ is the electro-mechanical coupling of the system, $\mathbf{C}^S$ is the capacitance of the system under constant strain, $\mathbf{F}$ is the force vector, and $\mathbf{Q}$ is the charge vector. $\mathbf{K}$, $\mathbf{p}$, and $\mathbf{C}^S$ can be non-linear functions of the independent variables $\mathbf{x}$ and $\mathbf{V}$. In this derivation, only quasi-static systems are being considered, so the dynamic terms are neglected. The use of non-linear material models in the desired form, like that presented by Fripp and Hagood[8] for electrostrictive materials, allow for a complete non-linear material model to be used in this derivation.

Given the framework of eqn. (2.22), it is necessary to understand the relations of the structural load that the coupled system works against. Generally the force-displacement relation for the load can be written as

$$\mathbf{F}_l = \mathbf{k}_l(\mathbf{x}_l)\mathbf{x}_l \tag{2.23}$$

where the subscript l refers to the generalized load. Note that the load relations are not constrained to be linear.

Compatibility and Equilibrium. In order to determine the work equations, it is necessary to determine some expressions that relate the state of the actuator to the state of the structure. The only assumption that is made in this derivation is that the structure and actuator have forces and displacements that are entirely working against each other. From this assumption, the following force balance equation can be expressed by forcing equilibrium

$$\mathbf{F} = \mathbf{F}_l \tag{2.24}$$

Substituting equations 2.23 and 2.22 in equation 2.24 results in the following expression

$$\mathbf{K}(\mathbf{x},\mathbf{V})\mathbf{x} - \mathbf{p}^{\mathbf{T}}(\mathbf{x},\mathbf{V})\mathbf{V} = \mathbf{k}_l(x_l)\mathbf{x}_l \tag{2.25}$$

Enforcing compatibility by requiring $\mathbf{x} = -\mathbf{x}_l$ results in the following expression from equation 2.25

$$\mathbf{x} = \frac{\mathbf{p}^T(\mathbf{x},\mathbf{V})\mathbf{V}}{\mathbf{K}(\mathbf{x},\mathbf{V}) + \mathbf{k}_l(\mathbf{x})} \tag{2.26}$$

This relationship is an implicit relationship between $\mathbf{x}$ and $\mathbf{V}$. The assumption used for the rest of the derivation is that by specifying a voltage level, this equation can be iteratively solved for a specific value of displacement. Therefore, the terms of the equation are assumed to be just dependent on the voltage of the system.

2.3.2 Work Expressions

Electrical Work

Now that the constitutive relations have been derived and an expression for $\mathbf{x}$ has been determined, it is possible to focus on deriving the work in and work out expressions for this actuator and structure system. Starting with the electrical work

$$W_E = \int_{Q_{initial}}^{Q_{final}} \mathbf{V}\delta\mathbf{Q} \tag{2.27}$$

The electrical work for actuator problems is the work into the system. Therefore, the following relation holds

$$W_{in} = W_E \tag{2.28}$$

It is generally desired to find all of the work terms as functions of the applied voltage, $\mathbf{V}$ since the voltage is applied to the system and is directly related to the displacement of the system. Therefore, to find a relation for the electrical work in terms of only voltage, we need to rewrite our expression for $\mathbf{Q}$, Eq. 2.22, without the displacement variable, $\mathbf{x}$. Doing this by substituting equation 2.26 into equation 2.22

$$\mathbf{Q} \;=\; \mathbf{p}(\mathbf{x},\mathbf{V})\mathbf{x} + \mathbf{C}^S(\mathbf{x},\mathbf{V})\mathbf{V} \tag{2.29}$$

$$\mathbf{Q} = \left(\frac{\mathbf{p^T(x,V)p(x,V)}}{\mathbf{K(x,V)+k}_l(x)} + \mathbf{C}^S\mathbf{(x,V)}\right)\mathbf{V} \tag{2.30}$$

Taking the variation of $\mathbf{Q}$ and substituting it into the electrical work expression, Eq. 2.27, results in

$$\begin{aligned} W_{in} = \int_{V_i}^{V_f} \Bigg\{ & \left[\frac{\mathbf{p}^T(\mathbf{V}) + \mathbf{V}\frac{\partial \mathbf{p}^T(\mathbf{V})}{\partial \mathbf{V}}}{\mathbf{K(V)+k}_l(\mathbf{V})} - \frac{\mathbf{p}^T(\mathbf{V})\mathbf{V}}{(\mathbf{K(V)+k}_l(\mathbf{V}))^2}\left(\frac{\partial \mathbf{K(V)}}{\partial \mathbf{V}} + \frac{\partial \mathbf{k}_l(\mathbf{V})}{\partial \mathbf{V}}\right)\right]\mathbf{p(V)} \\ & + \frac{\partial \mathbf{p(V)}}{\partial \mathbf{V}}\left(\frac{\mathbf{p}^T(\mathbf{V})\mathbf{V}}{\mathbf{K(V)+k}_l(\mathbf{V})}\right) + \mathbf{C}^S(\mathbf{V}) + \mathbf{V}\frac{\partial \mathbf{C}^S(\mathbf{V})}{\partial \mathbf{V}}\Bigg\}\mathbf{V}\delta\mathbf{V} \end{aligned} \tag{2.31}$$

Mechanical Work

The work into the structure is the work out of the system, defined by

$$W_M = \int_{x_{initial}}^{x_{final}} \mathbf{F}_l \delta \mathbf{x} \tag{2.32}$$

Since the work on the structure was defined as the work out of the system, the following can be written

$$W_{out} = W_M \tag{2.33}$$

Again, we want to find an expression for the mechanical work out of the system in terms of the applied voltage. This is possible through the use of equation 2.26. Therefore, determining the force in the system in terms of voltage by using equations 2.23 and equation 2.26

$$\mathbf{F}_l = \mathbf{k}_l(x)\mathbf{x} \tag{2.34}$$

$$\mathbf{F}_l = \frac{\mathbf{k}_l(x)\mathbf{p^T(x,V)V}}{\mathbf{K(x,V)+k}_l(x)} \tag{2.35}$$

Taking the variation of equation 2.26 and substituting into the work expression results in

$$W_{out} = \int_{V_i}^{V_f} \frac{\mathbf{k}_l(\mathbf{V})\mathbf{p}^T(\mathbf{V})}{\mathbf{K(V)+k}_l(\mathbf{V})}\left[\frac{\mathbf{p}^T(\mathbf{V}) + \mathbf{V}\frac{\partial \mathbf{p}^T(\mathbf{V})}{\partial \mathbf{V}}}{\mathbf{K(V)+k}_l(\mathbf{V})} - \frac{\mathbf{p}^T(\mathbf{V})\mathbf{V}}{(\mathbf{K(V)+k}_l(\mathbf{V}))^2}\left(\frac{\partial \mathbf{K(V)}}{\partial \mathbf{V}} + \frac{\partial \mathbf{k}_l(\mathbf{V})}{\partial \mathbf{V}}\right)\right]\mathbf{V}\delta\mathbf{V} \tag{2.36}$$

Initially, writing displacement as a function of applied voltage might seem odd since we are looking at the displacement of the spring. However, if we remember that the displacement of the system at any point in time is generated by the applied voltage in the active material at that time,

then writing the displacement this way makes sense.

Actuation Efficiency.

The actuation efficiency is the work out of the system divided by the work into the system. Therefore, equation 2.36 is divided by equation 2.31 to find the actuation efficiency.

2.4 Example of a One-dimensional Linear System

It is possible to illustrate the above derivation through the use of a one-dimensional sample system. The system considered is shown in fig. 2-2. The "three" direction of the system is along the central axis of the springs. Additionally, the spring and piezoelectric are assumed to be of equal cross-sectional area and length. Linear material and spring relations are used.

2.4.1 Material Relations.

The one-dimensional material parameters in the three direction are

$$S_3 = s_{33}^E T_3 + d_{33} E_3 \tag{2.37}$$

$$D_3 = d_{33} T_3 + \varepsilon_{33}^T E_3 \tag{2.38}$$

where s_{33}^E is the mechanical stiffness under constant Electric Field, $d_{33}$is the electro-mechanical coupling, and $\varepsilon_{33}^T$is the dielectric constant under constant stress, all in the "three-three" direction; and S_3 is the strain, T_3 is the stress, E_3 is the Electric Field, and D_3 is the electric displacement, all in the "three" direction.

Rearranging them into equations with stress as a free variable, the equations become

$$T_3 = c_{33}^E S_3 - e_{33} E_3 \tag{2.39}$$

$$D_3 = e_{33} S_3 + \varepsilon_{33}^S E_3 \tag{2.40}$$

by defining e_{33}, $c_{33}^E$and ε_{33}^Sas

$$c_{33}^E = \frac{1}{s_{33}^E} \tag{2.41}$$

$$e_{33} = d_{33}c_{33}^{E} \tag{2.42}$$

$$\varepsilon_{33}^{S} = \varepsilon_{33}^{T} - d_{33}{}^{2}c_{33}^{E} \tag{2.43}$$

where e_{33} is the electro-mechanical coupling of the system, $c_{33}^{E}$is the compliance of the active material under constant electric field, and $\varepsilon_{33}^{S}$is the dielectric constant under constant strain, all in the "three-three" direction. Equations 2.39 and 2.40 become the material relations used for the active material. It is now possible to use the generalized expressions of the governing equation and work expressions to find the work relations in this specialized case.

Finding Expressions for the Terms in the Governing Equation

To find the terms in the generalized governing equation for this specific example, the Ritz method was used. Therefore, the electrical and mechanical mode shapes that fit the boundary conditions of the problems must be found. The electrical mode shape chosen was

$$\psi_E = \frac{x}{l_p} \tag{2.44}$$

where x is the length along the center axis of the spring and l_p is the length of the piezoelectric material. The mechanical mode shape assumed is

$$\psi_M = \frac{x}{l_p} \tag{2.45}$$

These assumed mode shapes were used to find the stiffness term, K; the capacitance term, C^S; and the electro-mechanical coupling term, p. Finding the stiffness term results in

$$K_{33} = \frac{c_{33}^{E}A_p}{l_p} \tag{2.46}$$

Using the electrical mode shape of equation 2.44 results in a capacitance term of

$$C_{33}^{S} = \frac{\varepsilon_{33}^{S}A_p}{l_p} \tag{2.47}$$

In a similar manner, the electro-mechanical coupling term can be found as

$$p_{33} = \frac{e_{33}A_p}{l_p} \tag{2.48}$$

It is now possible to use equations 2.46, 2.47, and 2.48 in the previously derived expressions for work and actuation efficiency.

The final relation that needs to be derived in order to find the work expressions is the stiffness of the structure in terms of its compliance. As is found above, for a one-dimensional structure, the stiffness term is a combination of the compliance, length and cross-sectional area of the structure. Therefore, without derivation, the following relation is stated as the stiffness of the load spring

$$k_s = \frac{c_s A_s}{l_s} \tag{2.49}$$

where the subscript s refers to the spring. Since one of the initial assumptions in this example is that the piezoelectric material and spring have the same effective length and cross-sectional area, the following relations will be used

$$A_s = A_p = A \tag{2.50}$$

$$l_s = l_p = l \tag{2.51}$$

2.4.2 Electrical and Mechanical Work.

The electrical and mechanical work in the system can now be found using the relations derived in the previous section. The relations can be expressed in terms of K, C^S and p; or the volume terms can be explicitly expressed and the equations found in terms of c_{33}^E, ε_{33}^S, and e_{33}. Both will be done here.

From equation 2.31, the electrical work in expression is

$$W_{in}^{\bullet} = \frac{1}{2}\left(\frac{p_{33}^2}{K_{33} + k_s} + C_{33}^S\right) V^2 \tag{2.52}$$

Adding the definitions of K, C^S, p, and k_s found in equations 2.46, 2.47, 2.48, and 2.49 and using the area and length relations of equation 2.50 and equation 2.51 results in the following simplified expression for the electrical work

$$W_{in} = \frac{1}{2}\frac{A}{l}\left(\frac{e_{33}^2}{c_{33}^E + c_s} + \varepsilon_{33}^S\right) V^2 \tag{2.53}$$

The mechanical work out expression comes from equation 2.36. Adding in the terms from this

derivation results in

$$W_{out} = \frac{1}{2} k_s \left(\frac{p_{33}}{K_{33} + k_s} \right)^2 V^2 \tag{2.54}$$

Making the same substitutions as were made in the electrical work expression results in the following expression for mechanical work

$$W_{out} = \frac{1}{2} \frac{A}{l} c_s \left(\frac{e_{33}}{c_{33}^E + c_s} \right)^2 V^2 \tag{2.55}$$

The work relations can be found in terms of the material coupling coefficient, the stiffness ratio and work into an idealized capacitor. The material coupling coefficient for the extensional mode of operation[2] is

$$k_{33}^2 = \frac{{d_{33}}^2}{s_{33}^E \varepsilon_{33}^T} \tag{2.56}$$

The stiffness ratio of the system, a measure of relative stiffnesses of the elements, is

$$\alpha = \frac{k_s}{K} \tag{2.57}$$

The ideal work into a capacitor is

$$W_{ideal_in} = \frac{1}{2} \frac{A}{l} \varepsilon^T V^2 \tag{2.58}$$

From eqns. (2.31) and (2.36), the electrical and mechanical work expressions become

$$W_{in} = \left\{ 1 - \left(\frac{\alpha}{1+\alpha} \right) k_{33}^2 \right\} W_{ideal_in} \tag{2.59}$$

$$W_{out} = \frac{\alpha}{(1+\alpha)^2} k_{33}^2 W_{ideal_in} = \eta_{mech} k_{33}^2 W_{ideal_in} \tag{2.60}$$

where

$$\eta_{mech} = \left[\frac{\alpha}{(\alpha+1)^2} \right] \tag{2.61}$$

When the work output in written in a non-dimensionalized form, it is apparent that the work output is just a relation of the stiffness ratio multiplied by the material coupling coefficient. The stiffness ratio relation, henceforth referred to as η_{mech}, arises from the ratio of the work applied to the load over the energy available to do mechanical work. By examining the force-displacement diagram of the system, shown in fig. 2-3, the η_{mech} term can be explained. The area under the dashed line, the material load line, is the energy or work in the system available to do work on a

load. The area under the intersection of the solid line, the structural load line, and the material load line is the work put into the structure. η_{mech} is the ratio of these two values, the amount of work into the system compared to the available energy based on the stiffness ratio of the system.

2.4.3 Actuation Efficiency.

Using equations 2.53 and 2.55 to find the actuation efficiency expression results in

$$Ef = \frac{c_s \left(\frac{e_{33}}{c_{33}^E + c_s} \right)^2}{\frac{e_{33}^2}{c_{33}^E + c_s} + \varepsilon_{33}^S} \tag{2.62}$$

The expression for the actuation efficiency, eqn. (2.62), can be written in terms of the material coupling coefficient, k_{33}, and the compliance ratio, α, through the use of the relations found in eqns. (2.41) through (2.43) in order to illuminate the significance of the expression.

$$Ef = \frac{W_{out}}{W_{in}} = \frac{\left[\frac{\alpha}{(\alpha+1)^2} \right] k_{33}^2}{\left\{ 1 - \left(\frac{\alpha}{\alpha+1} \right) k_{33}^2 \right\}} \tag{2.63}$$

The numerator of eqn. (2.63) contains the term, $\left[\frac{\alpha}{(\alpha+1)^2} \right] = \eta_{mech}$, that quantifies the area under the material load line captured by the linear spring, or the ratio of the work done by the system to the energy available to do work. η_{mech} is the same quantity defined by Spangler and Hall[3] as η_{im} when discussing the maximum amount of strain energy transferable to a linear device. The effect of the load on the work into the system can be seen in the term $\left(\frac{\alpha}{\alpha+1} \right)$ in the denominator of eqn. (2.63). By setting this term equal to zero the load effects on the system are neglected and the expression looks like the expression for non-dimensionalized work output. Setting the stiffness ratio, α, to one reduces the new expression to the value found in the uncoupled analysis of the system efficiency of $\frac{1}{4}k_{33}^2$.

2.4.4 Results of the One-dimensional Simplification

It is necessary to look at what the expressions derived above mean for the design and performance of a simple one dimensional system. Figure 2-4 shows the actuation efficiency in the one-dimensional case as a function of the stiffness ratio, α, for various values of the coupling coefficient, k. Figure 2-4 also plots the variation of the non-dimensionalized work output for various values of the coupling

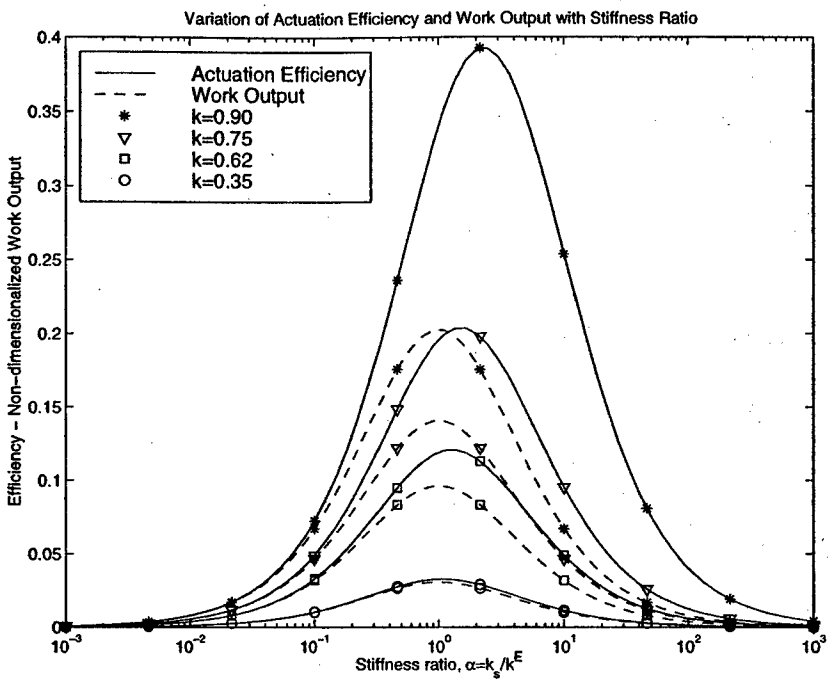

Figure 2-4: Actuation efficiency variation with structural stiffness for a one-dimensional system of an active material working against a linear load. The actuation efficiency is plotted for varying values of k, the coupling coefficient, and α, the stiffness ratio.

coefficient.

The figure shows that for small values of the coupling coefficient, the actuation efficiency closely matches the non-dimensionalized work output of the system because the electro-mechanical coupling is weak. However, for larger values of the coupling coefficient, the stronger electro-mechanical coupling results in a divergence of the actuation efficiency from the non-dimensionalized work output. Additionally, as the coupling coefficient increases, the peak actuation efficiency occurs at stiffness ratios greater than one, unlike the peak non-dimensionalized work output which always occurs at the impedance matched condition.

A common belief is that the maximum efficiency of a one-dimensional system working against a linear structure is a quarter of the square of the coupling coefficient. This occurs when the stiffness of the spring is equal to the stiffness of the piezoelectric material, making η_{mech} equal to one-quarter. Although this impedance matched condition provides the most work *done* by the active material, taking the load coupling of the system into account actually makes the most *efficient* stiffness ratio greater than 1 for large values of the coupling coefficient. The actuation efficiency at this larger

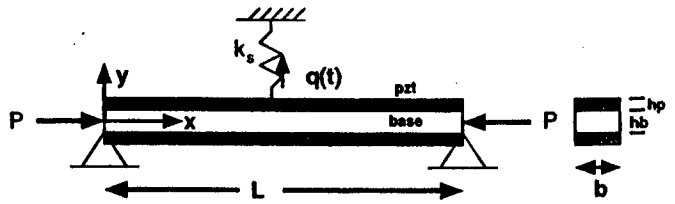

Figure 2-5: Model of bender structure being analyzed.

stiffness is also significantly higher than the maximum actuation efficiency predicted by the work output expression. Therefore, when systems are designed to maximize efficiency, it is actually beneficial to use an active material that is more compliant than the load it is working against given the active material has a large coupling coefficient. This also underscores the importance of using the fully coupled analysis when designing coupled systems for efficiency.

2.5 Example of a Bender Device

To further appreciate the importance of the load coupling on a system, the example structure presented by Lesieutre and Davis[1] as a method for increasing the device coupling coefficient is examined for its work output and efficiency characteristics. The model proposed by Lesieutre and Davis shown in fig. 2-5 is that of a bender, composed of two piezoelectric wafers bonded to a substrate, with a destabilizing preload on both ends. In this example problem, Lesieutre and Davis demonstrated the effect a destabilizing mechanical preload has on the value of the device coupling coefficient. Their derivation of a device coupling coefficient follows the derivation of a material coupling coefficient using the constitutive relations applicable to the device. Through the derivation, they demonstrate that an "apparent" definition of the device coupling coefficient goes to one as the preload applied goes to the critical buckling load. From this result, they imply that it is possible to get more work out of the device for the same amount of work applied to the device. The following sections will compare the device coupling coefficient in relation to the actuation efficiency.

2.5.1 Lesieutre and Davis' results

The governing equation presented by Hagood, Chung and von Flotow[7] shown in eqn. (2.22) is the starting point of the derivation done by Lesieutre and Davis. Because the system is a two-dimensional system, one would expect to use the full matrix relations. They, however, defined **q**

as the out-of-plane deflection of the system, allowing for a one-dimensional representation of the system. Therefore, the matrix relations defined in eqn. (2.22) become in-plane components with the exception of the electro-mechanical coupling term which has an in-plane and out-of-plane coupled relation.

The following mechanical and electrical assumed modes for a beam in bending were used.

$$\psi_M = \sin\left(\tfrac{\pi x}{L}\right) \quad \psi_E = \tfrac{y}{h_p}$$

The use of these mode shapes resulted in the following expressions for the stiffness, capacitance and electro-mechanical coupling of the beam without a preload.

$$K = \frac{\pi^4 b}{2L^3}\left[\frac{2c_p^E}{3}\left(h_p^3 + \frac{3}{2}h_b h_p^2 + \frac{3}{4}h_b^2 h_p\right) + \frac{h_b^3 c_b^E}{12}\right] \tag{2.64}$$

$$C^S = \frac{2\varepsilon_{33}^S Lb}{h_p} \tag{2.65}$$

$$p = 2be_{13}\frac{\pi}{L}\left(h_p + h_b\right) \tag{2.66}$$

Effect of the Device Preload

The axial preload on the system adds another work term to the expression used to derive eqn. (2.22). This work term is similar in nature to the stiffness term found above and is often seen as a stiffness reduction. Lesieutre and Davis included this axial preload term in the stiffness term, but found the preload term independently since the device preload adds to the total work done on the system. Using the assumed mechanical mode shape, the axial stiffness term is

$$K_G = P\frac{L}{2}\left(\frac{\pi}{L}\right)^2 \tag{2.67}$$

This term is subtracted from the stiffness term K of eqn. (2.64) resulting in a new stiffness term, $K_t = K - K_G$.

Device Coupling Coefficient

Lesieutre and Davis argue that although the mechanical preload adds to the amount of work put into the system, the work from the preload should be ignored when looking at the device coupling coefficient of the system since the preload can be applied statically. The device coupling coefficient

that they derive when just considering the electrical work is referred to as the "apparent" coupling coefficient. Since work is being done on the system by the preload, they also look at the coupling coefficient with the preload work added in, referred to as the "proper" coupling coefficient. The cycle that they use in the derivation of the device coupling coefficient is equivalent to the work cycle used in the material coupling coefficient derivation.

Their derivation results in the following "proper" and "apparent" coupling coefficients, rewritten from their original form as expressions in terms of a matrix coupling term, $k_m^2 = \frac{p^2}{K_t C^S}$

$$k_p^2 = \frac{k_m^2}{k_m^2 + 1 + \frac{K_G}{K_t} k_m^2} \tag{2.68}$$

$$k_a^2 = \frac{k_m^2}{k_m^2 + 1} \tag{2.69}$$

2.5.2 Work output approach

We now focus on finding the actuation efficiency of the system. A spring of stiffness k_s acting at the center of the beam represents the load. The electrical work into the system is found by simplifying the expression found in eqn. (2.31) for this example, resulting in

$$W_{in_E} = \frac{1}{2}\left(\frac{p^2}{K_t + k_s} + C^S\right) V^2 \tag{2.70}$$

There are two forms of mechanical work present in the system; the displacement that the spring sees and the work done on the system by the mechanical preload device. For this problem, the work into the spring is the work out of the system. The mechanical work done on the spring is

$$W_{out} = \frac{1}{2} k_s \left(\frac{p}{K_t + k_s}\right)^2 V^2 \tag{2.71}$$

The mechanical work done by the preload is found directly from the expression for the mechanical work using eqn. (2.67) as the stiffness seen by an axial load.

$$W_{in_M} = \frac{1}{2} K_G \left(\frac{p}{K_t + k_s}\right)^2 V^2 \tag{2.72}$$

Actuation Efficiency

To better illustrate the effect of the external load on the system performance, the derivation of the device coupling coefficient by Lesieutre and Davis[1] has also been adopted for the actuation efficiency. The "apparent" actuation efficiency is the ratio of the mechanical work out only to the electrical work in. The "proper" actuation efficiency includes the preload work with the electrical work. In coupled systems where work is being done on the environment, the "proper" definition of the efficiency is the correct efficiency expression since the preload work cannot be considered a steady-state source of energy in the system.

The "proper" actuation efficiency can be found in terms of the stiffness ratio $\alpha = \frac{k_s}{K_t}$, and matrix coupling term, k_m^2, as

$$Ef_p = \frac{W_{out}}{W_{in_E} + W_{in_M}} = \frac{\left[\frac{\alpha}{(1+\alpha)^2}\right] k_m^2}{\left(\frac{1}{1+\alpha}\right) k_m^2 + 1 + \frac{K_G}{K_t(1+\alpha)^2} k_m^2} \tag{2.73}$$

and the "apparent" actuation efficiency is

$$Ef_a = \frac{W_{out}}{W_{in_E}} = \frac{\left[\frac{\alpha}{(1+\alpha)^2}\right] k_m^2}{\left(\frac{1}{1+\alpha}\right) k_m^2 + 1} \tag{2.74}$$

2.5.3 Remarks on the Bender Device Example

In order to easily compare the device coupling coefficient and actuation efficiency expressions, sample values are presented in table 2.1. Figure 2-6 plots η_{mech} (eqn. (2.61)) times the square of the "apparent" coupling coefficient, η_{mech} times the square of the "proper" coupling coefficient, the "apparent" actuation efficiency, and the "proper" actuation efficiency all against the ratio of the preload value to the critical buckling load for this problem. The stiffness ratio, α, is 0.7 at zero preload value. The "apparent" device coupling coefficient goes to infinity as the mechanical preload increases. This is to be expected since K_t becomes small as the preload increases until K_G (eqn. (2.67)) exactly cancels K (eqn. (2.64)). However, the "apparent" actuation efficiency of the device does not go to infinity as would be assumed since the "apparent" device coupling coefficient does. As is also expected, the "proper" coupling coefficient goes to zero as K_t becomes small and K_G becomes large. However, the "proper" actuation efficiency does not approach zero or even follow the same downward trend of the "proper" coupling coefficient. The discrepancy is due to

Base Beam (aluminum)

h_b	thickness	0.0010
b	width	0.0100
L	length	0.1000
c_b^E	Young's Modulus	7.000e+10
ρ_b	density	2750

Piezoelectric Ceramic (PZT-5A; full set of material constants)

h_p	thickness	0.0005
c_p^E	Young's Modulus (constant electric field)	6.125e+10
e_p	piezoelectric coefficient	-10.48
ε_p^S	dielectric permittivity (constant strain)	1.330e-8
ρ_p	density	7250

Axial Load

P	axial load (compression is positive)	

Table 2.1: Definition of variables and sample numerical values for bender device problem as used by Lesieutre and Davis.

the relative output work value of the system.

The work in and work out of the system for various preload values are shown in fig. 2-7. Examining this figure explains the trends shown in fig. 2-6. Although the total work into the system increases with increasing preload more than the work out of the system, the relative increase of the work out is much greater than the relative increase of the work in.

The effect of load stiffness is illustrated in fig. 2-8. This figure plots the same equations as fig. 2-6 but against the stiffness ratio, α. The preload value used is 75% of the critical buckling load. As is shown, the stiffness of the load does influence the actuation efficiency of the system. The difference in the "proper" versus the "apparent" work ratio decreases as the stiffness of the load spring increases. Again, the actual work values divided are shown in fig. 2-9.

The results of the preloaded bender example show two things. First, it shows that for most conditions in this example, the device coupling coefficient can be used for an initial estimate of the efficiency of a system working against a load. The results also show that when an accurate value of the efficiency is needed, a fully coupled analysis is necessary. However, before any conclusive statements can be made about the device coupling coefficient's comparison to the actuation efficiency, the derivation of both quantities must be performed on additional devices and the results compared.

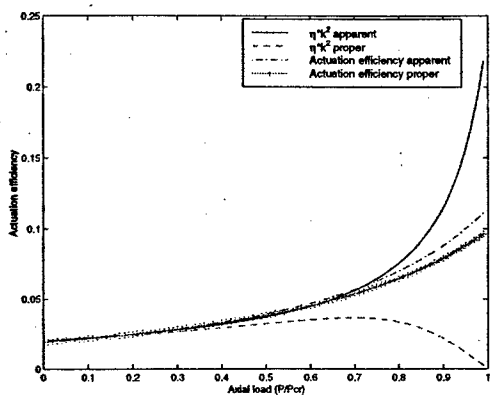

Figure 2-6: Actuation efficiency and device coupling coefficient against the mechanical preload of the system, plotted for $\frac{k_s}{K} = 0.7$.

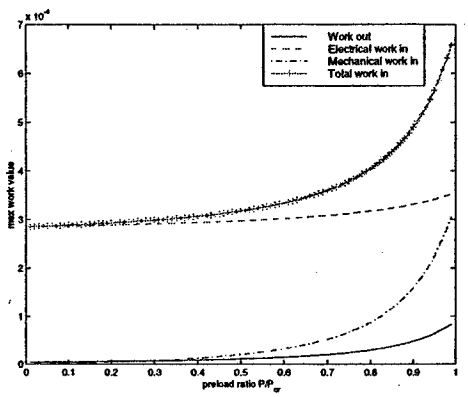

Figure 2-7: Work in and work out expressions plotted for varying values of system preload. Values plotted are the maximum work values assuming a 100 V peak input voltage.

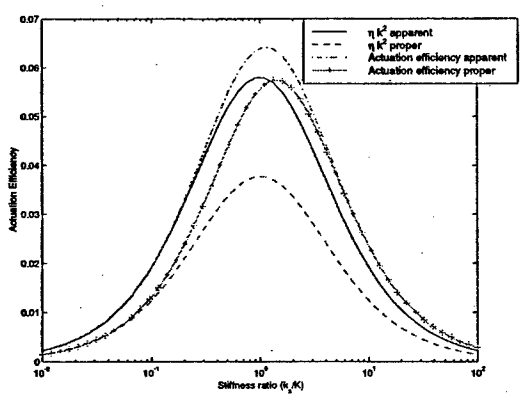

Figure 2-8: Actuation efficiency and device coupling coefficient against ratio of spring stiffness of the system, plotted for $\frac{P}{P_{cr}} = 0.75$.

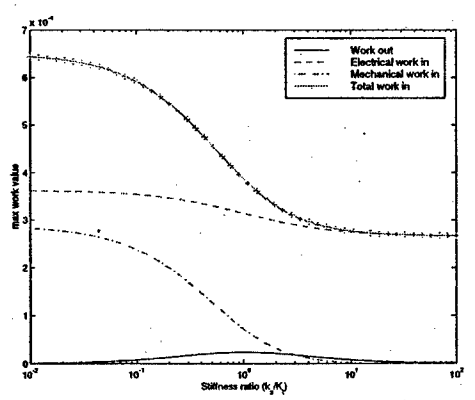

Figure 2-9: Work in and work out expressions plotted for varying values of stiffness ratio. Values plotted are the maximum work values over a cycle with 100 V maximum input voltage.

2.6 Coupled Actuation Efficiency of Non-linear Systems

Although examining the work output and actuation efficiency for work against a linear load gives insight into the work flow in a system, it doesn't provide a way to increase the work being done by the active material. However, by examining a system that is working against a non-linear load, it is possible to find a way to actually increase the work done on the load.

The motivation for looking into non-linear loads comes from the diagram showing the intersection of a material load line and a structural load line on a force-displacement graph, such as that shown in fig. 2-3. From this diagram, we know that the work out of the structure when working against a load is the area under the structural load line when it intersects with the material load line. It is also known that the total amount of energy available to do mechanical work is the area under the material load line. Therefore, the problem is to find a curve that encompasses more area under the material load line before they intersect and to determine if this new line actually increases the actuation efficiency of the active material.

Defining the non-linear loading function as a non-linear stiffness term, $k_s(q)$, the work ratio can be found by following the steps used in the general derivation presented in section 2.3. The same one dimensional spring system, shown in fig. 2-2, is used with a non-linear spring instead of a linear spring. Using linear material relations, the derivation equates forces and opposite deflections and solves for the work in and work out of the system.

2.6.1 Work derivation

Beginning with the system shown in fig. 2-2, where the material relationships are given in eqns. 2.39 and 2.40 and the spring relationship is given by:

$$F_s = k_s(x)x_s \tag{2.75}$$

Equating forces and opposite displacements, we have the following relationship for displacement similar to eqn. (2.26)

$$x = \frac{p_{33}V}{K_{33} + k_s(x)} \tag{2.76}$$

Unlike the linear case, eqn. (2.76) does not represent a closed form solution for displacement because the load stiffness, $k_s(x)$, varies with displacement. However, for a given value of voltage, V, eqn. (2.76) can be solved recursively to determine the value of displacement, x, and stiffness, $k_s(x)$,

that satisfies the relationship. Therefore, the displacement and load stiffness are only functions of the applied voltage and can be represented as $x(V)$ and $k_s(x(V))$ or simply $k_s(V)$.

Again, the integral form of the expression for work as presented in eqn. (2.32) is used. Simplifying eqn. (2.36) results in

$$W_M = \int_{V_i}^{V_f} \left(\frac{k_s(V)}{K_{33}+k_s(V)}\right) p_{33}V \left(\frac{p_{33}}{K_{33}+k_s(V)} - \frac{p_{33}V}{(K_{33}+k_s(V))^2}\frac{\partial k_s(V)}{\partial V}\right)\delta V \tag{2.77}$$

In the same manner, it is also possible to determine the energy into the system while working against a non-linear load. Simplifying the expression found in eqn. (2.31) results in the following equation for work in

$$W_{in} = \int_{V_i}^{V_f} \left\{C_{33}^S V + \frac{p_{33}^2 V}{K_{33}+k_s(V)}\left[1 - \frac{V}{K_{33}+k_s(V)}\frac{\partial k_s(V)}{\partial V}\right]\right\}\delta V \tag{2.78}$$

The actuation efficiency is found by dividing eqn. (2.77) by eqn. (2.78). Since linear material relations are being used, the actuation efficiency be written in terms of the material coupling coefficient as

$$\frac{W_{out}}{W_{in}} = \frac{\int_{V_i}^{V_f} k_{33}^2 \left(\frac{k_s(V)K_{33}}{(K_{33}+k_s(V))^2}\right)\left(1 - \frac{V}{K_{33}+k_s(V)}\frac{\partial k_s(V)}{\partial V}\right) V\delta V}{\int_{V_{initial}}^{V_{final}} \left\{1 - k_{33}^2 + k_{33}^2\left(\frac{K_{33}}{K_{33}+k_s(V)}\right)\left[1 - \frac{V}{K_{33}+k_s(V)}\frac{\partial k_s(V)}{\partial V}\right]\right\} V\delta V} \tag{2.79}$$

where $k_{33}^2 = \frac{{d_{33}}^2}{s_{33}^E \varepsilon_{33}^T}$.

2.6.2 Remarks on the Non-linear System Derivation

To illustrate the performance increases possible through the use non-linear loading functions, two sample non-linear loads are compared to the impedance matched linear load. The non-linear loading functions were chosen due to their similarity to physically achievable functions using zero spring rate suspension systems. Figure 2-10 depicts the two chosen functions and the linear function for comparison. The expressions used to find these loading functions are:

$$\begin{aligned}
\frac{F_{linear}}{F_{bl}} &= 1\frac{x}{x_{free}} \\
\frac{F_{non-linear1}}{F_{bl}} &= \frac{x}{x_{free}}\left(41\exp^{-5.45\left(\frac{x}{x_{free}}\right)^{\frac{1}{2}}}\right)
\end{aligned}$$

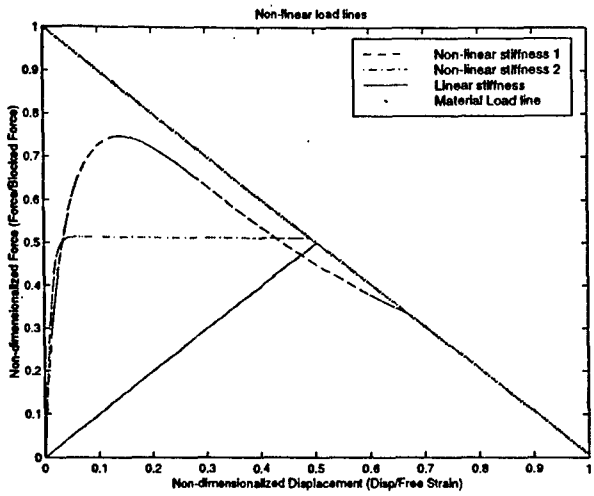

Figure 2-10: Linear and non-linear loading functions with the material load line at maximum applied voltage. The area under the curves represent the amount of output work is possible by each.

$$\frac{F_{non-linear2}}{F_{bl}} = \frac{1}{2}\left(\tanh\left(66\frac{x}{x_{free}}\right)\right)$$

The work out is the area under the loading function curve as depicted on the force-displacement diagram. Pictorially, it seems that the first function encloses twice the area of the linear function, signifying that there should be about twice the work out of the system. The second function looks like it encloses about three times the area of the linear system, corresponding to three times the work out of the system.

Optimal Trajectory Approach for Finding the Maximum. The Principle of Optimal trajectories seems well suited to a problem such as this where it is desired to find the maximum, or minimum, of a function given a set of conditions. Typically, a cost function in terms of x, $\dot{x}$, and t, where x is a state and t is time, is determined as an expression of what needs to be maximized as well as the conditions associated with maximizing it. For this problem, a problem statement might be: To maximize the area under the curve for a given arc length while making the end point lie on the material load line. With this problem statement, a cost function can be written, analyzed using the methods of optimal control, and a trajectory determined that will maximize the area under the curve. Since a function was needed merely to show that it is possible to get more work out of the system with a non-linear load than with a linear load, the maximum function was not found using

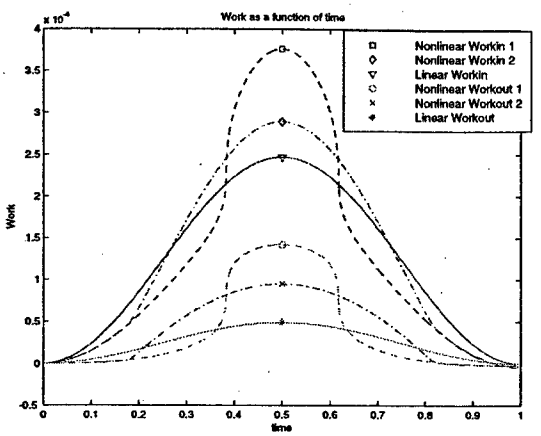

Figure 2-11: Instantaneous Work of non-linear loading functions. The first non-linear loading function can increase the work out of the system, compared to the linear load, by a factor of 3.

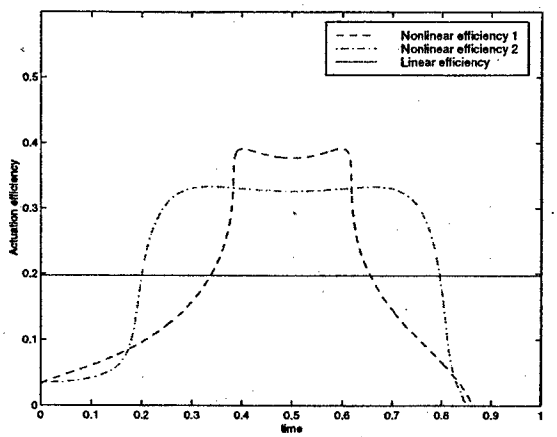

Figure 2-12: Actuation efficiency of non-linear loading functions. First non-linear loading function increases the efficiency of the system by a factor of 2.

this method, but rather a representative curve was chosen.

Results. In the following figures, an adaptive time step was used to ensure that all of system behavior was properly captured. The values used to plot the functions are a coupling coefficient of $k_{33} = 0.75$ and a stiffness ratio of 1 in order to compare the non-linear loading functions with the impedance matched design decision.

Figure 2-11 depicts the instantaneous work done by the system, eqns. (2.77) and (2.78). The work in and work out of the system while working against the two non-linear functions are compared to the work done when working against the linear function. The comparison shows a 99% increase in the work out done by the second non-linear function at the peak of the cycle. The work out of the first nonlinear function increases by 198% when compared to the linear function. However, there is also a corresponding increase in the work into the system when working against the non-linear loads.

Figure 2-12 shows the actuation efficiency of the system with each of the non-linear loading functions and the linear loading function, eqn. (2.63). The non-linear functions increase the actuation efficiency of the system significantly compared to the linear actuation efficiency even though there is an absolute increase in the work into the system. The second non-linear function increases the actuation efficiency of the system over the linear efficiency by 75%. The first non-linear loading function increases the actuation efficiency of the system by almost 100%.

These results show that the use of non-linear loading functions theoretically make it possible to increase the work out of the system for the same applied maximum electric field. Additionally, the increase in work output corresponds to an increase in the actuation efficiency of the system. Therefore, with the correct non-linear loading function, significant increases in the useful performance of active material systems may be possible.

2.7 Conclusions

The work presented demonstrates the need for using the fully coupled system equations when examining the actuation efficiency of a coupled system in normal operating conditions. It has shown that the electro-mechanical coupling terms affect the expected performance for linear systems as well as non-linear systems. The work has also demonstrated the importance of looking at the true actuation efficiency of a system rather than relying on the material coupling coefficient as an approximate measure of the actuation efficiency of a system. However, it was shown that the device coupling coefficient does give a reasonable initial approximation of the efficiency of a system.

Through the use of the work expressions for a system under constant operation while working against a load, it has been possible to demonstrate a method for achieving a higher actuation efficiency over the same voltage cycle by utilizing the coupled nature of the piezoelectric governing equations. The coupled nature allows for a greater actuation efficiency and work output of systems that are working against a non-linear loading function instead of a typical linear load.

To get the fullest application of this work, it is necessary to design loading devices that load the active material non-linearly while loading the object it is working against linearly. When an efficient device of this kind is developed, greater actuation efficiency of active materials can be achieved when they are working in many applications. This derivation can also be expanded to include other classes of materials with similar results.

Chapter 3

Design and Validation of the Component Testing Facility

3.1 Motivation for the Component Tester

In order to verify the proposed derivation of the actuation efficiency, it is necessary to devise a test where it is possible to measure the work, both mechanical and electrical work, of an active material while working against a load. The guidelines for the test are that it must uniaxially allow an active material to work against a specified load, either linear or non-linear, and electrical and mechanical work must be measured. These guidelines led to the design and fabrication of a comprehensive compressive testing machine.

The comprehensive compressive testing machine was designed and built to test many of the different testing environments needed to test active materials, typically stacks and single crystals. Therefore, many of the requirements and design decisions were not based solely on the testing requirements for the verification of work throughput in active materials working against loads.

3.2 Component Tester Design Requirements

The baseline requirements of the component tester are derived from general stack testing requirements. It is designed to be a full scale testing facility to comprehensively test most properties of active materials. Generally, the testing requirements are devised to enable testing that is not currently possible with commercially available machines. The eight main requirements identified

are:

- To provide uniaxial testing with load application up to 8900 N and programmable impedances with a force resolution of 100mN
- To provide closed-loop testing capabilities at frequencies up to 1 kHz
- To provide a testing facility that accommodates samples from 0 to 120 mm long
- To provide position sensing of up to 130 microns at an accuracy of 30 nm
- To provide temperature environments of -50 to 200°C
- To provide the capability to perform "free strain" and "blocked force" tests
- To compensate for non-parallelism in the sample faces
- The ability to test most kinds of piezoelectric, electrostrictive, magnetostrictive and magneto shape-memory materials

As the design progressed, it became apparent that some of these requirements were harder to meet than others. The main "design driver" requirement is the ability to test samples at 1 kHz. This requirement not only affected the mechanical design of the system by constraining the first axial mode to be above 1 kHz, but it also constrained the piezoelectric positioning units to certain stiffnesses and capacitances. The resolutions of these issues are explained in greater detail in sections 3.4.1, 3.5.4, and 3.5.5.

Since the temperature testing facility was not needed for the tests performed, a facility was designed but not constructed. The design is discussed in some detail in section 3.4.4, but is not carried farther than that.

The satisfaction of the rest of the design requirements is discussed throughout the following sections where the complete design is presented. Where applicable, the satisfaction of any particular design requirement is explicitly mentioned.

3.3 Review of Commercially Available and Published Designs

Before a full scale design and fabrication process was started, a variety of commercial testing facilities were examined to determine if they could meet the testing requirements. Machines from

both Mechanical Testing Systems, Inc. and Instron, Inc. were examined to see if their high frequency testing machines could meet the derived requirements for the component testing facility. Unfortunately, the machines produced by each company for high frequency testing either did not allow testing at high enough frequencies, or did not have the position and load resolution necessary to test the materials. An additional problem of the commercially available machines is that a programmable linear or non-linear impedance would be difficult to implement.

Designs published in recent literature were also examined to determine if a previously published design would provide some insight into the design of this testing facility. An important source of design ideas was a paper by P. Pertsch *et al*[9]. They presented the design of a uniaxial compressive loading device for small samples. The facility is circular with a bias load applied by screwing on a plate that works like a jar lid in conjunction with a spring of a test-specified stiffness. The design of the facility they presented was also designed for high frequency testing. From this device, the idea of circular sections to increase the natural frequency of the system was taken. This design modification almost doubled the natural frequency of the component testing facility, allowing for closed loop testing capabilities at much higher frequencies.

Also from published testing facility designs, ideas for smaller improvements for the testing machine were garnered, including different optical measurement systems[10], alignment solutions for uniaxial compressive testing[9, 11, 12, 13], and temperature testing ideas[14, 15]. The methods and benefits of different measurement techniques were weighed and the most practical and relevant ideas were incorporated into the design of the testing facility.

The final testing machine design was primarily based on the previous designs of compressive testing facilities in the Active Materials and Structures Laboratory at MIT; the most recent designed under Eric Prechtl. The previous testing facilities used a laser interferometry system for displacement measurements and a spring loaded screw for loading the system. These facilities were used to measure the compliance of different materials at low load levels and manually applied loading profiles. The basic shape of the testing facility follows the same design with modifications made to enable larger sample size, the incorporation of high frequency positioning devices and automated high frequency testing.

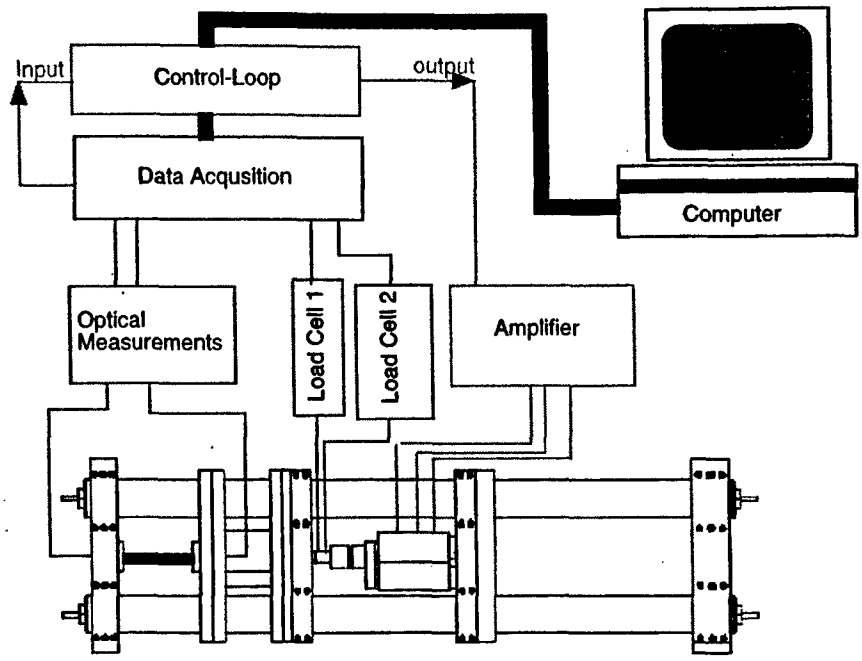

Figure 3-1: Schematic of the Compressive Testing Machine including the Electronic Operation of the System.

3.4 Component Testing Facility Design

The overall design of the component tester is split into the mechanical design and the electronic design. The mechanical design provides the mounting location and load application of the samples and enables the testing of many kinds of samples. The mechanical design carries the brunt of the innovative design in order to achieve the high frequency testing capability by requiring the first axial mode of the testing machine to be above 1 kHz. The electronic design provides the sensing and control capabilities of the testing facility and is primarily made up of commercially available products that have been selected for their sometimes unique ability to provide the exact combination of specifications needed. The electronic design enables some of the difficult measurement requirements to be met as well as providing the means to have closed loop control of the testing machine. A schematic of the component tester is shown in figure 3-1 while a picture of the mechanical design is shown in figure 3-2.

The design is centered around a large cage-like section that allows for the position adjustment necessary to test many different length samples. To avoid requiring the entire sample adjustment

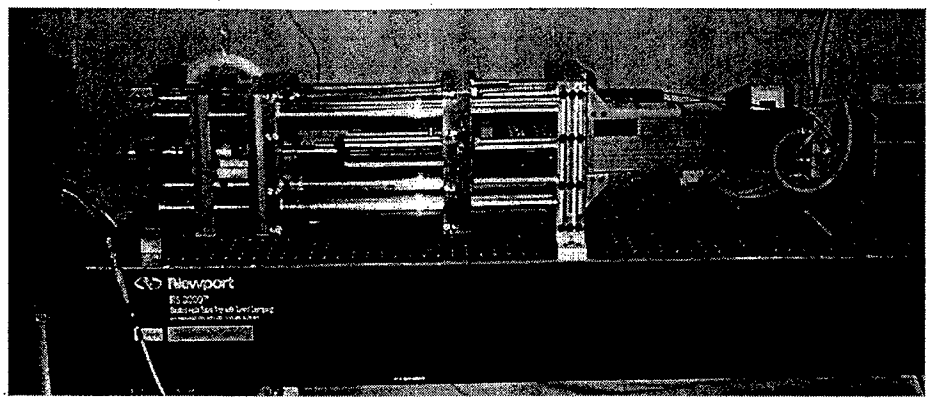

Figure 3-2: Compressive Testing Machine

cage to move during testing, a smaller circular section is suspended in the middle of the large pieces on a flexure mechanism. This circular section is the section that actually provides the high frequency motion to the sample. The circular plates are acted upon by a set of piezoelectric driving stacks that provide the small scale force and motion needed to test the samples. The piezoelectric stacks react against the back wall of the positioning cage which is attached to the large scale positioning device. The large scale positioning device adjusts the position of the entire cage to adjust for sample size and can provide a large preload to the sample when needed. The entire cage assembly is mounted on four rods through embedded bushings to provide ease of motion. Friction clamps from the cage to the rods are also attached to prevent the cage from shifting during sample testing and to provide a motion-free surface for the pzt driving stacks to react against. The entire assembly is equipped with panels that attach to the outside of the end-blocks and react the unfavorable shear and torsional loads that may arise at high frequencies.

Because of the natural split of the design, the different "halves" of the design are discussed as a group with attention paid to the critical components. After the discussion of the main design, the other system components are discussed and the design of the thermal testing facility is presented.

3.4.1 Mechanical Components

In general, there are two forms of mechanical components in the design; specially machined pieces and mechanical positioning and loading devices. The specially machined pieces were all designed with the use of the Parametric, Inc. program PRO Engineer. Most of these pieces were then sent to Hillcrest Precision Machine Corporation to produce the parts. The complete set of drawings are

BEST AVAILABLE COPY

found in Appendix A. There are seven primary parts to the machined parts and an additional four kinds of connecting pieces. The seven parts consist of two end blocks, the back piece of the mounting cage, the two outside front pieces of the mounting cage and the two inside pieces of the cage that provide for load application. The end blocks not only provide positioning of the large rods, but also provide a mounting surface for the sample, a load return path to react the large system loads through, and an attachment location so the machine stays on the table. The connecting pieces are the four large diameter outside steel or alumina rods, the three alumina braces that connect the two inside pieces to provide space for the displacement sensors, four steel rods that connect the the two front pieces of the mounting cage, and four adjustable threaded rods that provide a loading path between the front and back pieces of the mounting cage. The sample is mounted between one of the end blocks and the inside piece of the cage which both have tungsten carbide inserts that provide a stiff mounting surface for the sample. The materials used in the design were chosen for being low-compliance, low weight materials and the pieces were sized for the satisfaction of the functionality of the design while keeping the machine as small and light as practical.

There are three different positioning devices; a large scale linear positioner and two sets of piezoelectric small scale positioning devices. The large scale positioning device is a Morat, Inc. Flexline linear positioner. It provides for the positioning of the cage depending on sample size. It also can provide a large preload force of up to 20,000 N on the entire system while allowing very small motion with each turn of the motor. The piezoelectric positioning devices are two sets of three piezoelectric stacks manufactured by Kinetic Ceramics. One set of stacks has a large free displacement and a small blocked force while the other set has a larger blocked force and a small free displacement. The two different sets of stacks are necessary for getting the best performance of the system depending on the tests run and samples tested. The stiffer stacks allow for increased natural frequencies when a lower total displacement is acceptable. The stack selection was made in order to be able to test all samples identified in all kinds of tests with one set of stacks or the other. More about stack selection is identified in section 3.5.4.

3.4.2 Electronic Components

The electronic components are the core of the measurement and control systems of the testing machine. The measurement systems are the optical displacement sensors and the two load cells with their associated conditioning devices. The control system parts are the motor controller for

the linear positioner, the amplifier used to power the piezoelectric stacks, and the computer with its National Instruments/LabVIEW data acquisition and control hardware and software.

The measurement systems were chosen primarily for their range, sensitivity and frequency response. The position measurement system chosen is the MTI 2000 Photonic Sensor. It is a fiber optic measurement system that measures the displacement of a surface based on the intensity of light that is reflected into its receivers. With two probes measuring the displacement of each end of the sample, a differential measurement is taken that describes the motion of the sample. The range of the device is between 0.127 and 0.51 mm with a resolution of 25 μm. The system can measure displacements at a frequency up to 20 kHz. This device satisfies the displacement measurement requirement.

Two different load cells were chosen in order to satisfy the load sensitivity and frequency response requirement since no one load cell could adequately satisfy both parts of the requirement. The first load cell chosen is the Entran miniature load cell with a range of 13.350 N, a resolution of plus or minus 4.5 N, and a frequency response of DC to 700 Hz. The load cell is a strain gage-type load cell, so an amplifier conditions the signal for use in the control loop. The second load cell is a Kistler quartz load cell model 9212. It has a range of 22,250 N, a resolution of plus or minus 4.5 N and a frequency response of 1 to 3000 Hz. It is a high resolution quartz load cell; therefore, a charge amplifier conditions the signal from the load cell. Between the two load cells, the force measurement requirement is met.

The control systems power the positioning devices and are the output variables in the control loop. The amplifier was selected for its peak-to-peak voltage output characteristics, the peak current rating of the system and the frequency response of the system. The selected amplifier is made by Kinetic Ceramics and has a three channel output with an 800 V output, 1.5 Amp maximum current output per channel, and a frequency response of DC to 4 kHz. The other amplifiers considered and the basis of the performance requirements are explained further in section 3.5.5. The motor controller selected to power and control the 208V 3-phase AC motor in the linear positioner is an IDM variable frequency drive controller, 5M series. The controller was selected for its simple operation and its variable frequency control feature.

The final piece of the control system is the computer. A computer was needed to run the control system and take data from the many different instruments in the system. Since National Instruments' LabVIEW data acquisition system was selected as the software used, a computer that

was compatible with the software and configured to allow the software and hardware the highest possible performance was needed. This translated into a Gateway computer with a Pentium II 333 MHz processor, a free PCI expansion slot and 96 M-bytes of RAM. With this system it should be possible to control the system with six inputs and two outputs at 1 kHz.

3.4.3 Support Hardware

To make the testing machine into an independent testing facility, it was necessary to purchase some support hardware. The support hardware purchased was a dedicated optics table and an instrument rack. The optics table selected was a Newport Slimline series bench with a RS3000 series table top and isolated legs. It is a 30" by 72" table that only holds the testing machine and some of its instruments. The instrument rack houses the computer, monitor and data acquisition system.

3.4.4 Thermal Testing Facility Design

A thermal testing facility was designed to provide a thermal environment that can be controlled from -50 to 200°C. The design is based on a thermal testing design by D. Burianek and S.M. Spearing for testing a composite sample at 350°F[15]. The design consists of a hinged cylinder that fits the length of the sample and closes around the tungsten carbide inserts that are offset from the surface of the plate. The cylinder is an aluminum cylinder covered by an insulatory material. A sketch of the design is presented in figure 3-3. The shape of the container is cylindrical in order to allow the user to open the thermal chamber to position the sample before testing but while the facility is in place. The internal temperature is regulated through a hole in the enclosure designed to allow for a heat gun nozzle or a coolant system hose. The heated or cooled air is not released directly at the sample, but rather is deflected away from the sample by metal barriers that divert the flow around to the walls of the cylinder. An internal thermocouple should be used to regulate the temperature inside the cylinder, allowing for the heating or cooling element to be turned on when necessary through the use of a temperature regulator. The cooling equipment recommended for use in this system is the Cyrostream Cooler or similar system that is primarily used for cryogenic cooling of crystal samples. For heating the system, any variable-temperature heat gun would work. Temperature control of the inside of the cylinder can be achieved by using thermocouples and temperature regulatory systems by Omega.

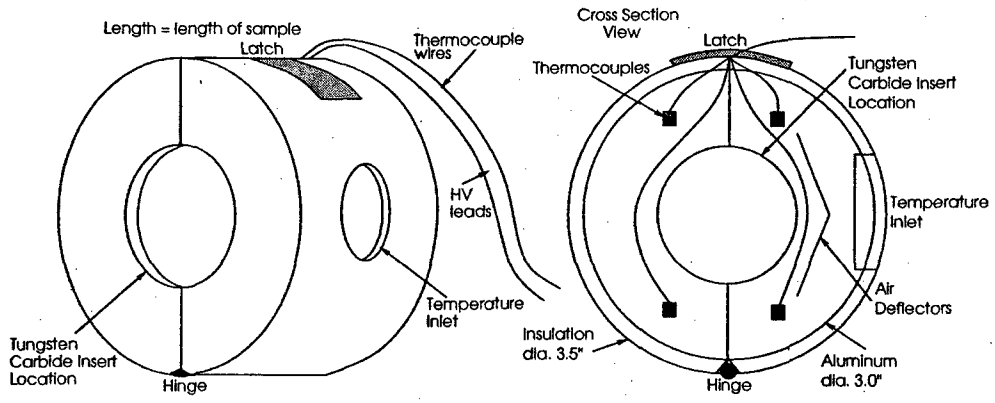

Figure 3-3: Sketch of Initial Design of a Temperature Testing Facility for use with the Component Testing Facility.

3.5 Design Issues

The following section describes how the different design decisions were made. The analysis performed for each decision and the different options examined are presented. A flow chart of the design process is presented in fig. 3-4. As can be seen, the design process was a highly iterative process in order to satisfy the design requirements completely. However, this analysis process enabled the best possible design decisions for meeting the specified requirements.

3.5.1 Compliance Budget

To size the plates and rod diameters it was necessary to construct a compliance budget to make sure that the stack displacement is not lost in compressing soft members in the load path of the machine and instead compresses the sample. Both axial and bending compliances were calculated and considered. Generally, the compliance of the plates are of the order of 10^{-9} in/lb and the compliance of the rods are on the order of 10^{-8} in/lb. The equations for finding the axial and bending compliance are:

$$c_{axial} = \frac{l}{EA} \tag{3.1}$$

$$c_{bend} = \frac{w}{2Eh^3t_p} \tag{3.2}$$

where l is the length, E is Young's Modulus, A is the cross sectional area, w is the width of a plate, h is the height of the plate, and t is the thickness of the plate. Only the axial compliance was found

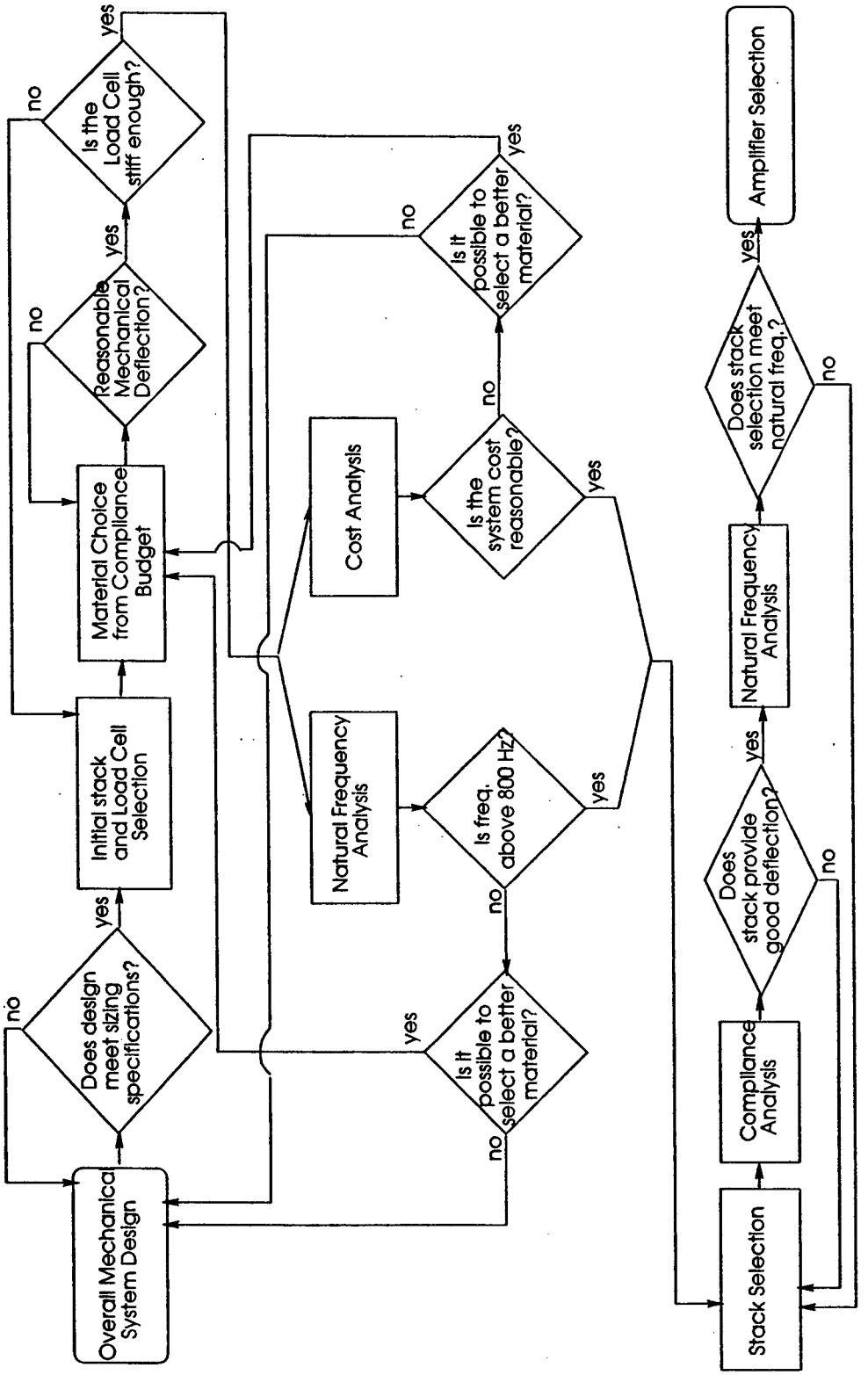

Figure 3-4: Flow Chart of the Process used in determining the final design decisions of the Compressive Testing Facility.

for rod elements while both the axial and bending compliance was found for plate elements. Adding the compliance of each piece together gives the total compliance of the system. The compliance is then compared to the driving stack compliance in order to determine how much stack deflection happens in the system. Once the deflection in the system is determined, then the deflection possible in the sample is found to make sure that it is significant enough to be measured during stiffness-type tests where the sample is not active. An example compliance budget is shown in figure 3-5. The spread sheet is set up so that material choice and part sizing is easily changed within the spread sheet. Part sizing to minimize compliance is traded with the desire to minimize weight in order to increase the natural frequency of the system.

3.5.2 Design for High Frequency First Mode

Since the major design requirement was to have the first axial mode of the system above 1 kHz, it was necessary to define a model that would compare the different material choices and sizes to determine how the material choice and configuration effects the natural frequency of the system. The stiffness and mass of the rods and plates were determined for each size and material choice. These values were put into a four node dynamic model. The model was a simple five spring-four mass model working against a wall. The pictorial representation of the model is shown in figure 3-6. The different masses are labeled in the figure. Since the outsides of the front plates of the cage are not moving during testing, the front plates are only the mass of the inside circular sections. The rods are the springs that connect the different pieces. The mass of the rods and braces are scaled and put into the masses of the ends. The spring between the front and back sections of the cage consists of the load cells and stack stiffnesses. The back of the cage is clamped to the large rods during high frequency operation, therefore the large rod stiffness is split into two pieces, the stiffness from the back wall to the back of the cage and the stiffness of the rods from the back of the cage to the front end piece. The braces between the inside sections of the front of the cage are the stiffness of the spring between those two sections. The stiffness of the rods was determined by the rod stiffness equation

$$k_{axial} = \frac{EA}{l} \tag{3.3}$$

where E is the Young's Modulus of the material, A is the cross-sectional area, and l is the length of the material. The mass of the plates were determined by the volume of the plate and the density of material used.

Compliance Budget			all dimensions in English units.							Good as of 10/28					
	Material Choices							PI pzt stack- used in calcs						PZT options	
	material	E (psi)	rho (slugs/in^3)					# in path	3					PI pzt stack-P247.80	
	steel	29000000	0.0087569444					pzt free	0.0031					pzt free	0.003149606
	aluminum	10500000	0.00303125					Kact	1809000					Kact	2905760
	tungstun	50000000	0.021											PI pzt stack-P242.40	
	beryllium	39000000	0.00236											pzt free	0.002362204
	alumina	51000000	0.00426											Kact	1760220
	lockallo	26900000	0.0023											PI pzt stack-P239.90	
component	Number	Type of deflect	length	Xsection area	width	height	Material	Stiffness	Compliance (1	Total component	mass (each) (slug			pzt free	0.007086614
Rods (activ	4	axial	24	3.1415927			alumina	51000000	1.4979289e-07	3.7448222e-08	0.17341591			Kact	167640
Brace	3	axial	3	0.44178647	&radius of .375		alumina	51000000	1.3314923e-07	3.3287308e-08	0.005646031			PI pzt stack-P242.30	
Plate-backl	1	axial	0.7	15.904313			aluminum	10500000	4.1917351e-05	4.1917351e-09	0.033746964			pzt free	0.001574803
	1	bending	2.5		0.7	2.5	aluminum	10500000	1.0884354e-08	1.0884354e-08				Kact	2380488
Plate-front	1	axial	0.7	15.904313			aluminum	10500000	4.1917351e-05	4.1917351e-09	0.033746964			KC pzt stack SDLF	
	1	bending	2.5		0.7	2.5	aluminum	10500000	1.0884354e-08	1.0884354e-08				pzt free	0.0031
Block	1	axial	1.5	58.5			aluminum	10500000	2.4420024e-09	2.4420024e-09	0.26599219			Kact	1809000
	1	bending	6		1.5	9.75	aluminum	10500000	2.0550711e-10	2.0550711e-10				KC pzt stack LDSF	
Loadcell	1	axial						%combo los	4.66e-07	4.66e-07				pzt free	0.0072
LC connecto	2	axial	0.15	0.19634954			steel	29000000	2.6342887e-08	5.2685774e-08	0.0002579133			Kact	774000
Wall Block	1	axial	2	58.5			aluminum	10500000	3.2560033e-09	3.2560033e-09	0.35465625				
	1	bending	6		2	9.75	aluminum	10500000	1.5413033e-10	1.5413033e-10					
Clamping pl	1	axial	1	42			aluminum	10500000	2.2675737e-05	2.2675737e-09	0.1273125				
	1	bending	3		1	3	aluminum	10500000	5.2910053e-09	5.2910053e-09					
Rod ends	4	axial	3	3.1415927			alumina	51000000	1.8724111e-08	4.6810277e-09	0.021676989				
align plate	1	axial	0.5	3.75			steel	29000000	4.5977011e-09	4.5977011e-09	0.01641927 1				
	1	bending	2		0.5	3	steel	29000000	2.5542784e-09	2.5542784e-09					
align rotat	1	axial	2	3.1415927			steel	29000000	2.1952406e-08	2.1952406e-08	0.055021505				
Plate-back2	1	axial	1	52.5			aluminum	10500000	1.814059e-09	1.814059e-09	0.15914063				
	1	bending	3		1	3	aluminum	10500000	5.2910053e-09	5.2910053e-09					
									TOTAL	1.5539441e-07					
specimen	1	axial	3.865	0.19634954			steel	29000000	6.7876839e-07	6.7876839e-07	0.0066455661				
							deflection of syst		Defsys	0.0018644482					
									Defspec	0.0015171242					
									loadspec	2235.1131					
									stress	11383.338					
							aluminum	10500000	3.8095238e-07	3.8095238e-07					
							deflection of syst		Defsys	0.0015265967					
									Defspec	0.0010842997					
									loadspec	2846.2866					
									stress	45540.586					

Figure 3-5: Sample compliance budget

BEST AVAILABLE COPY

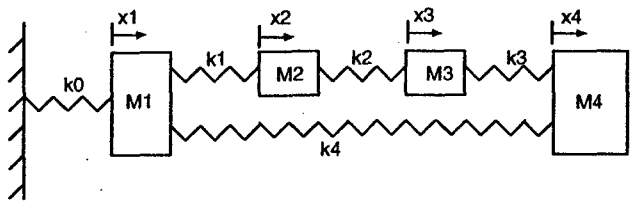

Figure 3-6: The four mass dynamic model of the system.

The compliance budget spread sheet was used to calculate the mass and stiffness of the different elements. This allowed for changes to the size and material choice of the different system elements to be recalculated automatically. The masses and stiffnesses were then put into a Matlab program that calculates the natural frequencies and frequency response of the system. The stiffness matrix was found to be

$$\mathbf{K} = \begin{bmatrix} k_0 + k_1 + k_4 & -k_1 & 0 & -k_4 \\ -k_1 & k_1 + k_2 & -k_2 & 0 \\ 0 & -k_2 & k_2 + k_3 & -k_3 \\ -k_4 & 0 & -k_3 & k_3 + k_4 \end{bmatrix} \tag{3.4}$$

where k_0 is the stiffness of the ends of the rods, k_1 is the combined stiffness of the stacks and load cells, k_2 is the stiffness of the braces, k_3 is the stiffness of the sample, and k_4 is the stiffness of the rods. The mass matrix is

$$\mathbf{M} = \begin{bmatrix} M_1 & 0 & 0 & 0 \\ 0 & M_2 & 0 & 0 \\ 0 & 0 & M_3 & 0 \\ 0 & 0 & 0 & M_4 \end{bmatrix} \tag{3.5}$$

where M_1 is the mass of back section of the cage, M_2 is the mass of the inside back piece of the front part of the cage plus a scaled mass of the braces, M_3 is the mass of the inside front piece of the front part of the cage plus a scaled mass of the braces, and M_4 is the mass of large end block, a scaled mass of the rods, and a scaled mass of the outside of the plates from the front cage section.

The eigenvalues of the square root of the **K** matrix divided by the **M** matrix were found, which are the modal frequencies of the system. A state space dynamic model using the above mass and stiffness matrices and assuming 1% damping was also constructed. The use of the dynamic model was important in deciding upon the final design of the testing machine since everything from piece sizing, material selection and general configuration affects the resonant response of the system. The

final decisions based on the design trades is presented in subsequent sections.

3.5.3 Rod and Plate Material Selection

The material choice for the rods and plates was very important for maximizing the frequency of the testing machine. Therefore, both traditional and non-traditional materials were considered for the construction of the machine. The materials compared for the plates were aluminum, steel, and beryllium. Although the beryllium plates gave the best system performance, the manufacturing and material cost was significant compared to the increased performance over the use of aluminum. As expected, the mass of the steel plates was significant and severely hindered meeting the frequency performance requirements of the testing machine.

The rod materials compared were steel, beryllium, and alumina. Generally the rod material had a greater impact on the natural frequency of the system than the plate material. Therefore, the rod material was the focus of a more detailed design study. Beryllium rods were eliminated immediately since a manufacturer that was willing to produce the rods with the desired tolerance was not found. Plots of the theoretical natural frequency of the system with the remaining rod material choices is plotted against cost to help quantify the performance relations. Eight different systems are plotted for each rod material choice; combinations of stack choice, either with one or three stacks; load cell choice, either with one or three Entran load cells; and plate material, either aluminum or beryllium plates. The comparison is shown in figure 3-7. The cost difference between the different rod choices is only the difference in the material and manufacturing costs of the rod material. The other cost differences are the stack, load cell, and plate cost differences which are constant for all of the rod choices.

The chosen design, was the alumina rods with aluminum plates, 3 stacks and 1 strain gage load cell. The alumina rods gave an increased performance of 200 Hz on average over steel rods. The single load cell was decided upon because it is possible to configure a system without load cells by mounting strain gages on the back plate to measure the load in the system. Using the strain gages would increase the possible system performance over the performance possible by using three load cells.

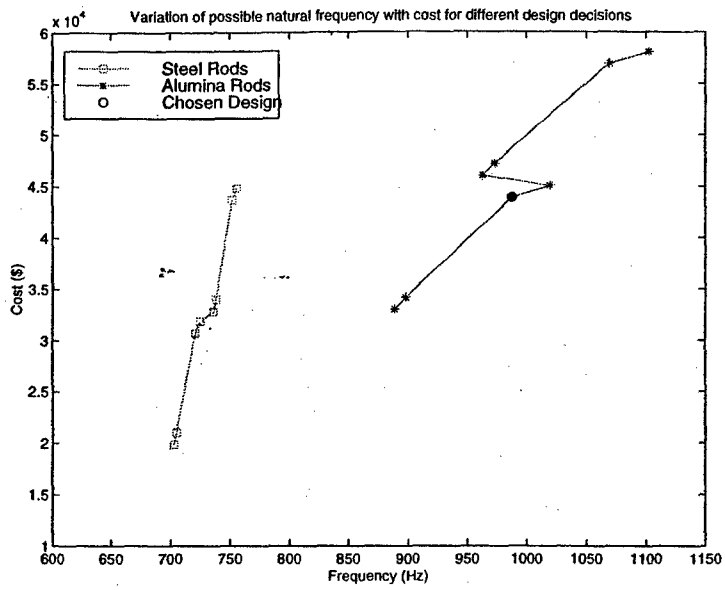

Figure 3-7: Natural Frequency Comparison for different rod materials and system configurations versus system cost. Rod materials plotted are Steel and Alumina.

3.5.4 Driving Piezostack Selection

As demonstrated in the above two sections, the piezoelectric stack selection has a significant impact on the natural frequency and compliance budget of the system. Because of this, the stack selection was arguably the most important selection for the best performance of the system. A variety of stacks were examined with different stiffness, free deflections, and natural frequencies. The comparison of the free deflection, blocked force and natural frequency of each of the stacks with the required free deflection, blocked force and natural frequency from the different samples to be tested is shown in figures 3-8 through 3-10. The stacks in the comparison are Polytec, PI stacks identified by their part number. From these comparisons it was determined that any one stack could not adequately test all of the samples. Therefore two different sets of stacks were selected for use depending on the type of testing to be done so that all of the sample types could be tested. Because the dual selection was necessary, it was decided to choose two stacks very different from each other to get the best range of system performance.

The samples that the stack performance was compared to are representative sample types that could be used in the testing machine. "XIRE" samples are stacks from Xinetics Inc. and properties were used from published properties from company papers[16]. "S" samples are from Sumitomo

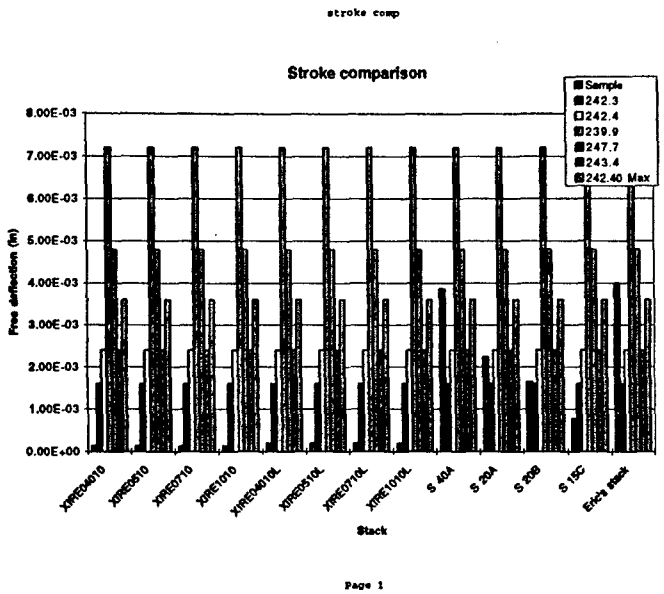

Figure 3-8: Free Deflection comparison of piezoelectric stacks to known samples to be tested.

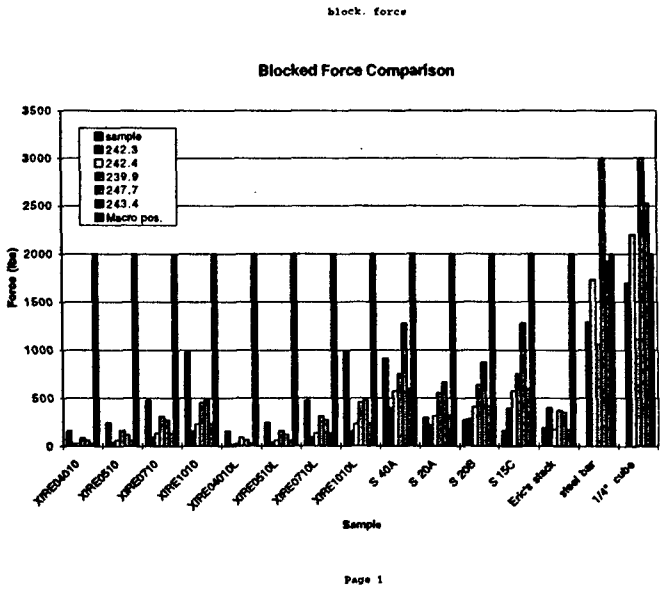

Figure 3-9: Blocked Force comparison of piezoelectric stacks to samples to be tested.

BEST AVAILABLE COPY

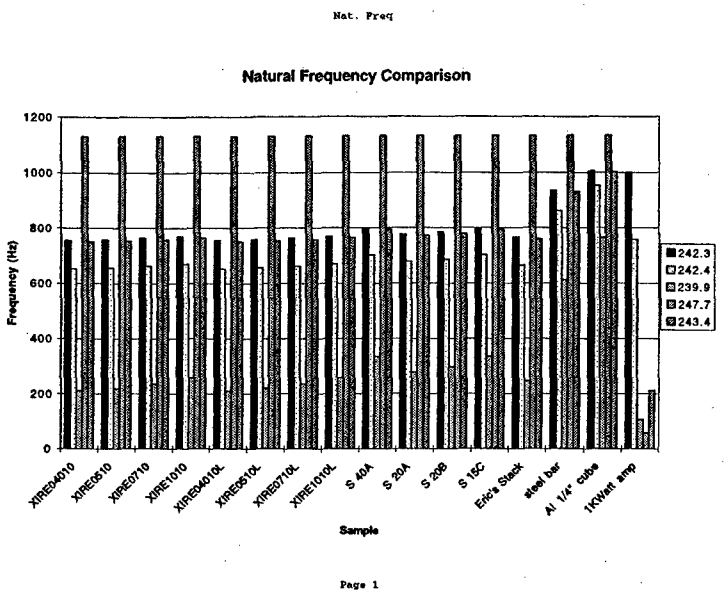

Figure 3-10: Natural Frequency comparison of piezoelectric stacks and samples tested.

Metals and properties were taken from their product literature[17]. "Eric's Stack" properties are based on the desired properties of a stack to use in the X-frame actuator designed by Eric Prechtl and Steve Hall[18]. The stack selected should have a larger free stroke then the samples in order to test the samples in "free strain" conditions. The blocked force of the stacks should also be larger than the blocked force of the sample in order to test the sample in the "blocked force" conditions. The natural frequency of the system should be as high as possible during the testing of each sample to allow characterization at high frequencies, therefore the selected stack should maximize the first resonance of the system.

Two kinds of Polytec, PI stacks were originally chosen to meet the system performance. They were stack models P242.40 and P239.90. However, because of incompatibilities in the electrical connections between the Polytec, PI stacks and the Kinetic Ceramic amplifier, the Polytec, PI stacks were returned for stacks supplied by Kinetic Ceramics that have similar performance metrics. The electrical connections between the Kinetic Ceramic stacks and amplifier are compatible, making the system safer to use.

BEST AVAILABLE COPY

3.5.5 Amplifier Selection

The amplifier was selected for its bandwidth, peak-to-peak voltage characteristics, current capability, and total cost. In order to be able to control each of the three stacks separately, it was necessary to have three different channels in the amplifier. This corresponded to either having one amplifier unit with three channels, or three amplifier units with one channel each. The combination of the bandwidth and power requirements made the choice of amplifier a difficult one since not many amplifiers are made that satisfy the requirements. The testing goals required that the amplifier have a bandwidth of DC to 1 kHz and produce about 1 kilowatt of power. The one kilowatt of power needed to be divided into 1000 V peak-to-peak and 1 Amp maximum current in order to effectively drive the large capacitance loads at high frequencies. This combination of requirements resulted in the choice of one amplifier, the Trek model P0617A. Although this amplifier could exactly match the technical requirements, the cost of $18,000 per channel made the amplifier financially infeasible. Since the bandwidth requirement could not be relaxed, the power requirement was relaxed to a 800 Watt requirement. At this lower power requirement, two options were possible; either the construction of an amplifier unit using APEX power amplifier SA16, or the purchase of amplifier unit from Kinetic Ceramics. Since building an amplifier unit is a time consuming project prone to many errors, the decision was made to buy a single, three channel amplifier that has bandwidth characteristics of DC to 3 kHz, a voltage level of 800 V peak-to-peak and a peak current value of 1.5 Amps per channel. The use of this amplifier should enable some level of voltage output at frequencies up to 1 kHz for the stacks selected.

3.5.6 LabVIEW Control Loop

The three main testing modes of the component testing facility are testing a sample against a programmable impedance, testing an active sample with a constant load, and testing an active sample under constant displacement. These three testing modes require that the state of the system is constantly monitored and modified, or actively controlled. Therefore, a control loop was implemented in LabVIEW. The control loop allows the user to specify what kind of control is wanted, what the target information or loading function is desired, and what other parameters are to be monitored and recorded at the same time. The input of the control loop is the displacement and force information from the displacement sensors and a load cell. The output of the control loop is the voltage level to supply to the driving stacks. The voltage level is determined by first

detecting what the desired change of the system is, and then calculating the necessary change in electric field.

The control loop implemented was designed using classical control techniques. A regulator was designed based on the experimentally derived frequency profile. The profile was found by taking transfer function of the input driving stacks to the sensor outputs. This frequency response was then analyzed and a controller designed to compensate the system. Since the requirement on this initial controller was to provide disturbance rejection of low frequency disturbances of less than one Hertz, the controller design has a low frequency roll-off in order to increase the high frequency noise rejection of the system. The non-compensated and compensated systems are shown in fig. 3-11. The transfer function of the controller is

$$G(s) = \frac{K\omega_0^2\omega_2^2\omega_3\left(s+\omega_1\right)\left(s+\omega_4\right)}{\omega_1\omega_4\left(s^2+2\zeta\omega_0 s+\omega_0^2\right)\left(s^2+2\zeta\omega_2 s+\omega_2^2\right)\left(s+\omega_3\right)} \tag{3.6}$$

where $\omega_0 = 2$ Hz, $\omega_1 = 7$ Hz, $\omega_2 = 40$ Hz, $\omega_3 = 0.2$ Hz, $\omega_4 = 1$ Hz, and $\zeta = 0.707$. This continuous system controller was transformed into a discrete time controller with a sampling frequency of 40 Hz. The transformed equation in difference form was used to implement the controller, resulting in the following controller representation.

$$\begin{aligned} u(k) &= 1.375u(k-1) + 0.3556u(k-2) - 0.8149u(k-3) - 0.184u(k-4) \\ &\quad +0.2618u(k-5) + 0.003068y(k) + 0.009598y(k-1) + 0.007714y(k-2) \\ &\quad -0.003769y(k-3) - 0.007625y(k-4) - 0.002673y(k-5) \end{aligned} \tag{3.7}$$

Verification of the Control Loop

To verify the operation of the control loop, tests were performed to see if the force present in the system could be held constant in the presence of a disturbance to the system. Three different piezoelectric stacks with different stiffnesses were used as disturbance sources. The stiffness of the stack determines the amount of authority the testing machine has to control its generated disturbance. Since the controller was designed to control low frequency disturbances, the input disturbance had a frequency of 0.025 Hz with many amplitudes for each of the disturbance sources. For all of the tests run, using the control loop with a gain of 12.6 allowed for the control of the force in the system to the order of the sensitivity of the load cell. A plot of a representative test

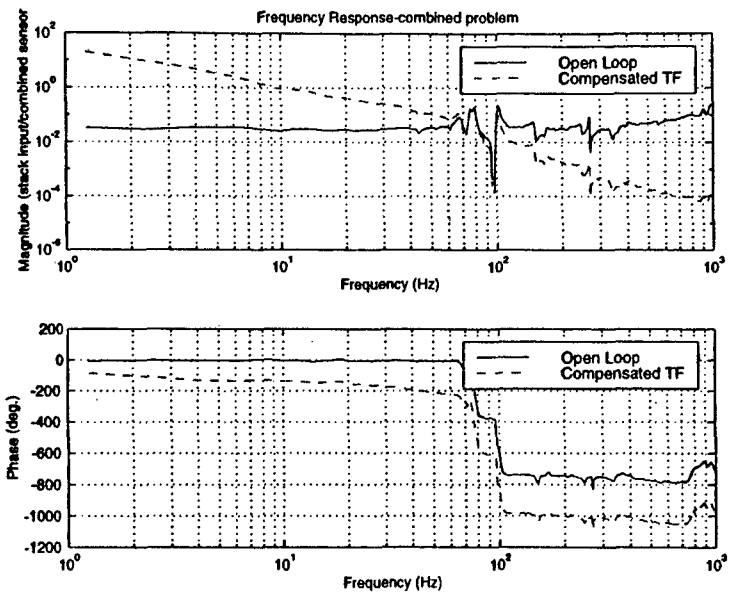

Figure 3-11: Transfer function of the compensated and uncompensated control loop for control of the testing machine.

run with a Sumitomo MLA-20B actuator is shown in fig. 3-12. As can be seen by the force and displacement time traces, the actuator was allowed to displace under constant force conditions.

3.5.7 Sample Alignment Mechanism

It was originally assumed that by using samples with spherical endcaps, bending within the sample would be minimized, allowing for accurate measurements of the axial displacement of the sample. However, the spherical endcaps resulted in large errors at small values of system preload, as can be seen in figures 3-13 and 3-14. These errors were eventually determined to be the result of Hertzian contact stiffnesses that were not originally predicted. To counteract that problem, a move to samples with flat ends was made. However, this move necessitated the design and construction of a device that eliminates bending in the sample due to non-parallelism of either the sample faces or machine faces. Typically, rocker-type mechanisms have been used to fulfill this role[11, 9, 12]. However, the spherical ends on the rocker would have the same problems that the spherical ends on the sample had. Therefore, a flexure mechanism was designed that had a very low bending stiffness with a moderate axial stiffness. This device, after its initial bending to counteract the face non-parallelism, has a known, constant stiffness that can be compensated for in the analysis of the data. The design of the mechanism is shown in fig. 3-15.

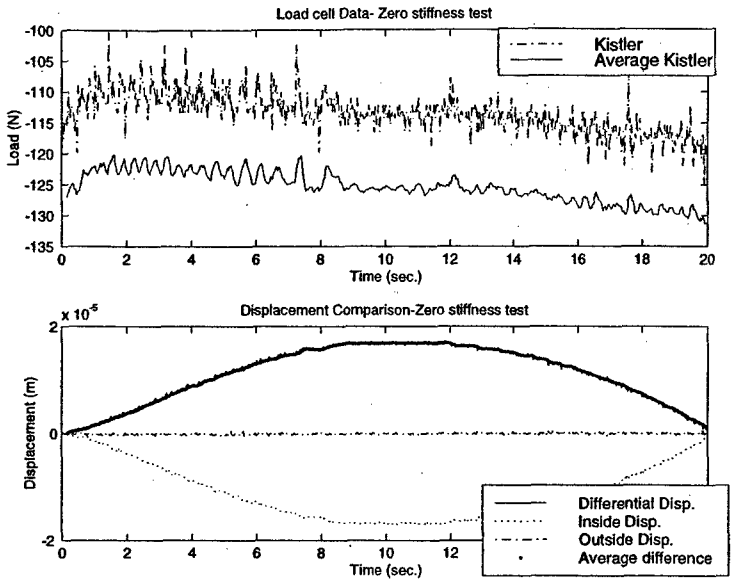

Figure 3-12: Representative time traces of a sample in the testing machine with the controller driving constant force tests in the presence of sample disturbance.

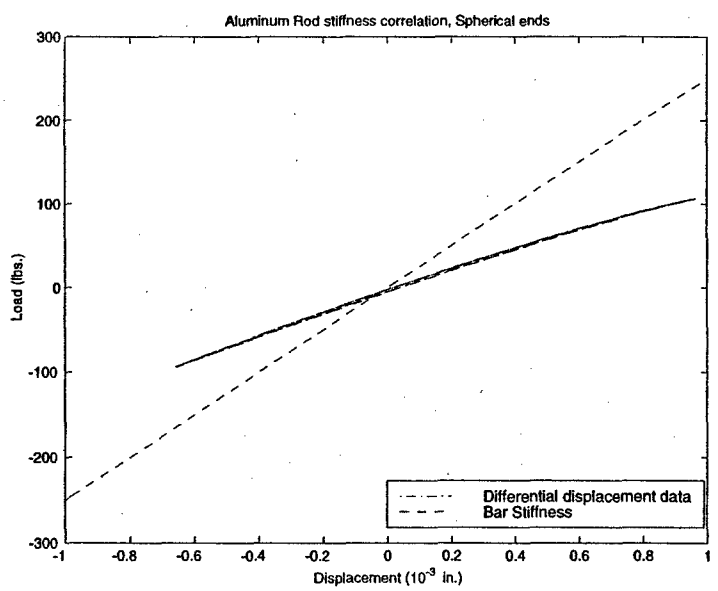

Figure 3-13: Mismatch in tested stiffness with theoretical stiffness for an aluminum bar with spherical endcaps under small preload values.

BEST AVAILABLE COPY

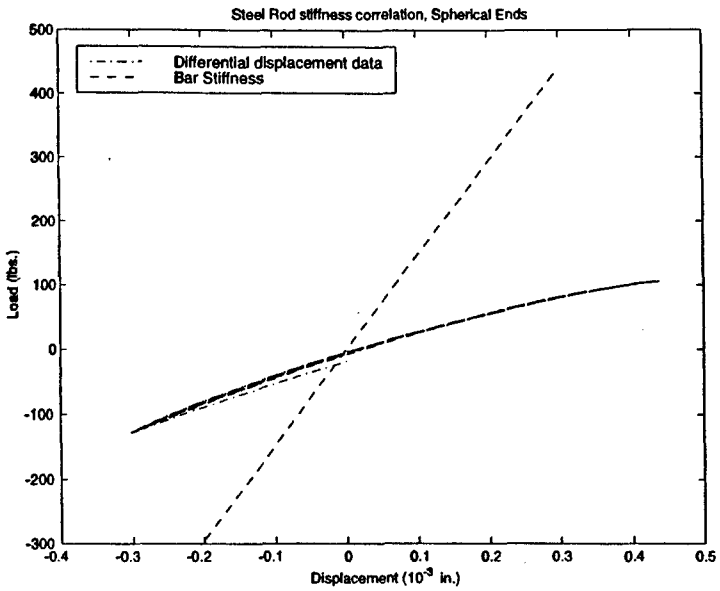

Figure 3-14: Mismatch in tested stiffness with theoretical stiffness for a steel bar with spherical endcaps under small preload values.

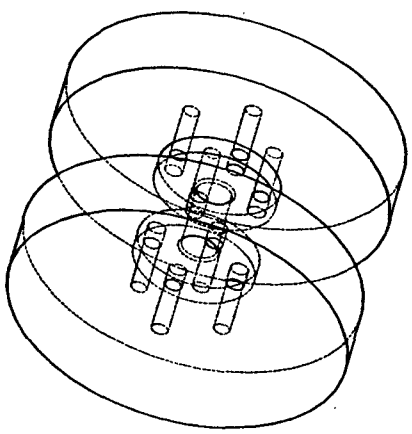

Figure 3-15: Alignment mechanism designed to compensate for the non-parallelism of sample faces.

3.6 Design Validation

To validate the design of the compressive testing facility after it was constructed, a series of tests were run to make sure the machine gave the expected results. The were two main items that needed to be checked; first that the load and displacement sensors were giving accurate readings, and second that the natural frequency of the system was near or above that predicted with the simple four node model.

The load and displacement sensors were tested along with the basic functionality of the testing machine by testing the stiffness of different samples with known stiffnesses. The two samples tested for accuracy were a steel rod and an aluminum rod. The steel rod has a length of 9.8 cm and a diameter of 1.27 cm, resulting in a theoretical stiffness of 257×10^6 N/m. The aluminum rod has a length of 8.34 cm and a diameter of 0.76 cm, resulting in a theoretical stiffness of 39.5×10^6 N/m. The stiffnesses measured by the testing machine resulted in the theoretical stiffness expected with the correction for the alignment mechanism for each of the samples. The results of these tests are shown in figures 3-16 and 3-17. Being able to consistently measure the correct stiffness of the samples gave confidence that the testing machine was accurately measuring the deflection of a sample at different load levels.

Th effect of sample placement on the stiffness measured is also an important factor to examine since it is impossible to always position the sample exactly in the center of the tungsten carbide inserts. Therefore, stiffness tests were performed on the steel and aluminum bars while placed in different positions on the inserts ranging from the top of the insert to the bottom. Results are presented in figs. 3-18 and 3-19. It is apparent from these figures that the stiffness variation with gross position change is very large. When reasonable effort is made to centrally locate the sample, variations of tested stiffness should be within 5% since the position changes represented in the figures are each over a quarter of an inch. However, it is important to be cognizant of the sample position.

The natural frequency of the system was measured with the large stack configuration and steel rods. The natural frequency was measured using 100 mV rms random noise inputs and taking transfer function data from a Tektronics 2630 personal Fourier analyzer. Transfer functions were taken from three different measuring locations; the position sensors, the Kistler load cell, and the Entran load cell. A steel bar was used as the sample during frequency response testing.

The first reading was the transfer function from the position sensors to the stack input. As

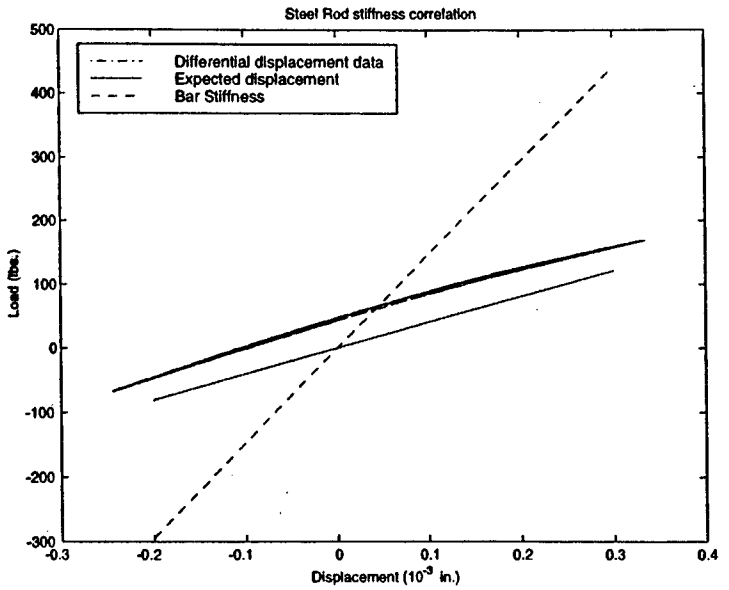

Figure 3-16: Stiffness information for a steel bar tested in the testing machine. The stiffness of the system is shown as seen by the strain gages, the displacement sensors and the expected measurement by the strain gages and displacement sensors.

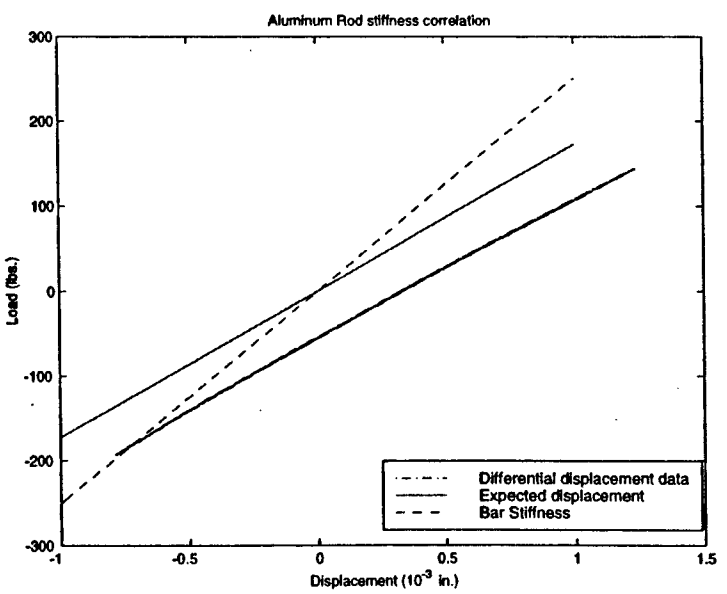

Figure 3-17: Stiffness information for an aluminum bar tested in the testing machine. The stiffness of the system is shown as seen by the displacement sensors, the theoretical stiffness, and expected displacement sensor readings.

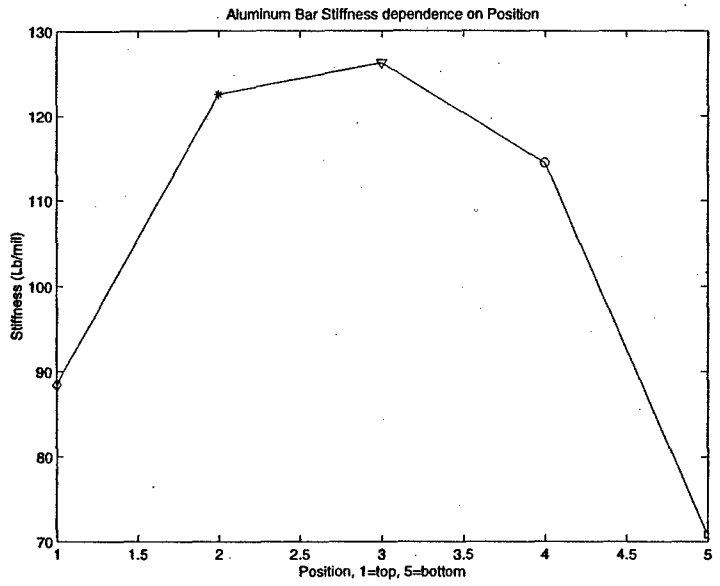

Figure 3-18: Variation of the stiffness of an aluminum rod based on position in the testing machine.

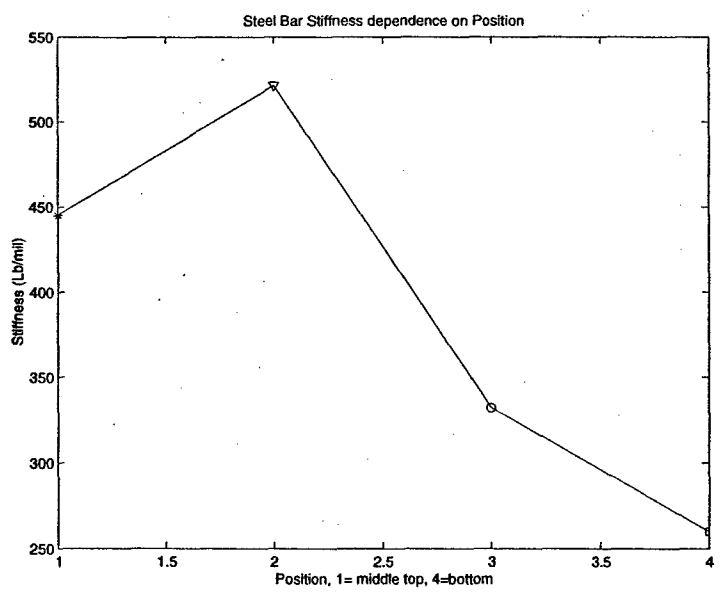

Figure 3-19: Variation of the stiffness of a steel rod based on position in the testing machine.

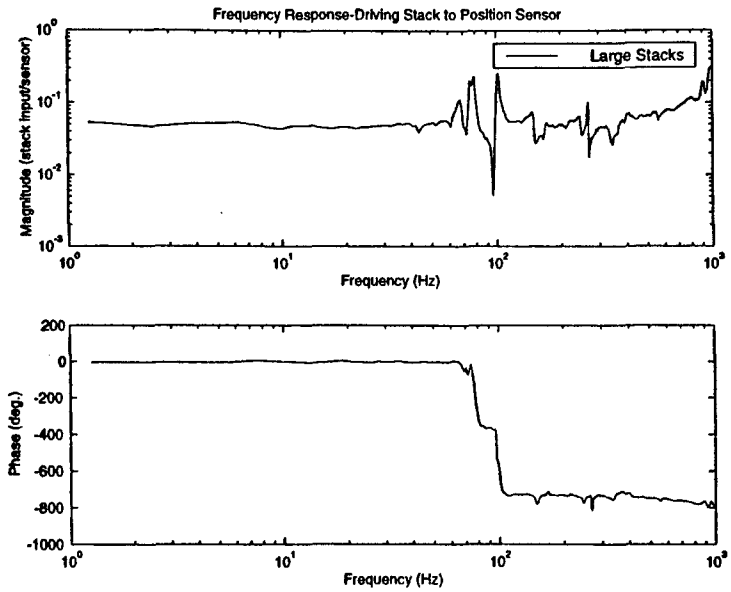

Figure 3-20: Transfer function from the optical displacement sensors to the input to the stack in the system configuration of the large stack and steel rods.

can be seen from figure 3-20, there is a small peak and resulting phase shift at a low frequency of about 80 Hz with a larger peak above 1 kHz. The first peak is a result of the position sensor stands vibrating like a flexible beam. The second peak is found in all of the transfer functions taken and is therefore probably the first mode of the system.

The next two transfer functions are from the Entran and Kistler load cells to the input to the stacks. These are presented in figure 3-21 and figure 3-22. Again, the first peak of the system is above 1 kHz in both of these figures. The Kistler load cell transfer function also includes a transfer function taken with the small stacks. The comparison of the data shows the peak shift in the small stack transfer function due to the greater stack stiffness.

The final transfer function presented is the expected transfer function that was predicted by the model. This transfer function is plotted in figure 3-23 for each of the four possible system configurations. Although the shape of the transfer function is the same as the transfer functions measured, the peaks for each of the systems is off by a few hundred Hertz. From these results, we can determine that the model predictions were conservative and closed-loop control of the system should be possible up to 500 Hz. The transfer function assumed an input force at mass two and shows the response of the displacement of x_3 from fig. 3-6.

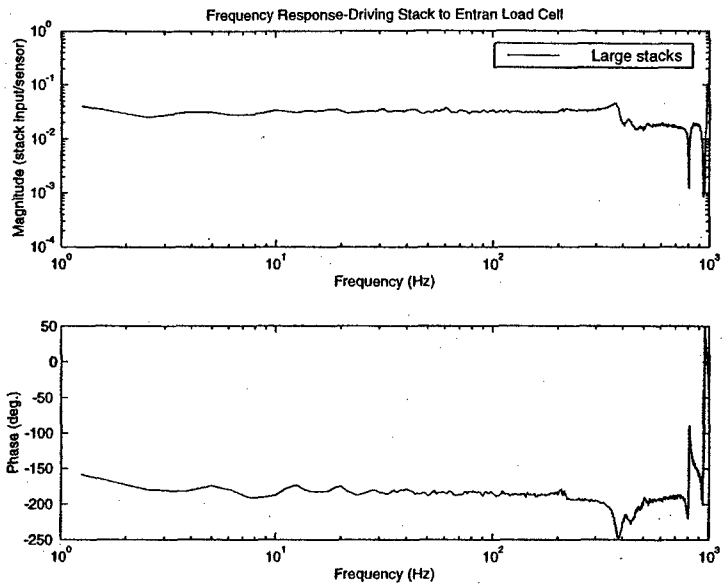

Figure 3-21: Transfer function from the Entran load cell to the input to the stack in both system configurations.

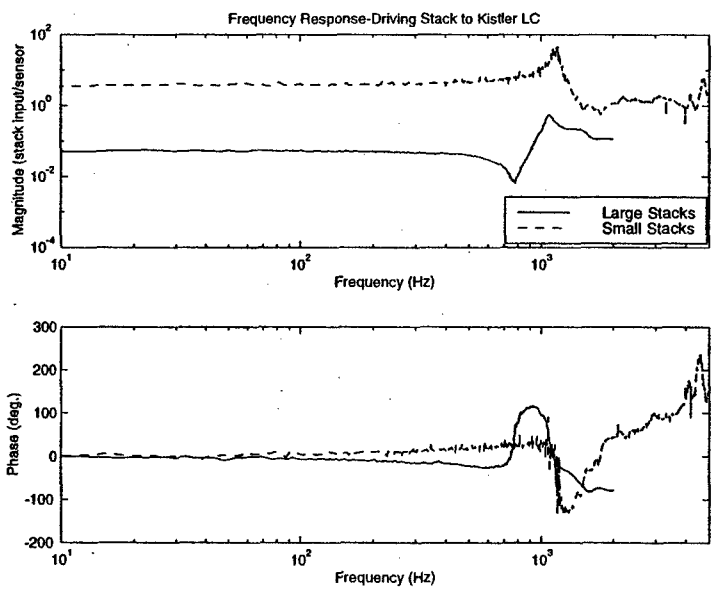

Figure 3-22: Transfer function from the Kistler load cell to the input to the stack in both system configurations.

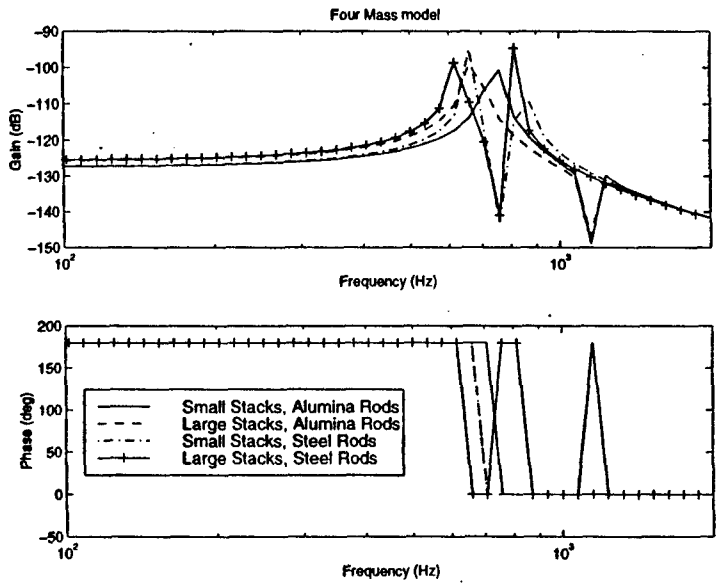

Figure 3-23: Transfer functions of the four system configurations as predicted by the four node model. Transfer functions were taken from a force input at mass two to a position measurement at mass three.

Chapter 4

Validation of Theoretical Results

4.1 Testing Methodology

The goal of testing is to validate the theoretical results derived in chapter 2 for the actuation efficiency and work output of a system. To validate the theory, it is necessary to measure the work of the system, both the electrical and mechanical work, when a sample is working against linear and non-linear loads. If the work measured is close to the work that the theory predicts for the choice of material and loading function, then it can be assumed that the theory is validated.

The tests should be taken on a uniaxial material working against a programmable uniaxial load. The most readily available uniaxial material is a multi-layered piezoelectric stack. Therefore, tests were taken with a sample stack and the electrical and mechanical work measured from the output of the stack. The only drawback of piezoelectric stacks is that their derived coupling coefficient is much lower than the typical bulk material coupling coefficient.

4.2 Measurement of Mechanical and Electrical Work

Measuring the mechanical work of the system is achieved by measuring the force and displacement at every time step and then integrating the force with respect to displacement. Since the component testing facility is designed to measure force and displacement, the mechanical work in the system comes directly from the integration of the measured parameters. The electrical work of the system is measured much the same way as the mechanical work by recording the current and voltage supplied to the tested sample. The Kepco amplifier used to run the sample has a current and voltage monitor integrated into the system. These values are measured through the data acquisition system. The

current measured by the system is multiplied by the voltage in the system at the same time and integrated with respect to time to find the electrical work in the system. The actuation efficiency is found by dividing the measured mechanical work by the measured electrical work.

4.3 Testing Plan

To verify the theory presented in Chapter 2 two different kinds of tests were used to compare to the theory. The first kind of test is the verification of figure 2-4, the variation of actuation efficiency and work output with stiffness ratio when a one-dimensional active material is working against a linear load. The second kind of tests verify the increase in work output and actuation efficiency by working against a non-linear load. The two types of tests are performed on a Sumitomo Corporation multi-layered actuator, part number 20B.

4.4 Test Specimen Selection and Information

4.4.1 Sample Selection

The sample selection was limited by the authority and performance of the testing machine when working against samples of different stiffnesses. Generally, the testing machine can test samples of all stiffnesses while simulating zero stiffness conditions up to simulating a load of the same stiffness as the sample. However, the testing machine is limited when simulating loads of stiffnesses much greater than the sample. Therefore, a sample of stiffness on the same order of the stiffness of the load chain, 17.5 N/μm while using the small stacks, was needed to be able to simulate linear loads of large relative stiffnesses and non-linear loads that have a large initial stiffness.

There were three stacks initially tested to determine which was the best stack to use for the complete battery of tests. The three stacks were an EDO corporation E-400P3 stack, a Polytec, PI P-820.30 series stack and a Sumitomo Corporation MLA-20B stack. The three stacks were tested for their suitability by taking a sweep of data with the stack working against linear loads of different stiffnesses. From this analysis, it was determined that the Sumitomo stack could be tested at the highest relative stiffness, and therefore was used in the subsequent function testing. The physical properties of the Sumitomo Corporation stack are presented in table 4.1[17].

Table 4.1: Physical Characteristics of the Sumitomo Corporation Stack MLA-20B.

Total length	41	mm
Active length	37	mm
Width	4.5	mm
Height	5.2	mm
Cross-sectional Area	23.4	mm^2
Layer thickness	0.18	mm
Number of Layers	200	
Maximum Voltage	250	V

4.4.2 Sample Information and Characterization

The Sumitomo actuator was tested to determine the mechanical and electrical properties of the stack. These values were then compared to the bulk material properties to ensure that the test results were reasonable values of the material properties. Tests were performed to determine the stack properties of stiffness, electro-mechanical coupling, and dielectric constant. The bulk material properties[17] and measured stack properties are compared in table 4.2.

Stiffness and Elastic Constant

Stiffness tests were performed on the actuator in the compressive testing facility. The actuator was placed in the machine with the alignment mechanism to ensure that there was no bending in the sample during testing. It was necessary to test the stiffness of the actuator at a small preload value to avoid coming close to the blocked force loading of the actuator. To allow this condition, the stacks were powered prior to applying the preload. When applying the preload, the Entran load cell output value was monitored with a multimeter to make sure that the actuator was not overloaded. The preload was applied through the use of the hand-crank on the linear positioner to better apply a known preload value of 45 N. The actuator was tested in its open circuit condition.

Tests were performed through the actuation of the small stacks in the loading path. The voltage signal sent to the stacks to apply the uniaxial load was

$$V_{appl} = |V_{max} \sin(0.2\pi t)| \tag{4.1}$$

Tests were performed for 15 seconds at 0.1 Hz and a maximum signal input to the KC amplifier of 7 V. It was necessary to use the above signal to test the actuator because the preload was applied

Table 4.2: Measured and Published material values for Sumitomo MLA-20B Actuator.

Material Property Item	Units	Bulk Material (SPEM-5D)	Stack Properties	Tested Stack Properties	
Stiffness (k^E)	N/μm	-	31.6*	18.3 ± 5%	
Elastic constant (s_{33}^E)	10^{-12}m^2/N	20.0	-	34.5*	
Capacitance (C^T)	nF	-	800 ± 20%	785 ± 39[1]	1050 ± 55[2]
Dielectric constant ($\epsilon_{33}^T/\epsilon_0$)	-	4300	3570*	3411[1]*	4568[2]*
X_0/E_0	μm/V	-	0.16	0.162	
Electro-mechanical coupling term (d_{33})	10^{-12} C/N	640	778*	788*	
Blocked Force	N	-	1200	-	
Free Strain	μm	-	42 ± 3	-	

[1] Measured using HP impedance analyzer [2] Measured during bench top testing

Values marked with an * are calculated based on measured values or values published in product literature[17]. Equations are presented in section 4.4.2.

with the driving stacks already powered. If a negative voltage was supplied to the KC amplifier to drive the stacks, the stacks would retract from their initial powered position. This could result in the actuator falling out of the testing machine, making the stiffness test fail and possibly cracking the ceramic. Representative time traces of the force and displacement measured are shown in fig. 4-1. The Kistler load cell was used as the force measurement in the system; the displacement was measured by the MTI Photonic sensors.

The displacement measured by the Photonic sensors is the combined displacement of the actuator and the alignment mechanism. To determine the displacement (and thereby the stiffness) of the actuator from the data, it was necessary to subtract the effect of the alignment mechanism. Since the stiffness of the alignment mechanism is known and the stiffness of the actuator is desired, it is easier to subtract the effect of the alignment mechanism from the correlated force and displacement information than from the displacement information alone. If k_{meas} is the slope of the line fit to the data taken, k^E is the stiffness of the actuator, and k_{align} is the stiffness of the alignment mechanism,

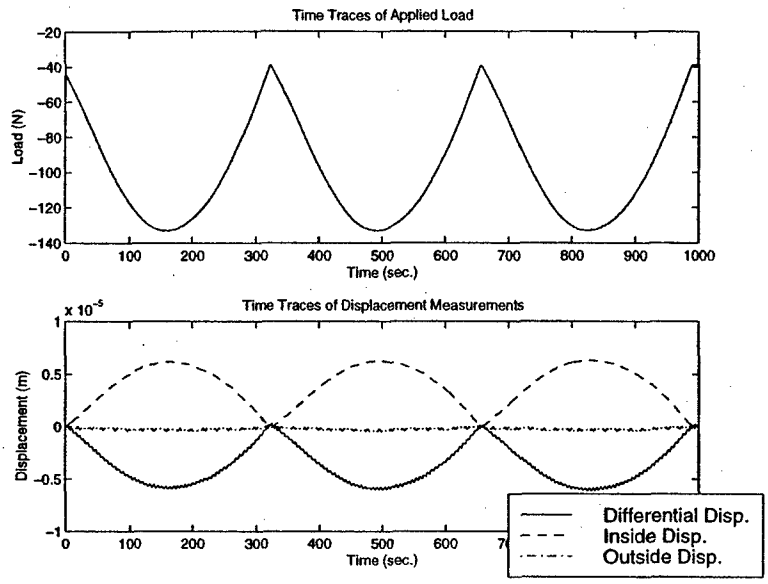

Figure 4-1: Time traces of the force and displacement measurements taken when finding the stiffness of the Sumitomo actuator.

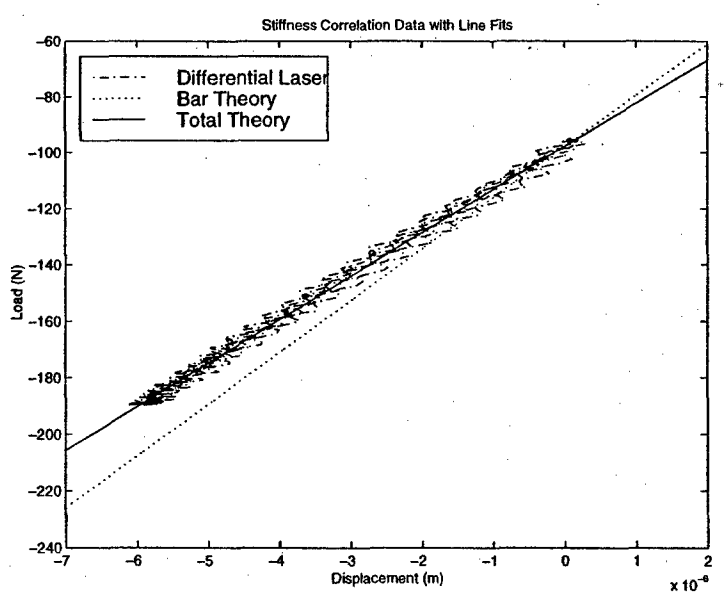

Figure 4-2: Data taken to find the stiffness of the Sumitomo stack.

then the three values can be related in the following way to determine the stiffness of the actuator

$$k^E = \frac{1}{\frac{1}{k_{meas}} - \frac{1}{k_{align}}} \tag{4.2}$$

where the stiffness of the alignment mechanism is known to be 97.3 N/μm. The line fit to the data was a least squares first order polynomial fit. Figure 4-2 shows the measured value of stiffness, k_{meas}, and the actuator stiffness, k^E, with the correlated displacement and force data. The data fit shown results in a stiffness value of the actuator of 18.3 N/μm. It should be noted that the 2 mm thick isolation plates on the ends of the actuator were assumed rigid when finding the stiffness of the actuator.

To find the elastic constant from the measured stiffness information, it is necessary to use the physical properties of the actuator. Generally, the axial stiffness of a bar is the Young's Modulus of the material multiplied by the cross-sectional area and divided by the length. However, since a uniaxial force was applied and the material was allowed to strain in all directions, the testing conditions allow only for the derivation of the elastic constant and not Young's Modulus from the test data. Therefore the equation that relates the measured stiffness value to the elastic constant is

$$s_{33}^E = \frac{A_{cr}}{k^E l} \tag{4.3}$$

where A_{cr} is the cross-sectional area of the actuator and l is the active length of the material. It should also be noted that solving this equation for stiffness is how the calculated stack stiffness was found from the bulk material properties, as presented in table 4.2.

The measured values of stiffness and elastic constant are considerably different from the bulk material values. The differences can largely be attributed to losses introduced in the manufacturing process and variations in the bulk material properties. In addition, small errors are introduced in the assumption that the insulation pieces are rigid and by neglecting the stiffness of the interface between the insulation pieces and the active part of the stack.

Capacitance and Dielectric Constant

The capacitance of the actuator was found in two ways. The first method involved taking admittance data with the Hewlett Packard Impedance Analyzer and finding an equivalent capacitance. The second method was taking benchtop data by applying various values of voltage and measuring

the current signal going to the actuator. Both of these methods are described in detail below.

The first method involved finding the equivalent capacitance of the actuator based on the frequency response of the stack with small applied voltages. Tests were taken through the use of the Hewlett Packard 4194A Impedance/Gain-Phase Analyzer. The maximum applied voltage from the Analyzer is 35 V, although it is likely that the actual applied voltage was far below the maximum value. The actuator was tested in free-free conditions. Admittance data was taken from 100 Hz to 10 kHz to avoid the first resonance of the actuator at 31 kHz. The response of an equivalent capacitance was automatically calculated based on the measured response of the actuator by using the functionality of the HP Analyzer. The resulting capacitance at constant stress is 785 nF.

Benchtop tests were also taken to find the capacitance of the actuator. The sample was tested in free-free conditions while being powered by a Trek 609D-6 High Voltage Amplifier. The National Instruments/LabVIEW Data Acquisition System was used to generate the input signal to the amplifier and record the time profiles of current and voltage. The current and voltage signals measured were the output signals from the current and voltage monitors on the Trek amplifier. The input and output voltage signals have a gain of 1000. The current signal has a scaling factor of 2 mA/V. The signal used as input to the amplifier is

$$V_{appl} = \frac{1}{2}V_{max}\sin(20\pi t) + \frac{1}{2}V_{max} \tag{4.4}$$

Tests were taken for 0.5 seconds at 10 Hz. Maximum voltage levels were taken from 25 V to 225 V at 25 V intervals. A representative time trace of the current and voltage data is shown in fig. 4-3.

The time integral of current was taken to find the charge on the electrodes. This new time trace was plotted versus voltage and the maximum voltage and largest current points were found for each test. The maximum values were plotted on a new graph with a least squares linear fit, as shown in fig. 4-4. The slope of the linear data fit is the tested capacitance of the actuator under constant stress, and has a value of 1050 nF.

The dielectric constant under constant stress can be found from the measured value of capacitance by using the physical stack properties. The equation that relates the capacitance and dielectric constant is

$$\varepsilon_{33}^{T} = \frac{C^{T} t_l}{A_{cr} N} \tag{4.5}$$

where t is the thickness of each layer and N is the number of layers in the actuator. This equation

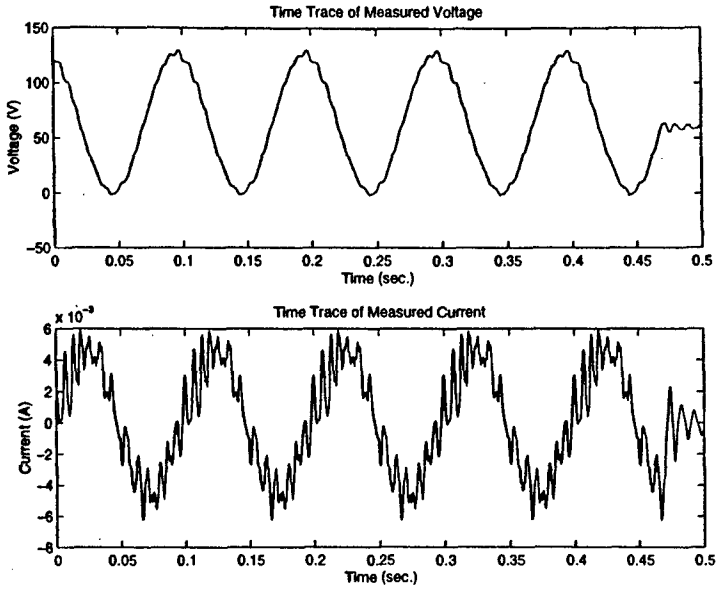

Figure 4-3: Representative time traces of Current and Voltage values measured while finding the capacitance of the Sumitomo actuator.

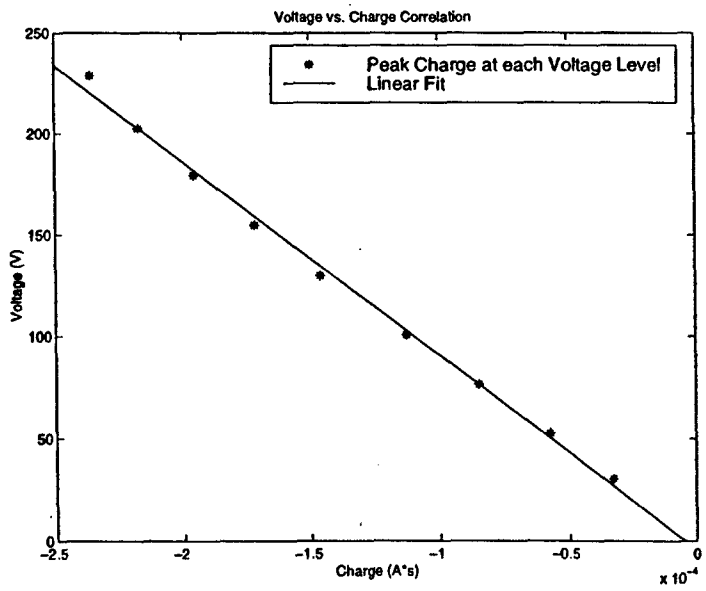

Figure 4-4: Test used to find the dielectric constant of the material at varying values of electric field.

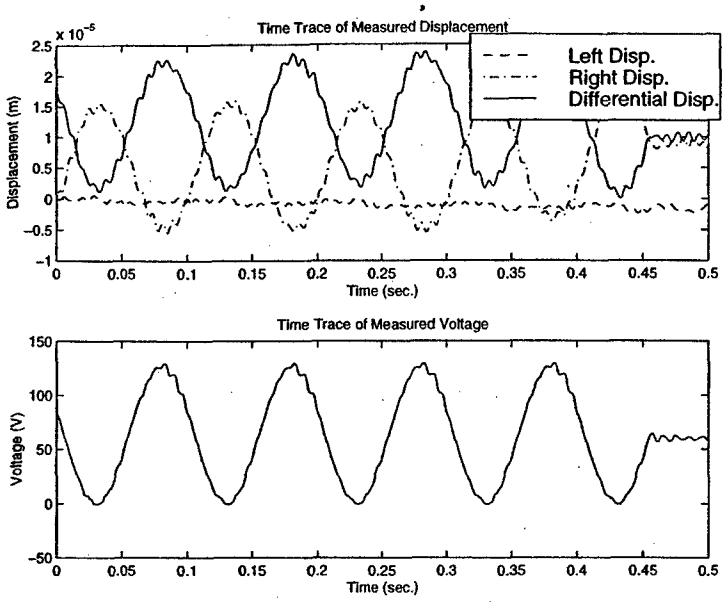

Figure 4-5: Representative time history of voltage and displacement measured when finding the electro-mechanical coupling in the Sumitomo actuator.

is used with the values presented in table 4.1 to find the calculated values of dielectric constant from the measured values of capacitance. The dielectric constant for the stack was found from the published capacitance from the same equation. Both measured values of capacitance translate into dielectric constants that are within the accuracy range of the published values for the bulk material and stack information.

Displacement vs. Voltage and the Electro-mechanical Coupling Term

Bench top displacement vs. voltage tests were taken in order to find an approximate value of the electro-mechanical coupling in the system. Tests were taken with the actuator in free-free conditions. Tests were taken with the same setup as the bench top dielectric tests were taken with the displacement measured using the Photonic sensors. The voltage was applied and monitored with the Trek amplifier. The input signal was generated and the results recorded using LabVIEW. The tests were taken at 10 Hz for 0.5 seconds. A representative time history of the voltage and displacement is shown in fig. 4-5. The maximum voltage and displacement value for each test was recorded and plotted to determine the displacement vs. voltage value. The correlation is shown in fig. 4-6. A least squares, linear fit to the data was performed and resulted in a measured value of 0.162 μm/V. The linear fit neglected the 175 V and 200 V data points when performing the fit.

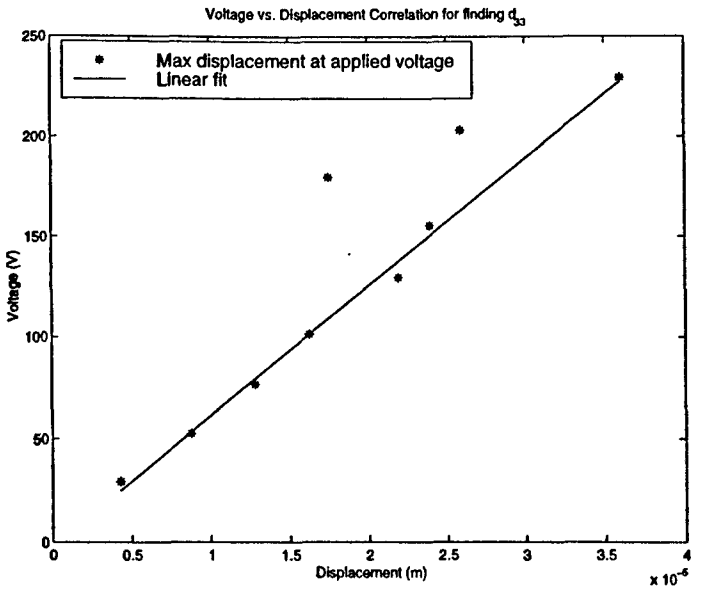

Figure 4-6: Test used to find the electro-mechanical coupling term of the Sumitomo stack at varying values of applied voltage.

The electro-mechanical coupling term can be found from the displacement vs. voltage value through the use of the physical properties of the stack. The equation that relates the two values is

$$d_{33} = \frac{\left(\frac{x}{V}\right) t_l}{l} \tag{4.6}$$

Using this equation with the measured value of displacement vs. voltage results in a electro-mechanical coupling term of 788 $\times 10^{-12}$ m/V. This equation is also used to convert the published stack value of displacement vs. voltage to the electro-mechanical coupling term.

4.4.3 Selection of Material Values and Coupling Coefficient

Before continuing, it is desirable to determine what range of values will be considered reasonable for each of the actuator properties. These values will then be used to determine what range of data should be taken for the linear and non-linear tests. Each of the values will be looked at in turn and ranges of reasonable values decided upon. The final range of values used is presented in table 4.3.

The first parameter considered is the elastic constant. Because the only published value of elastic constant is for the bulk material, it is difficult to justify the use of the derived stiffness value from the bulk material. However, the disparity between the value of the elastic constant for the

Table 4.3: Ranges of the Sumitomo material properties used in the theoretical comparison to the data.

Material Property		Average	Maximum	Minimum
Item	Units	Value	Value	Value
Elastic Constant	$10^{-12}\mathrm{m}^2/\mathrm{N}$	31.3	34.5	27.5
Dielectric Constant	$\varepsilon_{33}^T/\varepsilon_0$	4015	4818	3215
Electro-mechanical coupling	$10^{-12}\mathrm{m/V}$	785	824	746

bulk material and the derived elastic constant from the measured stiffness value makes it difficult to attribute the errors entirely to material inconsistencies and manufacturing tolerances. Therefore, a reasonable range of values to consider for the elastic constant is a range from the constant based on the measured stiffness value, 34.5 $\times 10^{-12}$ m^2/N, to a value halfway between the bulk and measured values at 27.5 $\times 10^{-12}$ m^2/N. Using this range of values should capture the actual stiffness of the stack.

Next, it is necessary to determine a reasonable range of values for the dielectric constant. Since there are many reasonable values to consider, and since the minimum and maximum values are both measured parameters, it is perhaps best to take an average of the values and consider a range of $\pm 20\%$ around that value. The average value of the dielectric constant is 4015 ε_0 with the upper and lower bounds at 4818 ε_0 and 3215 ε_0 respectively. This completely bounds all values found for the dielectric constant.

The electro-mechanical coupling term is the easiest value to bound because of the similarity in the published and measured values. It can be assumed that the bulk material value will not be as accurate because of the configuration issues. Therefore the value assumed for the electro-mechanical coupling term is 785 $\times 10^{-12}$ m/V with an error factor of 5%.

Finally, the coupling coefficient to be used must be determined from the published value, the tested value, and the values resulting from the different combinations of the stack properties. In terms of the fundamental properties of an active material, the coupling coefficient for the extensional mode of operation is defined as

$$k_{33}^2 = \frac{{d_{33}}^2}{s_{33}^E \varepsilon_{33}^T} \tag{4.7}$$

However, it is also possible to find the coupling coefficient in the extensional mode of operation by finding the resonance and anti-resonance of the sample. This method was used to find the published coupling coefficient of the bulk material and measured for the stack by using the HP analyzer. The

Table 4.4: Comparison of different possible material coupling coefficient values for the Sumitomo actuator.

Method of Obtaining Value			Coupling Coefficient k_{33}^2	Data Label
Bulk Material			0.72	-
Measured Stack Resonance			0.44	-
max s_{33}^E	max ε_{33}^T	max d_{33}	0.675	Theory 1
min s_{33}^E	min ε_{33}^T	min d_{33}	0.843	Theory 2
mean s_{33}^E	mean ε_{33}^T	mean d_{33}	0.745	Theory 3
max s_{33}^E	max ε_{33}^T	min d_{33}	0.611	Theory 4
min s_{33}^E	min ε_{33}^T	max d_{33}	0.932	Theory 5

equation used to relate the resonance and anti-resonance of the stack to the coupling coefficient is

$$k_{33} = \frac{\pi}{2}\frac{f_r}{f_a}\tan\left(\frac{\pi}{2}\frac{f_a - f_r}{f_r}\right) \tag{4.8}$$

where f_r and f_a are the resonant frequency and anti-resonant frequency respectively.

The measured stack coupling coefficient was found by taking the frequency profile of the stack with the HP impedance analyzer. The initial frequency sweep was taken over a range of frequencies from 100 Hz to 40 MHz. This initial sweep located the frequency in the 10 kHz decade. Then the sweep was changed to a sweep from 10 kHz to 100 kHz to find the actual value of the resonance. The resonant and anti-resonant values were measured from the analyzer through the use of the "min" and "max" functions and the values recorded. The resonant frequency was found to be 31.26 kHz and the anti-resonant frequency was 40.04 kHz. These values result in a coupling coefficient of 0.44.

A comparison of all of the coupling coefficient values is presented in table 4.4. The coupling coefficients found using the resonance method are presented first. Then the coupling coefficients found from combinations of different stack values are presented. As can be seen from the values, the different combinations of property values can result in a wide range of coupling coefficient values. It is important to again limit the range of values considered for the coupling coefficient while keeping in mind that this limitation will affect the effective range of material properties that are used.

Looking at the coupling coefficient values, it is difficult to just decide upon a range to use in the data analysis since each value of coupling coefficient depends on the use of specific stiffness, dielectric constant and electro-mechanical coupling values. In turn, each of these values will effect the predicted stiffness, work input, work output, and actuation efficiency values when analyzing

testing results. Therefore, the five values in table 4.4 based on material properties will be used in the analysis of the data with the corresponding material values used when more than just the coupling coefficient is needed.

4.5 Validation of Linear Loading of Piezoelectric Materials

Tests were performed on the stack while working against a linear load of different stiffnesses. The lower and upper bounds on the stiffness were determined by the amount of control that was required of the testing machine to achieve the stiffness value. Therefore, for a 200V maximum input voltage it was possible to test a range of stiffness ratios from 0.5 to 2. The voltage input to the stack was half of a cycle of a sinusoid with a maximum value of 200 V and a frequency of 0.025 Hz. The tests were performed using the controller designed for the testing machine and described in section 3.5.6. Tests were taken for 20 seconds at a 40 Hz sampling frequency with a gain of 12.6.

Two to three tests were performed at each stiffness value and the current, voltage, force and displacement time traces were recorded. Representative time traces of the values recorded are presented in fig. 4-7. The force and displacement measurements were generally noisy measurements that produced more noise in the system when integrated. Therefore, eight point data averages of the force, inside displacement and outside displacement values were performed. The averaged total displacement value was the difference of the averaged inside and outside displacement values. From the values recorded, the electrical and mechanical work was determined at each time through the following expressions.

$$W_{out} = \int_{x_i}^{x} F dx \tag{4.9}$$

$$W_{in} = \int_{t_i}^{t} VI dt \tag{4.10}$$

The integrals, when taken over the complete cycle, should return to zero assuming that none of the work was lost to the environment. Therefore, the important information is the time history of the electrical and mechanical work of the system.

The time history of electrical and mechanical work is shown in fig. 4-8 for a sample case of the active material working against a load of the same stiffness. The current data has a bias offset that is removed before taking the time integration of the product of the voltage and current so that the cycle work returns to zero. The bias current is $\pm 20\mu$A, considerably smaller than the peak current

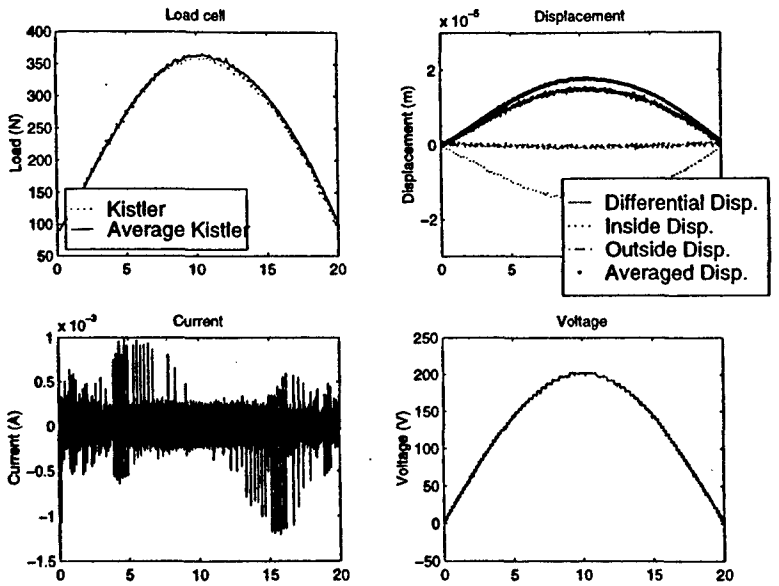

Figure 4-7: Representative time traces of the force, displacement, voltage and current data measured during testing a piezoelectric actuator working against a linear load.

values that are on the order of 1 mA. The force and displacement used to find the mechanical work are the 8 point averaged values.

The maximum value of the mechanical and electrical work was recorded for each test taken and averaged at each stiffness ratio. Additionally, the maximum value of the mechanical work for each test was divided by the maximum value of the electrical work for each test and then averaged at each stiffness ratio to determine the maximum actuation efficiency variation with stiffness ratio. These results are shown in figures 4-9, 4-10 and 4-11. In order to plot each value in relation to the stiffness ratio, an assumed actuator stiffness of 20.2 N/μm was used. The data points plotted are the average value of the tests taken at that stiffness ratio. The error bars illustrate the range of values recorded at each stiffness ratio.

The five theory lines shown in each figure are based on the variations of the assumed material properties, as described in section 4.4.3. The theory lines are based on the following equations for work output, work input and actuation efficiency of linear systems working against a linear load.

$$W_{out} = \frac{1}{2}\frac{A}{l}\varepsilon_{33}^{T}V^2N^2\left[\frac{\alpha}{(\alpha+1)^2}\right]k_{33}^2 \tag{4.11}$$

$$W_{in} = \frac{1}{2}\frac{A}{l}\varepsilon_{33}^{T}V^2N^2\left(1-\frac{\alpha}{\alpha+1}k_{33}^2\right) \tag{4.12}$$

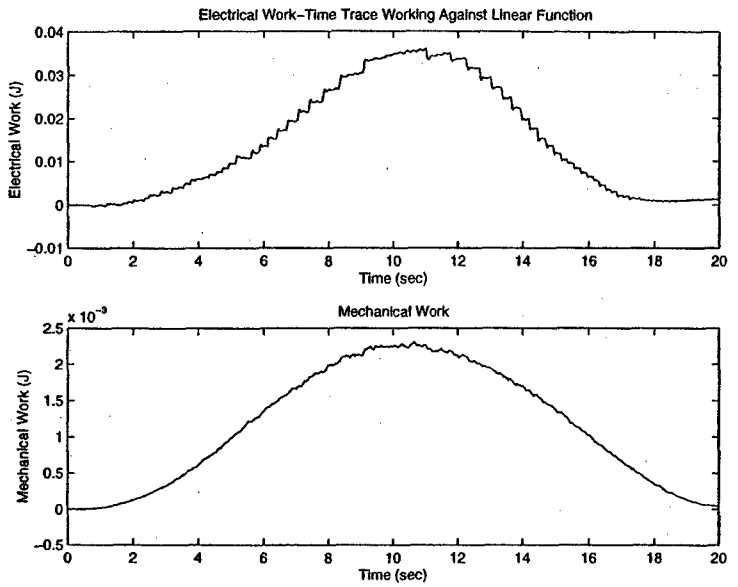

Figure 4-8: Electrical and Mechanical work of an active material working against a uniaxial load of the same stiffness, time traces.

$$Ef = \frac{\left[\frac{\alpha}{(\alpha+1)^2}\right] k_{33}^2}{1 - \frac{\alpha}{\alpha+1} k_{33}^2} \tag{4.13}$$

As can be seen from these equations, the most important single material value for fitting the experimental results and theoretical results is the dielectric constant of the material. However, the various values of coupling coefficient also significantly effect the data correlation. In addition, the elastic constant effects the theoretical fit to data since the assumed stiffness value effects what stiffness ratio value the work data is plotted at. Therefore, changing the actuator stiffness would shift the data points one direction or the other. The material constants that correspond to the data labels are shown in table 4.4.

The mechanical work data shows good correlation with the average theory lines as can be seen in fig. 4-9. Both the trend of the maximum work output location and the magnitude of the work output data correlate well with the expected results. The theory line that most closely matches the data is the "Theory 1" line, consisting of the maximum values of the material constants. This is expected since the tested values of the material constants lie in the upper region of the material values considered.

The electrical work data shown in fig. 4-10 does not correlate well with the expected theoretical

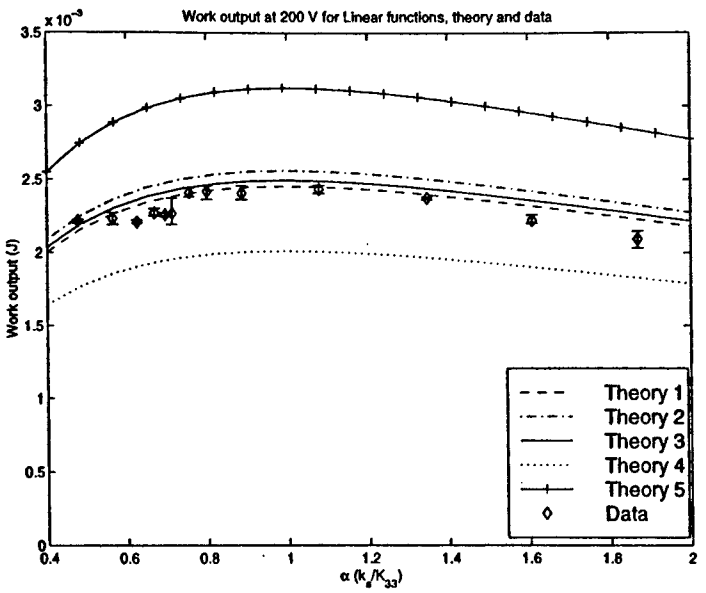

Figure 4-9: Maximum work output variation with stiffness ratio for an active material working against a linear load.

results. The data lies a factor of 2 or more above the expected theoretical results. A possible reason for this discrepancy is the frequency at which the actuator was run. The tests were taken at a very low frequency of 0.025 Hz. However, at frequencies this low, it is difficult to get accurate current data because most of the data occurs in current spikes, as can be seen in fig. 4-7. When dielectric constant values were measured at low frequencies, the values were often off by as much as a factor of 2 and sometimes more. Therefore, it is likely that the gross errors in the electrical work data are a product of the testing frequency and not the theory presented. Unfortunately, it is not possible to test a piezoelectric material working against a load in the component testing facility in its current configuration at a high enough frequency to get accurate current measurements. By eliminating the dynamics present in the displacement sensor stands and with a redesigned control loop it should be possible to take data at higher frequencies.

The actuation efficiency data is presented in fig. 4-11. Again, there is a significant mismatch in the data presented versus the expected theoretical results. The difference is due to the problems with the electrical work data. If the electrical work data more closely matched the expected results based on the theory, then it is likely that the actuation efficiency would also match the expected results since the mechanical work data closely matches the expected results. Unfortunately, the large values of electrical work make the variation in measured actuation efficiency with stiffness

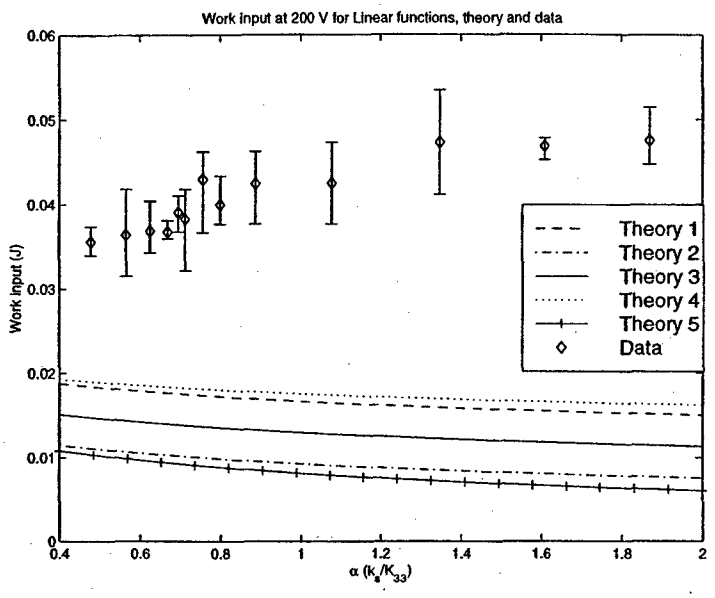

Figure 4-10: Maximum input work variation with stiffness ratio for an active material working against a linear load.

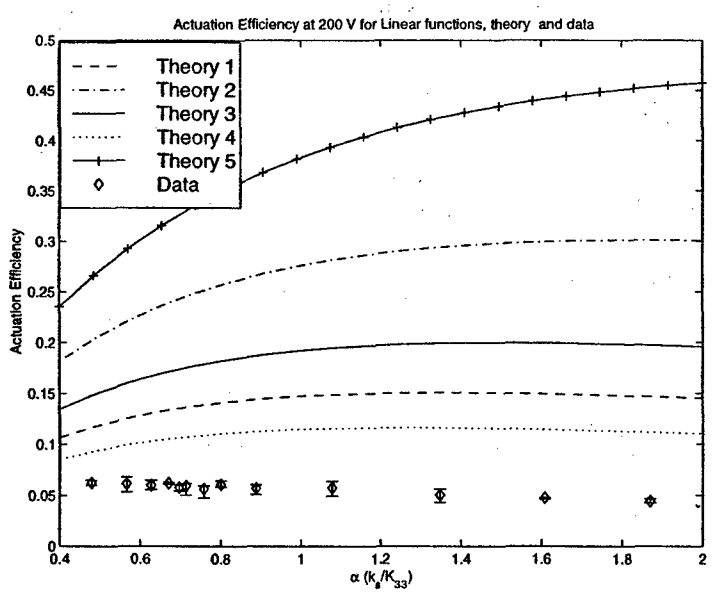

Figure 4-11: Maximum actuation efficiency variation with stiffness ratio for an active material working against a linear load.

ratio very small.

4.6 Validation of Non-linear Loading of Piezoelectric Materials

To validate the performance increases possible through the use of non-linear loading functions, tests were taken on the stack when working against the two types of loading functions used in the theoretical derivation. As a point of comparison, the performance found when the active material was working against non-linear loading functions was compared to the performance of the material when working against a linear loading function with the same stiffness value as the secant stiffness of the non-linear loading functions. This was done for four different stiffness values at two different voltage levels.

The non-linear loading functions were tested through the use of the programmable impedance functionality of the component testing facility. The functions were determined based on the desired range of stiffnesses and the desire to maximize the area under the material load line. However, the possible functions tested were limited by the initial stiffness of the function, since the non-linear functions that capture the most area have the largest initial stiffness. Unfortunately, the conditions on initial stiffness severely limited the functions that could be tested and in fact forced the testing of functions that made the controller on the edge of instability. Therefore, tests of the material working against some of the functions with high initial stiffnesses have severe startup transients that effect the maximum work values calculated.

The functions tested at a 200V input voltage and 150V input voltage are shown in figures 4-12 and 4-13, respectively. In each figure eleven different functions are shown, three functions at each of four stiffnesses with the exception of one "non-linear 1" function. The three different functions are a linear function, a "non-linear 1" function, and a "non-linear 2" function. The base equations for the "non-linear 1" and "non-linear 2" functions are

$$F_{n1} = Ax \exp \frac{-\sqrt{|x|}}{B} \tag{4.14}$$

$$F_{n2} = D \tanh (Cx) \tag{4.15}$$

Using the defined loading functions as input to the controller allowed for verification of performance increases through the use of non-linear loading functions.

Results of the tests were recorded and correlated similarly to the results of the linear tests.

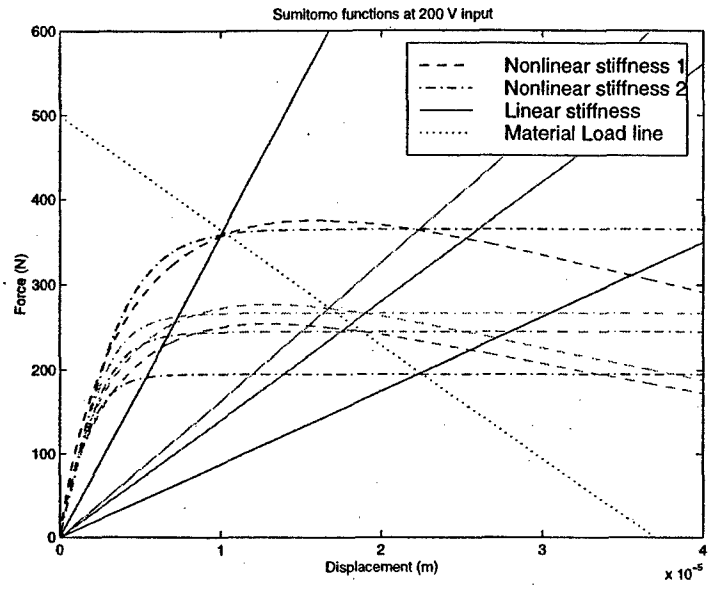

Figure 4-12: Non-linear and linear loads tested with a 200V stack input voltage, shown with the material load line on a force-displacement graph.

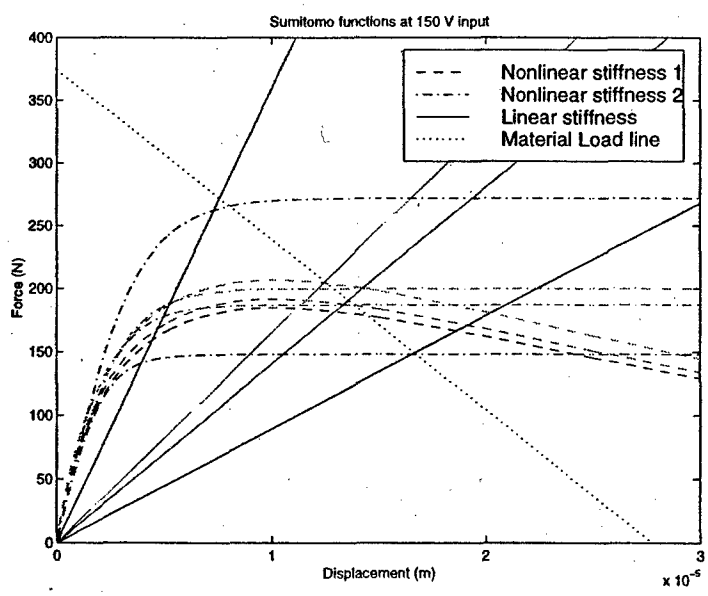

Figure 4-13: Non-linear and linear loads tested with a 150V stack input voltage, shown with the material load line on a force-displacement graph.

Again, multiple tests of each of the loading functions were performed and the results averaged. The maximum work output and work input for the different loading function tests are shown in figures 4-14 through 4-17 as a function of stiffness ratio. The figures show the results of the tests taken at both 150 V and 200 V. The non-linear functions are plotted against their secant stiffness ratio. An actuator stiffness of 20.2 N/μm was used in calculating the stiffness ratio. Again, the data point plotted is the averaged value of the tests taken at each stiffness with the error bars demonstrating the range of values recorded.

The mechanical work results for actuator inputs of 150 V and 200 V working against linear and non-linear functions are shown in figures 4-14 and 4-15. The data for the linear and non-linear tests are shown with the five theory lines based on work against a linear load. In both figures, the linear data points are within the range of expected results. The non-linear functions, however, show significant increases in the work output over the linear work output values. For example, the "non-linear 2" mechanical work is a factor of two greater than the "linear" mechanical work for a stiffness ratio of 0.7 and input voltage of 150 V. The "non-linear 1" mechanical work for the same test was almost a factor of three greater than the "linear" work. Generally, the mechanical work values show distinct increases by using non-linear loads instead of linear loads. However, it should be noted that the reduced performance levels at the higher values of stiffness ratio are due in large part to the problems testing these functions and should not be an indication of poor theoretical performance.

The electrical work results are presented in figures 4-16 and 4-17. Similarly to the linear electrical work data presented in fig. 4-10, the electrical work data presented in these figures are up to a factor of two above the expected values for electrical work. The mismatch is likely from the same frequency problems encountered in the linear work. However, it should be noted that the "non-linear" work data does follow a similar downward trend as the "theory" lines.

Increases in the actuation efficiency of a piezoelectric material can be seen when the device is working against a non-linear load verses a linear load. The actuation efficiency information is presented in figures 4-18 and 4-19. The results are plotted against the expected linear theoretical results from varying stiffness values and material coupling coefficient. At stiffness ratios close to one, increases of more than a factor of two are demonstrated at the 150 V input level. Unfortunately, in general the actuation efficiency is much less than the expected actuation efficiency. This is again due to the problems with the electrical work data and measuring current values. However, the

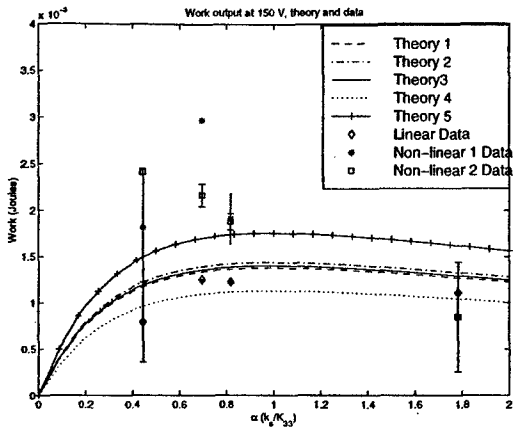

Figure 4-14: Work output values of the active material when working against linear and non-linear loading functions with an input value of 150 V verses the stiffness ratio of the linear load. Values are compared to the expected work output based on work against a linear function for multiple values of the material constants.

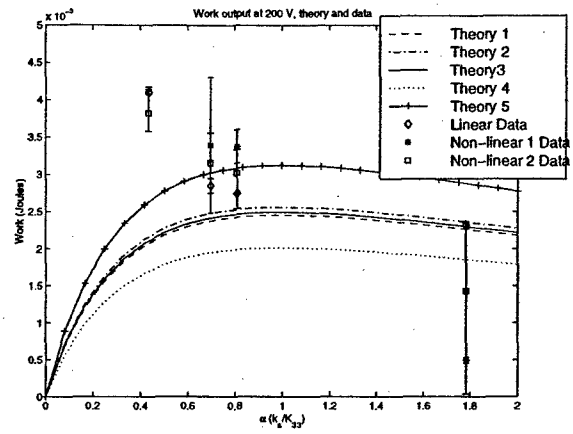

Figure 4-15: Work output values of the active material when working against linear and non-linear loading functions with an input value of 200 V verses the stiffness ratio of the linear load. Values are compared to the expected work output based on work against a linear function for multiple values of the material constants.

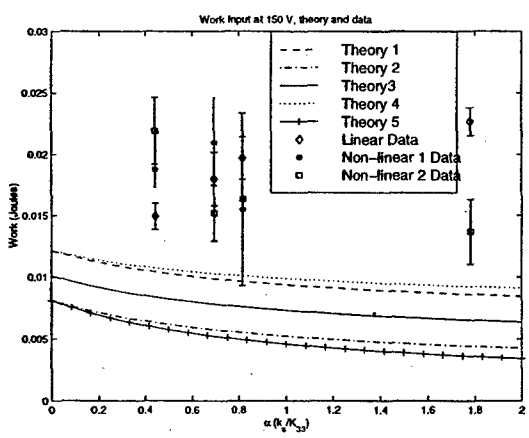

Figure 4-16: Work input values of the active material when working against linear and non-linear loading functions with an input value of 150 V verses the stiffness ratio of the linear load. Values are compared to the expected work input based on work against a linear function for multiple values of material constants.

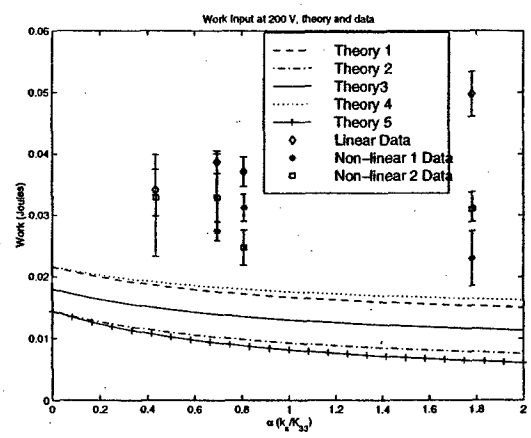

Figure 4-17: Work input values of the active material when working against linear and non-linear loading functions with an input value of 200 V verses the stiffness ratio of the linear load. Values are compared to the expected work input based on work against a linear function for multiple values of material constants.

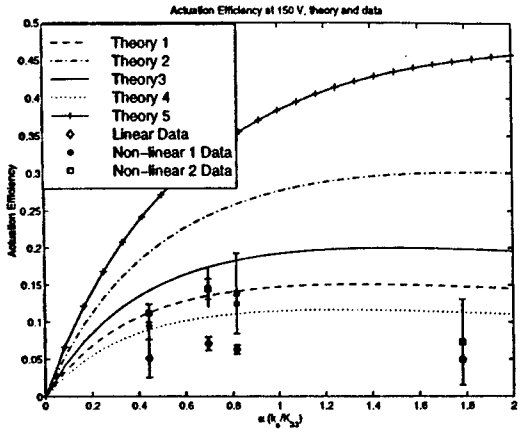

Figure 4-18: Actuation efficiency values of the active material when working against linear and non-linear loading functions with an input value of 150 V verses the stiffness ratio of the linear load. Values are compared to the expected work output based on work against a linear function for varying values of coupling coefficient.

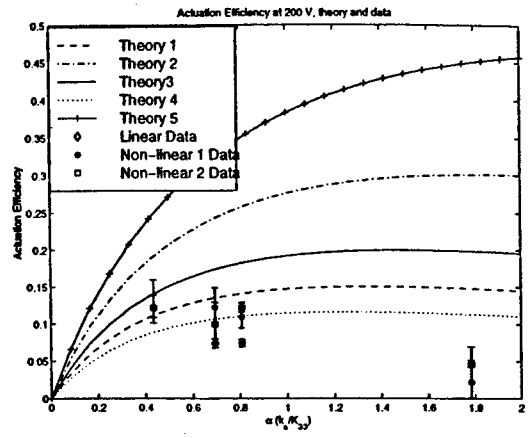

Figure 4-19: Actuation efficiency values of the active material when working against linear and non-linear loading functions with an input value of 200 V verses the stiffness ratio of the linear load. Values are compared to the expected work output based on work against a linear function for varying values of coupling coefficient.

hoped-for increases in actuation efficiency through the use non-linear loads is clearly demonstrated in the figures.

It should be noted that correlation of non-linear loading function secant stiffness with performance increases should not be made based on this data since the performance values are highly dependent on the actual loading function used. Instead, the general validation of increases in the performance of active materials working against non-linear loading functions verses linear loading functions should be understood.

4.7 Non-linear Loading Device

As mentioned at the end of Chapter 2, the increased work efficiency associated with a non-linear loading function is only useful if a method is devised to load the active material non-linearly while allowing a linear response of the structure being loaded. A common method of achieving a zero-rate spring stiffness is by configuring two springs into a triangle and looking at the behavior of the springs as they are loaded through the flat point of the system. Using this idea, a device was designed that, with the right spring selection, can non-linearly load the active material while linearly loading the structure. Obviously, this is only useful if the extra work from loading the

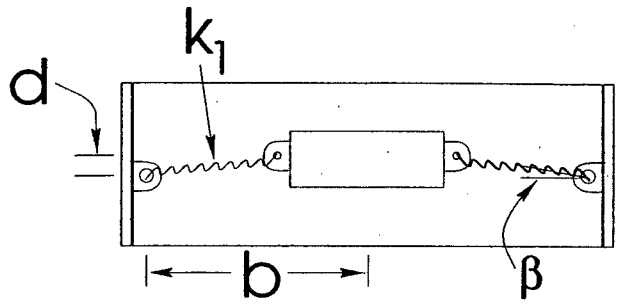

Figure 4-20: Non-linear loading device. Presented in cross-section. Dimensions labeled are the critical dimensions in the design.

material non-linearly is transmitted to the structure and not all used by the loading device.

The cross-sectional view of the proposed device is shown in figure 4-20. The device consists of four springs where the uncompressed positions of the springs makes the central platform above the spring hinge points by a specified angle. During operation the platform is pressed down through the plane of the hinges and farther down to actually stretch the springs on the other side. The critical dimensions of the device are the initial spring angle, the distance from the hinges to the center of the platform, and the stiffness of the side springs. These values are all sized to the active material used and the stiffness of the structure it is working against.

The equation that describes the operation of the springs with the load is the following

$$F = 4k_1 \frac{d}{b \sin \beta_i} (\cos \beta - \cos \beta_i)(d - x) + k_2 x \tag{4.16}$$

where the angles are defined as

$$\beta = \tan^{-1}\left(\frac{d-x}{b}\right) \tag{4.17}$$

$$\beta_i = \tan^{-1}\left(\frac{d}{b}\right) \tag{4.18}$$

and the stiffness of the load is k_2. The rest of the variables used are defined in fig. 4-20. This equation can be inserted into the non-linear analysis presented in Chapter 2. The sample case presented here uses eqns. 4.16, 4.17, and 4.18 with the values presented in table 4.5 to find the performance metrics of the system. The load lines used are presented in fig. 4-21.

The analytical results are shown in the work profiles presented in figure 4-22. The top two lines

Table 4.5: Values used in the analysis of the performance possible using the proposed design of the non-linear loading device.

Variables		Value
Load Stiffness	k_2	6×10^6 lb/in
Side Spring Stiffness	k_1	9×10^{12} lb/in
Baseline	b	0.0036 inches
Hinge Height	d	3.5×10^{-6} inches

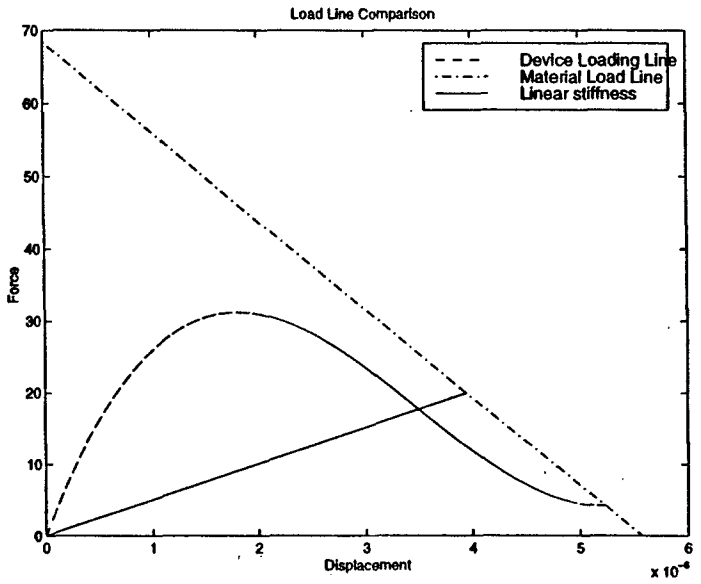

Figure 4-21: Load lines used in the analysis of the non-linear loading device.

in the figure are the work into the active material with and without the device. The next set of lines are the lines that describe the work output of the system. The top most of the second set of lines is the line that describes the work out of the active material and into the device and structure combined. The smoothest line is the linear work line. This is the line that describes the work into the structure when an unmodified material is working against a normal linear load. The final line that weaves through the rest of the lines is the amount of work that finally makes it into the structure from the active material and loading device. As can be seen in the picture, this value peaks at a 71% increase over the linear function.

The work efficiencies were then plotted in figure 4-23. There are three functions compared in this figure. The first one is the usual linear work equations that the non-linear loads have been compared to throughout the derivation of Chapter 2. The second item compared is the work out

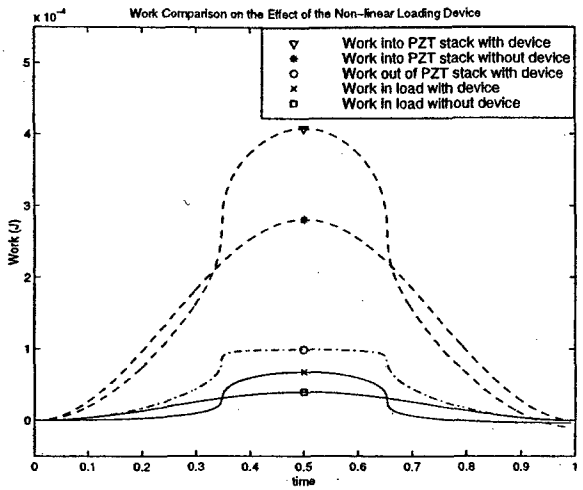

Figure 4-22: Work in and work out plotted for the non-linear loading device. Looks at the unmodified linear system and the work into and out of the active material and the work into the structure by using the non-linear loading device.

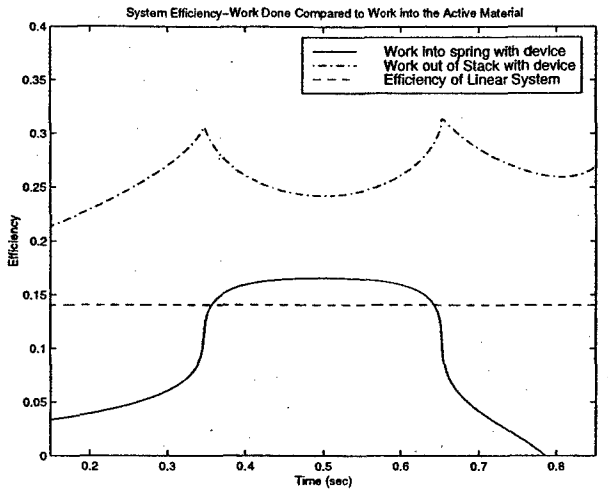

Figure 4-23: Work efficiency of the system using the proposed design of the non-linear loading device.

of the active material and into the loading device and structure combined divided by the work into the active material when loaded non-linearly. The third item compared is the same work into the active material, but the mechanical work-out is just the work that is being done on the structure. The last line is important in order to determine if the efficiency is actually increasing with the use of the device over the active material working against the structure without the aid of the device. The performance of this device demonstrates that it is realistic to design and build a device that can actually load an active material non-linearly in order to increase its performance output and transfer the increased performance to useful work on a linear load.

Chapter 5

Conclusions and Recommendations for Future Work

5.1 Conclusions of the Derivation of Actuation Efficiency and Work Output in Coupled Systems

The work presented demonstrates the need for using the fully coupled system equations when examining the actuation efficiency of an electro-mechanically coupled system in normal operating conditions. It has shown that the load coupling affects the expected performance for linear systems as well as non-linear systems. The work has also demonstrated the importance of looking at the true work efficiency of a system rather than relying on the material coupling coefficient as an approximate measure of the actuation efficiency of a system. However, it was shown that the device coupling coefficient does give a reasonable initial approximation of the efficiency of a system.

Through the use of the work expressions for a system under constant operation while working against a load, it has been possible to demonstrate a method for achieving a higher actuation efficiency over the same voltage cycle by utilizing the coupled nature of the piezoelectric material. The coupled nature allows for a significantly increased actuation efficiency and work output of systems that are working against a non-linear loading function instead of a typical linear load. A 200% increase in the work output achieved by a linear function has been demonstrated as possible through the use of a non-linear loading function.

The behavior seen in the theoretical examination of work in a coupled system have been experimentally verified. A Sumitomo multi-layered actuator was used to test the stiffness ratio correlation

of an active material working against a linear load. The work output values were verified and a discussion of the difficulties in achieving accurate work input values presented. The actuator was then loaded non-linearly. The increases in work output and actuation efficiency possible through the use of non-linear loading functions were verified.

Finally, the design for a device that could be used to load an active material non-linearly while loading a structure linearly was presented. The device was sized to maximize the work into the structure. Although the performance of the device does not match the performance possible through the use of the non-linear loading functions presented in Chapter 2, it does increase the amount of work delivered to the structure compared to the amount of work delivered from the active material working against the structure directly.

5.2 Recommendations for Future Work on the Analysis of Coupled Systems

The theoretical derivation of the work in coupled systems in has been demonstrated and the results for linear piezoelectric materials verified. However, there are many possible directions for the continuation of this work. One main direction is to expand the examples presented to include a non-linear material working against a linear load and a non-linear material working against a non-linear load. Only when these examples have been examined can it be stated that the work flow in piezoelectric materials has been fully explored and the main consequences for the design of systems discovered. It is likely that when looking at the non-linear region of the material, either further increases in the work output and actuation efficiency will be possible, or it will be found that non-linear material effects negate the positive effects found by using the linear material model. However, the importance of looking at the work flow is not diminished by a undesirable answer, rather the examination needs to be done in order to design systems most effectively.

A second avenue of exploration is to expand the work flow analysis to include other types of materials. Expanding the derivation for other materials that have material models in the correct two-block form, like the electrostrictive model presented by Fripp and Hagood[8], is a straight forward application of the equations presented. Exploration of the work flow for materials that do not have the correct form will require a more complete understanding of how energy is moving in the system and will likely run into the same type of problems that the derivation of a material coupling coefficient for non-piezoelectric materials has encountered[11].

In addition to these two main paths, it might be interesting to try to find the function that maximizes the actuation efficiency and work output of a material working against a non-linear function. Although restraints on the kind of function looked at is necessary, it would be interesting to see if the actuation efficiency is maximized with the same function that the work output is maximized with. This exploration could also be expanded to find the function that maximizes the work output or actuation efficiency of different classes of materials or kinds of piezoelectric materials.

A final area that is open for more work is the design of a device that effectively transfers the work done by the active material into the work done on the structure. The design of the non-linear loading device presented does increase the work done on the structure, however the increases possible by the system are not impressive. By looking at a different kind of loading device it should be possible to design a device which significantly increases the performance of the active material system.

5.3 Conclusions of the Design of the Component Testing Facility

A design was presented and validated for testing active materials in a uniaxial compressive testing facility. The facility was designed to be able to test relevant mechanical properties of active materials in a variety of testing conditions. The conditions that can be tested include testing at high preload values, testing at a variety of frequencies, and testing with constant force or constant displacement of the material tested. A design to include testing in thermal environments was also presented but not validated. A control loop was designed and tested that allows for constant force and constant displacement tests at frequencies up to 20 Hz. The parameters that are always measured in the testing system are the system force and sample displacement information. Other information can be recorded using the data acquisition system.

5.4 Recommendations for Future Work of the Component Testing Facility

The main improvement necessary for the desired operation of the component testing facility is a method of damping the vibrations in the position sensor stands in order to increase the testing frequency above 20 Hz. The damping should be possible by either isolating the disturbance source,

the interaction of motion of the endblock to the table surface, or by redesigning the method of mounting the stands to increase the natural frequency of the stands to above the frequency range of interest. With this improvement made, and the resulting redesign of the controller, it should be possible to test samples in the testing machine at frequencies up to 800 Hz. At this high frequency possible problems that might be encountered are the resonances of the testing machine, control loop speed limits from LabVIEW, or amplifier performance limits. However, the effects of most of these problems should be able to be reduced or eliminated without requiring the complete redesign of the testing facility.

The design of the component testing facility as presented is a comprehensive design for a limited range of tests. Currently, the tests must be in compression and must allow at least a small preload on the system. However, there are many kinds of active materials that should be tested in tension. Therefore, a primary recommendation for improving the Component Testing machine is to find a way to allow tensile tests while still allowing the system to perform compressive tests with the interchange of a few parts. In addition, there are parts of the design that a preliminary design was made, but the additional piece never built for the system. These include the thermal testing facility and a magnetic field yolk for testing magnetostricitve and magneto-shape memory materials at both AC and DC magnetic fields. A next-generation design of the testing facility is not needed at this point because the modularity of the current design allows for system modifications and improvements without having to redesign the entire apparatus. However, if a next generation design does become desired, the use of ball bearings over bushings is strongly recommended for ease of plate motion and alignment.

Appendix A

Component Testing Facility Drawings

The following pages contain the complete set of mechanical drawings for the Component Testing Facility. Materials used, tolerances and fasteners are noted on the pieces where appropriate. Additionally, the complete set of assembly drawings are included for further enlightenment on the design of the testing facility.

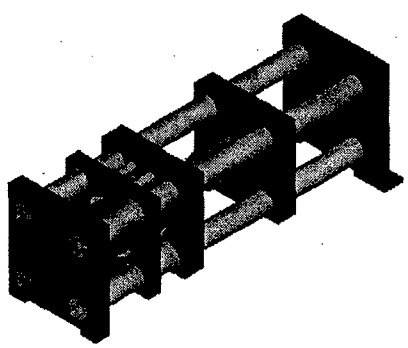

Figure A-1: Shaded parametric view of the model of the testing facility.

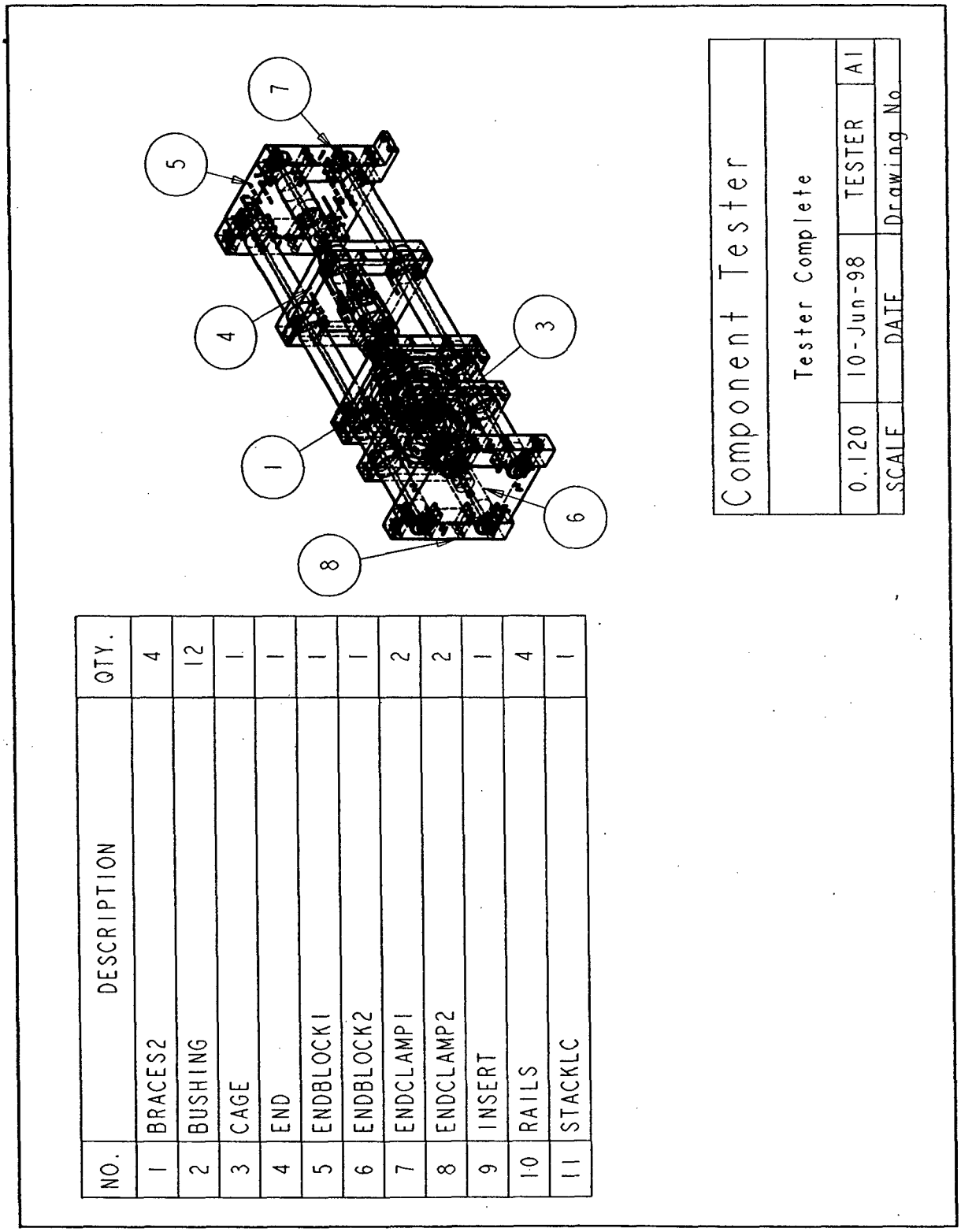

Figure A-2: Top Level Assembly Drawing.

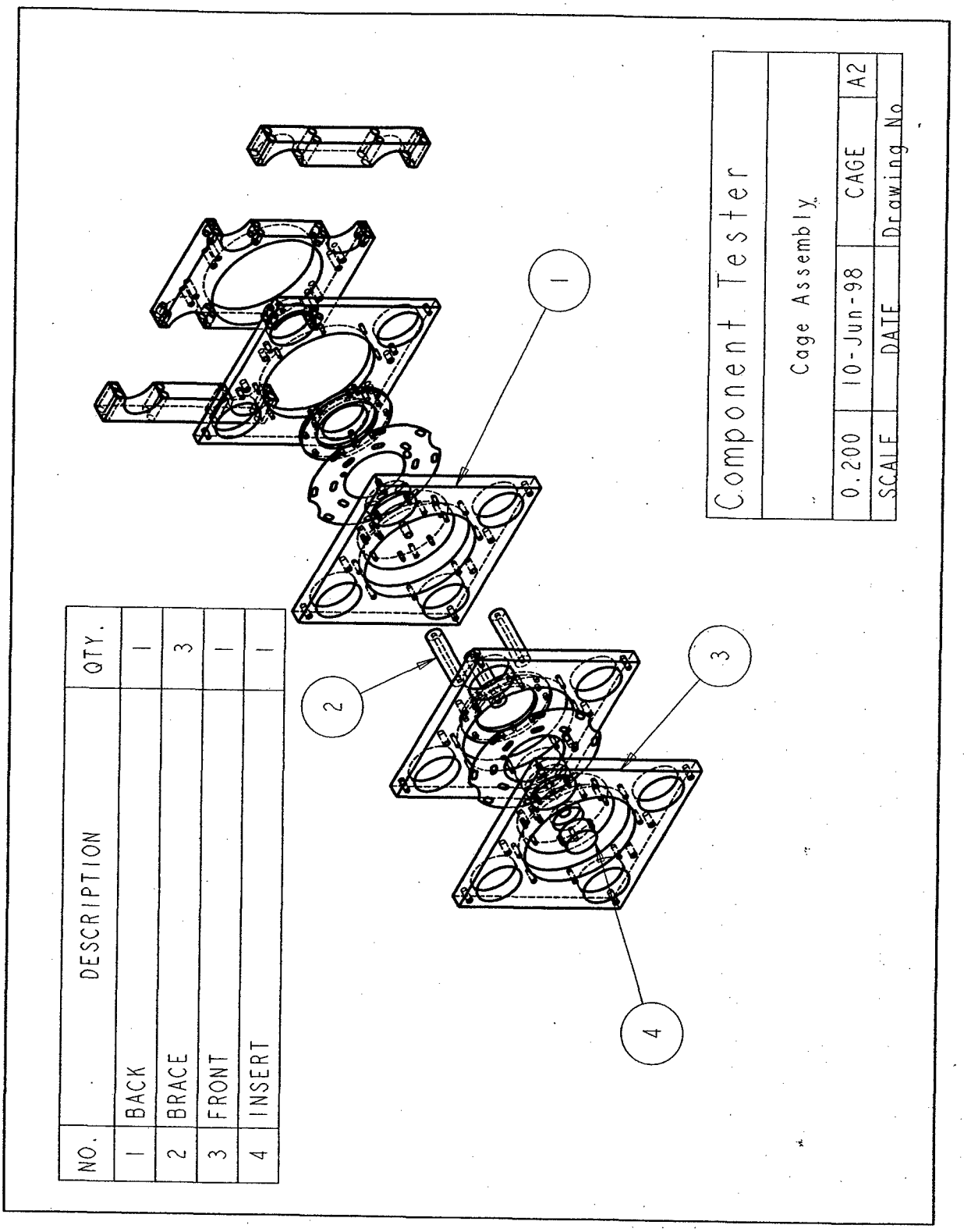

Figure A-3: Cage Assembly Drawing.

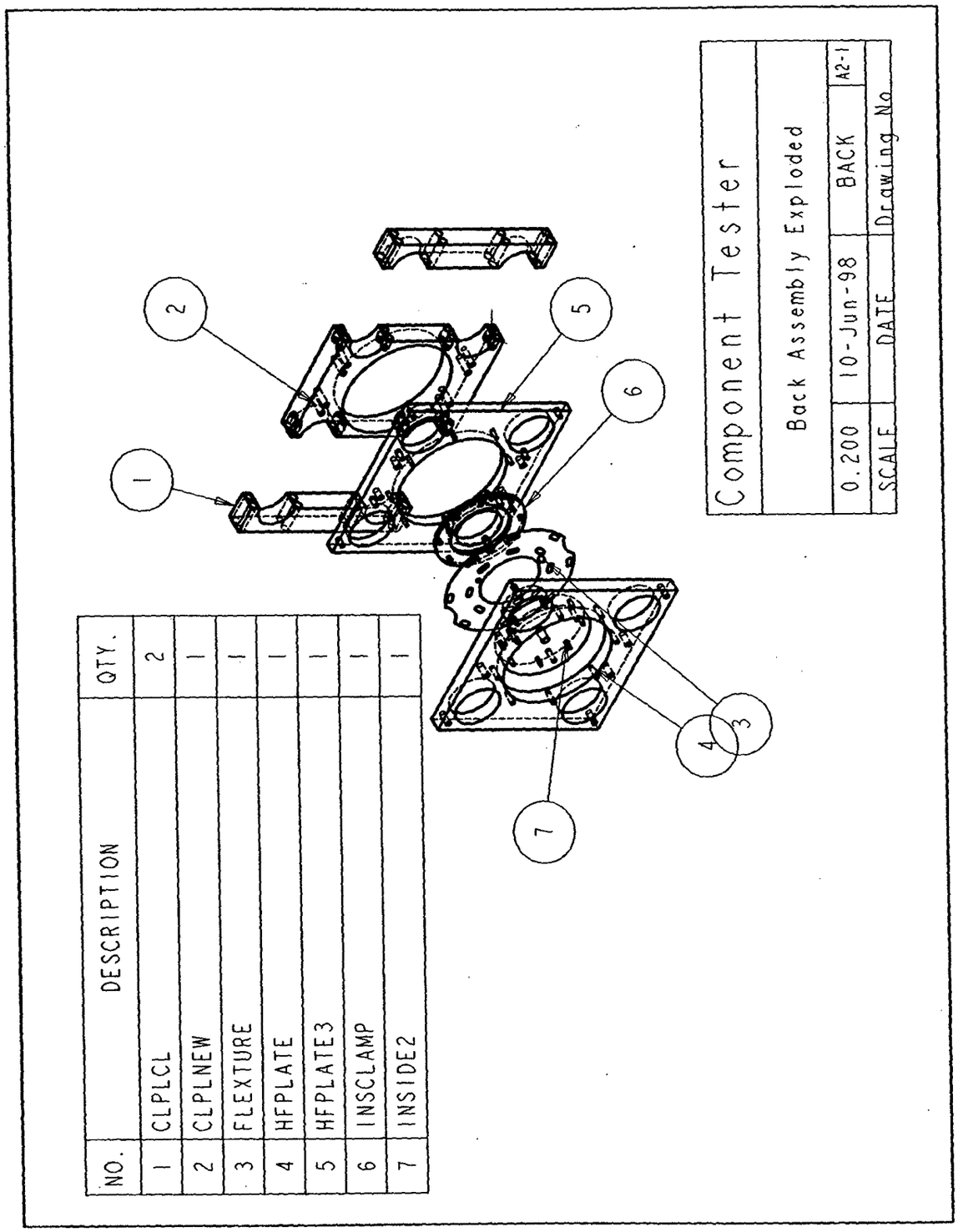

Figure A-4: Back Piece of Cage, Assembly Drawing.

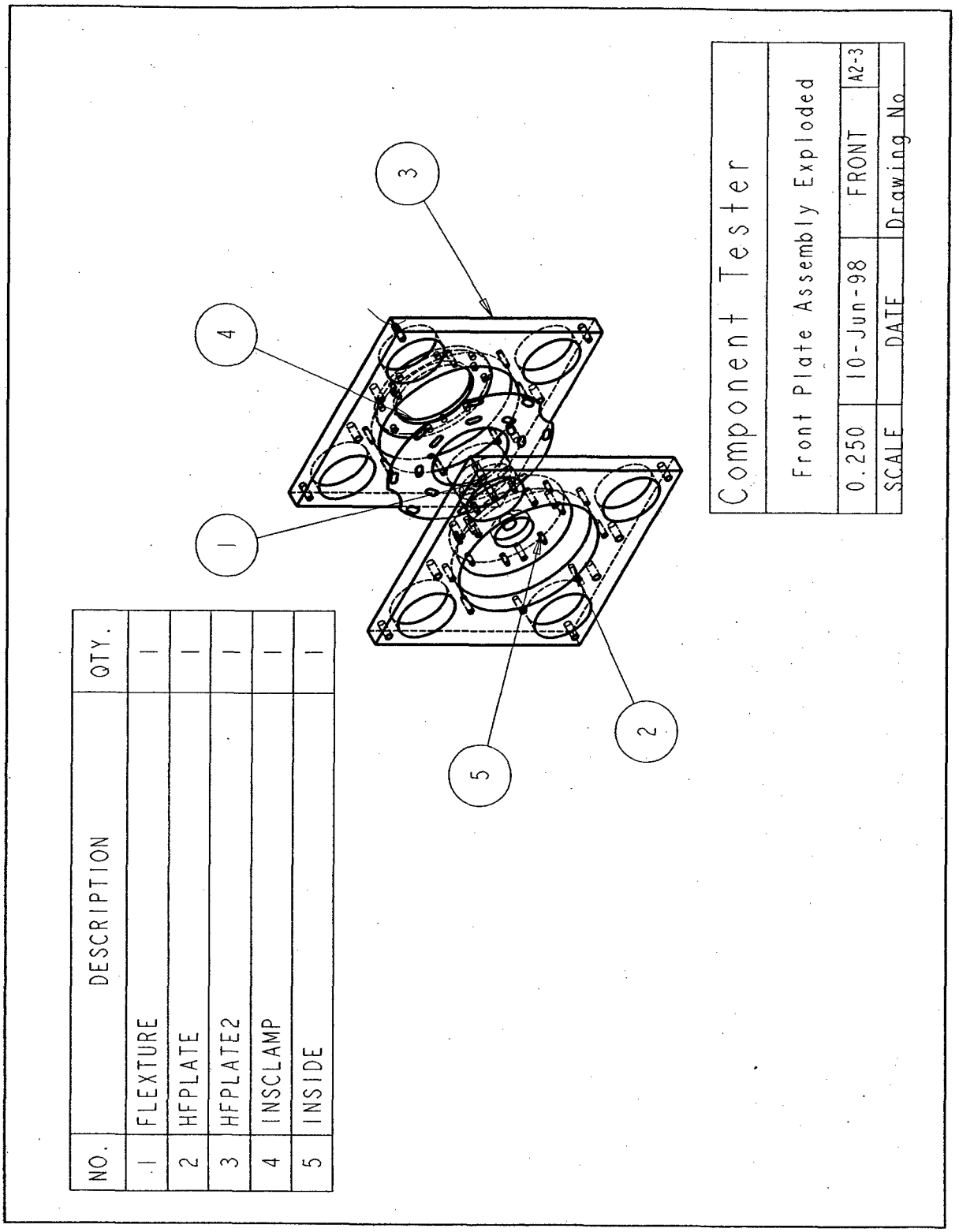

Figure A-5: Front Piece of Cage, Assembly Drawing.

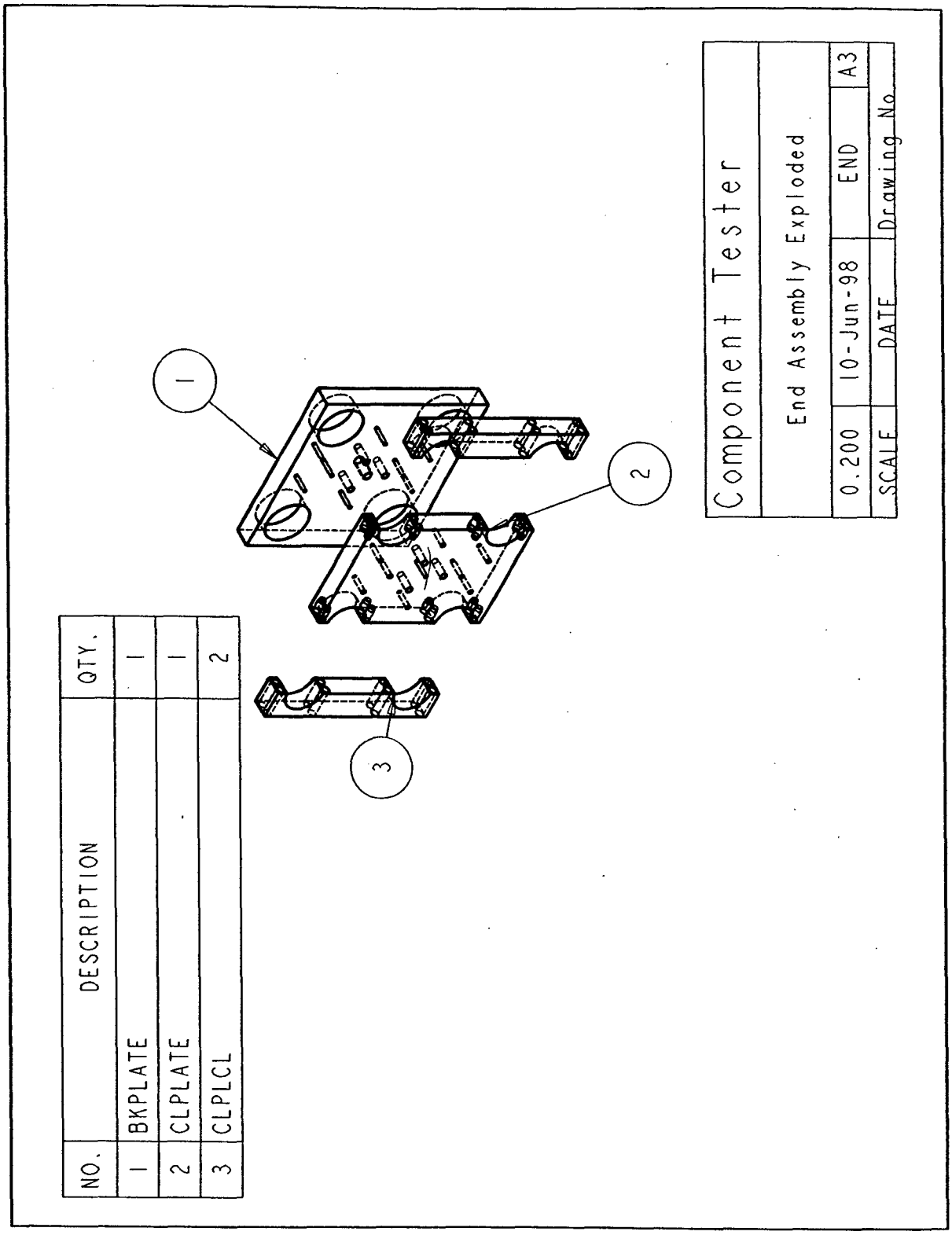

Figure A-6: End Piece Assembly Drawing.

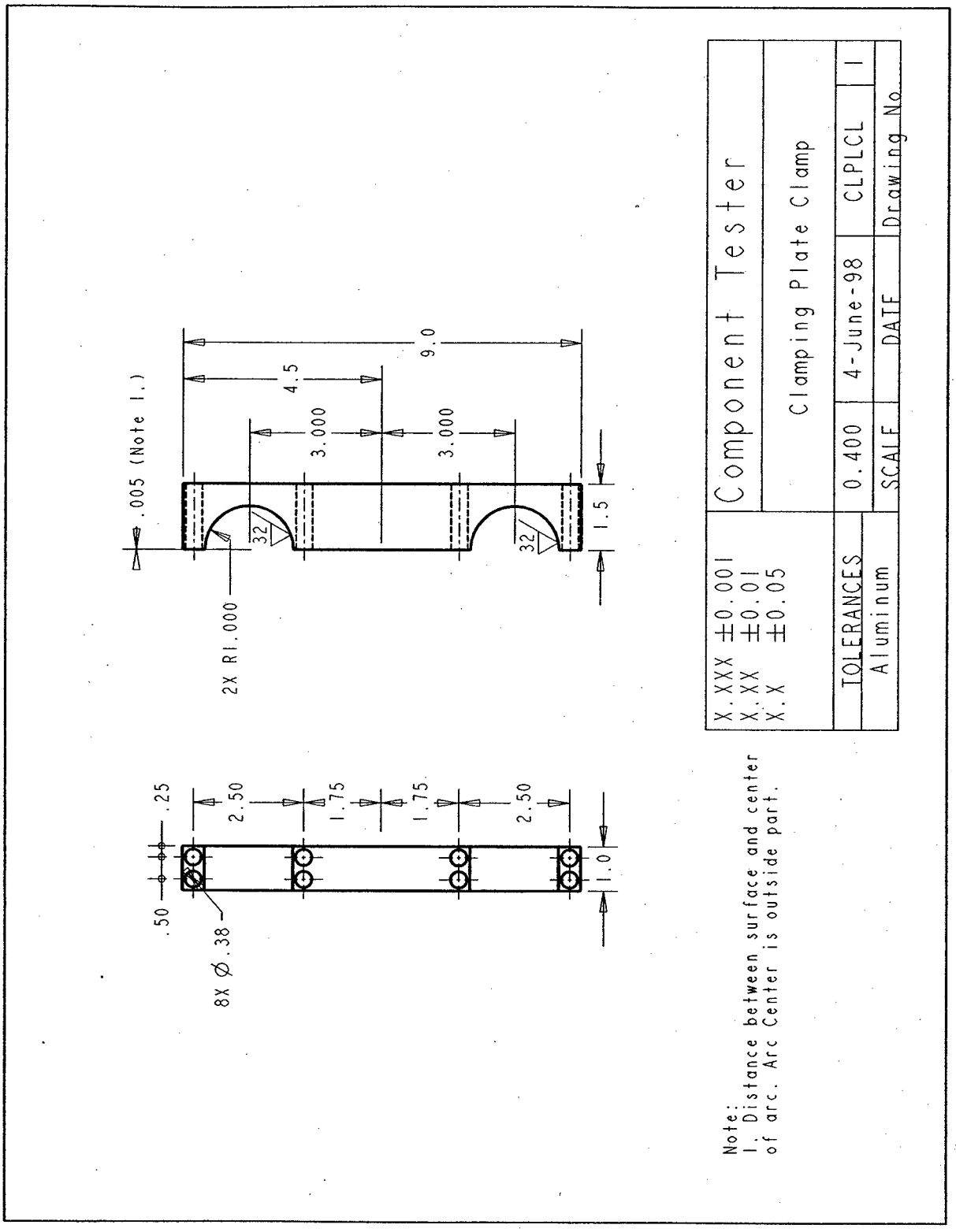

Figure A-7: Clamping Plate Clamp Part Drawing.

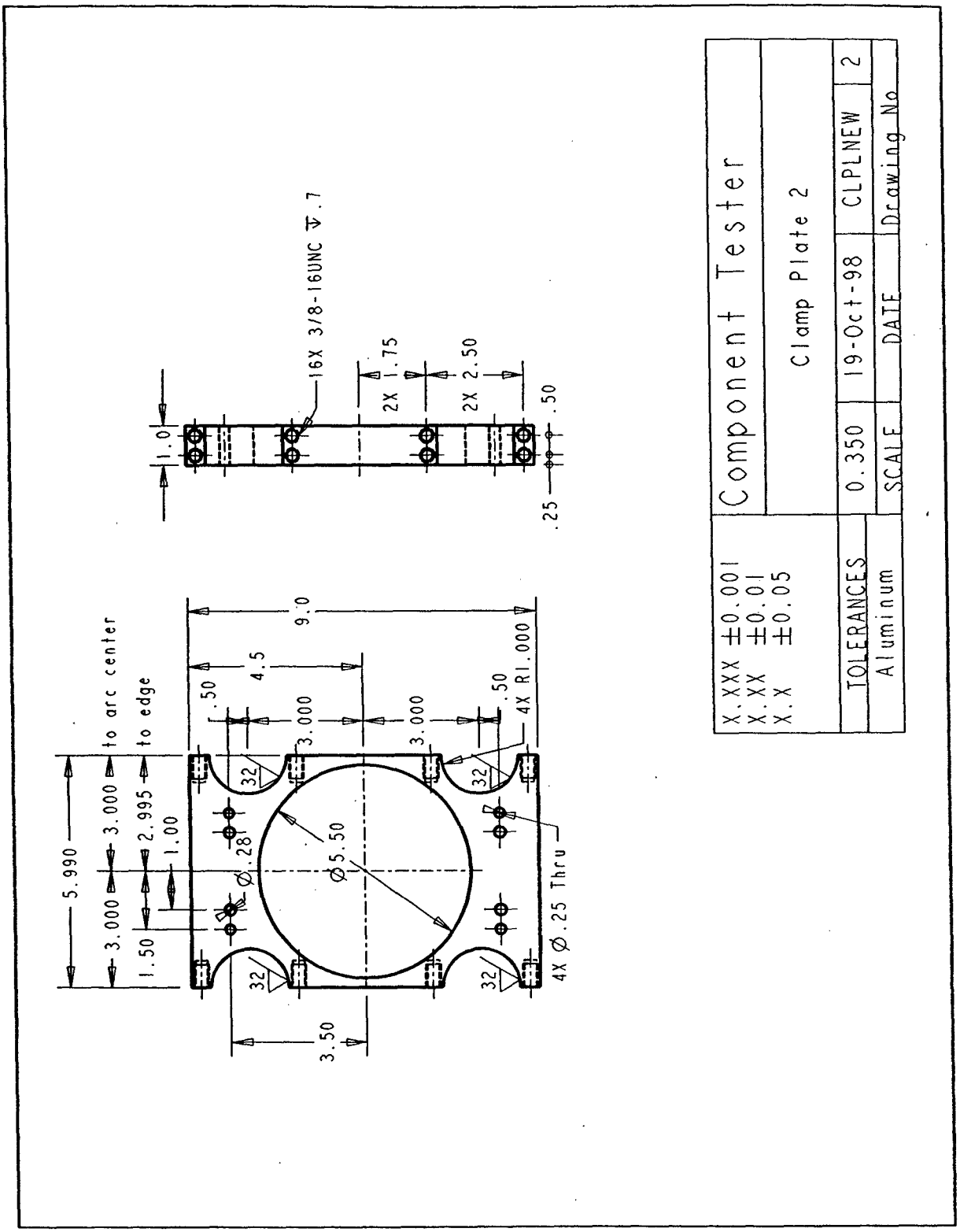

Figure A-8: Clamping Plate 2 Part Drawing.

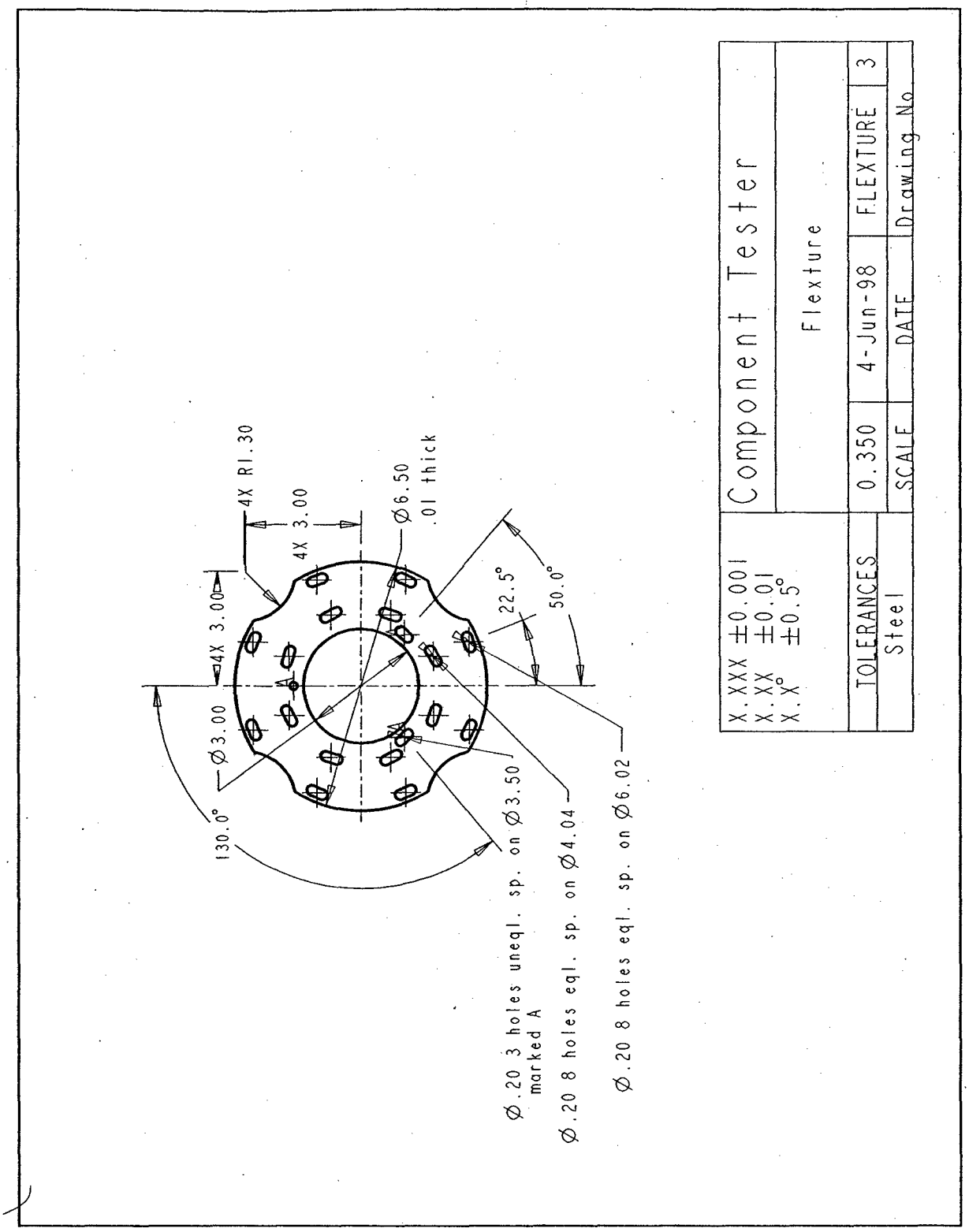

Figure A-9: Flexure Part Drawing.

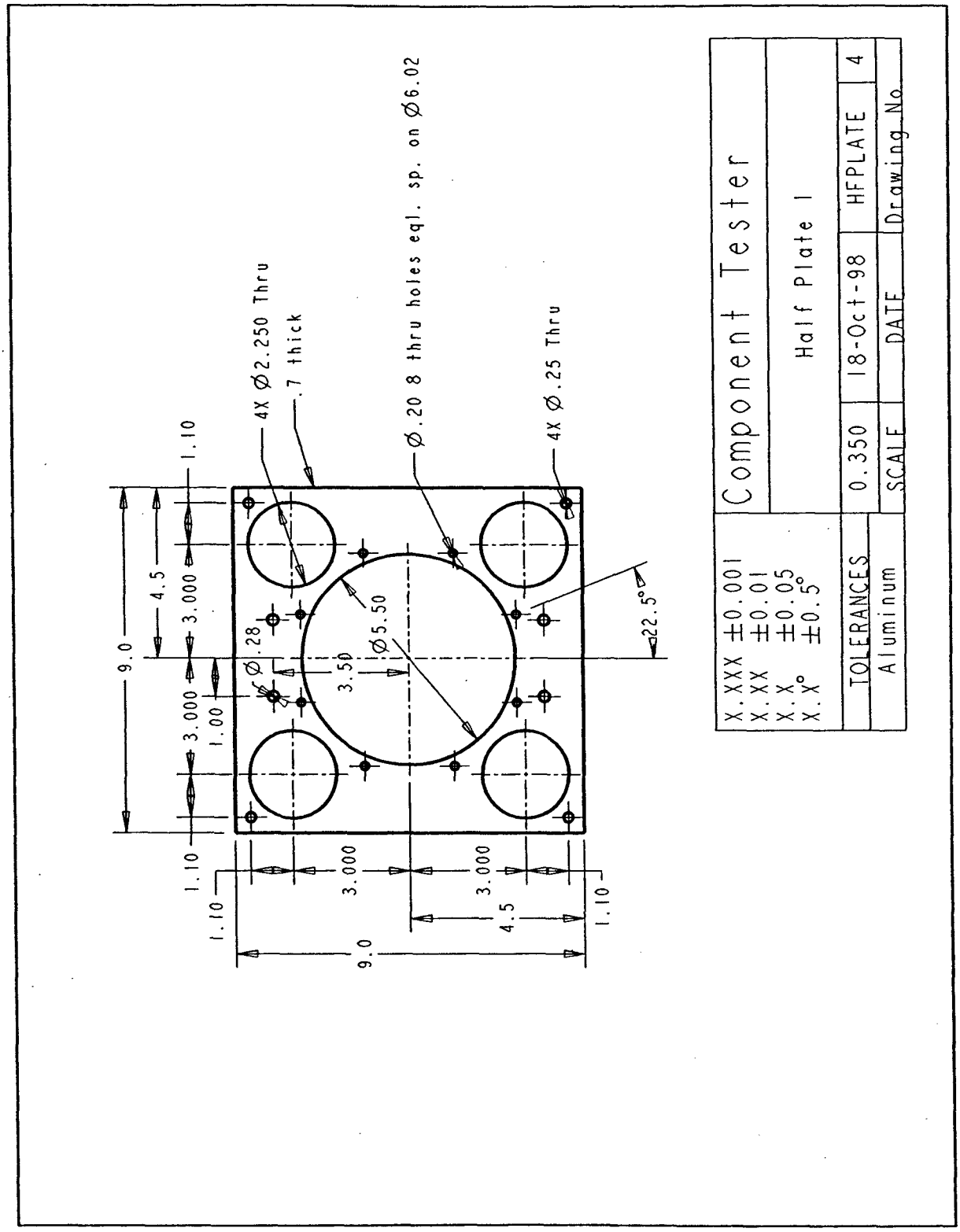

Figure A-10: Half Plate 1 Part Drawing.

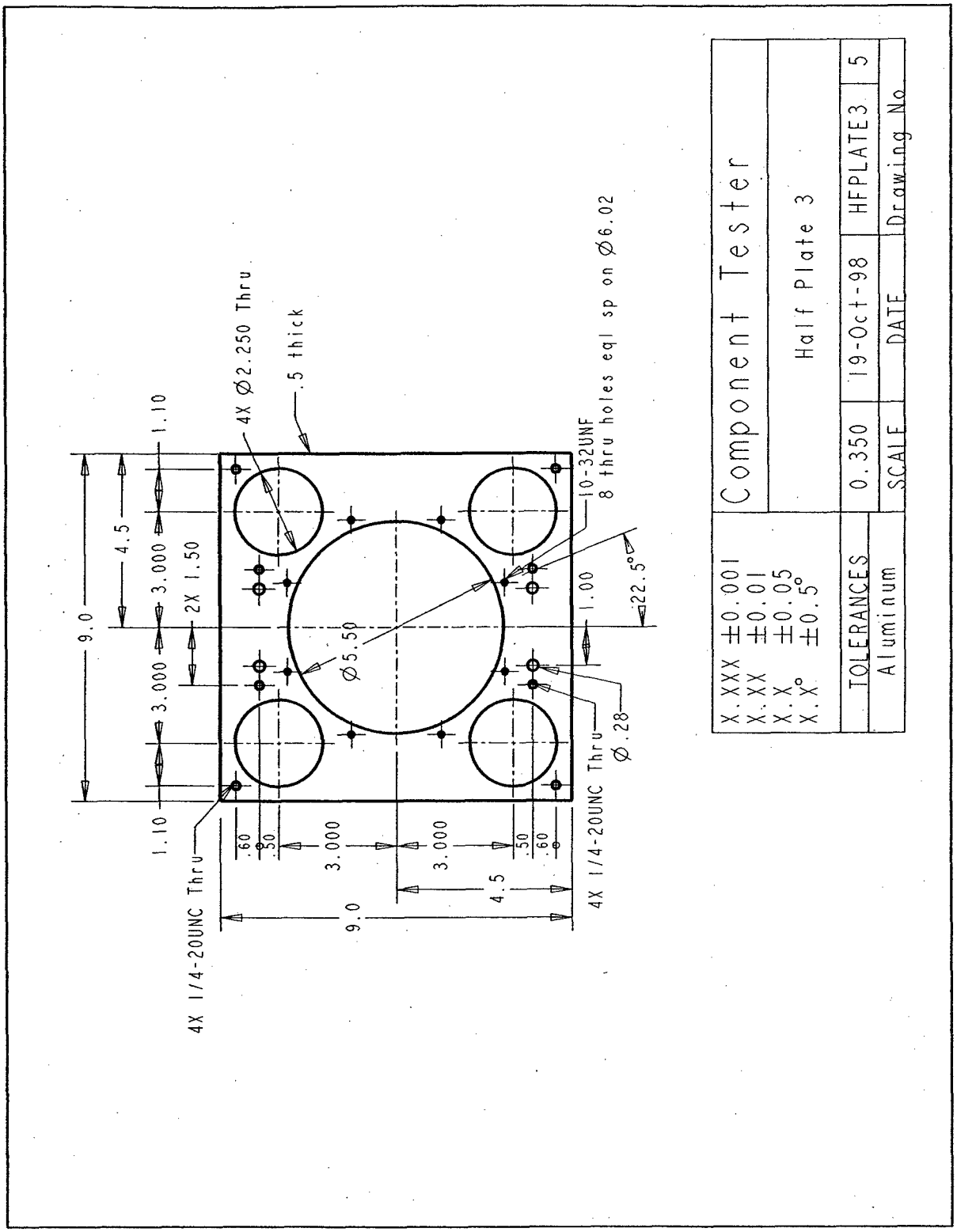

Figure A-11: Half Plate 3 Part Drawing.

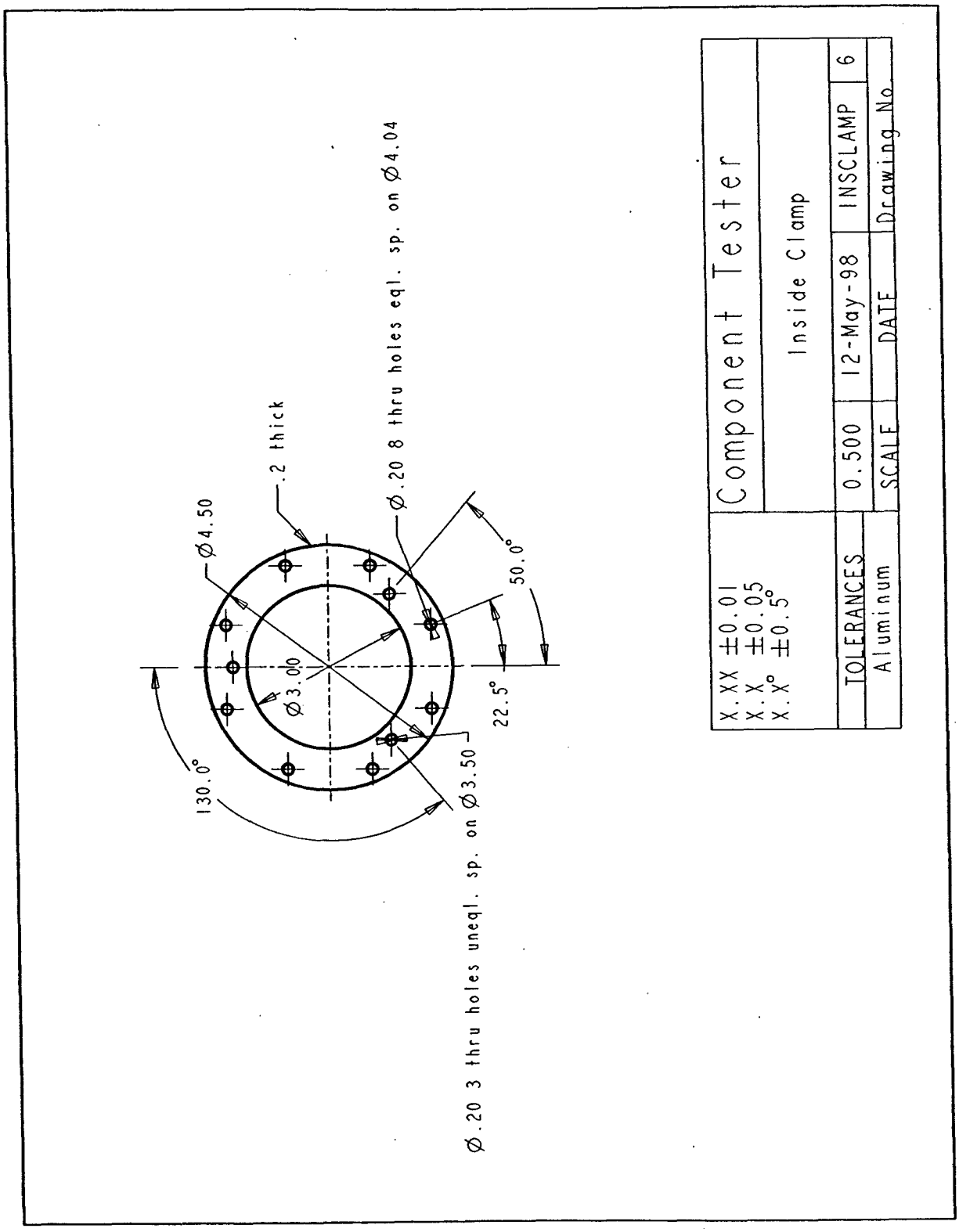

Figure A-12: Inside Clamp Part Drawing.

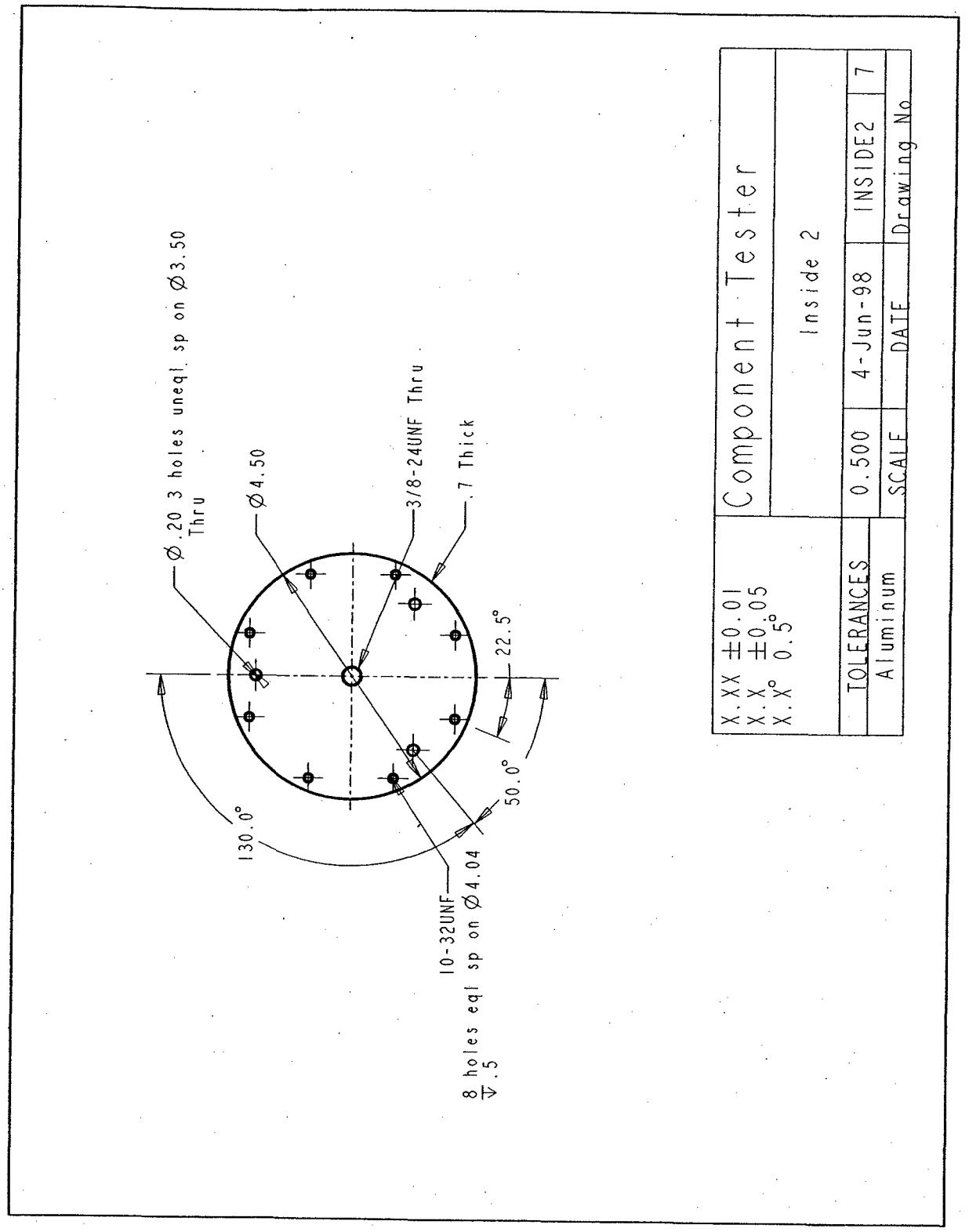

Figure A-13: Inside 2 Part Drawing.

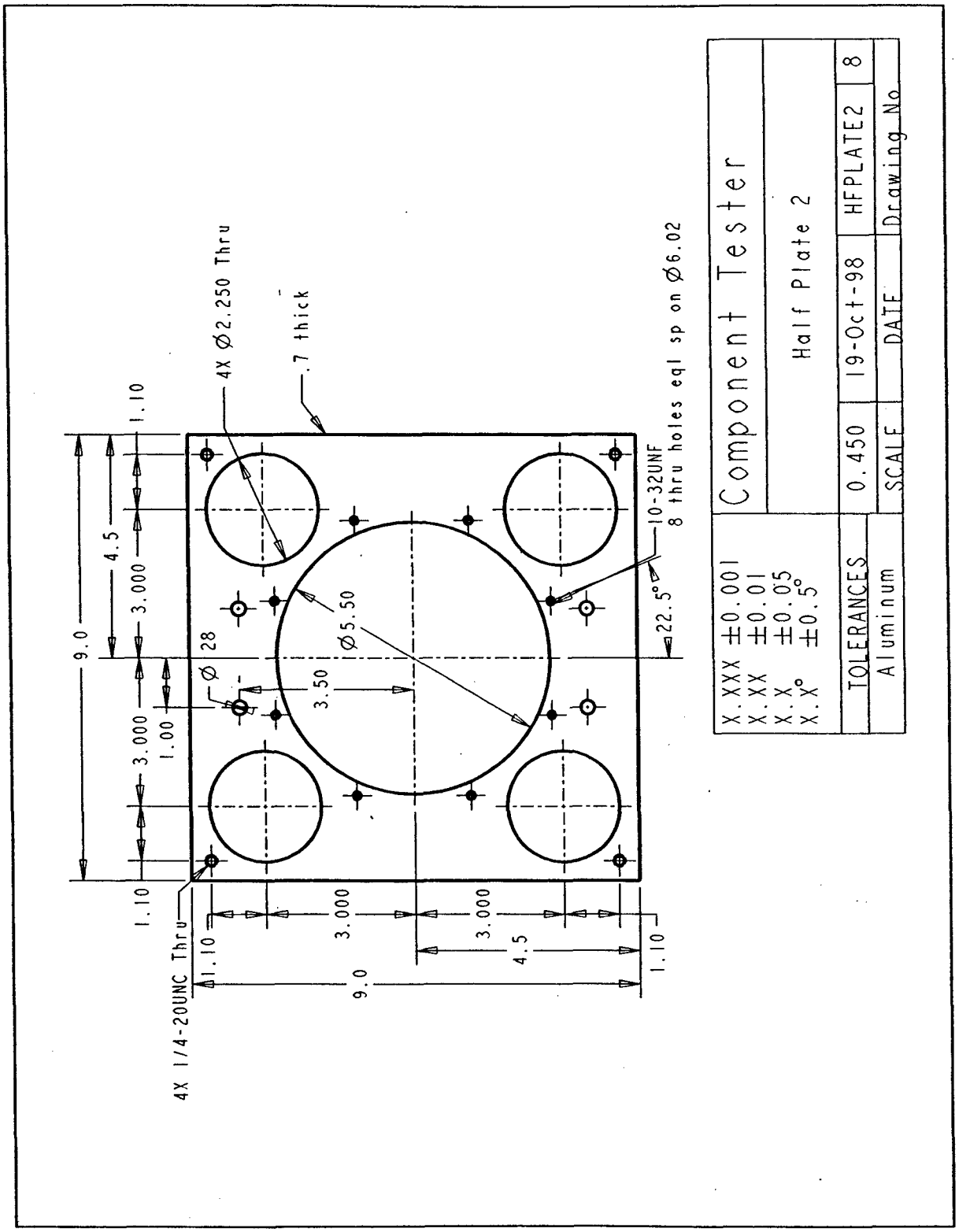

Figure A-14: Half Plate 2 Part Drawing.

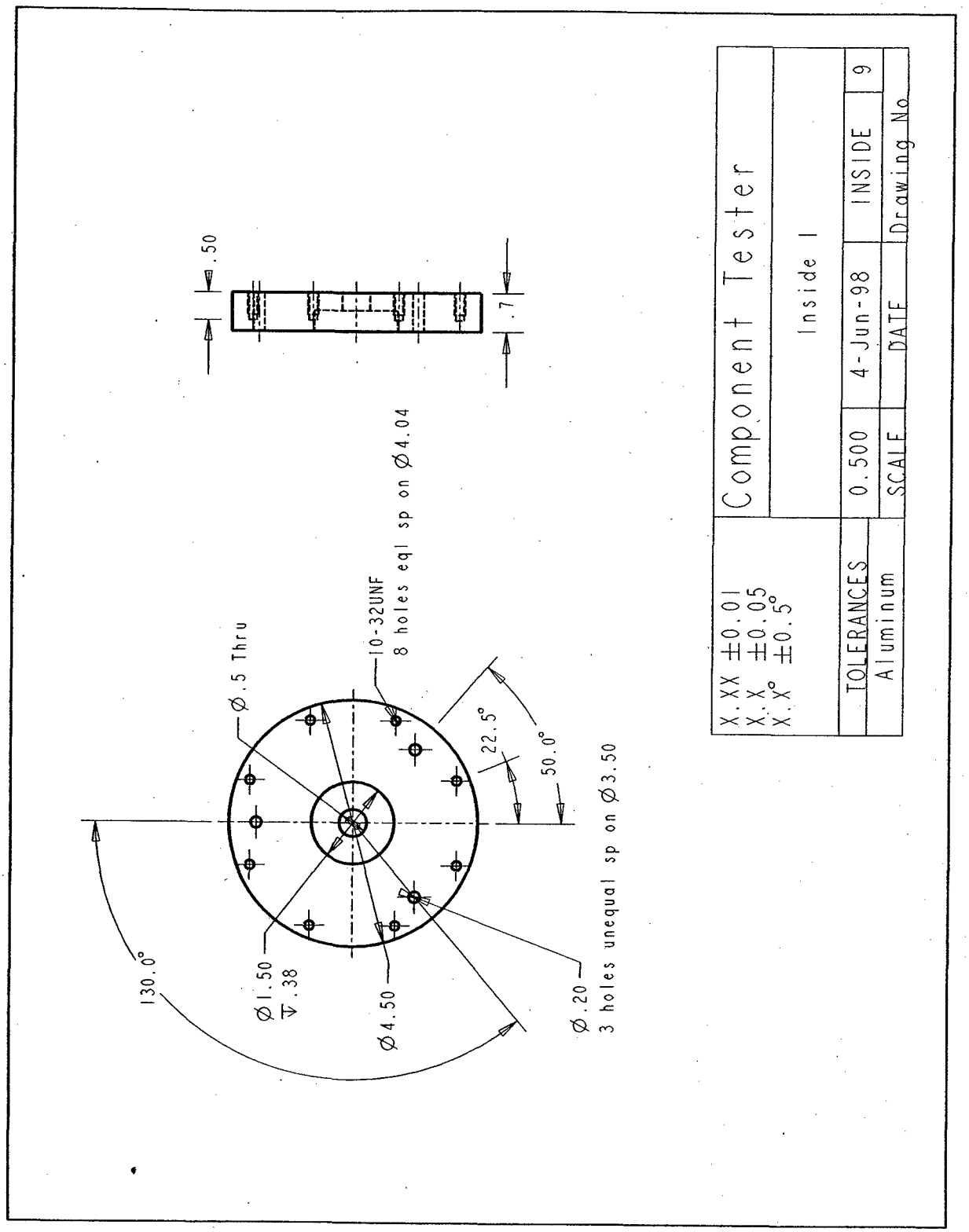

Figure A-15: Inside 1 Part Drawing.

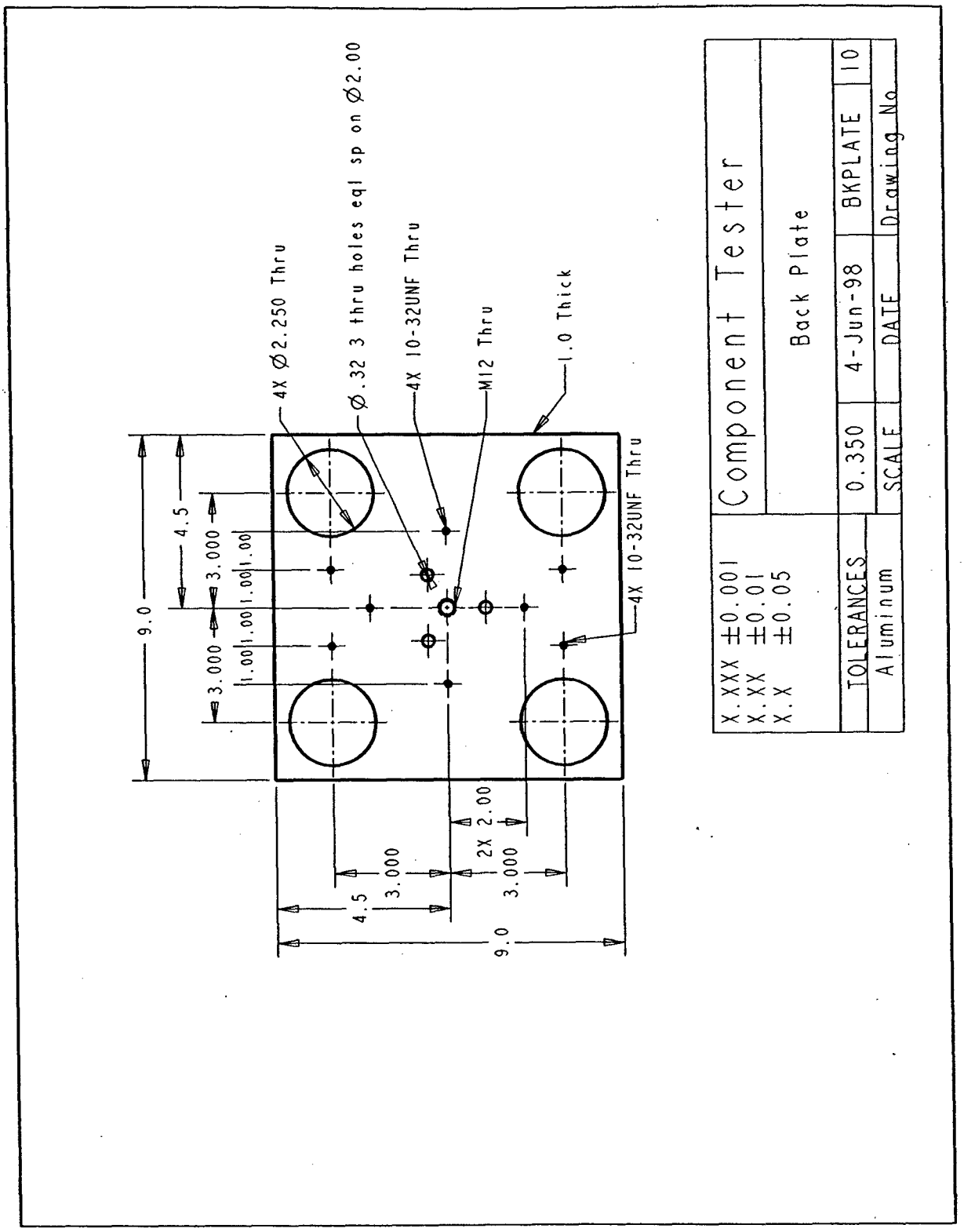

Figure A-16: Back Plate Part Drawing.

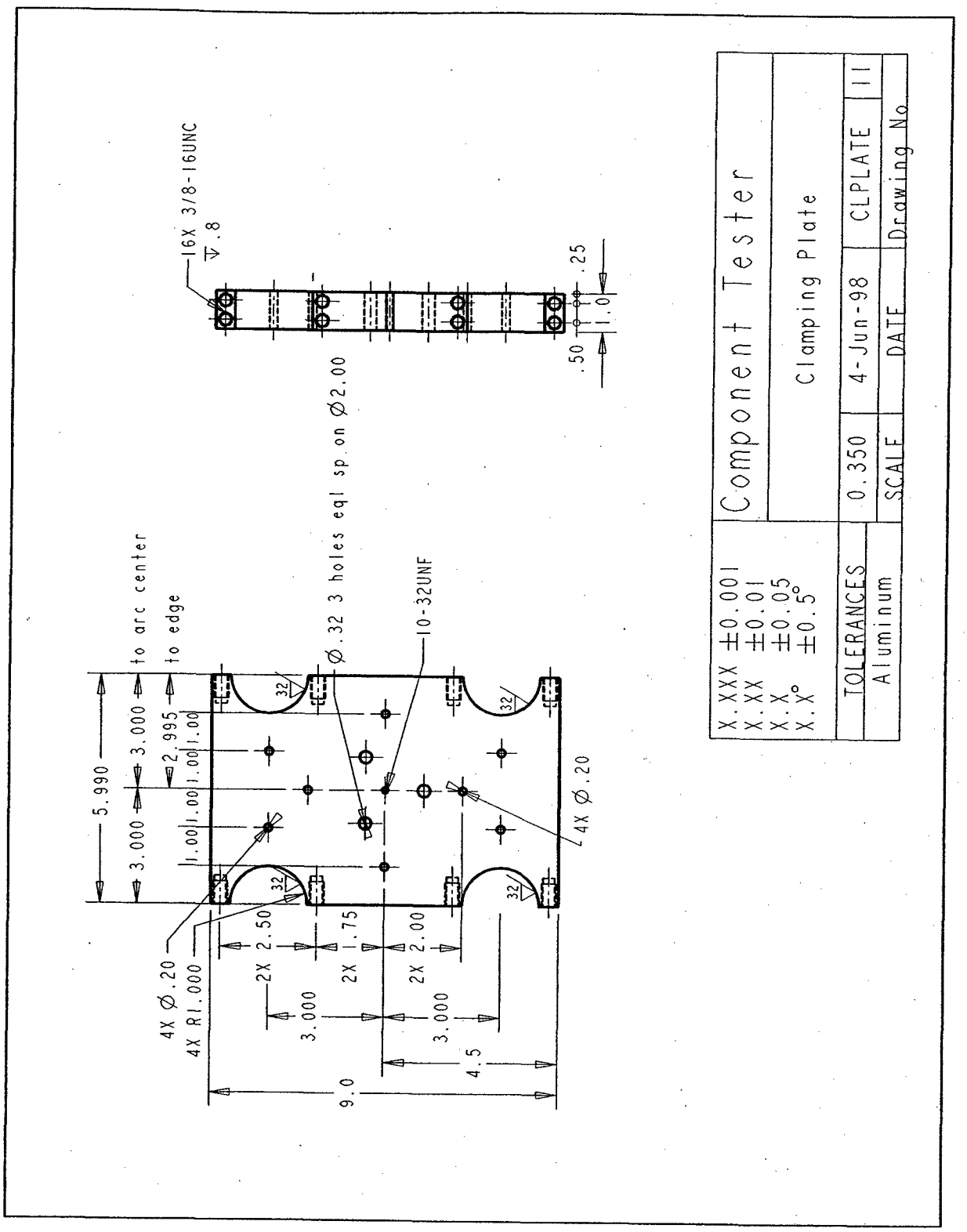

Figure A-17: Clamping Plate 1 Part Drawing.

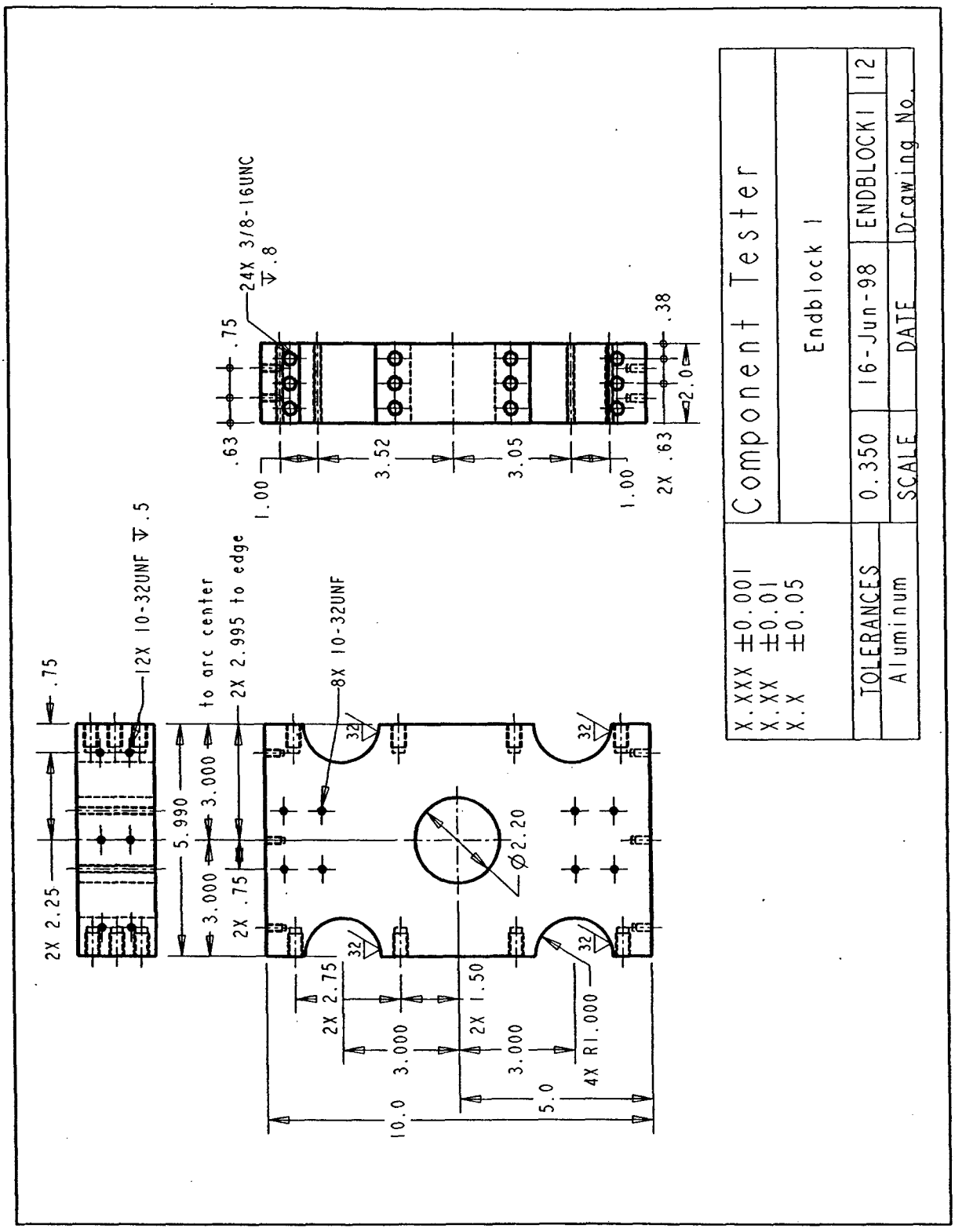

Figure A-18: End Block 1 Part Drawing.

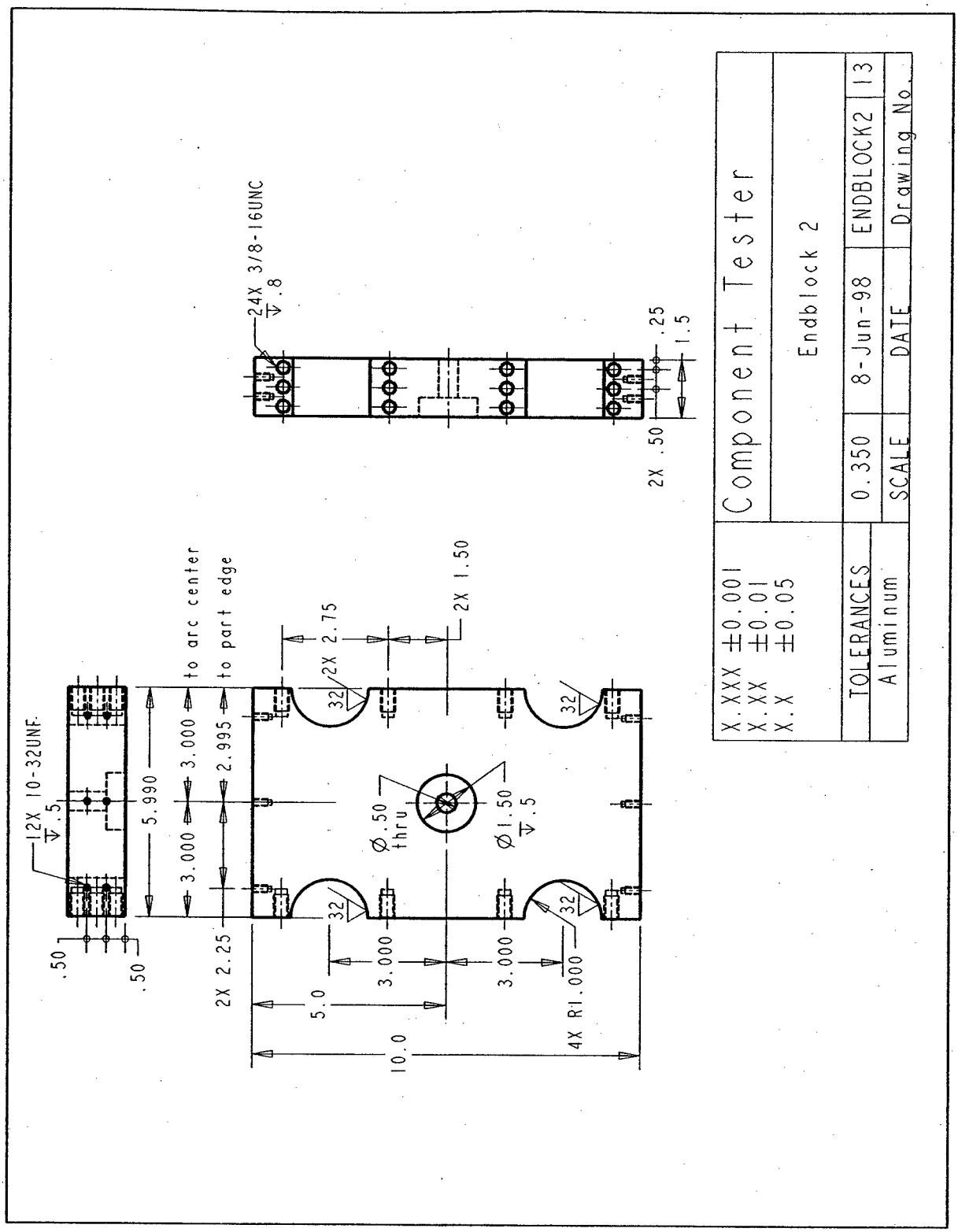

Figure A-19: End Block 2 Part Drawing.

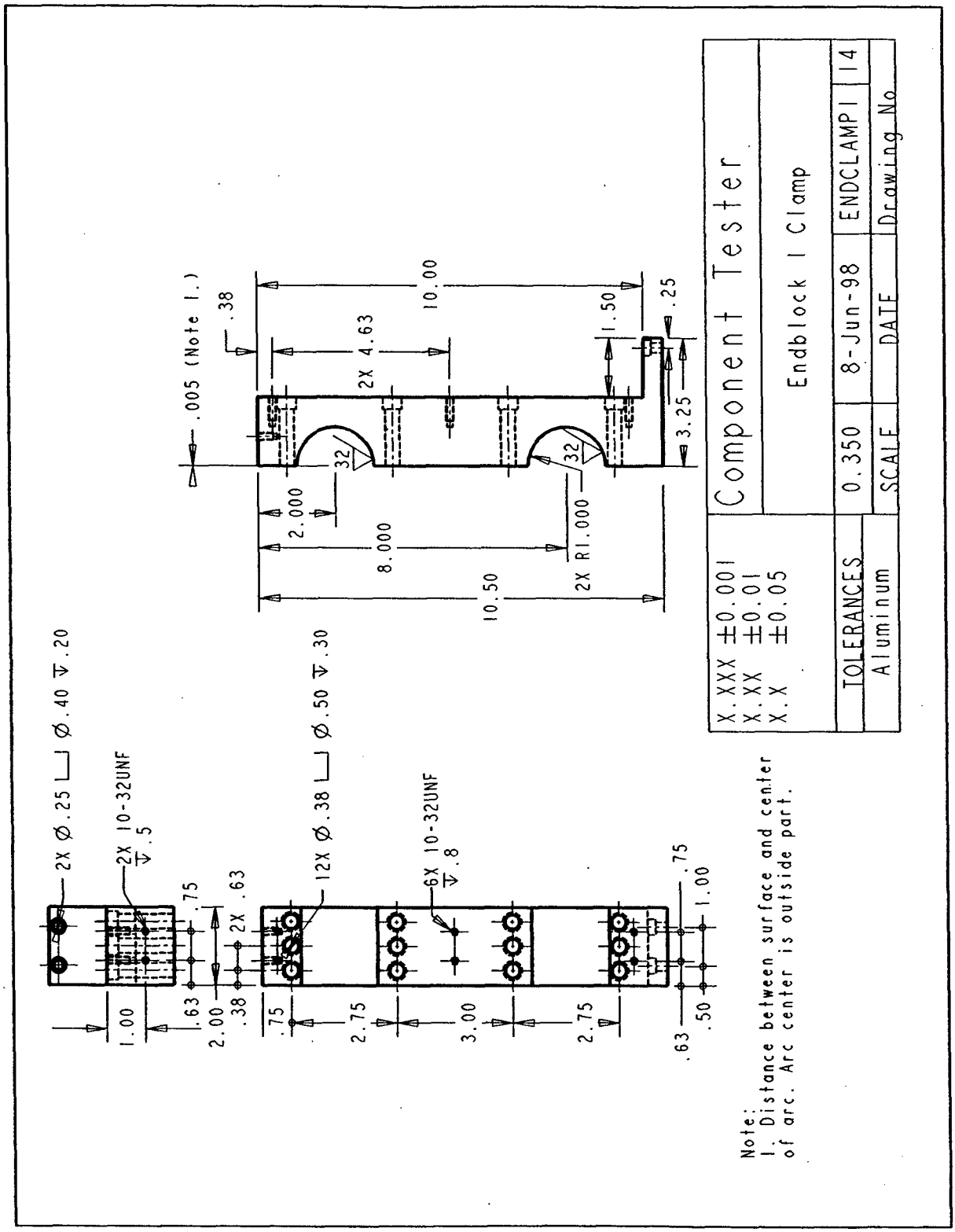

Figure A-20: End Clamp 1 Part Drawing.

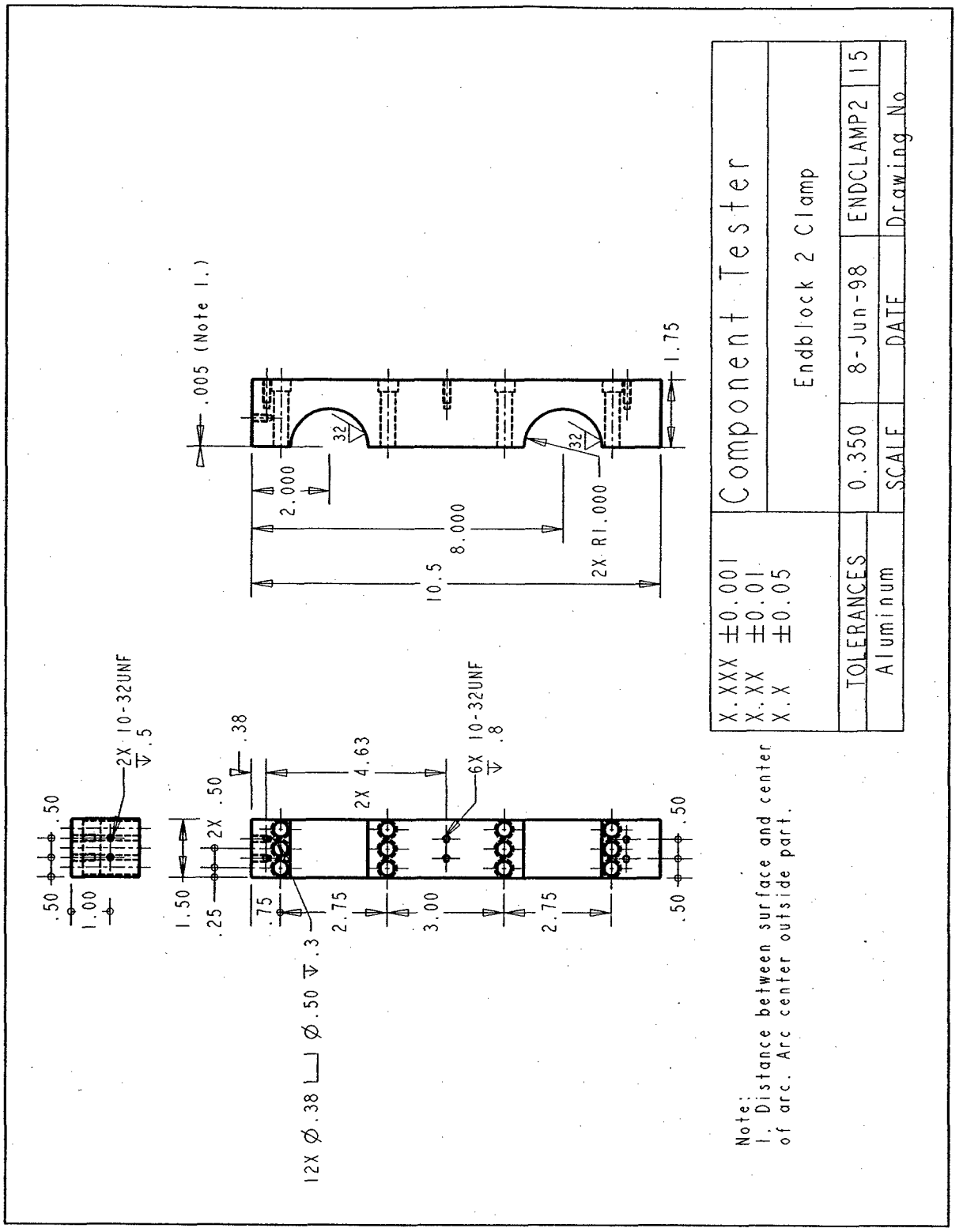

Figure A-21: End Clamp 2 Part Drawing.

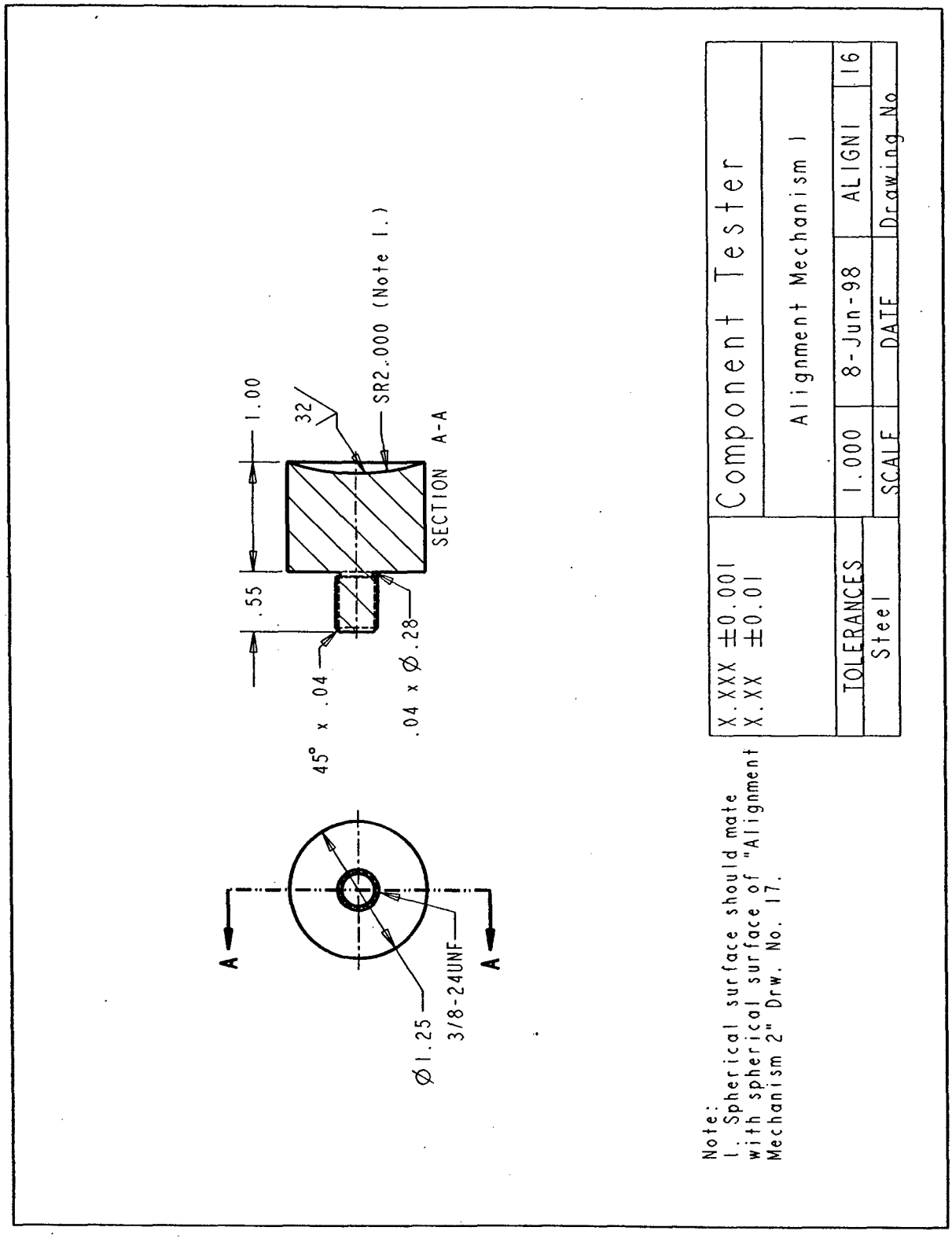

Figure A-22: Stack Alignment Mechanism 1 Part Drawing.

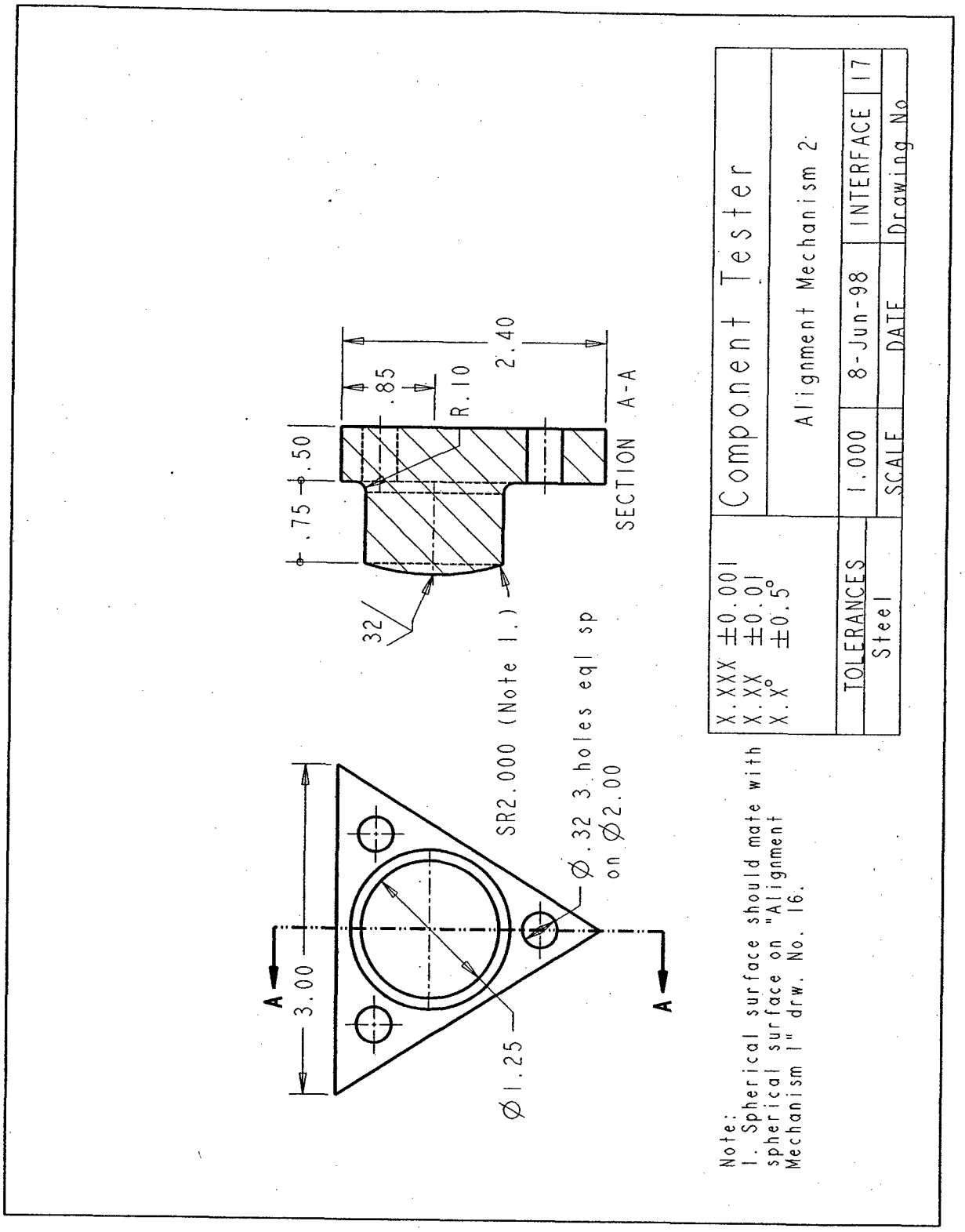

Figure A-23: Stack Alignment Mechanism 2 Part Drawing.

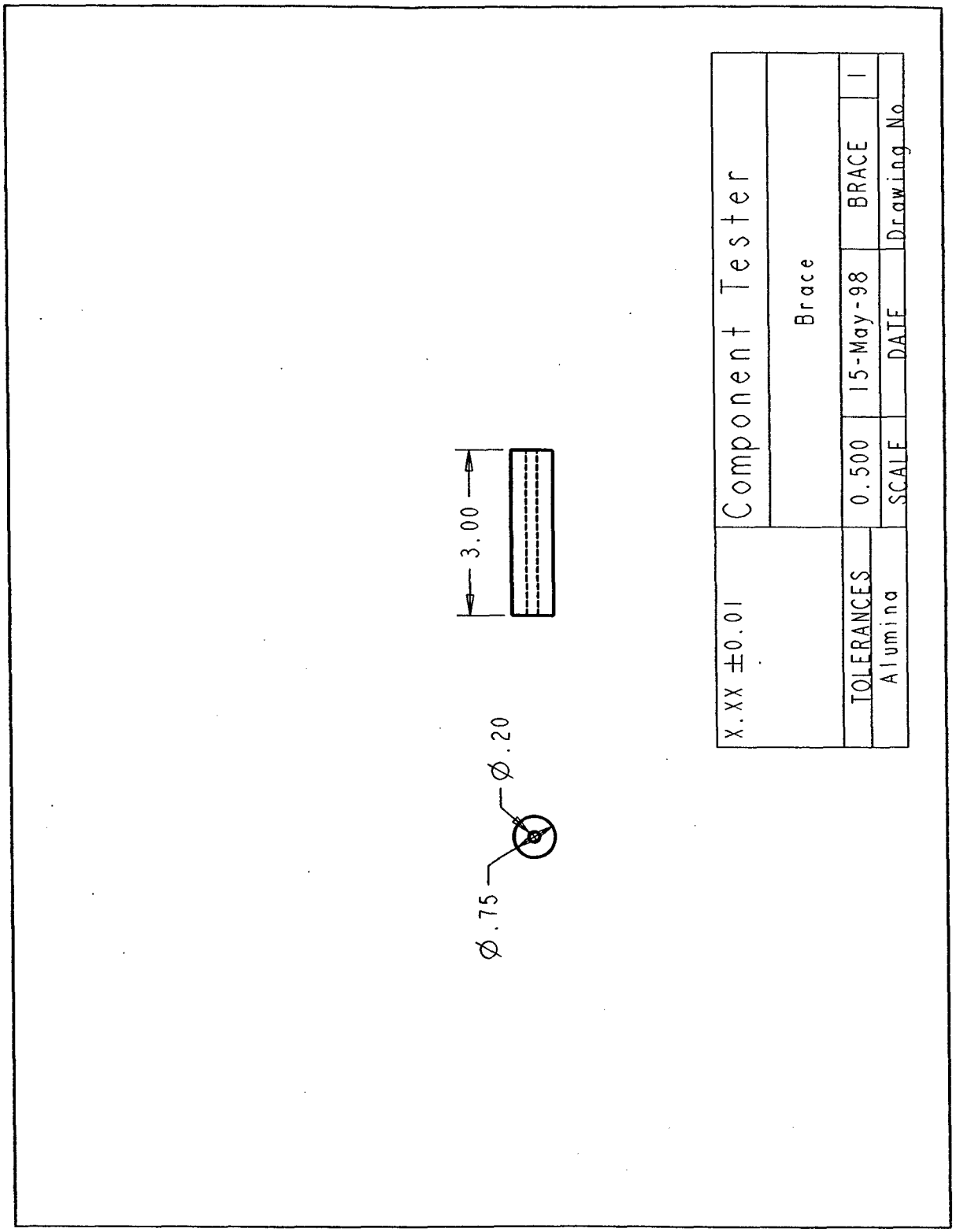

Figure A-24: Alumina Brace Part Drawing.

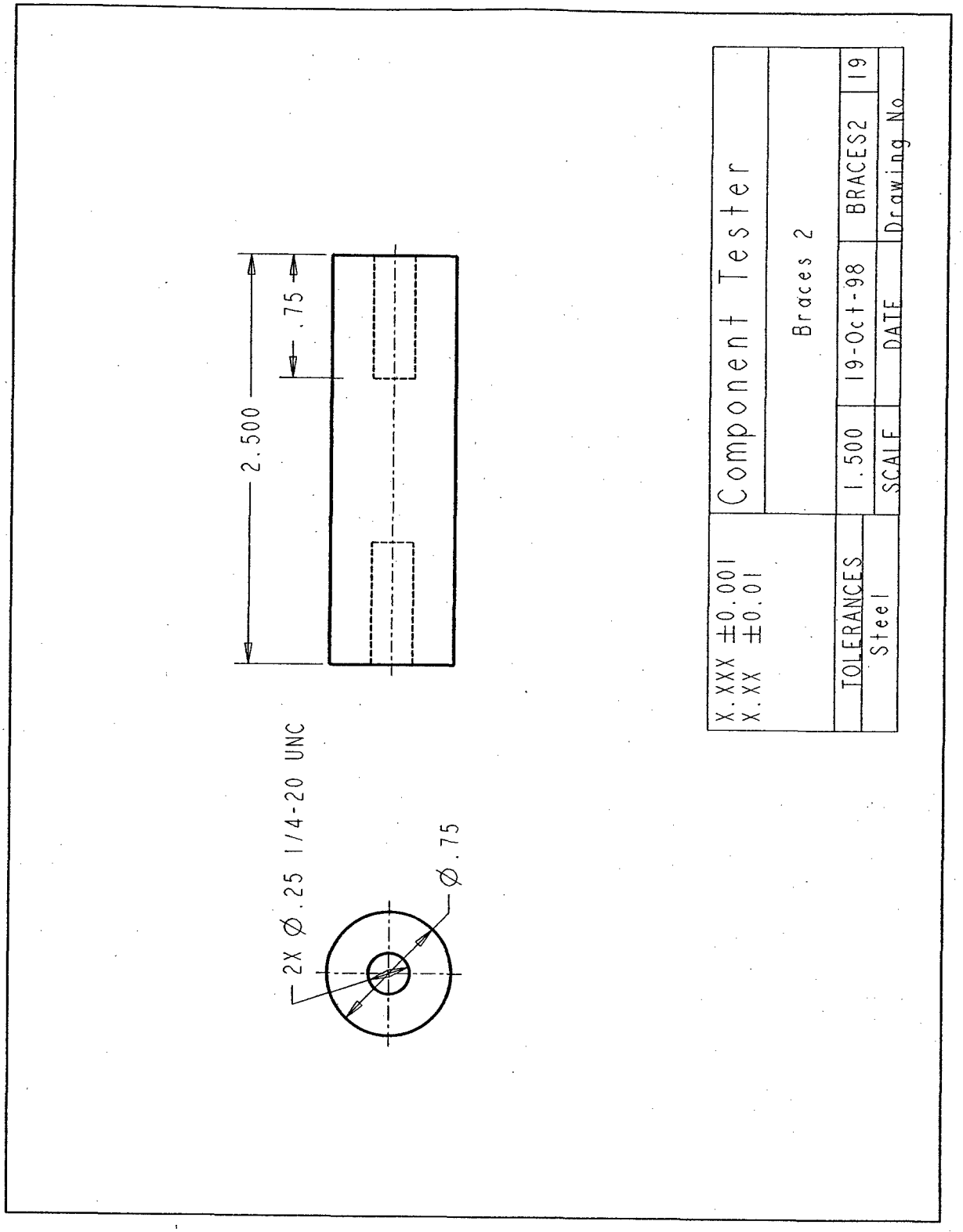

Figure A-25: Steel Braces Part Drawing.

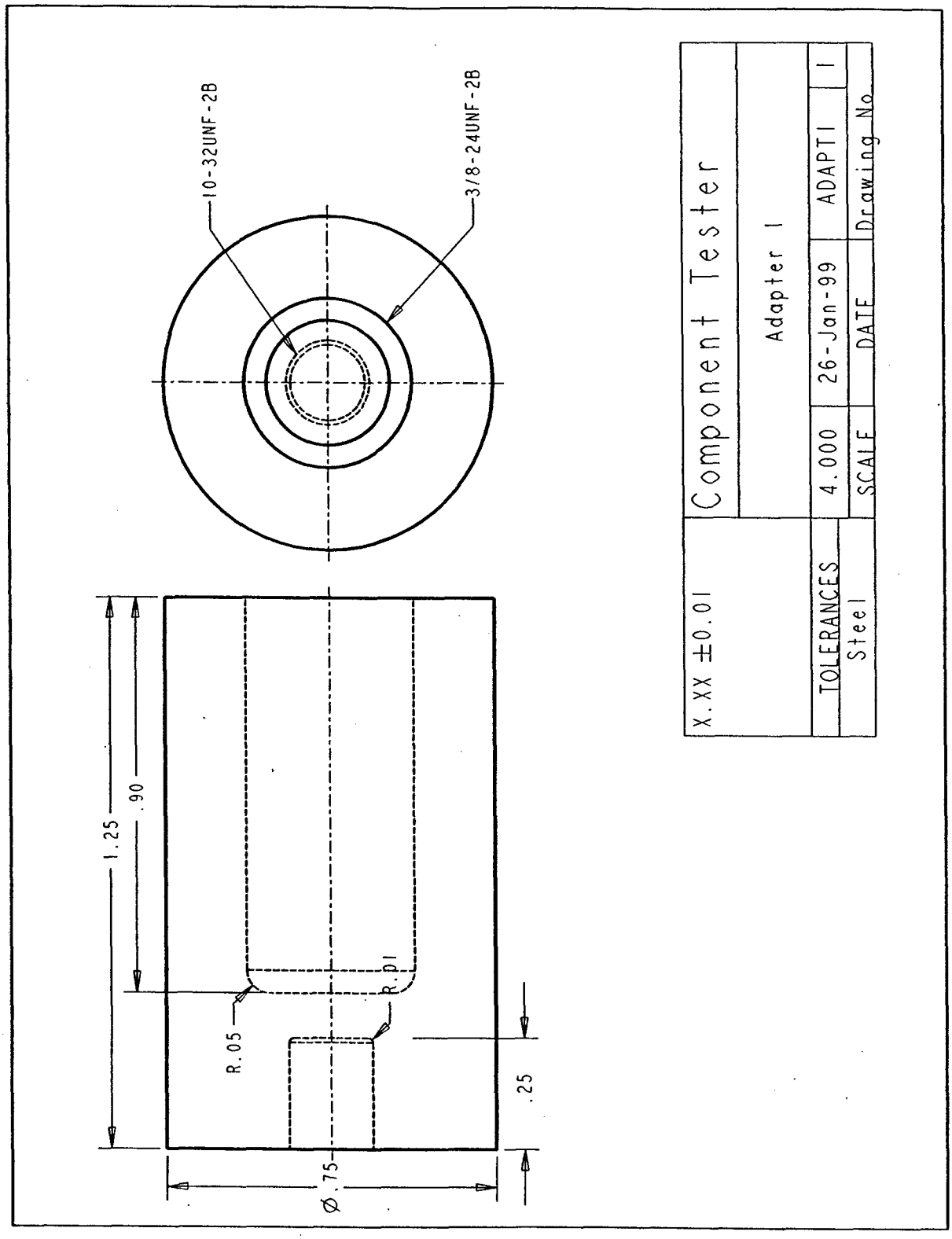

Figure A-26: Load Cell Adapter Part Drawing.

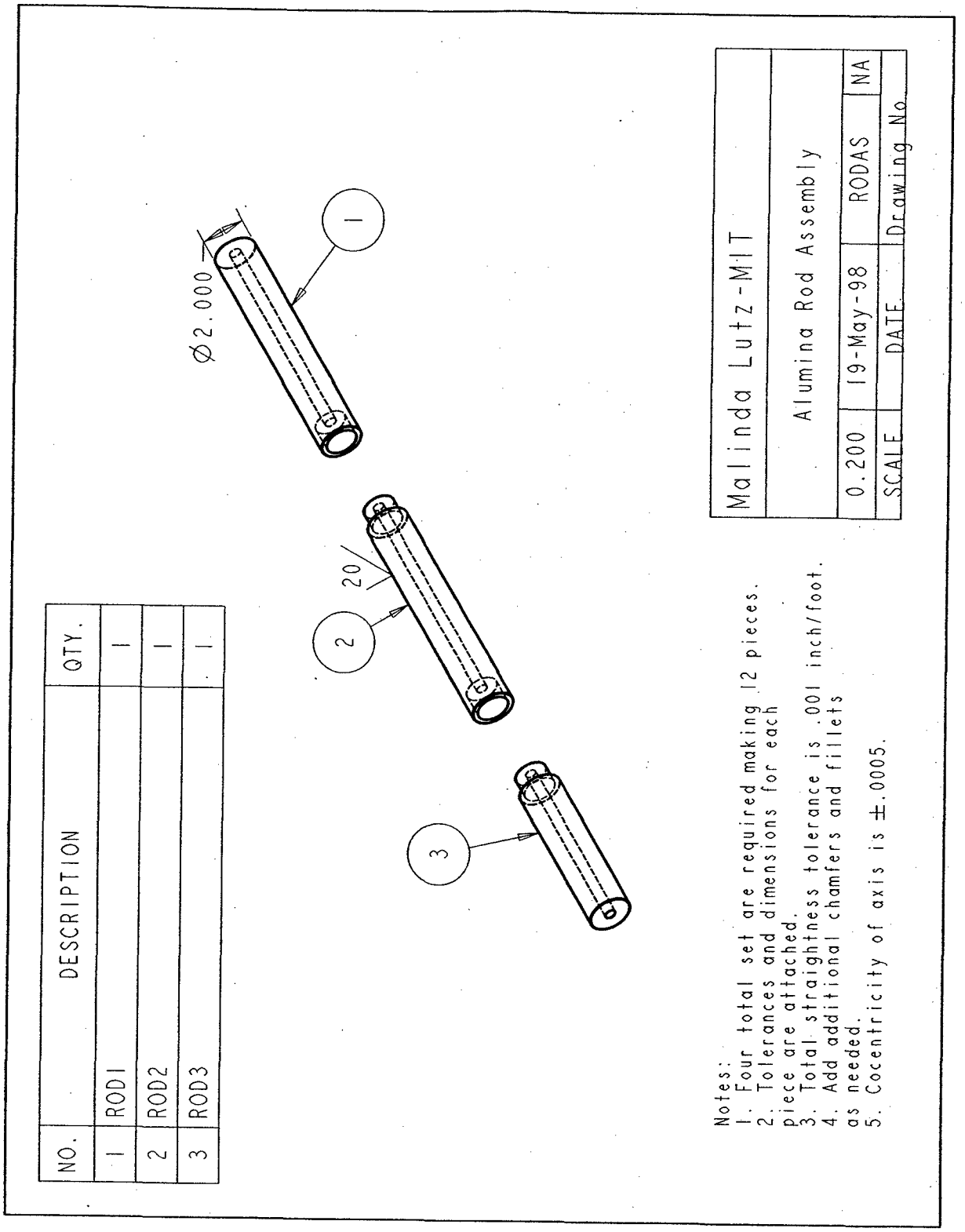

Figure A-27: Alumina Rod Assembly Drawing.

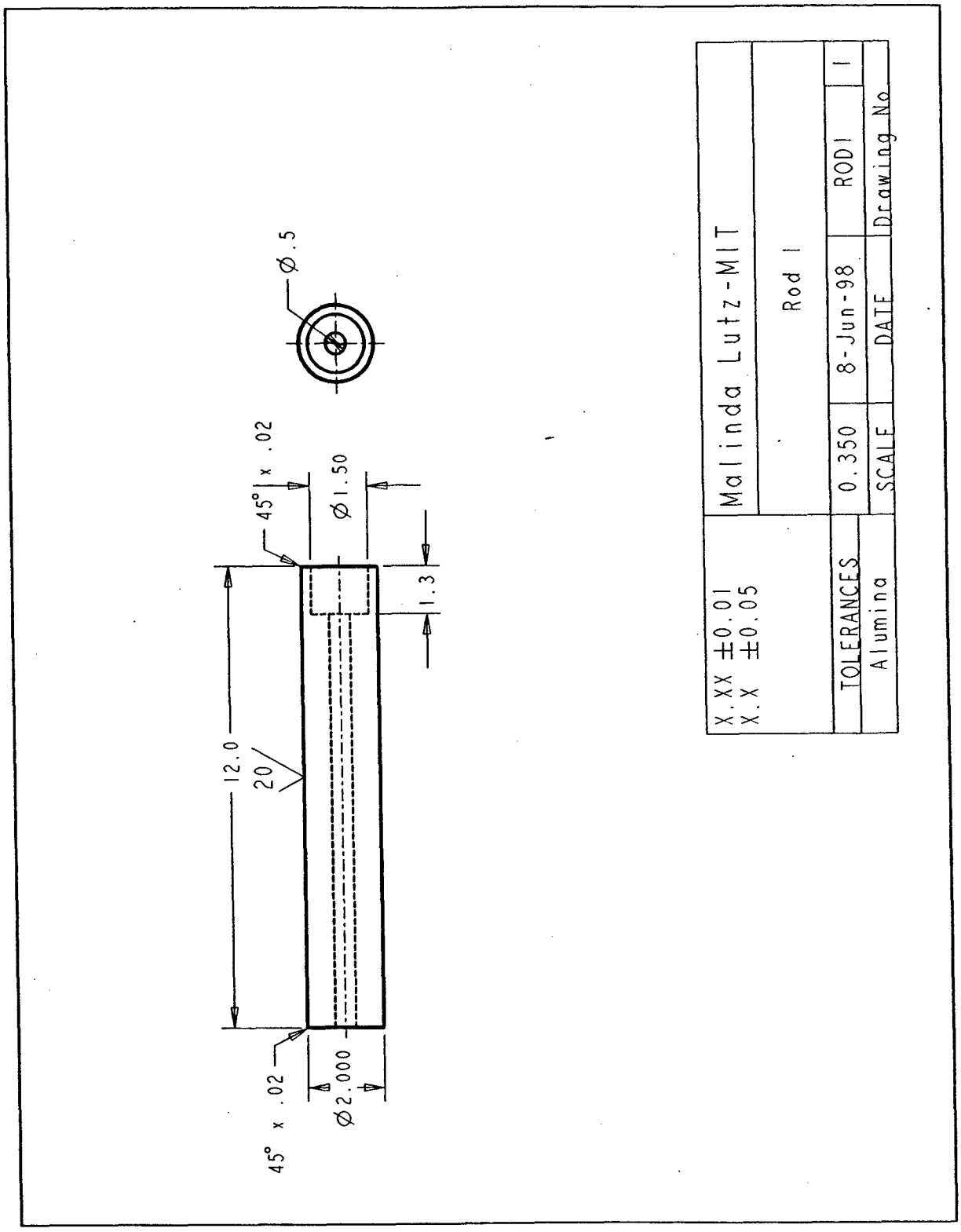

Figure A-28: Alumina Rod Part 1 Drawing.

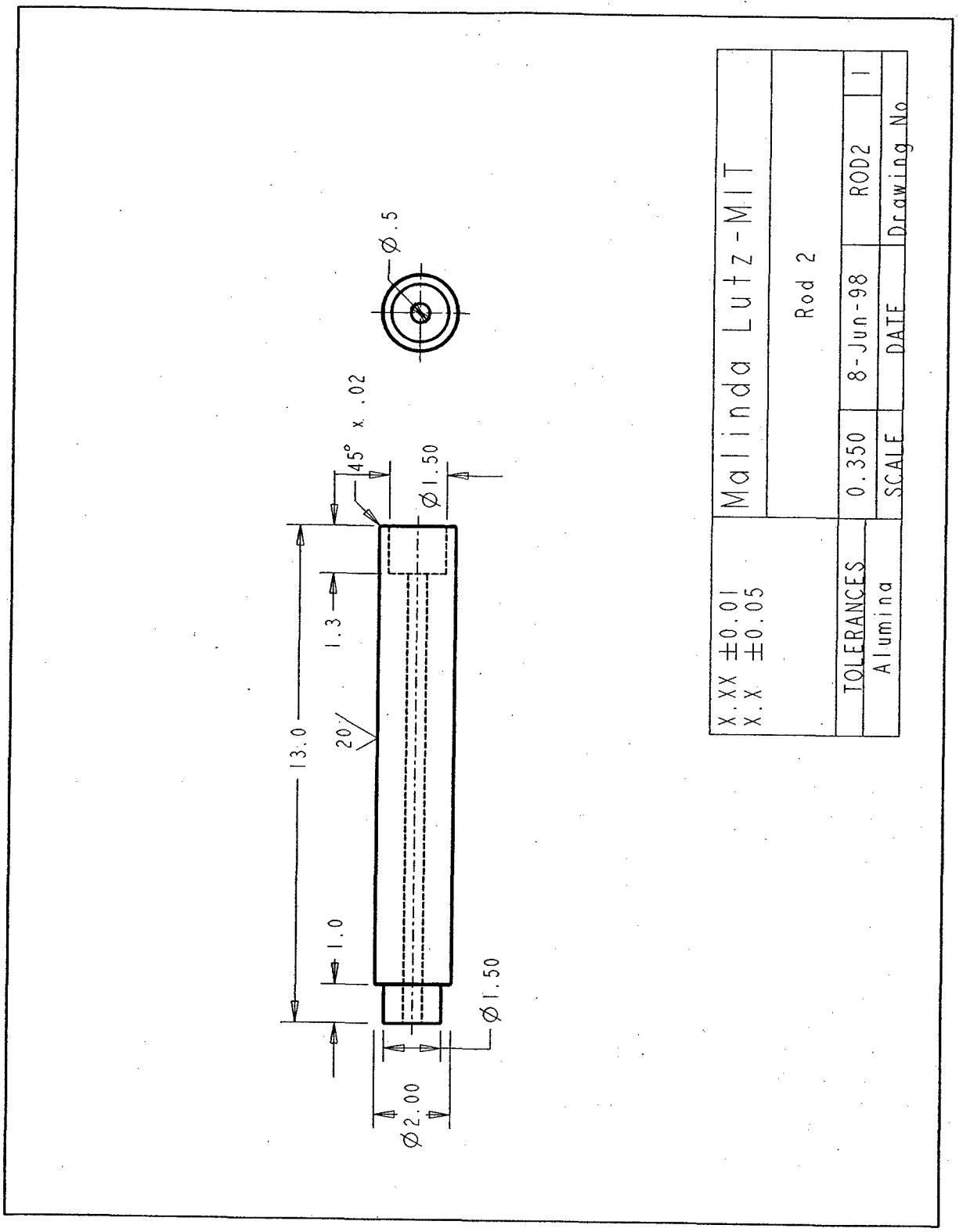

Figure A-29: Alumina Rod Part 2 Drawing.

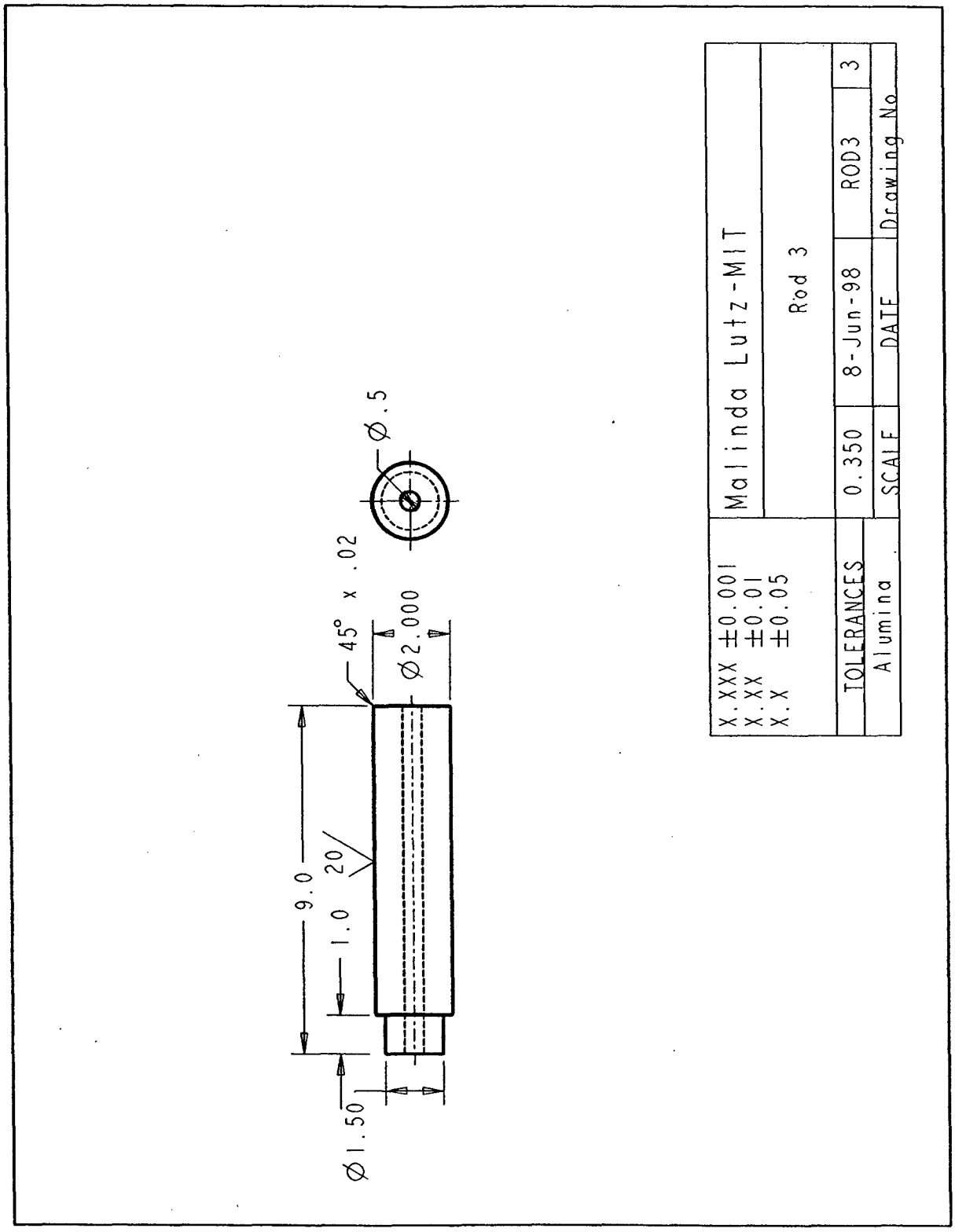

Figure A-30: Alumina Rod Part 3 Drawing.

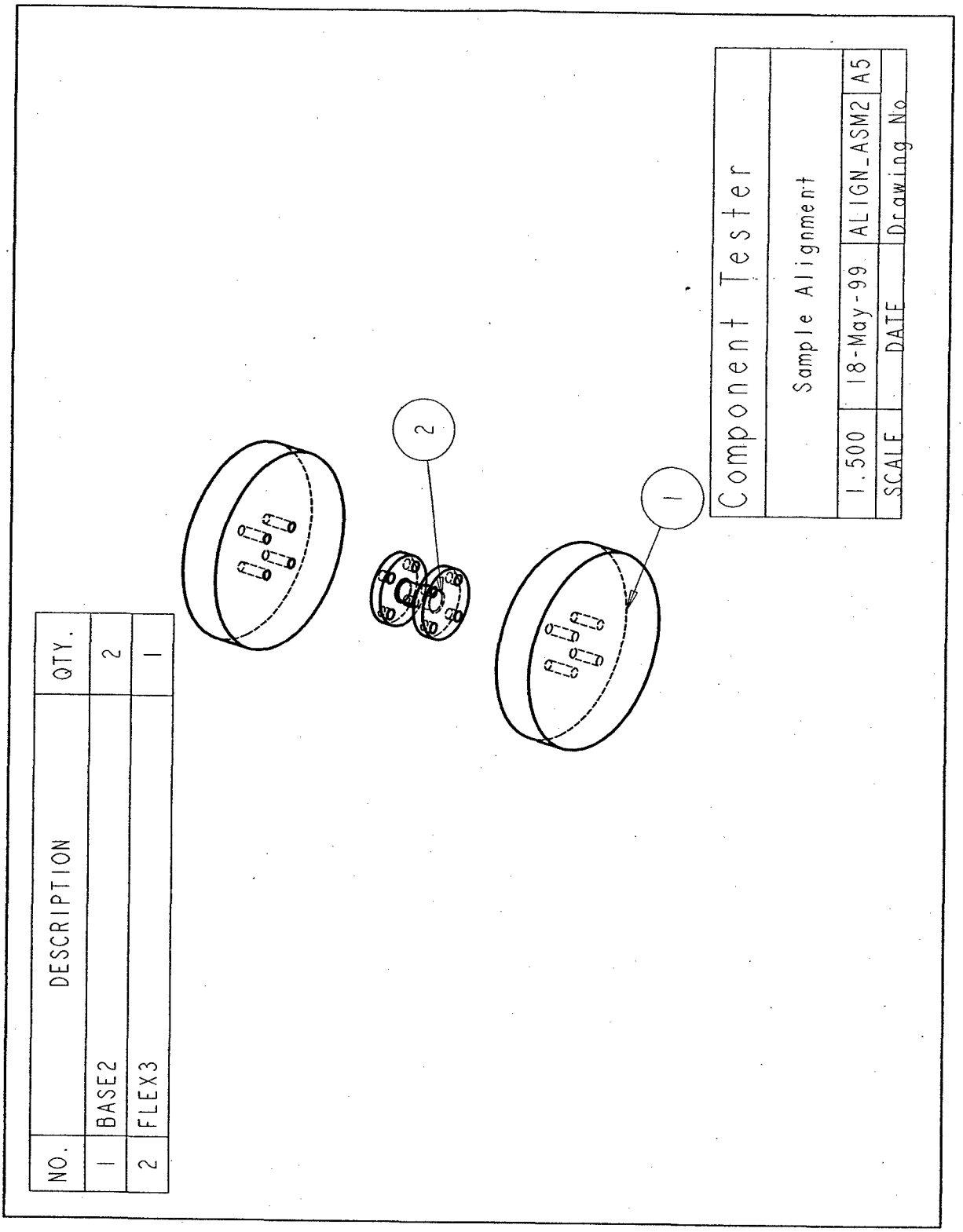

Figure A-31: Sample Alignment Assembly Drawing.

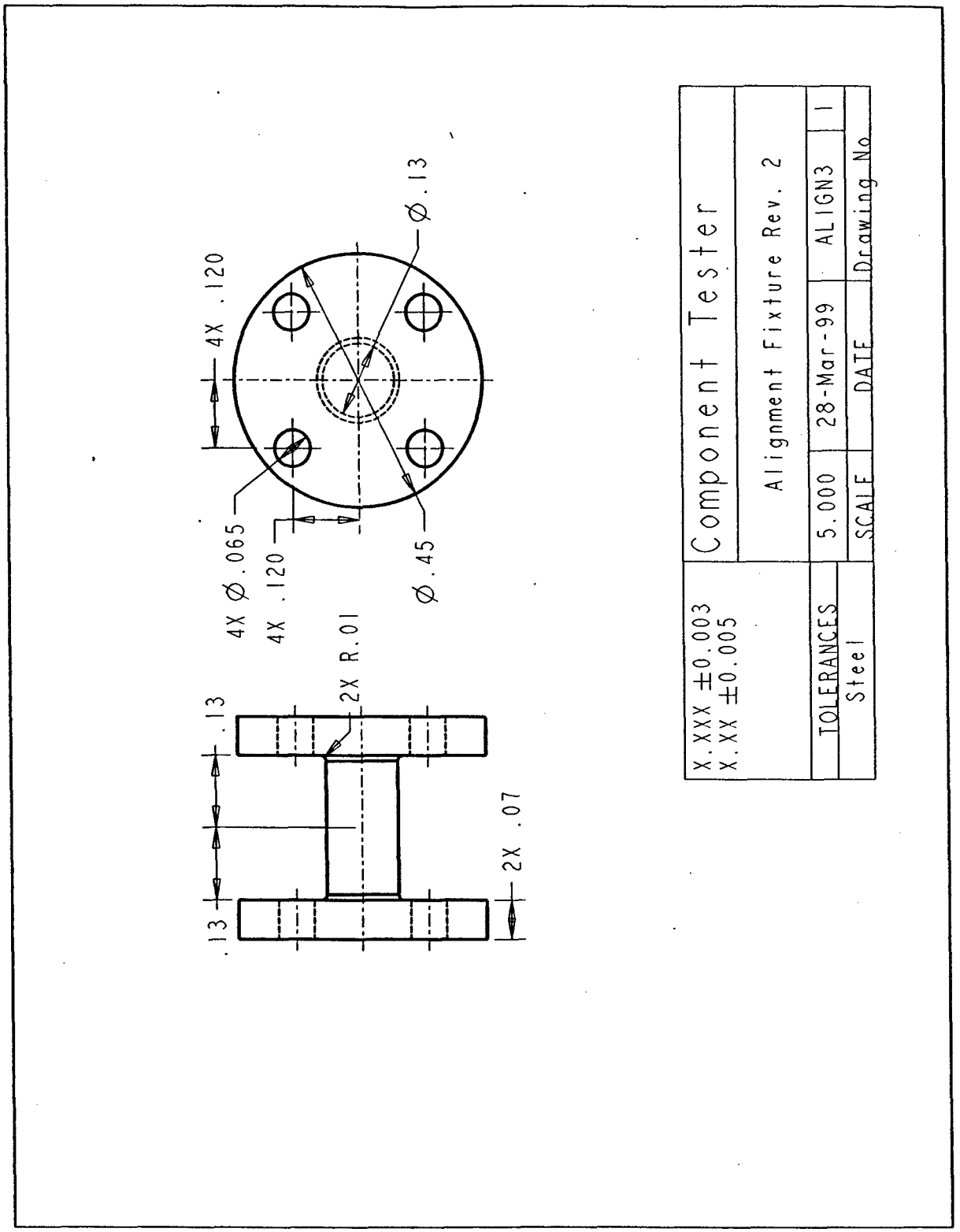

Figure A-32: Alignment Flexure Part Drawing.

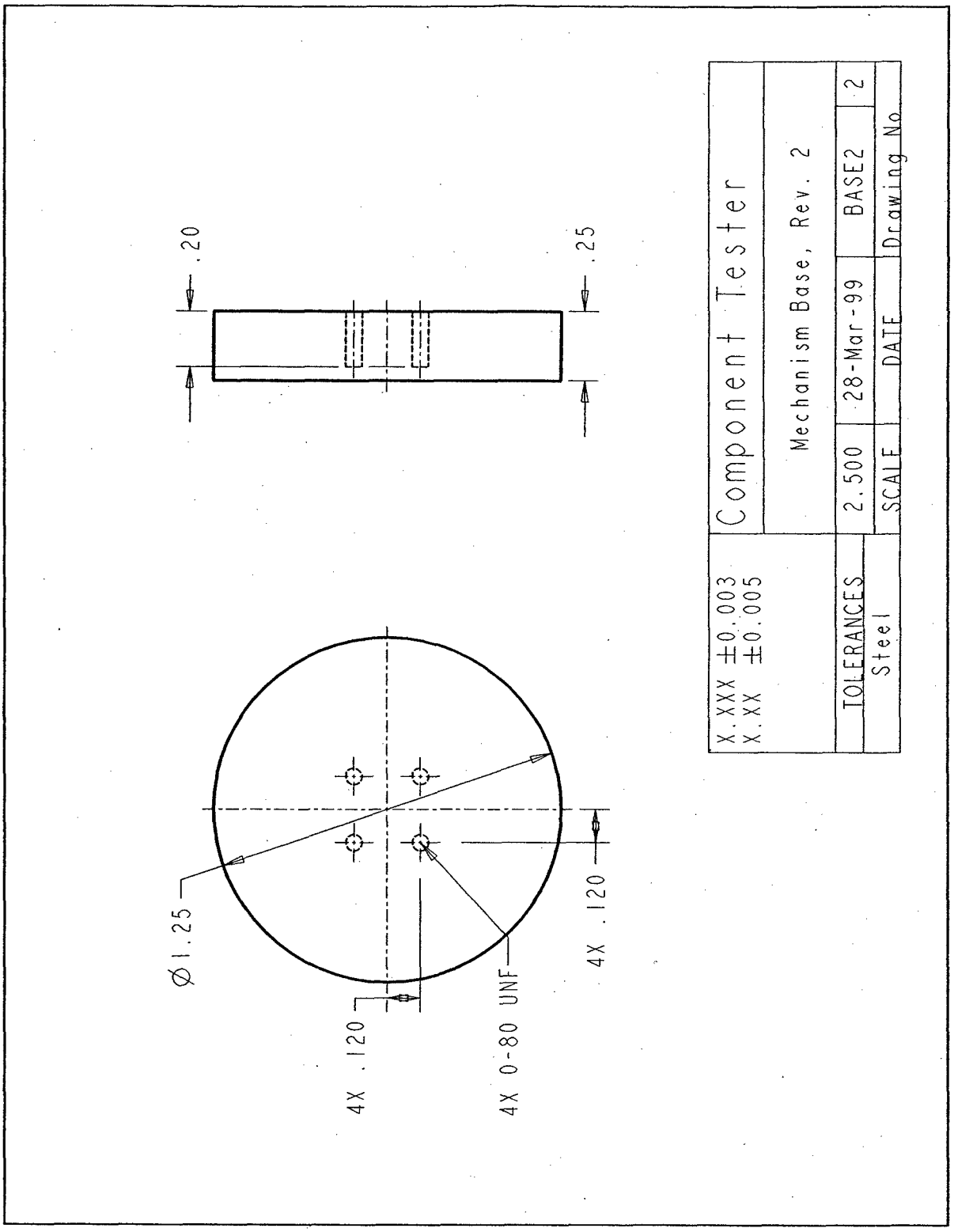

Figure A-33: Sample Alignment Base Part Drawing.

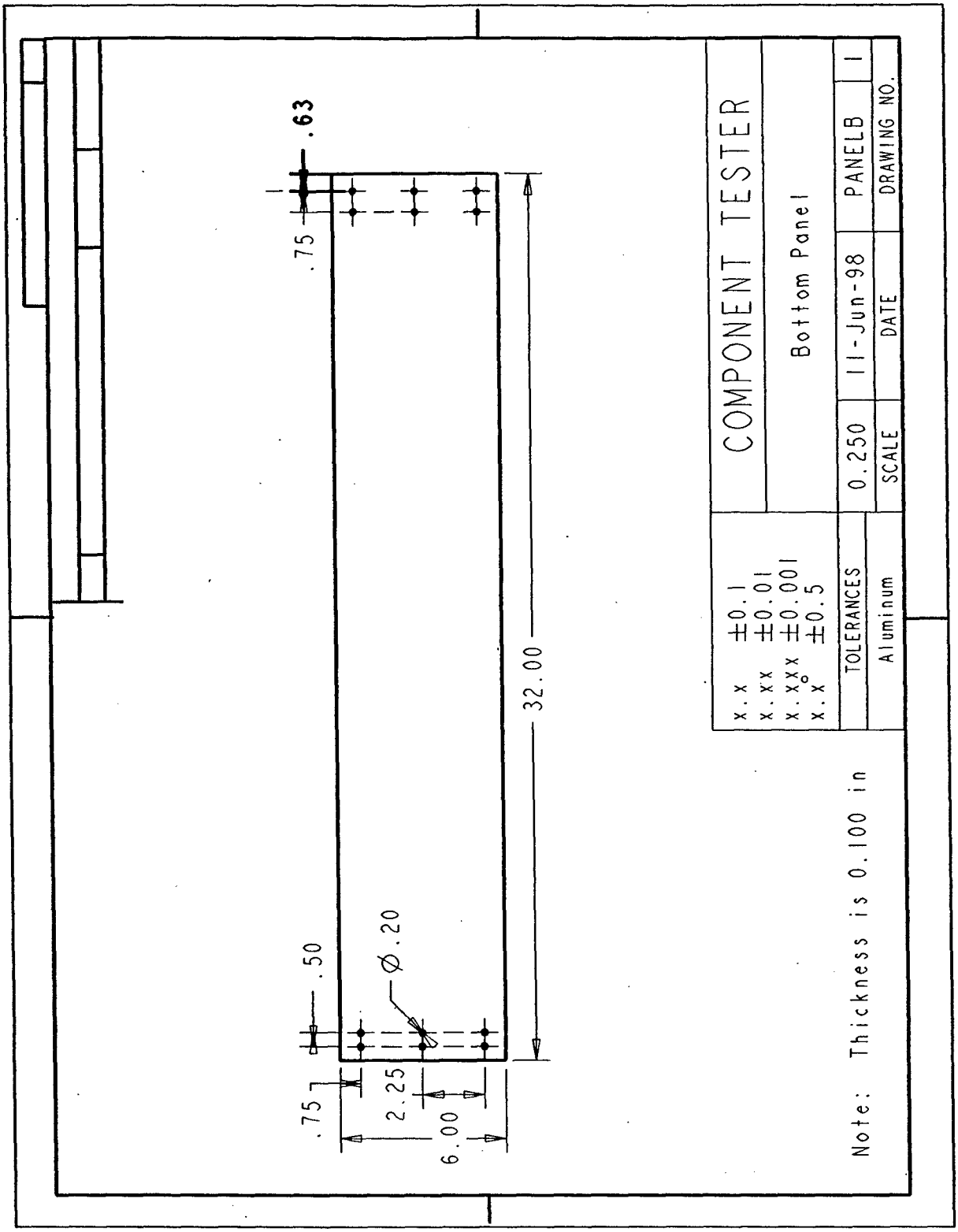

Figure A-34: Bottom Shear Panel Part Drawing.

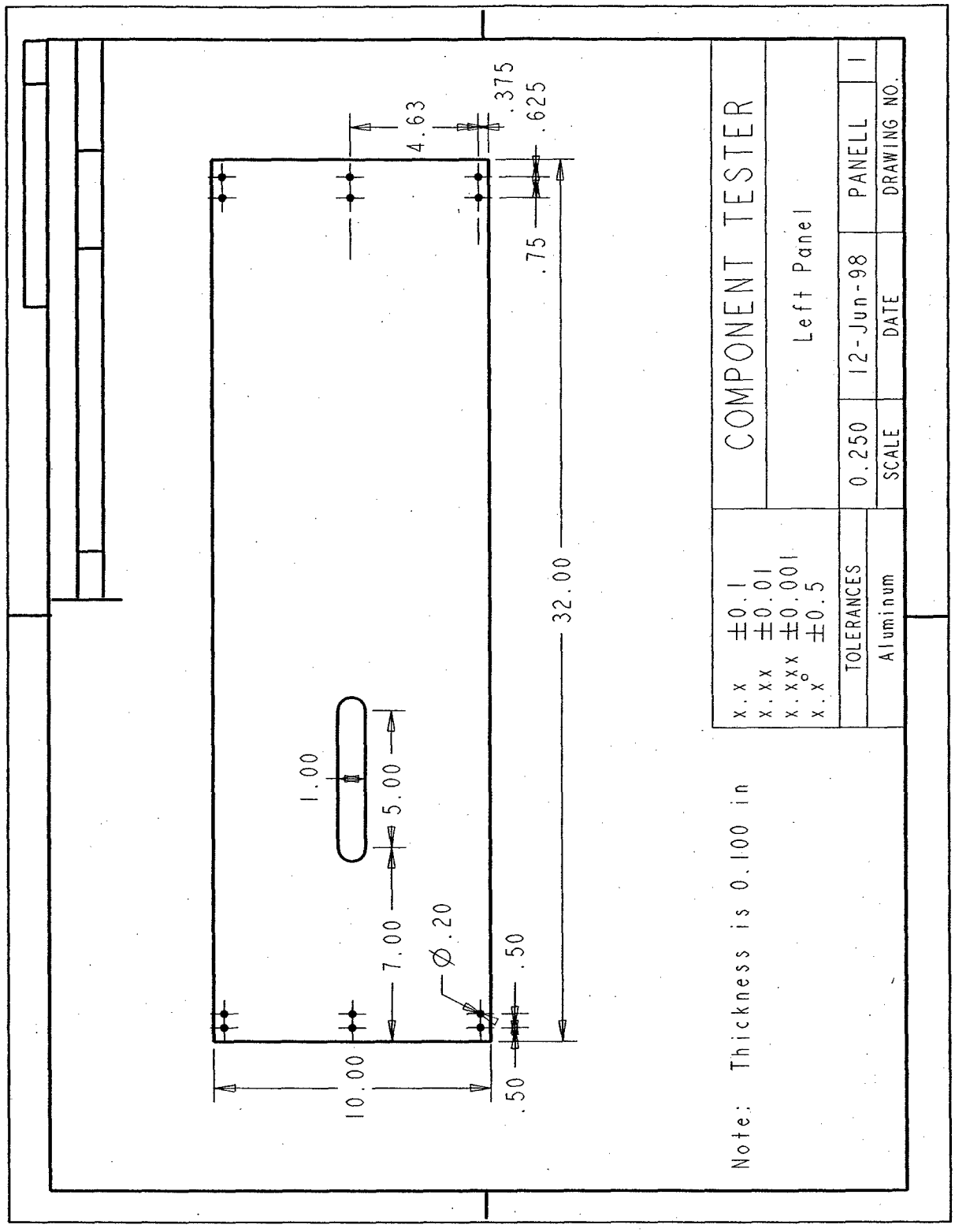

Figure A-35: Left Shear Panel Part Drawing.

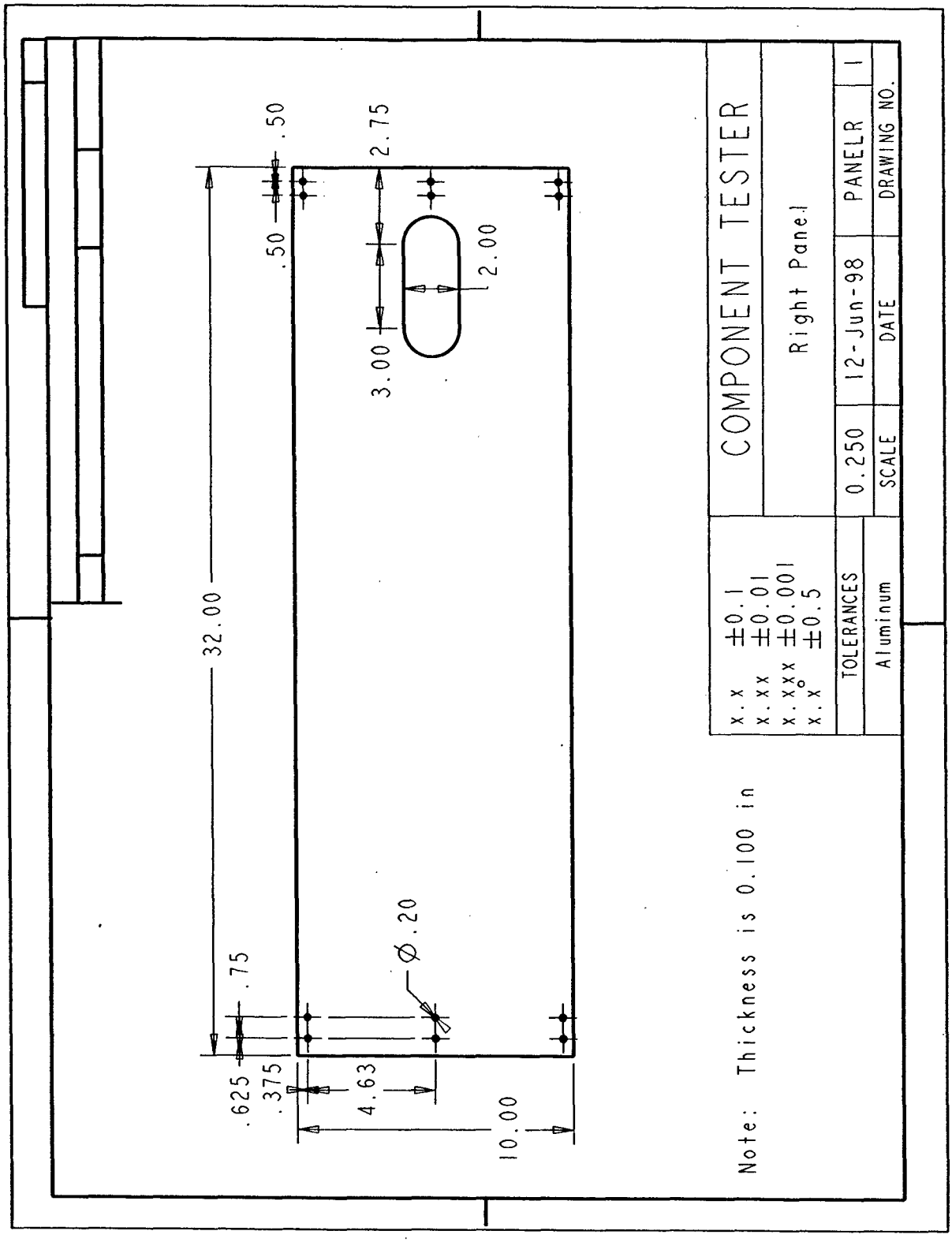

Figure A-36: Right Shear Panel Part Drawing.

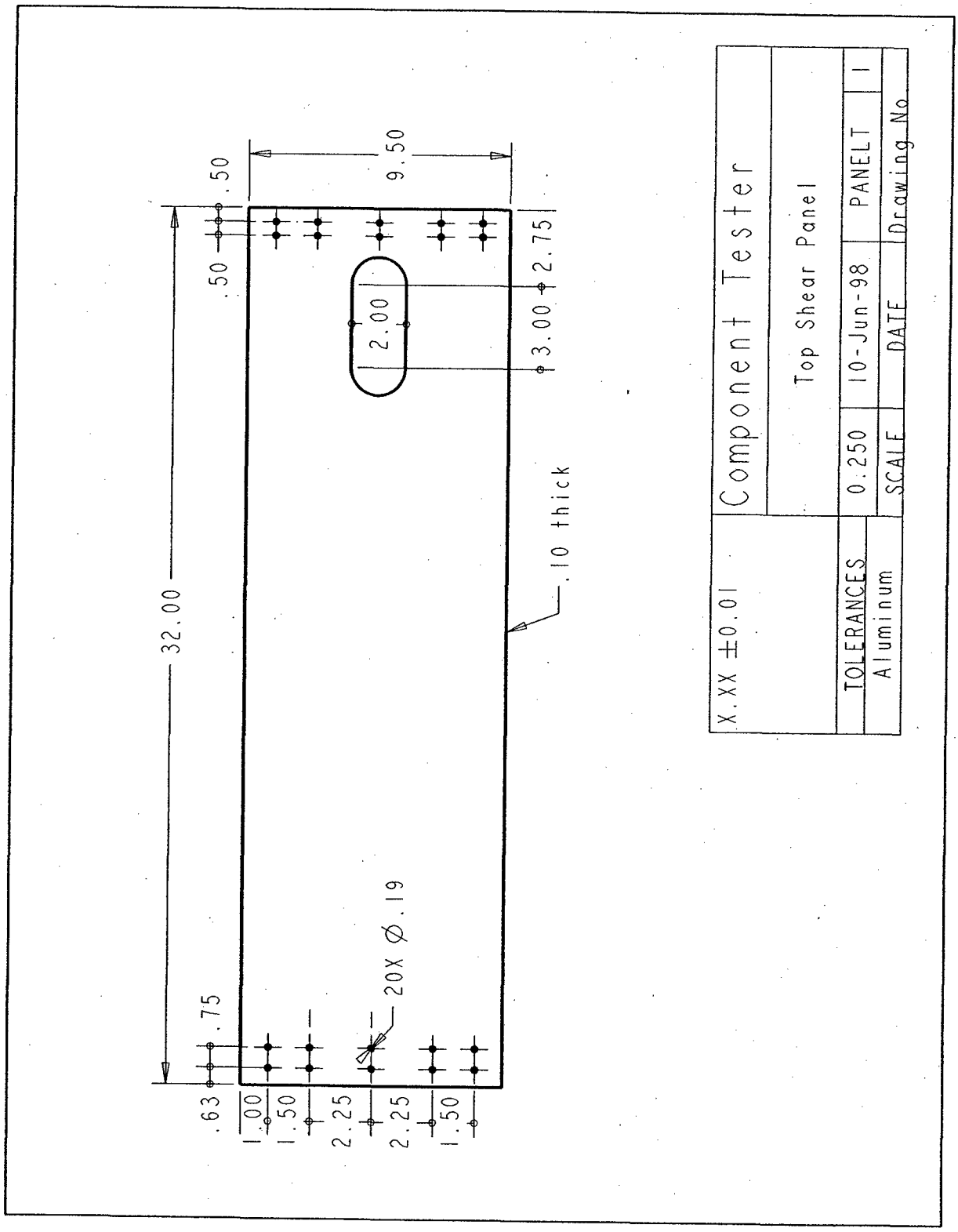

Figure A-37: Top Shear Panel Part Drawing.

Bibliography

[1] G. Lesieutre and C. Davis, "Can a coupling coefficient of a piezoelectric device be higher than those of its active material?," *Journal of intelligent material systems and structures* **8[10]**, p. 859, 1997.

[2] D. Berlincourt, "Piezoelectric crystals and ceramics," in *Ultrasonic Transducer Materials*, O. E. Mattiat, ed., Plenum Press, New York, 1971.

[3] R. L. Spangler and S. R. Hall, "Piezoelectric actuators for helicopter rotor control," in *Proceedings 31st Structures, Stuuctural Dynamics and Materials Conference*, (Long Beach, CA), 1990.

[4] S. R. Hall and E. Prechtl, "Development of a piezoelectric servoflap for helicopter rotor control," *Smart Mater. Struct.* **5**, pp. 26–34, 1996.

[5] *IEEE Standard on Piezoelectricity*, IEEE, Inc., 1978.

[6] D. Berlincourt, "Piezoelectric and ferroelectric energy conversion," *IEEE Transactions on Sonics and Ultrasonics* **SU-15(2)**, 1968.

[7] N. Hagood, W. Chung, and A. von Flowtow, "Modeling of piezoelectric actuator dynamics for active structural control," *Journal of intelligent material systems and structures* **1[3]**, pp. 327–354, 1990.

[8] M. L. R. Fripp and N. W. Hagood, "Distributed structural actuation with electrostrictors," *Journal of sound and vibration* **203(1)**, pp. 10–40, 1997.

[9] P. Pertsch, F. Bohrisch, G. Borchardt, B. Hoefer, H. Rohr, and E. Wehrsdorfer, "Properties of piezoelectric multilayer actuators under uniaxial compressive stress," in *New actuators*, H. Borgmann, ed., *Proceedings: International conference; 5th–1996 Jun:Bremen; Germany* , pp. 217–220, 1996.

[10] A. Wolff, D. Cramer, H. Hellebrand, I. Probst, and K. Lubtiz, "Optical two channel enlongation measurement of pzt piezoelectric multilayer actuators," in *ISAF '94*, R. Pandey, M. Liu, and A. Safari, eds., *Proceedings: 9th International symposium on applications of ferroelectrics* , pp. 755–757, 1994.

[11] C. Hom, S. Pilgrim, N. Shankar, K. Bridger, M. Massuda, and S. Winzer, "Calculation of quasi-static electromechanical coupling coefficient for electrostrictive ceramic materials," *IEEE Trans. of Ultrasonics, Ferroelectrics and Frequency Control* 41[4], pp. 542–551, 1994.

[12] H. Cao and A. G. Evans, "Nonlinear deformation of ferroelectric ceramics," *J. Am. Ceram. Soc.* **76**[4], pp. 890–896, 1993.

[13] M. Kondo and K. Ohya, "Effects of one-dimensional compressive stress on the properties of multilayer piezoelectric ceramic actuator," *NEC Research and Development* **32(2)**, pp. 220–226, 1991.

[14] E. Wehrsdorfer, G. Borchhardt, W. Karthe, and G. Helke, "Large signal measurements on piezoelectric stacks," *Ferroelectrics* **174**, pp. 259–275, 1995.

[15] D. Burianek, "Fatigue damage in titanium-graphite hybrid laminates," Master's thesis, MIT, 1998.

[16] M. Ealey, C. Pohlhammer, and J. Wellman, "New developments in pmn based multilayer actuators," in *SPIE Proceedings*, vol. 2865, 1996.

[17] Sumitomo Metals, Kanagawa, JAPAN, *Piezo Electric Products*, no. 73910 ed., 1997.

[18] E. Prechtl and S. R. Hall, "X-frame-actuator servo-flap acuation system for rotor control," in *Proceedings- SPIE The International Society for Optical Engineering*, vol. 3329[1] of *Smart structures and integrated systems*, pp. 309–320, SPIE, 1998.

2/26-11

REPORT DOCUMENTATION PAGE

Form Approved
OMB NO. 0704-0188

Public Reporting burden for this collection of information is estimated to average 1 hour per response, including the time for reviewing instructions, searching existing data sources, gathering and maintaining the data needed, and completing and reviewing the collection of information. Send comment regarding this burden estimates or any other aspect of this collection of information, including suggestions for reducing this burden, to Washington Headquarters Services, Directorate for information Operations and Reports, 1215 Jefferson Davis Highway, Suite 1204, Arlington, VA 22202-4302, and to the Office of Management and Budget, Paperwork Reduction Project (0704-0188,) Washington, DC 20503.

1. AGENCY USE ONLY (Leave Blank)	2. REPORT DATE 07/18/2003	3. REPORT TYPE AND DATES COVERED Final Technical Report: 05/01/1996 to 09/30/2001
4. TITLE AND SUBTITLE Development of Testing Methodologies for Nonlinear Solid State Actuation Materials; Performance Models for Underwater Transducers Incorporating Nonlinear Active Materials		5. FUNDING NUMBERS N00014-96-1-0691
6. AUTHOR(S) Nesbitt W. Hagood IV, Yong Shi , John E. Harper, and Malinda K. Lutz		
7. PERFORMING ORGANIZATION NAME(S) AND ADDRESS(ES) Massachusetts Institute Of Technology 77 Massachusetts Ave. Cambridge, MA 02139		8. PERFORMING ORGANIZATION REPORT NUMBER
9. SPONSORING / MONITORING AGENCY NAME(S) AND ADDRESS(ES) Office of Naval Research Ballston Centre Tower One 800 North Quincy St. Arlington, VA 22217-5660		10. SPONSORING / MONITORING AGENCY REPORT NUMBER

11. SUPPLEMENTARY NOTES
The views, opinions and/or findings contained in this report are those of the author(s) and should not be construed as an official Office of Naval Research position, policy or decision, unless so designated by other documentation.

12 a. DISTRIBUTION / AVAILABILITY STATEMENT Approved for public release; distribution unlimited.	12 b. DISTRIBUTION CODE

13. ABSTRACT (Maximum 200 words)

A derivation is presented and demonstrated for finding actuation efficiency and work output for electromechanically fully coupled, non-linear systems working against generalized quasi-static loads. A component testing facility with programmable impedance and closed-loop capability was designed, built, and operated to measure work output and actuation efficiency of a discrete actuator working against both linear and non-linear loads. The complete design of the testing facility is presented with an overview of the rationale behind its design decisions. Increases in the mechanical work output of the actuator were found to be possible by using non-linear loads instead of linear loads. Theory and formulation are presented, suitable for modeling and performance analysis of actuator and sensor devices composed of deformable, electromechanically coupled, highly insulating materials with non-linear response functions. The testing facility was renovated and used for feed-forward open-loop test methodology utilizing a Force-Voltage model developed from Ritz Formulation. Linear tests correlated well with theoretical prediction. Results show actuation efficiency of a non-linear system is about 200% that of a linear system, and its work output is about 245% that of the linear system. Research is recommended on behavior and performance of active materials and actuation efficiency of piezoelectrically-driven systems under dynamic loads.

14. SUBJECT TERMS Linear system, non-linear system, coupled system, actuator, sensor, transducer, input, output, impedance, closed-loop, loading function, actuation efficiency, electromechanical, piezoelectric, electroelastic, hydraulic, electric conduction, active material, magnetic shape memory alloy, magnetostrictive, electrostrictive, polymers, single crystal, ferroelectric, performance metric, load stiffness, material stiffness.	15. NUMBER OF PAGES 432 16. PRICE CODE

17. SECURITY CLASSIFICATION OR REPORT UNCLASSIFIED	18. SECURITY CLASSIFICATION ON THIS PAGE UNCLASSIFIED	19. SECURITY CLASSIFICATION OF ABSTRACT UNCLASSIFIED	20. LIMITATION OF ABSTRACT UL

NSN 7540-01-280-5500

Standard Form 298 (Rev.2-89)
Prescribed by ANSI Std. 239-18
298-102